Technische Universität München
TUM School of Engineering and Design

TUM

Entwicklung eines kompakten volloptischen Zugangs für Großmotoren und Anwendung für die Verbrennungsdiagnostik erneuerbarer Kraftstoffe

Stephan Bernhard Karmann

Vorwort und Danksagung

Die vorliegende Forschungsarbeit basiert auf den Ergebnissen und Erkenntnissen, welche ich während meiner Tätigkeit als wissenschaftlicher Mitarbeiter am Lehrstuhl für Verbrennungskraftmaschinen der Technischen Universität München von Mai 2015 bis Juli 2022 in zwei Forschungsprojekten HERCULES 2 und E2Fuels erarbeitet habe.

Ich möchte meinem Doktorvater Prof. i.R. Dr.-Ing. Georg Wachtmeister herzlich für die Betreuung der Arbeit und die einmalige Möglichkeit danken, meine Ideen zu verwirklichen. Herrn Prof. Dr.-Ing. Bert Buchholz gilt mein Dank für die Übernahme des Zweitgutachtens.

Eine Arbeit wie diese kann nur entstehen, wenn man mit seinen Aufgaben wächst, so bin ich dankbar, dies am Lehrstuhl für Verbrennungskraftmaschinen in einem Umfeld getan zu haben, in welchem man sich gegenseitig unterstützt und einem mannigfaltige Hilfe wiederfährt. Allen voran möchte ich mich bei Stefan Eicheldinger für unvergleichliche humorvolle Lektionen am Prüfstand und fachliche Diskussionen während der Co-Autorenschaften danken. Für die Unterstützung in CFD und Hardware Angelegenheiten möchte ich mich bei Kai Gaukel und Stephanie Frankl bedanken. Stefan Held gilt mein Dank als Retter in allen Matlab Angelegenheiten. Für das Lesen meiner Ausuferungen und deren Eingrenzung möchte ich Dominik Walligorsik an dieser Stelle herzlich danken. Allen hier nicht namentlich erwähnten Assistentenkollegen insbesondere allen Betreibern des Prüfstandes 7 gilt mein Dank und meine Hochachtung vor ihrem enormen Wissen und Können, den Prüfstand erfolgreich am Leben und Laufen zu halten. Meinem Oberingenieur Hr. Dr.-Ing. Maximilian Prager danke ich für das entgegengebrachte Vertrauen bei der Durchführung der Projekte und das Finden des ein oder anderen Fehlers in den Veröffentlichungen. Den Kollegen unseres direkten Projektpartners und meinen Co-Autoren, Christian Kunkel, Dr.-Ing. Stefan Weber und Dr.-Ing. Chrisitan Friedrich seitens der MAN Energies Solution danke ich für die gute Zusammenarbeit und die Unterstützung bei Aufbau, IBN und Durchführung der Versuche. Ebenso gilt mein Respekt und Dank dem Techniker Team der AnnA für so manch schnelle Lösung. Bei den Mitarbeitern der Werkstatt des Lehrstuhls, allen voran Patrick Ottiger und Siegfried Geiger, möchte ich mich für die Unterstützung bei Prüfstandsumbauten und der Teilefertigung bedanken. Wenn bei hoher Werkstattauslastung Bauteile dennoch schnell fertig sein mussten, konnte ich mich immer an eine Person wenden. Dieser gilt mein uneingeschränkter Dank neben den Bauteilen auch für alles, was hierhergeführt hat – meinem Vater Josef Karmann. Für das Verständnis und den Rückhalt meiner Mutter Angela Karmann über meinen bisherigen Lebensweg hinweg danke ich ihr sehr. Die Menschen, die das hier nicht mehr lesen werden, mir aber genau das ermöglicht haben, werde ich niemals vergessen – meine Großeltern Johanna und Josef Karmann.

Niemals zuletzt aber immer am Wichtigsten gehört meine ewig währende Liebe und mein Dank meiner Frau Carla. In der Rolle als Motivationstrainer hast du mich nach langen und längeren Arbeitszeiten aufgemuntert, in meinen zahlreichen Veröffentlichungen als Lektorin meine sprachlichen und grammatikalischen Irrungen gezeigt und immer einen roten Faden in meiner Schreiberei und unserem Leben gesucht.

Kurzzusammenfassung

Ziel der vorliegenden wissenschaftlichen Arbeit ist die Entwicklung einer kompakten Alternative zum Bowditch-Design zur Realisierung einer volloptischen Zugänglichkeit von Großmotoren für stationäre und mobile Anwendungen. Erste charakteristische optische Messungen der Verbrennung von nachhaltigen synthetischen Kraftstoffen bestätigen die erfolgreiche Umsetzung.

Die Entwicklung eines kompakten optischen Zugangs soll die Anwendung optischer und laseroptischer Messtechniken zur Verbrennungsdiagnostik vereinfachen und ermöglichen. Diese Methoden werden zum Ableiten phänomenologischer Verbrennungsmodelle, Validieren vorhandener Simulationsmodelle und experimentellen Optimieren der Verbrennung bisher vor allem in schnelllaufenden PKW-und LKW- Motoren angewandt. Insbesondere zum Vorantreiben einer Dekarbonisierung von Großmotoren durch erneuerbare synthetische Kraftstoffe soll der hier entwickelte optische Zugang beitragen.

Dazu ist neben einem kompakten seitlichen Zugang ein kompakter endoskopischer Zugang durch den Zylinderkopf für zwei verschiedene Großmotor Hubraumklassen entwickelt und für erste charakteristische Untersuchungen der Verbrennung alternativer Kraftstoffe angewendet worden. Der endoskopische Zugang besteht aus einer direkt in den Brennraum montierten Fisheye Optik mit 180 ° Sichtfeld, die speziell für diese Anwendung entwickelt worden ist. Die in einem mittelschnelllaufenden MAN 35/44DF Motor verwendete erste Fisheye Optik ist für die Anwendung in einem 4,8 l schnelllaufenden Großmotor verkleinert und weiter optimiert worden.

Für die Auswertung der Untersuchungen ist ein Postprocessing Algorithmus entwickelt worden, welcher die stark verzerrten Fisheye Bilder entzerrt und entsprechend aufbereitet. Mit der ersten entwickelten Optik ist die flüssige Strahleindringtiefe der Pilotkraftstoffe OME_{3-5} mit DMA verglichen worden. Der Vergleich zeigt in einem gefeuerten Betrieb des MAN 35/44DF Motors gute Übereinstimmungen mit der Theorie und in der Literatur gezeigten Untersuchungen an einer Einspritzkammer.

Der zweite entwickelte Zugang ist, neben der Untersuchung des Einflusses der Wasserstoffbeimischung von 2, 5, 10 und 40 %$_V$ Wasserstoff zu Methan gegenüber reinem Erdgas, für die experimentelle Abschätzung der Vergleichbarkeit des optisch zugänglichen Aufbaus zu seinem rein thermodynamischen Pendant verwendet worden. Der Vergleich zeigt eine hohe Übereinstimmung des thermodynamischen Verhaltens des optischen gegenüber dem rein thermodynamischen Motor. Die Versuchsergebnisse der Wasserstoffbeimischung auf die Verbrennung, zeigen mit Literaturergebnissen schnelllaufender Motoren eine gute Übereinstimmung. Die Ergebnisse aus den hier durchgeführten Untersuchungen können zur Optimierung künftiger defossilisierter Motorgenerationen beitragen.

Abstract

The aim of the present scientific work is the development of a compact alternative to the Bowditch design for the realization of full-optical accessibility of large bore engines covering stationary and mobile applications. First characteristic optical measurements of the combustion of sustainable synthetic fuels confirm the successful implementation.

The development of this more simple to realize optical access will enhance the application of optical and laser-optical measurement techniques for combustion diagnostics. These methods are used to derive phenomenological combustion models, validating existing simulation models and optimizing combustion, yet so far mainly applied in high-speed passenger car and commercial vehicle engines. In particular, the optical approach is developed to contribute to the decarbonisation of large-bore engines with renewable synthetic fuels. To enable full optical accessibility, a compact lateral access as well as an endoscopic access through the cylinder head has been developed for two different large-bore engine displacement classes. It was used for initial characterization investigations of the combustion of renewable fuels. The endoscopic access consists of a fisheye optical system with a 180 field of view, which has been developed and optimized for application directly in the combustion chamber.

The fisheye optic first applied in a medium-speed MAN 35/44DF engine is scaled down and further optimized for the application in a 4.8 l high-speed large bore engine. For the evaluation of the investigations, a post-processing algorithm has been developed, which rectifies the highly distorted fisheye images and processes them accordingly. Using the first developed optic the liquid jet penetration depth has been compared between the pilot fuels OME_{3-5} and DMA. The comparison conducted in a fired MAN 35/44DF engine shows good agreement with the theory and investigations shown in literature derived from an injection chamber.

The second developed approach, in addition to investigate the influence of hydrogen admixture of 2, 5, 10 and 40 %v hydrogen to methane versus pure natural gas, has been used further for the experimental estimation of the comparability of the optically accessible setup to its pure thermodynamic all metal counterpart. The comparison shows high agreement of the thermodynamic behavior of the optical versus the all-metal approach. The findings on the influence of hydrogen admixture on combustion are generally in good agreement with the findings from literature on high-speed small-scale engines. The knowledge gained from the investigations carried out here can contribute to the optimization of future generations of defossilized engines.

Inhaltsverzeichnis

Abbildungsverzeichnis

Tabellenverzeichnis

Formelzeichen

FEM

B	N	Äußere Kräfte
D	-	Differntialoperatoren Matrix
E	-	Materialgesetz
u	m	Verschiebung
λ	-	Lagrange Multiplikator
σ	N/mm²	Spannung

CFD

B	N	Äußere Kräfte
c_p	MJ/kg	Isobare Wärmekapazität
D		Deformationsrate
I	-	Einheitstensor
n	-	Normalenvektor
Pr	-	Prandtl Zahl
T	-	Spannungstensor
T	K	Temperatur
t	s	Zeit
u^+	-	Entdimensionierte Geschwindigkeit
V	m³	Volumen
y^+	-	Entdimensionierter Abstand
p	bar	Druck
q	W/m²	Wärmestromdichte
κ	-	Von Karman Konstante
ρ	kg/m³	Dichte
ϕ		Extensive Größe
Γ		Diffusiver Term

Optik

f	mm	Fokusabstand
f#	-	Blendenzahl
g	-	Abbildungsfunktion
u	-	Zur Oberfläche senkrecht stehender Normalenvektor
n	-	Brechzahl
r	mm	Radius
α	rad	Winkel
λ	nm	Wellenlänge
ϕ	rad	Winkel
Θ	rad	Winkel

Abkürzungen

Abkürzung

ASTI	Astigmatismus
BFL	Back focal length (Rückwärtiger Fokusabstand)
CCD	Charge coupled device
CFD	Computational fluid dynamics
CHT	Conjugate heat transfer
DF	Dual Fuel
DIST	Distortion (Verzerrung)
DLR	Deutsches Luft- und Raumfahrtzentrum
DMA	Marine destillate fuel
EFL	Effektive Fokuslänge
EU	Energieumsatzpunkt
FEM	Finite Elemente Methode
FKM	Forschungskuratorium Maschinenbau
HCF	High cycle fatigue
HGK	Hochgeschwindigkeitskamera
KPM	Kontrollpunktmuster
KW	Kurbelwellenwinkel
LCA	Longitudinale chromatische Aberration
LIF	Laser induzierte Fluoreszenz
LII	Laser induzierte Inkandeszenz
LKW	Lastkraftwagen
LVK	Lehrstuhl für Verbrennungskraftmaschinen
MTF	Modulation transfer function
NG	Natural gas (Erdgas)
nZOT	nach Zündung oberer Totpunkt
OME	Oxymethylenether
OPD	Optical path difference (optische Weglängendifferenz)
PFI	Port fuel injection
PIV	Particle image velocimetry
PKW	Personenkraftwagen
PSF	Point spread function
RCEM	Rapid compression expansion machine
RMS	Root mean square (quadratisches Mittel)
SI	Spark ignition (Funken Zündung)
SPH	Sphärische Aberration
TCA	Transversale chromatische Aberration
THC	Total hydrocarbon (Gesamt Kohlenwasserstoff)
TLIF	Tracer basierte laserinduzierte Fluoreszenz
UV	Ultraviolett
UVZK	Ungespülte Vorkammerzündkerze
vZOT	vor Zündung oberer Totpunkt
ZK	Zündkerze
λ	Verbrennungsluftverhältnis

1 Einleitung

Die Welt ist im Wandel. Geopolitische Veränderungen führen uns vor Augen, wie globalisiert unsere Handelsketten heute sind und wie wichtig der Transport von Gütern und die Bereitstellung von Energie und Energieträgern hierfür sind. Dabei führen uns die Auswirkungen des Klimawandels in Form von extremen Wettersituationen mehr denn je vor Augen, wie wichtig eine umweltfreundliche Bereitstellung dieser Energie ist. Somit ist die nachhaltige, kostengünstige und sozial verträgliche Versorgung von Energie eine der größten Herausforderungen unserer Zeit.

Der Ausbau erneuerbarer Energien und die Defossilisierung der Energieerzeugung und Antriebe ist ein Weg, diese herausfordernden Ziele anzugehen. Diese Maßnahmen sollen beitragen, die CO_2 Reduktion von 65 % gegenüber dem Stand von 1990 bis 2030 und 80-95 % bis 2050 (vgl. [1]) in den energienutzenden Sektoren der privaten Haushalte, industriellen Prozesse und im industriellen sowie individuellen Transport zu erreichen. Die Nutzung regenerativer Energien wie Solar- und Wasserkraft sind hinsichtlich ihrer regionalen und saisonalen Verfügbarkeit Schwankungen unterworfen. Zur Stabilisierung der Energieversorgung aus erneuerbaren Energien, muss Energie zur Kompensation von Residuallasten und Schwankungen kurz-, mittel- und langfristig gespeichert und bei Bedarf zur Verfügung gestellt werden können (vgl. [2]).

Ein entscheidender Ansatz ist dabei die Sektorenkopplung, welche durch einen Zusammenschluss von nachhaltiger Energieerzeugung und Energienutzung über den Transport und die Infrastruktur der Energie diese effizient speichert und verteilt. Zur Speicherung überschüssiger erneuerbarer Energie, produziert in Zeiten hoher Verfügbarkeit und geringer Nachfrage, ist das Power to X Verfahren ein im Fokus stehender Ansatz. Hierbei wird die elektrische Energie in Form gasförmiger (Wasserstoff) oder flüssiger Kraftstoffe (z.B. Oxygenate) chemisch gebunden. Diese Energieträger können als nachhaltige Kraftstoffe zur Rückverstromung und als Antriebsenergie genutzt werden. Das Power to Gas Verfahren, bei welchem gasförmige Kraftstoffe, insbesondere Wasserstoff mit einer Energiedichte von 350 kWh/Nm³ mit einem Wirkungsgrad von 64,1 % erzeugt, in Kavernenspeichern vorgehalten und verteilt werden können, bietet hier ein enormes Potential. In einem nachgelagerten Prozess kann mit einem Wirkungsgradverlust von 13,2 % Wasserstoff und CO_2 zu regenerativem Methan mit einer mittleren in Kavernenspeichern vorgehaltenen Energiedichte von 1100 kWh/Nm³ umgewandelt werden. Im Vergleich dazu kann mit Lithiumionen Batterien eine mittlere speicherbare Energiedichte von maximal 375 kWh/m³ erreicht werden. (vgl. [3])

Mit dem Schritt der Methanisierung des Wasserstoffs schließt sich der CO_2 Kreislauf von der Gewinnung des notwendigen Kohlenstoffes aus der Luft bis hin zur klimaneutralen Verbrennung des so hergestellten synthetischen Kraftstoffes. Das synthetisch erzeugte Methan kann direkt zur Substitution fossilen Erdgases in bestehenden Gasnetzen verwendet werden. Eine direkte Substitution des Erdgases durch reinen Wasserstoff ist aufgrund der Netzbeschaffenheit derzeit nicht umsetzbar. Je nach Verträglichkeit können Methan/Wasserstoffmischungen eine Übergangslösung darstellen. Somit ist eine auf Wasserstoff basierte Energieerzeugung möglich und momentan im Aufbau, sodass nach [4] kurzfristig von 8,3 %$_V$ mittelfristig von 22,2 %$_V$

1

und langfristig von 40 %$_V$ Wasserstoff im deutschen Erdgasnetz ausgegangen werden kann. Die Dekarbonisierung von Verbrennungskraftmaschinen ist ein guter Ansatz, da bereits 25 % des Weltenergiebedarfs damit bereitgestellt und dabei 10 % der Treibhausgasemissionen verursacht werden (vgl. [5]). Eine Beimischung von Wasserstoff zu Erdgas oder auch die Anwendung von flüssigen alternativen Kraftstoffen als Ersatz fossiler Energieträger verändern das Brennverhalten und bedürfen deshalb intensiver Untersuchungen für eine optimale Berücksichtigung der neuen Kraftstoffeigenschaften (vgl. [6]).

Ein bereits seit Beginn der Entwicklung von Verbrennungskraftmaschinen eingesetztes Hilfsmittel sind optisch zugängliche Motoren (vgl. [7])). Für schnelllaufende PKW- und LKW Motoren sind diese mittlerweile ein kommerziell erhältliches Werkzeug für optische- und laseroptische in situ Messungen. Diese werden genutzt, um Vorgänge während der Gemischentstehung (Ladungsbewegung), der Zündung (Kraftstoff-Luft-Interaktion bei DI Diesel-Motoren), der Verbrennung (Flammenfrontdetektion) und Emissionsentstehung (örtlich aufgelöste Speziesdetektion) beschreiben und durch geeignete abgeleitete Maßnahmen optimieren zu können. Für Großmotoren in der stationären und mobilen Anwendung ist die Untersuchungsdichte mit diesen Messtechniken im Vergleich deutlich geringer. Im Hinblick auf die Auswirkungen erneuerbarer Kraftstoffe auf das Brennverfahren sind diese aber nicht weniger von Bedeutung zur erfolgreichen Transition hin zu erneuerbaren Kraftstoffen.

Aus diesem Grund behandelt die vorliegende Arbeit die Entwicklung eines optischen Zugangs für Großmotoren, welcher die Anwendung von optischen Messtechniken zur Verbrennungsdiagnostik regenerativer Kraftstoffe ermöglicht. Damit soll es unter motorisch realistischen Bedingungen möglich sein, die Verbrennung zu beobachten und zu beschreiben. Hierfür ist an zwei Großmotoren unterschiedlicher Hubraumklassen mit 43 l und 4,8 l je eine volloptisch zugängliche Motorkonfiguration entwickelt worden. Diese wurde genutzt, um Einflüsse bei der Anwendung von nachhaltigen Kraftstoffen zu untersuchen. Realisiert wurde ein horizontales Sichtfeld durch eine 180 ° Fisheye Optik, welche in den Zylinderkopf integriert wird. Zur Auswertung der Untersuchungen ist ein entsprechendes Postprocessing entwickelt worden, mit dem u.a. die flüssigen Strahleindringtiefen eines OME$_{3-5}$ Pilotkraftstoffstrahls denen von DMA gegenübergestellt werden konnten. Dieses ist erweitert worden, um zeitlich aufgelöste Intensitätsverläufe der natürlichen Flammeneigenstrahlung der Verbrennung von Wasserstoff/Methanmischungen mit den thermodynamisch ausgewerteten Brennverläufen zu vergleichen, um so den Einfluss von Wasserstoff auf das Brennverhalten zu evaluieren. Experimentelle Vergleichsmessungen zwischen dem Motor mit optischem Zugang und dem thermodynamischen Pendant beweisen die Übertragbarkeit der Messungen und decken Unterschiede auf, welche bei der Einordnung der mit den optischen Zugängen abgeleiteten Ergebnisse berücksichtigt werden müssen.

2 Grundlagen und Stand der Technik

Eine Darstellung des aktuellen Standes der Technik und Forschung auf dem Gebiet der optischen Zugänglichkeit an Großmotoren und deren Nutzung für die Verbrennungsdiagnostik soll aufzeigen, welche spezifischen Randbedingungen bei der Entwicklung eines alternativen kompakten Zugangs für Großmotoren zu berücksichtigen sind. Analog des später aufgezeigten Entwicklungsprozesses, werden nachfolgend die hierfür verwendeten numerischen Simulationsmethoden der Finiten Elemente- und -Volumen Methode und die Grundlagen des Optikdesigns vorgestellt. Diese werden für die Beurteilung des entwickelten optischen Zuganges herangezogen. Eine Zusammenfassung bestehender Untersuchungen von wasserstoffbasierten nachhaltigen Kraftstoffen unterstreicht den Bedarf nach optischen Zugängen für Großmotoren als Grundvoraussetzung für weiterführende Versuche.

2.1 Optische Zugänglichkeit an Verbrennungskraftmaschinen

Optisch zugängliche Motoren sind so alt wie Verbrennungsmotoren selbst. 1872 verwendete Nicolaus Otto einen optischen Motor mit einem Glaszylinder, die sog. „Rauchmaschine", zur Untersuchung der Ladeluftverteilung während der vier Takte der innermotorischen Verbrennung (vgl. [7]). Gerade heute, wo Verbrennungsmotoren unter besonderem Druck zur Einhaltung von Abgasemissionen stehen, bieten optisch zugängliche Motoren die Möglichkeit, mit Hilfe optischer und laseroptischer Messtechnik Verbrennungsprozesse mit alternativen Kraftstoffen in situ zu untersuchen, zu verstehen und zu optimieren. Aus diesem Grund sind optische Motoren und die entsprechenden Messtechniken stetig verbessert und an die entsprechenden Gegebenheiten angepasst worden.

2.1.1 Optisch zugängliche Einhubtriebwerke (RCEM)

Neben den optisch zugänglichen Motoren haben sich RCEMs (Rapid compression expansion machine), sog. Einhubtriebwerke, für Grundlagenuntersuchungen der Verbrennung und Emissionsentstehung ohne die störenden Einflüsse realer Motoren, wie der Schmierölverbrennung, zur Erstellung von Reaktionskinetik Modellen etabliert. Nachteilig an diesen Maschinen ist, dass der Einfluss des Ladungswechsels auf die Gemischbildung vernachlässigt wird und meist nur ein bis wenige Hübe ausführbar sind. Anwendungsbeispiele finden sich z.B. in [8–10].

2.1.2 Einteilung und Klassifizierung optisch zugänglicher Motoren

Für die optische Zugänglichkeit an Verbrennungskraftmaschinen sind verschiedene Ausführungsformen verbreitet (vgl. [7]). Abbildung 1 zeigt die nach [11] erstellte und in **[12]**[1] in Hinblick auf Großmotoren erweiterte Übersicht kommerziell erhältlicher und in der Literatur veröffentlichten Ausführungsformen. Diese sind nach dem Grad des Eingriffes der optischen Einbauten in den thermodynamischen Motor gruppiert. Je nach Ausführungsform des Zugangs steigt der Grad der optischen Zugänglichkeit von minimal bis maximal invasiv in Hinblick auf das im Brennraum zu erreichende Sichtfeld, sowie die Möglichkeit der Einkopplung einer Beleuchtung. Im gleichen Maße wie die optische Zugänglichkeit steigt, sinkt die Vergleichbarkeit

---

[1] Die im weiteren Verlauf hervorgehobenen Publikationen sind durch den Verfasser dieser Arbeit erstellt worden.

des optisch modifizierten Motors zu seinem rein thermodynamischen Pendant. Die Reduzierung der Vergleichbarkeit wird vor allem durch den Einsatz der optischen Materialien, wie synthetischem Quarz oder Saphirglas, und deren abweichenden Eigenschaften gegenüber Stahl hervorgerufen. Die notwendigen Anpassungen des Motors zu deren Integration wie z.B. vergrößerte und vermehrte Spaltvolumina tragen ebenso zu einer reduzierten Vergleichbarkeit bei.
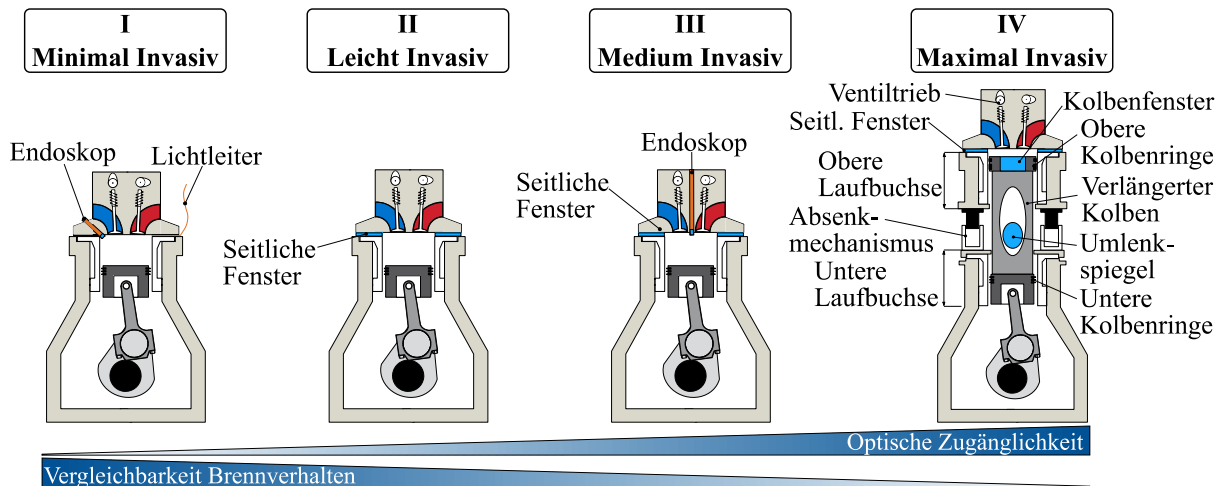
Abbildung 1 Einteilung optischer Zugangsmöglichkeiten für Verbrennungskraftmaschinen

Das **minimal invasive Konzept** fasst einzelne oder kombinierte faseroptische und endoskopische Zugänge zusammen. Faseroptische Leiter, integriert in Messzündkerzen, der Zylinderkopfdichtung, der Laufbuchse oder dem Zylinderkopf, können für passive, auf Chemilumineszenz basierte Verfahren und aktive, auf die Anregung von Spezies mit externen Leuchtquellen basierter Fluoreszenz- oder Extinktions Messtechniken verwendet werden (vgl. [13, 11]). Von verschiedenen Herstellern werden faseroptische Systeme integriert in eine Messzündkerze für passive Untersuchungen der Helligkeitsausbreitung z.B. einer Flammenfront oder zur Detektion des Klopfortes einer anormalen Verbrennung, wie in [14] durchgeführt, angeboten. Der Integrationsaufwand dieser optischen Elemente ist aufgrund des geringen Platzbedarfs vergleichsweise gering und kann ohne größere Anpassung von vorhandenen Bauteilen oder durch das Nutzen bereits vorhandener Öffnungen erfolgen. Diese Art des Zugangs ist vor allem für Serien- und Vollmotoren geeignet, ohne die Volllastfähigkeit der Motoren zu beeinflussen. Der größte Nachteil der Messmethode ist allerdings die beschränkte räumliche Information welche aus den tomografischen Verfahren resultiert (vgl. [11]). Für tomografische Aufnahmen können neben Raster, integriert in der Zylinderkopfdichtung und deren Ebene, faseroptische Sensoren wie in [15] zur Detektion der Flammenhüllkurve eingesetzt werden. Tsekenis [16] zeigt die Anwendung der chemischen Spezies Tomographie mittels Infrarot Absorption an einem Wärtsilä 6L20 vorkammergezündeten Groß-Gasmotor. Die faseroptischen Sensoren wurden hier in die Zylinderlaufbuchse integriert, um ein aus 31 Strahlen bestehendes Raster aufzuspannen und die Spezieskonzentration nahe den Austrittsöffnungen einer Vorkammer in den Fackelstrahlen zu bestimmen.

Endoskopische Zugänge mit starren oder flexiblen Endoskopen benötigen nur kleine Bohrungen zur Integration. Meist werden starre Endoskope (sog. Boroskope) aufgrund ihres besseren Auflösungsvermögens verwendet (vgl. [17]). Die Endoskope werden für verschiedene Anwendungen und Messtechniken in bestimmten Wellenlängenbereichen optimiert. Die Endoskope

4

werden aufgrund der hohen thermischen und mechanischen Belastungen nicht direkt in den Brennraum integriert, sondern mit einer Schutzhülse mit integriertem Brennraumfenster, meist aus Saphirglas, versehen. Diese weisen je nach Ausführungsform und integrierter Kühlung einen Durchmesser zwischen 8 und 14 mm auf. Die Integration muss dabei den Gegebenheiten des jeweiligen Motors und insbesondere der Zylinderkopfkühlung angepasst werden, sodass die Stabilität und Integrität des Brennraumes erhalten bleiben.

Die bildgebenden Verfahren werden für die Anwendung der passiven und aktiven Messtechniken verwendet. Für aktive Messtechniken wird ein zweites Endoskop für die Beleuchtung mittels Laserlichtschnitt rechtwinklig zum Beobachtungsendoskop integriert. Einer der größten Nachteile des Einsatzes eines Endoskops ist die oft geringe Blendenzahl und damit eine geringe Helligkeit der Aufnahmen. Dies verschlechtert das nutzbare Signal und verringert das Signal-Rauschverhältnis. Durch immer kleinere Endoskope bei gleichzeitiger Optimierung der optischen Eigenschaften sind auch diese für Serienvollmotoren und seriennahe Einzylinder ohne Reduzierung der Volllastfähigkeit geeignet. [11, 13]

Reichle zeigt die Entwicklung eines UV optimierten Endoskops unter Nutzung diffraktiver optischer Elemente in [18] für die Anwendung in einem PKW-Motor. Um das Sichtfeld zu erweitern, entwickelte Wilson in [19] eine in die Zündkerze eines Rasenmähermotors integrierte Fisheye Optik mit einem Durchmesser von 6 mm für den sichtbaren Spektralbereich. Mittels der Optik wurde die Verbrennung der vorgemischten Flamme über Aufnahmen der natürlichen Chemilumineszenz untersucht

Für Großmotoren zeigt Disch [20] die Integration eines Endoskops mit 100 ° Öffnungswinkel in die Starter-Druckluftbohrung eines Vorkammer gezündeten MAN 32/40 Gasmotors zur Beobachtung der natürlichen OH* Radikal Chemilumineszenz der Fackelstrahlen. Unfug [21] integriert ein Endoskop mit 90 ° Öffnungswinkel in einen MAN 32/44 common rail Dieselmotor anstelle eines der Auslassventile. Der Aufbau ist zur Untersuchung der Einspritzstrahlen mittels Mie-Streulicht, der Verbrennung mittels natürlicher Chemilumineszenz und der Rußbildung mittels zwei Farben-Pyrometrie genutzt worden.

Das **leicht invasive Konzept** bedient sich großflächiger optischer Zugänge, welche je nach vorhandenem Bauraum gestaltet werden. Bei dachförmigen Brennräumen besteht die Möglichkeit über integrierte trapezförmige Fenster die Mitte des Brennraums für Untersuchungen zugänglich zu machen (vgl. [11]). Da Großmotoren meist einen flachen Brennraum aufweisen ist diese Möglichkeit nicht geeignet. Brennraumfenster in einem Stahlring, welcher zwischen Zylinderkopf und Laufbuchse integriert wird, ermöglichen einen seitlichen Zugang zum Brennraum (vgl. Abbildung 1). Die Anzahl und Größe der Glasfenster ist durch das vorhandene Platzangebot und die anzuwendenden Messtechniken vorgegeben. So erfordern die aktiven Messtechniken zumindest zwei orthogonal angeordnete Fenster für Beleuchtung und Beobachtung. Diese Art der optischen Zugänglichkeit ist im Großmotorenbereich (vgl. [22–24]) weit verbreitet. Für die Brennraumfenster existieren generell zwei Ausführungsformen der brennraumseitigen Fensterflächen: gekrümmt, wie z.B. in [23–25] umgesetzt oder flach wie in [22]. Ein Nachteil der gekrümmten Fenster ist ein inhomogener Abbildungsmaßstab, welcher sich in einer Komprimierung der Bildinformation zum Rand hin äußert, eine Verschiebung des Fokus

durch die negative Zylinderlinse sowie Aberrationen (Astigmatismus), welche die Abbildungsqualität verschlechtern (vgl. [23, 25]). Diese Effekte müssen aufwändig durch weitere Korrekturoptiken und Postprocessing Algorithmen korrigiert werden. Dafür ermöglicht die negative Zylinderlinse eine Vergrößerung des Sichtfeldes. Meist wird die Krümmung dem Bohrungsdurchmesser äquivalent gewählt (vgl. [23, 24]), sodass bei den damit vorherrschenden Krümmungen eines Großmotors die Aberrationen reduziert werden. Neben den besseren optischen Eigenschaften verringert eine der Bohrung angepasste Krümmung zusätzliches Totvolumen und verbessert so die Vergleichbarkeit zum thermodynamischen Motor. Im Vergleich zu den endoskopischen und faseroptischen Zugängen bedarf dieser Zugang in beiden Varianten umfangreicher Modifikationen des Versuchsträgers, wodurch die Vergleichbarkeit zum Thermodynamikmotor sinkt. Dies ist insbesondere der Fall, wenn eine Anpassung der Kolbenringhöhe und damit des Feuersteges notwendig wird, um den Stahlring mit den Brennraumfenstern zu integrieren. Die Gestaltung des Zugangs weist ein meist großflächiges, vertikal im Brennraum liegendes Sichtfeld auf. Eine horizontale Beobachtungsebene, welche einen Blick in die Kolbenmulde während der Verbrennung erlaubt, ist nicht gegeben. Modifikationen des Kolbens in Form von Aussparungen, wie in [22] gezeigt, kompensieren diesen Nachteil teilweise. Allerdings gehen diese zu Lasten der Vergleichbarkeit mit dem Thermodynamikmotor.

Das **medium invasive Konzept** erweitert das leicht invasive um einen weiteren Zugang durch den Zylinderkopf. Damit wird das großflächige, rein vertikale Sichtfeld um ein horizontales Sichtfeld im Brennraum erweitert. Das horizontale Sichtfeld kann dabei unter anderem über die Integration eines Endoskops in den Zylinderkopf erfolgen. Dieses Konzept findet hauptsächlich im Großmotorenbereich Anwendung, da vor allem für PKW Motoren beide Sichtfelder mit einem ausreichenden Umfang endoskopisch realisiert werden können. Hult zeigt in [26] für einen in maritimen Antrieben eingesetzten MAN 4T50ME-X Zweitaktmotor ein Konzept mit mehreren horizontalen und vertikalen optisch nutzbaren Öffnungen im Zylinderkopf. Diese Anordnung wird durch das zentrale Auslassventil des Zweitaktmotors vereinfacht. Alle optischen Zugänge werden mit Saphirbrennraumfenstern von 46 mm Durchmesser zum Einkoppeln von Laserlichtschnitten und zum Auskoppeln der emittierten Strahlung der beobachteten Spezies versehen.

Das **maximal invasive Konzept** wird aufgrund seiner Komplexität hauptsächlich an PKW bis leichten LKW Motoren umgesetzt und basiert in der Regel auf dem 1961 erstmals vorgestellten Prinzip nach Bowditch [27]. Das Prinzip wird aufgrund seines vertikalen und horizontalen Beobachtungsfeldes als volloptisch zugänglicher Motor bezeichnet (vgl. [11]). Der optische Hauptzugang erfolgt von unten über ein in den Kolben integriertes Kolbenglas, welches den thermischen und mechanischen Randbedingungen aus der Verbrennung ausgesetzt ist und dementsprechend aus Saphir oder Quarzglas gefertigt wird. Der Kolben selbst wird verlängert, um einen stationär am Motorgehäuse angebrachten Umlenkspiegel über einen Ausbruch im Kolben zu integrieren. Diese Ausführung vermeidet eine Interferenz des sich oszillierend bewegenden Kolbens mit dem fixierten Spiegel und gewährleistet ein frei zugängliches Sichtfeld auf den Spiegel während des gesamten oder eines Teils des Kolbenhubes. Diese Verlängerung des Kolbens bzw. des Motors bedingt eine Aufteilung der Zylinderlaufbuchse in einen unteren, konventionell mit Öl geschmierten Teil und einen oberen, meist trockenen Teil, damit das Schmieröl den optischen Pfad nicht verschmutzt. Taschek [28] nutzt in diesem Bereich einen

ölgetränkten Filzring für eine Minimalschmierung, um konventionelle Kolbenringe nutzen zu können. Ungeschmierte Ausführungen haben sich allerdings vermehrt durchgesetzt und verwenden aus Kompressoren bekannte, selbstschmierende PTFE/Bronze oder Graphitringe, wie in [29] realisiert. Diese sind stark verschleißbehaftet und erhöhen damit den wartungstechnischen Aufwand während Messungen, zumal die konventionelle Anwendung nicht das Abdichten heißer Brennraumgase vorsieht. Der seitliche Zugang wird vor allem im PKW-Größenbereich (vgl. [11, 28, 30]) aber auch im LKW Größenbereich (vgl. [31]) durch synthetische Quarzglasringe realisiert, welche zwischen Zylinderkopf und oberer Zylinderbuchse verspannt werden. Alternativ kann analog dem leicht invasiven Konzept auch ein Stahlring mit integrierten Brennraumfenstern verwendet werden, wie in [29] für einen PKW-Motor, in [32] für LKW-Größe und in [33] für einen Großmotor gezeigt wird. Meist werden hydraulische Spannsysteme wie in [11, 30] umgesetzt, welche es ermöglichen, die Anordnung aus Glasring und oberer Zylinderbuchse abzusenken. Ein Absenkmechanismus ist für die Reinigung der Glaselemente von Verbrennungsrückständen erforderlich, welche bei zunehmender Kontamination die Lichtausbeute verringern. Die komplexen Modifikationen zur Integration der optischen Komponenten erfordern hier meist eine Anpassung der Lastgrenzen. Dies geschieht durch eine Reduktion der Motordrehzahl zur Kompensation der deutlich gestiegenen oszillierenden Massen. Daneben wird der Spitzendruck zur Kompensation der reduzierten Festigkeit der Glasbauteile eingeschränkt. Um die thermische Last auf die Glasbauteile und deren meist verklebten Stahl/Glas Verbindungen zu reduzieren wird eine Anpassung der Betriebsstrategie hin zu einem diskontinuierlichen Skipped Fire Betrieb vorgenommen.

Untersuchungen der Auswirkungen dieser Einschränkungen in Vergleich zu den jeweiligen thermodynamischen Motoren sind für PKW-Motoren in [34, 35] und leichte LKW Motoren in [36] durchgeführt worden. Kashdan [34, 35] weist im volloptischen Aufbau eine erhöhte Wandtemperatur durch die geringere Wärmeleitfähigkeit der Glasoberflächen im Brennraum nach. Diese erhöht die Restgastemperatur und damit den Druckanstieg im Brennraum und hat Einfluss auf die Emissionsentstehung. Hierzu trägt auch die erhöhte Kolbentemperatur des Glaskolbens bei. Die Abweichungen in der Temperatur werden durch einen Skipped Fire Betrieb reduziert. Durch dynamische Effekte kommt es zudem zu einer erhöhten Stauchung bzw. Längung des verlängerten optischen Kolbens gegenüber dem Konventionellen, was eine Anpassung des Verdichtungsverhältnisses erforderlich macht, um den Brennraumdruck dem Thermodynamikmotor anzugleichen. Colban [36] zeigt analog zu den Ergebnissen nach [34, 35], dass die Druck- und Wärmefreisetzungseigenschaften des optischen Motors durch das größere Spaltvolumen und die Nachgiebigkeit des verlängerten optischen Kolbens beeinflusst werden. Um ein vergleichbares thermodynamisches Grundverhalten zwischen dem optischen und dem thermodynamischen Motor zu gewährleisten werden daher Regelgrößen des volloptischen Motors wie Einlasstemperatur, Ladedruck, Kühlmitteltemperatur, Abgasgegendruck, und der Motorbetrieb hin zu einem Skipped Fire Betrieb adaptiert. Daneben werden geometrische Anpassungen wie beispielsweise an der Quetschspalthöhe vorgenommen. Mit diesen Einstellungen werden Abgasmessungen durchgeführt, welche ein gleiches Verhalten der Emissionen auf Veränderungen der Einspritzparameter als auch gleiche Extrema aufweisen. Dennoch zeigen diese Untersuchungen den notwendigen betrieblichen Aufwand, welcher für vergleichbare Ergebnisse zusätzlich zu den konstruktiven Änderungen für eine vergleichbare Ergebnisgüte getrie-

ben werden muss. Korb [33, 37] zeigt die Umsetzung eines volloptischen Motors nach Bowditch an einem 4,8 l Großmotor mit einem Hub von 210 mm und einer Bohrung von 170 mm. Merts [38] nutzt einen 8,8 l Großmotor mit einer Bohrung von 200 mm und einem Hub von 280 mm, ausgestattet mit einem volloptischen Zugang nach Bowditch zur Untersuchung des Dual Fuel Brennverfahrens in einem Skipped Fire Betrieb.

2.1.3 Ableiten von Randbedingungen für optisch zugängliche Großmotoren

PKW- und LKW Motoren weisen eine breite optische Untersuchungsdichte auf. Vor allem das Konzept des maximal invasiven volloptischen Zuganges ist durch ein kommerzielles Angebot weit verbreitet. Deutlich geringere am Weltmarkt abgesetzte Stückzahlen von Großmotoren tragen ebenso zu einer geringeren optischen Untersuchungsdichte bei. Wegen der langen Einsatzdauer solcher Motoren ist eine Optimierung hinsichtlich ihres Beitrags am weltweit ausgestoßenen CO_2 Anteils ein notwendiger Schritt hin zu einer nachhaltigen Energieversorgung.

Die geplante Messtechnik und die Zielstellung der Untersuchung bestimmen den Grad der Zugänglichkeit. Dennoch bleibt es das Hauptziel, den in Abbildung 1 gezeigten Zielkonflikt einer maximalen optischen Zugänglichkeit bei gleichzeitiger hoher Vergleichbarkeit aufzulösen. Dies ist für Großmotoren umso mehr der Fall, da die limitierten Sichtfelder von endoskopischen Zugängen einen weitaus geringeren beobachtbaren Anteil des deutlich größeren Brennraumes als im Vergleich zu kleinen Motoren zulassen. Gleichzeitig aber bedingt die Dimension dieser Motoren einen enormen Aufwand zur Realisierung des maximal invasiven Konzeptes und weist zudem, bedingt durch die damit einhergehenden extensiveren Anpassungen, ein verändertes Betriebsverhalten auf.

2.2 In der Arbeit angewandte optische Messtechniken

Wie bereits in Abschnitt 2.1.1 zusammengefasst, werden verschiedene berührungslose, optische Messtechniken angewandt, um die innermotorischen Phänomene während der Gemischbildung, Zündung, Verbrennung und Emissionsentstehung, unbeeinflusst durch die applizierte Technik selbst, zu untersuchen. Zudem haben optische Messverfahren gegenüber den etablierten Indiziermesstechniken, welche zur Beurteilung des Brennverlaufs und daraus abgeleiteter Größen wie der Emissionsbildung herangezogen werden, den Vorteil einer zeitlich zugeordneten, örtlichen Auflösung der Messgrößen. (vgl. [11, 39])
Die zahlreichen Messverfahren können in aktive und passive Messtechniken eingeteilt werden.

Die **aktiven** Messtechniken umfassen alle Methoden mit einer externen Beleuchtung des Beobachtungsfeldes. Meistens werden Lichtschnitte im Brennraum aus Laserlichtquellen fest definierter Wellenlängen für die jeweilige Anregung bestimmter zu detektierender Verbrennungs-Spezies (LIF), Partikel (LII), Stoffe zur Tracerung bestimmter Spezies (TLIF) oder der Strömung (PIV) herangezogen. Die Publikationen [11, 24, 25, 39] erklären diese Methoden und zeigen deren Anwendung. Neben Laserlichtquellen können auch breitbandig emittierende Lichtquellen eingesetzt werden, welche die Visualisierung der flüssigen Phase eines Kraftstoffstrahls im Brennraum erlauben. Das Mie Streulichtverfahren wurde für erste Messungen am untersuchten optischen Motor herangezogen und wird daher in Abschnitt 2.2.1 detaillierter erläutert.

Passive Methoden benötigen keine externen Lichtquellen und bedienen sich zur Beurteilung der Verbrennung des Eigenleuchtens der Flamme. Auch dieses Verfahren wird in der vorliegenden Arbeit genutzt, um erste Aussagen über die Verbrennung nachhaltiger wasserstoffbasierter Kraftstoffe zu generieren sowie die erfolgreiche Anwendung dieses Verfahrens mittels der neu entwickelten Zugänge zu zeigen.

2.2.1 Das aktive Messverfahren der Mie-Streuung

Die Streulichtmesstechniken können in elastische (Rayleigh- und Mie-Streuung) und inelastische Streuprozesse (Raman-Streuung z.B. in [40]) eingeteilt werden. Hierbei tritt Licht in Wechselwirkung mit Materie (Partikeln). Die Wechselwirkung kann dabei generell eine Beugung, Brechung, Absorption, Transmission sowie gerichtete oder ebene diffuse Reflexion sein. Die für diese Arbeit relevante elastische Streuung hat die Eigenschaft, dass während der Wechselwirkung keine Energie dauerhaft ausgetauscht wird. Damit kommt es zu keiner Frequenzverschiebung des reflektierten Lichts. Die weitere Unterscheidung der Rayleigh und Mie Streuung basiert auf der Partikelgröße, an der das Licht gestreut wird. Für die Rayleigh Streuung gilt, dass die Wellenlänge des Lichtes deutlich größer ist als der Partikel selbst.

2.2.2 Das passive Messverfahren des Flammeneigenleuchtens

Ohne zusätzliche Leuchtquelle nutzt dieses Messverfahren die Detektion der Eigenstrahlung der Flamme. Diese Eigenstrahlung stammt hauptsächlich aus zwei Mechanismen:

Die Chemilumineszenz entsteht durch die Emission von Lichtquanten beim diskreten Übergang der Elektronen angeregter, nicht stabiler Verbrennungsradikale in ihren energetisch stabileren Grundzustand. Die Anregung und Anhebung des Elektrons in einen energetisch instabilen Zustand kann durch die Energieaufnahme während einer chemischen Reaktion oder durch die Aufnahme von während einer Verbrennung freiwerdenden Wärmeenergie erfolgen. Die bei der Relaxation freiwerdende Energie zeigt sich aufgrund der Bohrschen Frequenzbedingung in einem diskreten Emissionsspektrum, abhängig vom jeweiligen angeregten Molekül oder Atom. Dieses diskontinuierliche Emissionsspektrum weist einzelne Spektrallinien auf, meist hervorgerufen durch die Anregung ungebundener Atome, und mehrere in Banden gruppierte Spektrallinien, wie sie durch die Anregung großer Moleküle hervorgerufen werden. Aufgrund des diskreten, einer Spezies zuzuordnenden Emissionsspektrums, sowie dem zeitlichen Verhältnis der Emission und den makroskopischen Zeitskalen der Verbrennung können mittels der Chemilumineszenz die einzelnen Phasen der Verbrennung mit ihren jeweiligen thermodynamischen Druck- und Temperaturrandbedingungen charakterisiert werden. [11, 39, 41]

Die Energieabgabe kann durch das Quenching erfolgen. Wenn angeregte Moleküle mit einem Stoßpartner, meist Sauerstoff, unter hohen Temperaturen und bei überstöchiometrischen Brennverfahren zusammenprallen, wird die Energie an den Stoßpartner ohne die detektierbare Emission von Licht übertragen. Dies hat eine reduzierte Intensität der Chemilumineszenz zur Folge. [11, 39, 41]

Abbildung 2 zeigt die für eine Kohlenwasserstoffflamme üblichen Emissionsspektren der während einer Verbrennung gebildeten Radikale OH*, CH* und C_2*. Das in Abbildung 2 dargestellte Emissionsspektrum des H_2O* Radikals ist bei einer Verbrennung von 30 %$_V$ Wasserstoff

und 70 %$_V$ Methan beobachtet worden. Das H_2O^* Radikal kann v.a. bei der Verbrennung von reinem Wasserstoff auch in Bereichen um 600 nm beobachtet werden. Die Anregung hierbei stammt allerdings nicht aus chemischen Reaktionen, vielmehr aus der thermischen Anregung durch die Flammentemperatur (vgl. [42, 43]). Dazu ähnlich ist die in Abbildung 2 gezeigte Schwarzkörperstrahlung. Diese entsteht ebenfalls aus thermischer Anregung von Rußpartikeln, der sog. Rußinkandeszenz, und trägt vor allem bei Diffusionsflammen einer lokalen unterstöchiometrischen Verbrennung zur messbaren Flammeneigenstrahlung bei. Diese Festkörperstrahlung emittiert ein breitbandiges Spektrum mit einem im Infrarotbereich liegenden temperaturabhängigen Maximum. Dieses kontinuierliche Spektrum mit einer höheren Intensität als die Chemilumineszenz überlagert den Messbereich des Flammeneigenleuchtens. Zudem kann der entstandene Ruß die Chemilumineszenz Strahlung absorbieren. Dies kann zu einem verschlechterten und teilweise gänzlichen Verlust der aus der Chemilumineszenz zu gewinnenden Informationen führen. [11]

In Abbildung 2 sind aus Übersichtlichkeit die weiteren Breitbandspektren, wie die des CO_2^* (@340-650 nm), dem HCO^* (@340-523 nm) und dem $HCHO^*$ (@340-523 nm) Radikal (vgl. [44, 45]) nicht dargestellt.
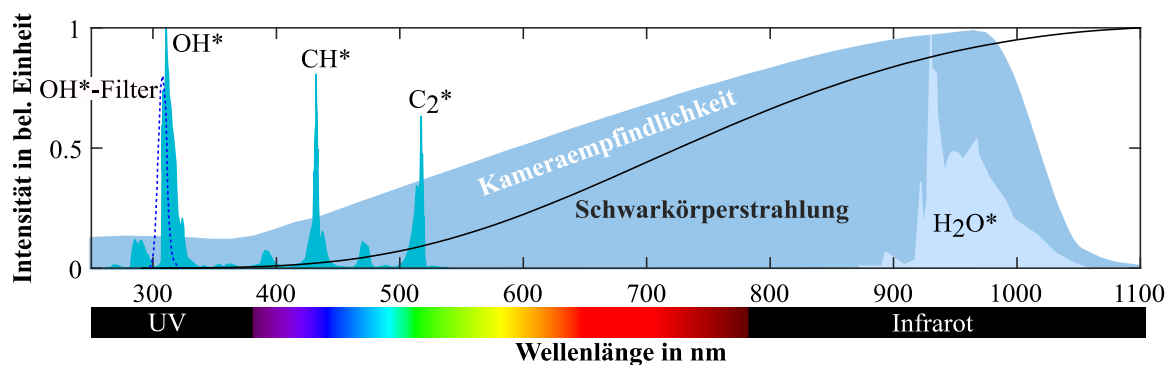
Abbildung 2 Emissionsspektren einer Kohlenwasserstoffflamme (Daten entnommen aus [42, 46, 47])

2.2.3   Optoelektronische Komponenten

Die optoelektronischen Komponenten dienen als Schnittstelle der optischen Komponenten, wie der verwendeten Objektive und Filter, und der elektronischen Umwandlung der damit aufgenommenen Lichtintensitäten. Für die in dieser Arbeit durchgeführten Messungen der natürlichen Chemilumineszenz und des Mie Streulichtes kommen hauptsächlich monochromatische und chromatische HGKs (Hochgeschwindigkeitskamera) zur Anwendung. Diese sind mit CCD Sensoren ausgestattet. Der Sensor der Farbkamera unterteilt jeden Pixel über Farbfilter in einen roten, grünen und blauen Anteil. Die auf Siliziumhalbleitern basierten Kamerasensoren weisen besonders im ultravioletten Spektralbereich eine reduzierte Empfindlichkeit auf (siehe Abbildung 2). Daher wird für die Aufnahme des natürlichen OH^*-Radikals ein zeitlich hochauflösender Bildverstärker verwendet. Diese auf dem Phosphoreszenz Prinzip basierende Verstärkung erlaubt es, die schwache Strahlung des natürlichen OH^*-Radikals zu beobachten. Im Infrarotbereich zeigen die Kamerasensoren dagegen eine erhöhte Empfindlichkeit, was die Detektion des Wasserradikals begünstigt (siehe Abbildung 2). Tabelle 3 in Anhang A.2 fasst die wichtigsten Eigenschaften der verwendeten HGKs zusammen.

2.3 Simulationsbasierte Entwicklung – Grundlagen

Die Entwicklung der optischen Zugänge für Großmotoren erfolgte hauptsächlich simulationsbasiert. Hierfür sind Methoden der 3D-CFD für die Ableitung thermischer Randbedingungen verwendet worden, welche Eingang in die Festigkeitsanalyse mittels FEM gefunden haben. Für die Durchführung der Simulationen wurde das Programm ANSYS Workbench verwendet. Die nachfolgenden Kapitel fassen die wichtigsten Grundlagen der Simulationsmethoden zusammen. Weiterhin ist für die Entwicklung und Auslegung der Optik das Programm OptaliX Pro der Firma Optenso zur Anwendung gekommen. Die Grundlagen des dort implementierten Raytracings werden im Folgenden zusammengefasst. Die Nutzung der simulationsbasierten Entwicklung unterstützt die Reduzierung von Prototypen, die Absicherung der Optimierungsschritte des Designprozesses sowie das Ableiten von Betriebsstrategien für den Versuchsaufbau.

2.3.1 Temperaturfeldbestimmung: Numerische Strömungsmechanik

Die in einem Verbrennungsmotor erzeugte Wärme wird aufgrund des Temperaturgefälles zwischen den Verbrennungsgasen und den Brennraumkomponenten an letztere mittels Strahlung und Konvektion übertragen (vgl. [48]). Eine Kühlung in Form einer wassergekühlten Zylinderlaufbuchse, spritzölgekühlter Kolben und wassergekühlter Zylinderköpfe sorgt für deren thermische Stabilität während des Betriebes über die Lebensdauer des Motors. Zur Berechnung der zulässigen Bauteiltemperaturen können gekoppelte Simulationen der Verbrennung und der Kühlwasserströmung durchgeführt werden. Entscheidend dafür ist, dass für die Berechnung entsprechende brennraumseitige Randbedingungen zur Verfügung stehen, welche z.B. aus 1D-Modellen abgeleitet werden können. Damit wird hauptsächlich die Kühlwasserströmung, welche zum Abtransport der Wärme durch erzwungene Konvektion genutzt wird, zum Gegenstand der Untersuchungen. Zur approximativen Bestimmung der erzwungenen Konvektion wird die 3D-CFD Methode verwendet.

Grundgleichungen der Strömungsmechanik – Navier Stokes Gleichungen

Die Navier Stokes Gleichungen beschreiben die Erhaltungsgleichungen der extensiven Eigenschaften einer Strömung für Masse, Impuls und Energie. Die Beschreibung eines abgeschlossenes Strömungsgebietes, dem Kontrollvolumen, kann allgemein nach Gleichung (1) erfolgen und setzt die Änderung der Menge einer extensiven Größe Φ innerhalb des Kontrollvolumens V in das Verhältnis zu den von außen auf das Kontrollvolumen V wirkenden Veränderungen der extensiven Größe Φ. [49]

$$\underbrace{\frac{\partial}{\partial t} \cdot \int_V \varrho \cdot \Phi \, dV}_{\substack{\text{Änderung innerhalb} \\ \text{des Volumens}}} + \underbrace{\int_S \varrho \cdot \Phi \cdot v \cdot n \, dS}_{\substack{\text{Zu– bzw. Abfluss über} \\ \text{Oberfläche von V}}} = \underbrace{\int_S \Gamma \cdot \nabla\phi \cdot n \, dS}_{\substack{\text{Diffusiver Transport}}} + \underbrace{\int_V q_\Phi \, dV}_{\substack{\text{Quellen und Senken}}} \tag{1}$$

$$\underbrace{\phantom{\frac{\partial}{\partial t} \cdot \int_V \varrho \cdot \Phi \, dV + \int_S \varrho}}_{\text{Änderungsrate der Menge von } \Phi \text{ innerhalb V}} \qquad \underbrace{}_{\text{von außen wirkende Veränderungen auf } \Phi}$$

Die Ableitung der Erhaltungsgleichungen für die verschiedensten Strömungsarten und beteiligten Energieaustauschformen, sowie eine vom Koordinatensystem unabhängige Darstellung mittels des Gaußschen Integralsatzes kann in der Fachliteratur gefunden werden. [49–51]

11

Für die vollständige Erfassung der Strömung werden zusätzlich die thermischen und kalorischen Zustandsgleichungen des Fluides benötigt (vgl. [51]). Die strömungsmechanischen Grundgleichungen müssen für die komplexen Kühlkanalstrukturen in Motoren und deren turbulenten Strömungsformen numerisch gelöst werden. Dies ist eine Grundvoraussetzung, um die Temperaturfelder der Motorkomponenten für eine nachfolgende mechanische Festigkeitsanalyse neu entwickelter Bauteile abzuleiten.

Turbulenzmodellierung – Reynolds gemittelte Navier Stokes Gleichungen

Turbulenzen, hervorgerufen durch Störungen der Strömung, weisen starke Variationen der Strömungsgrößen auf, welche einen Austausch von Impuls und Energie quer zur Hauptströmungsrichtung ermöglichen. Eine zeitliche und örtliche Auflösung dieser Fluktuationen ist aufgrund der starken Schwankung in Längen- und Zeitskala numerisch aufwändig und bedarf immenser Rechenkapazitäten. [49, 50]

Die sogenannte Reynoldsmittttelung zur näherungsweisen Lösung der turbulenten Navier Stokes Gleichungen ist für inkompressible Strömungen, wie sie in der Kühlwasserströmung von Verbrennungsmotoren vorliegen, ausreichend. Diese teilt die Strömungsgrößen Φ (z.B. Dichte, Geschwindigkeitskomponenten) in einen zeitlichen Mittelwert $\overline{\Phi}$ und eine Schwankungsgröße Φ' um das Mittel auf und ergibt angewendet auf die Navier Stokes Gleichungen eine Einpunktschließung. Aufgrund der Einpunktschließung sind zeitliche Änderungen der Strömungsgrößen an einem beliebigen Ort innerhalb der Strömung voneinander abhängig. Dies führt bei Einführung der Mittelung in die Impulserhaltung zu den sogenannten Reynoldsspannungen und zusätzlichen Termen, welche den turbulenten Skalarfluss darstellen (vgl. [49, 50]). Dies macht eine Modellierung der Turbulenz zur Beschreibung der zusätzlichen Terme notwendig.

Beschreibung der Grenzschicht und des Wärmeübergangs

In Wandnähe sinkt die Reynoldszahl aufgrund des Impulsaustausches zwischen den Fluidmolekülen und der Wand, bis die Strömung unmittelbar an der Wand aufgrund der Haftbedingung zum Erliegen kommt. Der Bereich der ansteigenden Geschwindigkeit bis hin zum Erreichen von 99% der Kernströmungsgeschwindigkeit wird als Grenzschicht bezeichnet. Die Modellierung der Turbulenz in diesem Bereich erfolgt durch sogenannte Wandfunktionen oder spezielle Low-Reynolds Turbulenzmodelle. [52, 53]

Da das k-ε Modell nicht in der Lage ist, die Turbulenz in Wandnähe zu beschreiben, werden hier zusätzliche Wandmodelle herangezogen. Dies führt zu einer stabileren Konvergenz durch eine gleichmäßigere Vernetzung im Wandnahen Bereich und einer geringeren Rechendauer. Das universelle Wandmodell basiert auf experimentellen Beobachtungen der Couette Strömung. Diese nutzt den über die Wandschubspannung und Dichte des Fluids entdimensionierten Wandabstand y^+ und die entdimensionierte Geschwindigkeit u^+ zur Beschreibung der Geschwindigkeit. Die Funktion wird dabei eingeteilt nach den drei Bereichen der Grenzschicht in viskose Unterschicht, Übergangsschicht und logarithmischen Bereich. Abbildung 3 zeigt diese Bereiche sowie die Annäherung durch die Wandfunktion. [53]

Ebenso wie die Grenzschicht der Strömungsgeschwindigkeit bildet sich eine thermische Grenzschicht für die im Kühlwassermantel eines Verbrennungsmotors vorkommende erzwungene

Konvektion. Damit sind die Strömungsgeschwindigkeit und die Temperaturverteilung miteinander über die Prandtl Zahl verbunden. Wie für die Strömung wird eine dimensionslose Temperatur T^+ definiert, mit welcher die Wärmestromdichte an der Wand berechnet wird. [54]
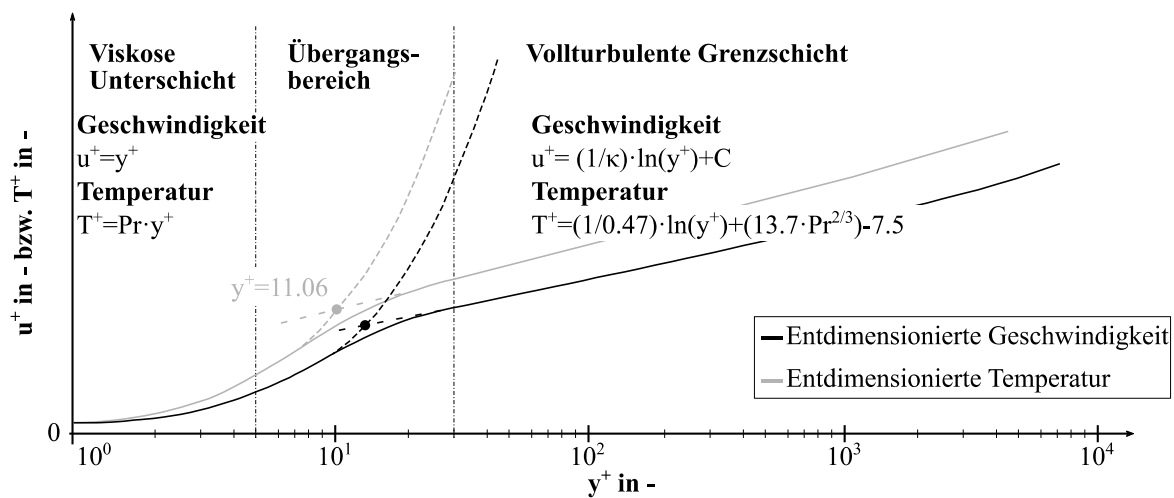

Abbildung 3 Universelles Wandgesetz der turbulenten Couette Strömung – (Pr=Prandtl Zahl, κ=Von Karman Konstante, C=experimentell bestimmte Konstante, (vgl. [50, 55]))

3D CFD - Finite Volumen Methode

Grundvoraussetzung zur Anwendung der CFD Methode und zur numerischen Lösung der RANS-Gleichungen ist eine Diskretisierung des Rechengebietes. Für die dreidimensionale Strömungssimulation wird die Finite Volumen Methode verwendet, welche das Rechengebiet in eine endliche Anzahl nicht überlappender Kontrollvolumina einteilt. Für die Simulation der hier verwendeten Temperaturfelder der Motorbauteile sind aufgrund der Komplexität des Kühlwasservolumens hauptsächlich unstrukturierte Tetraeder Gitter verwendet worden. Die Grenzschicht wird mit einer geringen Anzahl an Prismenschichten aufgelöst, um die idealen Voraussetzungen für die Wandfunktionen zu gewährleisten ($y^+ > 30$ vgl. [53]). Die Finite Volumen Methode berechnet die Ergebnisse für das Kontrollvolumen im Zentrum. Damit wird zur numerischen Approximation der Flüsse über die Kontrollvolumenflächen eine zweistufige Approximation notwendig, um zum einen das Flächenintegral mittels Quadratur anzunähern und zum anderen das Ergebnis aus der Mitte des Kontrollvolumens auf die Flächen des Volumens zu übertragen. Die hierfür verwendeten numerischen Methoden wie die Trapez- oder Mittelpunktsregel und die Aufwind Interpolation für die Berechnung der Werte auf den Kontrollvolumenflächen kann z.B. in [49, 53] gefunden werden.

2.3.2 Strukturmechanische Optimierung: Finite Elemente Methode

Die den Brennraum begrenzenden Bauteile sind neben den untersuchten thermischen Randbedingungen der Verbrennung mit hohen Spitzendrücken beaufschlagt. Die Kombination der verschiedenen Lasten führt zur notwendigen Untersuchung der HCF (High cycle fatigue). Dies erfolgt mittels einer statischen unidirektional schwach gekoppelten Simulation zwischen einer vorausgegangen 3D-CFD Berechnung des Temperaturfeldes, einer sog. CHT (conjugate heat transfere) Analyse und einer mechanischen FEM Simulation. Nachfolgend wird die FEM Methode vereinfacht zusammengefasst.

13

Grundgleichungen der Finite Elemente Methode – Lineare Elastizitätstheorie und Prinzip der virtuellen Arbeit

Die Grundgleichung der finiten Element Methode beruht auf der mathematischen Beschreibung der Elastizitätstheorie in Matrixschreibweise in einem karthesischen Koordinatensystem. Kleine, stetige und reversible Verformungen, hervorgerufen durch äußere und innere Kräfte, stehen hier über ein (nicht-)lineares Materialgesetz **E** in Zusammenhang. Insgesamt werden diese Zusammenhänge in den sechs kinematischen (Verschiebung-Verzerrung), sechs konstitutiven (Verzerrung-Spannung) und drei Gleichgewichts Gleichungen mit 15 Unbekannten (3 Verschiebungen $\boldsymbol{u}^t = [u_x u_y u_z]$, 6 Verzerrungen $\boldsymbol{\varepsilon}^t = [\varepsilon_{xx} \varepsilon_{yy} \varepsilon_{zz} \gamma_{xy} \gamma_{yz} \gamma_{zx}]$ und 6 Spannungen $\boldsymbol{\sigma}^t = [\sigma_{xx} \sigma_{yy} \sigma_{zz} \tau_{xy} \tau_{yz} \tau_{zx}]$) beschrieben. Gleichung (2) fasst den Zusammenhang zwischen der Spannung und Verzerrung über das Materialgesetz mit den Verformungen zusammen. Dieser Zusammenhang gilt für lineares, isotropes Werkstoffverhalten, wie es für die mechanische Simulation der entwickelten Konstruktionen verwendet worden ist. [56]

$$\boldsymbol{\sigma}^t = \boldsymbol{E} \cdot \boldsymbol{\varepsilon} = \boldsymbol{E} \cdot \underbrace{\boldsymbol{D}}_{Differentialoperatoren-Matrix} \cdot \boldsymbol{u} \tag{2}$$

$$D = \begin{bmatrix} \partial/\partial x & 0 & 0 & \partial/\partial y & 0 & \partial/\partial z \\ 0 & \partial/\partial y & 0 & \partial/\partial x & \partial/\partial z & 0 \\ 0 & 0 & \partial/\partial z & 0 & \partial/\partial y & \partial/\partial x \end{bmatrix}$$

Das Gleichgewicht der inneren Spannungen mit den äußeren Kräften, dargestellt in Gleichung (3), stellt eine wichtige Voraussetzung der Finiten Elemente Methode dar. Hier wird berücksichtigt, dass Anfangsspannungen $\boldsymbol{\sigma}_0$ oder Verzerrungen $\boldsymbol{\varepsilon}_0$ aus z.B. Wärmedehnungen oder Schraubenvorspannkräften vorhanden sein können.

$$\boldsymbol{D}^t \cdot \underbrace{\boldsymbol{\sigma}}_{\substack{\sigma_{el}+\sigma_0 \\ E \cdot (\varepsilon - \varepsilon_0)}} = \underbrace{\boldsymbol{B}}_{\text{äußere Kräfte}} \tag{3}$$

Aufbauend auf Gleichung (3) wird zum Lösen der Differentialgleichung das Variationsprinzip oder auch Prinzip der virtuellen Arbeit verwendet, welches in Gleichung (4) dargestellt ist. Für dieses Prinzip gilt, dass sich ein elastischer Körper mit einem bekannten äußeren und inneren Kräfteprofil (Eigengewicht, Fliehkräfte, etc.) im Gleichgewicht befindet, wenn die äußere und innere virtuelle Arbeit identisch ist. [56]

$$\overbrace{\delta\boldsymbol{u}^t \cdot \underbrace{\boldsymbol{B}}_{\text{äußere Kräfte}} + \int_V \delta\boldsymbol{u}^t \cdot \underbrace{\boldsymbol{p}}_{\text{innere Volumenkräfte}} dV + \int_S \delta\boldsymbol{u}^t \cdot \underbrace{\boldsymbol{q}}_{\text{Oberflächenlast}} dS}^{\text{Äußere virtuelle Arbeit}} \tag{4}$$

$$= \underbrace{\int_V \delta\boldsymbol{\varepsilon}^t \cdot \boldsymbol{\sigma} \, dV}_{\text{innere virtuelle Arbeit}}$$

Die finite Elemente Methode nähert die exakte Beschreibung der Identität (4) durch die Einführung eines Verschiebungsansatzes $\boldsymbol{u} = \boldsymbol{G} \cdot \boldsymbol{d}$ an, welcher die Knotenverschiebungen **d** über meist auf Polynomen basierten Funktionen $\boldsymbol{G}$ mit der Verschiebung des Volumens innerhalb der finiten Elemente verknüpft, welche die Struktur diskretisieren. Durch Einsetzen des Ver-

schiebungsansatzes in Gleichung (4) und einem linearem Materialgesetz, wird die Grundgleichung der FEM erhalten. Diese setzt eine Steifigkeit C mit den Knotenverschiebungen d des finiten Elements multipliziert mit den gesamten äußeren und inneren Kräften P gleich. [56, 57]

$$\underbrace{\int_V (D \cdot G)^t \cdot E \cdot (D \cdot G) \, dV \cdot d}_{C} = \underbrace{G^t \cdot F + \int_V G^t \cdot p \, dV + \int_O G^t \cdot q \, dO}_{P} \tag{5}$$

In Gleichung (5) wird der Grundgedanke der FEM ersichtlich, der reale Geometrien mittels mechanisch vollständig beschreibbaren kleinen, finiten Elementen annähert. Diese Elemente sind an das jeweilige zu lösende Problem hinsichtlich ihrer Dimensionalität (Linien-, Flächen-, Volumenelement) und Freiheitsgrade angepasst und weisen eine entsprechende Steifigkeit gegenüber der Verschiebung ihrer Knotenpunkte auf. Durch die Koppelung der Knoten untereinander, dem Zusammenbau der Elementsteifigkeiten zur Gesamtsteifigkeit und unter Berücksichtigung der Randbedingungen kann so die Verformung der Geometrie und über das Materialgesetz die hieraus entstehenden Spannungen bestimmt werden. [56]

Nichtlineare Finite Elemente Methode

Die in Gleichung (5) dargestellte Grundgleichung ist aufgrund der getroffenen Vereinfachungen linear. Werden Systeme berücksichtigt, deren Werkstoffverhalten nicht ideal elastisch ist und die eine geometrische Nichtlinearität (große Verformungen bei kleinen Verzerrungen) aufweisen, so wird die Steifigkeitsmatrix C von den Knotenpunkt-Verschiebungen d selbst abhängig. Zudem kann es durch nichtlineare Randbedingungen, wie sich öffnende oder schließende Kontakte zwischen Körpern, ebenfalls zu einer nicht linearen Steifigkeitsmatrix kommen.

Die entwickelten optischen Zugänge wurden in die Power Unit der verwendeten Motoren integriert und sind über nichtlineare Kontakte verbunden. Daher ist eine iterative Lösung des nichtlinearen Problems der Kontaktmodellierung notwendig. Generell wird eine Kontaktbedingung an den zuvor definierten Kontaktzonen für den jeweiligen Körper als eine Kraftrand- und Verschiebungsrandbedingung aufgefasst. Dies wird durch eine entsprechende Nebenbedingung über Lagrange-Multiplikatoren λ, welche die Kontaktkräfte in den Knotenpunkten des Kontaktkörpers beschreiben, mit in die iterative Lösung der nichtlinearen Grundgleichung über das Newton-Raphson Verfahren gelöst. Mittels des Coulombschen Reibungsgesetzes wird der aktuell vorliegende Kontaktzustand bestimmt (haftend, gleitend, kein Kontakt) und die entsprechenden geometrischen Kontaktbedingungen in der Matrix N umgesetzt. Gleichung (6) beschreibt das zu lösende Gleichungssystem, welches für die Verschiebung und die Kontakt-Knotenpunktkraft eine Linearisierung verwendet. [56, 58]

$$^{t+\Delta t}\begin{bmatrix} K_T(U) & N^t \\ N & 0 \end{bmatrix}^{(n-1)} \cdot \, ^{t+\Delta t}\begin{bmatrix} U^i - U^{(n-1)} \\ \lambda^i - \lambda^{(n-1)} \end{bmatrix} = \, ^{t+\Delta t}\begin{bmatrix} P - F(U) + R_c \\ \Delta \end{bmatrix}^{(n-1)} \tag{6}$$

Ausgehend von einer bekannten Lösung zum Zeitpunkt t wird die Lösung zum Zeitpunkt $t + \Delta t$ bestimmt. Für die Elastostatik wird als Zeitinkrement die Unterteilung der Lastschritte angesehen, mit welcher die äußeren Lasten auf die Struktur aufgebracht werden. Diese Unterteilung ist vor allem für die Konvergenz von Kontaktproblemen entscheidend. Die finale quasista-

tische Lösung wird aus der Überlagerung der Einzelschritte bestimmt. Mit n werden die Iterationsschritte des Newton-Raphson Verfahrens bezeichnet, welche zu jedem Zeitpunkt $t + \Delta t$ durchgeführt werden, um die Verschiebung $\boldsymbol{U}$ und die Kontakt-Knotenpunktkräfte $\boldsymbol{\lambda}$ zu bestimmen. Es werden so viele Iterationen n durchgeführt, bis die zwei Bedingungen

1. Die Materialüberlappung $^{t+\Delta t}\Delta^{(n-1)}$, welche während der Iteration entsteht, unter einen bestimmten festgelegten Grenzwert fällt.
2. Die Differenz aus den äußeren Kräften $\boldsymbol{P}$ und den elastischen Rückstellkräften $\boldsymbol{F(U)}$ an den Knoten den Kontakt-Knotenpunktkräften $\boldsymbol{R_c} = {}^{t+\Delta t}\boldsymbol{N}^{t,(n-1)} \cdot {}^{t+\Delta t}\boldsymbol{\lambda}^{(n-1)}$ entspricht. Dabei sind diese gleich null für alle Knoten außerhalb des Kontaktbereiches und innerhalb des Kontaktbereiches neben den Verschiebungen die zweite Unbekannte im Gleichungssystem (6).

erfüllt sind.

Gekoppelte thermische und strukturmechanische Berechnung

Die hier durchgeführte schwache Koppelung der CFD- und FEM- Simulation überlagert aus sequentiellen, unidirektionalen Berechnungen des Temperaturfeldes die daraus hervorgegangenen thermischen Spannungen mit Spannungen aus den mechanischen Belastungen. Dies ist in dem hier vorliegenden Anwendungsfall eine akzeptable Näherung, da die brennraumseitigen Randbedingungen als fixiertes Szenario gewählt wurden und der Einfluss der Brennraumwandtemperatur auf die Verbrennung vernachlässigt wird. Somit werden die Lastvektoren miteinander gekoppelt und das nichtlineare Gleichungssystem mit Kontaktbedingungen gelöst. [56]

Die Ergebnisse der gekoppelten thermischen und mechanischen Analyse werden nach der FKM Richtlinie [59] einem örtlichen Ermüdungsfestigkeitsnachweis unterzogen. Aus kritischen Ergebnissen können Anpassungen der Betriebsstrategie abgeleitet werden, um bei ausgeschöpften konstruktiven Maßnahmen durch eine Anpassung der Prozess-Randbedingungen einen sicheren Betrieb gewährleisten zu können.

2.3.3   Optikauslegung – Raytracing[2]

Die Funktionalität und Effektivität der optischen Bauteile entscheidet neben der Festigkeit der Konstruktion über die Realisierung des entwickelten optischen Zugangs. Dafür wurde eine optische Auslegung und Bewertung der entwickelten Optik mittels der Strahlengangdurchrechnung (Raytracing) durchgeführt.

Grundlegend wird in der **technischen Optik** die Ausbreitung des Lichtes und dessen Interaktion mit Materie (optische Medien, bzw. Linsen) zur Beschreibung der Abbildung optischer Systeme herangezogen. Dabei wird die Beschreibung der Ausbreitung des Lichtes in die Bereiche der Wellenoptik (Beugung, Interferenz, Polarisation) und der geometrischen Optik (Brechung und Reflexion) unterschieden (vgl. [60]). Die geometrische Optik beschreibt die Effekte ausreichend genau, wenn die Wellenlänge deutlich kleiner als die Abmessungen der zu untersuchenden Objekte ist. In der Regel wird aber eine kombinierte Betrachtung während der Ent-

---

[2] Die für die Optik verwendeten Begriffe werden im Anhang detailliert erläutert und im Fließtext kursiv gedruckt.

wicklung eines optischen Systems für die Beschreibung der auftretenden Effekte herangezogen (vgl. [61]).

Die **Wellenoptik** basiert auf der Ausbreitung des Lichtes als elektromagnetische Welle. Die physikalische Beschreibung der Ausbreitung basiert auf den vier Gleichungen nach Maxwell, welche zur zeitunabhängigen Helmholtzgleichung umgeformt werden [60–62]. Hieraus wird abgeleitet, dass sich aufgrund der Änderung des Brechungsindizes, hervorgerufen durch einen Medienwechsel, auch die Phasengeschwindigkeit der Welle ändert. Dies ist die Grundlage des Brechungsgesetzes, welches in der geometrischen Optik seine Anwendung findet (vgl. [63]).

Die **geometrische Optik** beschreibt die Ausbreitung der Wellenfronten des Lichtes eindimensional in vereinfachter Form von Strahlen (vgl. [60]). Die Lichtstrahlen werden dabei als die Normalen-Vektoren auf die Phasenflächen verstanden, welche den geometrischen Ort aller Punkte der von einem Objektpunkt ausgehenden Lichtwellen der gleichen Schwingungsphase beschreibt. Damit kann die Ausbreitung der Wellenfront des Lichtes mit Hilfe eines einfachen zweidimensionalen Strahlenganges durch ein optisches System beschrieben werden. Dabei werden drei Grundaxiome für die Ausbreitung der Strahlen nach [60, 63] angewendet:

1. Lichtstrahlen breiten sich in homogenen Medien geradlinig aus.
2. Lichtstrahlen interferieren nicht und sind damit voneinander unabhängig.
3. Die Interaktion an den Grenzflächen von Medien, durch welche das Licht hindurchtritt, unterliegen dem aus dem Fermatschen Prinzip abgeleiteten Brechungs- und Reflexionsgesetz.

Das Reflexionsgesetz beschreibt die Ausbreitung des Lichtes bei Auftreffen auf eine optisch reflektierende Oberfläche. Dabei gilt, dass der Winkel der einfallenden Welle (zwischen Lot und Lichtstrahl) gleich dem Winkel der reflektierten Welle ist. Je nach Einfallswinkel wird zwischen einer Teil- und Totalreflexion unterschieden. Bei Teilreflexionen wird die einfallende Welle unter Einhaltung des Energieerhalts zerlegt in einen reflektierten und einen gebrochenen Anteil. Das Brechen der Lichtwelle erfolgt an Grenzflächen von Medien mit unterschiedlichen Brechkräften n. Je nach Medieneigenschaft am Übergang wird der Strahl zum auf der optischen Oberfläche senkrecht stehenden Lot hin bzw. weggebrochen. Mit Hilfe des Brechungsgesetzes nach Snellius wird dieser Zusammenhang in Gleichung (7) vektoriell dargestellt.

$$n_i \cdot (\widehat{k}_i \cdot \widehat{u}_n) = n_t \cdot (\widehat{k}_t \cdot \widehat{u}_n) \tag{7}$$

Hierbei bestimmt n die Brechkraft, k den einfallenden bzw. den ausfallenden Strahl und u den senkrecht auf der Grenzfläche stehenden, in Richtung des Mediums zeigenden Einheitsvektor. Der Index i bestimmt den Ort vor Auftreffen auf eine Fläche und t den Ort bzw. das Medium danach. Der Brechungsindex ist meist Wellenlängen- und Temperaturabhängig und wird in *Dispersionsformeln* und Kennfeldern der Glashersteller für die Berechnung zugänglich gemacht (vgl. [60]).

Das **Raytracing** (Strahlverlaufsberechnung) beinhaltet die Beschreibung des Strahlenganges zur Bestimmung der Abbildung eines optischen Systems, wie es prinzipiell in Abbildung 4 dargestellt ist. Ein Objektpunkt emittiert Licht in Form von kugelförmigen Wellen. Die Wellenfronten passieren für die Abbildung des Punktes O das optische System, dargestellt durch

Strahlen als Normalen auf den Wellenfronten. Ein jeder Strahl wird exakt verfolgt. Dazu wird beim Auftreffen auf eine Fläche des optischen Systems der Strahl gebrochen und mittels des vektoriellen Snelliusschen Brechungsgesetzes Gleichung (7) bestimmt, wo der Strahl auf die nächste Fläche trifft. [63]

Zusätzlich zu einem Strahl in der Ebene der optischen Achse (*Meridionalstrahl*) wird auch ein dazu windschiefer Strahl (*Saggitalstrahl*) betrachtet und dessen Durchtritt durch das optische System im dreidimensionalen Raum berechnet. Dies wird notwendig, um die Abbildungsqualität eines optischen Systems anhand der Aberrationstheorie bestimmen zu können.
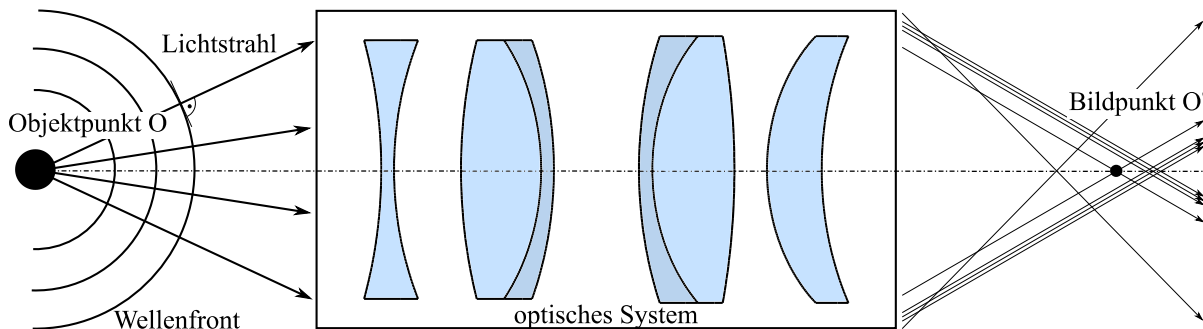
Abbildung 4 Entstehung von Aberrationen

2.4 Optik Design und Abbildungsmodelle für Fisheye Optiken[3]

Die Entwicklung der Optiken erfolgte nach dem in Abbildung 5 dargestellten Ablauf. Das Raytracing (Strahlverlaufsberechnung) ist dabei Kernbestandteil der in Abbildung 5 dargestellten Optimierung des aus der Literatur abgeleiteten Grunddesigns für die Randbedingungen eines Brennraums und die vorhandenen Aberrationen. Im Weiteren soll die Aberrationstheorie als Grundlage für die Entwicklung einer Optik zusammengefasst werden.
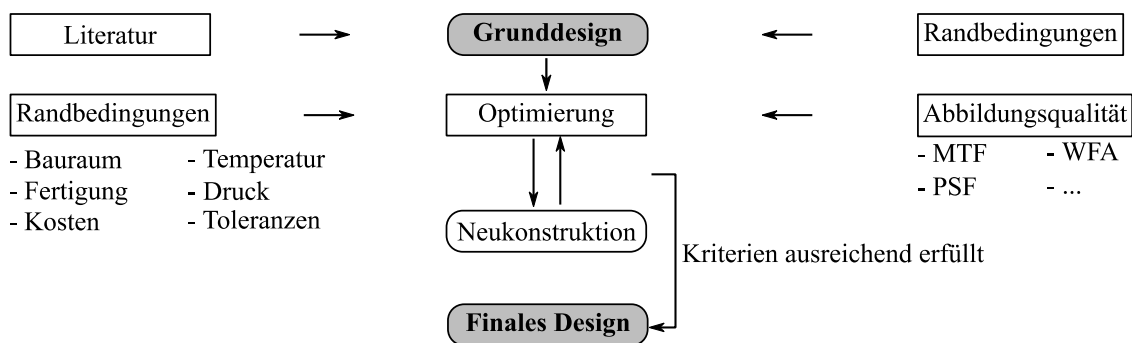
Abbildung 5 Vorgehen für die Entwicklung der Optiken

2.4.1 Aberrationstheorie

Abbildung 4 zeigt eine Abbildung eines Objektpunktes O durch ein optisches System, welches mittels der Strahlverlaufsberechnung bestimmt werden kann. Eine ideale Abbildung ist gegeben, wenn sich alle Strahlen exakt im Bildpunkt O' wieder vereinen. Allerdings entstehen Abbildungsfehler oder sog. Aberrationen in jedem optischen System, welches außerhalb der paraxialen Randbedingungen und mit polychromatischen Licht verwendet wird. Dies äußert sich

---

[3] Die für die Optik verwendeten Begriffe werden im Anhang detailliert erläutert und im Fließtext kursiv gedruckt.

darin, dass sich die Lichtstrahlen nicht exakt im Bildpunkt O' vereinen. Im paraxialen Gebiet mit kleinen *Aperturen* und *Feldwinkeln* wird eine ideale Abbildung eines kleinen Ausschnitts der ausgesandten Kugelwellen erreicht. Durch die Beschränkung auf kleine Feldwinkel bis zu 5° kann das Snelliussche Brechungsgesetzes aus Gleichung (7) durch eine Taylor-Reihenentwicklung, die nach dem ersten Glied mit vernachlässigbaren Fehlern abgebrochen wird (siehe Gleichung (8)), angenähert werden. [64]

$$n_1 \cdot \alpha_1 = n_2 \cdot \alpha_2 \qquad \text{mit der Taylor Reihe: } \sin(\alpha) \approx \alpha + \frac{\alpha^3}{3!} + \frac{\alpha^5}{5!} + \cdots \tag{8}$$

Aufgrund der Nichtlinearität des Brechungsgesetzes, welches in der Gaußschen Optik durch die paraxialen Vereinfachungen vernachlässigt wird, kommt es bei Verlassen des Paraxialgebietes und Berücksichtigung des zweiten Terms der Taylorreihenentwicklung zur Fehlertheorie dritter Ordnung nach Seidl. Diese Abweichungen äußern sich in einer nicht idealen Abbildung. Die quantitative Bestimmung und Korrektur der Aberrationen ist wesentlicher Bestandteil des Optikdesigns für eine optimale Abbildung des zu beobachtenden Objektes. Bei der optischen Auslegung eines Systems ist ein Kompromiss aus Abbildungsqualität und konstruktivem Aufwand notwendig, welcher die Anzahl an Elementen im System, deren Toleranzen, Fertigbarkeit und damit die Kosten des Systems festlegt. Abbildungsfehler dritter Ordnung werden bezüglich der Wellenlänge des Lichts in chromatische und monochromatische Aberrationen unterteilt. Die *chromatischen Fehler* können in longitudinale und transversale Fehler unterschieden werden und beruhen hauptsächlich auf der unterschiedlichen Brechkraft optischer Materialien für unterschiedliche Wellenlängen.

Die monochromatischen Aberrationen umfassen Abbildungsfehler, welche die Bildqualität verschlechtern, wie *sphärische Aberration*, *Koma* und *Astigmatismus* sowie Bild verformende Abbildungsfehler wie die *petzvalsche Bildfeldwölbung* und *Verzeichnung*. Die Abbildungsfehler dritter Ordnung werden für jede Fläche eines Linsensystems bestimmt und zur Gesamtabweichung aufaddiert. Die Berechnungsvorschriften der Seidlkoeffizienten können z.B. in [65] gefunden werden. Die Seidl Aberrationen bilden einen guten, für jede Fläche eines Elementes aufgelösten und einfach zu bestimmenden Wert für die Qualität der Abbildung. Mit diesen können Maßnahmen wie das Einfügen weiterer Linsen zur Verteilung der Brechkraft, der Kombination unterschiedlicher optischer Materialien, der Anpassung der Krümmungsradien z.B. durch den Einsatz von *asphärischen Linsen*, die optimale Wahl des Blendendurchmessers und deren Positionierungen im System sowie der Wahl der Abstände der Linsen zueinander umgesetzt werden. Generell zielen diese Maßnahmen auf einen homogenen und kontinuierlich verlaufenden Pfad der Lichtstrahlen ab. Meist treten die beschriebenen Aberrationen dritter Ordnung nicht isoliert auf. Sie überlagern und verstärken sich zum Teil gegenseitig und sind Voraussetzung für das Entstehen von bestimmten Fehlern, wobei die Korrektur eines Fehlers ohne die Korrektur des Anderen nicht erfolgen kann.

Die Fehler dritter Ordnung sind Teil der Wellenfrontaberration höherer Ordnungen und können damit auch aus diesen abgeleitet werden. Ein Vorgehen hierzu kann in z.B. [65] gefunden werden. Auch diese Fehler höherer Ordnung wurden für die Entwicklung der Optik in Form der Wellenfrontabweichung (OPD) mit herangezogen und eine detailliertere Beschreibung dieser kann z.B. in [65, 66] gefunden werden.

2.4.2 Gütekriterien für die Beurteilung einer Optik

Die Beurteilung der Abbildungsqualität soll anhand der entwickelten Optik für den mittelschnelllaufenden Großmotor MAN 35/44 DF, welche in Abschnitt 4.1 gezeigt wird, exemplarisch erläutert werden.

Das erste für die Beurteilung der Abbildungsqualität heranzuziehende Kriterium ist der Punktgrößendurchmesser. Dieser wird bestimmt, indem eine bestimmte Anzahl von Lichtstrahlen in definierten Wellenlängen und einer bestimmten Anordnung die Optik gleichzeitig passieren und auf einer Bildebene detektiert werden. Im theoretischen Idealfall wird jede Punktquelle wieder auf einen Punkt abgebildet. Dies ist in der Realität jedoch aufgrund von Beugungseffekten nicht möglich, sodass im besten Falle die Punktquelle als *Airy Scheibchen* abgebildet wird. Optiken, die solch ein Verhalten aufweisen, nennt man beugungsbegrenzt. Jedoch führen die Aberrationen zu Abweichungen der realen Abbildung im Vergleich zur beugungsbegrenzten bestmöglichen. Abbildung 6 zeigt für vier unterschiedliche Anordnungen der Punktquelle die sich ergebenden Bilder für die Frauenhofer Linien bei 486 nm, 587 nm und 656 nm mit 0 ° direkt auf der optischen Achse, bei 45 °, 70 ° und den maximal möglichen Feldwinkel 89,9 °. Das auf der 0 °-Achse liegende Feld leidet besonders unter der sphärischen Aberration, die sich in einer erhöhten Streuung der Punkte zeigt. Eine Vergrößerung des Feldwinkels führt zu einem verstärkten Astigmatismus, der sich in der Ausbreitung der Punkte in horizontaler und vertikaler Richtung äußert. Alle Bilder außerhalb der Achse zeigen die typische Kometenschweif ähnliche Koma-Aberration. Vor allem der Feldwinkel von 70 ° zeigt hier den stärksten Einfluss der Koma-Aberration durch einen in der Punktform zu erkennenden kleinsten und scharf abgegrenzten Kegel. Die mittlere-Punktgröße für die Referenzwellenlänge von 587 nm liegt für die vier dargestellten Felder im Bereich der Pixelgröße der verwendeten Kameras (vgl. Tabelle 3) und ergibt somit eine ausreichende Auflösung. Außerdem ist die Punktgröße für den maximalen Feldwinkel nur geringfügig kleiner als beim Winkel von 70 °, was auf eine bessere Aberrationskorrektur in diesem Bereich zurückzuführen ist.

Angewandte Wellenlänge in µm:	0,486
	0,587
	0,656

Durchmesser des Airy Scheibchens: 0,003mm

Feldwinkel	0°	45°	70°	89,9°
RMS SPD in mm	0,011	0,013	0,026	0,021
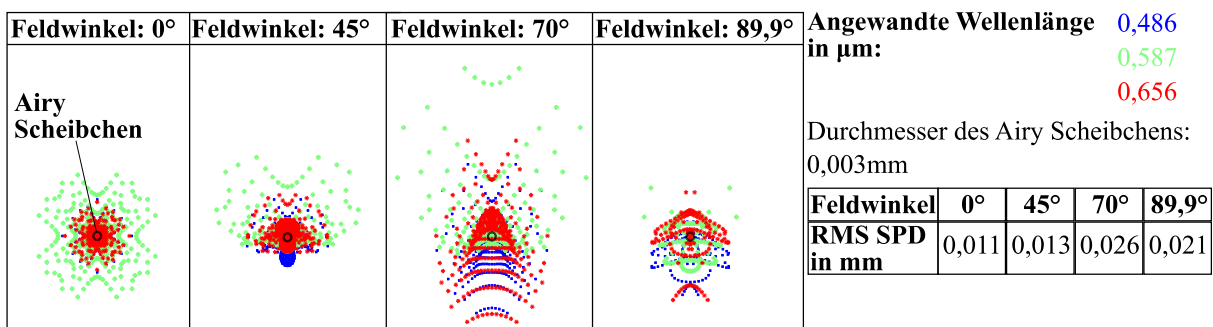
Abbildung 6 RMS SPD für Punktquellen bei 0 °, 45 °, 70 ° und 89,9 ° Feldwinkel

Wie bereits erwähnt, bilden die Abbildungsfehler dritter Ordnung nach Seidl ein für jede Fläche des Linsensystems auflösbares Kriterium, um Optimierungsschritte abzuleiten. Abbildung 7 zeigt eine solche qualitative Auflösung für alle 15 Glasflächen der Optik. Fläche 8 ist die physikalische Blende des Systems, deren Anordnung im System ebenso Auswirkungen auf die Abbildungsfehler hat. Das Diagramm zeigt den Aufbau des entwickelten Systems als Retrofokus System. Die negative Gruppe (Fläche 1-7) weist einen negativen Fokusabstand auf und erzeugt

Abbildungsfehler im System. Die positive Gruppe (Fläche 9-16) korrigiert diese Fehler weitestgehend.
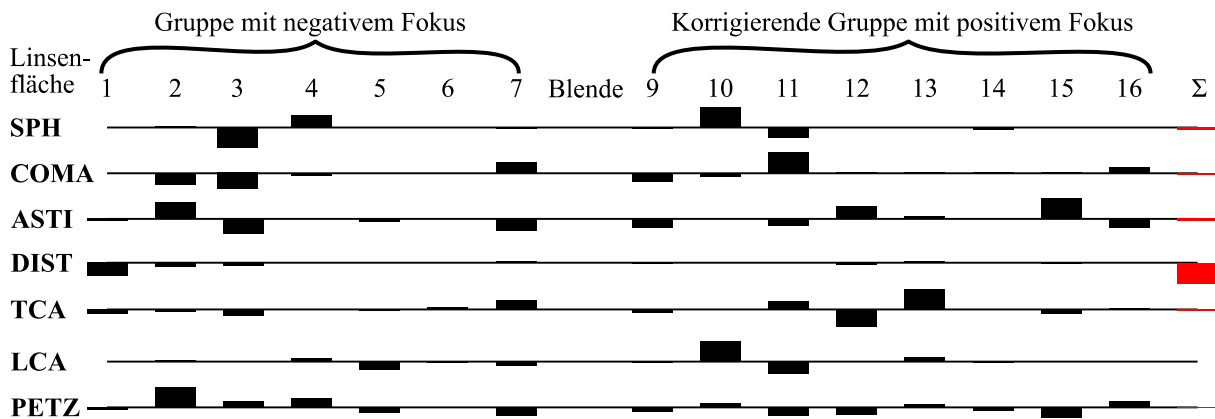
Abbildung 7 Seidl Aberrationen (SPH=Sphärische Aberration, COMA=Koma, ASTI=Astigmatismus, DIST=Verzerrung, TCA=Transversaler Farbfehler, LCA=Longitudinaler Farbfehler, PETZ=Petzval-Summe)

Die höherwertigen Abbildungsfehler können mit der optischen Wegdifferenz, welche die reale (durch das optische System deformierte) Wellenfront zur idealen (undeformierten) Form vom Scheitelpunkt bis zum Tal einer Lichtwelle bemisst, beschrieben werden. Die OPD Darstellung (vgl. Abbildung 8) hebt besonders die chromatischen Aberrationen hervor und ist ein Maß für die Qualität des Bildes und damit die Eignung der Optik für die Untersuchung und Visualisierung der Phänomene im Zylinder des Verbrennungsmotors. Für die tangentiale Ebene zeigt die Optik über alle Feldwinkel entlang des Durchmessers der *Eintrittspupille* ein gutes Verhalten der OPD. Das 89,9 °-Objekt zeigt eine maximale Abweichung von +3 Wellenlängen aufgrund der Koma, die sich in einer U-Form des Fächers äußert. Außerdem ist die sehr gute Korrektur der Farbabweichungen in der Tangentialebene nachzuvollziehen, welche sich in der Überdeckung der drei Wellenlängen äußert. Die äußeren Regionen leiden unter leichten axialen Farbaberrationen, sichtbar in der Änderung der Neigung der Kurven, die jedoch nahezu vernachlässigbar sind. Die Sagittalebene weist bis zum 70 °-Objekt ein gutes Verhalten bezüglich der Aberrationen auf. Insbesondere das 89,9 °-Objekt zeigt sphärische Aberrationen und Koma, welche sich in S-förmigen Linien mit einem längeren und kürzeren Teil der S-Form äußert.
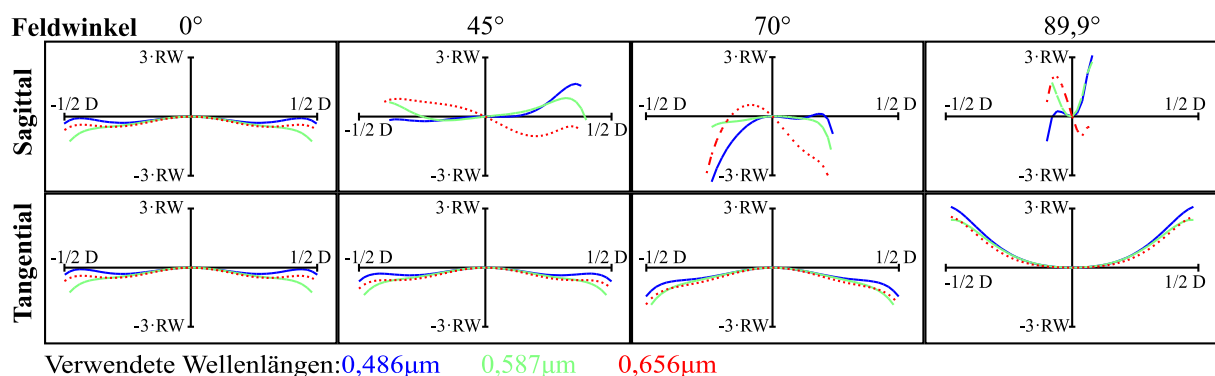

Abbildung 8 Optische Weglängendifferenz-OPD (D=Durchmesser Eintrittspupille, RW= Referenzwellenlänge)

Ein Vergleich zwischen den sagittalen und tangentialen Kurven außerhalb der optischen Achse zeigt den Astigmatismus im System. Die verkürzten Linien über dem normalisierten Durch-

messer der Eintrittspupille für die Feldwinkel 70 ° und 89,9 ° sind ein Hinweis auf Vignettierung im System. Außerdem gibt Abbildung 8 einen Hinweis auf einen leichten *Sphärochromatismus*, der sich in wechselnden Kurvenformen innerhalb eines Objektwinkels über die betrachteten Wellenlängen manifestiert.

Das Kriterium der *Modulationsübertragungsfunktion* (MTF) in Abhängigkeit des Feldwinkels gibt die Abbildungsqualität des Gesamtsystems und insbesondere die erzielbare Auflösung der Abbildung an. In der Literatur gibt es verschiedene Regeln für eine ausreichende Bildauflösung, wie die 30-50-Regel, die 50 % bei einer Anregung von 30 lp/mm und 30 % bei einer Anregung von 50 lp/mm fordert (vgl. [67]). Daneben ist ein weiteres Kriterium, dass die MTF bei 30 lp/mm über 90 % des Bildwinkels bei 20 % liegt. Gleichung (9) berechnet die maximal mögliche Anregungsfrequenz, die eine ideale und damit aberrationsfreie Optik erreichen kann. Mit den Werten der Optik aus Abschnitt 4.1 könnte eine Grenzfrequenz von 774 lp/mm erreicht werden.

$$f_{\xi c} = \frac{1}{\lambda \cdot f\#} \tag{9}$$

Abbildung 9 zeigt die MTF bezüglich der Bildauflösung bis zu einer Objektfrequenz von 50 lp/mm für vier Feldwinkel zwischen 0 und 89,9 °. Bezüglich der möglichen Kameraauflösung von 25 lp/mm für die monochromatische Kamera und 18 lp/mm für die Farbkamera (vgl. Tabelle 3), welche durch die Pixelgröße des Sensors begrenzt ist, zeigt die MTF der Fisheye Optik einen ausreichenden Wert größer 50 %. Darüber hinaus weist die MTF über das gesamte Sichtfeld eine Auflösung von 30 lp/mm auf, was den angeführten Regeln für eine gute Bildauflösung entspricht. Da die geplante Anwendung der Optik in einem Brennraum deutlich größere Strukturen abbildet, kann eine Kontrastgrenze gewählt werden, welche einer computergestützten Bildverarbeitung von standardmäßig mindestens 20 % genügt.
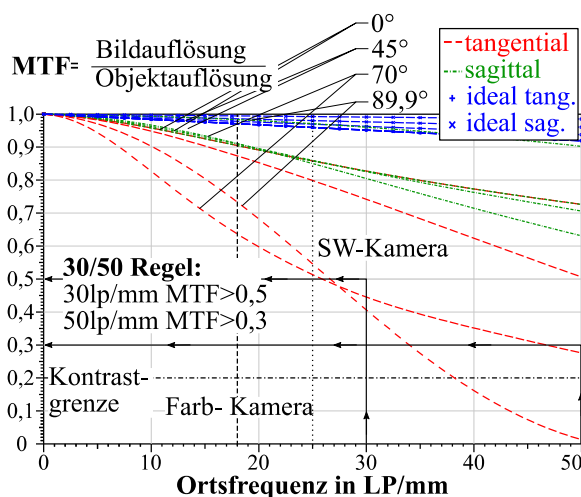
Abbildung 9 Modulations Übertragungsfunktion   **Abbildung 10** Toleranzanalyse
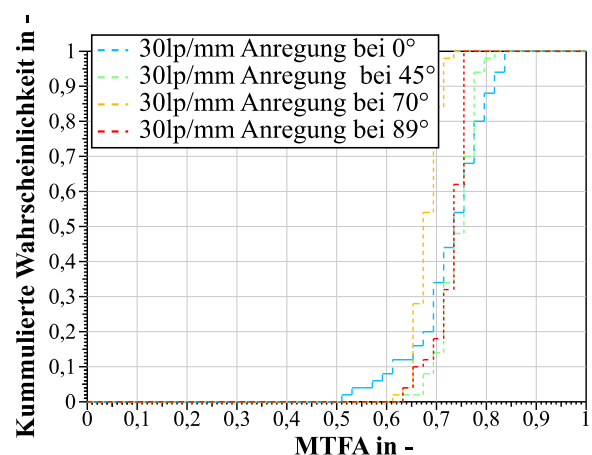
Neben den konstruktiven Abbildungsfehlern bestimmen Abweichungen durch die technische Herstellung der Linsenmaterialien, Linsen und Optiken sowie ihrer Montage die effektive Güte der optischen Abbildung. Diese müssen durch eine statistische Toleranzanalyse über das Raytracing analysiert und beherrscht werden. Die Toleranzen werden unter den Gesichtspunkten

der Herstellbarkeit, der ausgelegten optischen Abbildungsqualität und der Kosten festgelegt. Abbildung 10 zeigt das Ergebnis einer solchen Toleranzanalyse für vier Feldwinkel bei einer Anregung mit 30 lp/mm für die Berechnung der über die sagittale und tangentiale MTF gemittelten Übertragungsfunktion (MTFA). Die Analyse ist mit einem Erwartungswert der stochastischen Verteilung von 95 % durchgeführt worden. Die einzige zur Verfügung stehende Korrekturgröße während der Variation der Toleranzen ist - wie im späteren realen System - die Anpassung des rückwärtigen Fokus über ein Verschieben der Bildebene. Es ist ersichtlich, dass die MTFA von 65 % mit einer ausreichend hohen Wahrscheinlichkeit von >60 % unter den gewählten Toleranzen möglich ist.

2.4.3   Eigenschaften von Fisheye Optiken

Als Fisheye-Objektive werden Objektive bezeichnet, die ein Sichtfeld größer oder gleich 180 ° aufweisen und ihr Bild auf eine endliche, ebene Bildebene projizieren (vgl. [68], [69]). Sie werden in zirkuläre und Vollformat-Bildsysteme unterteilt. Zudem weisen sie relativ kleine Brennweiten (f<15) auf. Systeme, die ein eingeschränkteres Sichtfeld bei gleichen Abbildungseigenschaften aufweisen, werden als Quasi-Fisheye-Optiken bezeichnet. Das gebräuchlichste Design folgt dem Retrofokus-Ansatz, welcher jeweils aus einer Einheit mit negativer und einer mit positiver Brechung besteht. Die Verwendung des Retrofokus-Ansatzes führt in der Regel zu Systemen mit einer relativ großen vorderen *Apertur* und damit zu großen ersten Linsen. Die Minimierung dieser Linsen führt normalerweise zu einer geringeren optischen Bildqualität und geringerer numerischer Apertur und damit Lichtstärke. Zur Korrektur von Abbildungsfehlern wird in der Regel ein positives Element vor der Apertur in die negativ brechende Einheit platziert. Die positiv brechende Einheit ist für die Erzeugung des realen Bildes und die Hauptkorrektur der Aberrationen verantwortlich. In der Regel sorgt ein Doublett, bestehend aus einer positiven Bikonvexlinse mit niedrigem Brechungs- und Dispersionsindex verkittet mit einer negativen Linse mit hohem Brechungs- und Dispersionsindex in der positiven Einheit für eine Korrektur des Astigmatismus und der Petzvalsumme. Der oft nicht symmetrische Aufbau von Fisheye-Linsensystemen erfordert relativ komplexe Kompensationsmaßnahmen der Aberrationen, hauptsächlich Farblängsfehler, Astigmatismus und Bildfeldwölbung (Petzvalsumme), um eine optimale Bildqualität zu gewährleisten. (vgl. [70–72]).

Fisheye Optiken weisen aufgrund des großen Gesichtsfeldes eine stark negative, meist tonnenförmige Verzeichnung auf. Diese Art der Abbildung mit starker Verzeichnung folgt nicht mehr der einfachen perspektivischen Projektion, sondern wird durch alternative Ansätze beschrieben, welche im nachfolgenden Abschnitt genauer betrachtet werden (vgl. [73]). Die Verzeichnung beeinflusst Bildqualität und -fehler nicht. Es handelt sich lediglich um eine vom Einfallswinkel des Lichtstrahls abhängige Vergrößerung, die in einem Nachbearbeitungsschritt kalibriert werden kann (vgl. Abschnitt 2.4.5). Zudem bedingt die starke Verzeichnung, dass *Randstrahlen* näher in die Mitte des Bildes abgebildet werden als dies in klassischen Objektiven der Fall ist. Durch diese Komprimierung der Randbereiche einer Fisheye Optik wird die Intensität des Lichtes für große Feldwinkel erhöht und der Randlichtabfall ist nicht mehr proportional zu $\cos^4 \theta$ (vgl. [68, 69, 72]). Eine weitere Besonderheit der Fisheye Optiken, welche das ausgedehnte Sichtfeld erst ermöglichen, ist eine nicht konstante, senkrecht zur optischen Achse positionierte Eintrittspupille. Diese verschiebt sich in Richtung der ersten Linse und verkippt weg von der optischen Achse (vgl. [68, 69, 74]).

23

2.4.4 Modellvorstellung des Abbildungsprozesses von Fisheye Optiken

Aufgrund der dargestellten Besonderheiten bei der Fisheye Abbildung bedarf es angepasster Berechnungsmethoden zu ihrer Beschreibung. Die einfachste Beschreibung ist die perspektivische Projektion einer Lochblendenkamera. Sie wird für konventionelle Optiken mit einem Feldwinkel von bis zu 40 ° und damit vernachlässigbaren radialen Verzerrungen angewandt (siehe Gleichung (10)). Abbildung 11 (a) stellt die Projektion nach Gleichung (10) dar. Die perspektivische Projektion bildet den Punkt P(X, Y, Z) aus dem dreidimensionalen Raum auf die zweidimensionale Bildebene im Punkt p'(x', y', z') ab.

$$r = \underbrace{f}_{\text{Fokusabstand}} \cdot \tan (\underbrace{\theta}_{\text{Feldwinkel}}) \tag{10}$$

Durch Gleichung (10) ist ersichtlich, dass bei Erreichen eines Winkels von 90 ° die Abbildungsvorschrift einen beliebigen Punkt P(X,Y,Z) im dreidimensionalen Raum nicht mehr auf eine endliche Bildebene abbilden kann, da hier der Wert der tan-Funktion gegen unendlich strebt (siehe Abbildung 11 (a) und (b)). Fisheye Optiken weisen aber einen hohen Grad an oftmals nichtlinearer radialer Verzerrung auf, welche hier essentiell für die Abbildung ist. Für die Auslegung einer Fisheye Optik und Optimierung wird meist eine der vier Abbildungsvorschriften der stereographischen, äquidistanten, orthogonalen und Abbildung des gleichmäßigen Winkels herangezogen. Da die Optik aufgrund der Aberrationen diesen Abbildungsvorschriften nicht ideal folgt, werden allgemeiner formulierte mathematische Ansätze, meist bestehend aus Polynomgleichungen, zur Beschreibung der Projektion verwendet. Abbildung 11 (b) stellt drei dieser allgemeineren Ansätze (Scaramuzza [75], Kannala [76] und Micusik [77]) in unterschiedlicher Linienvariation den gewöhnlich zur Auslegung verwendeten Abbildungsvorschriften, dargestellt in unterschiedlichen Farben, gegenüber. Es wird hier bereits ersichtlich, dass je nach Ansatz der gewählten Funktion geringe Abweichungen im Ergebnis existieren. Diese sind für die stereographische Abbildung in Abbildung 11 (b) exemplarisch dargestellt.

Im Weiteren soll das Vorgehen nach Kannala-Brandt [76] herangezogen werden. Dieser nutzt einen Polynomansatz mit ungeraden Exponenten und hat sich für die vorliegende Anwendung als einfach anwendbar und gut geeignet herausgestellt. Wie in Abbildung 11 (a) dargestellt, wird eine Einheitssphäre (abgebildet als einfache Hemisphäre im Abstand z über der zweidimensionalen Bildebene im Ursprung des Kamerakoordinatensystems) in der dreidimensionalen Szene eingeführt. Ausgehend von einer Projektion jedes abzubildenden Punktes im dreidimensionalen Raum auf diese Einheitssphäre, wird jedem Punkt ein sogenannter Sichtstrahl $\Phi(\theta, \psi)$ mit der Einheitslänge 1 zugeordnet. Über die Zuordnung der Winkel θ und ψ zu dem jeweiligen Sichtstrahl kann die Vorwärtsprojektion g(Φ) aus dem dreidimensionalen in den zweidimensionalen Raum nach Gleichung (11) angegeben werden.

$$\mathbf{p} = r(\theta) \cdot (\cos\psi, \sin\psi)^T = g(\mathbf{\Phi}) \tag{11}$$
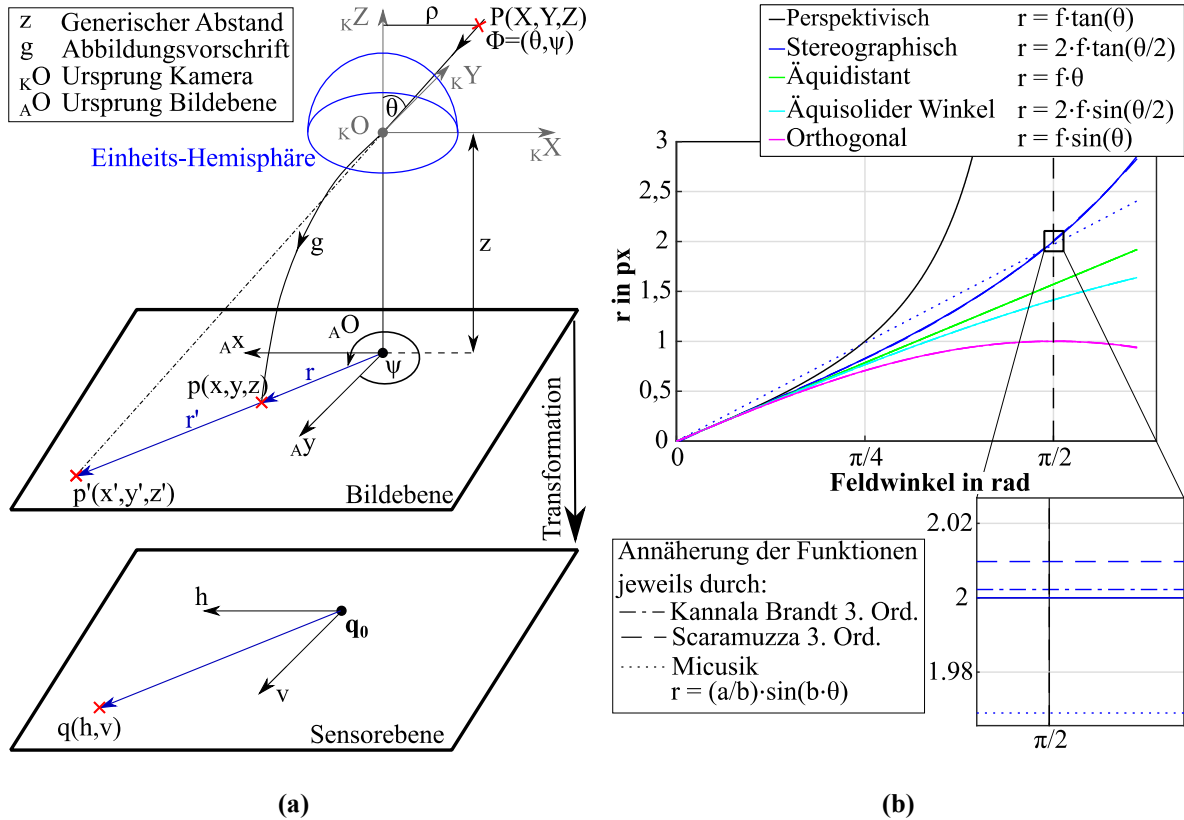
Abbildung 11 Fisheye Projektion (a) Lochkamera und Fisheye Projektion (nach [63], mod.)

(b) Abbildungsvorschriften (nach [63], mod.)

Die von Kannala in [76] genutzte Projektion beinhaltet zusätzlich zur rotationssymmetrischen radialen Verzerrung eine nicht rotationssymmetrische radiale $\Delta_r(\theta, \psi)$ und tangentiale Verzerrung $\Delta_t(\theta, \psi)$. Da diese allerdings oft vernachlässigbar klein sind, ergibt sich für die **Vorwärtsprojektion** $g(\boldsymbol{\Phi})$ nach [76]:

$$\mathbf{g}(\boldsymbol{\Phi}) = \underbrace{r(\theta)}_{k_1 \cdot \theta + k_2 \cdot \theta^3 + k_3 \cdot \theta^5 + k_4 \cdot \theta^7 + k_5 \cdot \theta^9 + \cdots} \cdot \begin{pmatrix} \cos\psi \\ \sin\psi \end{pmatrix} = \begin{pmatrix} {}_I x \\ {}_I y \end{pmatrix} \tag{12}$$

Die so projizierten Punkte werden zum Schluss noch auf den Kamerasensor projiziert (vgl. Abbildung 11 (a)). Dies erfolgt über eine einfache Skalierung der Punkte über die Faktoren m_h und m_v welche die Einheitslänge pro Pixel ausdrücken. Zudem wird das Verzerrungszentrum q_0 eingeführt, sodass die Ursprungskoordinaten der Bildebene in Einheitslänge nicht mit dem System in Pixel übereinstimmen müssen (vgl. Gleichung (13)).

$$\mathbf{q} = \begin{bmatrix} m_h & 0 \\ 0 & m_v \end{bmatrix} \cdot \boldsymbol{p} + \boldsymbol{q_0} \tag{13}$$

Dies liefert $(n+1)/2$ Freiheitsgrade aus dem Polynomgrad n die Skalierungskoeffizienten m_h und m_v als weitere Optimierungsparameter, um die Abbildung bestmöglich zu beschreiben. Die Bestimmung dieser Freiheitsgrade erfolgt durch eine Kalibrierung der Optik, deren Vorgehen im nächsten Abschnitt zusammengefasst wird.

25

2.4.5 Der Kalibrierprozess – Ableiten extrinsischer und intrinsischer Abbildungsparameter

Generell existieren verschiedene Möglichkeiten Optiken zu kalibrieren. Diese unterscheiden sich hauptsächlich:

- im verwendeten Ansatz der Projektionsfunktion
- im Start der Kalibrierung mit der Bestimmung der Vorwärts- (von 3D auf 2D) oder Rückwärtsprojektion (von 2D auf 3D), was Auswirkungen auf die Initialisierung der Optimierungsalgorithmen hat und damit auf die erreichbare Genauigkeit
- im verwendeten Kalibriermuster

Je nach verwendetem Kalibriermuster können nach [78] fünf unterschiedliche Methoden herangezogen werden: Linienbasierte Muster, Zweidimensionale Kalibriermuster, Selbstkalibrierung, Dreidimensionale Punktkalibrierung und Polarisationsbasierte Kalibrierung.

In der vorliegenden Arbeit wurde ein zweidimensionales Kalibriermuster gewählt, welches für die Verwendung der Projektionsvorschrift nach Kannala-Brandt geeignet ist (vgl. Abbildung 12). Grundsätzlich werden Aufnahmen des Kalibriermusters in verschiedenen Relativpositionen zur Optik aufgenommen. In den Aufnahmen werden dann die Pixel basierten Koordinaten der auf dem Kalibriermuster dargestellten Kontrollpunkte extrahiert. Hierfür kam das vom DLR entwickelte Tool CalDe zum Einsatz (siehe [79]). Mit den extrahierten Kontrollpunkten werden über eine Optimierung die extrinsischen (Rotationsmatrix R und Translation t zur Beschreibung der Relativen Lage des Kalibiermusters zur Optik) und intrinsischen Parameter (Fokusabstand, $(n + 1)/2$ Freiheitsgrade des Polynoms vom Grad n, das Verzerrungszentrum q_0 und die Skalierungsfaktoren m_h und m_v) bestimmt. Hierzu werden die Kontrollpunkte aus der zweidimensionalen Bildebene in die dreidimensionale Szene projiziert. Diese Projektion wird unter Optimierung der Parameterwerte solange iteriert, bis der Projektionsfehler im Subpixelbereich liegt. Dies ist möglich, da die Kontrollpunkte und insbesondere deren unveränderliche Abstände in der dreidimensionalen Szene bekannt sind und damit ein fixes Kriterium für die Optimierung bereitstellen.
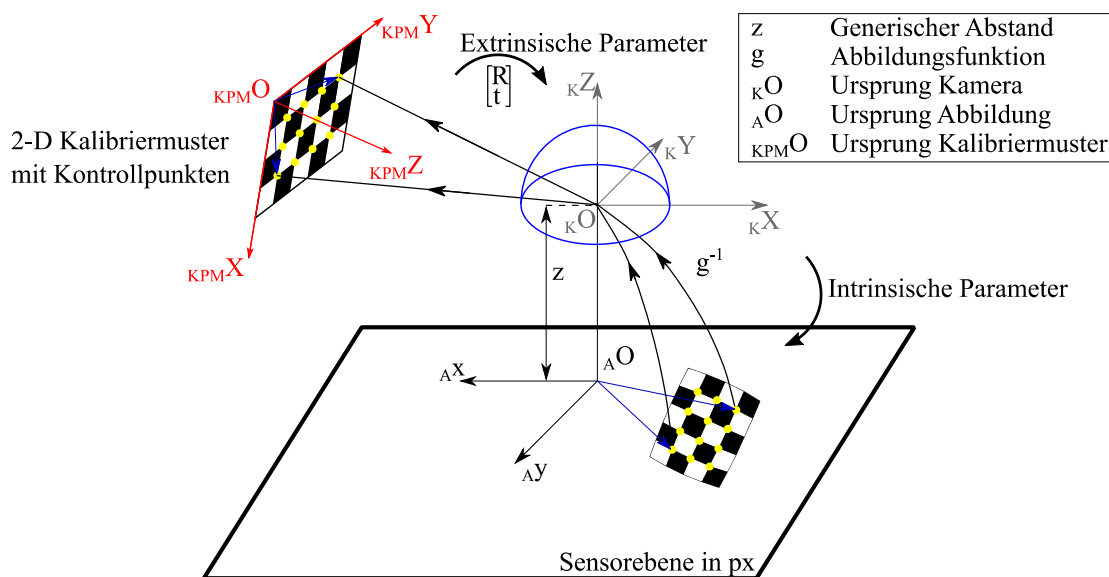

Abbildung 12 Kalibrierprozess: K=Kamera, A=Abbildung, KPM=Kontrollpunkt- Muster

Abbildung 12 zeigt das Vorgehen und die verwendeten Koordinatensysteme des Projektions-prozesses. Die letzte Skalierung von der Bildebene in die Kamerasensorebene ist hier bereits mit in den intrinsischen Parametern enthalten.

2.5 Verbrennung nachhaltiger wasserstoffbasierter Kraftstoffe

Mit dem entwickelten kompakten optischen Zugang soll das Verbrennungsverhalten von nach-haltigen Kraftstoffen untersucht werden. Das Interesse an solchen nachhaltigen Kraftstoffen hat in den letzten Jahren aufgrund des regulatorischen Drucks zur Emissionsreduzierung deutlich zugenommen, sodass zahlreiche simulative, thermodynamische und optische Untersuchungen von erneuerbaren Kraftstoffen meist an PKW- und LKW Motoren durchgeführt worden sind. Der Fokus dieser Arbeit liegt auf gasförmigen, Wasserstoff basierten Kraftstoffen, insbeson-dere Methan und Mischungen von Wasserstoff mit Methan, mit ihrem großen Potential einer nachhaltigen wasserstoffbasierten Energieversorgung. Abbildung 13 fasst relevante Untersu-chungen an funkengezündeten Motoren in Abhängigkeit der verwendeten Hubraumklasse, un-tersuchten maximalen H_2-Gehalte, der Untersuchungsart (optisch/thermodynamisch) und des realisierten effektiven bzw. indizierten Mitteldruckes zusammen. Diese Übersicht macht zudem noch einmal deutlich, dass optische Untersuchungen von Großmotoren ein bisher noch wenig genutztes Potential bieten.
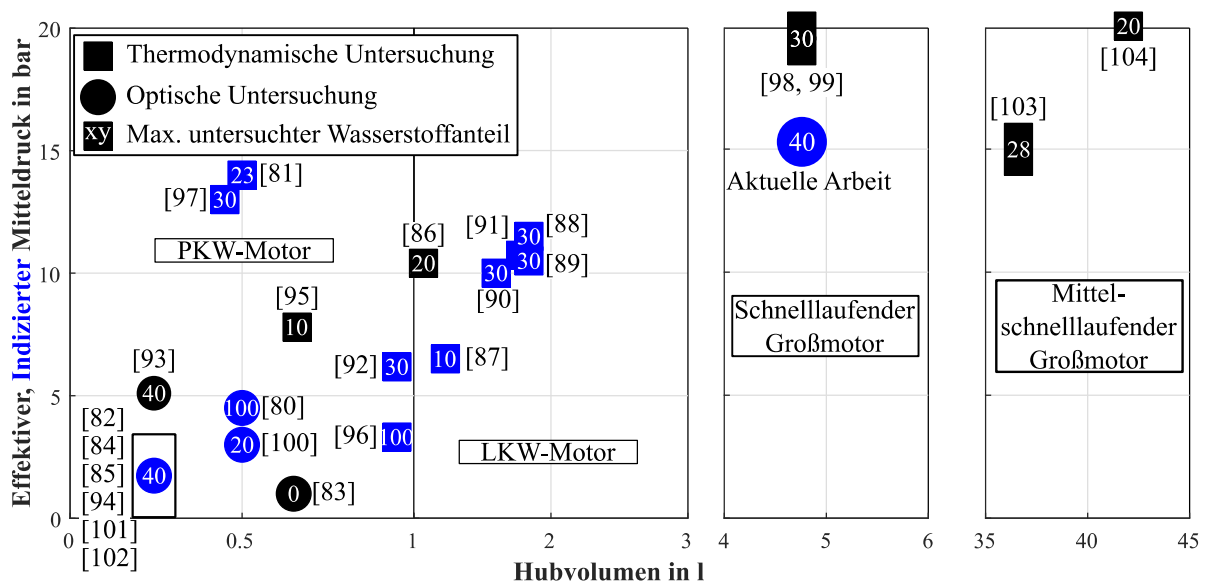
Abbildung 13 Übersicht durchgeführter Untersuchungen [80–104]

2.5.1 Motorische Verbrennung von Wasserstoff/Methanmischungen

Die Verbrennung von Methan-Wasserstoffgemischen folgt je nach Mischungsanteil den Reak-tionspfaden der Methanverbrennung. Der Hauptpfad der C1-Reaktionen (vgl. Abbildung 14) gibt dabei ausreichend die Verbrennung von überstöchiometrischen und stöchiometrischen Ge-mischen wieder (vgl. [105]). In unterstöchiometrischen Gemischen kommt es zur Rekombina-tion des CH_3 Radikals mit anderen CH_3 Radikalen zu Ethan C_2H_6 und damit zu einer Ketten-verzweigung und dem C2-Reaktionspfad, welcher unter anderem zu Rußbildung führt. Generell dominieren wenige Hauptreaktionen den parallelen und zum Teil konkurrierenden Ablauf der Reaktionen. Diese beschränken sich auf den Verbrauch von CH_4 und O_2 und die Oxidation von

CO zu CO_2. Diese bestimmen zudem die Kettenverzweigung und den Reaktionsabbruch und damit die Reaktionsgeschwindigkeit. Für die reine Methanverbrennung läuft die Oxidation zu CO hauptsächlich über den C1-Hauptpfad. [105, 106] In Abhängigkeit der Verbrennungsrandbedingungen, wie dem Luftanteil, der Temperatur und des Druckes, sowie dem Vorhandensein weiterer Kraftstoffe wie Wasserstoff, verschieben sich die Gleichgewichtsreaktionen und damit die Konzentration bestimmter Radikale (insbesondere des OH* Radikals) und schließlich die Produkte bzw. Emissionen.

Abbildung 14 C1 und C2 Reaktionspfad der Methanverbrennung und eingezeichnete Radikale nach [107, 105]

Garcia-Armingol et al. [108, 109] beschreibt die Auswirkungen einer Wasserstoffzumischung auf die vorgemischte Methanverbrennung und deren globale Intensitäten der Flammeneigenstrahlung in ein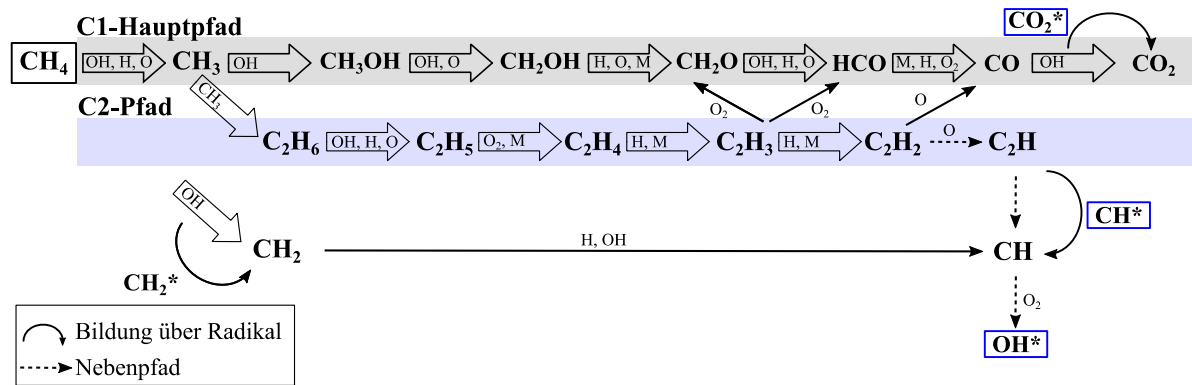em kontinuierlichen Brenner. Hier wird festgestellt, dass global mit zunehmendem Wasserstoffanteil die Kohlenstoffbasierten Radikale (CH*, C_2*, CO_2*) abnehmen und damit die Intensitäten der in Abbildung 2 dargestellten Banden. Bis 40 %$_V$ Wasserstoff sind noch geringe Restintensitäten der CH*- und C_2* Radikale vorhanden, welche ab 50 %$_V$ beinahe vollständig verschwinden. Das gleiche Verhalten wird von Ballester et.al. [110] in einer Brennkammer gezeigt. Die Intensität der Hydroxylradikale geht mit zunehmendem Wasserstoffanteil ebenso zurück, obwohl die Produktion aufgrund des vermehrten Wasserstoffangebotes steigen müsste. In Summe wird die Konzentration der OH*-Radikale aber nicht höher, da die Reaktion (14) aufgrund mangelnder CH*-Radikale nicht stattfindet. Oh et al [111] zeigt an einer nicht vorgemischten Flamme, dass mit zunehmender Wasserstoffkonzentration die lokale OH*-Radikal Konzentration steigt, wohingegen die globale sinkt. Dies wird der Abhängigkeit der OH*-Radikal Bildung von den CH*-Radikalen (vgl. Reaktion (14)) zugeschrieben, welche hauptsächlich in der Reaktionszone der Flamme abläuft.

$$CH^* + O_2 \leftrightarrow OH^* + CO \tag{14}$$

Reyes et.al [112] zeigt in einer Brennkammer mit konstantem Volumen die Auswirkungen der Wasserstoffzumischung bis 100 %$_V$ zu Erdgas auf die Emissionsintensität der OH*- und CH*-Radikale. Hier wird eine Zunahme der lokalen OH*-Intensität vor allem für Mischungen größer 50 %$_V$ beobachtet. Ähnliches wird auch in [113] gezeigt. Anstelle der aus der Methanverbrennung bekannten Radikale treten Spektren im Infrarotbereich bis 600 nm auf. Diese stammen nach [46, 43, 108] aus der Anregung des erhöhten Wasseranteils.

2.5.2 Übersicht und Ergebnisse durchgeführter Untersuchungen

Die auf den Kraftstoffeigenschaften basierenden Auswirkungen von Wasserstoffbeimischungen auf das Brennverhalten sind in der Literatur mit optischen und thermodynamischen Untersuchungen evaluiert worden. Einige ausgewählte Ergebnisse mit Fokus auf optische Untersuchungen sollen in diesem Abschnitt kurz zusammengefasst werden.

Untersuchungen an PKW-Motoren

Untersuchungen an volloptisch zugänglichen PKW-Motoren sind hauptsächlich mit Zündkerze und PFI Einbringung des Wasserstoff/Methangemisches in einem Verhältnis von 0 bis zu 40 %$_V$ durchgeführt worden.

In [97] werden die Einflüsse der Wasserstoffzumischung von 5 %$_V$, 10 %$_V$ und 20 %$_V$ auf die Flammenfrontgeschwindigkeiten untersucht. Es wurde eine Geschwindigkeitserhöhung mit steigendem Wasserstoffanteil gegenüber reinem Methan festgestellt. Für die Untersuchungen werden Hochgeschwindigkeitskameras mit UV-Bildverstärkern verwendet. Es wird eine stärkere Flammenfrontfaltung sowohl bei zunehmendem Wasserstoffanteil, als auch noch stärker ausgeprägt bei höheren Luft-Kraftstoff Verhältnissen gezeigt. Zudem steigt mit zunehmenden Wasserstoffanteilen die Eindringtiefe der Flamme in das Feuerstegvolumen und reduziert THC-Emissionen gegenüber einer reinen Methanverbrennung. Aufgrund der Verwendung eines volloptischen Motors mit Glaskolben und vergrößerten Spaltvolumina fällt der Effekt im Vergleich zu einem Thermodynamik-Motor jedoch überproportional hoch aus. Martinez [114] bestätigt die Ergebnisse aus [97] und weist ebenso mit einem volloptisch zugänglichen PKW Motor die Zunahme der Flammenfrontfaltung unter Erhöhung des Wasserstoffgehalts von 25 %$_V$ und 50 %$_V$ nach.

Di Iorio [101, 98] untersucht an einem volloptisch zugänglichen PFI SI PKW Motor die Flammenfrontausbreitung mittels Spektroskopie des Flammeneigenleuchtens vom UV- bis hin in den sichtbaren Bereich. Die Untersuchungen beinhalten Versuche mit reinem Methan als Referenz und Wasserstoffbeimischungen von 20 %$_V$ und 40 %$_V$, welche unter stöchiometrischen Bedingungen verbrannt werden. Im UV-Bereich zeigen das natürliche OH* (@310 nm) und das CH* (@431 nm) Radikal als Indikatoren der Flammenfront deren Ausbreitung im Brennraum. In den optischen Aufnahmen wird eine für höhere Wasserstoffanteile beschleunigte radiale Ausbreitung der Flammenfront hin zu den Brennraumwänden gegenüber einer Verbrennung mit reinem Methan beobachtet. Dies wird durch die gesteigerte laminare Brenngeschwindigkeit der Mischungen erklärt. Die höhere Brenngeschwindigkeit wird auf die vermehrte Bildung von Wasserstoff, Sauerstoff und Hydroxyl Radikale zurückgeführt, welche die Kettenverzweigungsreaktionen der Verbrennung begünstigen. Methan zeigt im Gegensatz zu den Mischungen eine stärker gefaltete Flammenfront im Gegensatz zu den Untersuchungen aus [97]. Erklärt wird dies über vier Effekte, welche zu einer gleichmäßigeren Ausbreitung der Flammenfront durch Wasserstoffbeimischung führen können:

1. Die schnellere laminare Brenngeschwindigkeit des Wasserstoffs.
2. Die geringere Entflammungsenergie und weitere Zündgrenzen von Wasserstoff bedingen eine bessere Zündung nicht verbrannter Kraftstoffbereiche.

3. Die durch Wasserstoffzumischung mögliche dickere Flamme (vgl. [115]) reagiert weniger intensiv auf lokale Schwankungen der Turbulenz.

4. Die hohe Diffusivität des Wasserstoffs von 3,8-mal der von Methan, welche eine schnellere Durchmischung unverbrannter Zonen mit Wasserstoff fördert und damit über ein homogeneres Gemisch für eine schnellere Zündung sorgt.

Untersuchungen an Großmotoren

Für einen Vollmotor mit 36,3 l je Zylinder hat Portin [102] den Effekt einer Wasserstoffzumischung von bis zu 60 %$_V$ zu Erdgas gezeigt. Mit steigender Zumischung wurde ein besserer Wirkungsgrad unter einem Stickoxid äquivalenten Betrieb bei gleichzeitiger Reduzierung der THC Emissionen erreicht. Die Motorregelung wurde auf die geringere Klopffestigkeit des Brenngases angepasst, wobei Vorzündungen zur Einschränkung des Betriebsbereichs führten.

Wahl [103] untersucht an einem 42,3 l mittelschnelllaufenden Großmotor mit gespülter Vorkammer die Auswirkungen von 10 %$_V$ und 20 %$_V$ Wasserstoffbeimischung gegenüber reinem Erdgas. Durch die Zumischung von Wasserstoff wird eine höhere Klopfneigung festgestellt, welche durch eine Verschiebung des Zündzeitpunktes kompensiert wird. Mit höheren Anteilen Wasserstoff wird eine Stabilisierung der Verbrennung beobachtet, was in einer Erweiterung der Magerlaufgrenze resultiert. Für einen Stickoxid äquivalenten Betrieb kann aufgrund der geringen Zunahme der Stickoxidemissionen bei der untersuchten Wasserstoffbeimischung diese durch die Stabilisierung der Verbrennung über ein Abmagern der Betriebspunkte oder frühere Zündzeitpunkte kompensiert werden. In diesem Betrieb zeigen erst Verbrennungsluftverhältnisse über 2.1 eine Reduktion der THC Emissionen. Dies wird durch die eingeschränkten Anpassungsmöglichkeiten des Zündzeitpunktes (NOx äquivalenter Betrieb) erklärt, welcher erst mit höheren Verbrennungsluftverhältnissen aufgrund geringerer Verbrennungstemperaturen wieder hin zu späteren Zeitpunkten verschoben werden kann.

Korb und Kawauchi [82, 87] untersuchen an einem 4,8 l Einzylinder und an einer RCEM die Beimischung von 10 und 30 %$_V$ Wasserstoff zu Erdgas. Neben den bekannten Effekten wie

- der Erweiterung der Magerlaufgrenze
- der Reduzierung der THC Emissionen von bis zu 44% bei einer Beimischung von 30 %$_V$
- des kürzeren scheinbaren Zündverzugs und der kürzeren Brenndauer

werden Vorzündungen beschrieben, welche die Betriebsgrenzen weiter einschränken. Mittels der Schlieren Messtechnik wurden in der RCEM Flammenkerne außerhalb der Flammenfront beobachtet, welche eine Selbstzündung dieser Bereiche belegen. Die Häufigkeit der Selbstzündung steigt mit zunehmendem Wasserstoffanteil. Jedoch führen diese nicht zu ähnlich starken Druckanstiegen, wie sie im Motor noch vor der Hauptverbrennung beobachtet worden sind. Ein weiterer Erklärungsansatz für die Vorzündungen ist die für erhöhte Anteile von Wasserstoff höhere Verbrennungstemperatur, welche zur Hot Spot Bildung im Brennraum und dadurch Selbstentzündung führen kann.

2.5.3 Zusammenfassung

Die Zumischung von Wasserstoff zu Erdgas oder regenerativ erzeugtem Methan zur Anwendung in einer motorischen Verbrennung weist aufgrund der Kraftstoffeigenschaften des Wasserstoffes eine erhöhte Gefahr für anormale Verbrennung in Form von Klopfen, Vorentflammung oder Rückzündung [116] auf. Wie im vorangegangenen Abschnitt dargestellt, erweist sich die Vorentflammung als der den Betriebsbereich begrenzende Faktor für PFI Motoren mit Zündkerze oder ungespülter Vorkammer. Neben den Risiken bietet die Zumischung aber auch einige Vorteile für die Verbrennung hinsichtlich Wirkungsgrad und Emissionen. Abbildung 15 fasst basierend auf den Kraftstoffeigenschaften des Wasserstoffes ohne Berücksichtigung des Brennverfahrens die Auswirkungen der Kraftstoffeigenschaften des Wasserstoff bei Zumischung zu Methan bzw. Erdgas vereinfacht zusammen. Tabelle 1 zeigt zudem die unterschiedlichen Kraftstoffeigenschaften von Methan im Vergleich zu Wasserstoff. Die deutlich reduzierte Dichte des Wasserstoffs gegenüber Methan zeigt, dass der massenbezogene Heizwert um 41,67 % höher ist. Die um den Faktor 4,86 erhöhte laminare Brenngeschwindigkeit des Wasserstoffs hat hier positive Auswirkung auf die Brenndauer, die Magerlaufgrenze und damit auf den Wirkungsgrad von mit Wasserstoffmischungen betriebenen Motoren. Zudem erweitert die geringere Zündenergie von Wasserstoff die Magerlaufgrenze gegenüber des aufgrund seiner Tetraeder Struktur ansonsten stabileren und damit zündunwilligeren Kraftstoffs Methan.
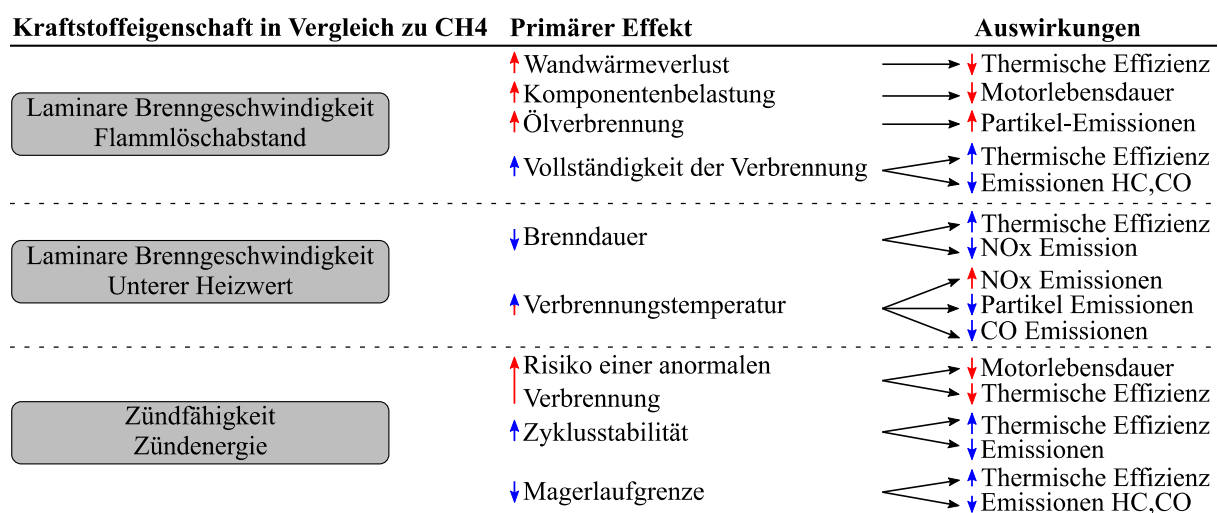
Abbildung 15 Auswirkungen der Kraftstoffeigenschaften von Wasserstoff auf die innermotorische Verbrennung bei der Zumischung zu Methan im Vergleich zu reinem Methan (Negativ, Positiv)

Tabelle 1 Kraftstoffeigenschaften von Methan CH_4 und Wasserstoff H_2 (vgl. [117])

Kraftstoffeigenschaften	H_2	CH_4
Dichte in kg/m³	0,08	0,65
Zündfähigkeit in Luft in %$_V$	4-75	5-15
Selbstzündtemperatur in Luft in K	858	813
Minimale Zündenergie in mJ	0,02	0,28
Laminare Brenngeschwindigkeit in m/s	1,85	0,38
Adiabate Flammentemperatur in K bei $\lambda = 1$	2390	2226
Flammlöschabstand in mm	0,64	2,03
Unterer Heizwert MJ/kg	120	50

3 Ziele der Forschungsarbeit

In den Abschnitten 2.1 und 2.5 wird gezeigt, dass der optische Zugang eines Verbrennungsmotors als Grundvoraussetzung für die Anwendung optischer- und laseroptischer Messverfahren dient. Mittels dieser Messverfahren werden vor allem im PKW und LKW Hubraumklassenbereich Maßnahmen zur Verbesserung der Gemischbildung, Entflammung, Verbrennung und Emissionsreduzierung konventioneller und erneuerbarer synthetischer Kraftstoffe phänomenologisch charakterisiert, bewertet und optimiert. Mit den Ergebnissen werden Modelle und Simulationstools zur Vorausberechnung künftiger neuer Motorgenerationen validiert und weiterentwickelt. Jedoch zeigen die veränderten Größen- und Zeitskalen abweichende Effekte in Großmotoren wie (vgl. [118]):

- vergrößerte Entflammungswege und deren Auswirkungen auf die Entflammung, Flammenausbreitung und Durchbrand, und damit auf die innermotorische Emissionsentstehung
- vergrößerte Spaltvolumina aus den an die Größenverhältnisse angepassten Toleranzen und den damit einhergehenden größeren, nicht von der Flammenfront erfassten Bereichen, welche direkt auf die innermotorischen Emissionen angerechnet werden müssen
- verändertes Temperatur- und Energiedichte-Niveau

Daher ist ein Übertrag der Erkenntnisse aus Untersuchungen an kleinhubigen Triebwerken nicht ausreichend, um Verbrennungsphänomene in Großmotoren detailliert beschreiben und nachvollziehen zu können. Dies gewinnt insofern an aktueller Bedeutung, als dass Großmotoren betrieben mit nachhaltig erzeugten synthetischen Kraftstoffen im Rahmen eines Sektorübergreifenden Ansatzes ausschlaggebend zu einer umweltfreundlichen Energieversorgung beitragen können. Damit werden Untersuchungen an optischen Großmotoren im Rahmen der Verbrennungsoptimierung synthetischer Kraftstoffe für Großmotoren notwendig. Bisher ausgeführte Konzepte der optischen Zugänglichkeit dargestellt in Abschnitt 2.1 führen zu folgenden identifizierten Restriktionen:

Die **Komplexität** der in PKW und LKW Motoren häufig umgesetzten volloptischen Zugänge nach dem Bowditch Prinzip vervielfacht sich für Großmotoren mit der Zunahme der Abmessungen. Aufgrund der Zunahme der Abmessungen verteuern sich die Bauteile. Der konstruktive und fertigungstechnische Aufwand nehmen ebenfalls zu.

Die **Reduktion der Vergleichbarkeit** eines volloptischen Zugangs nach Bowditch kann z.B. für Grundlagenuntersuchungen der Entflammung durch verschiedene Zündquellen in Kauf genommen werden. Realitätsnahe Untersuchungen wie z.B. des Flammenausbrandes oder der Interaktion des Schmieröls mit der Verbrennung und deren Auswirkungen können dagegen nicht sinnvoll abgebildet werden.

Das **limitierte Sichtfeld** häufig eingesetzter endoskopischer Zugänge führt durch die größere Dimension eines Großmotors zur Notwendigkeit der Fokussierung auf bestimmte Bereiche des Brennraums und zur Vernachlässigung anderer. Für eine ganzheitliche Betrachtung zur Identifizierung von der die Verbrennung beeinflussenden Effekten müssen mehrere Zugänge geschaffen und entweder synchron oder sequentiell in unterschiedlichen Experimenten aufgenommen werden. Der Aufwand und die Komplexität der Versuche steigen an.

Um die Durchführung von Untersuchungen zur Generierung von neuen Erkenntnissen über die Verbrennung synthetischer erneuerbarer Kraftstoffe als Grundlage weiterer Optimierungen zu erleichtern, werden folgende Ziele mittels der vorliegenden Arbeit verfolgt:

- Entwicklung eines kompakten optischen Zugangs an Großmotoren mit weniger konstruktivem Aufwand gegenüber dem bekannten Bowditch Prinzip, bei gleichzeitig hohem Vergleichspotential zum thermodynamischen Pendant und maximalem Sichtfeld im Vergleich zu reinen Endoskop-Lösungen.

- Ableiten eines simulativ gestützten Auslegungs- und Absicherungsverfahrens zur Gewährleistung des optimalen Designs hinsichtlich Festigkeit, Sichtfeld, optischer Abbildungsqualität und Betriebssicherheit.

- Aufbau und Inbetriebnahme des Konzepts an einem Prüfstand für mittelschnelllaufende Großmotoren.

- Ableiten einer Betriebsstrategie für den optischen Motor und Nachweis der Funktionalität des Prüfstandes.

- Experimentelle Untersuchungen des synthetischen Dieselersatzkraftstoffes OME zur Dekarbonisierung eines mittelschnelllaufenden DF Großmotors.

- Entwicklung einer Postprocessing Toolbox zur Evaluierung der Messdaten.

- Übertragung und Weiterentwicklung des Konzeptes auf einen Motor geringeren Hubraums.

- Experimentelle Untersuchung der Vergleichbarkeit des neu entwickelten optischen Zugangs.

- Realitätsnahe experimentelle Untersuchung von Wasserstoff/Methanmischungen mit dem neu entwickelten optischen Zugang zur Verifizierung der erfolgreichen Umsetzung.

4 Ergebnisse der Entwicklung und Versuchsauswertung

In Abschnitt 2.1 ist zusammenfassend dargestellt worden, welche optischen Zugangsarten für Großmotoren bereits realisiert worden sind und welche Anforderungen sich an die Entwicklung eines alternativen Konzeptes stellen. In **[12]** wird anhand dieser Anforderungen ein Bowditch Konzept für einen mittelschnelllaufenden Großmotor konzeptioniert und zwei alternativen optischen Zugängen gegenüber gestellt. Anhand der Kriterien der Vergleichbarkeit zwischen optisch zugänglichem Motor und thermodynamischen Pendant, der Sichtfläche und der Komplexität der Aufbauten wird das im weiteren Verlauf realisierte und weiterentwickelte Konzept ausgewählt. Die Realisierung und Anwendung wird in den nachfolgenden Abschnitten aufgezeigt und ist Kernbestandteil dieser Arbeit.

4.1 Realisierung eines kompakten optisch voll zugänglichen mittelschnelllaufenden Großmotors

Die Veröffentlichung *Realization of a Fully Optically Accessible Medium Speed Large Bore Engine Using a Fisheye Optic*, 2020 erschienen als Konferenzbeitrag der virtuellen 28. Konferenz zu Nukleartechnik verbunden mit der ASME 2020 Power Conference **[119],** beschreibt die Realisierung und Verifizierung des in **[12]** konzipierten kompakten volloptischen Zugangs für Großmotoren. Abbildung 16 zeigt den volloptischen Zugang mit Fisheye Optik für den MAN 35/44 DF. Dieser besteht aus zwei Teilen. Der seitliche Zugang, umgesetzt als Ring zwischen Zylinderkopf und Zylinderlaufbuchse, nimmt die vier optischen und senkrecht zueinanderstehenden Fenster mit Zylinderlinse auf. Die Entwicklung und ein Anwendungsbeispiel unter Serienlast des MAN 35/44DF wurden in **[120]** detailliert beschrieben. Die Fisheye Optik mit 54 mm Durchmesser der ersten Linse kann zusätzlich zu den seitlichen optischen Zugängen anstelle des Hauptinjektors in einen modifizierten Zylinderkopf integriert werden.
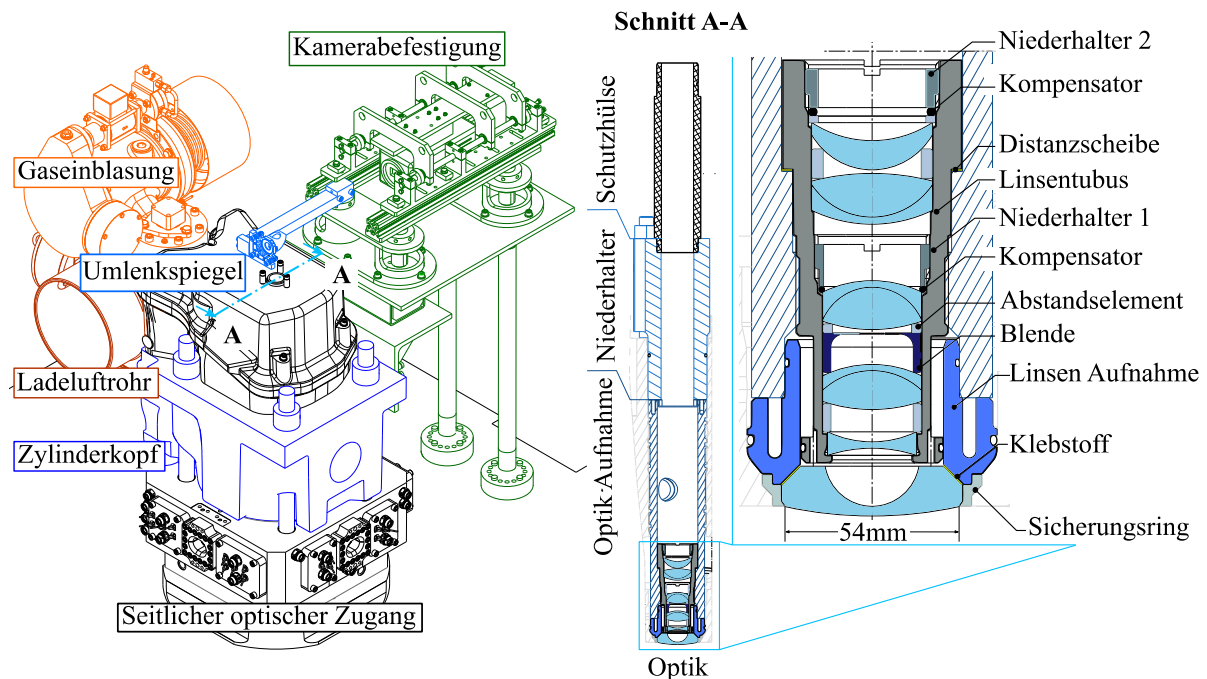

Abbildung 16 Aufbau des volloptischen mittelschnelllaufenden Großmotors

Die Optik wurde auf diesen Durchmesser zusammen mit einer Festigkeitsbetrachtung des Zylinderkopfes optimiert und der notwendige Skipped Fire Betrieb des optischen Aufbaus simulativ evaluiert. Mit den 54mm Durchmesser der ersten Linse wird ein 180° Sichtfeld in den Brennraum während eines Motorbetriebs unter einem reduzierten Spitzendruck von 170 bar realisiert. Die Entwicklung der Optik nach dem Retrofokus Prinzip wird in der Veröffentlichung beschrieben und resultiert in einer Länge der Optik von 127,4 mm, einer Bildgröße von 20 mm im Durchmesser und einer Blendenzahl f# von 2,2. Die Bewertung der optischen Eigenschaften zeigt eine ausreichende Abbildungsqualität mit einer MTF größer der Kontrastgrenze von 0,2 bis zur Auflösungsgrenze der verwendeten Kamera.

Die simulativen Festigkeitsuntersuchungen sind mit zwei experimentellen Aufbauten zur Charakterisierung der kritischen Temperaturen für die Bauteilfestigkeit für zwei Laststufen (85 % und 40 % der Nominallast) überprüft worden. Der erste Aufbau nutzt einen nicht an die Fisheye Optikaufnahme angepassten Zylinderkopf. Dieser weist Temperaturmessstellen nahe des Flammdecks an Positionen auf, welche durch die Integration der Optik im modifizierten Zylinderkopf nicht mehr vorhanden sind. Der zweite Aufbau nutzt den optischen Aufbau mit einer Stahllinse und darin integrierten Thermoelementen. Ein in die Linsenaufnahme integriertes Thermoelement nahe der Klebestelle zwischen erster Linse und Aufnahme wird verwendet, um die Temperatur an dieser betriebskritischen Stelle zu überwachen.

Der Vergleich der simulativen und der experimentellen Ergebnisse zeigt Unterschiede aufgrund der gewählten Randbedingungen. Simulation und Versuch zeigen jedoch eine ausreichende ertragbare Betriebsdauer bei Heranziehen der Messwerte des Thermoelementes in der Linsenaufnahme, welches für die automatisierte Betriebsstrategie des Motors verwendet wird. Eine experimentelle Lastvariation unter konstantem Verbrennungsluftverhältnis von 2,3 bestimmt die jeweils mögliche gefeuerte Betriebsdauer bis zum Erreichen der festigkeitsbedingten Temperaturgrenze von 200 °C am Flammdeck. Unter 85 % Nominallast können bis zu 16s gefeuerter Motorbetrieb unter den gewählten Randbedingungen realisiert werden. Damit stehen 50 Arbeitsspiele als Einschwingphase und weitere 50 aufeinanderfolgende Arbeitsspiele für die Aufnahme der Bilder bei einer Motordrehzahl von 750 U/min zur Verfügung.

Die Funktionsfähigkeit der Optik und des gesamten Aufbaus konnte mit der angepassten Betriebsstrategie durch erste Aufnahmen der natürlichen Flammeneigenstrahlung der DF-Verbrennung mit vorgemischtem Erdgas und DMA Pilotzündung gezeigt werden. Die Aufnahmen zeigen die für eine Fisheye Optik charakteristische tonnenförmige Verzeichnung, sodass eine entsprechende Entzerrung der Bilder für weitere optische Auswertungen notwendig ist.

Individueller Beitrag: Der Verfasser dieser Arbeit hat die vorliegende Veröffentlichung angefertigt. Die Ausarbeitung, die Durchführung der Simulationen, deren Auswertung, Interpretation und das Ableiten der Randbedingungen für die Betriebsstrategie sind durch den Verfasser der vorliegenden Arbeit durchgeführt worden. Die Implementierung der Betriebsstrategie am Versuchsmotor bei der MAN Energy Solution SE erfolgte durch Hr. Dr.-Ing. Friedrich. Die experimentellen Untersuchungen sind von Hr. Dr.-Ing. Friedrich bei der MAN Energy Solution SE in Abstimmung mit dem Verfasser der Arbeit durchgeführt worden. Die Auswertung und Interpretation der Messdaten wurden durch den Verfasser der vorliegenden Arbeit durchgeführt.

4.2 Mie Streulicht Untersuchungen an DMA und OME$_{3-5}$ Pilotkraftstoffstrahlen am mittelschnelllaufenden DF Motor

Weitere Untersuchungen sollen das Potential des entwickelten kompakten volloptischen Zugangs für Großmotoren für die optische Verbrennungsdiagnostik aufzeigen. Die Veröffentlichung *Development of an Optical Investigation Method for Diesel and Oxymethylen Ether Spray in a Large-Bore Dual-Fuel Engine Using a Fisheye Optical System,* erschienen 2022 im International Journal of Engines der SAE **[121]**, beschreibt die Anwendung der entwickelten Optik für Mie-Streulichtaufnahmen von DMA und OME$_{3-5}$ Pilotkraftstoffstrahlen in einem MAN 35/55DF Einzylinder Versuchsmotor. Es wird zudem die Entwicklung eines Auswertungs-Algorithmus gezeigt, welcher es ermöglicht, von den verzerrten zweidimensionalen Aufnahmen der Fisheye Optik eine virtuelle dreidimensionale Rückprojektion in den Brennraum des Motors zu berechnen. Dieser basiert auf den in den Abschnitten 2.4.4 und 2.4.5 gezeigten Abbildungseigenschaften. Zudem wird die Annahme getroffen, dass die beiden betrachteten Einspritzstrahlen eine Ebene aufspannen, deren Lage durch die Düsengeometrie vorgegeben ist. Abbildung 17 beschreibt das Vorgehen der virtuellen dreidimensionalen Rückprojektion.
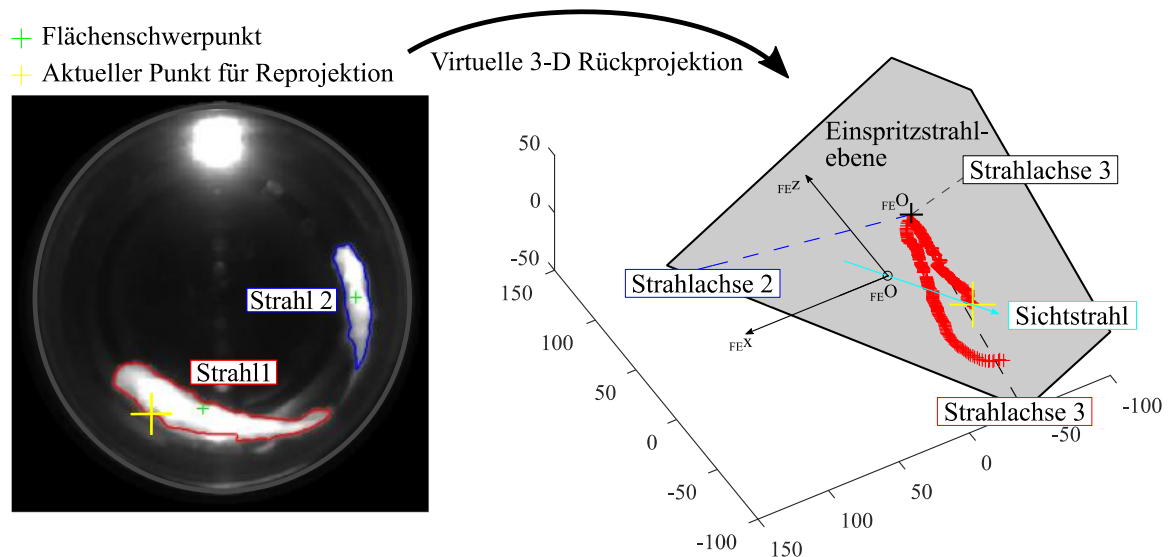
Abbildung 17 Prinzip der virtuellen dreidimensionalen Rückprojektion (PI=Pilotinjektor, FE=Fisheye)

Die experimentellen Untersuchungen sind unter gleicher Energiemenge und gleicher Kraftstoffmasse der beiden Pilotkraftstoffe DMA und OME$_{3-5}$ durchgeführt worden.

Aufgrund der um den Faktor 1,9 höheren Dichte von OME$_{3-5}$ gegenüber DMA verlängert sich die notwendige Einspritzdauer des Dreilochinjektors. Dies wirkt sich wiederum auf die Zündung des vorgemischten Erdgas-Kraftstoffgemisches aus und führt je nach gewählten Einspritzparametern zu einer veränderten Verbrennung und Emissionsentstehung.

Unter einer konstanten Kraftstoffmasse beider Pilotkraftstoffe, zeigt sich für DMA ein tieferes Eindringen der flüssigen Phase als für OME$_{3-5}$, was zu einem besseren Strahlaufbruch und einer besseren Erfassung der vorgemischten Zylinderladung während des Zündvorgangs führt. Die Erhöhung des Einspritzdruckes hat nur geringe Auswirkungen auf die Eindringtiefe. Für einen Einspritzdruck von 1600 bar zeigt sich für DMA eine für Strahl 1 um 11,25 % geringere Ein-

dringtiefe als unter 1200 bar. Die aus dem höheren Einspritzdruck stammende erhöhte Geschwindigkeit führt zu kleineren Kraftstofftröpfchen und damit zur schnelleren Verdampfung des Kraftstoffes. Des Weiteren führt ein späterer Einspritzbeginn bei 25 °KW vZOT zu höheren Brennraumtemperaturen, was die Verdampfung des Kraftstoffes weiter unterstützt. Weiter bremst ein höherer Brennraumdruck bei späteren Einspritzzeitpunkten den flüssigen Anteil des Kraftstoffstrahls ab und reduziert so die flüssige Eindringtiefe.

Bei gleichem Einspritzdruck und Variation des Einspritzzeitpunktes wird die mittlere flüssige Eindringtiefe beider Kraftstoffe aufgrund des höheren Gegendrucks und höherer Verdampfungsanteile reduziert. Im Schnitt ist die mittlere flüssige Eindringtiefe für den höheren Kraftstoffdruck unterhalb der Messungenauigkeit von 2,1 mm, welche hauptsächlich aus der Kalibrierung der Optik resultiert, und wird damit als praktisch identisch betrachtet.

DMA weist gegenüber OME_{3-5} einen um den Faktor 2,19 geringeren Energieinhalt auf. Dies macht eine Erhöhung der Kraftstoffmasse zum Erreichen des gleichen Energieinhaltes notwendig. Unter gleicher Energiemenge zeigt der Injektor für DMA aufgrund der geringeren Kraftstoffmasse und der damit verbundenen geringsten Bestromungszeit unter höchstem Einspritzdruck eine geringere Verdampfungsneigung als für die Untersuchungen unter äquivalenter Kraftstoffmasse. Dies kann am Betrieb des Injektors nahe der minimalen Betriebsgrenze liegen. Das Verhalten des Pilotkraftstoffes folgt damit den erwarteten und in der Literatur an Einspritzkammerprüfständen beobachteten Ergebnissen. Damit ist die Leistungsfähigkeit des entwickelten optischen Zugangs in Kombination mit der implementierten Auswerteroutine bestätigt worden.

Individueller Beitrag: Der Verfasser dieser Arbeit hat die vorliegende Veröffentlichung angefertigt. Die Ausarbeitung, die Entwicklung der Auswerteroutine, die Durchführung der Versuche, deren Auswertung und Interpretation sind durch den Verfasser der vorliegenden Arbeit durchgeführt worden. Die experimentellen Untersuchungen wurden von Hr. Dr.-Ing. Weber bei der MAN Energy Solution SE begleitet. Hr. Dr. Stürzl hat in Diskussionen und seinem Review zur Entwicklung der Auswerteroutine beigetragen.

Wie Abschnitt 4.2 zeigt, ist die Kombination einer Fisheye Optik mit einem seitlichen optischen Zugang ein vielversprechender Ansatz für die Verbrennungsdiagnostik an Großmotoren. Aus diesem Grund soll das entwickelte Konzept im Weiteren für einen schnelllaufenden Großmotor verkleinert, optimiert und für erste Untersuchungen des Einflusses von Wasserstoffbeimischungen zu Methan auf das Brennverhalten angewandt werden. Zudem soll eine Abschätzung vorgenommen werden, inwiefern der optisch zugängliche Motor mit dem thermodynamischen Pendant vergleichbar bleibt, um die Aussagekraft solcher Untersuchungen zu verifizieren.

4.3 Realisierung eines optisch vollzugänglichen schnelllaufenden Großmotors

Die Optimierung des Zugangs aus Abschnitt 4.1 hinsichtlich mechanischer Integration sowie der Optik ist in der Veröffentlichung *Design of an Endoscopic Fully Optically Accessible High-Speed Large-Bore Engine* beschrieben [122]. Diese ist 2022 im SAE International Journal of Engines erschienen. Der Zugang ist für einen Forschungsmotor des Lehrstuhls für Verbrennungskraftmaschinen der TUM auf Basis der MTU 4000 Baureihe verkleinert und verbessert worden.

Der seitliche Zugang wird über einen Ring zwischen Zylinderkopf und Zylinderlaufbuchse umgesetzt. Für ein maximales Sichtfeld, wird ein UV-optimiertes Endoskop der Firma LaVision mit einem Öffnungswinkel von 50 ° verwendet. Es wird zeitgleich das Flammeneigenleuchten und die natürliche OH*-Chemilumineszenz über einen optischen Zugang mit Hilfe eines Strahlteilers aufgenommen.

Die Erweiterung des seitlichen Zugangs um das Fisheye Endoskop, das anstelle des Auslassventils integriert wird, erfordert eine Anpassung des Zylinderkopfes und des Ventiltriebes(vgl. Abbildung 18). Dies hat erhebliche Einflüsse auf das Ladungswechselverhalten des Motors. Diesem wird mittels Absenken des Abgasgegendrucks auf Umgebungsbedingungen und dem Vergrößern des Ventilhubs des verbliebenen Ventils begegnet.
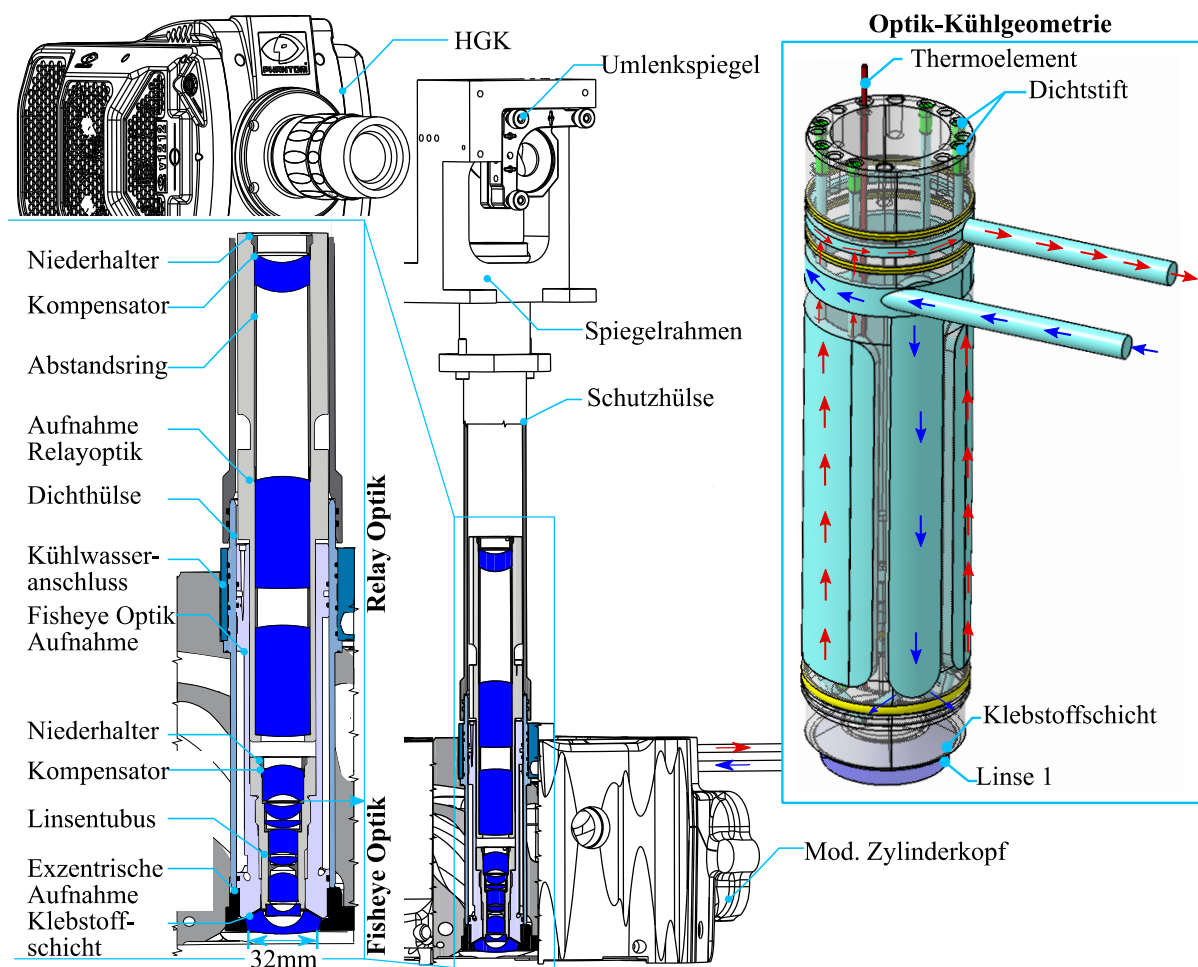

Abbildung 18 Fisheye Optik Zugang am schnelllaufenden Großmotor (HGK=Hochgeschwindigkeitskamera)

Der Effekt der Maßnahmen ist mittels CFD-Strömungssimulationen untersucht und bewertet worden. Mit einem erhöhten Massenstrom des im Zylinder befindlichen Restgases in den Ansaugtrakt um 33 % und einer Abweichung des Abgasmassenstroms um 0,4 % gegenüber dem thermodynamischen Pendant ohne Modifikationen werden die Maßnahmen als ausreichend für einen Versuchsbetrieb betrachtet.

Aufgrund des silkonbasierten Hochtemperaturklebstoffes, welcher zum Haltern der ersten Linse in der Aufnahme der Fisheye Optik verwendet wird, müssen die thermischen Belastungen über einen Skipped Fire Motorbetrieb ähnlich dem in Abschnitt 4.1 reduziert werden. Weiter ist die Absenkung des Verbrennungsspitzendruckes auf 170 bar aufgrund der Modifikationen des Zylinderkopfs zur Integration der Optik aus Festigkeitsgründen unerlässlich.

Die Optik weist eine Blendenzahl von 2,2, eine numerische Apertur von 0,18 und einen effektiven Fokus von 4 mm auf. Die reine Fisheye Optik erzeugt ein Bild mit einem Durchmesser von 9 mm. Dieses wird durch die Relay Optik mit dem Faktor 2:1 vergrößert. Damit konnte gegenüber der Optik aus Abschnitt 4.1 der Durchmesser der ersten Linse um 40,7 % verringert werden. Zudem ist die hier eingesetzte Linse aufgrund der kleineren Fläche stabiler und damit aus Quarzglas ausführbar, günstiger und besser verfügbar.

Die MTF Werte der kombinierten Einheit weisen nach der in Abschnitt 2.4.2 gezeigten 30/50 Regel für den maximalen Feldwinkel ein gutes Auflösungsvermögen auf. Die Seidl –Aberrationen zeigen für das Fisheye Endoskop eine ausgezeichnete Farbkorrektur (TCA, LCA), welche unerlässlich für den kombinierten Einsatz mit der Hochgeschwindigkeitsfarbkamera sind. Durch die Kombination der Fisheye Optik mit der Relayoptik steigen vor allem die Sphärische Aberration und der Astigmatismus an. Beide Fehler liegen in einem nach den getroffenen Abschätzungen akzeptablen Rahmen.

Die Abbildungsqualität der Optik gegenüber der in Abschnitt 4.1 gezeigten ersten Variante konnte, trotz reduzierter Größe, durch die gewonnenen Erkenntnisse verbessert werden. Die simulativen Untersuchungen des weiterentwickelten optischen Zugangs weisen die Funktionalität der mechanischen und optischen Eigenschaften nach.

Individueller Beitrag: Der Verfasser dieser Arbeit hat die Veröffentlichung angefertigt. Die Ausarbeitung, die Durchführung der Simulationen, deren Auswertung sowie Interpretation sind durch den Verfasser der vorliegenden Arbeit durchgeführt worden. Die finalen Designs, welche in der Veröffentlichung gezeigt werden, sind durch den Verfasser dieser Arbeit ausgearbeitet worden und beruhen auf den Grundlagen, welche in den studentischen Arbeiten der Co-Autoren Hr. Hannes Röhrle, M.Sc. (Röhrle 2019) und Hr. Bernhard Klier, M.Sc. (Klier 2019) entwickelt wurden. Diese Arbeiten wurden durch den Verfasser der vorliegenden Arbeit betreut.

4.4 Experimenteller Vergleich der optisch zugänglichen Motoren mit dem Thermodynamik Motor

Die Integration optischer Komponenten verändert in Abhängigkeit des Grads der optischen Zugänglichkeit die Vergleichbarkeit des Betriebsverhaltens gegenüber des ursprünglichen Thermodynamikmotors (vgl. Abschnitt 2.1.2). Damit gilt es herauszufinden, inwieweit die Versuchsergebnisse des entwickelten optischen Motors auf das thermodynamische Pendant übertragbar sind. Die Veröffentlichung *Experimental comparison between an optical and an all-metal large bore Engine*, 2022 [123] im International Journal of engine research erschienen, vergleicht das thermodynamische Verhalten der zwei entwickelten optischen Zugänge untereinander sowie den volllastfähigen optischen Motor zusätzlich mit dem thermodynamischen Pendant. Beide Vergleiche sind unter 750 U/min mit reinem Erdgas und einer ungespülten Vorkammerzündkerze unter einem geometrischen Verdichtungsverhältnis von 11,6 durchgeführt worden. Tabelle 2 fasst die Versuchsbedingungen zusammen. Das Brennverhalten wird jeweils hinsichtlich Brenngeschwindigkeit, Brenndauer zwischen EU10 und EU90, indiziertem Wirkungsgrad, Verbrennungsstabilität und Wärmefreisetzungsrate beurteilt.

Tabelle 2 Übersicht der Vergleiche zwischen den optischen und thermodynamischen Versuchsträgern

Vergleich 1: Thermodynamikmotor (1) und volllastfähiger optischer Zugang (2)		
Versuchsaufbau	1	2
Betriebsart	kontinuierlich	kontinuierlich
Variation	EU50, λ	EU50, λ
Last (p_{mi})	21 bar	21 bar
Vergleich 2: Volllastfähiger optischer Zugang (2) und volloptischer Zugang (3)		
Versuchsaufbau	2	3
Betriebsart	kontinuierlich	diskontinuierlich – Skipped Fire
Variation	EU50 @ λ=1,7	EU50 @ λ=1,7
Last (p_{mi})	16 bar	16 bar

Die Wärmefreisetzung für eine Verbrennungsschwerpunktlage von 8 °KW nZOT und ein Verbrennungsluftverhältnis von 1,7 führt in Vergleich 1 zu einer Verschiebung der Zündung um 2,25 °KW für den Versuchsaufbau 2 gegenüber 1. Dies liegt an tendenziell schlechteren Zündbedingungen durch geringere Brennraumtemperaturen bedingt durch die integrierte Kühlung in Versuchsaufbau 2. Dies resultiert in einer im Durchschnitt 11 % bzw. 3 °KW längeren Brenndauer des Versuchsaufbaus 2. Der indizierte Wirkungsgrad dagegen ist im Mittel 0,9 % geringer. Dies resultiert aus erhöhten Wandwärmeverlusten an die kälteren Brennraumwände und den vergrößerten Spaltvolumina aus der Integration des optischen Aufbaus. Diese führen zu einem erhöhten Anteil an unverbrannten Kohlenwasserstoffen.

Die Verbrennungsstabilität zeigt ein gegensätzliches Verhalten, sodass für den Versuchsaufbau 2 eine stabilere Verbrennung beobachtet werden konnte. Eine mögliche Erklärung kann hier die veränderte Verformung der Zylinderlaufbuchse aus dem optischen Aufbau und damit ein erhöhter Schmieröleintrag in den Brennraum sein. Das Schmieröl entflammt bei Erreichen der Selbstzündtemperatur und unterstützt die Verbrennung als im Brennraum verteilte zusätzliche Zündquellen. Vor allem bei hohen Verbrennungsluftverhältnissen kommt es zu einer deutlichen

Diversifizierung der Verbrennungsstabilität, da bei niedrigeren Verbrennungsluftverhältnissen dessen positiver Einfluss auf die Zünd- und Verbrennungsbedingungen überwiegt.

Unterschiede in der Emissionsentstehung sind vor allem im Anteil der unverbrannten Kohlenwasserstoffe mit 50 % aufgrund der größeren Spaltvolumina des Versuchsaufbaus 2 deutlich. Die Stickoxidemissionen dagegen sind hier tendenziell aufgrund der kühleren Brennraumwand geringer, dafür steigen die Kohlenstoffmonoxid Emissionen an.

Für Vergleich 2 zwischen den optischen Aufbauten ist trotz des Skipped Fire Betriebs zur Harmonisierung des Verbrennungsschwerpunktes auf 8 ° KW nZOT lediglich eine Verschiebung des Zündzeitpunktes von 0,75 °KW des Versuchsaufbaus 3 gegenüber des Versuchsaufbaus 2 notwendig. Werden die Brenndauern über die untersuchten Verbrennungsschwerpunkte verglichen, wird hier eine Erhöhung in der Hauptverbrennung von EU10-50 um gemittelt 10 % und der Nachverbrennung gemittelt um 9 % für den Aufbau 3 erkennbar. Der indizierte Wirkungsgrad ist hier ebenfalls wie erwartet im Mittel 1,7 % geringer. Dies liegt am Skipped Fire Betrieb, zusätzlichen Spaltvolumina und dem veränderten Ladungswechsel. Versuchsaufbau 3 zeigt für die Verbrennungsstabilität unter günstigen frühen Schwerpunktlagen und damit günstigen Zündzeitpunkten gegenüber dem Versuchsaufbau 2 eine Abweichung von 0,5 %. Mit späteren Verbrennungsschwerpunktlagen steigt die Abweichung auf 1,2 %. Der Skipped Fire Betrieb des Versuchsaufbaus 3 trägt unter diesen Bedingungen weiter zur Verschlechterung der Zünd- und Verbrennungsbedingungen bei.

Während des Aufnahmezeitfensters der thermodynamischen Daten im Skipped Fire Betrieb des Versuchsaufbau 3 ist der eingeregelte Gasmassenstrom mit einer Spitzenabweichung von 0,35 % stabil und genau. Der Luftmassenstrom weist eine maximale Abweichung von 1,7 % auf. Dies wirkt sich auf das Ziel Verbrennungsluftverhältnis mit lediglich 1,58 % aus. Aufgrund der starken Verbrennungstemperaturabhängigkeit reicht die mit dem Versuchsaufbau 3 erreichbare Messzeit nicht aus, um die Einschwingphase der Stickoxidemissionsbildung aufzunehmen. Deshalb können die gemessenen Werte nur als Tendenzen interpretiert werden.

Die Stickoxidwerte des Versuchsaufbaus 3 unter Skipped Fire Betrieb und abgesenkter Kühlwassertemperatur für eine maximale Betriebszeit sind geringer als für den Versuchsaufbau 2 unter kontinuierlicher Last und einer standardmäßigen Kühlmitteltemperatur von 85 °C. Die erhöhten THC Emissionen im Skipped Fire Betrieb hängen unter anderem mit dem leicht schlechteren Wirkungsgrad des Versuchsaufbaus 3 und dessen größeren Spaltvolumina zusammen. Bezüglich der CO Emissionen zeigen beide Aufbauten ein annähernd ähnliches Verhalten, was auf eine ähnliche Ausbrandphase schließen lässt.

Die experimentell ermittelten Abweichungen zeigen die thermodynamische Vergleichbarkeit der Aufbauten und damit die Übertragbarkeit von Versuchsergebnissen auf das thermodynamische Pendant.

4.5 Optische Untersuchungen mit Wasserstoff/Erdgas Mischungen unter seriennaher Volllast am schnelllaufenden Großmotor

Nachdem die Vergleichbarkeit des optisch zugänglichen Versuchsmotors mit seinem thermodynamischen Pendant verifiziert wurde, werden die Auswirkungen einer Wasserstoffbeimischung zu Methan auf die Verbrennung von 2/98 %$_V$, 5/95 %$_V$, 10/90 %$_V$ und 40/60 %$_V$ Wasserstoff/Methan hinsichtlich der Brenndauer, Wärmefreisetzung, Verbrennungsstabilität, dem Zündverzug und indiziertem Wirkungsgrad untersucht. Die Veröffentlichung *Optical and thermodynamic investigations of a methane and hydrogen blend fueled large bore engine*, 2022 **[124]** im International Journal of engine research der SAGE erschienen, beschreibt die optischen und thermodynamischen Ergebnisse aus Versuchsreihen mit dem volllastfähigen optischen Aufbau.

Die Untersuchungen sind unter einem indizierten Mitteldruck von 21 bar, einer Drehzahl von 750 U/min sowie einem geometrischen Verdichtungsverhältnis von 11,6 durchgeführt worden. Abbildung 19 vergleicht die Ergebnisse für konstante Stickoxidemissionen und für den bestmöglichen Wirkungsgrad jeweils bezogen auf die Basisversuche mit Erdgas und zeigt die Vorteile einer Wasserstoffbeimischung. Die Mischungsverhältnisse sind aufgrund deren hohem kurz-, mittel- und langfristigem Potential der Beimischung von Wasserstoff in das deutsche Erdgasnetz gewählt worden.

Für die Einstellung der gleichen Stickoxidemissionen bei einem Verbrennungsschwerpunkt von 8 °KW nZOT wird das Verbrennungsluftverhältnis angepasst. Abbildung 19 (a) zeigt, dass der Wirkungsgrad über den Anstieg der Wasserstoffbeimischung aufgrund der Erweiterung der Magerlaufgrenze ansteigt. Die Verbrennungsinstabilität nimmt für steigende Wasserstoffanteile gegenüber reinem Erdgas tendenziell zu, da ein Ausgleich der Stickoxidemissionen durch Erhöhung des Verbrennungsluftverhältnisses erfolgt. Dies ist notwendig, um die mit der Wasserstoffbeimischung steigenden Verbrennungstemperaturen zu kompensieren. Gleichzeitig sinkt aber die Verbrennungsstabilität bei hohen Verbrennungsluftverhältnissen vor allem für den Referenzkraftstoff Erdgas und damit auch für die Mischungen mit geringem Wasserstoffanteil.
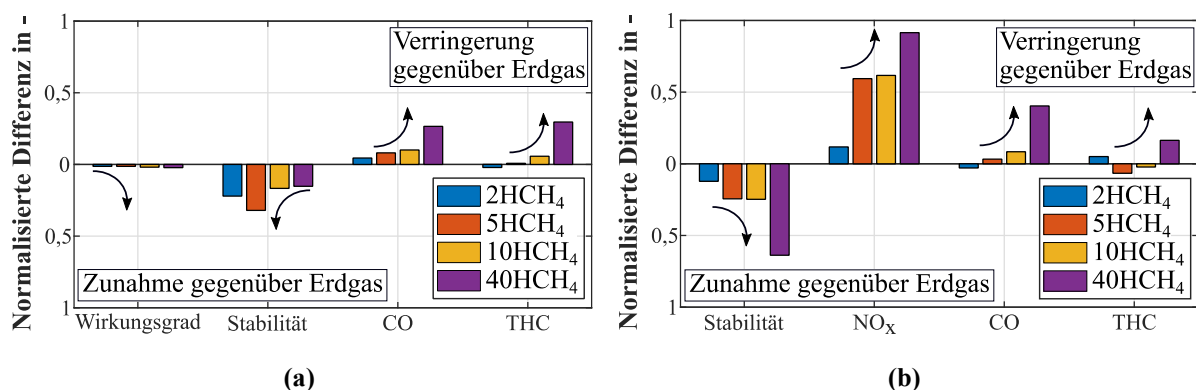

Abbildung 19 Einfluss von Wasserstoff H$_2$ auf die Verbrennung (a) NOx Äquivalent (b) Bester Wirkungsgrad

Die THC-Emissionen verringern sich aufgrund des günstigeren C/H-Verhältnisses der Mischungen gegenüber Erdgas, sowie der vollständigeren Verbrennung. Ebenso verringern sich

die CO-Emissionen aufgrund des geringeren C/H-Verhältnisses der Mischungen und ausreichend hoher Temperaturen in der Ausbrandphase. Für die Vergleiche des sich einstellenden besten Wirkungsgrades bei 8 °KW nZOT Verbrennungsschwerpunktlage jedes Kraftstoffgemisches zeigt sich in Abbildung 19 (b), dass die Verbrennungsinstabilität mit einem Anstieg der Wasserstoffbeimischung zunimmt. Dies liegt daran, dass der höchste Wirkungsgrad bei hohen Verbrennungsluftverhältnissen erreicht wird, welche tendenziell schlechtere Zünd- und Verbrennungsrandbedingungen aufweisen. Die Stickoxidemissionen sinken mit zunehmendem Verbrennungsluftverhältnis und den dadurch sinkenden Verbrennungstemperaturen trotz steigender Wasserstoffbeimischung stärker. Die übrigen Emissionen sinken aus dem gleichen Grund.

Zusätzlich zu den thermodynamischen Ergebnissen konnten durch den seitlichen optischen Zugang parallel die natürliche OH* Radikal- und sichtbare Flammenchemilumineszenz detektiert werden. Die Breitbandstrahlung der Flammenchemilumineszenz wird mit einer Hochgeschwindigkeitsfarbkamera aufgezeichnet. Die Aufnahmen zur Detektion der Emissionen im UV-Bereich nutzen eine monochromatische bildverstärkte Hochgeschwindigkeitskamera mit einem Bandpassfilter im Bereich von 300-315 nm (vgl. Abbildung 2), um das natürliche OH*-Radikal in einem Wellenlängenbereich um 309 nm selektiv detektieren zu können. Zündung und Start der Verbrennung werden allerdings durch die Kolbenbewegung verdeckt. Durch eine Erhöhung der Wasserstoffbeimischung steigt die Intensität der OH- und Breitband Chemilumineszenzen an. Es kommt aufgrund der erhöhten Wasserstoffkonzentration zu einer vermehrten lokalen Bildung emittierender Radikale während der Verbrennung. Dieser Effekt wird ebenso für die Entstehung des natürlichen OH*- Radikals und der damit einhergehenden erhöhten Strahlungsintensität des detektierten UV-Signals vermutet, da aufgrund niedriger Mischungsverhältnisse ausreichend Kohlenstoff für die in Gleichung (15) beschriebene Reaktion als Hauptreaktionspfad für die OH*-Radikal Bildung lokal zur Verfügung steht.

Mit zunehmendem Anteil an Wasserstoff dominieren die aus höheren Verbrennungstemperaturen angeregten Breitbandemissionen. Die Abnahme beider Intensitäten über die Zunahme des Verbrennungsluftverhältnisses ist ebenfalls durch eine abnehmende Verbrennungstemperatur erklärbar. Das Ende der Verbrennung, definiert als 95 % Energieumsatzpunkt, stimmt mit dem Ende der OH*-Radikal-Intensität zusammen. Im Breitbandspektrum klingt die Intensität erst nach dem Ende der Verbrennung ab. Dies weist auf eine Nachoxidation außerhalb der aufgenommen Strahlung im UV-Bereich hin. Diese ist intensiver für höhere Anteile Wasserstoff in der Kraftstoffmischung und zeigt damit einen Einfluss aus erhöhten Verbrennungstemperaturen.

Generell stimmen die aus den seitlichen Zugängen aufgenommenen optischen Aufnahmen gewonnenen Erkenntnisse mit den aus den thermodynamischen Messwerten abgeleiteten Eigenschaften der Verbrennung überein, sodass diese als plausibel anzusehen sind.

Individueller Beitrag: Der Verfasser dieser Arbeit hat die vorliegende Veröffentlichung angefertigt. Die Konzeptionierung, Ausarbeitung, die Auswertung, graphische Darstellung und Interpretation der Versuchsergebnisse wurden durch den Verfasser der vorliegenden Arbeit durchgeführt. Hr. Eicheldinger, M.Sc. hat die Versuchsdurchführung am Prüfstand unterstützt.

## 4.6 Untersuchungen am schnelllaufenden volloptisch zugänglichen Groß-motor

Für ein erweitertes Sichtfeld wird der Versuchsaufbau aus Abschnitt 4.5 um die in Abschnitt 4.3 entwickelte Fisheye Optik erweitert. Damit wird ein Blickfeld von oben auf den Brennraum ermöglicht. Die Veröffentlichung *Optical and Thermodynamic Investigations of a Methane- and Hydrogen- Blend-Fuelled Large-Bore Engine Using a Fisheye Optical System*, erschienen 2023 im Energies Journal der MDPI **[125]**, stellt die Ergebnisse der so durchgeführten Versuche vor. Es werden die beiden Zündsysteme ungespülte Vorkammer (UVZK) mit sieben Bohrungen einer Ringelektroden-Zündkerze (ZK) für die Kraftstoffmischungen 5/95 %$_V$, 10/90 %$_V$ H_2/CH_4 und NG (Erdgas) anhand thermodynamischer und optischer Untersuchungen der natürlichen Flammenchemilumineszenz gegenübergestellt. Die Versuche wurden unter einem geometrischen Verdichtungsverhältnis von 11,6 und einer Motordrehzahl von 750 U/min im Skipped Fire Betrieb durchgeführt.

Aus den thermodynamischen Vergleichen zeigt sich eine schnellere Verbrennung für die UVZK gegenüber der ZK. Dies äußert sich für die UVZK mit einer Reduktion der Brenndauer um 11,87 % im Vergleich zur ZK für die Verwendung von NG und 18,29 % für 10HCH$_4$. Dies resultiert u.a. aus einem kürzeren Zündverzug zwischen ZK und UVZK für NG mit 73 % und für 10HCH$_4$ mit 67 % bei λ=1,7. Der positive Einfluss der Wasserstoffzumischung auf die Verbrennung äußert sich bei der verwendeten ZK und hohem λ stärker als bei der verwendeten UVZK. Dennoch bewirkt bereits die geringe Zumischung von 10 %$_V$ Wasserstoff eine maximale Steigerung des indizierten Wirkungsgrads für die UVZK von 0,8 % gegenüber Erdgas.

Ein Vergleich des Intensitätsverlaufes des Flammeneigenleuchtens mit der aus der Brennverlaufsberechnung abgeleiteten gemittelten Brennraumtemperatur zeigt eine zunehmende Abweichung der Maximalwerte für späte Verbrennungsschwerpunkte auf maximal 3,35°KW für NG. Dieser Abstand kann aus einer verschleppten Verbrennung mit einem längeren, weniger intensiven sichtbaren Ausbrand resultieren. Einen deutlicheren Einfluss zeigt die Erhöhung des Verbrennungsluftverhältnisses auf den Abstand des Helligkeits- und Temperaturmaximums. Hier reduziert neben einer verschleppten Verbrennung noch das Sauerstoff-Quenching die Intensität der natürlichen Flammeneigenstrahlung. Generell zeigt das Verbrennungsluftverhältnis die größten Auswirkungen auf die Intensität der Flammeneigenstrahlung. Der Unterschied zwischen den verschiedenen Kraftstoffgemischen ist für frühe Verbrennungsschwerpunkte gering. Im Vergleich der beiden Zündsysteme zeigt die UVZK um bis zu 20 % höhere Intensitäten der natürlichen Flammeneigenstrahlung.

Die Interpretation der Flammenfarbe erfolgt an den Umsatzpunkten EU5, 10, 50 und 95. Hierbei zeigt sich eine Abhängigkeit der Flammenfarbe vom Verbrennungsluftverhältnis exemplarisch dargestellt in Abbildung 20 für die UVZK. Für ein niedriges Verbrennungsluftverhältnis dominieren in den frühen Phasen der Verbrennung mit EU5 und 10 bereits erste orange bis rötliche Anteile. Lediglich an den Flammenfronten sind bläuliche Anteile des CH*-Radikals zu erkennen. Dies ist für beide Zündsysteme sowie für den Referenzkraftstoff NG und die maximal untersuchte Zumischung mit 10 %$_V$ Wasserstoff zu beobachten. Aufgrund der höheren Verbrennungstemperatur und der niedrigen Verbrennungsluftverhältnisse dominiert eine gelbe Farbe die Verbrennung und ist ein Hinweis auf das C_2*-Radikal.

Verbrennungsluftverhältnis 1,5
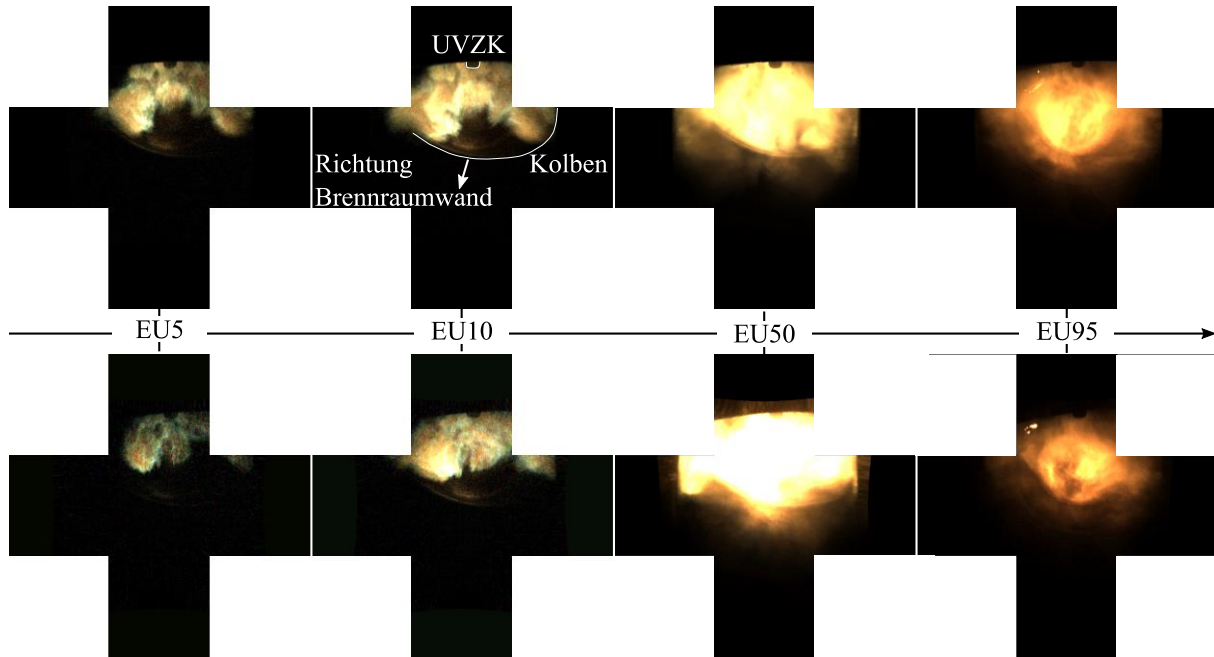
Verbrennungsluftverhältnis 1,7

Abbildung 20 Bilderserie des 25. Arbeitsspiels für 10HCH4 bei EU5, 10, 50, 95 mit UVZK bei λ 1,5 und 1,7

Daneben erhöht die Verbrennungstemperatur die Hintergrundstrahlung und überlagert den in der Intensität schwächeren blauen Anteil der Flamme aus dem CH*-Radikal. Mit voranschreitender Energiefreisetzung konzentrieren sich in der Kolbenmulde hauptsächlich helle orange bis gelbe Anteile der Flamme. Bei Verbrennungsende EU95 ist in der Kolbenmulde eine rötliche Restintensität sichtbar. Diese kann aus thermisch angeregtem Wasser stammen und ist umso heller, je höher die Brennraumtemperaturen ausfallen.

Für die Verbrennung mit der ZK zeigt sich von Beginn an eine durchgehende, flächige Verbrennung. Dahingegen zeigt die ungespülte Vorkammer eine Formation der Flammenfront aus der Vereinigung der Fackelstrahlen, welche aus der UVZK austreten (vgl. Abbildung 20). Mit einer virtuellen Rückprojektion (vgl. Abschnitt 4.2) wird in der frühen Phase der Verbrennung der nach unten gerichtete, zur Zylinderachse parallele Fackelstrahl in eine quasi dreidimensionale Darstellung überführt und die Länge des Fackelstrahls bestimmt. Die Auswertung zeigt die Interaktion des Fackelstrahls mit der Kolbenmulde. Zwischen dem Referenzkraftstoff und der maximalen untersuchten Zumischung von 10 $\%_V$ zeigen sich in den Aufnahmen keine besonderen Unterschiede hinsichtlich Intensität oder Farbe der Flamme. Dafür scheint die Zumischung und deren Auswirkung auf die Brenngaseigenschaften zu gering. Lediglich für die Variation des Verbrennungsluftverhältnisses zeigen sich Änderungen in der Intensität und der Farbe der Fackelstrahlen. Mit geringerem Verbrennungsluftverhältnis bekommen die Spitzen der Fackelstrahlen eine leicht orange Färbung. Zudem nimmt die Verbrennungsgeschwindigkeit zu und die Intensität der Fackelstrahlen resultiert in einem hellen gelben Leuchten.

Individueller Beitrag: Der Verfasser dieser Arbeit hat die vorliegende Veröffentlichung angefertigt. Die Konzeptionierung, Ausarbeitung, Auswertung, graphische Darstellung und Interpretation der Versuchsergebnisse sind durch den Verfasser der vorliegenden Arbeit durchgeführt worden. Hr. Eicheldinger, M.Sc. hat die Versuchsdurchführung am Prüfstand unterstützt.

5 Diskussion und Einordnung der Ergebnisse

Verglichen mit dem Konzept nach Bowditch ist der hier entwickelte kompakte Zugang hinsichtlich der Komplexität durch seine geringere Anzahl an Bauteilen, geringen Modifikationen am Grundmotor und dem besseren Verhältnis von erzielbarem Sichtfeld zu Größe des Zugangs deutlich überlegen. Dennoch bedingen v.a. die Modifikationen des Zylinderkopfs und die verwendete Klebstoffverbindung der ersten Fisheye Linse eine Einschränkung in Form eines Skipped Fire Motorbetriebs zur Vermeidung thermischer bzw. mechanischer Überlasten. Ein entsprechend gegossener Zylinderkopf, in dem die Aufnahme einer solchen Optik bereits vorgesehen ist, würde diesen Nachteil kompensieren, den Aufwand zur Realisierung aber vergrößern.

Im nHCFen kompakten Design kann der Anteil gefeuerter Zyklen des Skipped Fire Betriebs vor allem für die zweite, optimierte Optik im Gegensatz zu einem Konzept nach Bowditch, das zwischen 50 und 200 Arbeitsspiele erlaubt, abhängig vom Motor Betriebspunkt auf bis zu 460 Arbeitsspiele erhöht werden. Dies ist aufgrund der deutlich kleineren wärmeübertragenden Linsenfläche der Fisheye Optik gegenüber dem großen Kolbenfensterdurchmesser eines Bowditch Designs möglich. Weiteres Verbesserungspotential würde hier ein Wechsel von Luft- auf Wasserkühlung bieten. Dies hätte durch die längere mögliche Betriebsdauer vor allem den Vorteil, dass eine längere Einschwingdauer der Abgasmesstechnik mit stabileren Stickoxid Emissionen über die Abgasstrecke ermöglicht wird.

Ein weiterer Vorteil des kompakten Zugangs ist, dass der Öleintrag über die Kolbenringe in den Brennraum und damit die aus der Verbrennung der Öltröpfchen induzierten Vorentflammungen beobachtet werden können. Diese sind vor allem für die Untersuchungen von wasserstoffhaltigen Brenngasen aufgrund der höheren Reaktivität und damit verbundenen anormalen Verbrennungen (vgl. [116]), induziert aus der Ölverbrennung, interessant. Dieser Vorteil kann aber auch als Nachteil ausgelegt werden, soll die Verbrennung ohne störende Einflüsse und Strahlungsüberlagerung aus der Öltropfenverbrennung für das Ableiten von Modellvorstellungen verwendet werden. Hierfür bietet das Konzept nach Bowditch die besseren Möglichkeiten mit einem Trockenlauf in der oberen Laufbuchse. Dennoch bietet der hier entwickelte Zugang für die innermotorische Verbrennung realitätsnähere Randbedingungen.

Das Sichtfeld der entwickelten Fisheye Optiken umfasst den gesamten Bohrungsdurchmesser. Die Auflösungsgüte der Optiken ist abhängig von der Entfernung des zu detektierenden Events zur Optik und nimmt in den Randbereichen aufgrund der tonnenförmigen Verzeichnung eines Fisheyes ab. Dennoch wird ein größeres Sichtfeld ermöglicht als durch in anderen Arbeiten eingesetzte Endoskope (vgl. Abschnitt 2.1.2). Je nach Ausführung des Kolbenfensters in einem Bowditch Konzept wird ein bestimmter Teil des Randbereichs für die Halterung des Kolbenfensters benötigt und ist für optische Aufnahmen nicht nutzbar. Die meist planparallelen Flächen am Kolbenfenster nach Bowditch erlauben dafür eine einfache lineare Zuordnung der Pixel zur realen Fokusebene. Für die hier entwickelten Fisheye Optiken muss ein Postprocessing der Aufnahmen und dafür eine aufwändigere Kalibrierung mit deutlich höherem Abweichungspotential durchgeführt werden. Eine Verbesserung der Kalibrierung führt direkt zu einer besseren Qualität und Aussagekraft der ausgewerteten Messergebnisse.

Im Vergleich zur ersten entwickelten Optik weist die zweite, verkleinerte Optik wegen der Einführung einer zusätzlichen Relayoptik eine bessere Lichteffizienz bei einer gleichzeitigen Verbesserung der Abbildungsqualität auf. Diese bietet zusätzliches Optimierungspotential, über einen symmetrischen Aufbau und eine Verlängerung des rückwärtigen Fokus die Lichteffizienz weiter zu steigern. Damit können die Belichtungszeit der Kamera reduziert und die zeitliche Auflösung der Verbrennungsaufnahmen verbessert werden. Ebenso können *Asphären* in der Optik zur kombinierten Aberrationskorrektur eingesetzt werden. Dies reduziert die Anzahl benötigter Linsen, erhöht damit durch geringere Reflexionen an den Linsenflächen die Lichteffizienz und verbessert die Abbildungsqualität. Einziger Nachteil sind die mit der aufwändigen Fertigung verbundenen hohen Kosten. Zudem kann das hier entwickelte Konzept mit einer UV-fähigen Fisheye Optik erweitert werden. Dies Bedarf einer Überarbeitung der verwendeten Linsen hin zu deutlich kostspieligeren und schlecht verfügbaren Materialien, welche einen Transmissionsbereich im UV-Wellenlängenbereich aufweisen. Mit einer solchen Optik wird die Anwendung von laserbasierten Messverfahren ermöglicht. Damit können weitere quantifizierbare Messgrößen wie die Ladungsverteilung und eine Bestimmung der Flammenfrontausbreitung über die selektive Detektion der Verbrennungsspezies durchgeführt werden. Neben der erweiterten Anwendung einer solchen UV-fähigen Optik, ist das Postprocessing zur 3D-Darstellung bei definierten Laser-Lichtschnitten um ein vielfaches einfacher und eine örtliche Zuordnung mit nur einer Kamera über den gezeigten Reprojektionsalgorithmus möglich.

Bisher nutzte lediglich Wilson [19] eine Fisheye Optik zur Aufnahme der natürlichen Flammeneigenstrahlung in einem 146 cm³ Rasenmäher Motor mit seitlichen, hängenden Ventilen. Zusätzlich zur Fisheye Optik wird, wie in der hier dargestellten weiterentwickelten Variante, eine Relayoptik eingesetzt. Ebenso wird, wie in der vorliegenden Arbeit eine Entzerrung der Bilder für eine höhere Güte der Ergebnisse verwendet. Im Gegensatz zu der Arbeit nach Wilson wird in der vorliegenden Arbeit die einfache Entzerrung zu dem dargestellten Reprojektionsalgorithmus weiterentwickelt. Der bedeutendste Unterschied zur Arbeit von Wilson ist allerdings die Motorgröße, für welche die Optik entwickelt wurde und die nach Kenntnisstand des Verfassers bisher einzigartig ist. Die Randbedingungen und der erforderliche Änderungsaufwand sind, verglichen mit einem Rasenmäher Motor mit einem Verdichtungsverhältnis von 6:1, um ein Vielfaches anspruchsvoller und erfordern eine deutlich aufwändigere Integration der Optik in den Motor. Zusätzlich trägt die Entwicklung eines seitlichen Zugangs zur Realisierung eines kompakten Konzepts der volloptischen Zugänglichkeit zur innovativen Erweiterung der Anwendung von Fisheye Optiken für die Verbrennungsdiagnostik bei. Abbildung 13 zeigt zudem, dass vor allem auf dem Gebiet der Großmotoren ein Nachholbedarf an u.a. optischen Untersuchungen zu v.a. nachhaltigen Kraftstoffen besteht. Untersuchungen der Verbrennung alternativer Kraftstoffe mit den entwickelten Zugängen tragen hier zur Schließung dieser Lücke bei. Zudem validieren die Untersuchungen das entwickelte Konzept.

Am Einzylinderforschungsmotor wurden mit der ersten Fisheye Optik und der Beleuchtung über den seitlichen Zugang Mie-Streulichtaufnahmen des Pilotkraftstoffeinspritzstrahls während des Motorbetriebs aufgenommen (vgl. Abschnitt 4.2). Es konnten aufgrund der Anordnung der Optik, des Pilotinjektors und der Abbildungsqualität der Optik zwei der drei Kraftstoffstrahlen komplett für eine Auswertung nutzbar aufgelöst werden. Wird die Positionierung

der Injektordüse und der Optik auf annähernd gleicher Höhe bündig mit dem Flammdeck berücksichtigt, zeigt sich hier das enorme Potential der Anwendung einer Fisheye Optik für die Verbrennungsdiagnostik aus dem 180 ° Sichtfeld. Die entwickelte Reprojektionsmethode der Einspritzstrahlkontur in eine quasi 3D-Darstellung ermöglicht eine quantitative Aussage über die flüssige Strahleindringtiefe. Validierungsversuche zeigen, dass die Reprojektionsmethode eine gemittelte Genauigkeit von 2,1 mm aufweist. Diese Abweichung entsteht hauptsächlich durch Kalibrierungsungenauigkeiten und kann durch deren Optimierung weiter reduziert werden. Die ausgewerteten Versuchsergebnisse zeigen einen kürzeren und kompakteren Einspritzstrahl des verwendeten OME$_{3-5}$ gegenüber dem Referenzkraftstoff DMA. Die mittlere flüssige Strahleindringtiefe zeigt über die durchgeführten Variationen des Kraftstoffdruckes und die Variation der Injektorbestromung ein plausibles Verhalten, vergleichbar mit den Ergebnissen aus [126] ermittelt an einer Einspritzkammer. Die entwickelte Methodik kann also mit den Versuchen verifiziert werden.

Die in Abschnitt 4.4 gezeigten Versuche mit dem seitlichen Zugang unter Volllast gegenübergestellt mit Versuchen am thermodynamischen Pendant bestätigen die Vergleichbarkeit der Ergebnisse des weiterentwickelten optischen Zugangs. Die Abweichungen in den Versuchsergebnissen sind vornehmlich in erhöhten Abgasemissionen analog den Versuchsergebnissen aus [34, 36] an einem volloptischen Motor nach Bowditch zu finden und können auf größere Spaltvolumina (vgl. [127]) durch die Integration der optischen Einbauten, insbesondere der Fisheye Optik, zurückgeführt werden.

Des Weiteren erfolgte eine Charakterisierung des Einflusses einer Wasserstoffzumischung auf das Brennverhalten des mittels ungespülter Vorkammerzündkerze gezündeten vorgemischten Magergasmotors unter seriennaher Volllast ohne Integration der Fisheye Optik (siehe Abschnitt 4.5). Die Ergebnisse stimmen mit den Erkenntnissen aus dem dargestellten Stand der Technik (vgl. Abschnitt 2.5) überein. Der für die Erdgas-Verbrennung optimierte Forschungsmotor und die ungespülte Vorkammerzündkerze sowie die reduzierte Motordrehzahl tragen dazu bei, dass Erdgas in den tendenziell fetteren Betriebsbereichen bereits eine gute Verbrennungsstabilität aufgrund der Zünd- und Brennbedingungen aufweist. Damit zeigt Methan gegenüber den Wasserstoffbeimischungen mit einem Verbrennungsluftverhältnis von 1,5 bis zur Magerlaufgrenze des Motors bei 1,8 eine ähnliche Verbrennungsstabilität. Ein ähnliches Verhalten wird z.B. in [128] an einem vorgemischten Zündkerzen gezündeten PKW Motor bis zu dessen Magerlaufgrenze beschrieben. Die maximale Wasserstoffzumischung von 40 %$_v$ zeigt in der vorliegenden Arbeit sogar eine geringere Verbrennungsstabilität. Erst für höherer Verbrennungsluftverhältnisse ab 1,8 ändert sich dies und die Wasserstoffbeimischung zeigt eine Stabilisierung der Verbrennung und Erweiterung der Magerlaufgrenze.

Mit der optimierten Fisheye Optik sind außerdem Mischungen von Wasserstoff zu Methan im Vergleich zu reinem Erdgas betrachtet worden (siehe Abschnitt 4.6). Die optischen Aufnahmen zeigen eine Intensitätszunahme der natürlichen Eigenstrahlung für frühe Verbrennungsschwerpunkte, niedrige Verbrennungsluftverhältnisse und höhere Zumischungen von Wasserstoff. Die Intensität hat dabei sowohl eine starke Abhängigkeit vom Verbrennungsluftverhältnis und der daraus resultierenden Änderung der Brennraumtemperaturen, als auch von der Zunahme des Sauerstoff-Quenchings mit den angeregten Molekülen. Die Flammenfarbe zeigt ebenso eine

starke Abhängigkeit vom Verbrennungsluftverhältnis, was sich in der Auswertung der Fackelstrahlen bei Verwendung der ungespülten Vorkammerzündkerze fortsetzt.

Dies zeigt, dass der für Erdgas optimierte Magergasmotor für die geringe Zumischung von 10 %$_V$ Wasserstoff gut geeignet ist und die Verbrennung durch die Wasserstoffbeimischung positiv zu mehr Wirkungsgrad hin beeinflusst werden kann. Eine kurzfristige Zumischung von 10 %$_V$, um durch erneuerbare Energien erzeugten Wasserstoff nutzbar zu machen, welcher im Erdgasnetz gespeichert werden kann, scheint damit ein vielversprechender erster Schritt in Richtung einer nachhaltigen Energieversorgung.

Korb [37, 129, 127] zeigt erste thermodynamische und optische Untersuchungen mit einem Zugang nach dem Bowditch Konzept am gleichen Grundmotor, an dem auch die hier dargestellte optimierte Variante der volloptischen Zugänglichkeit entwickelt und die Versuche zur Charakterisierung der Einflüsse des Wasserstoffanteils auf das Brennverfahren durchgeführt worden sind. Neben einem anderen Zylinderkopf und Steuerzeiten sind im Gegensatz zu den Untersuchungen nach Korb in der vorliegenden Arbeit andere Mischungsverhältnisse untersucht worden. Zudem ist die Charakterisierung der Verbrennung mit einem volllastfähigen optisch zugänglichen Motor durchgeführt worden. Die zusätzliche Anwendung der Fisheye Optik erweitert das Sichtfeld und die Einblicke während der Verbrennung unter realitätsnahen motorischen Bedingungen. Dadurch gelingt eine erste Charakterisierung der Verbrennung von Wasserstoff/Methanmischungen mit zusätzlichen optischen Aufnahmen.

Die vorliegende Arbeit trägt neben dem Aufzeigen des Potentials des entwickelten kompakten volloptischen Zugangs für Großmotoren für die Charakterisierung und Bewertung erneuerbarer Kraftstoffe zur weiteren Verständnisbildung des Einflusses von Wasserstoffbeimischung auf das magergasmotorische Brennverfahren bei.

6 Zusammenfassung und Ausblick

Die vorliegende Arbeit zeigt die Entwicklung eines kompakten Konzeptes für die vollständige optische Zugänglichkeit an Großmotoren für die in situ Verbrennungsdiagnostik. Im Gegensatz zu den aufwändigen Modifikationen nach dem Bowditch Prinzip mit einem optischen Zugang durch den Kolben sowie den daraus resultierenden Nachteilen wird die Entwicklung und Realisierung eines kompakteren optischen Zugangs über eine Fisheye Optik im Zylinderkopf dargestellt. Diese ist einfacher in den Motor zu integrieren, die Verbrennung daher dem thermodynamischen Pendant ähnlicher und die Optik bietet mit einem 180 ° Sichtfeld mit hoher Tiefenschärfe einen umfassenden Beobachtungsraum für die Verbrennungsdiagnostik. Ergänzt wird das horizontale Sichtfeld mit einem seitlichen Zugang für die Beleuchtung des Brennraums bzw. die Beobachtung aus einem anderen Blickwinkel. Eine Weiterentwicklung der Fisheye Optik bei annähernder Halbierung des Durchmessers und gleichzeitiger Verbesserung der Abbildungsqualität ermöglicht die Anwendung dieses Zugangs auch für kleinere Hubraumklassen und vereinfacht gleichzeitig die Integration in größere.

Anwendungen der entwickelten Zugänge zur Charakterisierung der Verbrennung von regenerativen Kraftstoffen in optischen und thermodynamischen Versuchen bestätigen das Potential des entwickelten kompakten volloptischen Zugangs und zeigen den Einfluss von Wasserstoff/Methangemischen auf die Verbrennung. Neben der Erweiterung der Magerlaufgrenze des Motors und der damit möglichen Wirkungsgradsteigerung zeigen optische Aufnahmen der Verbrennung bei Verbrennungsende mit zunehmenden Wasserstoffanteil eine Restintensität aus möglichem thermisch angeregtem Wasser. Die natürliche Flammeneigenstrahlung zeigt aufgrund der höheren Verbrennungstemperaturen der Wasserstoff/Methanmischungen höhere Intensitäten. Eine geringe Zumischung von Wasserstoff bis 10% zeigt keine signifikanten Auswirkungen auf die Flammenfarbe, sodass diese der reinen Erdgasverbrennung ähnlich ist.

Das entwickelte leistungsstarke Postprocessing ermöglicht eine quantitative Auswertung der stark verzerrten optischen Fisheye Aufnahmen. Künftige Optimierungen hinsichtlich der konträren Kriterien Abbildungsqualität, Lichtstärke und Baugröße können zu einer noch einfacheren Integration mit einer verbesserten Ergebnisqualität beitragen. Zudem kann eine solche Optik auch für die Anwendung im UV-Bereich appliziert werden. Damit wären laserbasierte Messverfahren möglich, mit denen z.B. auch die Verbrennung von reinem Wasserstoff untersucht werden kann. Mit der entwickelten Optik ist der Grundstein gelegt, damit künftige Wasserstoff basierte Brennverfahren untersucht und hinsichtlich Effizienz, Emission und Nachhaltigkeit optimiert werden können.

Literaturverzeichnis

[1] *Burchardt, J.; Franke, K.; Herhold, P. et al.:* Klimapfade 2.0 – Ein Wirtschaftsprogramm für Klima und Zukunft. BDI Ausgabe Oktober 2021.

[2] *Trost, T.; Horn, S.; Jentsch, M. et al.:* Erneuerbares Methan – Analyse der CO2-Potenziale für Power-to-Gas Anlagen in Deutschland. *In:* Zeitschrift für Energiewirtschaft 36 (2012), Heft 3, S. 173-190. https://doi.org/10.1007/s12398-012-0080-6.

[3] *Zapf, M.:* Stromspeicher und Power-to-Gas im deutschen Energiesystem – Rahmenbedingungen, Bedarf und Einsatzmöglichkeiten. Springer Vieweg, Wiesbaden, 2017.

[4] *Krause, H.; Werschy, M.; Franke, S. et al.:* Untersuchungen der Auswirkungen von Gasbeschaffenheitsänderungen auf industrielle und gewerbliche Anwendungen Ausgabe April 2014.

[5] *Reitz, R.D.; Ogawa, H.; Payri, R. et al.:* IJER editorial: The future of the internal combustion engine. *In:* International Journal of Engine Research 21 (2020), Heft 1, S. 3-10. https://doi.org/10.1177/1468087419877990.

[6] *Onorati, A.; Payri, R.; Vaglieco, B.M. et al.:* The role of hydrogen for future internal combustion engines. *In:* International Journal of Engine Research 23 (2022), Heft 4, S. 529-540. https://doi.org/10.1177/14680874221081947.

[7] *Miles, P.C.:* The History and Evolution of Optically Accessible Research Engines and Their Impact on Our Understanding of Engine Combustion. *In: Grauer, D.K.* (ed.): Proceedings of the ASME Internal Combustion Engine Division fall technical conference - 2014 – Presented at the ASME 2014 Internal Combustion Engine Division fall technical conference, October 19 - 22, 2014, Columbus, Indiana, USA. American Society of Mechanical Engineers, no. 2. ASME, Columbus, Indiana, USA, 2014.

[8] *Schneider, B.; Schürch, C.; Boulouchos, K. et al.:* The Flex-OeCoS—a Novel Optically Accessible Test Rig for the Investigation of Advanced Combustion Processes under Engine-Like Conditions. *In:* Energies 13 (2020), Heft 7, S. 1794. https://doi.org/10.3390/en13071794.

[9] *Tanaka, S.; Ayala, F.; Keck, J.C.:* A reduced chemical kinetic model for HCCI combustion of primary reference fuels in a rapid compression machine. *In:* Combustion and Flame 133 (2003), Heft 4, S. 467-481. https://doi.org/10.1016/S0010-2180(03)00057-9.

[10] *Mittal, G.; Sung, C.-J.:* A RAPID COMPRESSION MACHINE FOR CHEMICAL KINETICS STUDIES AT ELEVATED PRESSURES AND TEMPERATURES. *In:* Combustion Science and Technology 179 (2007), Heft 3, S. 497-530. https://doi.org/10.1080/00102200600671898.

[11] *Bensing, D.:* Aufbau eines optisch zugänglichen Einzylinder-Viertaktmotors und charakterisierende Messungen, Universität Duisburg-Essen, Dissertation, 2013.

[12] *Karmann, S., Prager, M.; Wachtmeister, G.:* Conceptual Investigations on Full Optical Accessibility to Large-Bore Medium-Speed Engines. *In:* SAE Int. J. Engines, Vol. 12 (2019), Iss. 3. https://doi.org/10.4271/03-12-03-0020.

[13] *Goschütz, M.:* Endoskopische Brennraumdiagnostik im seriennahen Ottomotor durch Chemilumineszenz und laserinduzierte Fluoreszenz. Duisburg-Essen, Universität Duisburg-Essen, Dissertation, 2018.

[14] *Ohler, S.:* Entwicklung und Vergleich von Kriterien zur Erkennung der klopfenden Verbrennung in Ottomotoren. Hamburg, Helmut-Schmidt-Universität / Universität der Bundeswehr Hamburg, Dissertation, 2014.

[15] *Han, K.-M.; Velji, A.; Spicher, U.:* A New Approach for Three-Dimensional High-Speed Combustion Diagnostics in Internal Combustion Engines. *In:* SAE Technical Paper Series, SAE Technical Paper Series. SAE International400 Commonwealth Drive, Warrendale, PA, United States, 2006.

[16] *Tsekenis, S.A.; Wilson, D.; Lengden, M. et al.:* Towards in-cylinder chemical species tomography on large-bore IC engines with pre-chamber. *In:* Flow Measurement and Instrumentation 53 (2017), S. 116-125. https://doi.org/10.1016/j.flowmeasinst.2016.04.006.

[17] *Reling, J.; Flögel, H.-H.; Werschy, M.:* Technische Endoskopie – Grundlagen und Praxis endoskopischer Untersuchungen, Kontakt & Studium Heft 597, expert Verl., Renningen-Malmsheim, 2001.

[18] *Reichle, R.; Pruss, C.; Gessenhardt, C. et al.:* Diffractive/refractive (hybrid) UV-imaging system for minimally invasive metrology: design, performance, and application experiments. *In:* Applied optics 51 (2012), Heft 12, S. 1982-1996. https://doi.org/10.1364/AO.51.001982.

[19] *Wilson, T.S.:* The research and development of in situ non-intrusive optical and temperature diagnostics in an internal combustion engine, University of Warwick, PhD, 2002.

[20] *Disch, C.; Waldenmaier, U.:* High-Speed Flame Chemiluminescence Investigations of Prechamber Jets in a Lean Mixture Large-Bore Natural Gas Engine Ausgabe 2013.

[21] *Unfug, F.:* Experimentelle und numerische Untersuchung der Verbrennung eines mittelschnelllaufenden 4-Takt Dieselmotors. Dissertation. Karlsruher Institut für Technologie, Forschungsberichte aus dem Institut für Kolbenmaschinen, Karlsruher Institut für Technologie (KIT)Bd. 2013,7, Logos Berlin, Berlin, 2013.

[22] *Epp, M.:* Optische Untersuchungen einer Einspritzstrategie mit früher Voreinspritzung an einem schweröltauglichen mittelschnelllaufenden Commen Rail-Großdieselmotor. Rostock, Universität Rostock, Dissertation, 2013.

[23] *Wellander, R.; Rosell, J.; Richter, M. et al.:* Study of the Early Flame Development in a Spark-Ignited Lean Burn Four-Stroke Large Bore Gas Engine by Fuel Tracer PLIF. *In:* SAE International Journal of Engines 7 (2014), Heft 2, S. 928-936. https://doi.org/10.4271/2014-01-1330.

[24] *Duong, J.:* Combustion Visualization in a Large Bore Gas Engine. Lund, Lund University, Thesis for the Degree of Licentiate in Engineering, 2013.

[25] *Wellander, R.:* Multi-Dimensional Quantitative Laser-based Diagnostics Development and Practial Applications, Lund University, Sweden, Doctoral Thesis, 2014.

[26] *Hult, J.; Mayer, S.:* A methodology for laser diagnostics in large-bore marine two-stroke diesel engines. *In:* Measurement Science and Technology 24 (2013), Heft 4, S. 45204. https://doi.org/10.1088/0957-0233/24/4/045204.

[27] *Bowditch, F.W.:* A New Tool for Combustion Research A Quartz Piston Engine. *In:* SAE Technical Paper (1961), Heft 610002. https://doi.org/10.4271/610002.

[28] *Marco Taschek:* Einsatz qualitiver und quantitiver optischer Messverfahren an einem Diesel Transparentmotor, Universität Erlangen-Nürnberg, 2007.

[29] *Beatrice, C.; Bertoli, C.; d'Ascoli, G. et al.:* Design of a small displacement transparent research engine equipped with a common-rail diesel injection system. *In: :* 2001 Internal Combustion Engines. Istituto Motori C.N.R; Diesel Engine and Fuel Department, SAE Technical Paper Series. SAE International400 Commonwealth Drive, Warrendale, PA, United States, 2001.

[30] *Fuyuto, T.; Matsumoto, T.; Hattori, Y. et al.:* A New Generation of Optically Accessible Single-Cylinder Engines for High-speed and High-load Combustion Analysis. *In:* SAE International Journal of Fuels and Lubricants 5 (2012), Heft 1, S. 307-315. https://doi.org/10.4271/2011-01-2050.

[31] *Aronsson, U.:* Processes in Optical Diesel Engines. Division of Combustion Engines, Lund University, Sweden, Doctoral Thesis, 2011.

[32] *Pöllmann, S.; Härtl, M.; Wachtmeister, G.:* Injection Process of the Synthetic Fuel Oxymethylene Ether: Optical Analysis in a Heavy-Duty Engine. *In: :* SAE Technical Paper Series, SAE Technical Paper Series. SAE International400 Commonwealth Drive, Warrendale, PA, United States, 2020.

[33] *Korb, B.; Gleis, S.:* Auslegung und Entwicklung eines volloptischen Einzylinder-Groß-motors mittels Ansys Workbench und einer vereinfachten FKM-Richtlinie. *In: :* Ansys Conference & 33. CADFEM Users' Meeting, 2015.

[34] *Kashdan, J.T.; Thirouard, B.:* A Comparison of Combustion and Emissions Behaviour in Optical and Metal Single-Cylinder Diesel Engines. *In:* SAE International Journal of Engines 2 (2009), Heft 1, S. 1857-1872. https://doi.org/10.4271/2009-01-1963.

[35] *Kashdan, J.; Thirouard, B.:* Optical Engines as Representative Tools in the Development of New Combustion Engine Concepts. *In:* Oil & Gas Science and Technology – Revue d'IFP Energies nouvelles 66 (2011), Heft 5, S. 759-777. https://doi.org/10.2516/ogst/2011134.

[36] *Colban, W.F.; Kim, D.; Miles, P.C. et al.:* A Detailed Comparison of Emissions and Combustion Performance Between Optical and Metal Single-Cylinder Diesel Engines at Low Temperature Combustion Conditions. *In:* SAE International Journal of Fuels and Lubricants 1 (2009), Heft 1, S. 505-519. https://doi.org/10.4271/2008-01-1066.

[37] *Korb, B.:* Beitrag zur Charakterisierung des homogenen Magerbrennverfahrens bei Groß-gasmotoren mittels experimenteller Methoden im Hinblick auf Verbrennung, Wirkungs-grad und Emissionen. München, Technische Universität München, Dissertation, 2021.

[38] *Merts, M.; Derafshzan, S.; Hyvönen, J. et al.:* An optical investigation of dual fuel and RCCI pilot ignition in a medium speed engine. *In:* Fuel Communications 9 (2021), S. 100037. https://doi.org/10.1016/j.jfueco.2021.100037.

[39] *Greis, E.A.:* Laseroptische Untersuchungen des Verbrennungsprozesses in einem PKW-Dieselmotor. Aachen, Rheinisch-Westfälische Technische Hochschule, Dissertation, 2007.

[40] *Stenhouse, I.A.; Williams, D.R.; Cole, J.B. et al.:* CARS measurements in an internal combustion engine. *In:* Applied optics, Vol. 18 (1979), Iss. 22, pp. 3819-3825. https://doi.org/10.1364/AO.18.003819.

[41] *Geßenhardt, C.:* Endoskopische Bestimmung des Temperaturfeldes im Brennraum von Ottomotoren mittels laserinduzierter Fluoreszenz. Fakultät für Ingenieurweissenschaften, Abteiilung Maschinenbau, Universität Duisburg-Essen, Doctoral dissertation, 2013.

[42] *Oh, S.; Park, Y.; Seon, G. et al.:* Impacts of N2 and CO2 diluent gas composition on flame emission spectroscopy for fuel concentration measurements in flames. *In:* International Journal of Heat and Mass Transfer 149 (2020), S. 119174. https://doi.org/10.1016/j.ijheatmasstransfer.2019.119174.

[43] *Schefer, R.W.; Kulatilaka, W.D.; Patterson, B.D. et al.:* Visible emission of hydrogen flames. *In:* Combustion and Flame 156 (2009), Heft 6, S. 1234-1241. https://doi.org/10.1016/j.combustflame.2009.01.011.

[44] *Catapano, F.; Di Iorio, S.; Sementa, P. et al.:* Characterization of CH 4 and CH 4 /H 2 Mixtures Combustion in a Small Displacement Optical Engine. *In:* SAE International Journal of Fuels and Lubricants 6 (2013), Heft 1, S. 24-33. https://doi.org/10.4271/2013-01-0852.

[45] *Gaydon, A.:* The Spectroscopy of Flames. Springer Netherlands, Dordrecht, 1974.

[46] *Brockhinke, A.; Krüger, J.; Heusing, M. et al.:* Measurement and simulation of rotationally-resolved chemiluminescence spectra in flames. *In:* Applied Physics B 107 (2012), Heft 3, S. 539-549. https://doi.org/10.1007/s00340-012-5001-1.

[47] *Karmann, S.; Mühlthaler, M.; Prager, M. et al.:* A method for measuring in-cylinder λ-distribution in medium-speed DF engines. Lehrstuhl für Verbrennungskraftmaschinen Ausgabe 2016.

[48] *van Basshuysen, R.; Schäfer, F.:* Handbuch Verbrennungsmotor – Grundlagen, Komponenten, Systeme, Perspektiven ;Springer Vieweg, Wiesbaden, 2017.

[49] *Ferziger, J.H.; Perić, M.:* Numerische Strömungsmechanik. Springer, Berlin, 2008.

[50] *Laurien, E.; Oertel, H.:* Numerische Strömungsmechanik. Springer Fachmedien Wiesbaden, Wiesbaden, 2013.

[51] *Lecheler, S.:* Numerische Strömungsberechnung – Schneller Einstieg durch ausführliche praxisrelevante Beispiele, Studium, Vieweg + Teubner, Wiesbaden, 2009.

[52] *Herwig, H.; Schmandt, B.:* Strömungsmechanik – Physik – mathematische Modelle – thermodynamische Aspekte. Springer Berlin Heidelberg, Berlin, Heidelberg, 2015.

[53] *Schwarze, R.:* CFD-Modellierung – Grundlagen und Anwendungen bei Strömungsprozessen, Springer eBook Collection, Springer, Berlin, Heidelberg, 2013.

[54] *Beate Wötz:* Numerische Modellierung turbulenter Strömun mit Wärmeübergnag in einer konvektiv gekühlten Turbinenschaufel. Aachen, Rheinisch-Westfälischen Technischen Hochschule Aachen, Dissertation, 2018.

[55] *Gersten, K.:* Strömungsmechanik – Grundlagen der Impuls-, Wärme- und Stoffübertragung aus asymptotischer Sicht, Grundlagen und Fortschritte der Ingenieurwissenschaften, Vieweg & Teubner, Wiesbaden, 2014.

[56] *Klein, B.:* FEM – Grundlagen und Anwendungen der Finite-Element-Methode im Maschinen- und Fahrzeugbau, Vieweg Studium : Technik, Friedr. Vieweg & Sohn Verlag, Wiesbaden, 2007.

[57] *Mathiak, F.U.:* Die Methode der finiten Elemente (FEM) – Einführung und Grundlagen. Neubrandenburg, Hochschule Neubrandenburg, Vorlesungsskript, 2010.

[58] *Gebhardt, C.:* Praxisbuch FEM mit ANSYS Workbench – Einführung in die lineare und nichtlineare Mechanik. Hanser Verlag, München, 2014.

[59] *Forschungskuratorium Maschinenbau:* Rechnerischer Festigkeitsnachweis für Maschinenbauteile aus Stahl, Eisenguss- und Aluminiumwerkstoffen. Forschungskuratorium Maschinenbau, FKM-Richtlinie, VDMA-Verl., Frankfurt am Main, 2012.

[60] *Litfin, G.:* Technische Optik in der Praxis. Springer-Verlag, Berlin/Heidelberg, 2001.

[61] *Gross, H.:* Fundamentals of Technical optics, Handbook of optical systemsVol. 1, Wiley-VCH, Weinheim, 2005.

[62] *Thiele, R.:* Optische Netzwerke – Ein feldtheoretischer Zugang ; mit 12 Tabellen sowie 904 Formeln und 29 Aufgaben mit Lösungen. Friedr. Vieweg & Sohn Verlag | GWV Fachverlage GmbH Wiesbaden, Wiesbaden, 2008.

[63] *Hecht, E.:* Optik. Oldenbourg, München, 2009.

[64] *Gross, H. (ed.):* Handbook of optical systems, Volume 3, Aberration theory and correction of optical systems. Wiley-VCH, Weinheim, 2007.

[65] *Gross, H.; Zügge, H.; Peschka, M. et al.:* Aberration Theory and Correction of Optical Systems, Handbook of optical systemsVolume 3, Wiley-VCH, Weinheim, 2007.

[66] *Kingslake, R.; Johnson, R.B.:* Lens design fundamentals. Academic Press, Ansterdam, 2010.

[67] *Sasián, J.:* Image Evaluation // Introduction to Lens Design, Heft 5, Cambridge University Press, 2019.

[68] *Gross, H.; Blechinger, F.; Achtner, B. (eds.):* Survey of Optical Instruments, Handbook of optical systemsVolume 4, Wiley-VCH, Weinheim, 2008.

[69] *Martin, C.B.:* Design issues of a hyperfield fisheye lens. *In: Sasian, J.M.; Koshel, R.J.; Manhart, P.K. et al.* (Hrsg.): Novel Optical Systems Design and Optimization VII, SPIE Proceedings Heft 5524. SPIE, Bellingham, WA, 2004, S. 84-92.

[70] *Laikin, M.:* Lens design, Optical engineering Heft 48, Marcel Dekker, New York, 1995.

[71] *Samy, A.M.; Gao, Z.:* Simplified compact fisheye lens challenges and design. *In:* Journal of Optics 44 (2015), Heft 4, S. 409-416. https://doi.org/10.1007/s12596-015-0260-y.

[72] *Kumler, J.; Bauer, M.; (Keine Angabe):* Fisheye lens designs and their relative performance // Fish-eye lens designs and their relative performance. *In:* Proceedings of SPIE Vol.4093 (2000), S. 360.

[73] *Zhang, B.L.; Zhang, S.J.; Ding, W.Q. et al.:* Fisheye Lens Distortion Calibration Based on the Lens Charactetic Curves. *In:* Applied Mechanics and Materials 519-520 (2014), S. 636-639. https://doi.org/10.4028/www.scientific.net/AMM.519-520.636.

[74] *Thoby, M.:* LPP Theory, 2009, http://michel.thoby.free.fr/Fisheye_history_short/Beyond-the-pupil.html [Zugriff am: 21.06.2019].

[75] *Scaramuzza, D.; Martinelli, A.; Siegwart, R.:* A flexible technique for accurate omnidirectional camera calibration and structure from motion. *In: :* Computer Vision Systems, 2006 ICVS'06. IEEE International Conference on. IEEE, 2006, S. 45.

[76] *Kannala, J.; Brandt, S.S.:* A generic camera model and calibration method for conventional, wide-angle, and fish-eye lenses. *In:* IEEE transactions on pattern analysis and machine intelligence 28 (2006), Heft 8, S. 1335-1340. https://doi.org/10.1109/TPAMI.2006.153.

[77] *Micusík, B.; Pajdla, T.:* Structure from motion with wide circular field of view cameras. *In:* IEEE transactions on pattern analysis and machine intelligence, Vol. 28 (2006), Iss. 7, pp. 1135-1149. https://doi.org/10.1109/TPAMI.2006.151.

[78] *Puig, L.; Bermúdez, J.; Sturm, P. et al.:* Calibration of omnidirectional cameras in practice: A comparison of methods. *In:* Computer Vision and Image Understanding 116 (2012), Heft 1, S. 120-137. https://doi.org/10.1016/j.cviu.2011.08.003.

[79] *K. H. Strobl; W. Sepp; S. Fuchs et al.:* DLR CalDe and DLR CalLab. Institute of Robotics and Mechatronics, German Aerospace Center (DLR), http://www.ro-botic.dlr.de/callab/.

[80] *Akansu, S.O.; Kahrman, N.; CEPER, B.:* Experimental study on a spark ignition engine fuelled by methane–hydrogen mixtures. *In:* International Journal of Hydrogen Energy 32 (2007), Heft 17, S. 4279-4284. https://doi.org/10.1016/j.ijhydene.2007.05.034.

[81] *Sagar, S.M.V.; Agarwal, A.K.:* Experimental investigation of varying composition of HCNG on performance and combustion characteristics of a SI engine. *In:* International Journal of Hydrogen Energy 42 (2017), Heft 18, S. 13234-13244. https://doi.org/10.1016/j.ijhydene.2017.03.063.

[82] *Kawauchi, S.; Korb, B.; Wachtmeister G. et al.:* Understanding of combustion process in apremixed lean burn gas engine fueled withhydrogen enriched natural gas. *In:* CIMAC (Hrsg.), Helsinki, 2016.

[83] *Bhasker, J.P.; Porpatham, E.:* Effects of compression ratio and hydrogen addition on lean combustion characteristics and emission formation in a Compressed Natural Gas

fuelled spark ignition engine. *In:* Fuel 208 (2017), S. 260-270.
https://doi.org/10.1016/j.fuel.2017.07.024.

[84] *Biffiger, H.; Soltic, P.:* Effects of split port/direct injection of methane and hydrogen in a spark ignition engine. *In:* International Journal of Hydrogen Energy 40 (2015), Heft 4, S. 1994-2003. https://doi.org/10.1016/j.ijhydene.2014.11.122.

[85] *Di Iorio, S.; Sementa, P.; Vaglieco, B.M.:* Analysis of combustion of methane and hydrogen–methane blends in small DI SI (direct injection spark ignition) engine using advanced diagnostics. *In:* Energy 108 (2016), S. 99-107. https://doi.org/10.1016/j.energy.2015.09.012.

[86] *Hora, T.S.; Shukla, P.C.; Agarwal, A.K.:* Particulate emissions from hydrogen enriched compressed natural gas engine. *In:* Fuel 166 (2016), S. 574-580. https://doi.org/10.1016/j.fuel.2015.11.035.

[87] *Korb, B.; Kawauchi, S.; Wachtmeister, G.:* Influence of hydrogen addition on the operating range, emissions and efficiency in lean burn natural gas engines at high specific loads. *In:* Fuel 164 (2016), S. 410-418. https://doi.org/10.1016/j.fuel.2015.09.080.

[88] *Lim, G.; Lee, S.; Park, C. et al.:* Effects of compression ratio on performance and emission characteristics of heavy-duty SI engine fuelled with HCNG. *In:* International Journal of Hydrogen Energy 38 (2013), Heft 11, S. 4831-4838. https://doi.org/10.1016/j.ijhydene.2013.01.188.

[89] *Liu, J.; Duan, X.; Yuan, Z. et al.:* Experimental study on the performance, combustion and emission characteristics of a high compression ratio heavy-duty spark-ignition engine fuelled with liquefied methane gas and hydrogen blend. *In:* Applied Thermal Engineering 124 (2017), S. 585-594. https://doi.org/10.1016/j.applthermaleng.2017.06.067.

[90] *Park, C.; Kim, C.; Choi, Y. et al.:* Operating strategy for exhaust gas reduction and performance improvement in a heavy-duty hydrogen-natural gas blend engine. *In:* Energy 50 (2013), S. 262-269. https://doi.org/10.1016/j.energy.2012.10.048.

[91] *Park, C.; Lee, S.; Lim, G. et al.:* Full load performance and emission characteristics of hydrogen-compressed natural gas engines with valve overlap changes. *In:* Fuel 123 (2014), S. 101-106. https://doi.org/10.1016/j.fuel.2014.01.041.

[92] *Santoli, L.* de*; Lo Basso, G.; Bruschi, D.:* Energy characterization of CHP (combined heat and power) fuelled with hydrogen enriched natural gas blends. *In:* Energy 60 (2013), S. 13-22. https://doi.org/10.1016/j.energy.2013.07.012.

[93] *Tangöz, S.; Akansu, S.O.; Kahraman, N. et al.:* Effects of compression ratio on performance and emissions of a modified diesel engine fueled by HCNG. *In:* International

Journal of Hydrogen Energy 40 (2015), Heft 44, S. 15374-15380. https://doi.org/10.1016/j.ijhydene.2015.02.058.

[94] *Catapano, F.; Di Iorio, S.; Magno, A. et al.:* A comprehensive analysis of the effect of ethanol, methane and methane-hydrogen blend on the combustion process in a PFI (port fuel injection) engine. *In:* Energy 88 (2015), S. 101-110. https://doi.org/10.1016/j.energy.2015.02.051.

[95] *Catapano, F.; Di Iorio, S.; Sementa, P. et al.:* Analysis of energy efficiency of methane and hydrogen-methane blends in a PFI/DI SI research engine. *In:* Energy 117 (2016), S. 378-387. https://doi.org/10.1016/j.energy.2016.06.043.

[96] *Chen, L.; Wei, H.; Zhang, R. et al.:* Effects of spark plug type and ignition energy on combustion performance in an optical SI engine fueled with methane. *In:* Applied Thermal Engineering 148 (2019), S. 188-195. https://doi.org/10.1016/j.applthermaleng.2018.11.052.

[97] *Peñaranda, A.; Martinez Boggio, S.D.; Lacava, P.T. et al.:* Characterization of flame front propagation during early and late combustion for methane-hydrogen fueling of an optically accessible SI engine. *In:* International Journal of Hydrogen Energy 43 (2018), Heft 52, S. 23538-23557. https://doi.org/10.1016/j.ijhydene.2018.10.167.

[98] *Di Iorio, S.; Sementa, P.; Vaglieco, B.M.:* Optical diagnostics for the analysis of hydrogen–methane blend combustion in internal combustion engines. *In: Barbir, F.; Basile, A.; Veziroğlu, T.N.* (eds.): Hydrogen energy conversion, Woodhead publishing series in energynumber 85. Elsevier/WP Woodhead Publishing, Amsterdam, 2016, pp. 233-261.

[99] *Merola, S.S.; Di Iorio, S.; Irimescu, A. et al.:* Spectroscopic characterization of energy transfer and thermal conditions of the flame kernel in a spark ignition engine fueled with methane and hydrogen. *In:* International Journal of Hydrogen Energy 42 (2017), Heft 18, S. 13276-13288. https://doi.org/10.1016/j.ijhydene.2017.03.219.

[100] *Soltic, P.; Hilfiker, T.:* Efficiency and raw emission benefits from hydrogen addition to methane in a Prechamber–Equipped engine. *In:* International Journal of Hydrogen Energy 45 (2020), Heft 43, S. 23638-23652. https://doi.org/10.1016/j.ijhydene.2020.06.123.

[101] *Di Iorio, S.; Sementa, P.; Vaglieco, B.M.:* Experimental investigation on the combustion process in a spark ignition optically accessible engine fueled with methane/hydrogen blends. *In:* International Journal of Hydrogen Energy 39 (2014), Heft 18, S. 9809-9823. https://doi.org/10.1016/j.ijhydene.2014.04.065.

[102] *Portin, K.; Stegar, J.; Monnet, G. et al.:* Hydrogen as fuel for Wärtsilä gas engines. *In:* CIMAC (Hrsg.), Helsinki, 2016.

[103] *Wahl, J.; Kallo, J.:* Quantitative valuation of hydrogen blending in European gas grids and its impact on the combustion process of large-bore gas engines. *In:* International Journal of Hydrogen Energy 45 (2020), Heft 56, S. 32534-32546. https://doi.org/10.1016/j.ijhydene.2020.08.184.

[104] *Cruccolini, V.; Discepoli, G.; Cimarello, A. et al.:* Lean combustion analysis using a corona discharge igniter in an optical engine fueled with methane and a hydrogen-methane blend. *In:* Fuel 259 (2020), S. 116290. https://doi.org/10.1016/j.fuel.2019.116290.

[105] *Franz Joos:* Technische Verbrennung – Verbrennungstechnik, Verbrennungsmodellierung, Emissionen, SpringerLink Bücher, Springer Berlin Heidelberg, Berlin, Heidelberg, 2006.

[106] *Warnatz, J.; Maas, U.; Dibble, R.W.:* Verbrennung – Physikalisch-Chemische Grundlagen, Modellierung und Simulation, Experimente, Schadstoffentstehung, Springer e-Book Collection, Springer Berlin Heidelberg, Berlin, Heidelberg, 2001.

[107] *Kammerstätter, S.:* Verbrennungsablauf und Schadstoffbildung in Erdgas Großmotoren mit Vorkammerzündung. München, Technische Universität München, Dissertation, 2012.

[108] *García-Armingol, T.; Ballester, J.:* Flame chemiluminescence in premixed combustion of hydrogen-enriched fuels. *In:* International Journal of Hydrogen Energy 39 (2014), Heft 21, S. 11299-11307. https://doi.org/10.1016/j.ijhydene.2014.05.109.

[109] *García-Armingol, T.; Ballester, J.:* Influence of fuel composition on chemiluminescence emission in premixed flames of CH4/CO2/H2/CO blends. *In:* International Journal of Hydrogen Energy 39 (2014), Heft 35, S. 20255-20265. https://doi.org/10.1016/j.ijhydene.2014.10.039.

[110] *Ballester, J.; Hernández, R.; Sanz, A. et al.:* Chemiluminescence monitoring in premixed flames of natural gas and its blends with hydrogen. *In:* Proceedings of the Combustion Institute 32 (2009), Heft 2, S. 2983-2991. https://doi.org/10.1016/j.proci.2008.07.029.

[111] *Oh, J.; Noh, D.; Ko, C.:* The effect of hydrogen addition on the flame behavior of a non-premixed oxy-methane jet in a lab-scale furnace. *In:* Energy 62 (2013), S. 362-369. https://doi.org/10.1016/j.energy.2013.09.049.

[112] *Reyes, M.; Tinaut, F.V.; Giménez, B. et al.:* Effect of hydrogen addition on the OH* and CH* chemiluminescence emissions of premixed combustion of methane-air mixtures. *In:* International Journal of Hydrogen Energy 43 (2018), Heft 42, S. 19778-19791. https://doi.org/10.1016/j.ijhydene.2018.09.005.

[113] *Nilsson, E.J.K.; van Sprang, A.; Larfeldt, J. et al.:* The comparative and combined effects of hydrogen addition on the laminar burning velocities of methane and its blends with ethane and propane. *In:* Fuel 189 (2017), S. 369-376. https://doi.org/10.1016/j.fuel.2016.10.103.

[114] *Martinez, S.; Lacava, P.; Curto, P.L. et al.:* Effect of Hydrogen Enrichment on Flame Morphology and Combustion Evolution in a SI Engine Under Lean Burn Conditions. *In: :* SAE Technical Paper Series, SAE Technical Paper Series. SAE International400 Commonwealth Drive, Warrendale, PA, United States, 2018.

[115] *Wang, J.; Wei, Z.; Zhang, M. et al.:* A review of engine application and fundamental study on turbulent premixed combustion of hydrogen enriched natural gas. *In:* Science China Technological Sciences 57 (2014), Heft 3, S. 445-451. https://doi.org/10.1007/s11431-014-5471-y.

[116] *Eicheldinger, S.; Karmann, S.; Prager, M. et al.:* Optical screening investigations of backfire in a large bore medium speed hydrogen engine. *In:* International Journal of Engine Research (2021), Special issue on the current and future use of H2 and H2 based e-fuels in combustion engines and fuel cells, 146808742110531. https://doi.org/10.1177/14680874211053171.

[117] *Verhelst, S.; Wallner, T.:* Hydrogen-fueled internal combustion engines. *In:* Progress in Energy and Combustion Science 35 (2009), Heft 6, S. 490-527. https://doi.org/10.1016/j.pecs.2009.08.001.

[118] *Zacharias, F.:* Gasmotoren, Vogel-Fachbuch, Vogel, Würzburg, 2001.

[119] *Karmann, S.; Friedrich, C.; Prager, M. et al.:* Realization of a Fully Optically Accessible Medium Speed Large Bore Engine Using a Fisheye Optic. *In: :* ASME 2020 Power Conference. American Society of Mechanical Engineers, Virtual, Online, 08042020.

[120] *Karmann, S., Kunkel, C., Prager, M., and Wachtmeister, G; Karmann, S.B.; Kunkel, C. et al.:* A New Optical Access for Medium Speed Large Bore Marine Engines under Full-Load Operating Conditions. *In:* SAE Int. J. Engines 14 (2021), 14 // 6. https://doi.org/10.4271/03-14-06-0052.

[121] *Karmann, S.B.; Weber, S.; Stürzl, W. et al.:* Development of an Optical Investigation Method for Diesel and Oxymethylene Ether Spray in a Large-Bore Dual-Fuel Engine Using a Fisheye Optical System. *In:* SAE International Journal of Engines 16 (2023), Heft 5. https://doi.org/10.4271/03-16-05-0036.

[122] *Karmann, S.B.; Röhrle, H.; Klier, B. et al.:* Design of an Endoscopic Fully Optically Accessible High-Speed Large-Bore Engine. *In:* SAE International Journal of Engines 15 (2022), Heft 6. https://doi.org/10.4271/03-15-06-0042.

[123] *Karmann, S.; Eicheldinger, S.; Prager, M. et al.:* Experimental comparison between an optical and an all-metal large bore engine. *In:* International Journal of Engine Research (2022), 146808742210827. https://doi.org/10.1177/14680874221082794.

[124] *Karmann, S.; Eicheldinger, S.; Prager, M. et al.:* Optical and thermodynamic investigations of a methane and hydrogen blend fueled large bore engine. *In:* International Journal of Engine Research (2022), Special issue on the current and future use of H2 and H2 based e-fuels in combustion engines and fuel cells, 146808742110667. https://doi.org/10.1177/14680874211066735.

[125] *Karmann, S.; Eicheldinger, S.; Prager, M. et al.:* Optical and Thermodynamic Investigations of a Methane- and Hydrogen-Blend-Fueled Large-Bore Engine Using a Fisheye Optical System. *In:* Energies, Vol. 16 (2023), Iss. 4, p. 1590. https://doi.org/10.3390/en16041590.

[126] *Honecker, C.; Neumann, M.; Glueck, S. et al.:* Optical Spray Investigations on OME3-5 in a Constant Volume High Pressure Chamber. *In: :* SAE Technical Paper Series, SAE Technical Paper Series. SAE International400 Commonwealth Drive, Warrendale, PA, United States, 2019.

[127] *Kuppa, K.; Nguyen, H.D.; Goldmann, A. et al.:* Numerical modelling of unburned hydrocarbon emissions in gas engines with varied fuels. *In:* Fuel 254 (2019), S. 115532. https://doi.org/10.1016/j.fuel.2019.05.115.

[128] *Ma, F.; Wang, Y.; Liu, W. et al.:* Experimental study on thermal efficiency and emission characteristics of a lean burn hydrogen enriched natural gas engine. *In:* International Journal of Hydrogen Energy 32 (2007), Heft 18, S. 5067-5075. https://doi.org/10.1016/j.ijhydene.2007.07.048.

[129] *Korb, B.; Kuppa, K.; Nguyen, H.D. et al.:* Experimental and numerical investigations of charge motion and combustion in lean-burn natural gas engines. *In:* Combustion and Flame 212 (2020), S. 309-322. https://doi.org/10.1016/j.combustflame.2019.11.005.

[130] *Naumann, H.; Schröder, G.; Löffler-Mang, M.:* Handbuch Bauelemente der Optik – Grundlagen, Werkstoffe, Geräte, Messtechnik. Hanser, München, 2014.

[131] *Gerhard, C.:* Tutorium Optik. Springer Berlin Heidelberg, Berlin, Heidelberg, 2016.

[132] *Demtröder, W.:* Experimentalphysik 2 – Elektrizität und Optik, Springer-Lehrbuch, Springer Berlin Heidelberg, Berlin, Heidelberg, 2017.

Betreute Studienarbeiten

Während der Anstellung des Autors als wissenschaftlicher Mitarbeiter entstanden unter seiner Betreuung nachfolgende Studienarbeiten. Der Autor dankt den Studentinnen und Studenten für ihren großartigen Einsatz, die hervorragenden Ergebnisse und ihren Beitrag zum Gelingen der Konstruktionen, Simulationen und Experimente.

Röhrle, H.M.: Entwicklung und Konstruktion eines minimal-invasiven optischen Zugangs für einen schnelllaufenden Großmotor, Masterarbeit 2019

Klier, B.: Optimierung einer Weitwinkeloptik für den Einsatz in einem Verbrennungsmotor, Semesterarbeit 2019

Bombelli, A.: Optimierung eines seitlichen Zugangs für einen optisch vollzugänglichen schnelllaufenden Einzylinder-Groß-Motor. Bachelorarbeit 2018

Niesl, C.: Abbildung des Gemischbildungsprozesses eines optisch zugänglichen Groß-DF-Einzylinder-Forschungsmotors und Voruntersuchungen zur Verbrennung mittels 3D-CFD unter Berücksichtigung der Realgeometrie, Semesterarbeit 2018

Kink, K.: Entwicklung und Konstruktion eines Ventiltriebs für einen optisch vollzugänglichen Groß Einzylinder DF-Motor, Bachelorarbeit 2017

Neureiter, M.: Entwicklung und Konstruktion eines optischen Kolbens für einen optisch vollzugänglichen Groß Einzylinder DF-Motor, Bachelorarbeit 2017

Köhler, P.: Entwicklung und Konstruktion eines Grundaufbaus für einen optisch vollzugänglichen Groß-Einzylinder-DF-Motor, Bachelorarbeit 2017

Milchev, K.: Untersuchung verschiedener Vernetzungsstrategien zur Erstellung einer Ladungswechselsimulation eines opt. zugänglichen Groß-DF-Motors, Bachelorarbeit 2017

Equiza, M.: Kühlwassersimulation eines seitlichen optischen Zugangs an einem Groß DF Einzylinder Forschungsmotor, Masterarbeit 2017

Baran, F. W.: Simulative Analyse eines Pleuels und des Gleitlagerschmierspaltes in einem Schiffsdieselversuchsmotors, Masterarbeit 2017

Maas, P.: Berechnung und Simulation eines innovativen alternativen optischen Zugangs für Großmotoren durch den Zylinderkopf, Semesterarbeit 2017

Wilhelm, S.: Entwicklung und Bewertung von Konzepten zur optischen Zugänglichkeit durch den Kolben an einem Groß-Dual-Fuel Einzylinder Forschungsmotor, Bachelorarbeit 2016

Fritz, P.: Strömungssimulation des Kühlmantels eines optisch zugänglichen Groß DF Einzylinder Forschungsmotors, Bachelorarbeit 2016

Schneider, E: Optimierung eines optischen seitlichen Zugangskonzeptes an einem Groß Dual Fuel Einzylinderforschungsmotor, Bachelorarbeit 2016

Nedvidek, M.: Vergleich der Realisierbarkeit verschiedener Umsetzungsmöglichkeiten zur optischen Zugänglichkeit an einem Groß-Dual-Fuel- Einzylinder-Forschungsmotor und Weiterentwicklung eines bestehenden Konzepts, Bachelorarbeit 2016

Schneider, E: Optimierung eines optischen seitlichen Zugangskonzeptes an einem Groß Dual Fuel Einzylinderforschungsmotor, Bachelorarbeit 2016

Publikationsliste

Karmann, S.; Eicheldinger, S.; Prager, M.; Jaensch, M.; Wachtmeister, G. Optical and Thermo-dynamic Investigations of a Methane- and Hydrogen-Blend-Fueled Large-Bore Engine Using a Fisheye Optical System. *Energies* 2023, *16*, 1590. https://doi.org/10.3390/en16041590

Karmann, S., Weber, S., Stürzl, W., Prager, M. et al., "Development of an Optical Investigation Method for Diesel and Oxymethylene Ether Spray in a Large-Bore Dual-Fuel Engine Using a Fisheye Optical System," SAE Int. J. Engines 16(5):2023, doi:10.4271/03-16-05-0036.

Karmann, S.; Eicheldinger, S.; Prager, M.; Jaensch, M.; Wachtmeister, G. Experimental Comparison Between an Optical and an All-Metall Large Bore Engine. International Journal of Engine Research 2022,146808742210827. doi: 10.1177/14680874221082794.

Karmann, S.; Eicheldinger, S.; Prager, M.; Wachtmeister, G. Optical and thermodynamic investigations of a methane and hydrogen blend fueled large bore engine. International Journal of Engine Research 2022,146808742110667. doi: 10.1177/14680874211066735.

Karmann, S., Röhrle, H., Klier, B., Prager, M. et al., "Design of an Endoscopic Fully Optically Accessible High-Speed Large-Bore Engine," *SAE Int. J. Engines* 15(6):2022, https://doi.org/10.4271/03-15-06-0042

Eicheldinger, S.; Karmann, S.; Prager, M.; Wachtmeister, G. Optical screening investigations of backfire in a large bore hydrogen engine. International Journal of Engine Research 2021,146808742110531. doi: 10.1177/14680874211053171.[4]

Karmann, S., Kunkel, C., Prager, M.; Wachtmeister, G., "A New Optical Access for Medium Speed Large Bore Marine Engines under Full-Load Operating Conditions," *SAE Int. J. Engines* 14(6):867-883, 2021, https://doi.org/10.4271/03-14-06-0052 .

Frankl S, Gleis S, Karmann S, Prager M, Wachtmeister G. Investigation of ammonia and hydrogen as CO2-free fuels for heavy duty engines using a high pressure dual fuel combustion process. *International Journal of Engine Research*. 2021;22(10):3196-3208. doi:10.1177/1468087420967873

Karmann, S, Friedrich, C, Prager, M; Wachtmeister, G. "Realization of a Fully Optically Accessible Medium Speed Large Bore Engine Using a Fisheye Optic." *Proceedings of the ASME 2020 Power Conference collocated with the 2020 International Conference on Nuclear Engineering. ASME 2020 Power Conference*. Virtual, Online. August 4–5, 2020. V001T03A008. ASME. https://doi.org/10.1115/POWER2020-16477

Karmann, S., Prager, M.; Wachtmeister, G., "Conceptual Investigations on Full Optical Accessibility to Large-Bore Medium-Speed Engines," *SAE Int. J. Engines* 12(3):291-308, 2019, https://doi.org/10.4271/03-12-03-0020 .

---

[4] Die Autoren Stefan Eicheldinger und Stephan Karmann teilen sich die Erstautorenschaft und haben zu gleichen Teilen zu dieser Veröffentlichung beigetragen.

Karmann, S., Rösler, S., Wachtmeister, G., Fischer, P. et al., "Co-Simulation Study of the Split-Crankshaft Engine's Electromechanical Clutch Unit," *SAE Int. J. Engines* 11(1):79-94, 2018, https://doi.org/10.4271/03-11-01-0006.

Baumgartner, L.S.; Karmann, S.; Backes, F.; Stadler, A.; Wachtmeister, G. „Experimental Investigation of Orifice Design Effects on a Methane Fuelled Prechamber Gas Engine for Automotive Applications", SAE Technical Papers 2017, doi:10.4271/2017-24-0096

Karmann, S.; Mühlthaler, M.; Prager, M.; Wachtmeister, G.; Unfug, F. „A method for measuring in-cylinder λ-distribution in medium-speed DF engines" 2016, Horizon 2020

A. Anhang

A.1 Definitionen von Begrifflichkeiten zur Beschreibung optischer Systeme

Die nachfolgenden Definitionen bieten einen Überblick über in der Arbeit verwendete Begrifflichkeiten aus der Optik. Für eine tiefergehende Beschreibung und formelmäßige Darstellung von Abhängigkeiten zwischen den erklärten Begriffen muss aufgrund deren Umfangs auf die einschlägige Fachliteratur nach ([60, 63, 130, 131]) verwiesen werden.

Asphäre

Asphären sind rotationssymmetrische Linsen bei denen der Krümmungsradius radial vom Mittelpunk an mindestens einer Stelle abweicht.

Dispersion

Unter Dispersion wird die Abhängigkeit des Brechnungsindex oder besser der Ausbreitungsgeschwindigkeit in einem Medium von der Wellenlänge verstanden.

Doublet

Als Doublet werden zwei miteinander verkittete Linsen bezeichnet.

Transversal und longitudinal

Transversal bedeutet quer zur Richtung der Lichtausbreitung. Longitudinal dagegen beschreibt die Richtung in Lichtausbreitung.

Apertur und Feldblende

Die Apertur ist die maximale Öffnungsweite in einem optischen System, durch welche Lichtstrahlen treten können. Meist wird in optischen Systemen eine variable, kreisförmige Aperturblende eingesetzt, um Bilder abblenden zu können. Damit kann u.a. die Schärfentiefe angepasst werden. Die Anpassung des Aperturdurchmessers wird durch die Blendenzahl f# beschrieben. Der maximale Durchmesser beeinflusst den maximal auflösbaren Bereich einer Optik. Zusammen mit der Brennweite bestimmt die Apertur die Lichtstärke der Optik. Eine größere Apertur führt damit zu helleren und besser aufgelösten Bildern. [63]
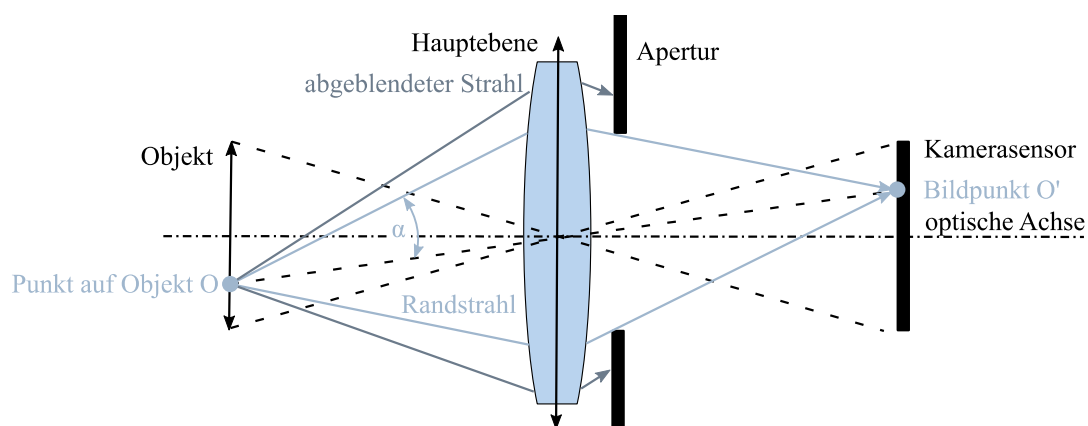

Abbildung 21 Apertur (nach [63], mod.)

Abbildung 21 zeigt die Abbildung eines auf einem Objekt liegenden Punktes O auf den Bildpunkt O' durch eine einfache Sammellinse und einer dahinter liegenden Aperturblende. Die Randstrahlen bestimmen den maximal möglichen halben Öffnungswinkel α. Alle Strahlen, welche von dem Objektseitigen Punkt O ausgehen und einen größeren Winkel aufweisen, werden abgeblendet. Das Bild wird dadurch dunkler. Die Feldblende begrenzt das Gesichtsfeld eines optischen Systems und schränkt die Bildgröße ein. Diese ist meist durch die Größe des Kamerasensors begrenzt. [63]

Eintrittspupille und Austrittspupille

Als Eintrittspupille wird das virtuelle Bild der Aperturblende bezeichnet, welches entsteht, wenn die Blende von der Eintrittsseite des Lichtes in eine Optik betrachtet wird. Diese ist ein Maß des an der Abbildung beteiligten Lichtes, da die Eintrittspupille den Öffnungswinkel eines geraden noch einzufangenden Strahlenbündels auf der Objektseite definiert. Damit hat sie Einfluss auf die resultierende Lichtstärke im optischen System.

Die Austrittspupille definiert genau den umgekehrten Fall, nämlich den Öffnungswinkel, des aus der Optik austretenden Lichtbündels. Befindet sich keine Linse nach der Aperturblende, so entspricht die Größe der Austrittspupille dem freien Durchmesser der Aperturblende. [63]

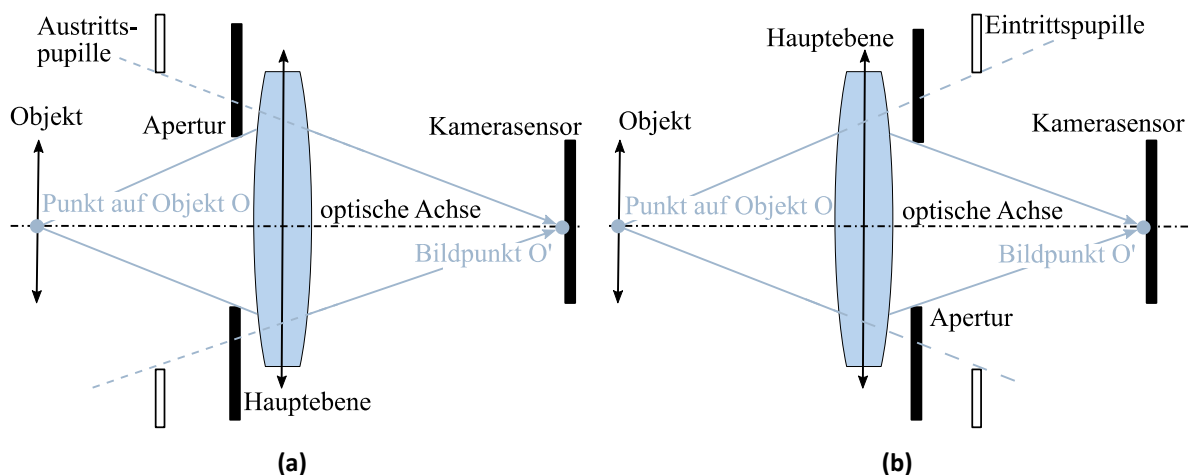Abbildung 22 zeigt die Bestimmung der Ein- und Austrittspupille.

Abbildung 22 (a) Eintritts (b)Austrittspupille (nach [63], mod.)

Feldwinkel

Der Feldwinkel ist eine Kenngröße des Sichtfeldes einer Optik. Dieser beschreibt auf Objektseite den doppelten Winkel zwischen der optischen Achse und einem vom Rande des Objektes verlaufenden Hauptstrahls. [63]

Feldlinsen

Eine Feldlinse wird nahe des vom Objektiv produzierten reellen Bildes angeordnet. Feldlinsen reduzieren Lichtverluste und Bildabschattungen wie sie bei Optiken aus mehreren Linsen durch die wiederholte Abbildung entstehen. Starre Stablinsen Endoskope nutzen diese, um die Lichtverluste zu reduzieren.

Hauptstrahl

Der Hauptstrahl repräsentiert als Zentralstrahl ein kegelförmiges Strahlenbündel ausgehend vom Objekt. Abbildung 23 zeigt die Konstruktion des Hauptstrahls exemplarisch nach [63] an einem optischen System mit drei Linsen. Dieses wir ausgehend von einem nicht auf der optischen Achse liegenden Punktes auf Objektseite, z.B. den äußersten Punkte des Objektes, im Raytracing für die Berechnung der Abbildungsfehler verwendet.

Der Hauptstrahl tritt in das optische System entlang einer Linie ein, deren gedachte Verlängerung durch den Mittelpunkt der Eintrittspupille verläuft (vgl. Abbildung 23). Je nach Lage der Apperturblende zwischen Ein- und Austritt verläuft der Hauptstrahl danach durch deren Mittelpunkt. Bei Verlassen des optischen Systems geschieht dies entlang einer Linie, deren Verlängerung den Mittelpunkt der Austrittspupille schneidet. [63]
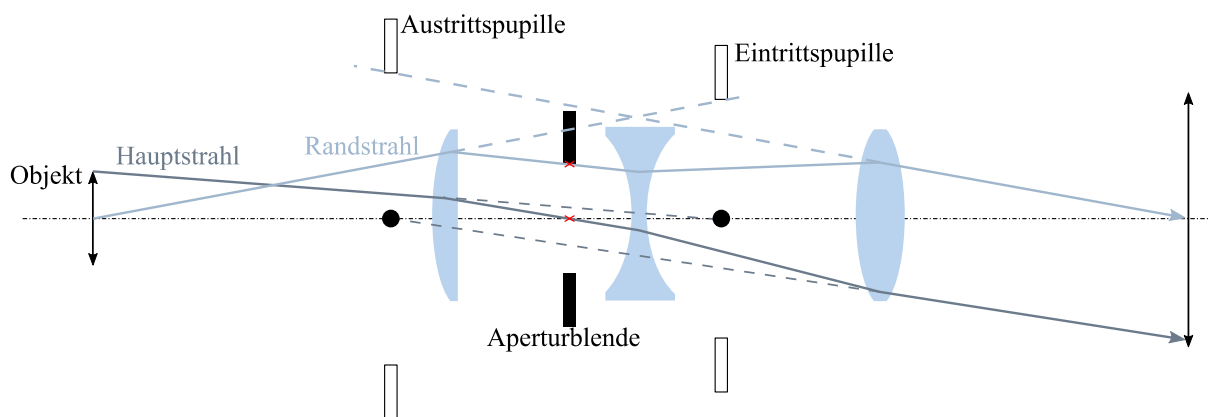
Abbildung 23 Konstruktion des Haupt- und Randstrahls (nach [63], mod.)

Randstrahl

Der Randstrahl verläuft ausgehend von der optischen Achse zum Rand der Eintrittspupille. Die Achse kann hier auch der Hauptstrahl sein womit der Randstrahl die Grenze des durch den Hauptstrahl repräsentierten kegelförmigen Strahlenbündels wiederspiegelt. [63]

Die Konstruktion des Randstrahls ausgehend von einem Punkt auf der optischen Achse ist nach [63] in Abbildung 23 dargestellt.

Meridional- und Saggitalebene

Der Begriff Meridionalebene bezeichnet eine jede Ebene, welche durch die optische Achse und einen beliebigen Objektpunkt verlaufen.

Die Saggitalebene enthält den Hauptstrahl eines beliebigen Strahlenbündels und steht senkrecht auf der Meridionalebene

Airy Scheibchen

In der Optik sind die Airy-Scheibe (Beugungsscheibe) und das Airy-Muster Beschreibungen des am besten fokussierten Lichtpunkts, den eine perfekte Linse mit kreisförmiger Öffnung erzeugen kann. Die Auflösung ist dabei begrenzt durch die Beugung des Lichts. Die Intensität

des Lichtes reduziert sich damit auf 84% innerhalb des Airy Scheibchens. Damit kann ein Lichtpunkt durch eine Optik aufgrund der auftretenden Beugung niemals auf einen Punkt abgebildete werden. [63]

Sphärische Aberrationen (Öffnungsfehler)

Achsensymmetrisch einfallende Strahlen weisen bei Verlassen des Systems und Schnitt mit der optischen Achse unterschiedliche Schnittweiten auf. Strahlen im Paraxialgebiet, mit kleinen Feldwinkeln, schneiden sich im paraxialen Bildpunkt. Bei Verlassen des Paraxialgebietes kommt es aufgrund der stärkeren Brechung des Lichtes am Rand einer sphärischen Linse zur Entstehung weiterer, näher an der letzten Linsenfläche liegende Schnittpunkte. Es wird hier je nach Lage der Schnittpunkte zum Gaußschen Punkt die positive, vor dem Punkt verlaufende, und negative, nach dem Punkt entstehende sphärische Aberration unterschieden. Die einhüllende Kurve der zueinander verlaufenden Strahlen in der Meridionalebene bildet die sog. Kaustik, deren Spitze der paraxiale Bildpunkt ist. Im Schnitt der Bildebene mit den Lichtstrahlen entsteht ein Zerstreuungskreis durch die unterschiedlichen Schnittweiten und erzeugt damit eine unscharfe Abbildung. Abbildung 24 zeigt bei parallel einfallenden Strahlen an einer bikonvexen Linse die Entstehung der Kaustik (einhüllende Kurve).

Für ein möglichst kontrastreiches Bild muss daher die Bildebene so positioniert werden, dass die Randstrahlen maximal fokussiert werden. Dieser Ort entspricht dem Zerstreuungskreis mit dem kleinstmöglichen Durchmesser am Ort der Kaustik mit der größten Einschnürung. Alternativ ist die mittlere Bildebene aus maximalem und minimalem Abstand der Schnittpunkte zur Linse eine weitere Möglichkeit, die Bildebene zu positionieren. Für die Gaußsche Bildebene im paraxialen Bildpunkt ergeben sich der laterale und axiale Öffnungsfehler in Abhängigkeit der Strahlhöhe. Die sphärische Aberration für nicht paraxiale Strahlen weist eine Abhängigkeit der Brennweite von der Blendenöffnung auf. [63]

Um die sphärische Aberration zu korrigieren, werden sog. Linsen bester Form verwendet. Da hier vor allem die Krümmung der Linse einen großen Einfluss hat, wird diese optimiert bzw. um die gleiche Brechkraft zu gewährleisten auf mehrere Linsen verteilt. Daneben können asphärische Linsen für eine komplette Korrektur eingesetzt werden. [130]
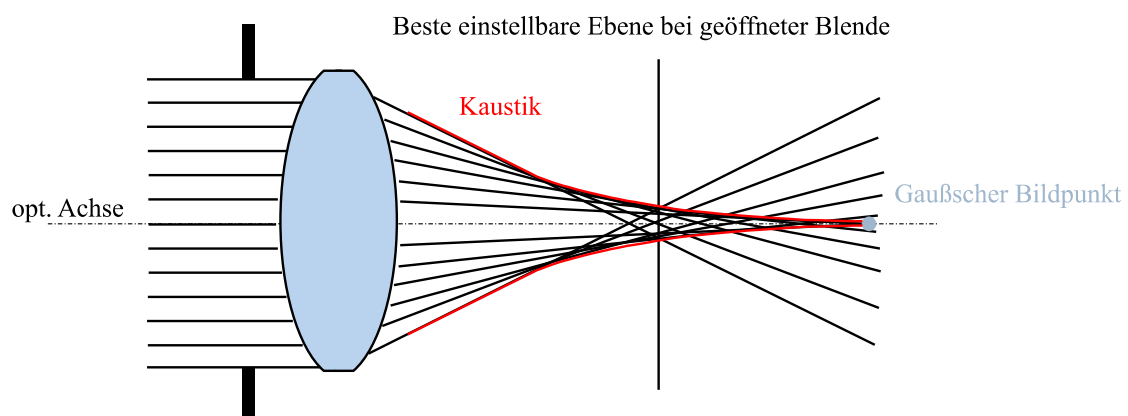

Abbildung 24 Sphärische Aberration Öffnungsfehler (nach [130], mod.)

Koma (Asymmetriefehler)

Befinden sich Objektpunkte außerhalb der optischen Achse und treffen deren parallele Lichtstrahlen unter einem Winkel zur optischen Achse geneigt auf eine Linse, so ist analog zur sphärischen Aberration und der unterschiedlich starken Brechung kein gemeinsamer Schnittpunkt aller Strahlen zu erreichen. Stattdessen werden die Lichtstrahlen und deren Schnittpunkte weg von der optischen Achse zum Rand der Linse hin verschoben. In der Bildebene ergeben sich im einfachsten Fall der Koma nicht konzentrisch liegende sowie unterschiedlich große Ringe. Damit variiert der transversale Abbildungsmaßstab je nach Linsenzone bzw. dem Ort auf der Linse auf den die Strahlen treffen (1 und 1' vgl. Abbildung 25). Dies wird in Abbildung 25 durch einen größeren Kreisdurchmesser für die Randstrahlen als für mittlere Strahlenbündel deutlich. Erfahren Randstrahlen die größte Vergrößerung, wird die Koma als positiv, erfahren Randstrahlen die geringste Vergrößerung als negativ definiert. [63]
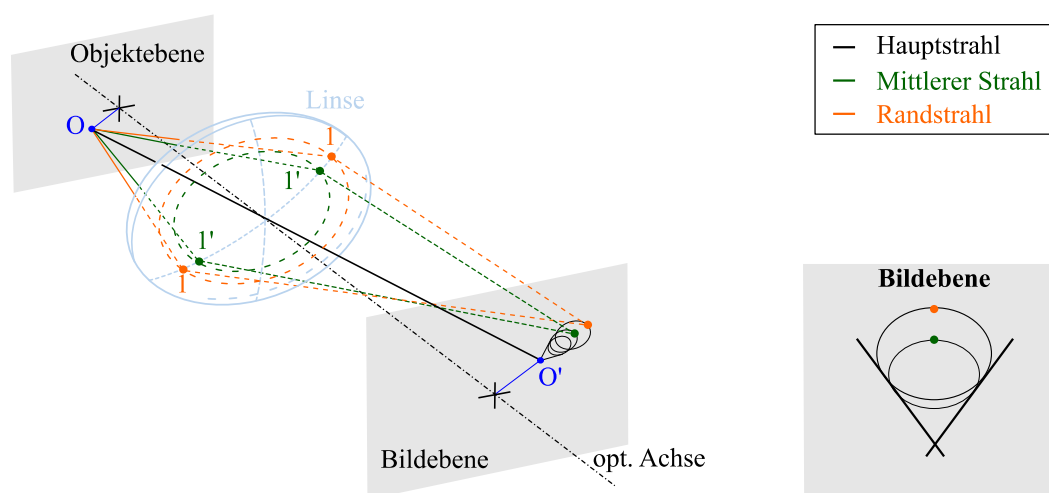
Abbildung 25 Darstellung einer positiven Koma (nach [63], mod.)

Astigmatismus (Punktlosigkeit)

Für objektseitige Punktquellen außerhalb der optischen Achse trifft der Strahlkegel des Lichtes asymmetrisch auf die Linse. Zur Beschreibung des damit ebenfalls windschiefen Hauptstrahles wird dieser in zwei Ebenen betrachtet – der Meridional- und der dazu senkrecht stehenden Sagittalebene. Für beide Ebenen ergeben sich aufgrund des ungleichen Schnittes mit der Linse und der dadurch entstehenden Radien unterschiedliche Brennweiten. Dies wirkt sich auf die Abbildung dahingehend aus, dass an zwei zueinander versetzten Orten Bildpunkte (primäre und sekundäre Linienbildung siehe Abbildung 26) entstehen, welche eine scharfe Abbildung des Objektes verhindern. Der Unschärfekreis entsteht zwischen meridionalem und sagittalem Brennpunkt und bildet den Objektpunkt als unscharfen Kreis ab. Das entstehende primäre Bild wird, da es auf der Meridionalebene senkrecht steht, auch als Meridional- oder Tangential-Bild bezeichnet. Das zur Sagittalebene senkrecht stehende Bild wird als Sagittal-oder radiales Bild bezeichnet. Damit werden alle radialen Konturen auf der Saggitalschale und alle tangentialen auf der Meridionalschale abbgebildet. Beide Schalen berühren sich im Gaußpunkt. Die Erweiterung der meridionalen und saggitalen Ebene wird durch die Bildfeldwölbung notwendig. Der Astigmatismus ist von der Linsenkrümmung und der Blendenposition abhängig und kann über deren Anpassung optimiert werden. [63, 130]
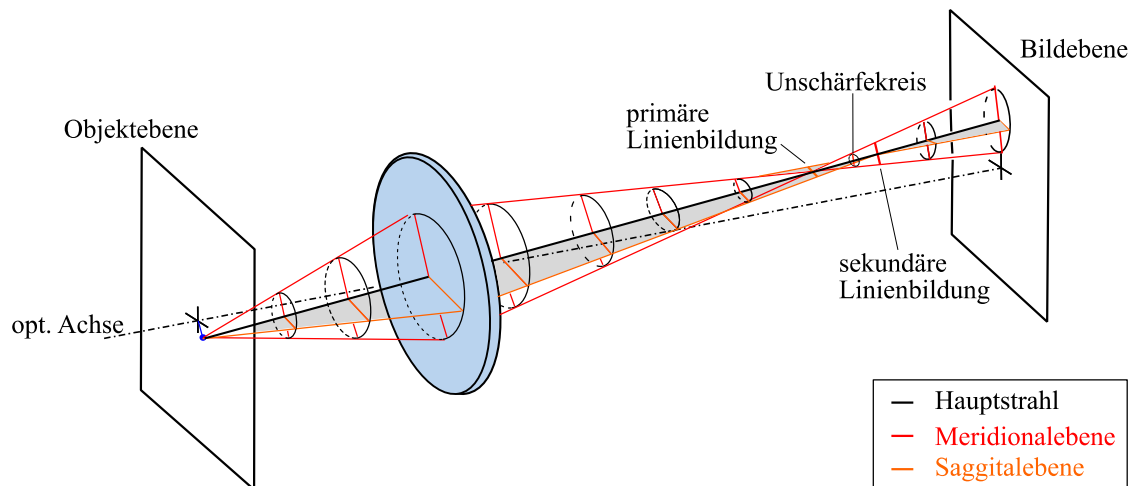
Abbildung 26 Astigmatismus (nach [63], mod.)

Bildfeldwölbung

Selbst bei ausreichenden Maßen zum Beheben des Astigmatismus werden ebene, senkrecht zur optischen Achse stehende Objekte nicht auf eine flache Ebene abgebildet. Dies liegt daran, dass achsparallele und schräg einfallende Lichtstrahlen unterschiedlich gebrochen werden. [132]

Abbildung 27 zeigt die Entstehung der Bildschale für eine Bikonvexlinse. Josef Maximilian Petzval entwickelte 1843 eine Formel zu Berechnung der Bildfeldwölbung. Durch den Einsatz einer dünnen plankonkaven Feldlinse mit einer planen Seite als Bildseite und einer konkaven Objektseite kann die Bildfeldwölbung reduziert werden. Daneben können auch dicke Menisken und Linsengruppen in Form von Triplets oder zwei ausgleichende Linsen in einigem Abstand zur Korrektur eingesetzt werden. [64]
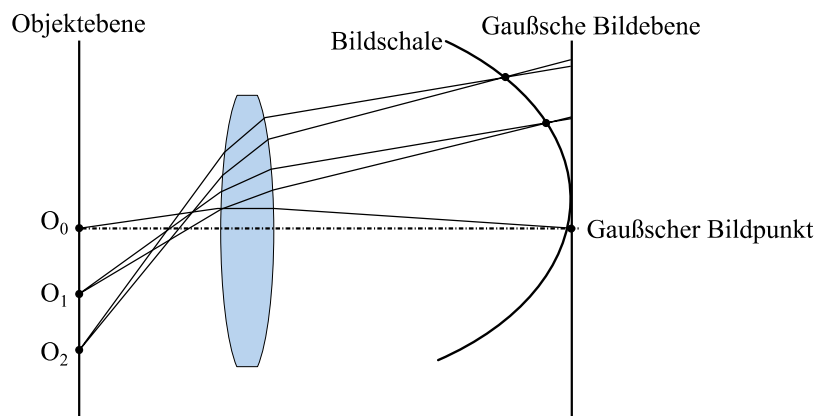
Abbildung 27 Bildfeldwölbung (nach [132], mod.)

Verzeichnung

Als Verzeichnung wird die rein geometrische Veränderung der Abbildung bezeichnet. Diese ist im Gegensatz zu den bisher genannten Aberrationen ohne Einfluss auf Kontrast und Auflösung der Abbildung. Dieser rein monochromatische Fehler beschreibt die Abweichung der idealen von der realen Bildhöhe und ist somit ein vom Feldwinkel abhängiger Bildmaßstabsfehler. Die

Verzeichnung kann über eine entsprechende Kalibrierung der Optik kompensiert werden. Generell wird zwischen einer tonnenförmigen (Abbildung 28 (b)) und einer kissenförmigen (Abbildung 28 (c)) Verzeichnung unterschieden. [64]

Möglichkeiten zur Reduktion der Verzeichnung sind das Aufteilen der Brechkraft auf mehrere Linsen und die Reduzierung der Schnitthöhe an der Linse. Daneben besteht die Möglichkeit eines symmetrischen Aufbaus des optischen Systems zur Reduktion der Verzeichnung. [64]
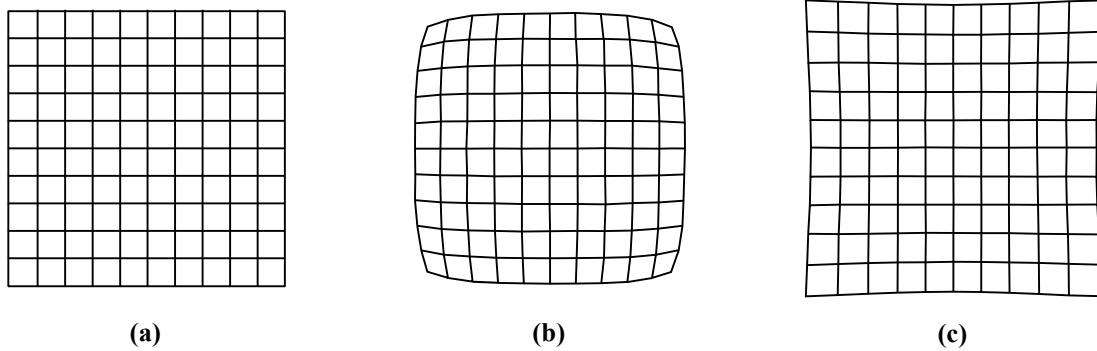

<center>(a)   (b)   (c)</center>

Abbildung 28 Verzeichnungen (a) Unverzerrt (b) Tonnenförmige Verzeichnung (c) Kissenförmige Verzeichnung

Chromatische Aberration (Farblängs- und -querfehler)

Neben den monochromatischen Aberrationen existieren von der Wellenlänge und damit vom Material und dessen Dispersion abhängige chromatische Fehler.

Einer dieser Fehler ist der Farblängsfehler (longitudinale chromatische Aberration). Durch die Wellenlängenabhängigkeit des Brechungsindex, kommt es für verschiedene Wellenlängen zu unterschiedlichen Schnittweiten mit der optischen Achse. Der Fehler äußert sich in unscharfen und falsch farbigen Bildrändern. Abbildung 29 (a) zeigt diese Art des Fehlers. [64, 130]
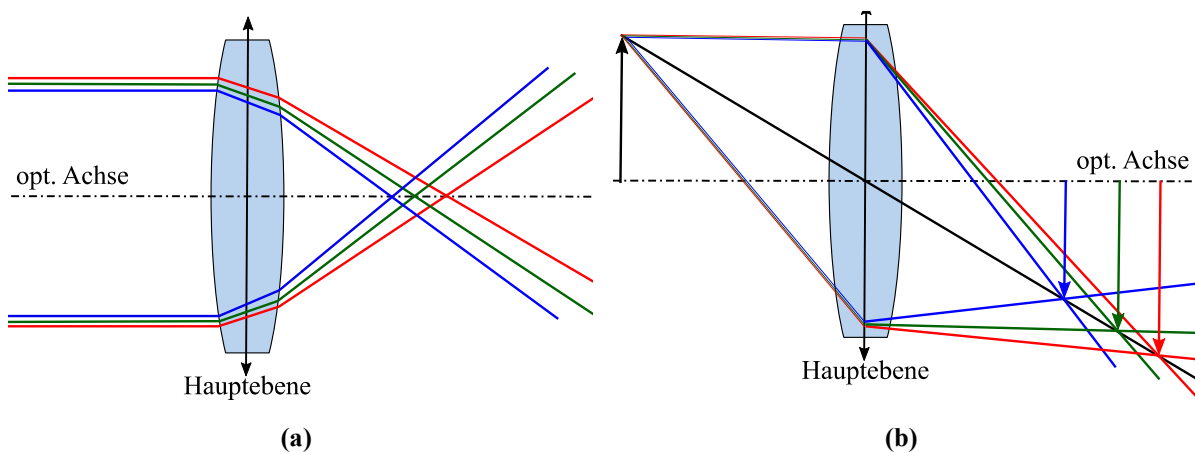

<center>(a)   (b)</center>

Abbildung 29 Chromatische Aberrationen (a) Farblängsfehler (b) Farbquerfehler

Zur Korrektur dieses Fehlers wird die Abbezahl verwendet. Diese beschreibt die relative Änderung des Brechungsindexes abhängig von der Wellenlänge und ist definiert in Gleichung (15) als das Verhältnis der Brechzahl bezogen auf bestimmte Wellenlängen, wie z.B. die sogenannten Fraunhofer Linien. Hier kann aber auch jede beliebige Definition der Wellenlängen je nach

Einsatzzweck der Optik vorgenommen werden. Mit der geeigneten Glaswahl, welche die Abbezahlen des gesamten Systems beeinflusst, oder der Kombination von Linsen als verkittete Doublets kann der Farblängsfehler korrigiert werden. [64, 130]

$$\nu = \frac{n_d - 1}{n_F - n_C} \tag{15}$$

In Abhängigkeit der Wellenlänge ändert sich mit dem Brechungsindex auch die Bildvergrößerung. Der Farbvergrößerungsfehler bzw. Fabrquerfehler (transversale chromatische Abberation) ist damit ein die Bildebene betreffender Fehler. Der Fehler äußert sich auch durch Farbränder an Kontrastkanten, wo starke Übergänge von hell nach dunkel auftreten. Abbildung 29 (b) stellt diesen Fehler für einen Objektpunkt außerhalb der optischen Achse dar. Im Gegensatz zu den Farblängsfehlern kann dieser Fehler nicht durch eine Reduzierung der Blende korrigiert werden. [64, 130]. Analog dem longitudinalem Farbfehler kann aber die Wahl der Glassorten, mit der entstehenden Kombination der Abbezahlen, sowie ein symmetrischer Aufbau der Optik zur Kompensation des Fehlers beitragen.

Vignettierung

Die Vignettierung oder auch Randlichtabfall beschreibt die Verringerung der Helligkeit am Bildrand. Liegen Objektpunkte außerhalb der optischen Achse können neben der Aperturblende auch weitere Bauelemente die Lichtmenge durch das System beschränken. Die durchgelassene Strahlungsintensität ist dabei proportional zu $\cos(\phi)^4$, wobei Φ den Feldwinkel darstellt. [130]

Spherochromatismus

Spherochromatismus beschreibt die von der Wellenlänge abhängige sphärische Aberration. [66]

MTF

Die Modulations Übertragungsfunktion beschreibt die Fähigkeit eines optischen Systems Details eines Objektes zu beschreiben. Diese Eigenschaft schwarze und weiße Bereiche örtlich diskret voneinander abgrenzen zu können wird über eine Anregung des Systems getestet. Die Anregung erfolgt als streifenförmiges Muster mit abwechselnden weißen und schwarzen Linien mit einem Abstand von 1/Anregung. Eine hohe MTF spricht für eine gute Unterschiedung für schmale Linienbreiten. Die MTF is multiplikativ für die Anwendung mehrere optischer Systeme zur Abbildung eines Objektes. [66]

Apertur

Die (numerische) Apertur ist ein Maß für das Auflösungsvermögen bzw. des Vermögens einer Optik eine Menge an Licht aufzunehmen. Die Apertur ist abhängig vom Feldwinkel und der Brechkraft der Optik. Eine größere Apertur bedeutet eine größere aufzunehmende Lichtmenge und damit eine bessere Auflösung von Objektdetails. [63]

A.2 Kameradaten

Tabelle 3 Kameradaten

	Phantom v12.1	Phantom v711	Phantom v2011
Hersteller	Vision Research	AMETEK	AMETEK
Sensor	CMOS	CMOS	CMOS
Sensorgröße	1280x800	1280x800	1280x800
Pixelgröße	20 μm	20 μm	28 μm
Grenzauflösung	25 lp/mm	25 lp/mm	18 lp/mm
Aufnahmegeschwindigkeit bei Vollauflösung	6,2 k	7,5 kHz	22,5 kHz

B. Veröffentlichungen

B.1 Veröffentlichung 1 im Original

Karmann, S, Friedrich, C, Prager, M, & Wachtmeister, G. "Realization of a Fully Optically Accessible Medium Speed Large Bore Engine Using a Fisheye Optic." Proceedings of the ASME 2020 Power Conference collocated with the 2020 International Conference on Nuclear Engineering. ASME 2020 Power Conference. Virtual, Online. August 4–5, 2020. V001T03A008. ASME. https://doi.org/10.1115/POWER2020-16477

Reprinted with permission from ASME

©ASME

Dear Stephan Karmann,

It is our pleasure to grant you permission **to use all or any part of** the following ASME paper "Realization of a Fully Optically Accessible Medium Speed Large Bore Engine Using a Fisheye Optic," by Stephan Karmann, Christian Friedrich, Maximilian Prager, Georg Wachtmeister, Paper No: POWER2020-16477, cited in your letter for inclusion for a thesis entitled Entwicklung eines kompakten volloptischen Zugangs für Großmotoren und Anwendung für die Verbrennungsdiagnostik erneuerbarer Kraftstoffe to be published by Technical University of Munich.

Permission is granted for the specific use as stated herein and does not permit further use of the materials without proper authorization. Proper attribution must be made to the author(s) of the materials. Please note: if any or all of the figures and/or Tables are of another source, permission should be granted from that outside source or include the reference of the original source. ASME does not grant permission for outside source material that may be referenced in the ASME works.

As is customary, we request that you ensure full acknowledgment of this material, the author(s), source and ASME as original publisher.

Many thanks for your interest in ASME publications.

Sincerely,

Beth Darchi

Publishing Administrator

ASME

2 Park Avenue, 6th Floor

New York, NY 10016-5990

POWER2020-16477

REALIZATION OF A FULLY OPTICALLY ACCESSIBLE MEDIUM SPEED LARGE BORE ENGINE USING A FISHEYE OPTIC

Stephan Karmann[1]; Christian Friedrich[2]; Maximilian Prager[1]; Georg Wachtmeister[1]

[1]Technical University Munich Chair for Internal Combustion Engines
[2]MAN Energy Solutions SE

ABSTRACT

To address one of the main environmental concerns, the engine out emissions, an enhanced understanding of the combustion process itself is fundamental. Recent optical and laser optical measurement techniques provide a promising approach to investigate and optimize the combustion process regarding emissions. These measurement techniques are already quite common for passenger car and truck size engines and significantly contribute to their improvement. Transferring these measurement techniques to large bore engines from low to high speed is still rather more uncommon especially due to the bigger challenges caused by the engine size and thus much higher stability requirements and design effort for optical accessibility. To cover this new field of research a new approach for a medium speed large bore engine was developed using a fisheye optic mounted centrally in the cylinder head to design a fully optically accessible engine test bench. This new approach is detailed with a test setup layout and a stability concept consisting of cooling systems and the development of a suitable operation strategy based on simulation and experimental verification. The design of this single cylinder engine with 350mm bore and 440mm stroke providing 530kW nominal load at 750 rpm was tested up to 85% nominal load in skipped fire engine operation mode. The measurements of the flame chemiluminescence of a dual fuel combustion of the diesel gas type present proof of the feasibility of the new design as a starting point for future systematic studies on the combustion process of large bore engines

Keywords: fully optical engine, large bore engine, fisheye optic

NOMENCLATURE

FE	Fisheye	HS	High speed
IV	Intake valve	SOE	Start of energizing
EV	Exhaust valve	TDC	Top dead center
HSC	High speed cam	PIV	Particle image velocimetry

1. INTRODUCTION

One of the main challenges in the current debate on environmental friendly and sustainable energy supplies are seasonal and regional fluctuations of regenerative energy generation e.g. by solar, water and wind plants that are not in time with the actual energy demand. This means high demand may not be satisfiable from existing plants in time while at other times too much energy is produced that needs to be efficiently stored and at a later time efficiently reconverted to energy.

Power to X describes the carbon neutral synthetization of gaseous or liquid e-fuels from renewable electricity and presents a promising approach to solve the issue of storing and later re-using surplus energy. The generated e-fuels provide carbon neutral and sustainable energy sources to apply for energy generation on demand as well as in heating, industry and transportation to replace the current fossil fuels like natural gas, coal, diesel or gasoline. Prerequisites - besides a continuous expansion of renewable energy installations - are the possibility of both long term and seasonal storage of the generated e-fuels and the optimization of energy generation with those new fuels. One possibility for long-term storage of the e-fuels is to feed the gaseous e-fuels hydrogen or methane into the natural gas infrastructure and storage system. The stored e-fuel can later be used in unit-type power plants (retro grid conversion) to intercept seasonal or regional residual loads stabilizing and securing the availability of renewable energy. The efficiency and sustainability of the underlying energy generation processes on the other hand rely on the improvement of the applied internal combustion engines to overcome existing limitations concerning reliability, effectiveness and especially environmental issues.

Recent optical and laser optical measurement techniques provide a promising approach to investigate the combustion process from the in cylinder air-fuel distribution and charge motion to the combustion itself. This allows the observation of the combustion flame's chemiluminescence or the species

radicals in the flame that define the emission formation and enable to deduce reaction kinetics (cf. [1]) and thus the efficiency and properties of the combustion. These measurement techniques are state of the art for passenger car and truck size engines. Transferring these measurement techniques to large bore engines used for a combined heat and power generation from low to high speed proves rather more challenging.

2. OPTICAL ACCESSIBLE ENGINES

The scope of optical and laser optical measurement techniques ranges from single cylinder research engines up to full engines of car and truck size. Depending on the measurement technique, the investigation goals and the engine type, different degrees of optical accessibility are necessary respectively feasible. Figure 1 based on [2, 3] summarizes the different degrees of optical accessibility referenced by literature. Generally, a larger optical access requires an increased amount of fragile glass components and adaptions to the engine geometry to mount them. Several investigations conduct comparisons on the differences between an optical and an all-metal engine describing changes in e.g. emission, mixing and combustion due to design and necessary operation mode adaptions like the reduction of the maximum bearable load and speed to protect the glass components from damage (cf. [4–6]). Table 1 depicts an overview of already implemented optical engines and possible investigations assigned to the different degrees of optical accessibility shown in Figure 1.
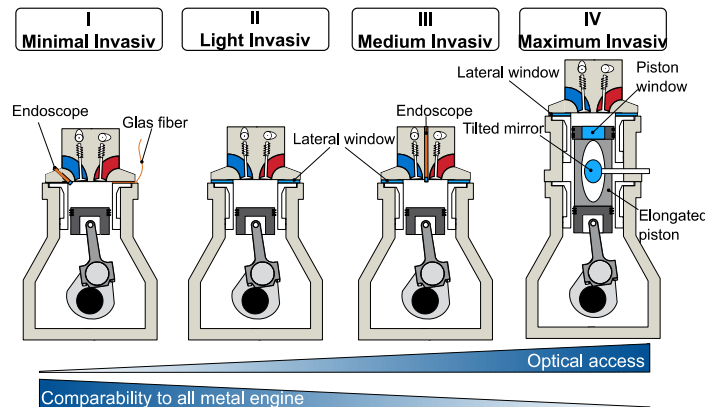

Figure 1 Degrees of optical accessibility

Large bore four stroke engines are often implemented as optical engines of degree I or II. These degrees of optical accessibility are mostly suited to investigate a defined part of the combustion chamber with a vertical field of view according to the focus of the investigation (e.g. injection process of diesel engine). One advantage of those concepts is the implementation with a limited effort maintaining a maximum of the engine's stability and comparability to the all-metal engine, e.g. concerning the piston lubrication properties of a completely unchanged crank train in contrast to the degree IV. The degree IV is known as fully optically accessible engine according to the Bowditch principle (cf. [7]) with a lateral and horizontal optical access. To design an optical engine of degree IV of marine or stationary engine size is very complex due to its extent and thus higher stability issues. So far, only one execution with a swept volume of 5l has been published (cf. Table 1). A design study to develop a large bore medium speed engine with degree IV and an eight times larger engine volume is presented in [3]. The study emphasizes the immense effort for such a realization and presents possible alternative concepts. One of the alternatives for a fully optically accessible engine as presented in [3] integrated a fisheye optic into the cylinder head to enlarge the field of view and to circumvent the necessary engine modifications to integrate a plain piston window. The realization of this alternative is described in the following sections.

Table 1 Overview of conducted optical engines

Bore/Stroke	Measurement	Deg.	Source
320/440	Flame emission	I	[8]
340/430	LIF	II	[9]
340/400	HS flame propagation	II	[10]
320/400	Fuel jet breakup, flame emission	I	[11]
500/2200	Fuel jet ignition, PIV	III	[12–14]
170/210	HS flame propagation, OH chemiluminescence, PIV	IV	[15–17]
200/280	CST with IR absorption	I	[18]
Passenger car/ Truck size engine			
84/90	OH LIF	I	[2]
75/88,3	PIV	IV	[19]
79,5/95,9	LIF, Raman spectroscopy	IV	[20]

3. DESIGN AND ASSEMBLY OF THE FULLY ACCESSIBLE OPTICAL ENGINE

3.1 Description of the assembly

The medium invasive concept III presents an optimal compromise of near realistic properties, near realistic behavior of the engine and feasibility. The final implementation consists of a central optical access from the cylinder head above and four sealable lateral accesses through the cylinder wall. All accesses are perpendicularly arranged to enable optimal measurement accessibility and quality. The experimental layout determines the amount of used optical inserts for both excitation and observation. Unused lateral accesses can be closed via steel inserts to allow for a more realistic engine behavior.

A 45° tilted mirror is mounted at the engine's top and redirects the fisheye optic's field of view to the vertically mounted imaging system. This arrangement prevents the imaging system from direct damage in case of a failure of the optical system. The designed fisheye optic consists of nine lenses divided in two clamped lens settings mounted in a lens tube (cf. Figure 2). The optic unit mount replaces the engine's central main injector used for the diesel operation mode of the DF-engine. Both lens settings can be focused and adjusted by spacers. To allow for thermal expansion two compensator rings are integrated within the optical assembly. The front sapphire lens exposed to the combustion chamber boundary conditions is glued to the mount with a thermal stable silicon glue. A locking ring prevents the lens from falling into the engine in case of a failing adhesive.
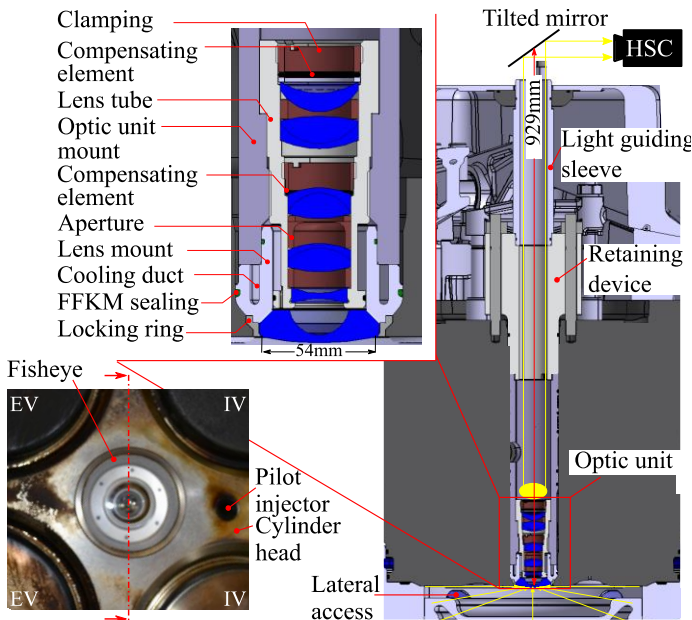
Figure 2 Sectional view of the fisheye optic

In case of leakage of the adhesive joint the lens tube offers several drill holes and grooves at it's circumference to release the combustion pressure and prevent the lenses from damage. A retaining device fixes the optic unit mount to the cylinder head against the combustion pressure. The cylinder head itself is a series part modified to fit the top and lateral access. On top of the retaining device the light sleeve encloses the optical path and seals it against the oil mist of the valve train. Around the lens tube an additional water-cooling system (cf. 3.2) sealed by FFKM gaskets was constructed to lessen the thermal stress on the less durable lenses. The cylinder liner as well as the piston rings were lowered by 10 mm to gain sufficient installation space for the lateral accesses. An optical ring contains the optical inserts. A locking plate fixes both elements and the cylinder liner with four engine tie rods. Metal gaskets between the cylinder head and optic ring as well as optic ring and cylinder liner seal the combustion chamber.
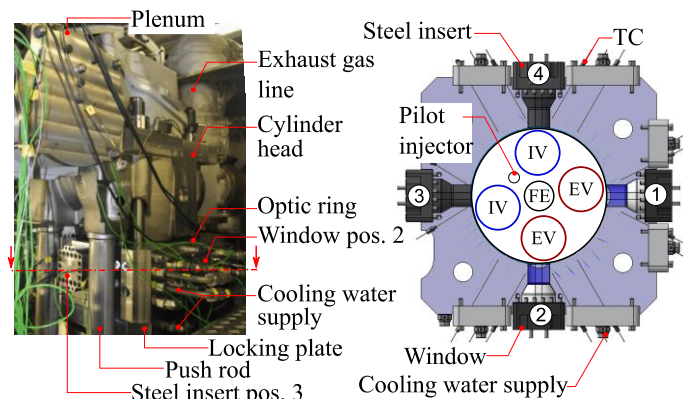
Figure 3 Sectional view of the lateral access

The optic ring made of 36NiCrMo16 is inlaid with four perpendicular openings for either optical or steel inserts (cf. Figure 3). The optical inserts are rectangular quartz profiles glued into a mounting structure. Their surfaces facing the combustion chamber are machined as cylindrical lense with a radius of 45mm and an aperture angle of 45° to enhance the lateral field of view. Between tests, the openings also provide a relatively easy access to clean the first lens of the fisheye optic from combustion residues and oil spill from the piston rings.

3.2 Description of the cooling concept

The mounting of optical elements as windows and lenses can either be realized by clamping of metal and glass elements or bonding with appropriate glues. Clampings are always at risk of leakage and damaging of the weaker glass material due to stress peaks by the different heat expansion coefficients (cp. Table 2). Using silicon based glues as applied for the first lens of the optic and the quartz glass window of the lateral optical inserts results in limitations concerning endurable temperatures (cp. [21]). This works for the quartz glass inserts due to the low heat conductivity of quartz glass and the relatively long distance between the combustion facing surface of the quartz glass window and the adhesive joint applied between the window and the mount on the outer side of the cylinder. The first lens of the fisheye optic on the other hand is made of sapphire glass with a much higher heat conductivity. Moreover, the adhesive joint of the first lens is quite close to the combustion heat and therefore at a much higher risk of overheating. Therefore, all following considerations for the optical cooling concept focus on steps to avoid overheating of this adhesive joint.

Table 2 Material property overview

	α $\frac{1}{K}10^{-6}$	$\lambda.$ $\frac{W}{mK}$	c $\frac{J}{kgK}$	$\varrho \frac{kg}{dm^3}$	σ_T MPa	σ_C MPa	T °C
Quartz	0.57	1.5	0,77	2,20	50	1150	1068
Sapphire	6.2	40	750	4	190	2000	2000
42CroMo4	12	42	470	7.72	840	n.a.	500
Titanium	9	22	560	4,43	895	n.a.	400
Glue	n.a.	n.a.	n.a.	1.1	6	n.a.	250

Cylinder head, fisheye optic, optic ring and cylinder liner have their own independent cooling water supply. This allows individual adjustment of the component temperatures to a previously defined, endurable level. Thermocouples integrated into the optic ring and lens mount serve to monitor and maintain these limits. Figure 4 shows the fisheye optic's cooling duct. Two ring-shaped channels at the upper part of the mount of the optic unit in combination with two riser liners realize the cooling water supply of the lower ring channel. This ring channel is quite close to the adhesive joint to guarantee a maximum heat dissipation. Due to the relatively low heat conductivity of the glue a high temperature gradient between the lens mount and the sapphire lens is necessary. Therefore, the fisheye optic cooling duct uses pure water at a minimum available temperature of 15°C.
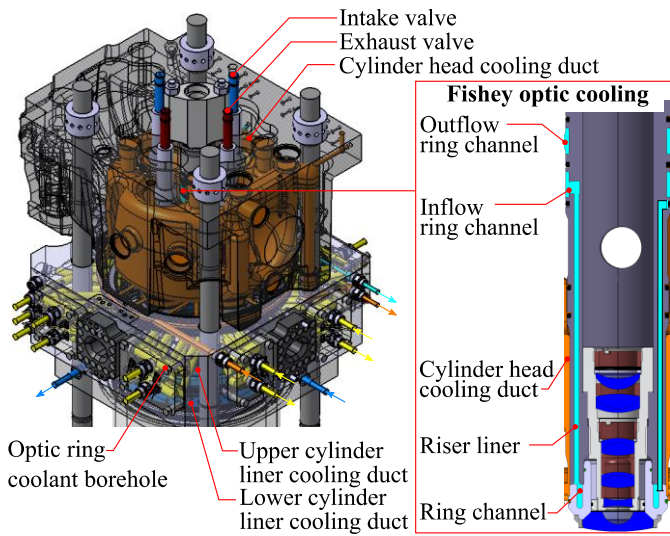
Figure 4 Cooling concept

4. DERIVATION OF A TESTING RIG OPERATION STRATEGY

While the installation of additional cooling systems increases the stability of the optical components, the engine operation strategy still needs to be adapted, as the optical elements cannot withstand a normal engine run for long. Due to a lack of examples for optical components in a combustion engine this size, combined and simplified CHT and mechanical strength simulations supported the design process to find an optimal compromise between the maximum field of view and stability conditions. The analysis of their results along with real engine experiments led to an optimal testing rig operation strategy determining the maximum endurable load. Figure 5 illustrates the development process from the design concept to the final engine operation strategy.
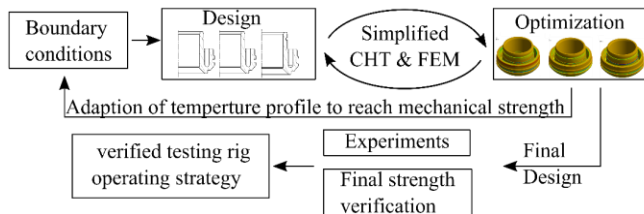
Figure 5 Derivation of the testing rig operation strategy

4.1 Stationary CHT Simulation

The setup of the simulation model is based on the findings of [22] with simplifications to create a fast model usable for the design process and operating behavior estimation under worst case conditions as well as to conduct a maximum endurable load estimation. First, a stationary CHT-Simulation determined the temperature profile under worst-case full load conditions derived from simplified CFD (Computational Fluid Dynamics) results. To save computational effort the model is constricted to the main parts of the top access (cylinder head, optic assembly, pilot injector). This is suitable because the separate fed cooling ducts and the very small contact surface between the optic ring and the

cylinder head for heat exchange (18% of the fire deck surface) generate only a very limited heat flux between these two parts.
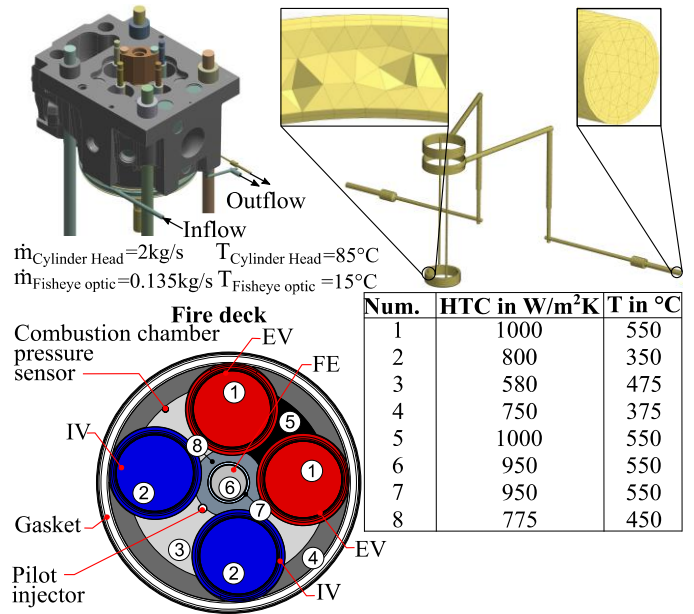

$\dot{m}_{\text{Cylinder Head}}$=2kg/s $T_{\text{Cylinder Head}}$=85°C
$\dot{m}_{\text{Fisheye optic}}$=0.135kg/s $T_{\text{Fisheye optic}}$=15°C

Num.	HTC in W/m²K	T in °C
1	1000	550
2	800	350
3	580	475
4	750	375
5	1000	550
6	950	550
7	950	550
8	775	450

Figure 6 Model setup of CHT Simulation

Figure 6 depicts the model, the main boundary conditions of the fire deck and the created mesh of the fisheye cooling duct's fluid domain. Figure 9 presents the contacts defined between the engine parts. The Reynolds-Averaged-Navier Stokes (RANS) equation models the fluid flow with a $k\varepsilon$-turbulence model and a RMS convergence criteria of $1 \cdot 10^{-4}$. The complete mesh consists of almost $18 \cdot 10^6$ elements. The unstructured tetrahedral mesh uses inflation layers with a set up chosen to avoid a complete resolution of the viscous sublayer that would otherwise result in a poor mesh quality due to layer elements with a small aspect ratio leading to bad convergence behavior (cf. [23]). Furthermore, as it is not feasible to resolve the boundary layer sufficiently, the recommended ANSYS scalable wall function with y^+-values between 30 and 200 (cf. [23–25]) was used.

An analysis of the temperature profile at the adhesive joint between lens and lens mount shows the impossibility of a
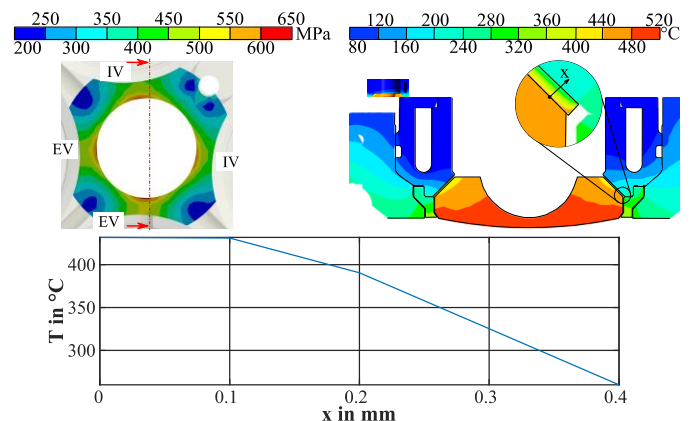

Figure 7 Temperature, max. compressive stress at the cylinder head

stationary engine run as the glue's maximum endurable temperature is exceeded over the complete thickness of the adhesive (cf. Figure 7). Furthermore, the cylinder head is at risk of mechanical failure due to temperature induced compressive stress located at the increased recess for the fisheye optic (cf. Figure 7) that is slightly higher than the material's compression strength of 650MPa (cp. [26]). To prevent the optical top access from damage the determination of an endurable engine load is therefore necessary.

4.2 Transient CHT and Stability Investigation

The definition of a final temperature limit for the cylinder head and the adhesive joint is crucial for the stability verification and a determining factor for the development of the testing rig operation strategy as depicted in Figure 5. These limits are estimated from a transient CHT simulation based on the static model and a time step of 1ms. Instead of a sapphire lens, the transient model uses a metal lens dummy equipped with five temperature measurement points used for later experimental verification of the testing rig operation strategy (cf. Figure 11). The temperature profile derived from this simulation setup is mapped onto the sapphire lens model for a strength evaluation. This approach seems valid as the specific material parameters like heat capacity, heat conductivity and density of metal are similar to sapphire (cf. Table 2) leading to an almost similar temperature behavior. Six further temperature measurement points are defined at the lens mount (TM) the locking ring (TC1-TC3) and the cylinder head (TC4, TC5). In contrast to the simulation setup, the experimental setup 1 (cf. Figure 11) cannot integrate the thermocouples at the locking ring but tracks the temperature in the cylinder head at these positions (TC1-TC3) instead.
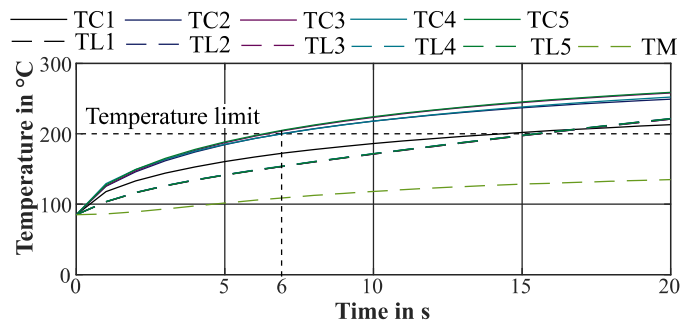
Figure 8 Temperature trace for measurement position TC=Cylinder head, TL=Steel lens, TM=Lens mount

Figure 8 depicts the simulated transient heating curve from a preconditioned engine temperature of 85°C at the start of combustion for the duration of 20s. The locking ring has low cooling properties because of the small heat dissipating surfaces connected to the cylinder head and lens mount. The temperature at the locking ring (TC1 – TC3) is higher than at the cylinder head (TC4, TC5), but in contrast to the temperatures of the cylinder head not decisive for the strength verification. Therefore, positions TC5 and especially TC4 in the CHT simulation setup are used to determine a temperature limit that

prevents the engine parts from damage. To determine and verify the effectiveness of this temperature limit a strength evaluation according to the proceeding described in [26] was set up over several temperature profiles leading to a temperature limit of 200°C. Figure 9 depicts the reduced engine assembly focused on the main parts of the optical top access, which are in the flux of force, that sets up the FEM model.
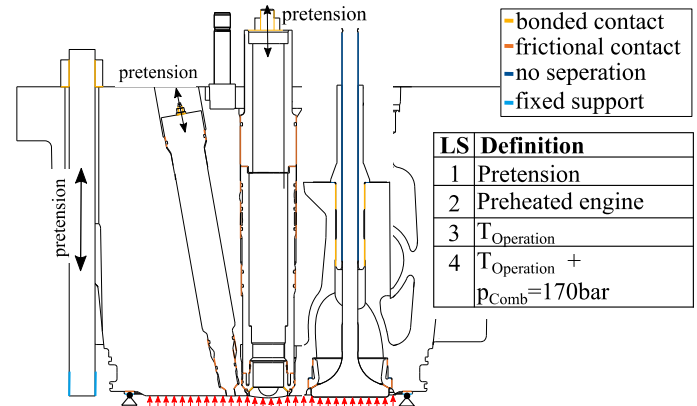
Figure 9 Simulation model contact and load

The simulation setup uses elastic temperature dependent material models, 63 contacts with their appropriate fit treatment and a mesh element amount of $2 \cdot 10^6$ containing refinements of contact regions and evaluation points. The glue's material model is assumed as elastic according to [15]. This material parametrization presents the main uncertainty in the model but the best compromise because of the lack of proper material data in literature to replicate the glue's hyper-elastic material behavior. Furthermore the simplification is based on former design experience of [15]. To validate the assumptions, the lens strength as well as the glue's sealing properties were verified in a test setup using a pressure chamber filled with oil up to 200bar hydrostatic excitation (cf. Figure 10). The final design impinged with the thermal boundary conditions of 200°C derived from the transient CHT proved feasible e.g. for the sapphire lens with a safety margin of eight (cf. Figure 10).
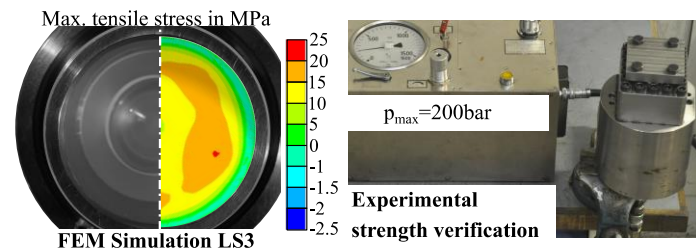
Figure 10 Sapphire lens strength verification
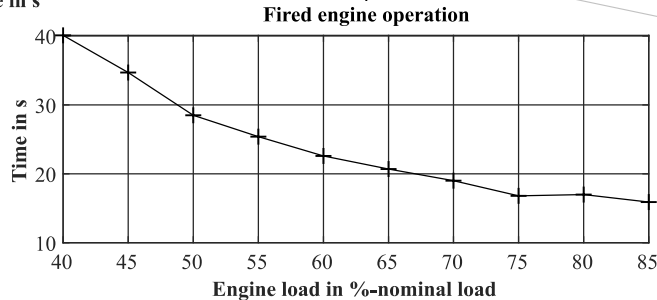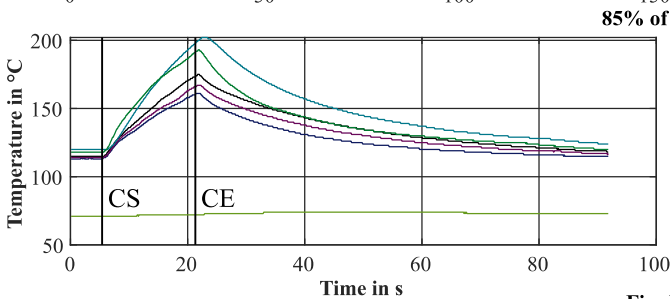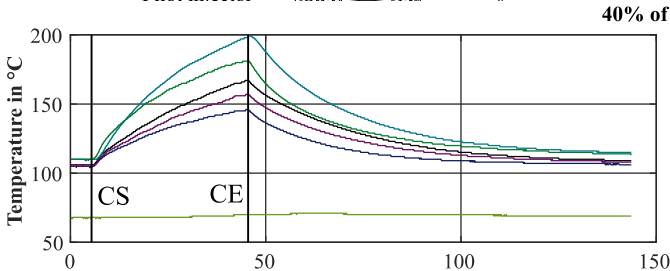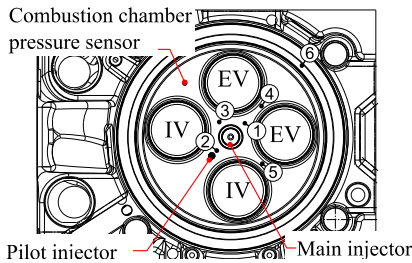
4.3 Testing rig operating strategy

To keep the engine temperatures below the temperature limit a skipped fire operation mode usually deployed for degree IV optical engines provides the best course of action. It consists of a certain number of fired engine cycles until a critical temperature is reached followed by motored cycles without

Copyright © 2020 ASME

combustion to cool down to the initial engine temperature bevor starting the fired cycles again.

Usually 50-100 cycles are sufficient to get a stable combustion behavior and conduct measurements (cf. [21]). Two preliminary experiments were set up to determine the details of the skipped fire operation mode for the large bore engine test rig. One set up focuses on the characteristic of the cylinder head temperature around the critical point at the central bore while the second one determines the temperature behavior of the adhesive joint. Both temperatures are crucial for the stability of the optical setup as explained in section 4.1.

The first experimental setup uses six thermocouples mounted in an unchanged series part cylinder head to determine the fire deck's temperature profile to the later realized optic top access (cf. Figure 11). An engine load variation from 40% up to 85% of the engine's nominal load at an almost constant λ of 2.3 and SOE at 25° before TDC was carried out. The energetic share of diesel of 5.4 to 2.75% varied depending on the load point.

Figure 11 depicts the transient temperature profile of the six thermocouples. The determined limit of 200°C is set as described in Figure 8 by a transient CHT simulation. Due to the inertia of the temperature conduction and the thermocouples, this temperature limit is set to 195°C. The injection of the pilot fuel stops if any of the thermocouples detects this temperature limit. To determine the fired engine run time, Figure 11 shows the combustion start (CS) and end time (CE).

The second setup focuses on the adhesive joint and uses a steel lens instead of the sapphire one, equipped with five thermocouples. A sixth thermocouple behind the adhesive joint glued into the lens mount determines the temperature profile (cf. Figure 11). This sixth thermocouple, also installed for later use with the real sapphire lens, supports the control of the skipped fire engine operation mode. The temperature at this special thermocouple derived from the same simulation as for the deduction of the cylinder head's temperature limit amounts to 130°C (cf. Figure 8).

Experimental setup 1: Cylinder head with thermocouples

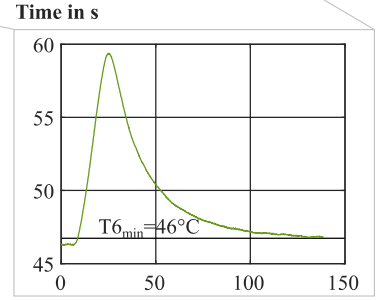**Experimental setup 2: Steel lense with thermocouples**

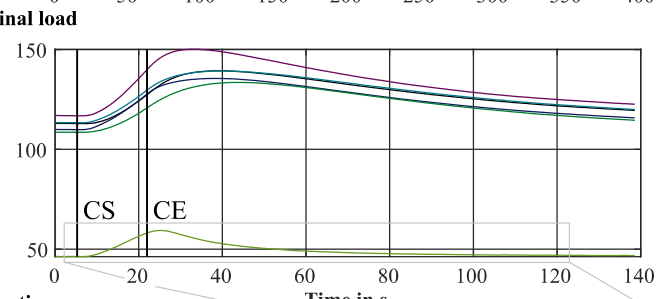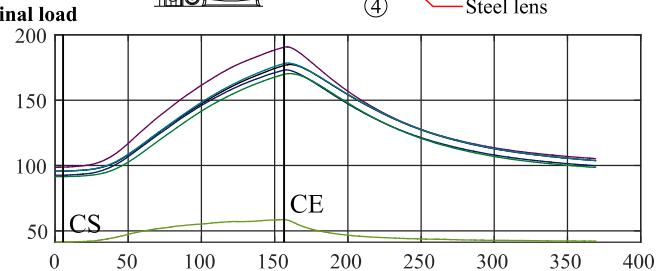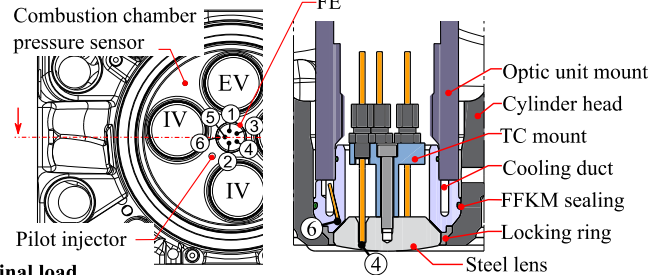**Figure 11** Experimental setup for testing rig operation determination (CS=combustion start, CE=Combustion end)

Besides the description of the two experimental setups, Figure 11 depicts the transient temperature profiles of two load variations with identic engine parameters. It is evident that the cylinder head in setup 1 reaches its temperature limit of 200°C for both loads faster according to a higher load.

For setup 2, the thermocouple 6 does not reach the temperature limit. Even the steel lens temperature (T1-5) remains under the glue's critical temperature of 250°C for both loads. Therefore, the cylinder head is the determining part for the maximum temperature and thus the maximum fired engine operation duration. This difference in the warm up behavior can be explained by a comparison of the area of heat-absorbing surfaces of both components. They differ by a factor of 16 for the heat-up when the fire deck surface without valves is taken into account. During the cooling of the components, it is exactly the other way around. The surface of the cylinder head that dissipates heat during the charge exchange is considerably larger than that of the lens, so that the cooling time of the tests with the second set-up is decisive to determine the operational limits. Figure 11 shows the firing duration for the load variation ranging from a maximum of almost 40s to the minimum of about 16s. This corresponds to a maximum of 250 respectively to 100 fired cycles. The number of feasible fired cycles seems sufficient for a stable engine run and recording.

Using the full optical engine design, the temperature measurement points in the cylinder head are not realizable. Therefore, only the thermocouple behind the adhesive layer is available to control the skipped fire operation. Due to the constant motor parameters used, a correlation between the measurement points of the two test setups is possible. Thus, by monitoring the temperature of the thermocouple positioned in the lens mount, the temperature of the flame deck can be deduced based on the same amount of heat introduced in both experiment setups for the same engine load.

The recording of measurement data is only triggered in fired cycles. Equation 1 determines the start temperature of the recording. Figure 11 determines the Temperature $T6_{min} = 46°C$ as lowest reachable temperature during the externally motored cool down phase of the skipped fire operation mode. The constant value A describes the temperature when an almost stable combustion is reached.

$$T_{Start} = T6_{min} + \frac{A - T6_{min}}{2} \qquad (1)$$

Furthermore, the constant A determines the possible amount of recorded cycles. The value could be adapted with regard to the engine behavior resulting in constant combustion conditions. Reaching the maximum temperature of 57°C determined from the experimental investigation to keep within the cylinder head's limit temperature of 200°C the pilot injection is interrupted and the combustion stops. The engine is motored externally and cools down until a new fired cycle with recordings can be started.

5. DESCRIPTION OF THE FISHEYE OPTIC IMAGING SYSTEM

The fisheye optic imaging system was especially developed for the observation of engine in-cylinder phenomena with a maximum field of view. The fisheye optic's design was developed using the optical engineering software OpTaliX Pro for raytracing and optimization. Concerning geometrical (installations space), thermal and mechanical as well as optical boundary conditions (field of view, design wavelengths) a base design derived from literature reviews (e.g. [27]) was optimized to reach the optical quality criteria e.g. the modulation transfer function, spot diameter, optical path difference and third order Seidl aberrations.

Geometrical boundaries set up from conducted stability investigations (cf. section 4.2) determine the material of the first lens (sapphire), its diameter as well as the diameters of the subsequent lenses. Besides, the engine dimension determines the field of view from a minimum of 150° to a maximum of 180°. The minimum field of view is set to the bore diameter in a distance of 37mm corresponding to the mid plane of the lateral access whereas the cylinder head's fire deck limits the maximum field angle. The optical and laser optical investigation methods usually used in state of the art combustion analysis determine the wavelength band the optical system has to be sensitive for. Experiments like PIV, flame chemiluminescence, two-color pyrometry, Mie scattering and Schlieren photography are conductible within a spectral wavelength from e.g. 400nm to 750nm. The skip of the UV-region facilitates the optic design. These measurement techniques mainly use a high-speed camera for recording. The high-speed camera for the test rig set-up is a Phantom v.12.1 with a sensor size of 25.6mm x 16mm and a maximum resolution of 1280x800 pixels. With the pixel size of 20µm, the camera has an estimated MTF value of 25lp/mm.

Concerning the defined design parameters Figure 12 depicts the final optimized retro focus like lens design consisting of nine lenses and three cemented doublets to reduce several of the occurring image aberrations. The lenses one and two realize strong ray bending to realize the 90° field angle. The design offers a fisheye specific small equivalent focal length of 10mm to realize a large field of view and a f#-number of 2.2 for a light intense system and therefore a bright image with a high contrast and an improved signal to noise ratio.
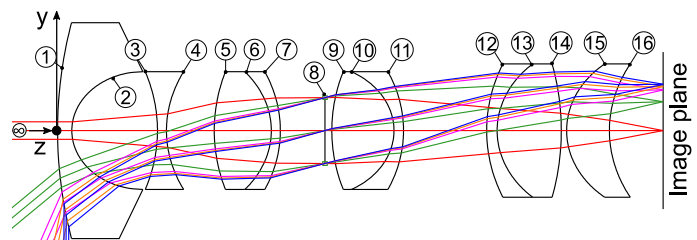

Figure 12 Fisheye optic design

The designed fisheye optic was optimized regarding small aberration errors and a high contrast defined by a high MTF (Modulation Transfer Function). Figure 13 depicts the MTF versus the field angle of the finalized optic. The depicted plot determines the imaging quality of a specific optic. The quality is measured as the resolution of a tangential and sagittal excitation with a pattern of black and white bars measured in lines per

millimeter and is shown over the entire field angle respectively the object space. The higher the resolution (MTF-value) the better a pattern structure is resolved on the image. As usually observed, the sagittal excitation shows a better resolution across the field angle than the tangential. Nevertheless, the designed fisheye optic shows a sufficient resolution concerning the 30lp/mm of 40% or higher (cf. Figure 13). Besides, the realized 30lp/mm is an even finer excitation than the camera's sensor is capable of processing and thus sufficient. Even for a structure with an object size of 0.032mm (60lp/mm) the optic shows a sufficient resolution up to a field angle of 74°. The contrast limit is set to the Rayleigh criteria [28].
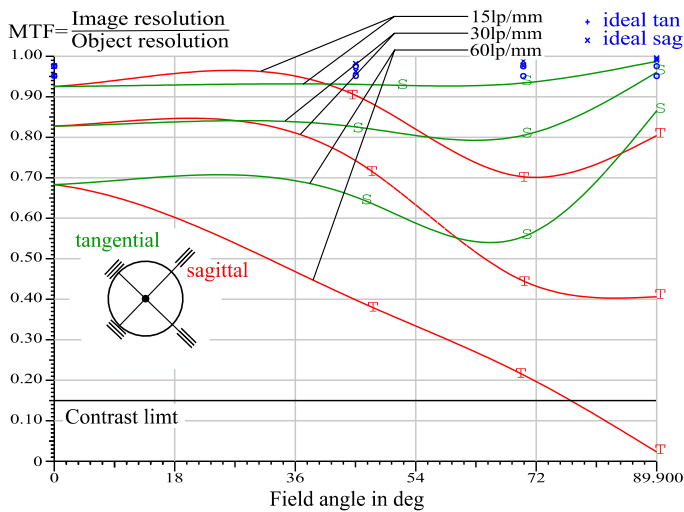

Figure 13 MTF vs. field angle

The final resolution of the complete imaging system depends on all the interacting components (objectives and camera) used to form the image of the combustion chamber. Due to the relatively long distance from the image of the fisheye optic to the camera sensor plane (1.4m cf. Figure 2) a second objective with a large focus is needed for the imaging onto the camera sensor. Besides a large focus, a small f#-number to keep the image brightness high is desirable. The fisheye optic's intermediate image guidance was realized using a Sigma macro objective with a fixed focus of 180mm and a f#-number of 2.8. A further integrated tele-converter with a magnification of the focus of 1.4 enhances the resolution and leads to a focus length of 252mm and a reduced f#-number of 3.92. The camera equipped with the tele-converter and the Sigma objective has an optimal working distance of 449mm. As the actual distance is much longer, it is not possible to use the full sensor frame for the resulting image. Only about one tenth of the pixels could be used resulting in an image size of 310x310 pixels. Compared to the theoretically maximum possible resolution this seems a quite less resolved and small image. But an ideal objective to use the complete sensor resolution needs a focal length of 700mm, which corresponds to relatively poor light efficiency. Therefore, the compromise used for the investigations concerning the focus and f#-number seems reasonable as it results in a better light efficiency. An initial operation test investigating the natural

flame luminosity of a dual fuel combustion of the diesel gas type proves the final sufficiency of the image resolution and states the concept's feasibility.

6. EXPERIMENTAL INVESTIGATION OF THE FLAME CHEMILUMINESCENCE

6.1. Experimental setup

Figure 14 depicts the schematic layout of the test bench. The full optical engine is based on a MAN 35/44 DF single cylinder research engine. Table 3 lists its specifications. The engine provides two common rail fuel injection systems for the pilot and main fuel injection. For the conducted optical investigations in the gas engine mode, the central main injection system in the cylinder head was removed from the testing rig and replaced by the optical access. An external natural gas processing plant with buffer storage guarantees a constant gas quality (methane number 80) and thus a stable engine operation behavior. The processed natural gas is pre-mixed into the intake duct after a buffer tank near the engine via a gas valve and a connected branch lance. The engine's charge air is externally conditioned depending on the operating point. The charge exchange is controlled by a bottom camshaft, which actuates two intake and two exhaust valves. An adjustable exhaust flap simulates the turbocharger's exhaust gas backpressure. Independent and monitored media circuits for cooling water and lubricating oil enable optimal supply conditions for a reliable controllable engine operation. The test bench has a full indicating system of intake, exhaust and combustion pressure. Occurring engine vibrations are compensated by a second-order mass balancing system. The engine itself is coupled to a dynamometer controlling the engine speed to constant 750rpm during motored and fired engine operation. The testing rig offers operation automation and a measurement and data acquisition system for engine control and measurement data handling. (cf. [29])
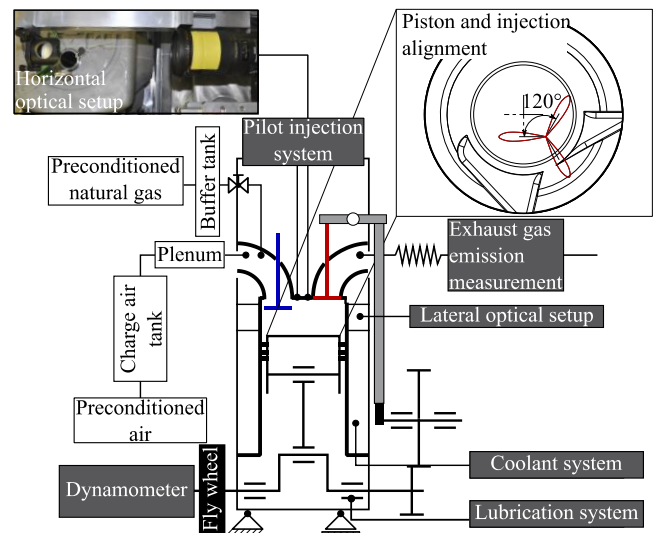

Figure 14 Schematic of the engine test bench

The setup also includes an adapted piston top part with two

perpendicular cutouts, which can be used to observe the phenomena within the piston bowl via the lateral optical accesses. The pilot injector has three spray holes evenly spaced around the circumference with a diameter of 0.24mm at the outlet. The positioning of the injection spray is shown in the sketch from a top view (cf. Figure 14). The optical setup is arranged in a way so that the horizontal and vertical field of view can be recorded simultaneously with two cameras. The top access is mounted with the fisheye optic and focused on the lateral access mid plane. In addition, glass inserts are installed in the perpendicular lateral positions 1 and 2 to observe the piston bowl (cf. Figure 3) or use for Mie scattering excitation with a flash lamp.

Table 3 Engine Specifications

Displacement	42.3dm³	Stroke	440mm
Bore	350mm	Connecting rod length	989mm

6.2. Flame Chemiluminescence

The flame chemiluminescence of the dual fuel combustion ranges in wavelengths from 280 to 610nm. According to [30], it mainly consists of four parts:
- the broadband chemiluminescence caused by radicals as CO_2^* and CHO^*
- the incandescence of soot
- the chemiluminescence of OH* and CH* radicals
- the chemiluminescence of CH_2O^* radicals

Figure 15 presents an image series of the combustion flame chemiluminescence starting at 4° crank angle before firing TDC with the first recor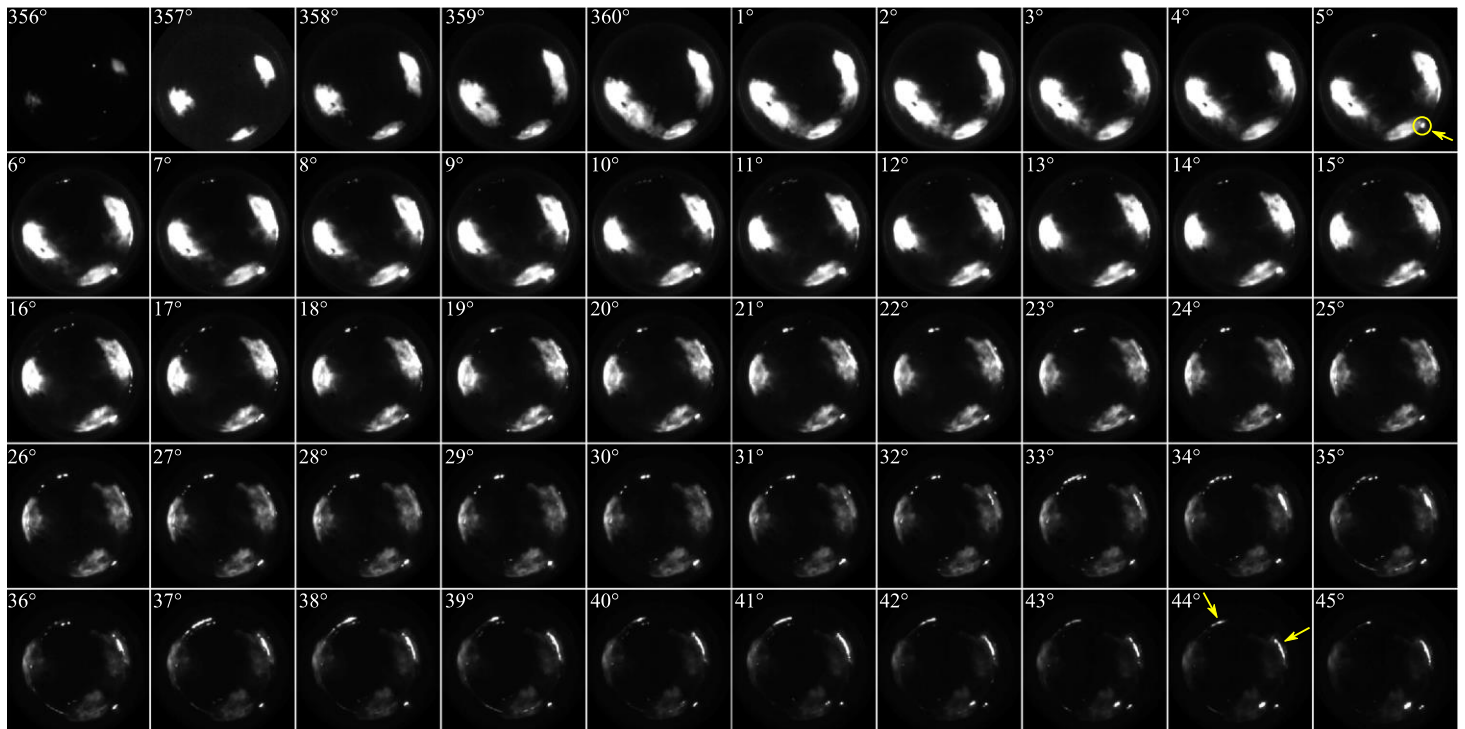ded luminosity of the combustion. The combustion is depicted for 85% nominal engine load. Start of injection energizing (SOE) was determined at 25° before firing TDC. The gas injection started at 420° after firing TDC. In combination with $1600 bar$ rail pressure and 3.7ms energizing duration a 3.3% share of diesel is provided at a λ of 2.

The images presented in Figure 15 are taken from the 12th out of at least 23 imaged cycles. The images were captured with a frequency of 4.5kHz resulting in a 1° resolved engine cycle. Exposure time for the images was 20μs. The images shown are post-processed to compensate for the relative movement between the camera arrangement and the fisheye optic. The post-processing consists of intensity based image registration using Matlab's one plus one evolutionary algorithm.

For a better understanding of the local assignment of the depicted combustion in Figure 15, Figure 16 shows the approximated position of the engine center as well as the pilot injector's position and spray cone orientation. The cone orientation corresponds with the location of the highly intense sooty combustion. Furthermore, Figure 16 depicts the piston respectively cylinder liner boundary beneath the steel insert mounted in the also visible optic ring.

Figure 15 shows the location of the combustion starting at 4° before firing TDC and at 21° after SOE, which corresponds to 4.67ms at 750rpm. The combustion in the outer regions is determined by a high intensity emitted primarily by the soot incandescence of the injected pilot fuel amount. Furthermore, the pilot injector's dripping after the injection is visible with an intense luminous sooty combustion beginning at 5°CA. Beside the injector dripping, a high intensity combustion at the outer piston, especially at the cylinder liner, is visible. The location and the high intensity of the emission indicates oil combustion.

Figure 15 Combustion image series for 85% engine load from 356°CA to 73°CA in 1°CA steps

The components that are decisive for the tribological system and adapted for the optical system, such as the cylinder liner and piston, can be a cause of the increased oil ingress and burn-off. The much less intense combustion progress towards the center of the combustion chamber is probably due to the emissions of the other mentioned radicals.

7. DISCUSSION OF THE NEW OPTICAL ACCESS

7.1 Engine setup and operation strategy

During the conducted experiments the test engine endured the 85% engine load without damage. Nevertheless, it was not possible to record the planned 50 cycles in a row without reaching the defined temperature limits. The engine control interrupts the combustion by stopping the injection as it reaches the implemented critical temperatures before the 50 cycles are recorded. The amount of recorded cycles deviates from at least 15 to 35 depending on the engine heat up which is dependent on the engine load and operation parameters. Especially influential is the injection timing, which controls the combustion process and heat release. Adjusting the design's cooling concept even more or adapting the testing rig strategy with an adapted temperature independent recording procedure could improve this issue. In addition, each measurement point could be approached several times with the same engine parameter leading to the same behavior in order to increase the recorded cycles for a later statistical evaluation of the combustion process.

7.2 Optical quality and fisheye optic imaging

The optical quality presented in the images of Figure 15 seems sufficient to resolve the large-scale combustion process. The designed optics' light efficiency is sufficient to capture the high intensity of the soot incandescence as well as part of the much less intense emission of the remaining species. Furthermore, the spatial resolution for the large-scale combustion is high enough to determine their location in the combustion chamber and to observe their radial propagation. Besides, the field of view as well as the depth of view are large enough to observe the whole combustion chamber. It is possible to observe the complete height of the steel insert visible in Figure 16.

The upper edge of the component is 7.4mm below the fire deck. This corresponds to a field angle of at least 87.5° and a field of view of 175°. The following comparison emphasizes the advantage of the fisheye optic. A concept realized with an endoscope only provides a field angle of 55° (cf. [31]) resulting in a comparable less field of view of 110°. This large field of view is only possible due to the fisheye optic's typical barrel distortion also depicted in Figure 16 where the straight lines of the checkerboard pattern are displayed as curved. To overcome this non-uniform magnification and undistort the image a complex post processing is necessary as it is done in e.g. [31–33] for applications in robotics.

Although the image series of the combustion is distorted and needs further image processing for detailed analysis the following results can be derived from the images:
- Location of high sooty combustion

- Location of combustion start
- Awareness of oil combustion
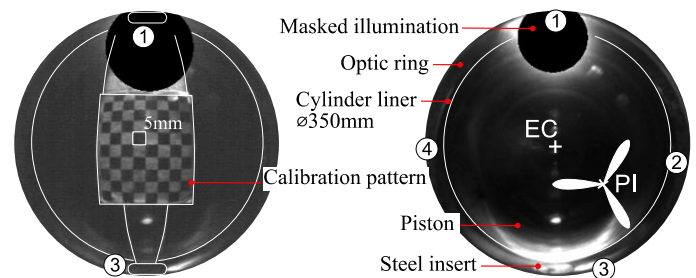- Occurance of injector dripping

Figure 16 Determination of the field of view (EC=Engine center)

8. CONCLUSION

The presented optical medium speed dual fuel single cylinder research engine provides a bore of 350mm and a stroke of 440mm producing 530kW at 750rpm. A newly developed fisheye optic top access provides a maximum horizontal field of view of up to 150° and additionally four possible lateral optical accesses. Stability issues were solved with a cooling concept and an individually adapted skip fire engine operation strategy. First chemiluminescence tests were executed as proof of concept depicting interesting insights into the combustion process. Further investigations are planned. To increase the significance of the results, a suitable post-processing routine has to be implemented to solve the imaging challenges and improve the analysis of the observed phenomena.

AUTHOR CONTRIBUTIONS

The complete writing, data preparation, post-processing and evaluation, the whole design of the optical test engine and simulative investigations belong to S. Karmann. C. Friedrich conducted the experimental measurements, derived and implemented the testing rig control algorithm at the MAN Energy Solutions SE. The remaining co-authors supported the work with their expertise and reviews.

CONTATCT INFORMATION

Stephan Karmann: karmann@lvk.mw.tum.de

REFERENCES

[1]   M. Aldén et al. , Visualization and understanding of combustion processes using spatially and temporally resolved laser diagnostic techniques, Proceedings of the Combustion Institute, vol. 33, no. 1, pp. 69–97, 2011.

[2] D. Bensing, Aufbau eines optisch zugänglichen Einzylinder-Viertaktmotors und charakterisierende Messungen, Universität Duisburg-Essen, 2013.

[3] Karmann, S., Prager, M. and G. Wachtmeister, Conceptual Investigations on Full Optical Accessibility to Large-Bore Medium-Speed Engines, SAE Int. J. Engines, vol. 12, no. 3, 2019.

[4] W. F. Colban et al., A Detailed Comparison of Emissions and Combustion Performance Between Optical and Metal Single-Cylinder Diesel Engines at Low Temperature Combustion Conditions, SAE Int. J. Fuels Lubr., vol. 1, no. 1, pp. 505–519, 2009.

[5] J. Kashdan and B. Thirouard, Optical Engines as Representative Tools in the Development of New Combustion Engine Concepts, Oil Gas Sci. Technol. – Rev. IFP Energies nouvelles, vol. 66, no. 5, pp. 759–777, 2011.

[6] J. T. Kashdan and B. Thirouard, A Comparison of Combustion and Emissions Behaviour in Optical and Metal Single-Cylinder Diesel Engines, SAE Int. J. Engines, vol. 2, no. 1, pp. 1857–1872, 2009.

[7] F. W. Bowditch, A New Tool for Combustion Research A Quartz Piston Engine, SAE Technical Paper, no. 610002, 1961.

[8] F. Unfug, Experimentelle und numerische Untersuchung der Verbrennung eines mittelschnelllaufenden 4-Takt Dieselmotors, KIT, Berlin, 2013.

[9] R. Wellander et al., Study of the Early Flame Development in a Spark-Ignited Lean Burn Four-Stroke Large Bore Gas Engine by Fuel Tracer PLIF, SAE Int. J. Engines, vol. 7, no. 2, pp. 928–936, 2014

[10] J. Duong, Combustion Visualization in a Large Bore Gas Engine, Lund University, Lund, 2013.

[11] C. Disch and U. Waldenmaier, High-Speed Flame Chemiluminescence Investigations of Prechamber Jets in a Lean Mixture Large-Bore Natural Gas Engine, CIMAC, Shanghai, 2013.

[12] J. Hult and S. Mayer, A methodology for laser diagnostics in large-bore marine two-stroke diesel engines, Meas. Sci. Technol., vol. 24, no. 4, p. 45204, 2013.

[13] S. Mayer, J. Hult, K. J. Nogenmyr, and S. Clausen, Eds., Advanced optical development tools for two-stroke marine diesel engines, CIMAC, Shanghai, 2013.

[14] S. Mayer, Ed., In-Situ Optical Combustion Diagnostics On A Large Two-Stroke Marine Diesel Engine, CIMAC, Bergen Norway, 2010.

[15] B. Korb and S. Gleis, Auslegung und Entwicklung eines volloptischen Einzylinder-Großmotors mittels Ansys Workbench und einer vereinfachten FKM-Richtlinie, Ansys Conference & 33. CADFEM Users' Meeting, 2015.

[16] S. Gleis et al., Investigation of the High-Pressure-Dual-Fuel (HPDF) combustion process of natural gas on a fully optically accessible research engine, JSAE/SAE Fuels and Lubricants International Meeting, 2019.

[17] S. Frankl, S. Gleis, and G. Wachtmeister, Interpretation of Ignition and Combustion in a Full-Optical High-Pressure-Dual-Fuel (HPDF) Engine using 3D-CFD Methods, CIMAC, Vancouver, 2019.

[18] S. A. Tsekenis et al., Towards in-cylinder chemical species tomography on large-bore IC engines with pre-chamber, Flow Measurement and Instrumentation, vol. 53, 2017

[19] M. Jakob, "Optical Investigation of Diesel-Engine Related Combustion Processes, RWTH, Aachen, 2014.

[20] E. A. Greis, Laseroptische Untersuchungen des Verbrennungsprozesses in einem PKW-Dieselmotor, RWTH, Aachen, 2007.

[21] S. Karmann et al., "A method for measuring in-cylinder λ-distribution in medium-speed DF engines," 2016.

[22] G. Cicalese, et al., "A Comprehensive CFD-CHT Methodology for the Characterization of a Diesel Engine: from the Heat Transfer Prediction to the Thermal Field Evaluation," SAE Technical Paper 2017-01-2196, 2017.

[23] J. H. Ferziger and M. Perić, Numerische Strömungsmechanik. Berlin, 2008.

[24] H. Punekar and S. Das, "Numerical Simulation of Subcooled Nucleate Boiling in Cooling Jacket of IC Engine," SAE Technical Paper 2013-01-1651, 2013.

[25] E. Laurien and H. Oertel, Numerische Strömungsmechanik, Wiesbaden, 2013.

[26] Forschungskuratorium Maschinenbau, Rechnerischer Festigkeitsnachweis für Maschinenbauteile aus Stahl, Eisenguss- und Aluminiumwerkstoffen, 6th ed. Frankfurt am Main: VDMA-Verl., 2012.

[27] A. M. Samy and Z. Gao, Simplified compact fisheye lens challenges and design, J Opt, vol. 44, no. 4, 2015,

[28] D. Malacara and Z. Malacara, Handbook of optical design, 2nd ed. New York, 2004.

[29] C. Friedrich and G. Wachtmeister, Entwicklung einer Methode zur Verkürzung des modellbasierten Applikationsprozesses in der Großmotorenentwicklung: Übertrag vom Einzylinder- auf den Vollmotor mittels generierter Transferfunktionen, München, 2018.

[30] A. Srna et al., Characterization of the spectral signature of dual-fuel combustion luminosity: Implications for evaluation of natural luminosity imaging, Appl. Phys. B, vol. 125, no. 7, p. 1174, 2019.

[31] J. Reling, H.-H. Flögel, and M. Werschy, Technische Endoskopie: Grundlagen und Praxis endoskopischer Untersuchungen. Renningen-Malmsheim: expert Verl., 2001.

B.2   Veröffentlichung 2 im Original

Karmann, S., Weber, S., Stürzl, W., Prager, M. et al., "Development of an Optical Investigation Method for Diesel and Oxymethylene Ether Spray in a Large-Bore Dual-Fuel Engine Using a Fisheye Optical System," SAE Int. J. Engines 16(5):2023, doi:10.4271/03-16-05-0036.

B.2   **Veröffentlichung 2 im Original**

CCC **Marketplace**

This is a License Agreement between Stephan Bernhard Karmann ("User") and Copyright Clearance Center, Inc. ("CCC") on behalf of the Rightsholder identified in the order details below. The license consists of the order details, the Marketplace Permissions General Terms and Conditions below, and any Rightsholder Terms and Conditions which are included below.

All payments must be made in full to CCC in accordance with the Marketplace Permissions General Terms and Conditions below.

Order Date	15-Apr-2023	Type of Use	Republish in a thesis/dissertation
Order License ID	1345358-1		
ISSN	1946-3944	Publisher	SAE International
		Portion	Chapter/article

LICENSED CONTENT

Publication Title	SAE International journal of engines	Rightsholder	SAE International
		Publication Type	Journal
Article Title	Development of an Optical Investigation Method for Diesel and Oxymethylene Ether Spray in a Large-Bore Dual-Fuel Engine Using a Fisheye Optical System	Issue	5
		Volume	16
		URL	http://www.sae.org
Author/Editor	Society of Automotive Engineers.		
Date	01/01/2009		
Language	English		
Country	United States of America		

REQUEST DETAILS

Portion Type	Chapter/article	Rights Requested	Main product
Page Range(s)	All	Distribution	Worldwide
Total Number of Pages	19	Translation	Original language of publication
Format (select all that apply)	Print, Electronic	Copies for the Disabled?	No
Who Will Republish the Content?	Academic institution	Minor Editing Privileges?	No
		Incidental Promotional Use?	No
Duration of Use	Life of current edition		
Lifetime Unit Quantity	Up to 499	Currency	EUR

NEW WORK DETAILS

Title	Entwicklung eines kompakten volloptischen Zugangs für Großmotoren und Anwendung für die Verbrennungsdiagnostik erneuerbarer Kraftstoffe	Institution Name	Technical University of Munich
		Expected Presentation Date	2023-10-31
Instructor Name	Prof. i.R. Dr.-Ing. Georg Wachtmeister		

ADDITIONAL DETAILS

| Order Reference Number | N/A | The Requesting Person/Organization to Appear on the License | Stephan Bernhard Karmann |

REQUESTED CONTENT DETAILS

Title, Description or Numeric Reference of the Portion(s)	Development of an Optical Investigation Method for Diesel and Oxymethylene Ether Spray in a Large-Bore Dual-Fuel Engine Using a Fisheye Optical System	Title of the Article/Chapter the Portion Is From	Development of an Optical Investigation Method for Diesel and Oxymethylene Ether Spray in a Large-Bore Dual-Fuel Engine Using a Fisheye Optical System
Editor of Portion(s)	Karmann, Stephan Bernhard; Weber, Stefan; St?rzl, Wolfgang; Prager, Maximilian; Jaensch, Malte; Wachtmeister, Georg	Author of Portion(s)	Karmann, Stephan Bernhard; Weber, Stefan; St?rzl, Wolfgang; Prager, Maximilian; Jaensch, Malte; Wachtmeister, Georg
Volume of Serial or Monograph	16	Issue, if Republishing an Article From a Serial	5
Page or Page Range of Portion	All	Publication Date of Portion	2022-12-07

Marketplace Permissions General Terms and Conditions

The following terms and conditions ("General Terms"), together with any applicable Publisher Terms and Conditions, govern User's use of Works pursuant to the Licenses granted by Copyright Clearance Center, Inc. ("CCC") on behalf of the applicable Rightsholders of such Works through CCC's applicable Marketplace transactional licensing services (each, a "Service").

1) Definitions. For purposes of these General Terms, the following definitions apply:

"License" is the licensed use the User obtains via the Marketplace platform in a particular licensing transaction, as set forth in the Order Confirmation.

"Order Confirmation" is the confirmation CCC provides to the User at the conclusion of each Marketplace transaction. "Order Confirmation Terms" are additional terms set forth on specific Order Confirmations not set forth in the General Terms that can include terms applicable to a particular CCC transactional licensing service and/or any Rightsholder-specific terms.

"Rightsholder(s)" are the holders of copyright rights in the Works for which a User obtains licenses via the Marketplace platform, which are displayed on specific Order Confirmations.

"Terms" means the terms and conditions set forth in these General Terms and any additional Order Confirmation Terms collectively.

"User" or "you" is the person or entity making the use granted under the relevant License. Where the person accepting the Terms on behalf of a User is a freelancer or other third party who the User authorized to accept the General Terms on the User's behalf, such person shall be deemed jointly a User for purposes of such Terms.

"Work(s)" are the copyright protected works described in relevant Order Confirmations.

2) Description of Service. CCC's Marketplace enables Users to obtain Licenses to use one or more Works in accordance with all relevant Terms. CCC grants Licenses as an agent on behalf of the copyright rightsholder identified in the relevant Order Confirmation.

3) Applicability of Terms. The Terms govern User's use of Works in connection with the relevant License. In the event of any conflict between General Terms and Order Confirmation Terms, the latter shall govern. User acknowledges that Rightsholders have complete discretion whether to grant any permission, and whether to place any limitations on any grant, and that CCC has no right to supersede or to modify any such discretionary act by a Rightsholder.

4) Representations; Acceptance. By using the Service, User represents and warrants that User has been duly authorized by the User to accept, and hereby does accept, all Terms.

5) Scope of License; Limitations and Obligations. All Works and all rights therein, including copyright rights, remain the sole and exclusive property of the Rightsholder. The License provides only those rights expressly set forth in the terms and conveys no other rights in any Works

6) General Payment Terms. User may pay at time of checkout by credit card or choose to be invoiced. If the User chooses to be invoiced, the User shall: (i) remit payments in the manner identified on specific invoices, (ii) unless otherwise specifically stated in an Order Confirmation or separate written agreement, Users shall remit payments upon receipt of the relevant invoice from CCC, either by delivery or notification of availability of the invoice via the Marketplace platform, and (iii) if the User does not pay the invoice within 30 days of receipt, the User may incur a service charge of 1.5% per month or the maximum rate allowed by applicable law, whichever is less. While User may exercise the rights in the License immediately upon receiving the Order Confirmation, the License is automatically revoked and is null and void, as if it had never been issued, if CCC does not receive complete payment on a timely basis.

7) General Limits on Use. Unless otherwise provided in the Order Confirmation, any grant of rights to User (i) involves only the rights set forth in the Terms and does not include subsequent or additional uses, (ii) is non-exclusive and non-transferable, and (iii) is subject to any and all limitations and restrictions (such as, but not limited to, limitations on duration of use or circulation) included in the Terms. Upon completion of the licensed use as set forth in the Order Confirmation, User shall either secure a new permission for further use of the Work(s) or immediately cease any new use of the Work(s) and shall render inaccessible (such as by deleting or by removing or severing links or other locators) any further copies of the Work. User may only make alterations to the Work if and as expressly set forth in the Order Confirmation. No Work may be used in any way that is unlawful, including without limitation if such use would violate applicable sanctions laws or regulations, would be defamatory, violate the rights of third parties (including such third parties' rights of copyright, privacy, publicity, or other tangible or intangible property), or is otherwise illegal, sexually explicit, or obscene. In addition, User may not conjoin a Work with any other material that may result in damage to the reputation of the Rightsholder. Any unlawful use will render any licenses hereunder null and void. User agrees to inform CCC if it becomes aware of any infringement of any rights in a Work and to cooperate with any reasonable request of CCC or the Rightsholder in connection therewith.

8) Third Party Materials. In the event that the material for which a License is sought includes third party materials (such as photographs, illustrations, graphs, inserts and similar materials) that are identified in such material as having been used by permission (or a similar indicator), User is responsible for identifying, and seeking separate licenses (under this Service, if available, or otherwise) for any of such third party materials; without a separate license, User may not use such third party materials via the License.

9) Copyright Notice. Use of proper copyright notice for a Work is required as a condition of any License granted under the Service. Unless otherwise provided in the Order Confirmation, a proper copyright notice will read substantially as follows: "Used with permission of [Rightsholder's name], from [Work's title, author, volume, edition number and year of copyright]; permission conveyed through Copyright Clearance Center, Inc." Such notice must be provided in a reasonably legible font size and must be placed either on a cover page or in another location that any person, upon gaining access to the material which is the subject of a permission, shall see, or in the case of republication Licenses, immediately adjacent to the Work as used (for example, as part of a by-line or footnote) or in the place where substantially all other credits or notices for the new work containing the republished Work are located. Failure to include the required notice results in loss to the Rightsholder and CCC, and the User shall be liable to pay liquidated damages for each such failure equal to twice the use fee specified in the Order Confirmation, in addition to the use fee itself and any other fees and charges specified.

10) Indemnity. User hereby indemnifies and agrees to defend the Rightsholder and CCC, and their respective employees and directors, against all claims, liability, damages, costs, and expenses, including legal fees and expenses, arising out of any use of a Work beyond the scope of the rights granted herein and in the Order Confirmation, or any use of a Work which has been altered in any unauthorized way by User, including claims of defamation or infringement of rights of copyright, publicity, privacy, or other tangible or intangible property.

11) Limitation of Liability. UNDER NO CIRCUMSTANCES WILL CCC OR THE RIGHTSHOLDER BE LIABLE FOR ANY DIRECT, INDIRECT, CONSEQUENTIAL, OR INCIDENTAL DAMAGES (INCLUDING WITHOUT LIMITATION DAMAGES FOR LOSS OF BUSINESS PROFITS OR INFORMATION, OR FOR BUSINESS INTERRUPTION) ARISING OUT OF THE USE OR INABILITY TO USE A WORK, EVEN IF ONE OR BOTH OF THEM HAS BEEN ADVISED OF THE POSSIBILITY OF SUCH DAMAGES. In any event, the total liability of the Rightsholder and CCC (including their respective employees and directors) shall not exceed the total amount actually paid by User for the relevant License. User assumes full liability for the actions and omissions of its principals, employees, agents, affiliates, successors, and assigns.

12) Limited Warranties. THE WORK(S) AND RIGHT(S) ARE PROVIDED "AS IS." CCC HAS THE RIGHT TO GRANT TO USER THE RIGHTS GRANTED IN THE ORDER CONFIRMATION DOCUMENT. CCC AND THE RIGHTSHOLDER DISCLAIM ALL OTHER WARRANTIES RELATING TO THE WORK(S) AND RIGHT(S), EITHER EXPRESS OR IMPLIED, INCLUDING WITHOUT LIMITATION IMPLIED WARRANTIES OF MERCHANTABILITY OR FITNESS FOR A PARTICULAR PURPOSE. ADDITIONAL RIGHTS MAY BE REQUIRED TO USE ILLUSTRATIONS, GRAPHS, PHOTOGRAPHS, ABSTRACTS, INSERTS, OR OTHER PORTIONS OF THE WORK (AS OPPOSED TO THE ENTIRE WORK) IN A MANNER CONTEMPLATED BY USER; USER UNDERSTANDS AND AGREES THAT NEITHER CCC NOR THE RIGHTSHOLDER MAY HAVE SUCH ADDITIONAL RIGHTS TO GRANT.

13) Effect of Breach. Any failure by User to pay any amount when due, or any use by User of a Work beyond the scope of the License set forth in the Order Confirmation and/or the Terms, shall be a material breach of such License. Any breach not cured within 10 days of written notice thereof shall result in immediate termination of such License without further notice. Any unauthorized (but licensable) use of a Work that is terminated immediately upon notice thereof may be liquidated by payment of the Rightsholder's ordinary license price therefor; any unauthorized (and unlicensable) use that is not terminated immediately for any reason (including, for example, because materials containing the Work cannot reasonably be recalled) will be subject to all remedies available at law or in equity, but in no event to a payment of less than three times the Rightsholder's ordinary license price for the most closely analogous licensable use plus Rightsholder's and/or CCC's costs and expenses incurred in collecting such payment.

14) Additional Terms for Specific Products and Services. If a User is making one of the uses described in this Section 14, the additional terms and conditions apply:

a) *Print Uses of Academic Course Content and Materials (photocopies for academic coursepacks or classroom handouts).* For photocopies for academic coursepacks or classroom handouts the following additional terms apply:

i) The copies and anthologies created under this License may be made and assembled by faculty members individually or at their request by on-campus bookstores or copy centers, or by off-campus copy shops and other similar entities.

ii) No License granted shall in any way: (i) include any right by User to create a substantively non-identical copy of the Work or to edit or in any other way modify the Work (except by means of deleting material immediately preceding or following the entire portion of the Work copied) (ii) permit "publishing ventures" where any particular anthology would be systematically marketed at multiple institutions.

iii) Subject to any Publisher Terms (and notwithstanding any apparent contradiction in the Order Confirmation arising from data provided by User), any use authorized under the academic pay-per-use service is limited as follows:

A) any License granted shall apply to only one class (bearing a unique identifier as assigned by the institution, and thereby including all sections or other subparts of the class) at one institution;

B) use is limited to not more than 25% of the text of a book or of the items in a published collection of essays, poems or articles;

C) use is limited to no more than the greater of (a) 25% of the text of an issue of a journal or other periodical or (b) two articles from such an issue;

D) no User may sell or distribute any particular anthology, whether photocopied or electronic, at more than one institution of learning;

E) in the case of a photocopy permission, no materials may be entered into electronic memory by User except in order to produce an identical copy of a Work before or during the academic term (or analogous period) as to which any particular permission is granted. In the event that User shall choose to retain materials that are the subject of a photocopy permission in electronic memory for purposes of producing identical copies more than one day after such retention (but still within the scope of any permission granted), User must notify CCC of such fact in the applicable permission request and such retention shall constitute one copy actually sold for purposes of calculating permission fees due; and

F) any permission granted shall expire at the end of the class. No permission granted shall in any way include any right by User to create a substantively non-identical copy of the Work or to edit or in any other way modify the Work (except by means of deleting material immediately preceding or following the entire portion of the Work copied).

iv) Books and Records; Right to Audit. As to each permission granted under the academic pay-per-use Service, User shall maintain for at least four full calendar years books and records sufficient for CCC to determine the numbers of copies made by User under such permission. CCC and any representatives it may designate shall have the right to audit such books and records at any time during User's ordinary business hours, upon two days' prior notice. If any such audit shall determine that User shall have underpaid for, or underreported, any photocopies sold or by three percent (3%) or more, then User shall bear all the costs of any such audit; otherwise, CCC shall bear the costs of any such audit. Any amount determined by such audit to have been underpaid by User shall immediately be paid to CCC by User, together with interest thereon at the rate of 10% per annum from the date such amount was originally due. The provisions of this paragraph shall survive the termination of this License for any reason.

b) *Digital Pay-Per-Uses of Academic Course Content and Materials (e-coursepacks, electronic reserves, learning management systems, academic institution intranets).* For uses in e-coursepacks, posts in electronic reserves, posts in learning management systems, or posts on academic institution intranets, the following additional terms apply:

i) The pay-per-uses subject to this Section 14(b) include:

A) Posting e-reserves, course management systems, e-coursepacks for text-based content, which grants authorizations to import requested material in electronic format, and allows electronic access to this material to members of a designated college or university class, under the direction of an instructor designated by the college or university, accessible only under appropriate electronic controls (e.g., password);

B) Posting e-reserves, course management systems, e-coursepacks for material consisting of photographs or other still images not embedded in text, which grants not only the authorizations described in Section 14(b)(i)(A) above, but also the following authorization: to include the requested material in course materials for use consistent with Section 14(b)(i)(A) above, including any necessary resizing, reformatting or modification of the resolution of such requested material (provided that such modification does not alter the underlying editorial content or meaning of the requested material, and provided that the resulting modified content is used solely within the scope of, and in a manner consistent with, the particular authorization described in the Order Confirmation and the Terms), but not including any other form of manipulation, alteration or editing of the requested material;

C) Posting e-reserves, course management systems, e-coursepacks or other academic distribution for audiovisual content, which grants not only the authorizations described in Section 14(b)(i)(A) above, but also the following authorizations: (i) to include the requested material in course materials for use consistent with Section 14(b)(i)(A) above; (ii) to display and perform the requested material to such members of such class in the physical classroom or remotely by means of streaming media or other video formats; and (iii) to "clip" or reformat the requested material for purposes of time or content management or ease of delivery, provided that such "clipping" or reformatting does not alter the underlying editorial content or meaning of the requested material and that the resulting material is used solely within the scope of, and in a manner consistent with, the particular authorization described in the Order Confirmation and the Terms. Unless expressly set forth in the relevant Order Conformation, the License does not authorize any other form of manipulation, alteration or editing of the requested material.

ii) Unless expressly set forth in the relevant Order Confirmation, no License granted shall in any way: (i) include any right by User to create a substantively non-identical copy of the Work or to edit or in any other way modify the Work (except by means of deleting material immediately preceding or following the entire portion of the Work copied or, in the case of Works subject to Sections 14(b)(1)(B) or (C) above, as described in such Sections) (ii) permit "publishing ventures" where any particular course materials would be systematically marketed at multiple institutions.

iii) Subject to any further limitations determined in the Rightsholder Terms (and notwithstanding any apparent contradiction in the Order Confirmation arising from data provided by User), any use authorized under the electronic course content pay-per-use service is limited as follows:

A) any License granted shall apply to only one class (bearing a unique identifier as assigned by the institution, and thereby including all sections or other subparts of the class) at one institution;

B) use is limited to not more than 25% of the text of a book or of the items in a published collection of essays, poems or articles;

C) use is limited to not more than the greater of (a) 25% of the text of an issue of a journal or other periodical or (b) two articles from such an issue;

D) no User may sell or distribute any particular materials, whether photocopied or electronic, at more than one institution of learning;

E) electronic access to material which is the subject of an electronic-use permission must be limited by means of electronic password, student identification or other control permitting access solely to students and instructors in the class;

F) User must ensure (through use of an electronic cover page or other appropriate means) that any person, upon gaining electronic access to the material, which is the subject of a permission, shall see:

- a proper copyright notice, identifying the Rightsholder in whose name CCC has granted permission,

- a statement to the effect that such copy was made pursuant to permission,

- a statement identifying the class to which the material applies and notifying the reader that the material has been made available electronically solely for use in the class, and

- a statement to the effect that the material may not be further distributed to any person outside the class, whether by copying or by transmission and whether electronically or in paper form, and User must also ensure that such cover page or other means will print out in the event that the person accessing the material chooses to print out the material or any part thereof.

G) any permission granted shall expire at the end of the class and, absent some other form of authorization, User is thereupon required to delete the applicable material from any electronic storage or to block electronic access to the applicable material.

iv) Uses of separate portions of a Work, even if they are to be included in the same course material or the same university or college class, require separate permissions under the electronic course content pay-per-use Service. Unless otherwise provided in the Order Confirmation, any grant of rights to User is limited to use completed no later than the end of the academic term (or analogous period) as to which any particular permission is granted.

v) Books and Records; Right to Audit. As to each permission granted under the electronic course content Service, User shall maintain for at least four full calendar years books and records sufficient for CCC to determine the numbers of copies made by User under such permission. CCC and any representatives it may designate shall have the right to audit such books and records at any time during User's ordinary business hours, upon two days' prior notice. If any such audit shall determine that User shall have underpaid for, or underreported, any electronic copies used by three percent (3%) or more, then User shall bear all the costs of any such audit; otherwise, CCC shall bear the costs of any such audit. Any amount determined by such audit to have been underpaid by User shall immediately be paid to CCC by User, together with interest thereon at the rate of 10% per annum from the date such amount was originally due. The provisions of this paragraph shall survive the termination of this license for any reason.

c) *Pay-Per-Use Permissions for Certain Reproductions (Academic photocopies for library reserves and interlibrary loan reporting) (Non-academic internal/external business uses and commercial document delivery).* The License expressly excludes the uses listed in Section (c)(i)-(v) below (which must be subject to separate license from the applicable Rightsholder) for: academic photocopies for library reserves and interlibrary loan reporting; and non-academic internal/external business uses and commercial document delivery.

i) electronic storage of any reproduction (whether in plain-text, PDF, or any other format) other than on a transitory basis;

ii) the input of Works or reproductions thereof into any computerized database;

iii) reproduction of an entire Work (cover-to-cover copying) except where the Work is a single article;

iv) reproduction for resale to anyone other than a specific customer of User;

v) republication in any different form. Please obtain authorizations for these uses through other CCC services or directly from the rightsholder.

Any license granted is further limited as set forth in any restrictions included in the Order Confirmation and/or in these Terms.

d) *Electronic Reproductions in Online Environments (Non-Academic-email, intranet, internet and extranet).* For "electronic reproductions", which generally includes e-mail use (including instant messaging or other electronic transmission to a defined group of recipients) or posting on an intranet, extranet or Intranet site (including any display or performance incidental thereto), the following additional terms apply:

i) Unless otherwise set forth in the Order Confirmation, the License is limited to use completed within 30 days for any use on the Internet, 60 days for any use on an intranet or extranet and one year for any other use, all as measured from the "republication date" as identified in the Order Confirmation, if any, and otherwise from the date of the Order Confirmation.

ii) User may not make or permit any alterations to the Work, unless expressly set forth in the Order Confirmation (after request by User and approval by Rightsholder); provided, however, that a Work consisting of photographs or other still images not embedded in text may, if necessary, be resized, reformatted or have its resolution modified without additional express permission, and a Work consisting of audiovisual content may, if necessary, be "clipped" or reformatted for purposes of time or content management or ease of delivery (provided that any such resizing, reformatting, resolution modification or "clipping" does not alter the underlying editorial content or meaning of the Work used, and that the resulting material is used solely within the scope of, and in a manner consistent with, the particular License described in the Order Confirmation and the Terms.

15) Miscellaneous.

a) User acknowledges that CCC may, from time to time, make changes or additions to the Service or to the Terms, and that Rightsholder may make changes or additions to the Rightsholder Terms. Such updated Terms will replace the prior terms and conditions in the order workflow and shall be effective as to any subsequent Licenses but shall not apply to Licenses already granted and paid for under a prior set of terms.

b) Use of User-related information collected through the Service is governed by CCC's privacy policy, available online at www.copyright.com/about/privacy-policy/.

c) The License is personal to User. Therefore, User may not assign or transfer to any other person (whether a natural person or an organization of any kind) the License or any rights granted thereunder; provided, however, that, where applicable, User may assign such License in its entirety on written notice to CCC in the event of a transfer of all or substantially all of User's rights in any new material which includes the Work(s) licensed under this Service.

d) No amendment or waiver of any Terms is binding unless set forth in writing and signed by the appropriate parties, including, where applicable, the Rightsholder. The Rightsholder and CCC hereby object to any terms contained in any writing prepared by or on behalf of the User or its principals, employees, agents or affiliates and purporting to govern or otherwise relate to the License described in the Order Confirmation, which terms are in any way inconsistent with any Terms set forth in the Order Confirmation, and/or in CCC's standard operating procedures, whether such writing is prepared prior to, simultaneously with or subsequent to the Order Confirmation, and whether such writing appears on a copy of the Order Confirmation or in a separate instrument.

e) The License described in the Order Confirmation shall be governed by and construed under the law of the State of New York, USA, without regard to the principles thereof of conflicts of law. Any case, controversy, suit, action, or proceeding arising out of, in connection with, or related to such License shall be brought, at CCC's sole discretion, in any federal or state court located in the County of New York, State of New York, USA, or in any federal or state court whose geographical jurisdiction covers the location of the Rightsholder set forth in the Order Confirmation. The parties expressly submit to the personal jurisdiction and venue of each such federal or state court.

Last updated October 2022

Development of an Optical Investigation Method for Diesel and Oxymethylene Ether Spray in a Large-Bore Dual-Fuel Engine Using a Fisheye Optical System

Stephan Bernhard Karmann,[1] Stefan Weber,[2] Wolfgang Stürzl,[3] Maximilian Prager,[1] Malte Jaensch,[1] and Georg Wachtmeister[1]

[1]Technical University of Munich, Germany
[2]MAN Energy Solutions, Germany
[3]DLR Institute of Robotics and Mechatronics, Germany

Abstract

Optical combustion phenomena investigation is a common tool for passenger car and automotive engines. Large-bore engines for stationary and mobile applications, on the other hand, have a lower optical examination density. This is mainly due to the technically more complex design of the optical accesses that have to provide a larger field of view and withstand high mechanical and thermal loads. Nevertheless, an optical investigation of in-cylinder phenomena in large-bore engines is essential to optimize efficient and environmentally friendly combustion processes using new sustainable e-fuels. To realize a simple optical access with maximum observability of the combustion chamber, a fisheye optic for the direct integration into internal combustion engines was developed and used for in-cylinder Mie-scattering investigations of diesel and Oxymethylene Ether (OME_{3-5}) pilot fuel spray of natural gas dual-fuel combustion processes in a MAN 35/44DF single-cylinder research engine. As this special application of a fisheye lens poses some technical challenges, a special image processing procedure is necessary for result evaluation. This innovative postprocessing of the fisheye images comprises a calibration of the fisheye optic and a virtual three-dimensional (3D) re-projection method. Investigations prove the accuracy of the method to be within 2.1 mm. To prove the advantage of the method, optical spray investigations of two different fuels using Mie-scattering in the skipped-fire optical accessible medium-speed large-bore engine are carried out under realistic engine conditions. With the newly developed post-processing procedure, it was possible to derive the mean liquid penetration depth of the in situ investigations. Further, the post-processing includes a rectification of the fisheye images to improve the observability of the pilot fuel spray in the fired combustion engine. The analysis reveals a more compact and dense spray for OME_{3-5} compared to marine diesel fuel (DMA) as well as about 39% reduced liquid penetration length.

1. Introduction

Regenerative energies from wind and sun are not constantly regionally and seasonally available. Different types of storage concepts are available to provide a long-term (several months), mid-term (several days), and short-term (several hours) buffering of residual loads to ensure a constant and safe supply of energy for the consumers. Various technologies such as pumped storage power plants, battery grids, a coupling of demand and supply sectors, and the Power to X approach offer the possibility of efficient generation, distribution, and storage of sustainable energy. In particular, the Power to X process, in which green surplus energy is converted into liquid or gaseous carbon-neutral or free energy sources, provides a promising possibility of long-term storage. The hydrogen produced here can be used in a wide variety of applications. One possibility is the direct use or further processing into sustainable fuels (methane, oxymethylene ether [OME], ethanol, ammonia, etc.) for use in combustion engines for energy recovery or in the field of freight transportation. In order to increase the efficiency of large-bore engines, most frequently used for regenerative fuels, the optical investigation of the combustion phenomena is important. By using optical and laser-optical measuring methods in combination with thermodynamic investigations, the mixture formation, combustion, and emission generation can be investigated to support the combustion model development of sustainable fuels. With improved calculation tools, future engine generations can be designed with greater efficiency.

The effectiveness of an experimental thermodynamic optimization of the dual-fuel combustion process in terms of main engine parameter variation (e.g., injection pressure and start of energizing [SOE]) was, e.g., described in [1] with presenting beneficial effects on carbon dioxide (CO_2) and particle emission. Fraioli [2] conducted numerical investigations with experimental validation on the same engine with 0.48L displacement using a dual-fuel combustion process and proved the effectiveness of numerical investigations. Gleis et al. investigated the combustion of alternative e-fuels in a high-pressure dual-fuel combustion process [3, 4] with beneficial effects on soot efficiency and knock limits with optical measurement techniques using a Bowditch [5] type fully optically accessible engine. Frankl et al. [6] provided numerical computational fluid dynamics (CFD) investigations with optical investigations of the same high-pressure dual-fuel single-cylinder research engine with 4.8L displacement. However, especially optical investigations require efficient optical accessibility into these engines, with minimum adaption of the original engine to gain maximum comparability. Due to the engine dimensions for stationary as well as mobile applications like ships and railways, the realization of optical accessibility requires a higher effort regarding design, build, and operations depending on the degree of accessibility (cf. [7]). For this application, an approximately equidistant fisheye optic has been developed (cf. [8]) for direct integration in the combustion chamber of a MAN 35/44DF test engine.

The successful implementation and setup is described in [8]. Due to the distorting properties of fisheye lenses, it is necessary to post process the captured images. The following describes the development, implementation, and use of this procedure for investigations of Mie-scattering images of the pilot fuel injection of the dual fuel combustion process during skipped-fire engine operation.

2. Fisheye Lens Imaging

Fisheye lenses provide a large field of view of 180° up to 280° and are usually applied in robotics, tele-operated driving, photography, and scientific observations (cf. [9]). The realization of such a large field of view is possible due to the fisheye-specific geometrical distortion of the shapes of the imaged objects. To compensate for this distortion, a post-processing projection algorithm is applied to the recorded image series. The following sections provide the theoretical background of imaging for the postprocessing, that is, projection schemes as well as an overview of available fisheye image distortion models and a summary of calibration possibilities of these models.
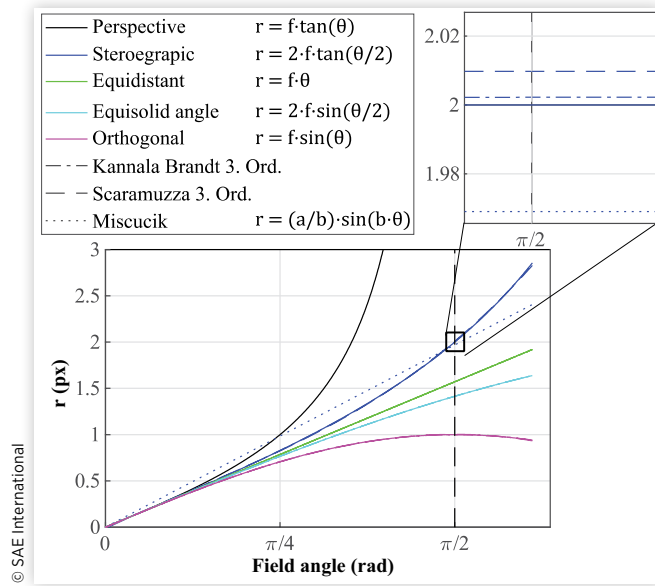
2.1. Fisheye Imaging Model

The mapping of real-world three-dimensional (3D) conditions onto a two-dimensional (2D) camera sensor can generally be defined as a 2D projection. This ideal concept can be described in its simplest form with, for example, the pinhole camera projection (perspective projection function cf. Equation 1). For many images with a relatively small viewing angle of up to 40°, this perspective projection is suitable. This is especially true as radial distortions are usually not very pronounced within that type of optic due to real lens effects and can therefore be neglected.

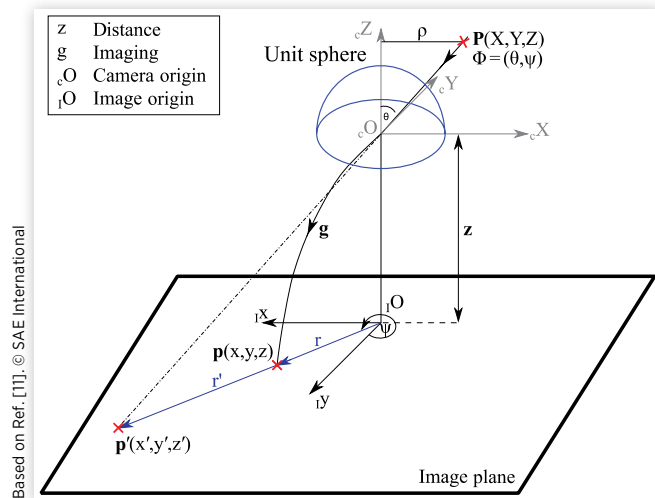$$r = f \cdot \tan(\Theta) \qquad \text{Eq. (1)}$$

For fisheye lenses with a field angle of $\theta \geq 90°$, the image description with the simple perspective projection according to Equation 1 is no longer possible. Figure 1 shows that an infinitely large radius would result in the perspective projection if the angle approaches 90°. Therefore, a significant radial distortion of the optic is necessary to realize the large field of view, which can no longer be neglected.

Fisheye optics, therefore, exhibit strong, often nonlinear distortions [10]. The general concept describing the fisheye image projection uses a spherical camera model and is shown in Figure 2 (cf. [11, 12]). Here, the projection of a 3D point $\mathbf{P}(X, Y, Z)$ is shown resulting in $\mathbf{p}'(x, y, z)$ onto the image plane using the perspective pinhole model with the distance z equals the focal length. For angles $\theta \geq 90°$, the perspective mapping can no longer project the point P onto a finite plane because the size of radius r would reach infinity [11].

FIGURE 1 Overview of projection functions.

Hence, other mapping models must be resorted to. A common approach for omnidirectional and fisheye optics is the unit sphere approach. Imaging a point P taken with a fisheye optic now projects this point via the unit hemisphere at the distance z which could equal the focal length (cf. [11]) and the imaging function **g** onto the image plane as **p**(x, y, z), where r < r′. This ensures projection onto a finite image plane for angles of θ ≥ 90°. The intermediate step of assuming a unit hemisphere is used to assign each imaged point to an incident ray vector **Φ** pointing from the center of the hemisphere, that is, the center of the camera $_c$O to the point in the 3D scene P. The two angles ψ and Θ describe the vector direction. The angles are determined in the respective projection plane of the incident ray vector (cf. Figure 2). The angle θ thus indicates the angle relative to the vertical axis z and the angle ψ, the

FIGURE 2 Fisheye imaging camera model.

angle to the y-axis (cf. [13]). Equation 2 summarizes this procedure as a forward projection, from the 3D space to the 2D image plane.

$$\mathbf{p} = r(\theta) \cdot (\cos \psi, \sin \psi)^{\mathrm{T}} = g(\mathbf{\Phi}) \qquad \text{Eq. (2)}$$

Figure 1 further shows the perspective projections and usual imaging rules for fisheye optics (stereographic, equidistant, equisolid) that refer to the function r(Θ) in Equation 2. Especially, the equidistant projection is often used for the design of fisheye lenses—as well as for the optics used in the following (cf. [8]). As a common approach to describe ideal projections, mathematical approximations are being used. These approximations are often based on polynomials of different degrees. Figure 1 shows this for the models according to Kannala and Brandt (cf. [11]), Scaramuzza (cf. [14]), and Miscucik (cf. [15]), as an example of a non-polynomial-based model. The disadvantage of Miscucik's non-polynomial-based model for stereographic projection is clearly visible. The other models follow the ideal imaging rules with much smaller deviations.

Due to tolerances like decenter and tilt resulting from manufacturing imprecisions and assembly of each optical lens, the real image rarely follows the represented ideal imaging function with respect to the camera sensor center. Because of this, the approximated common projection rules are usually supplemented using various mathematical approaches for modeling radial and tangential distortion effects arising from the real optic. These models also include the shift of the optical center. The mathematical approaches try to approximate the real mapping of the optical via a generally valid formulation using additional distortion terms to the projection **g** (see Equation 4) as shown in Equation 3 (cf. [10]). Here, $\mathbf{u_t}$ and $\mathbf{u_r}$ are the unit vectors in the radial and tangential direction in the Cartesian image plane coordinate system (COS). The terms $\Delta_r(\theta, \psi)$ and $\Delta_t(\theta, \psi)$ describe an unsymmetrical tangential and radial distortion term (cf. [11]).

$$\mathbf{p} = r(\theta) \cdot \mathbf{u_r}(\psi) + \Delta_r(\theta, \psi) \cdot \mathbf{u_r}(\psi) + \Delta_t(\theta, \psi) \cdot \mathbf{u_t}(\psi) \quad \text{Eq. (3)}$$

The radius r(θ) is the result from the mapping of the incoming ray to the image plane and is summarized with Equation 4 according to [11] using, e.g., an odd polynomial approach to define **g**.

$$\mathbf{g}(\mathbf{\Phi}) = \underbrace{\frac{r(\Theta)}{k_1 \cdot \theta + k_2 \cdot \theta^3 + k_3 \cdot \theta^5 + k_4 \cdot \theta^7 + k_5 \cdot \theta^9 + \cdots}} \cdot \begin{pmatrix} \cos \psi \\ \sin \psi \end{pmatrix} = \begin{pmatrix} _I x \\ _I y \end{pmatrix} \qquad \text{Eq. (4)}$$

At the final step, the Cartesian image plane coordinates have to be transformed into a pixel (px)-based description. Hence Equation 5 describes this affine transformation with the principal point $\mathbf{q_0}$, which may deviate from the metric image plane origin and the number of pixels per unit length in the horizontal and vertical direction of the image m_h, m_v.

$$\mathbf{q} = \begin{bmatrix} m_h & 0 \\ 0 & m_v \end{bmatrix} \cdot \mathbf{p} + \mathbf{q_0} \qquad \text{Eq. (5)}$$

With Equations 3, 4, and 5 the projection model consists of three composite functions:

- Equation 4 describes the transformation of the ray direction to the metric image plane system,

- Equation 3 describes the distortion mapping from the ideal to the distorted points in the metric image plane.

- Equation 5 describes the final mapping from the metric to the pixel-based description of the image plane.

All imaging projection approaches necessitate a physical calibration of the optical test setup in order to determine the parameters of the mathematical distortion and projection functions. This calibration process will be detailed in the following.

Generally, images with large fields of view also suffer from vignetting (edge light fall-off). However, due to their strong distortion, fisheye lenses exhibit less vignetting here due to the violation of the cos^4 law. Nevertheless, there is also a nonlinear edge light fall-off here, which can be countered by mathematical models of the light distribution and an appropriate calibration (cf. [10]).

2.2. Calibration Process

Calibration generally is a two-step process consisting of the choice of a suitable camera, namely, projection model and calibration process as well as the calibration as such. Puig et al. [12] presented an overview of calibration procedures for omnidirectional cameras, classifying them into five calibration types (line based, 2D-pattern calibration, 3D-point based, self-calibration, polarization imaging). They differ mainly in the number of necessary views of a specified calibration pattern, its dimension, and the underlying calibration model. The 2D-pattern calibration was deemed the most suitable for the herein-used application as the 2D patterns provide both easily detectable control points and several suitable calibration models. Figure 3 illustrates the relations for calibration with a control point pattern. It illustrates the different relevant COSs (CPP = Calibration Point Pattern, C = Camera, I = Image) which are used to describe the projection. The calibration process is used to determine the so-called intrinsic and extrinsic camera parameters according to the selected camera model. The extrinsic parameters describe the location of the camera in the 3D scene and the position of the objects in the 3D scene to the corresponding camera COS. A translation vector $\mathbf{t}$ and a rotation matrix $\mathbf{R}$ summarize this description. The intrinsic parameters describe the camera-specific properties like focal length, the distortion center ($\mathbf{q_0}$, cf. Equation 5), and the transition of the camera coordinate-system-specific description into an image plane and thus a pixel-based description (m_h, m_v, cf. Equation 5). The imaging function itself (Equations 4 and 3) is one of the intrinsic parameters. The $\frac{n+1}{2}$ parameters of, e.g., the Kannala-Brandt polynomial-based equation (cf. Equation 4) are calculated as

FIGURE 3 Camera calibration concept.

© SAE International
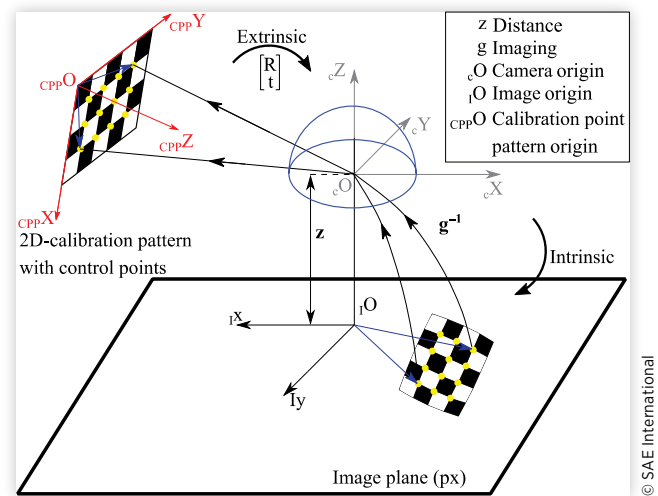
a result of the calibration process. They are estimated by a linear least squares minimization of the calculated forward and backward projection of the control points of the calibration pattern.

3. Experimental Setup

The following section contains the test bench design as well as a brief summary of the fuel properties and pilot fuel injection settings used for the conducted experiments.

3.1. Test Bench Design

Figure 4 depicts the test bench based on a MAN 35/44DF engine. The engine provides two injectors. The fisheye endoscope replaces the centrally mounted main injector, which is
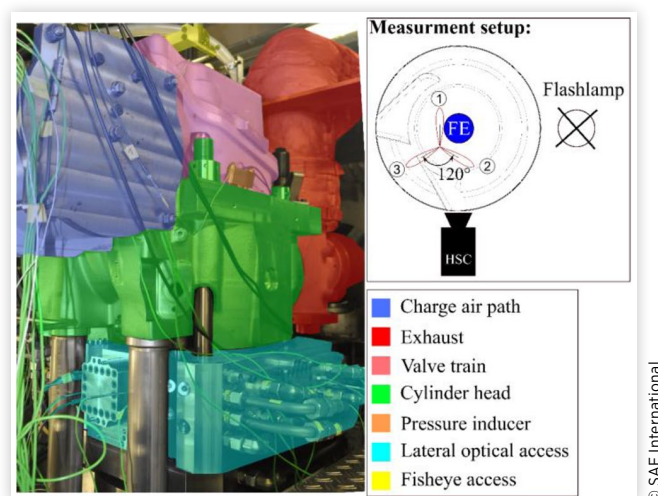
FIGURE 4 Experimental setup.

© SAE International

TABLE 1 Pilot injector specifications.

Amount of injection holes	3
Elevation angle	70°
Spray hole outlet diameter	0.16 mm
Maximum pressure	1600 bar
Hydraulic nozzle flow rate	481 cm³/30 s at 100 bar

© SAE International

TABLE 2 Engine specifications.

Displacement	42.3 dm³	**Stroke**	440 mm
Bore	350 mm	**Connecting rod length**	989 mm
Nom. speed	750 rpm	**Compression ratio**	12.2

© SAE International

not necessary as no pure diesel operation mode is used. The second injector mounted eccentrically between the intake valves provides the diesel pilot injection to ignite the premixed natural gas air mixture. The details of the pilot injector are summarized in Table 1. Figure 4 shows the spray orientation and the pilot injector position in the combustion chamber from a top view. The engine was operated in skipped-fire mode at 85% nominal engine load. The skipped-fire engine operation mode is described in detail in [8]. The reduction in load and the limited amount of fired cycles is necessary due to the adaptions of the cylinder head to fit the fisheye endoscope and the optic itself, especially the adhesive mount of the first lens.

Table 2 provides the test bench main data. For the herein-conducted measurements, the engine setup offers two optical accesses: the lateral and the fisheye endoscope access (cf. Figure 4).

The lateral access is realized with four quartz glass windows mounted in a ring introduced between the cylinder head and cylinder liner. Karmann et al. described the lateral access in [16]. Via each lateral window, a vertical field of view of the combustion chamber is possible. Furthermore, the accesses can be used for the illumination of the Mie-scattering images with a flash lamp. The lateral setup is depicted in Figure 5. To gain direct insight into the piston bowl by the lateral accesses as well, the engine piston is modified with two recesses (cf. Figure 4).

Figure 6 depicts the fisheye endoscope access through the cylinder head. The first lens directly facing the combustion

FIGURE 5 Lateral optical access.
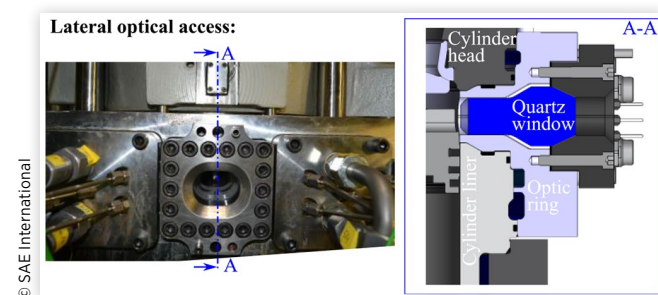
**FIGURE 6** Fisheye endoscopic access.
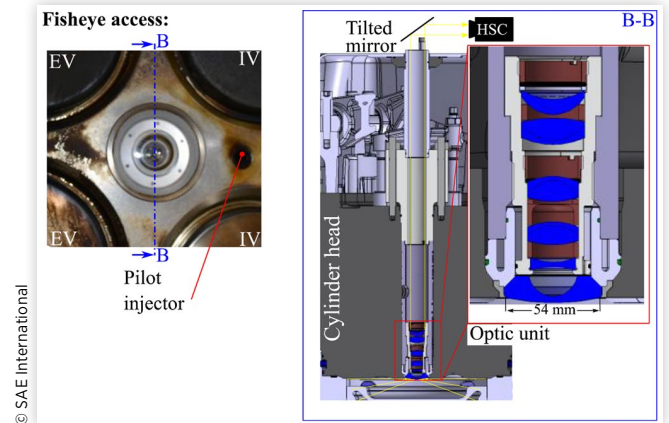
has a diameter of 54 mm. The image projected by the optic is redirected by a 45° tilted mirror on the outside of the engine to a monochromatic Phantom v2011 high-speed camera. The mirror decouples the image-capturing system from the engine. The camera is equipped with a Nikon teleconverter 1.4 magnifying the image captured with the Sigma f180 macro objective mounted on the camera front. The camera setup takes pictures with a resolution of 1°CA at 750 rpm nominal engine speed resulting in an exposure time of 330 μs. A detailed description of the fisheye endoscope is given by Karmann et al. [8] covering the experimental setup development of the optical engine and a detailed description of the engine operating conditions.

3.2. Field of View

As the field of view and the distortion of images recorded with a fisheye optic are quite unusual, Figure 7 depicts an overview of the fisheye field of view to gain an understanding of the

FIGURE 7 Field of view of the fisheye endoscope (EC = Engine center).
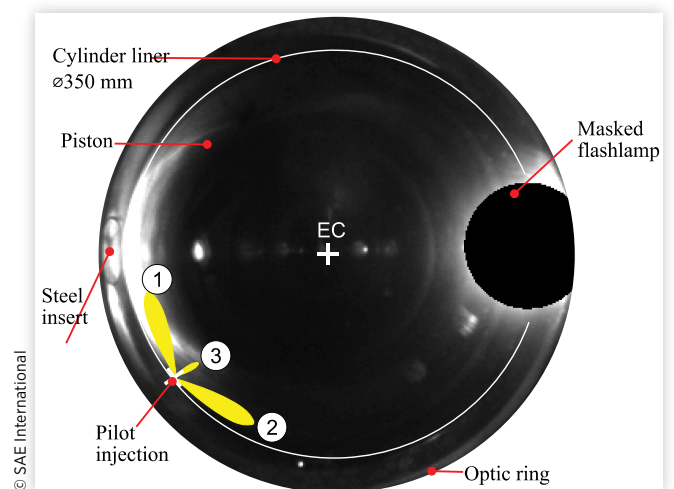
image composition. The field of view is similarly oriented as the top view in Figure 4. The bright spot of the illumination source (flash lamp) is covered for better differentiation. The position of the fuel jets is schematically indicated. Due to fisheye-specific imaging, close objects appear to be more distorted than objects in distance. Therefore, the piston, that is, the bore of the engine appears relatively undistorted in the images while the outer regions show a growing distortion effect. To the left of Figure 7, the steel insert mounted in one of the lateral accesses of the optic ring is visible opposite to the flash lamp.

3.3. Fuel Properties

The conducted experiments use a marine diesel fuel (DMA ISO8217) and for the second test series an OME_{3-5} blend as pilot fuel to ignite the premixed natural gas with a stoichiometric air-to-fuel ratio of 2. For a detailed overview of the OME fuel, synthetization and investigations as a sustainable replacement for fossil diesel fuels, e.g., [17, 18, 19, 20, 21], can be considered. Both fuel properties are summarized in Table 3. The diesel equivalent is calculated according to [17] and determines the volumetric energy content of the considered fuel to diesel.

According to the fuel properties, the following must be considered for the energetically equal replacement of DMA by OME_{3-5}:

- Increased density by a factor of 1.19 for OME_{3-5}
- Reduced energy content of OME_{3-5} by a factor of 2.19

This results in a 54.3% reduced volumetric energy content of OME_{3-5} being energetically comparable to DMA.

3.4. Derivation of the Injection Parameters

Using the same pilot injector and an energetically equivalent amount of pilot fuel for the two test series necessitates an adapted energizing time of the injector. As the injector characteristics for both fuels are not part of the presented investigation, comparable flow curves of a similar injector for DMA were adjusted by scaling.

According to Bernoulli's equation, the energy flow is calculated (cf. Equation 6) with some simplifications and the assumption of a steady flow of an incompressible fluid with no friction (cf. [17]). Further, the effect of the cylinder pressure at SOE on the injection rate is negligible, and the measured rail pressure equals the injection pressure.

$$\dot{E} = \underbrace{\frac{\pi}{4} \cdot d_{Nozzle}^2 \cdot n_{Nozzle}}_{cross-sectional\ area} \cdot LHV \cdot \sqrt{2 \cdot \varrho_{Fuel} \cdot p_{Rail}} \qquad Eq.\ (6)$$

Figure 8 depicts the energy flow depending on the rail pressure. The significant difference in the curve values emphasizes the need for an injection time adaption to realize the equal amount of energy content between both fuels. The difference in the courses of the two energy flows is the square root of the related fuel density and the LHV if the fuel density influence on the solenoid injector needle movement is neglected that arises due to the differing densities of OME_{3-5} compared to that of diesel observed in [22] for a commercial engine injector similar to the one used here. Due to the lack of experimental results regarding the used injector, the described procedure was developed to estimate the appropriate injection timings for an almost constant amount of energy by each fuel injection for each investigated fuel. Further, the procedure is used to define a mass equivalent amount for both fuels.

Thus, the following evaluation of the conducted experiments contains the analysis of a pilot fuel injection under energy and mass equivalent boundary conditions. The SOE of the pilot fuel injections is set in two steps at 30°CA bFTDC and 25°CA bFTDC for both fuel studies, and an additional SOE of 15°CA bFTDC for the OME_{3-5} blend is set in this study to conduct a more detailed investigation. For each step, the rail pressure is varied in two steps at 1200 bar and 1600 bar.

The conducted investigations are summarized in Table 4 and depict the investigated fuel, the amount of pilot fuel m_{Fuel}, time of injector energizing $t_{Energizing}$, injection rail pressure p_{Rail}, SOE, and the pilot fuel energy share compared to the total provided fuel (NG + pilot fuel) energy.

TABLE 3 Fuel properties (*according to PDF specified in EN15940 lower heating value [LHV] = 43.8 MJ/kg and density ρ = 750 kg/m³).

	DMA	OME_{3-5}
Density (kg/m³)	890	1060
Kinematic viscosity (mm²/s at 40°C)	4	1.2
LHV (MJ/kg)	42	19.16
Boiling point range (°C)	160–400	157–259
Flash point (°C)	60	70
Diesel equivalent* (m^3_{fuel}/m^3_{Diesel})	0.914	1.6822
Volumetric energy content (MJ/m³)	37,380	20,309
L_{min} (—)	14.59	5.8333

© SAE International

FIGURE 8 Comparison of DMA and OME_{3-5} energy injection rate.
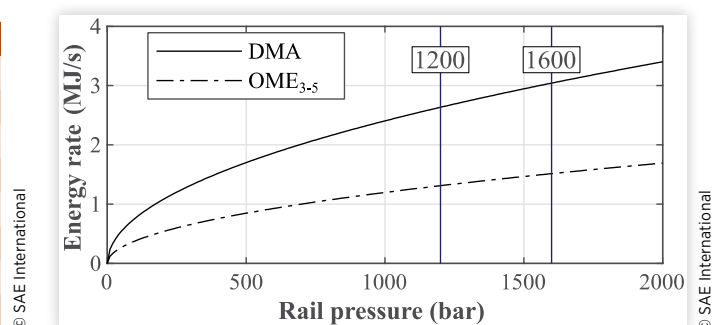
© SAE International

TABLE 4 Experiments at 80% nominal engine load—Mass equivalent and energy equivalent.

Fuel	m_{Fuel} (g/cycle)	$t_{Energizing}$ (ms)	p_{Rail} (bar)	SOE (°CA bTDC)	$E_{pilot\text{-}fuel}$ (%)
DMA	0.12	2.31 2.01	1200, 1600	30, 25	3
DMA	0.24	4.57 3.8	1200, 1600	30, 25	5
$OME_{3\text{-}5}$	0.24	3.74 3.19	1200, 1600	30, 25, 15	2
$OME_{3\text{-}5}$	0.29	4.57 3.86	1200, 1600	30, 25, 15	3

© SAE International

3.5. Derivation of the AHRR

The indicated combustion chamber pressure is recorded with a resolution of 0.1°CA between 30°CA bFTDC and 90°CA aFTDC covering the combustion. The recorded pressure is corrected using a two-point polytropic offset approach, filtered, and used as the mean value for the calculation of the apparent heat release rate (AHRR) shown in Equation 7 according to [23]. The cylinder pressure is averaged over the recorded fired cycles during the image recording. Equation 7 uses a constant isentropic coefficient κ = 1.32 suitable to combustion conditions and equal to the parameters chosen in [24].

$$\frac{dQ_H}{d\varphi} = \frac{\kappa}{\kappa - 1} \cdot p(\varphi) \cdot \frac{dV}{d\varphi} + \frac{1}{\kappa + 1} \cdot V(\varphi) \cdot \frac{dp}{d\varphi} \qquad \text{Eq. (7)}$$

4. Development of the Image Evaluation Procedure

The image evaluation procedure developed for the images captured with the fisheye endoscope consists of three main steps: Calibration of the optical system and preprocessing and postprocessing of the captured images. The following sections describe these steps in detail.

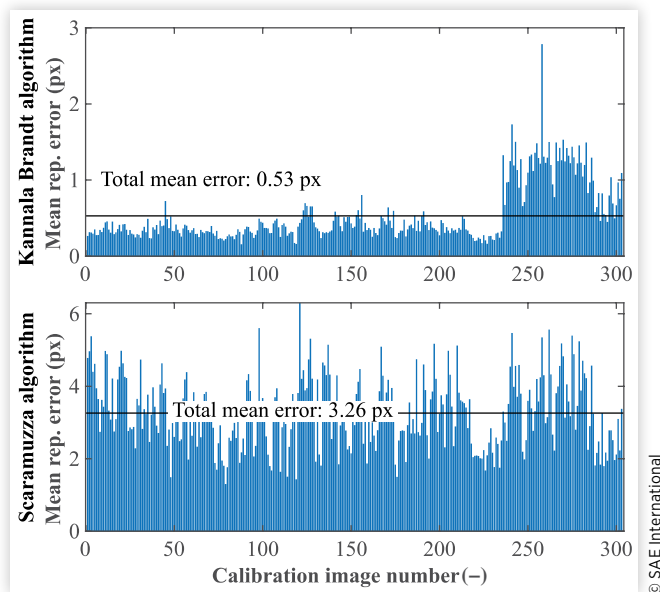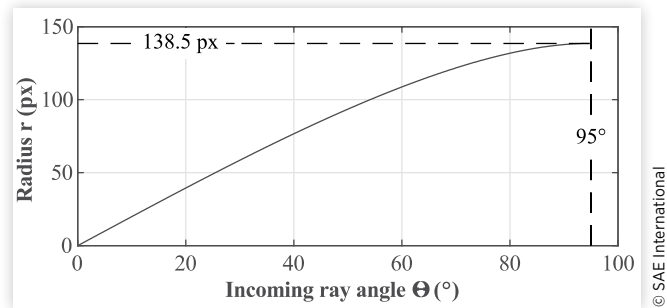## 4.1. Calibration of the Fisheye Endoscope

As already mentioned in Section 2 the images recorded through a fisheye optic require a distortion correction to acquire a rectified in-cylinder view. Two approaches, the Kannala-Brandt [11] and Scaramuzza [14, 25] procedures, were deemed suitable and are compared to each other in the following. Both approaches are control point based and use polynomial projection algorithms of different degrees to fit the real radial distortion of the optical system. The recordings of the calibration images of the control point pattern are conducted on the optical system outside of the engine, using a test setup with similar mounting conditions and distances compared to the test rig. This enables the recording of the control point pattern, as the space in the combustion chamber is too limited to insert the checkerboard calibration pattern of 297 × 420 × 10 mm in the needed varying angles and positions. Besides using the calibration test setup out of the engine allows better illumination as a homogenous illumination of the combustion chamber with limited space is difficult to realize. Further, the calibration setup enables additional calibration with additional patterns to determine the imaging quality of the optic as well as the feasible calibration quality. The control points used by the calibration algorithms are derived from the corners of the checkerboard pattern of black and white squares with a size of 25 mm. The corner feature detection algorithm CalDe provided by the DLR (cf. [26]) was applied here to predominantly automatically extract the control point information from the calibration picture series.

Overall, 303 calibration pictures with different alignments to the camera were captured with the imaging system and have been evaluated with the corner detection algorithm in CalDe. Figure 9 depicts the re-projection error of the two different calibration algorithms for all 303 calibration images. The error is calculated as a mean error for each original and re-projected control point on the calibration pattern in each view. Each algorithm calculates the re-projection of the calibration pattern in the scene to the camera sensor using the polynomial projection function (cf. Figure 3).

Due to the better performance of the Kannala-Brandt algorithm, the further proceeding is based on the forward projection function calculated by this algorithm and depicted in Figure 10. The backward projection function is easily derived as the inverse of the shown data.

The Kannala-Brandt model is also capable of an additional tangential distortion, but this was not used as the algorithm shows already a sufficiently good performance without it. To improve the total mean error, the 303 calibration images are filtered to neglect calibration points and images with high errors above 2 px that are mainly due to bad detection of the control points. The remaining 235 images result in a total mean error of 0.137 px and a maximum calibrated view angle of 95° in a maximum radius of 138.5 px in the image starting at the distortion center.

FIGURE 9 Mean re-projection error for Kannala-Brandt and Scaramuzza algorithms.


4.2. Image Preprocessing

The image preprocessing consists of five steps:

- Basic image arithmetic
- Compensation for the image movement
- Cut of the image shape to the region of interest (ROI)
- Image binarization
- Injection jet detection

The application of those steps on an example image is depicted in Figure 11. After the image import and file type conversion, the images are transformed to fit a view from the top into the engine. The transformation consists of a rotation and a vertical twist, depending on the camera orientation in the setup and the used mirror. As the camera is not rigidly aligned to the mirror, a relative motion between the deflection mirror and the camera occurs that has to be compensated before further postprocessing. Figure 11 depicts this motion by marking the

FIGURE 11 Preprocessing.

motion path with the centers of the circular fisheye images. The Matlab intensity-based image registration algorithm uses the bright spot produced by the flash lamp of the Mie-scattering experimental setup as a fixed reference position to compensate for this planar relative motion. As the motion consists of a rigid transformation without any tilt, the compensation works quite well. After the motion compensation, the image is cut to the ROI limited to the circular fisheye image on the camera sensor. For the cutout picture, the pixel size is reduced from 1280×840 to 400×400 per image capturing the complete combustion chamber of the engine. All images are binarized and cleared from background artifacts to enable automatic detection of the start and end of the injection as well as the injection jets. The binarization threshold mainly determines the accuracy of the jet detection. A constant threshold experimentally determined to gain the best fit for all experiments is therefore set individually for OME_{3-5} and DMA due to their different densities resulting in altered conditions for the Mie scattering.

Although there are three jets in the experimental setup, the optic is only capable of imaging and detecting two jets sufficiently for further postprocessing. They are pointing toward the optic and can easily be observed over the image series. The third jet on the other hand is directed away from the optic resulting in a kind of top view and is located at the largest distance from the optic. This large distance together with the fisheye optic imaging results in strongly distorted images of this jet positioned in the border region of the image and partly overlaid by Jet 1. As the resolution of the camera is limited and the amount of information per pixel in the border region of the image is high, the imaging system is not capable of a sufficient resolution to evaluate this jet.

FIGURE 10 Forward projection.
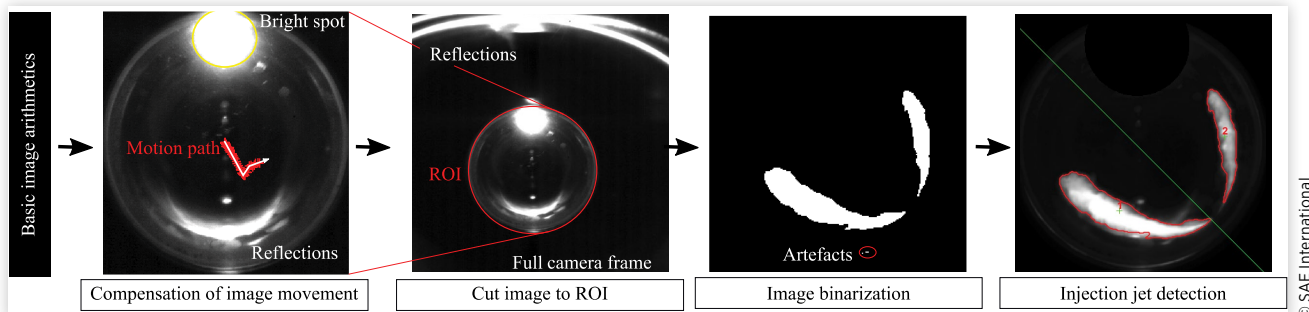
4.3. Image Postprocessing

The image postprocessing consists of two main tasks: One is the derivation of the liquid penetration length. The second uses the calibration information to undistort the image with a calibrated projection for a better visualization of the injection.

The image postprocessing to derive the injection-jet-related measures such as the liquid penetration length is based on the depicted calibration (cf. Section 4.1) and the following described processing.

With a fisheye optic, a simple pixel-to-length calibration is not possible due to the strong distortion and therefore nonlinear imaging. Generally, no depth information can be derived from only one camera as in this (fisheye) imaging process. Therefore, a virtual 3D remap of the jet contour will be carried out to derive the appropriate measures.

For this virtual 3D remapping, the following assumptions are made:

- The view axis is parallel to the cylinder liner axis.

- Both fuel jet axis 1, j_1, and jet axis 2, j_2, span a plane in which both jets remain during the injection.

- The calibration fits the conditions of the optic mounted in the engine.

- Manufacturing tolerances of the engine assembly are neglected.

With these assumptions made, Figure 12 depicts the geometric relations between the different parts and their COSs to determine the virtual 3D mapping of the fuel jet contour pixels. The forward projection model parametrized by the calibration measurements is applied to calculate the ray incident angle of each pixel belonging to one of the jet contours determined in the preprocessing (cf. Section 4.2). With this incident angle θ, the appropriate line of sight (cf. Figure 13)

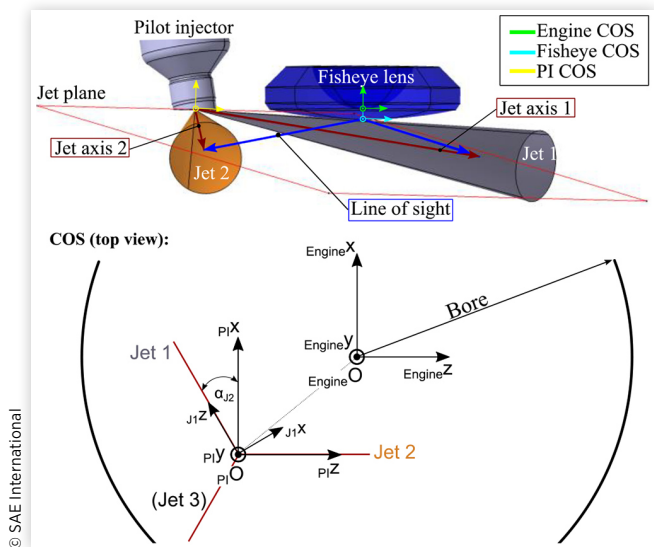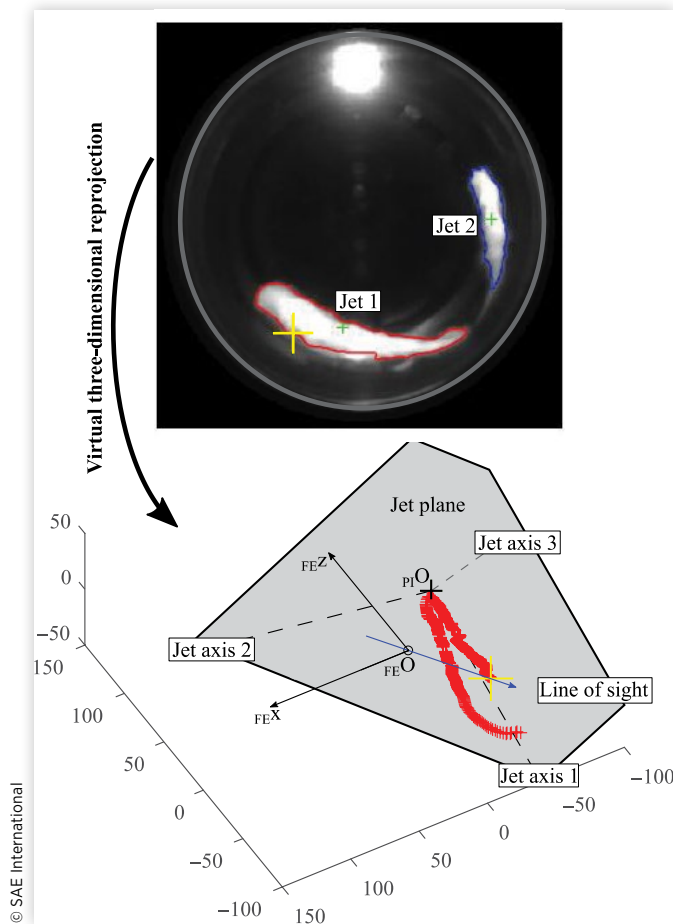**FIGURE 12**   Geometric relations and definition of the COS.

FIGURE 13   Virtual 3D re-projection.

Φ_n for each pixel from 1 to n of the spray contour can be derived. The fisheye optic COSs is coincident with the engine center system and can be shifted in the y-direction.

This shift corresponds to the camera position in the real world and is a possible optimization factor to better fit the imaged scene to the real world.

The top view shows the used COSs and transformations necessary to set up the linear system of equations for the calculation of the intersection of each line of sight with the theoretical jet plane derived from the two jet axis j_1 and j_2 in the engine OS specified by the injector positioning (cf. Equation 8).

$$\left[\mathbf{j}_1, \mathbf{j}_2, \frac{\Phi_n}{|\Phi_n|} \right] \cdot \lambda = {}_{FE}\mathbf{O} - {}_{PI}\mathbf{O}$$

$$\mathbf{j}_1 = \mathbf{R}_{PI\,y}\left(-\alpha_{J_1}\right)\mathbf{R}_{J1\,x}\left(\beta_J\right)\begin{bmatrix} 1 \\ 0 \\ 0 \end{bmatrix},$$

$$\mathbf{j}_2 = \mathbf{R}_{PI\,x}\left(\beta_J\right)\begin{bmatrix} 0 \\ 0 \\ 1 \end{bmatrix} \qquad \text{Eq. (8)}$$

By solving the linear system of equations of the jet contour projections, the contour of the fuel jet is transferred from the 2D camera sensor image into 3D coordinates as shown in Figure 13. This data is used to calculate the liquid penetration length of the two jets.

4.4. Quality Estimation of the Virtual 3D Re-projection

To verify the method of the virtual 3D re-projection method described in Section 4.3, several test images with a black and white checkerboard pattern with four rows and five columns and a square size of 13 mm are taken at three different distances from the first lens. The first distance of 35 mm equals the distance of the focus plane used in the test setup as well as in the engine. The pattern was oriented perpendicular to the optic at random positions to cover the entire field of view. With the information on the distance between the planar pattern and the lens, the distance between the control points can be calculated using the virtual 3D re-projection method.

Figure 14 depicts the standard deviation of the measured pattern square size to the real value of 13 mm in three different distances over all captured images spread across the optic field of view. With a maximum standard deviation at a distance of 50 mm and 80 mm, the optic and the method is capable of a mean re-projection error of 2.1 mm. The error is related to the amount and quality of the calibration images, as well as the detection of the control points in the image. The quality of the detection of the control points in the image relies on the imaging quality of the optic as well as the used detection algorithm. Nevertheless, a mean error of 2.1 mm seems acceptable compared to the dimension of the observable field of view of the bore area with a diameter of 350 mm.

4.5. Image Undistortion

Due to the strong distortion of fisheye optics that enables the 180° field of view the second path of the postprocessing consists of the undistortion of the captured images for better visibility and validation of the experiments. This proceeding is basically only a further projection of the hemispherical field of view of the fisheye image with an array of different

pinhole projections similar to [27, 28]. It results in some discontinuities in the final image, but also offers further insights. Figure 15 depicts the proceeding concept. Using the projection function the undistorted pixel points (i…j) for the piecewise projection in 3D coordinates can be transferred to the distorted image pixels. This creates a corresponding 3D undistorted to distorted pixel transfer map corresponding to the used amount of projections k (k = 1, 2, 3, 4, 5 in Figure 15). A simple 2D interpolation between both maps creates the image parts for the assembly of the undistorted image. The creation of each 3D pixel point is realized by simple orthogonal rotations of the pixel field (i…j) in the distance f. Because of the interpolation, the images become slightly blurry and artifacts can occur. Nevertheless, the undistorted image shows the third injection jet as well as the effect of the undistortion through the straightening of the injection lines as depicted in Figure 15.

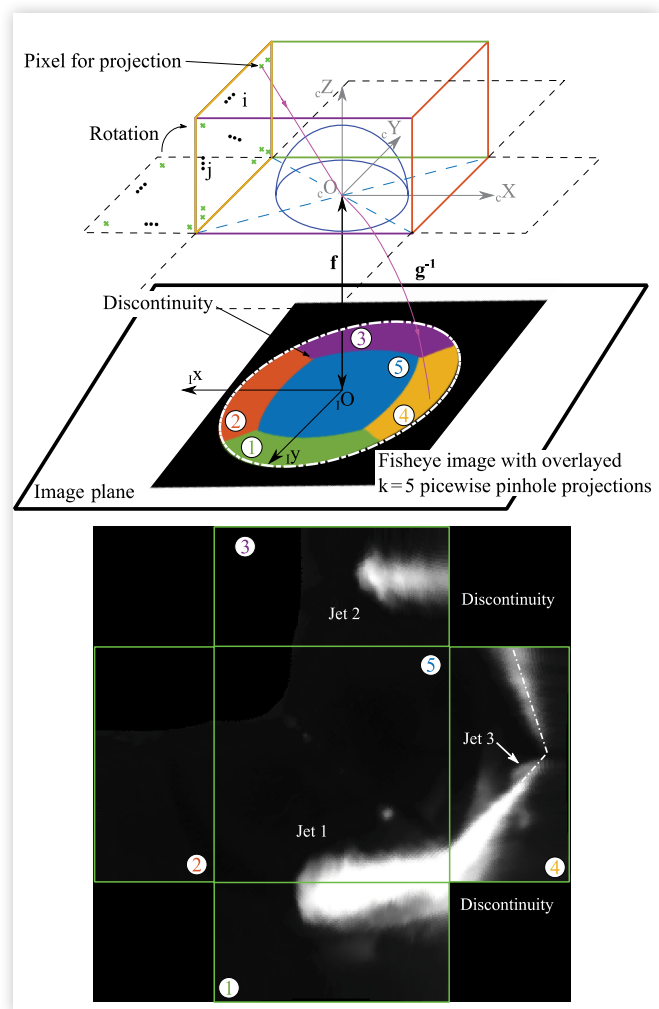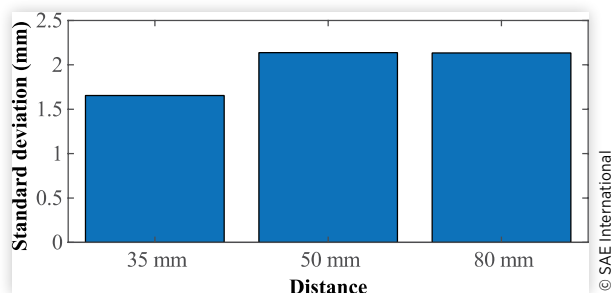**FIGURE 15** Piecewise pinhole projection for undistortion.

© SAE International

FIGURE 14 Standard deviation of virtual 3D test re-projection.

© SAE International

5. Experimental Results

The following presents the results of the conducted Mie-scattering investigations. To determine the potential of OME_{3-5} as a replacement for DMA, two comparisons regarding a mass equivalent amount of OME_{3-5} and DMA as well as an energy equal content of injected OME_{3-5} and DMA are presented. The results focus on the derived liquid penetration length, combustion chamber pressure, and heat release. For dual-fuel combustion, the penetrated volume and concentration distribution of the pilot fuel in the combustion chamber are important measures determining the combustion efficiency and emission (cf. [24]).

5.1. Mass Equivalent Pilot Fuel Injection of OME_{3-5} and DMA

A mass equivalent pilot fuel injection of OME_{3-5} and DMA results in a reduced amount of pilot fuel energy using OME_{3-5}. This results in a deteriorated ignition behavior due to an increased ignition delay (cf. [29]) that leads to a retarded combustion with decreased combustion temperature and a deteriorated thermal combustion efficiency (cf. [30]). OME_{3-5} partially compensates for this effect with its shorter ignition delay due to a higher cetane number compared to diesel fuels (cf. [31, 32]).

Table 5 summarizes the apparent start of combustion (ASOC) as the first recorded and detectable combustion event in the visible spectral range arising from the natural flame chemiluminescence of dual-fuel combustion. The so-derived values show a reasonable trend that with earlier SOE and higher combustion pressure, the ASOC becomes earlier. This is due to a better mixing and fuel preparation especially due to the higher injection pressure resulting in smaller fuel droplets. Further comparing the different fuels, OME_{3-5} shows almost similar ignition delays that fit the aforementioned compensational effect.

Nevertheless, experiments with a mass equivalent amount of pilot fuel can be used to characterize the influence of the different fuel properties on the injection.

Due to deteriorated ignition conditions of DMA arising from the skipped fire engine operation, the latest SOE of

15°CA bFTDC was neglected for the investigations due to unstable and incomplete combustion.

Figure 16 shows the comparison of the injected mass equivalent amount of OME_{3-5} and DMA for a rail pressure of 1200 bar. Figure 17 includes the comparison for 1600 bar rail pressure. Both figures include the AHRR, the combustion chamber pressure, and the mean liquid penetration length of both visible jets derived from the post-processing algorithm detailed in Section 4 as well as the undistorted image series of the injection at 25°CA bFTDC SOE.

In both figures, a deeper penetration length of the DMA jets compared with OME_{3-5} is obvious, and the liquid penetration length of both fuels increases with an increased rail pressure at early SOE and decreases with a later SOE due to higher counter pressure in the combustion chamber. Further increased evaporation at conditions of late SOE due to higher temperature leads to a decrease in the mean liquid penetration depth. Higher rail pressures additionally result in higher injection velocities and thus smaller fuel droplets supporting their evaporation, and lead to a reduction of the liquid penetration depth. Thus, the increase of the rail pressure on the liquid penetration depth especially for late SOE turns out to be low. Similar findings are made in [31].

For both rail pressure levels, DMA shows an increased apparent heat release during precombustion of the pilot fuel visible in the AHRR. This results from deeper penetration resulting in a better mixture preparation of the pilot fuel with the natural gas and air mixture in the combustion chamber. The image series states the deeper penetration as well as a broader spray cone of DMA compared to OME_{3-5}. Both result in better fuel preparation. The determining factor for the increased apparent heat release during precombustion is the higher amount of ignition energy of the mass equivalent DMA compared to OME_{3-5}.

5.2. Energy Equivalent Pilot Fuel Injection for OME_{3-5} and DMA

Using an energy equivalent amount of mass for OME_{3-5} and DMA results in increased energizing times of the solenoid valve injector for OME_{3-5} compared to DMA due to the reduced lower heating value and the different densities ($E_{DMA}/E_{OME} = 1.84$). As the injector has not been optimized for OME_{3-5}, a large spread to gain the appropriate energy equivalent mass for both fuels is needed, resulting in a significantly shorter energizing time for DMA and a longer one for OME_{3-5}. Table 4 summarizes the duration of energizing of the injector for the investigated points in Figures 18 and 19.

Figure 18 shows the comparison of both fuels for a rail pressure of 1200 bar. The mean liquid penetration length depicted is derived from the postprocessing of the captured Mie-scattering images detailed in Section 4 for both visible jets 1 and 2 as well as for the investigated SOE timings.

As a later SOE as 25°CA bFTDC leads to incomplete combustion of the engine operated in skipped fire during

TABLE 5 Apparent start of combustion ASOC.

OME_{3-5}				DMA			
p_{Rail} (bar)	SOE (°CA)	ASOC (°CA)	Δt_{Ign} (ms)	p_{Rail} (bar)	SOE (°CA)	ASOC (°CA)	Δt_{Ign} (ms)
1200	−33	−4	6.4	1200	−30	−4	5.8
1200	−25	−3	4.9	1200	−25	−5	4.4
1200	−15	−2	2.9	1200	−15	—	—
1600	−30	−6	5.3	1600	−30	−6	5.3
1600	−25	−5	4.4	1600	−25	−5	4.4
1600	−15	−1	1.3	1600	−15	—	—

FIGURE 16 Comparison of mass equivalent injected mass for OME and DMA at 1200 bar rail pressure: red = Jet 1, blue = Jet 2, Piecewise pinhole projection according to Figure 15.
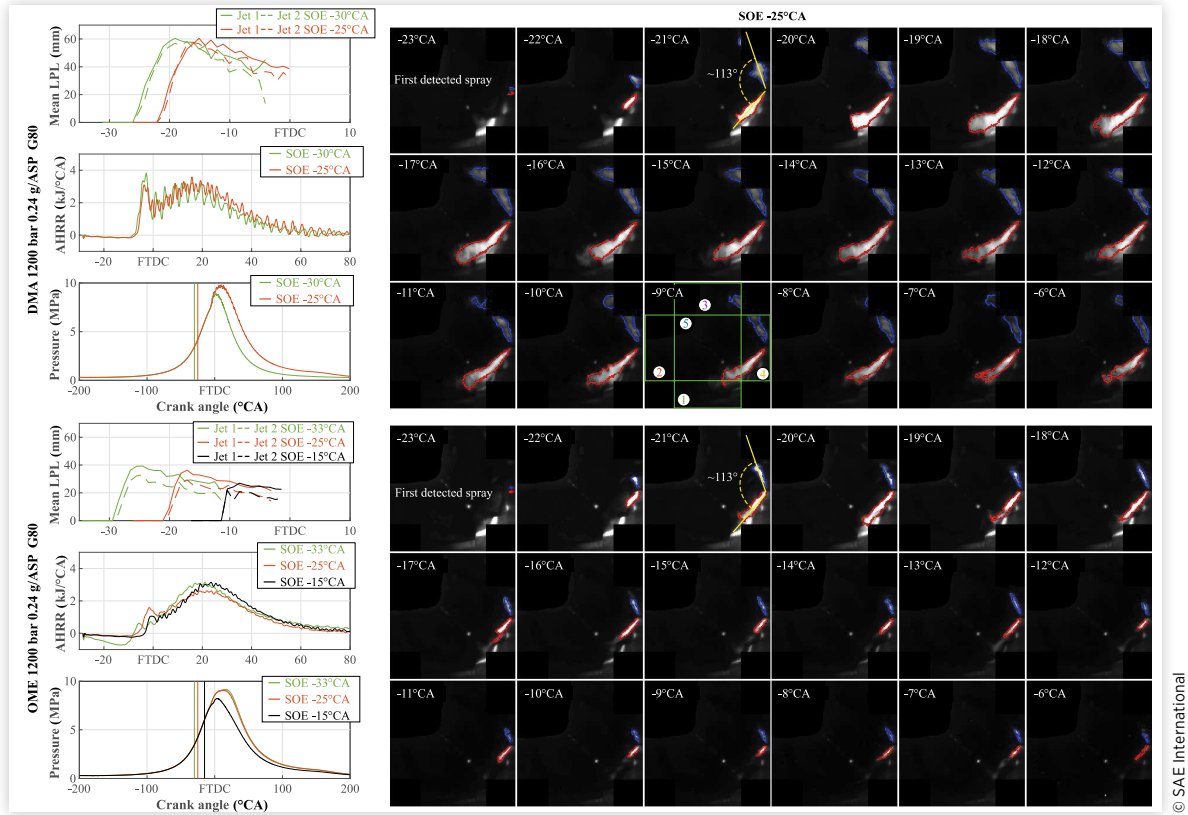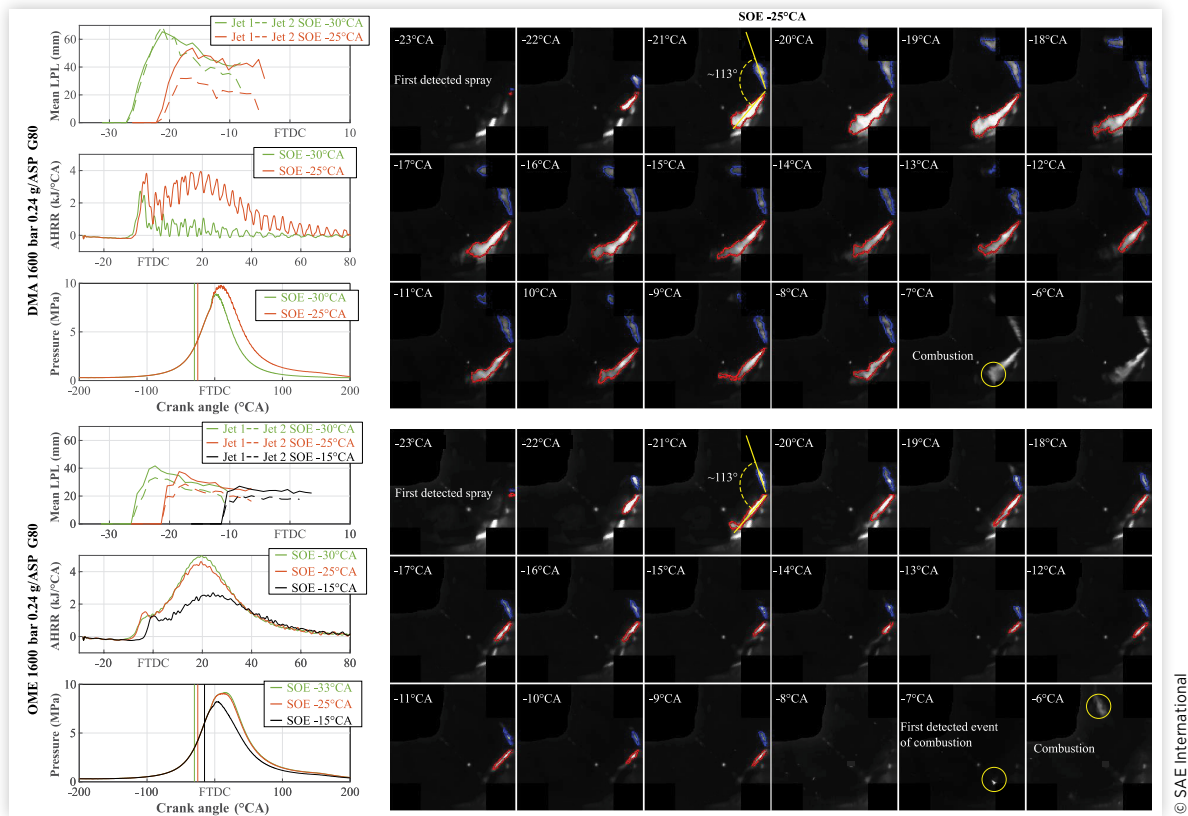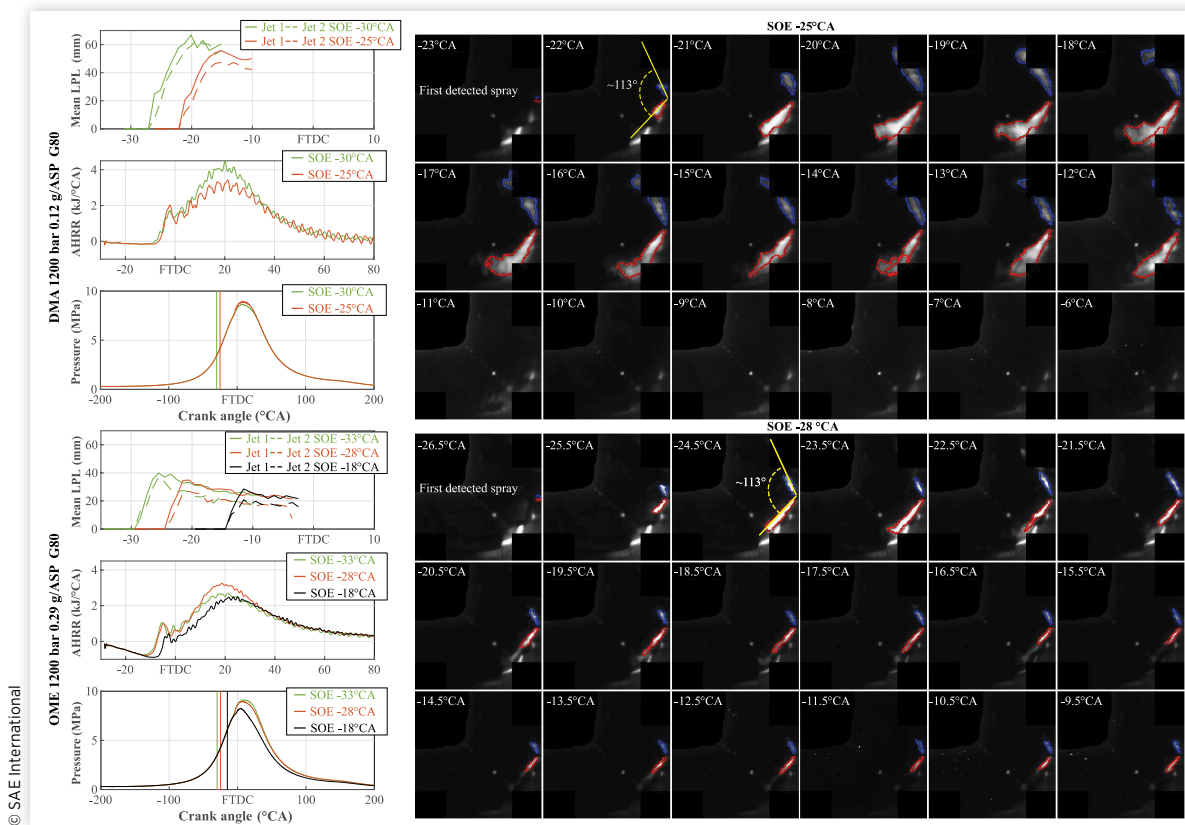

© SAE International

FIGURE 17 Comparison of mass equivalent injected mass for OME and DMA at 1600 bar rail pressure: red = Jet 1, blue = Jet 2.

© SAE International

FIGURE 18 Comparison of energy equivalent injected mass for OME and DMA at 1200 bar rail pressure: red = Jet 1, blue = Jet 2.

FIGURE 19 Comparison of energy equivalent injected mass for OME and DMA at 1600 bar rail pressure: red = Jet 1, blue = Jet 2.

© SAE International

13
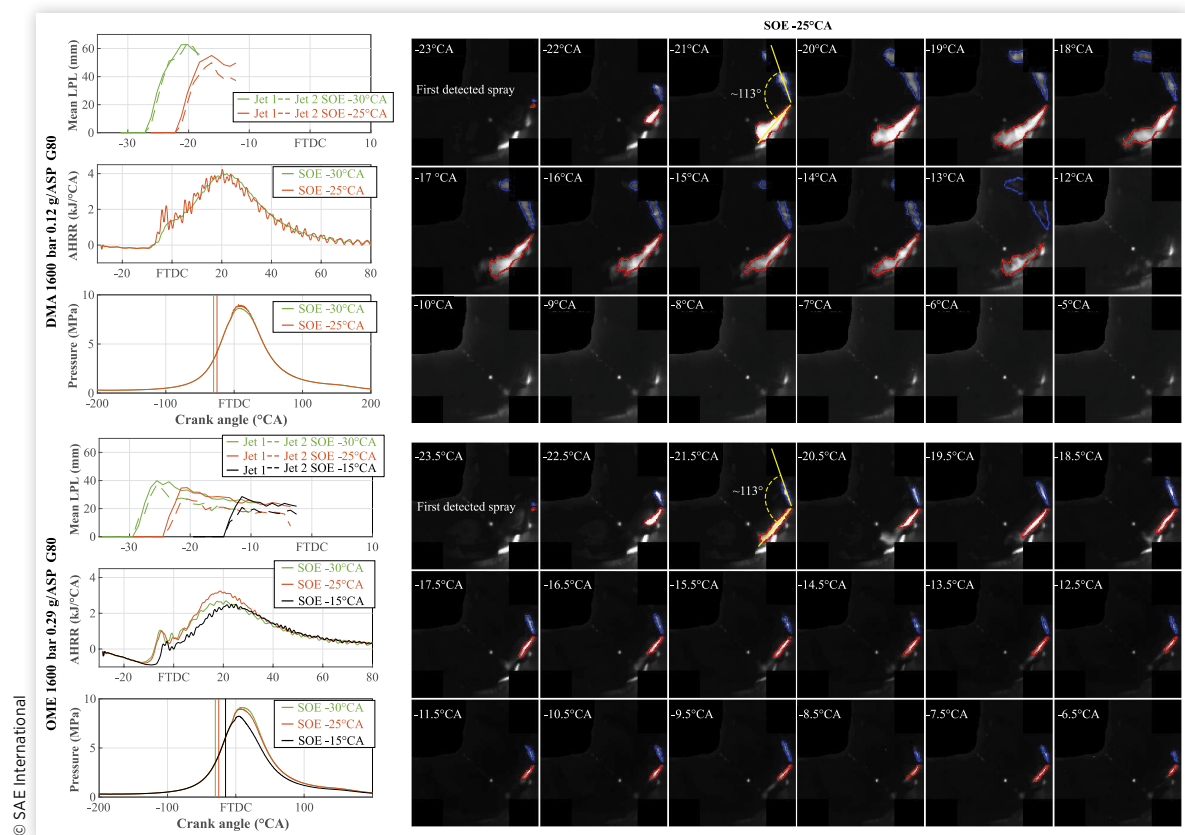
the DMA investigations, these operation points were neglected. The skipped-fire engine operation conditions result in reduced combustion chamber temperature and therefore deteriorated ignition conditions for the DMA. Further, the lower amount of DMA pilot fuel leads to nonoptimal injection conditions and therefore to a deteriorated fuel distribution and preparation. With an SOE of 30°CA bFTDC, the maximum shown AHRR is increased up to 30% due to a deeper penetration (20%) of the fuel into the combustion chamber resulting in greater areas with pilot fuel and an enhanced ignition of the premixed NG and air. The deeper penetration is also possible as, at 30°bFTDC SOE, the reduced combustion chamber pressure results in a lower density of the air-fuel mixture and thus results in less deceleration of the pilot fuel. Further, the earlier injection of the fuel leads to an elongated preparation time for the pilot fuel to mix with the combustion chamber charge. The earlier SOE shows a slightly earlier start of combustion as well as a slightly steeper increase in the AHRR due to better fuel preparation.

A quite similar behavior can be observed for the OME investigations. To prove the advantages of an SOE of ~30°CA bFTDC, the investigated timings are slightly modified with an offset of 3°CA. The injection timing of 28°CA bFTD results in an up to 28% higher maximum of the AHRR as well as the highest AHRR increase rate. The peak pressure of the pilot fuel combustion until the main combustion starts is similar for the two earlier timings of 33°CA and 28°CA bFTDC. The earliest timing shows a slightly higher peak of the pilot fuel combustion due to a deeper penetration of 14% and therefore intensified combustion of the pilot fuel. Nevertheless, as both early timings result in similar combustion of the pilot fuel, this hints at a well mixing of pilot fuel and cylinder charge, and a possible optimum of the SOE is assumed between both values.

At the latest injection of the tests with an SOE of 18°CA bFTDC, the penetration length is retarded due to the highest combustion chamber pressure and charge density at the start of injection. Due to a reduced time for pilot fuel mixing the pre-combustion peak is less, but the heat release is faster. Due to the late SOE, the main combustion is retarded. Further, comparing the combustion chamber pressure, an early SOE leads to a less pronounced pressure increase after the pre-combustion that can be explained by the aforementioned behavior.

Comparing the AHRR of OME_{3-5} and DMA a lower pre-peak is observable for OME_{3-5} than for DMA. Further, the maximum AHRR is also less for OME_{3-5} than for DMA (25%).

This can be explained by the different injection behaviors depicted in the image series of Figure 18. OME_{3-5} offers a more dense and compact spray as well as a shorter penetration length. This is mostly due to the increased amount of mass which is needed to gain the same amount of energy for both fuels.

Compared to DMA where the spray breakup seems wider, the smaller amount of mass increases the velocity of the fuel and therefore results in a 63% deeper penetration. In the detection of both fuels, a difference of ~2°CA between the SOE and the detection of the first visible spray occurs resulting in ~0.4 ms at 750 rpm engine speed, which can be explained by the inertia effects of the electronic actuation and needle lift of the injector. Experiments to evaluate this effect for OME_{3-5} and diesel are carried out in [32], summarizing a similar range for the delay using similar injectors.

Figure 19 shows the comparison of both fuels at a rail pressure of 1600 bar. Especially for the DMA, the AHRRs of both SOEs are practically equal with only a slight decrease in maximum value. Further, the SOE of 30°CA bFTDC of the DMA is more convenient resulting in a more stable combustion and better ignition. The presented penetration length is a bit reduced compared to the operating condition of the injector at 1200 bar. The reason for this is the used injector activation duration that had to be decreased to guarantee the same amount of mass for both settings. The additional decrease causes the injector to work close to its minimum possible energizing time resulting in a deteriorated injection. The AHRR derived from the combustion of OME_{3-5} shows the same behavior as for the operation at 1200 bar rail pressure. Here the SOE of 15°CA bFTDC results in less intense combustion because of a delay in the AHRR and less amount of heat release.

Comparing the combustion of DMA to OME_{3-5}, the differences diminish distinctly. The peak of the pre-combustion is almost equal and the maximum value differs only by 2.5%. This is due to a higher penetration length (10%) of the OME_{3-5} compared with the values using a rail pressure of 1200 bar, as well as the slightly deteriorated injection of DMA. Nevertheless, the OME_{3-5} spray is more compact and dense compared to the DMA jet.

Comparing the liquid penetration length of both fuels and at both rail pressure levels, it is obvious that the length of the OME_{3-5} jets is 35% up to 50% less depending on the SOE. Further, the liquid penetration length shows a reasonable behavior concerning the length increase with earlier SOEs due to lower counterpressure in the combustion chamber and an increase in injection pressure due to an increased momentum.

Similar to the findings of [32], the delay of the injection is slightly reduced with increasing pressure up to ~0.3 ms.

6. Summary and Discussion

The publication presents a new approach for optical investigations of large-bore engines and the development of a complex imaging post-processing procedure with algorithms to automatically undistort the recorded picture series and objectively evaluate the optical test results.

6.1. Discussion of the Image-Processing Algorithm

The image-processing algorithm relies on two main assumptions which cause uncertainties in the derived values.

The first is the fisheye imaging model that was chosen as the model developed by Kannala and Brandt [11] which necessitates calibration of the extrinsic and intrinsic parameters. Dependent on the quality of this calibration, the derived image post-processing results show a certain deviation from the real conditions. As validated in Section 4.1, the accuracy of the calibration shows good results for the re-projection error in the subpixel range. For the calibrated optic, a deviation of 2.1 mm was estimated for the processed images derived from tests with a simple test procedure.

Both the calibration and the test of sufficiency were carried out in a test rig offering the same installation conditions as in the engine, but not the appropriate temperature conditions during a skipped-fire engine operation. The engine operating temperature only affects the back-focus of the fisheye optic. The further used Sigma macro objective in front of the camera is mounted outside of the engine just like the camera itself and operates under room temperature, same as that used for recording the calibration images. Due to the available depth of focus of the Sigma macro objective, the small deviation of the back-focus of the fisheye optic can be compensated and therefore is negligible. Hence, the provided detection accuracy of 2.1 mm in a large-bore engine with a bore diameter of 350 mm seems sufficient (0.57%).

The second is necessary because of the missing depth information using the fisheye optic. For deriving the depth information, two aligned cameras are needed to gather two different images of the scene for simultaneous localization and stereo processing. Here, as only one camera is used, the assumption of the two jets being oriented within a plane is used to substitute the need for the second camera. This assumption leads to only a projection of the real jet behavior to this plane and is founded on the injector orientations defined by the assembly design. Nevertheless, a validation of CFD results using the same projection method seems a possible way to further use the results.

Under these preconditions, the different injection behavior of mass equivalent and energy equivalent amounts of pilot fuel mass into a dual-fuel engine under skipped-fire operation conditions is presented.

6.2. Discussion of the Results for Mass Equivalency

Honecker et al. [31] investigated the liquid penetration length of OME$_{3-5}$ using Mie scattering in a constant-volume high-pressure chamber and derived a liquid penetration length under 527°C and 50 bar counterpressure of ~30 mm for diesel and ~22 mm for OME$_{3-5}$ at 1000 bar rail pressure. The investigations presented here derive an almost doubled liquid penetration length of both fuels OME$_{3-5}$ and DMA at elevated injection rail pressure as well as a different volume under almost similar counterpressure and temperature conditions. Nevertheless, the findings of [31] can be used to compare the basic behavior. Further [31] also observes the same diminishing influence of rail pressure increase on liquid penetration depth as investigated here due to increased evaporation for OME$_{3-5}$.

Similar to the findings of [19, 31, 33] are the observed decreased ignition delays of OME$_{3-5}$. Those are also experienced here by compensating for the decreased amount of ignition energy provided by a mass equal amount of OME$_{3-5}$ compared to DMA. Here the liquid penetration length of DMA reaches a maximum of 69 mm under 1600 bar rail pressure, whereas the maximum of OME$_{3-5}$ reaches 42 mm. This results in an increased liquid penetration length of DMA compared to OME$_{3-5}$ with a difference of ~39%. Due to the image series, a more compact and dense spray of OME$_{3-5}$ compared to DMA is visible. This is due to the higher density and lower viscosity of OME$_{3-5}$, which should be considered if OME$_{3-5}$ is used to decarbonize dual-fuel engines. Modifications of the injector could improve the pilot fuel preparation. The derived characteristic of the liquid penetration length seems reasonable as the influence of the SOE, rail pressure, and fuel properties are in good accordance.

6.3. Discussion of the Results for Energy Equivalency

To gain the same energy equivalent amount of pilot fuel for both DMA and OME, the amount of OME$_{3-5}$ has to be increased by a factor of 1.84. Increasing the amount of pilot fuel results in an increased particle mass, especially for the diesel pilot fuel as reported in [29]. This is compensated using OME$_{3-5}$ due to its oxygen content and therefore less critical. Nevertheless, using the same energy equivalent amount of both fuels results in a large discrepancy of energizing times of the injector with a relative difference of 56% from the minimum value to the maximum. Especially for DMA, this results in a nonoptimal operation of the injector close to its minimum energizing time and leads to deteriorated spray formation compared to the mass equivalent amount of OME$_{3-5}$. Therefore, the liquid penetration length of DMA is decreased compared to its mass equivalent operation. For the OME$_{3-5}$ the liquid penetration length is almost similar to its operation with a mass equivalent amount due to an almost similar amount of fuel and injector energizing time. Comparing both fuels, OME$_{3-5}$ shows a shorter liquid penetration length of about 35% at the maximum arising length. This contributes to an improved combustion behavior resulting in faster combustion using DMA as pilot fuel. Nevertheless, both fuels almost provide similar combustion behaviors. Due to this, the investigations not only prove the new optical investigation

approach but also supports the possible replacement of the fossil pilot fuel with a regenerative one.

For both investigations comparing a mass and an energy equivalent amount of pilot fuel, the derived injection parameters contain uncertainties as only a scale-up approach for the usage of OME_{3-5} within the same injector was used. All the effects which are already investigated in, e.g., [22, 32], lead to different injection behavior. They necessitate an optimization of the injection parameters and injector geometries that was so far neglected in the herein-presented test series but should be taken into account if OME_{3-5} replaces fossil fuels as a pilot energy carrier in dual-fuel engines.

7. Conclusion and Outlook

A new approach for in situ optical engine measurements with a focus on image postprocessing is presented for regenerative pilot fuel to conventional comparisons in a MAN35/44DF large-bore combustion engine using a fisheye optical system as optical access. Spatial projection and image detection algorithms are applied to derive the liquid penetration length of DMA and OME_{3-5} pilot fuel injection. The effort to process images recorded through a fisheye optic is much higher and more complex than for normal optics due to their high spatial distortion. Nevertheless, using such an optic increases the field of view significantly compared to standard optics and thus improves the effectiveness of optical investigations. It also simplifies the optical access design as stated in detail in [7]. The new optical access with the fisheye optic mounted even at the cylinder head flame deck allows for the observation of the injection jets emanating from the injector. The new approach for virtual 3D reconstruction of the distorted images shows a sufficient accuracy of 2.1 mm that could also be used for 3D-CFD simulation verification if the same re-projection method is used for those.

The herein-derived optical data processed with the new approach are in good accordance with the physically valid behavior and literature investigations. For more detailed future investigations, the light efficiency of the optic could be improved with a relay optic as it was done in [34] to decrease the exposure time and increase the temporal resolution. Further, an in-cylinder calibration method could be developed to calibrate the optic directly in the engine and improve the projection accuracy of the image postprocessing further.

Author Contributions

The optical setup (development and design), the development and implementation of the preprocessing and postprocessing and interpretation of the optical data, and the complete preparation of the images and writing belong to Stephan Karmann.

Stefan Weber supported the experiments at the testing rig at MAN Energy Solutions. Wolfgang Stürzl supported the development of the optical preprocessing with his expertise and reviews. The remaining co-authors supported the work with their reviews.

Acknowledgments

Contact Information

Stephan Karmann
stephan.karmann@tum.de

Nomenclature

aFTDC - After firing top dead center

AHRR - Apparent heat release rate

ASOC - Apparent start of combustion

bFTDC - Before firing top dead center

COS - Coordinate system

DF - Dual fuel

DMA - Marine diesel fuel

EC - Engine center

FE - Fisheye

HPDF - High-pressure dual fuel

HSC - High-speed camera

LHV - Lower heating value

LPL - Liquid penetration length

NG - Natural gas

OME - Oxymethylene ether

PI - Pilot injector

ROI - Region of interest

SOE - Start of energizing

References

1. Belgiorno, G., Di Blasio, G., and Beatrice, C., "Parametric Study and Optimization of the Main Engine Calibration Parameters and Compression Ratio of a Methane-Diesel Dual Fuel Engine," *Fuel* 222 (2018): 821-840, doi:10.1016/j.fuel.2018.02.038.

2. Fraioli, V., Beatrice, C., Di Blasio, G., Belgiorno, G. et al., "Multidimensional Simulations of Combustion in Methane-Diesel Dual-Fuel Light-Duty Engines," SAE Technical Paper 2017-01-0568, 2017, https://doi.org/10.4271/2017-01-0568.

3. Gleis, S., Frankl, S., Prager, M., and Wachtmeister, G., "Optical Analysis of the Combustion of Potential Future e-Fuels with a High Pressure Dual Fuel Injection System," in *14. Internationales AVL Powertrain Diagnostik Symposium*, Baden-Baden, Germany, 2020.

4. Gleis, S., Frankl, S., Waligorski, D., Prager, M. et al.,
    "Investigation of the High-Pressure-Dual-Fuel (HPDF)
    Combustion Process of Natural Gas on a Fully Optically
    Accessible Research Engine," in *2019 JSAE/SAE Powertrains,
    Fuels and Lubricants International Meeting*, Kyoto,
    Japan, 2019.

5. Bowditch, F., "A New Tool for Combustion Research A
    Quartz Piston Engine," SAE Technical Paper 610002, 1961,
    https://doi.org/10.4271/610002.

6. Frankl, S., Gleis, S., and Wachtmeister, G., "Interpretation of
    Ignition and Combustion in a Full-Optical High-Pressure-
    Dual-Fuel (HPDF) Engine Using 3D-CFD Methods," in
    *CIMAC CONGRESS 19, 29th CIMAC World Congress on
    Combustion Engine, Meeting the Future of Combustion
    Engines*, Vancouver, BC, Canda, June 10-14, 2019.

7. Karmann, S., Prager, M., and Wachtmeister, G., "Conceptual
    Investigations on Full Optical Accessibility to Large-Bore
    Medium-Speed Engines," *SAE Int. J. Engines* 12, no. 3 (2019):
    291-308, doi:10.4271/03-12-03-0020.

8. Karmann, S., Friedrich, C., Prager, M., and Wachtmeister,
    G., "Realization of a Fully Optically Accessible Medium
    Speed Large Bore Engine Using a Fisheye Optic," in *ASME
    2020 Power Conference*, Virtual, Online, August 4, 2020.

9. Ying, X., Hu, Z., and Zha, H., "Fisheye Lenses Calibration
    Using Straight-Line Spherical Perspective Projection
    Constraint," in: Narayanan, P.J., Nayar, S.K., and Shum, H.Y.
    (eds), *Computer Vision—ACCV 2006*, vol. 3852 (Berlin/
    Heidelberg: Springer, 2006), 61-70, doi:10.1007/11612704_7.

10. Hughes, C., Glavin, M., Jones, E., and Denny, P., "Review of
    Geometric Distortion Compensation in Fish-Eye Cameras,"
    in *IET Irish Signals and Systems Conference (ISSC 2008)*,
    Galway, 2008, 162-167, doi:10.1049/cp:20080656.

11. Kannala, J. and Brandt, S.S., "A Generic Camera Model and
    Calibration Method for Conventional, Wide-Angle, and
    Fish-Eye Lenses," *IEEE Transactions on Pattern Analysis and
    Machine Intelligence* 28, no. 8 (2006): 1335-1340, doi:10.1109/
    TPAMI.2006.153.

12. Puig, L., Bermúdez, J., Sturm, P., and Guerrero, J.J.,
    "Calibration of Omnidirectional Cameras in Practice: A
    Comparison of Methods," *Computer Vision and Image
    Understanding* 116, no. 1 (2012): 120-137, doi:10.1016/j.
    cviu.2011.08.003.

13. Kanatani, K., "Calibration of Ultrawide Fisheye Lens
    Cameras by Eigenvalue Minimization," *IEEE Transactions
    on Pattern Analysis and Machine Intelligence* 35, no. 4 (2013):
    813-822, doi:10.1109/TPAMI.2012.146.

14. Scaramuzza, D., Martinelli, A., and Siegwart, R., "A Flexible
    Technique for Accurate Omnidirectional Camera
    Calibration and Structure from Motion," in *Computer Vision
    Systems, 2006 ICVS'06. IEEE International Conference on*,
    New York, 2006, 45.

15. Micusík, B. and Pajdla, T., "Structure from Motion with
    Wide Circular Field of View Cameras," *IEEE Transactions on
    Pattern Analysis and Machine Intelligence* 28, no. 7 (2006):
    1135-1149, doi:10.1109/TPAMI.2006.151.

16. Karmann, S., Kunkel, C., Prager, M., and Wachtmeister, G.,
    "A New Optical Access for Medium Speed Large Bore

    Marine Engines under Full-Load Operating Conditions,"
    SAE Int. J. Engines 14, no. 6 (2021): 867-883, doi:10.4271/03-
    14-06-0052.

17. Pélerin, D., Gaukel, K., Härtl, M., and Wachtmeister, G.,
    "Nitrogen Oxide Reduction Potentials Using Dimethyl Ether
    and Oxymethylene Ether in a Heavy-Duty Diesel Engine,"
    SAE Technical Paper 2020-01-5084, 2020, https://doi.
    org/10.4271/2020-01-5084.

18. Held, M., Tönges, Y., Pélerin, D., Härtl, M. et al., "On the
    Energetic Efficiency of Producing Polyoxymethylene
    Dimethyl Ethers from CO_2 Using Electrical Energy," *Energy
    Environ. Sci.* 12, no. 3 (2019): 1019-1034, doi:10.1039/
    C8EE02849D.

19. Pélerin, D., Gaukel, K., Härtl, M., Jacob, E. et al., "Potentials
    to Simplify the Engine System Using the Alternative Diesel
    Fuels Oxymethylene Ether OME1 and OME3−6 on a Heavy-
    Duty Engine," *Fuel* 259 (2020): 116231, doi:10.1016/j.
    fuel.2019.116231.

20. Pöllmann, S., Härtl, M., and Wachtmeister, G., "Injection
    Process of the Synthetic Fuel Oxymethylene Ether: Optical
    Analysis in a Heavy-Duty Engine," SAE Technical Paper
    2020-01-2144, 2020, https://doi.org/10.4271/2020-01-2144.

21. Dworschak, P., Härtl, M., and Wachtmeister, G.,
    "Oxymethylene Ethers: Quantifying the Effect of Fuel Chain
    Length and Water Emulsification on Emissions and
    Combustion in a Heavy-Duty Diesel Engine via Linear
    Regression Analysis," *SAE Int. J. Fuels Lubr.* 14, no. 3 (2021):
    141-160, doi:10.4271/04-14-03-0009.

22. Peter, A., Siewert, B., Riess, S., Strauss, L. et al., "Mixture
    Formation Analysis of Polyoxymethylenether Injection,"
    Atomization and Sprays 30, no. 11 (2020): 843-859,
    doi:10.1615/AtomizSpr.2020035250.

23. Bargende, M., "Ein Gleichungsansatz zur Berechnung der
    instationären Wandwärmeverluste im Hochdruckteil von
    Ottomotoren," Dissertation, Technische Universität
    Darmstadt, Darmstadt, 1990.

24. Weber, S., Stegmann, R., Prager, M., and Wachtmeister, G.,
    "The Effect of Inlet Valve Timing and Engine Speed on Dual
    Fuel NG-Diesel Combustion in a Large Bore Engine," *SAE Int.
    J. Engines* 11, no. 2 (2018): 229-246, doi:10.4271/03-11-02-0015.

25. Scaramuzza, D. and Siegwart, R., "A Practical Toolbox for
    Calibrating Omnidirectional Cameras," 2007, I-Tech
    Education and Publishing, Austria, doi:10.3929/
    ethz-a-005657929.

26. Strobl, K.H., Sepp, W., Fuchs, S., Paredes, C. et al., "DLR
    CalDe and DLR CalLab," Oberpfaffenhofen, Germany,
    accessed 01 August 2022, http://www.robotic.dlr.de/callab/.

27. Caruso, D., Engel, J., and Cremers, D., "Large-Scale Direct
    SLAM for Omnidirectional Cameras," in *2015 IEEE/RSJ
    International Conference on Intelligent Robots and Systems
    (IROS)*, Hamburg, Germany, 2015, 141-148, doi:10.1109/
    IROS.2015.7353366.

28. Wang, Y. et al., "CubemapSLAM: A Piecewise-Pinhole
    Monocular Fisheye SLAM System," In: Asian Conference on
    Computer Vision. Springer, Cham, 2018, 11366 (2019): 34-49,
    doi:10.1007/978-3-030-20876-9_3.

29. Zhou, L. et al., "Effect of the Diesel Injection Timing and the Pilot Quantity on the Combustion Characteristics and the Fine-Particle Emissions in a Micro-Diesel Pilot-Ignited Natural-Gas Engine," *Proceedings of the Institution of Mechanical Engineers, Part D: Journal of Automobile Engineering* 227, no. 8 (2013): 1142-1152, doi:10.1177/0954407013480452.

30. Ryu, K., "Effects of Pilot Injection Timing on the Combustion and Emissions Characteristics in a Diesel Engine Using Biodiesel–CNG Dual Fuel," *Applied Energy* 111 (2013): 721-730, doi:10.1016/j.apenergy.2013.05.046.

31. Honecker, C., Neumann, M., Glueck, S., Schoenen, M. et al., "Optical Spray Investigations on OME3-5 in a Constant Volume High Pressure Chamber," SAE Technical Paper 2019-24-0234, 2019, https://doi.org/10.4271/2019-24-0234.

32. Gelner, A., Höß, R., Zepf, A., Härtl, M. et al., "Engine Operation Strategies for the Alternative Diesel Fuel Oxymethylene Ether (OME): Evaluation Based on Injection Rate Analyzer and 0D-/1D-Simulation," SAE Technical Paper 2021-01-1190, 2021, https://doi.org/10.4271/2021-01-1190.

33. Barro, C., Parravicini, M., and Boulouchos, K., "Neat Polyoxymethylene Dimethyl Ether in a Diesel Engine; Part 1: Detailed Combustion Analysis," *Fuel* 256 (2019): 115892, doi:10.1016/j.fuel.2019.115892.

34. Karmann, S., Röhrle, H., Klier, B., Prager, M. et al., "Design of an Endoscopic Fully Optically Accessible High-Speed Large-Bore Engine," *SAE Int. J. Engines* 15, no. 6 (2022): 773-789, doi:10.4271/03-15-06-0042.

B.3 Veröffentlichung 3 im Original

Karmann, S., Röhrle, H., Klier, B., Prager, M. et al., "Design of an Endoscopic Fully Optically Accessible High-Speed Large-Bore Engine," SAE Int. J. Engines 15(6):2022,
https://doi.org/10.4271/03-15-06-0042

B.3 Veröffentlichung 3 im Original

![CCC] **Marketplace**

This is a License Agreement between Stephan Bernhard Karmann ("User") and Copyright Clearance Center, Inc. ("CCC") on behalf of the Rightsholder identified in the order details below. The license consists of the order details, the Marketplace Permissions General Terms and Conditions below, and any Rightsholder Terms and Conditions which are included below.

All payments must be made in full to CCC in accordance with the Marketplace Permissions General Terms and Conditions below.

Order Date	15-Apr-2023	Type of Use	Republish in a thesis/dissertation
Order License ID	1345357-1		
ISSN	1946-3944	Publisher	SAE International
		Portion	Chapter/article

LICENSED CONTENT

Publication Title	SAE International journal of engines	Publication Type	Journal
		Start Page	773
Article Title	Design of an Endoscopic Fully Optically Accessible High-Speed Large-Bore Engine	End Page	789
		Issue	6
		Volume	15
Author/Editor	Society of Automotive Engineers.	URL	http://www.sae.org
Date	01/01/2009		
Language	English		
Country	United States of America		
Rightsholder	SAE International		

REQUEST DETAILS

Portion Type	Chapter/article	Rights Requested	Main product
Page Range(s)	All	Distribution	Worldwide
Total Number of Pages	17	Translation	Original language of publication
Format (select all that apply)	Print, Electronic	Copies for the Disabled?	No
Who Will Republish the Content?	Academic institution	Minor Editing Privileges?	No
Duration of Use	Life of current edition	Incidental Promotional Use?	No
Lifetime Unit Quantity	Up to 499	Currency	EUR

NEW WORK DETAILS

Title	Entwicklung eines kompakten volloptischen Zugangs für Großmotoren und Anwendung für die Verbrennungsdiagnostik erneuerbarer Kraftstoffe	Institution Name	Technical University of Munich
		Expected Presentation Date	2023-10-31
Instructor Name	Prof. i.R. Dr.-Ing. Georg Wachtmeister		

ADDITIONAL DETAILS

Order Reference Number	N/A

The Requesting Person/Organization to Appear on the License	Stephan Bernhard Karmann		

REQUESTED CONTENT DETAILS

Title, Description or Numeric Reference of the Portion(s)	Design of an Endoscopic Fully Optically Accessible Large-Bore Engine	Title of the Article/Chapter the Portion Is From	Design of an Endoscopic Fully Optically Accessible High-Speed Large-Bore Engine
Editor of Portion(s)	Karmann, Stephan Bernhard; R?hrle, Hannes; Klier, Bernhard; Prager, Maximilian; Wachtmeister, Georg	Author of Portion(s)	Karmann, Stephan Bernhard; R?hrle, Hannes; Klier, Bernhard; Prager, Maximilian; Wachtmeister, Georg
Volume of Serial or Monograph	15		
		Issue, if Republishing an Article From a Serial	6
Page or Page Range of Portion	773-789		
		Publication Date of Portion	2022-02-01

Marketplace Permissions General Terms and Conditions

The following terms and conditions ("General Terms"), together with any applicable Publisher Terms and Conditions, govern User's use of Works pursuant to the Licenses granted by Copyright Clearance Center, Inc. ("CCC") on behalf of the applicable Rightsholders of such Works through CCC's applicable Marketplace transactional licensing services (each, a "Service").

1) Definitions. For purposes of these General Terms, the following definitions apply:

"License" is the licensed use the User obtains via the Marketplace platform in a particular licensing transaction, as set forth in the Order Confirmation.

"Order Confirmation" is the confirmation CCC provides to the User at the conclusion of each Marketplace transaction. "Order Confirmation Terms" are additional terms set forth on specific Order Confirmations not set forth in the General Terms that can include terms applicable to a particular CCC transactional licensing service and/or any Rightsholder-specific terms.

"Rightsholder(s)" are the holders of copyright rights in the Works for which a User obtains licenses via the Marketplace platform, which are displayed on specific Order Confirmations.

"Terms" means the terms and conditions set forth in these General Terms and any additional Order Confirmation Terms collectively.

"User" or "you" is the person or entity making the use granted under the relevant License. Where the person accepting the Terms on behalf of a User is a freelancer or other third party who the User authorized to accept the General Terms on the User's behalf, such person shall be deemed jointly a User for purposes of such Terms.

"Work(s)" are the copyright protected works described in relevant Order Confirmations.

2) Description of Service. CCC's Marketplace enables Users to obtain Licenses to use one or more Works in accordance with all relevant Terms. CCC grants Licenses as an agent on behalf of the copyright rightsholder identified in the relevant Order Confirmation.

3) Applicability of Terms. The Terms govern User's use of Works in connection with the relevant License. In the event of any conflict between General Terms and Order Confirmation Terms, the latter shall govern. User acknowledges that Rightsholders have complete discretion whether to grant any permission, and whether to place any limitations on any grant, and that CCC has no right to supersede or to modify any such discretionary act by a Rightsholder.

4) Representations; Acceptance. By using the Service, User represents and warrants that User has been duly authorized by the User to accept, and hereby does accept, all Terms.

5) Scope of License; Limitations and Obligations. All Works and all rights therein, including copyright rights, remain the sole and exclusive property of the Rightsholder. The License provides only those rights expressly set forth in the terms and conveys no other rights in any Works

6) General Payment Terms. User may pay at time of checkout by credit card or choose to be invoiced. If the User chooses

to be invoiced, the User shall: (i) remit payments in the manner identified on specific invoices, (ii) unless otherwise specifically stated in an Order Confirmation or separate written agreement, Users shall remit payments upon receipt of the relevant invoice from CCC, either by delivery or notification of availability of the invoice via the Marketplace platform, and (iii) if the User does not pay the invoice within 30 days of receipt, the User may incur a service charge of 1.5% per month or the maximum rate allowed by applicable law, whichever is less. While User may exercise the rights in the License immediately upon receiving the Order Confirmation, the License is automatically revoked and is null and void, as if it had never been issued, if CCC does not receive complete payment on a timely basis.

7) General Limits on Use. Unless otherwise provided in the Order Confirmation, any grant of rights to User (i) involves only the rights set forth in the Terms and does not include subsequent or additional uses, (ii) is non-exclusive and non-transferable, and (iii) is subject to any and all limitations and restrictions (such as, but not limited to, limitations on duration of use or circulation) included in the Terms. Upon completion of the licensed use as set forth in the Order Confirmation, User shall either secure a new permission for further use of the Work(s) or immediately cease any new use of the Work(s) and shall render inaccessible (such as by deleting or by removing or severing links or other locators) any further copies of the Work. User may only make alterations to the Work if and as expressly set forth in the Order Confirmation. No Work may be used in any way that is unlawful, including without limitation if such use would violate applicable sanctions laws or regulations, would be defamatory, violate the rights of third parties (including such third parties' rights of copyright, privacy, publicity, or other tangible or intangible property), or is otherwise illegal, sexually explicit, or obscene. In addition, User may not conjoin a Work with any other material that may result in damage to the reputation of the Rightsholder. Any unlawful use will render any licenses hereunder null and void. User agrees to inform CCC if it becomes aware of any infringement of any rights in a Work and to cooperate with any reasonable request of CCC or the Rightsholder in connection therewith.

8) Third Party Materials. In the event that the material for which a License is sought includes third party materials (such as photographs, illustrations, graphs, inserts and similar materials) that are identified in such material as having been used by permission (or a similar indicator), User is responsible for identifying, and seeking separate licenses (under this Service, if available, or otherwise) for any of such third party materials; without a separate license, User may not use such third party materials via the License.

9) Copyright Notice. Use of proper copyright notice for a Work is required as a condition of any License granted under the Service. Unless otherwise provided in the Order Confirmation, a proper copyright notice will read substantially as follows: "Used with permission of [Rightsholder's name], from [Work's title, author, volume, edition number and year of copyright]; permission conveyed through Copyright Clearance Center, Inc." Such notice must be provided in a reasonably legible font size and must be placed either on a cover page or in another location that any person, upon gaining access to the material which is the subject of a permission, shall see, or in the case of republication Licenses, immediately adjacent to the Work as used (for example, as part of a by-line or footnote) or in the place where substantially all other credits or notices for the new work containing the republished Work are located. Failure to include the required notice results in loss to the Rightsholder and CCC, and the User shall be liable to pay liquidated damages for each such failure equal to twice the use fee specified in the Order Confirmation, in addition to the use fee itself and any other fees and charges specified.

10) Indemnity. User hereby indemnifies and agrees to defend the Rightsholder and CCC, and their respective employees and directors, against all claims, liability, damages, costs, and expenses, including legal fees and expenses, arising out of any use of a Work beyond the scope of the rights granted herein and in the Order Confirmation, or any use of a Work which has been altered in any unauthorized way by User, including claims of defamation or infringement of rights of copyright, publicity, privacy, or other tangible or intangible property.

11) Limitation of Liability. UNDER NO CIRCUMSTANCES WILL CCC OR THE RIGHTSHOLDER BE LIABLE FOR ANY DIRECT, INDIRECT, CONSEQUENTIAL, OR INCIDENTAL DAMAGES (INCLUDING WITHOUT LIMITATION DAMAGES FOR LOSS OF BUSINESS PROFITS OR INFORMATION, OR FOR BUSINESS INTERRUPTION) ARISING OUT OF THE USE OR INABILITY TO USE A WORK, EVEN IF ONE OR BOTH OF THEM HAS BEEN ADVISED OF THE POSSIBILITY OF SUCH DAMAGES. In any event, the total liability of the Rightsholder and CCC (including their respective employees and directors) shall not exceed the total amount actually paid by User for the relevant License. User assumes full liability for the actions and omissions of its principals, employees, agents, affiliates, successors, and assigns.

12) Limited Warranties. THE WORK(S) AND RIGHT(S) ARE PROVIDED "AS IS." CCC HAS THE RIGHT TO GRANT TO USER THE RIGHTS GRANTED IN THE ORDER CONFIRMATION DOCUMENT. CCC AND THE RIGHTSHOLDER DISCLAIM ALL OTHER WARRANTIES RELATING TO THE WORK(S) AND RIGHT(S), EITHER EXPRESS OR IMPLIED, INCLUDING WITHOUT LIMITATION IMPLIED WARRANTIES OF MERCHANTABILITY OR FITNESS FOR A PARTICULAR PURPOSE. ADDITIONAL RIGHTS MAY BE REQUIRED TO USE ILLUSTRATIONS, GRAPHS, PHOTOGRAPHS, ABSTRACTS, INSERTS, OR OTHER PORTIONS OF THE WORK (AS OPPOSED TO THE ENTIRE WORK) IN A MANNER CONTEMPLATED BY USER; USER UNDERSTANDS AND AGREES THAT NEITHER CCC NOR THE RIGHTSHOLDER MAY HAVE SUCH ADDITIONAL RIGHTS TO GRANT.

13) Effect of Breach. Any failure by User to pay any amount when due, or any use by User of a Work beyond the scope of the License set forth in the Order Confirmation and/or the Terms, shall be a material breach of such License. Any breach not cured within 10 days of written notice thereof shall result in immediate termination of such License without further notice. Any unauthorized (but licensable) use of a Work that is terminated immediately upon notice thereof may be liquidated by payment of the Rightsholder's ordinary license price therefor; any unauthorized (and unlicensable) use that

is not terminated immediately for any reason (including, for example, because materials containing the Work cannot reasonably be recalled) will be subject to all remedies available at law or in equity, but in no event to a payment of less than three times the Rightsholder's ordinary license price for the most closely analogous licensable use plus Rightsholder's and/or CCC's costs and expenses incurred in collecting such payment.

14) Additional Terms for Specific Products and Services. If a User is making one of the uses described in this Section 14, the additional terms and conditions apply:

a) *Print Uses of Academic Course Content and Materials (photocopies for academic coursepacks or classroom handouts).* For photocopies for academic coursepacks or classroom handouts the following additional terms apply:

i) The copies and anthologies created under this License may be made and assembled by faculty members individually or at their request by on-campus bookstores or copy centers, or by off-campus copy shops and other similar entities.

ii) No License granted shall in any way: (i) include any right by User to create a substantively non-identical copy of the Work or to edit or in any other way modify the Work (except by means of deleting material immediately preceding or following the entire portion of the Work copied) (ii) permit "publishing ventures" where any particular anthology would be systematically marketed at multiple institutions.

iii) Subject to any Publisher Terms (and notwithstanding any apparent contradiction in the Order Confirmation arising from data provided by User), any use authorized under the academic pay-per-use service is limited as follows:

A) any License granted shall apply to only one class (bearing a unique identifier as assigned by the institution, and thereby including all sections or other subparts of the class) at one institution;

B) use is limited to not more than 25% of the text of a book or of the items in a published collection of essays, poems or articles;

C) use is limited to no more than the greater of (a) 25% of the text of an issue of a journal or other periodical or (b) two articles from such an issue;

D) no User may sell or distribute any particular anthology, whether photocopied or electronic, at more than one institution of learning;

E) in the case of a photocopy permission, no materials may be entered into electronic memory by User except in order to produce an identical copy of a Work before or during the academic term (or analogous period) as to which any particular permission is granted. In the event that User shall choose to retain materials that are the subject of a photocopy permission in electronic memory for purposes of producing identical copies more than one day after such retention (but still within the scope of any permission granted), User must notify CCC of such fact in the applicable permission request and such retention shall constitute one copy actually sold for purposes of calculating permission fees due; and

F) any permission granted shall expire at the end of the class. No permission granted shall in any way include any right by User to create a substantively non-identical copy of the Work or to edit or in any other way modify the Work (except by means of deleting material immediately preceding or following the entire portion of the Work copied).

iv) Books and Records; Right to Audit. As to each permission granted under the academic pay-per-use Service, User shall maintain for at least four full calendar years books and records sufficient for CCC to determine the numbers of copies made by User under such permission. CCC and any representatives it may designate shall have the right to audit such books and records at any time during User's ordinary business hours, upon two days' prior notice. If any such audit shall determine that User shall have underpaid for, or underreported, any photocopies sold or by three percent (3%) or more, then User shall bear all the costs of any such audit; otherwise, CCC shall bear the costs of any such audit. Any amount determined by such audit to have been underpaid by User shall immediately be paid to CCC by User, together with interest thereon at the rate of 10% per annum from the date such amount was originally due. The provisions of this paragraph shall survive the termination of this License for any reason.

b) *Digital Pay-Per-Uses of Academic Course Content and Materials (e-coursepacks, electronic reserves, learning management systems, academic institution intranets).* For uses in e-coursepacks, posts in electronic reserves, posts in learning management systems, or posts on academic institution intranets, the following additional terms apply:

i) The pay-per-uses subject to this Section 14(b) include:

A) Posting e-reserves, course management systems, e-coursepacks for text-based content, which grants authorizations to import requested material in electronic format, and allows electronic access to this material to members of a designated college or university class, under the direction of an instructor designated by the college or university, accessible only under appropriate electronic controls (e.g., password);

B) Posting e-reserves, course management systems, e-coursepacks for material consisting of photographs or other still images not embedded in text, which grants not only the authorizations described in Section 14(b)(i)(A) above, but also the following authorization: to include the requested material in course materials for use consistent with Section 14(b)(i)(A) above, including any necessary resizing, reformatting or modification of the resolution of such requested material (provided that such modification does not alter the underlying editorial content or meaning of the requested material, and provided that the resulting modified content is used solely within the scope of, and in a manner consistent with, the particular authorization described in the Order Confirmation and the Terms), but not including any other form of manipulation, alteration or editing of the requested material;

C) Posting e-reserves, course management systems, e-coursepacks or other academic distribution for audiovisual content, which grants not only the authorizations described in Section 14(b)(i)(A) above, but also the following authorizations: (i) to include the requested material in course materials for use consistent with Section 14(b)(i)(A) above; (ii) to display and perform the requested material to such members of such class in the physical classroom or remotely by means of streaming media or other video formats; and (iii) to "clip" or reformat the requested material for purposes of time or content management or ease of delivery, provided that such "clipping" or reformatting does not alter the underlying editorial content or meaning of the requested material and that the resulting material is used solely within the scope of, and in a manner consistent with, the particular authorization described in the Order Confirmation and the Terms. Unless expressly set forth in the relevant Order Conformation, the License does not authorize any other form of manipulation, alteration or editing of the requested material.

ii) Unless expressly set forth in the relevant Order Confirmation, no License granted shall in any way: (i) include any right by User to create a substantively non-identical copy of the Work or to edit or in any other way modify the Work (except by means of deleting material immediately preceding or following the entire portion of the Work copied or, in the case of Works subject to Sections 14(b)(1)(B) or (C) above, as described in such Sections) (ii) permit "publishing ventures" where any particular course materials would be systematically marketed at multiple institutions.

iii) Subject to any further limitations determined in the Rightsholder Terms (and notwithstanding any apparent contradiction in the Order Confirmation arising from data provided by User), any use authorized under the electronic course content pay-per-use service is limited as follows:

A) any License granted shall apply to only one class (bearing a unique identifier as assigned by the institution, and thereby including all sections or other subparts of the class) at one institution;

B) use is limited to not more than 25% of the text of a book or of the items in a published collection of essays, poems or articles;

C) use is limited to not more than the greater of (a) 25% of the text of an issue of a journal or other periodical or (b) two articles from such an issue;

D) no User may sell or distribute any particular materials, whether photocopied or electronic, at more than one institution of learning;

E) electronic access to material which is the subject of an electronic-use permission must be limited by means of electronic password, student identification or other control permitting access solely to students and instructors in the class;

F) User must ensure (through use of an electronic cover page or other appropriate means) that any person, upon gaining electronic access to the material, which is the subject of a permission, shall see:

  ○ a proper copyright notice, identifying the Rightsholder in whose name CCC has granted permission,

  ○ a statement to the effect that such copy was made pursuant to permission,

  ○ a statement identifying the class to which the material applies and notifying the reader that the material has been made available electronically solely for use in the class, and

  ○ a statement to the effect that the material may not be further distributed to any person outside the class, whether by copying or by transmission and whether electronically or in paper form, and User must also ensure that such cover page or other means will print out in the event that the person accessing the material chooses to print out the material or any part thereof.

G) any permission granted shall expire at the end of the class and, absent some other form of authorization, User is thereupon required to delete the applicable material from any electronic storage or to block electronic access to the applicable material.

iv) Uses of separate portions of a Work, even if they are to be included in the same course material or the same university or college class, require separate permissions under the electronic course content pay-per-use Service. Unless otherwise provided in the Order Confirmation, any grant of rights to User is limited to use completed no later than the end of the academic term (or analogous period) as to which any particular permission is granted.

v) Books and Records; Right to Audit. As to each permission granted under the electronic course content Service, User shall maintain for at least four full calendar years books and records sufficient for CCC to determine the numbers of copies made by User under such permission. CCC and any representatives it may designate shall have the right to audit such books and records at any time during User's ordinary business hours, upon two days' prior notice. If any such audit shall determine that User shall have underpaid for, or underreported, any electronic copies used by three percent (3%) or more, then User shall bear all the costs of any such audit; otherwise, CCC shall bear the costs of any such audit. Any amount determined by such audit to have been underpaid by User shall immediately be paid to CCC by User, together with interest thereon at the rate of 10% per annum from the date such amount was originally due. The provisions of this paragraph shall survive the termination of this license for any reason.

c) *Pay-Per-Use Permissions for Certain Reproductions (Academic photocopies for library reserves and interlibrary loan reporting) (Non-academic internal/external business uses and commercial document delivery).* The License expressly excludes the uses listed in Section (c)(i)-(v) below (which must be subject to separate license from the applicable Rightsholder) for: academic photocopies for library reserves and interlibrary loan reporting; and non-academic internal/external business uses and commercial document delivery.

i) electronic storage of any reproduction (whether in plain-text, PDF, or any other format) other than on a transitory basis;

ii) the input of Works or reproductions thereof into any computerized database;

iii) reproduction of an entire Work (cover-to-cover copying) except where the Work is a single article;

iv) reproduction for resale to anyone other than a specific customer of User;

v) republication in any different form. Please obtain authorizations for these uses through other CCC services or directly from the rightsholder.

Any license granted is further limited as set forth in any restrictions included in the Order Confirmation and/or in these Terms.

d) *Electronic Reproductions in Online Environments (Non-Academic-email, intranet, internet and extranet).* For "electronic reproductions", which generally includes e-mail use (including instant messaging or other electronic transmission to a defined group of recipients) or posting on an intranet, extranet or Intranet site (including any display or performance incidental thereto), the following additional terms apply:

i) Unless otherwise set forth in the Order Confirmation, the License is limited to use completed within 30 days for any use on the Internet, 60 days for any use on an intranet or extranet and one year for any other use, all as measured from the "republication date" as identified in the Order Confirmation, if any, and otherwise from the date of the Order Confirmation.

ii) User may not make or permit any alterations to the Work, unless expressly set forth in the Order Confirmation (after request by User and approval by Rightsholder); provided, however, that a Work consisting of photographs or other still images not embedded in text may, if necessary, be resized, reformatted or have its resolution modified without additional express permission, and a Work consisting of audiovisual content may, if necessary, be "clipped" or reformatted for purposes of time or content management or ease of delivery (provided that any such resizing, reformatting, resolution modification or "clipping" does not alter the underlying editorial content or meaning of the Work used, and that the resulting material is used solely within the scope of, and in a manner consistent with, the particular License described in the Order Confirmation and the Terms.

15) Miscellaneous.

a) User acknowledges that CCC may, from time to time, make changes or additions to the Service or to the Terms, and that Rightsholder may make changes or additions to the Rightsholder Terms. Such updated Terms will replace the prior terms and conditions in the order workflow and shall be effective as to any subsequent Licenses but shall not apply to Licenses already granted and paid for under a prior set of terms.

b) Use of User-related information collected through the Service is governed by CCC's privacy policy, available online at www.copyright.com/about/privacy-policy/.

c) The License is personal to User. Therefore, User may not assign or transfer to any other person (whether a natural person or an organization of any kind) the License or any rights granted thereunder; provided, however, that, where applicable, User may assign such License in its entirety on written notice to CCC in the event of a transfer of all or

substantially all of User's rights in any new material which includes the Work(s) licensed under this Service.

d) No amendment or waiver of any Terms is binding unless set forth in writing and signed by the appropriate parties, including, where applicable, the Rightsholder. The Rightsholder and CCC hereby object to any terms contained in any writing prepared by or on behalf of the User or its principals, employees, agents or affiliates and purporting to govern or otherwise relate to the License described in the Order Confirmation, which terms are in any way inconsistent with any Terms set forth in the Order Confirmation, and/or in CCC's standard operating procedures, whether such writing is prepared prior to, simultaneously with or subsequent to the Order Confirmation, and whether such writing appears on a copy of the Order Confirmation or in a separate instrument.

e) The License described in the Order Confirmation shall be governed by and construed under the law of the State of New York, USA, without regard to the principles thereof of conflicts of law. Any case, controversy, suit, action, or proceeding arising out of, in connection with, or related to such License shall be brought, at CCC's sole discretion, in any federal or state court located in the County of New York, State of New York, USA, or in any federal or state court whose geographical jurisdiction covers the location of the Rightsholder set forth in the Order Confirmation. The parties expressly submit to the personal jurisdiction and venue of each such federal or state court.

Last updated October 2022

Design of an Endoscopic Fully Optically Accessible High-Speed Large-Bore Engine

Stephan Bernhard Karmann,[1] Hannes Röhrle,[1] Bernhard Klier,[1] Maximilian Prager,[1] and Georg Wachtmeister[1]

[1]Technical University of Munich, Germany

Abstract

Rising engine efficiency and exhaust limitations demand a deeper knowledge of the combustion process. State-of-the-art investigations use laser optical test equipment that relies on optical accesses into the engine. In this article, a new endoscopic, fully optical access for a high-speed large-bore engine is demonstrated. The successfully realized concept consists of two individually usable accesses: The lateral access with a vertical field of view is realized via a ring, which is inserted between the cylinder liner and cylinder head. The ring offers several screw-in positions for an ultraviolet (UV)-enhanced endoscope. This access can be used independently for full-load investigations of the mixture formation and combustion processes taking place inside the cylinder; The second access from above is realized by inserting a self-developed fisheye endoscope. The endoscope replaces one of the exhaust valves and supplements the lateral access with a horizontal field of view covering nearly the whole combustion chamber. The development of the optical design of the fisheye endo-scope using ray tracing is detailed for this type of all-optical engine. The materials and design changes made for the second access reduce the convertible engine load. Thus finite element method (FEM), conjugate heat transfer (CHT), and multibody simulations validate strength and temperature behavior under engine conditions. A similar concept was already implemented and successfully tested at a dual-fuel engine with 40 l displacement. With the current investigations, it is shown that this concept represents a reasonable and feasible solution for in situ engine investigations for smaller engines as well, here with a bore of 170 mm and a stroke of 210 mm resulting in a 4.8 l displacement. For this reason, the design shown here approximately halves the diameter of the fisheye optics compared to the design already implemented. The main focus is thus on reducing the installation space of the optical accesses while at the same time optimizing the optical imaging properties and the field of view. The significantly reduced concept shown here, in turn, has the possibility of being integrated more efficiently into an engine with a larger displacement class through a reduced modi-fication effort, thus simplifying the in-situ investigations and enhancing the likeness to the original engine.
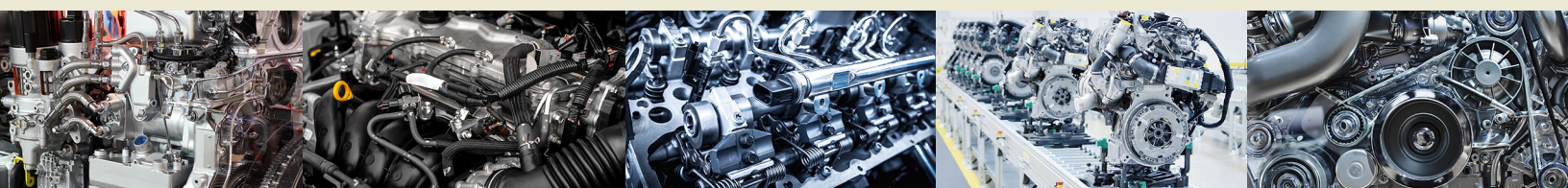
1. Introduction

In state-of-the-art energy networks, combustion engines can serve as a bridging technology in the energy transition. Regeneratively produced fuels such as hydrogen and methane, which are used to store seasonally and regionally fluctuating renewable energies, can be converted into electricity used as fuel for combustion engines in an environmentally friendly manner. This approach complements decentralized energy distribution and supports a sector coupling approach.

However, the influence of renewable fuels, especially hydrogen, but also hydrogen/methane or natural gas mixtures, on the combustion process still needs to be investigated and optimized in more detail for large-bore engines used for stationary power generation applications. For this purpose, optically accessible engines can serve as a key technology to observe mixture formation, inflammation, flame propagation, and abnormal combustion, the latter especially using hydrogen as the most reactive fuel. Such investigations in combination with all-metal engine experiments can contribute to enhance engine performance by reducing fuel consumption and in-engine emission formation and to increase efficiency and reliability. These investigations and their methods are quite common for passenger car and truck size engines using typical fuels (diesel, gasoline), as described in [1, 2, 3], as well as alternative and regenerative fuels like OME, an example given in [4, 5]. The combined use of an all-metal engine and a fully optically accessible engine, for example, to investigate the diesel spray influence on combustion and reduce the NOx soot trade-off is depicted in [6, 7]. For large-bore engines, the application of optical and laser optical measurements is still quite rare and usually conducted by a single lateral optical access only. Examples of this are given in [8]. A fully optical access according to the Bowditch principle, which is described in [9] for this size of engines, has been realized successfully and used for optical combustion analysis. Gleis used a fully optically accessible large-bore engine to describe the high-pressure dual-fuel combustion process with natural gas and diesel in [10]. In [11] the combustion of potential renewable fuels such as methanol and hydrogen was observed and described in the same engine, and the potential of those fuels concerning emission and efficiency was stated. Both [12, 13] use experimental data from a fully optically accessible large-bore engine to verify and validate numerical computational fluid dynamics (CFD) calculations of lean natural gas combustion with natural chemiluminescence observations of a high-pressure dual-fuel combustion with particle image velocimetry and natural chemiluminescence experiments, respectively. A realization for even larger engines is theoretically investigated, e.g., in [14]. As the Bowditch principle for large-bore engines requires a high design effort, an already-realized alternative using a lateral access similar to [15] but extended with a horizontal field of view (FOV) using a fisheye optic is presented in [16]. This concept provides some advantages such as a reduced design and invest effort, as well as a more realistic engine behavior as the piston lubrication could be preserved.

In the following sections this promising approach is adapted for a smaller engine size with a bore of 170 mm and a stroke of 210 mm. The design and numerical investigations of the optical as well the engine components and the necessary design modifications are presented in the following sections detailing the raised adaptations due to smaller construction space.

2. Design Description of the Endoscopic Fully Optically Accessible Engine

The endoscopic fully optical access has been developed for the cost-efficient use of series components in order to ensure the lowest possible test bench modification effort and an easy-to-use system adaptable for further testing rig variations or even the adaptation of other series engines, if available. It is important that the access shows high comparability of its engine behavior with that of a thermodynamically equivalent setup. As a further requirement, it should be possible to observe combustion anomalies that occur when using regenerative produced fuels, in particular pure hydrogen or hydrogen/methane blends. For this reason, the design is made up of two individually usable accesses. A lateral access with a vertical FOV is designed for full-load operation. This access can be used e.g. to investigate abnormal combustion phenomena, as it is done in [17]. A combination with a fisheye endoscope allows an additional vertical and, therefore, enhanced FOV. Due to design constraints, the engine load has to be reduced to prevent the optical elements from failing. Figure 1 shows the overall setup of both accesses implemented at the test bench of the Chair of Internal Combustion Engines. The realized test engine is a 4.8 l research engine, which can be operated with different ignition systems (spark plug, scavenged or unscavenged prechamber, pilot ignition) and different combustion processes (dual fuel in high- and low-pressure variants, gas operation with loads up to 30 bar p_{mi}). Based on the design studies in [18], the new setup is depicted in Figure 2. The endoscope ring mounting the high-efficiency ultraviolet (UV) endoscope is placed between the cylinder head and cylinder liner. Two sealings made of nickel are induced at these positions. Slight modifications at the cylinder head are necessary to increase the available installing space for the optical access. Furthermore, the cylinder liner is lowered by the height of the endoscope ring and shortened in order to maintain the piston's lower clearance dimension. Furthermore, the anti-bore polish ring is removed. This is possible as the test engine is run for fewer operating hours than required to really benefit from the effect of the anti-bore polish ring. Due to a high top land of the aluminum piston, an adjustment of the piston ring package is not necessary as

FIGURE 1 Lateral access sectional views (EV = Exhaust valve, IV = Intake valve, FEO = Fisheye optic), Mounting Positions 1-3.
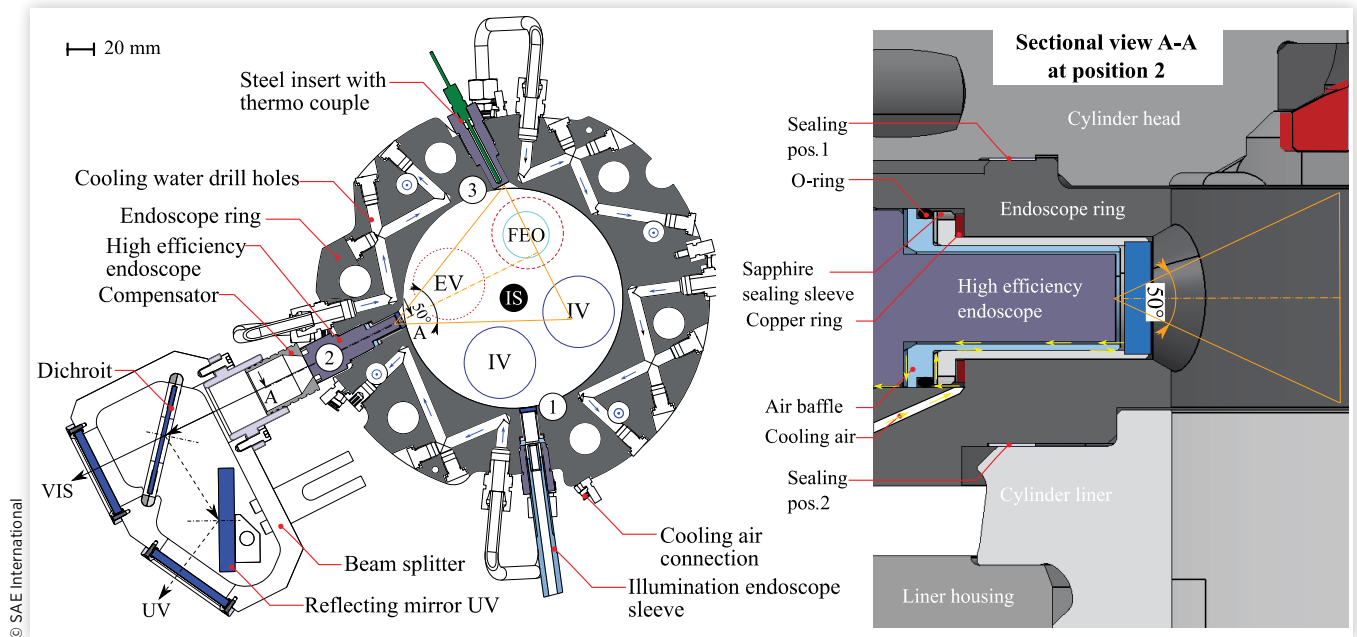
the first piston ring cannot pass the gap between the cylinder liner and endoscope ring. As the lateral endoscopic access is designed for engine full-load operating conditions, it has to withstand high combustion peak pressure and thermal loads. The latter condition is met by an appropriate cooling system. The engine's series cooling duct is extended with drill holes in the endoscope ring guiding the water closer to the combustion chamber from the cylinder head to the cylinder liner and back to the controlled cooling water conditioning system (cf. Figure 2). Furthermore, the air cooling of the endoscope and the steel inserts prevents over-heating. A close look at the cooling concept is provided in Subsection 3.1 with the numerical treatment under worst-case full-load conditions. Besides the high thermal load, the

high combustion pressure has to be met by the design. The relatively closely spaced accesses for the endoscope, there-fore, minimize the occurring load from combustion pressure. Furthermore, sapphire, as the most stable glass material, is pressed into a titanium sleeve. The sapphire sealing sleeve has been designed by FOS Messtechnik GmbH for up to 300 bar pressure and 600°C.

The access size allows a maximum field of observation with a field angle of the endoscope of up to 50° and three possible positions to mount (cf. Figure 2).

Figure 3 depicts the observable FOV in the combustion chamber focused at a distance of −116 mm. With at least >82.5 mm distance from the optic in a horizontal line, the cylinder head, cylinder liner, endoscope ring ignition system,

FIGURE 2 Engine setup at the testing rig.
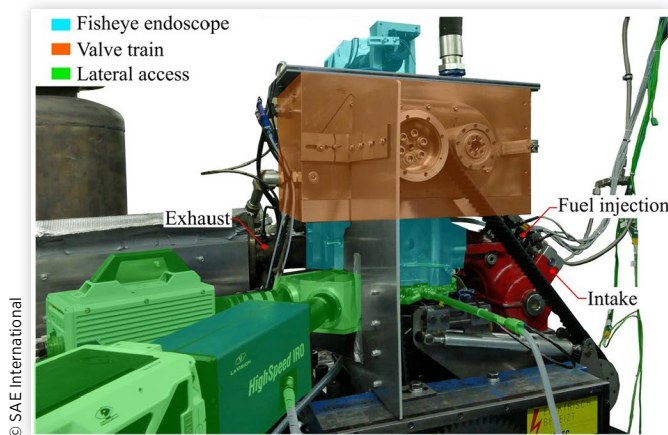
FIGURE 3 Vertical FOV (FEO = Fisheye optic).
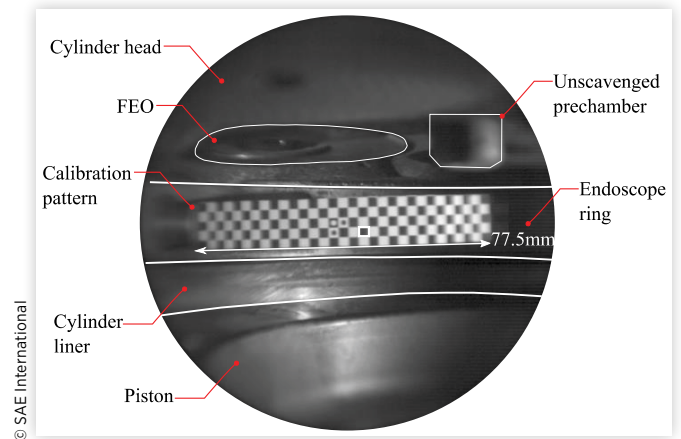
piston, and fisheye optic are visible. Parts outside the limited focus plane are blurred. An example of this is the unscavenged prechamber spark plug depicted in Figure 3. Furthermore, a slight barrel distortion is visible and typical for endoscopic imaging. In addition, by using only the endoscope, a beam splitter can be integrated into the beam path. It splits the image of the endoscope into the visible spectral component and the UV component. With this application, the flame chemiluminescence and the combustion's UV chemiluminescence can be recorded simultaneously, as in the application depicted in [10]. This allows the generation of two sets of different measurement data at the same time, reducing the overall testing time.

3. Design of the Full-Load Optical Configuration

The full-load configuration consists only of the endoscopic lateral optical access using a slightly modified cylinder head to fit the endoscope ring. As this setup is developed for full-load continuous engine operation with higher stability requirements, the following sections depict simulative fatigue investigations carried out during the design process to confirm the feasibility of the full-load configuration.

3.1. Conjugate Heat Transfer (CHT) Simulation of the Cooling Concept

The engine's cooling duct consists of the all-metal engine's water cooling extended by the cooling of the endoscope ring and the air cooling of the endoscope. Figure 2 depicts the airflow of the endoscope's cooling. The cooling air restricted by the copper ring and the O-ring flows inward via radially integrated recesses on the sapphire sealing sleeve. Grooves on the air baffle direct the cooling air at its outer surface toward the sapphire window. Here the cooling air absorbs the heat from the sapphire window and is then directed inside the air baffle into the environment. For this purpose, grooves are integrated on the sealing surface between the endoscope and the air baffle through which the air can leak. Likewise, grooves are provided in the endoscope ring's screw-in thread of the endoscope to allow cooling air flow into the environment.

The effectiveness of the cooling concept is estimated using a simulation model consisting of the parts and fluid volumes depicted in the overview in Figure 4. The thermal boundary conditions are derived as a mean value from pressure analysis of the all-metal engine run up to an extended load of 30 bar mean effective pressure described in [19]. Figure 4 depicts these boundary conditions. This mean value setup describes a sufficient worst-case scenario to derive an adequate temperature distribution for a worst-case fatigue proof. The stationary Reynolds-averaged Navier-Stokes equation (RANS) CHT simulation is carried out similar to [18] using 17.2×10^6 (85.7% air volume, 6% solid, 8.3% water volume) elements and the k-ε turbulence model for the engine's water and air-cooling duct with a root mean square (RMS) convergence criteria of 10^{-4}. The water flow is defined as incompressible whereas the airflow compressibility is visible by the occurring pressure shock depicted in Figure 5.

As this simulation is a worst-case scenario, the velocity profile of the air cooling will not show this behavior because, on the one hand, manufacturing tolerances widen the critical cross section and, on the other hand, due to a missing sealing of the endoscope housing, the air mass flow leaks via this part and decreases the velocity, correspondingly the pressure, and reduces the probability of a pressure shock. With this setting the minimum possible air mass flow is simulated, resulting in a theoretical maximum temperature of the endoscope and the sapphire window. With a maximum temperature of the endoscope of 137°C, the simulation confirms a lower temperature than the endurable temperature of 200°C, which is set by

FIGURE 4   Boundary conditions for CHT simulation of the full-load configuration.
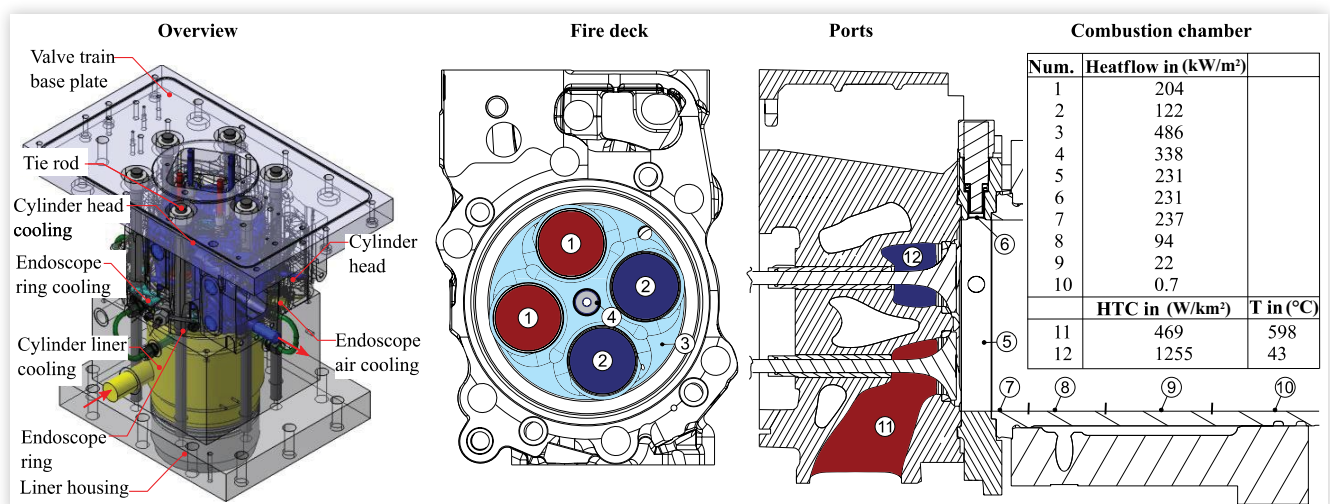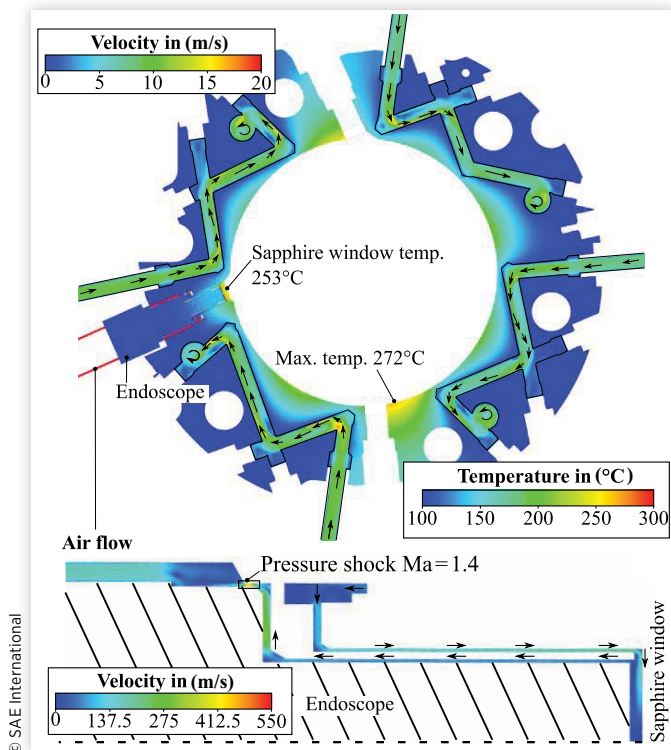

Num.	Heatflow in (kW/m²)	
1	204	
2	122	
3	486	
4	338	
5	231	
6	231	
7	237	
8	94	
9	22	
10	0.7	
	HTC in (W/km²)	T in (°C)
11	469	598
12	1255	43

© SAE International

FIGURE 5 Cooling water, airflow, and temperature distribution at the endoscope ring sectional view.

FIGURE 6 FEM contact and load step (LS) definition for full-load configuration.

LS	Definition
1	Tie rod pretension 180 kN
2	Pre-tension + full load temperature profile
3	Pre-tension + temp. profile combustion pressure 25 MPa

the supplier. Figure 5 depicts the stationary results of the simulation for a sectional view through the midplane of the endoscope ring. The figure depicts the temperature distribution of the endoscope ring with its maximum of 272°C and the sapphire window temperature of 253°C. This temperature is less than the endurable 600°C of the sapphire sealing sleeve, and therefore not critical. Further, the cooling water flow velocity is depicted. The additional water-cooling effect of the endoscope ring is visible with a maximum effect at the drill tips pointing toward the most-strained positions at the endoscope drill holes. Nevertheless, the highest temperature values occur at the endoscope Mounting Positions 2 and 3, as the cooling water cannot reach these positions due to installing space constraints for the drill bores that were optimized for maximum diameter and the possibility of manufacturing and optimum positioning.

The water pipe flow shows typical behavior with dead water areas at the sharp bending as well as a swirl in the volume where the water is guided upward to the cylinder head. With this valid behavior of the flow and temperature, the CHT simulation seems valid for a worst-case fatigue proof.

3.2. Result of the Fatigue Proof

The finite element method (FEM) model is set up with the parts, loads, and simulation steps listed in Figure 6. As the newly designed endoscope ring is of interest, the following

evaluation focuses on this part. Table 1 summarizes the data used according to the proceeding of [20] for the fatigue proof. The FEM model uses 2.1×10^6 elements and 45 contact definitions as depicted in Figure 6. The material models are defined as elastic with thermal dependence.

The dynamic utilization ratio of the high cycle fatigue treats the Load Steps 2 and 3 with the maximum rising temperature and combustion pressure. The dynamic utilization ratio is not critical and is less than 1. The static proof regarding the maximum thermal-induced stress of the preloaded assembly offers static utilization ratios greater than 1. Figure 7 depicts these locations with their static utilization ratio at a mean static safety margin of 2.4. A utilization ratio above one would result in increased material utilization. A comparison of these locations to the effective yield strength shows no critical stress or strain especially at Position 1 (cf. Figure 7) and is therefore acceptable for the experimental full-load engine operation.

Furthermore, the maximum possible pretension and no plastic strain factor are considered for this worst-case

TABLE 1 Material properties 42CrMo4V used for fatigue proof.

Tensile strength R_m	865 MPa	Mean static safety margin	2.4
Yield stress R_p	634 MPa	Mean dynamic safety margin	1.2
Fatigue strength	546 MPa		

FIGURE 7 Static utilization ratio at critical locations with a mean static safety margin of 2.4.

**FIGURE 8** Fisheye endoscope access (HS camera = High-speed camera).
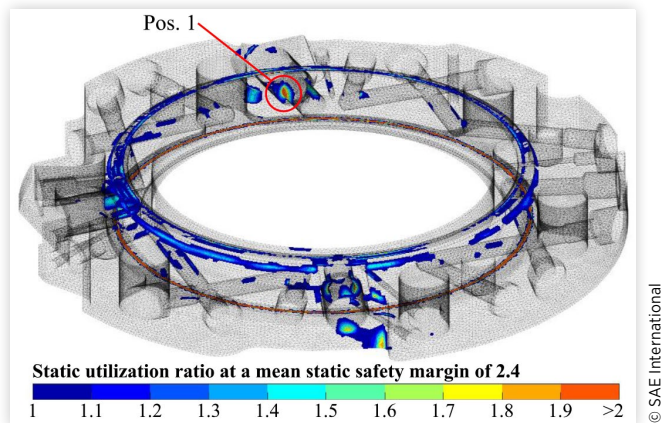
simulation of the setup. Therefore, a failure of the endoscope ring is considered unlikely. The remaining parts show sufficient fatigue under the chosen worst-case condition.

4. Design of the Fisheye Endoscope Access

The fully optically accessible setup uses a fisheye optic designed comparable to [16] and depicted in Figure 8. In contrast to [16], this approach pursues the integration of a much smaller optic in the cylinder head by replacing an exhaust valve similar to [21] implemented with a simple endoscope which achieves a much smaller FOV than a fisheye optic is capable of. The exhaust valve seat is replaced by an eccentric mount which fixes the fisheye optic mount to the cylinder head. In addition to the thread for the screw connection between the eccentric mount and the fisheye optic mount, the eccentric mount acts as a securing element in case the adhesive bond between the front lens and the fisheye optic mount fails. Furthermore, the eccentric mount protects the adhesive bond from the direct flame interference of the combustion. The small axial metal contact between the fisheye optic mount and eccentric mount seals the optic against the combustion chamber pressure. As the bore of the valve guiding sleeve has to be extended to provide enough installing space for the optic, another sealing sleeve has to be pressed and glued into the cylinder head to seal the cylinder head's cooling duct against the exhaust channel. A further O-ring mounted axially seals the cylinder head's cooling duct against the oil-filled valve train area. The protection tube further seals the optical path against oil spill from the valve train and positions the 45° deflection mirror on top of the optic. The use of a deflection mirror allows the secure mount of the high-speed camera outside the engine, preventing direct engine oscillation or any failure of the design from damaging the camera. To cool the adhesive bond between the front lens and the fisheye optic
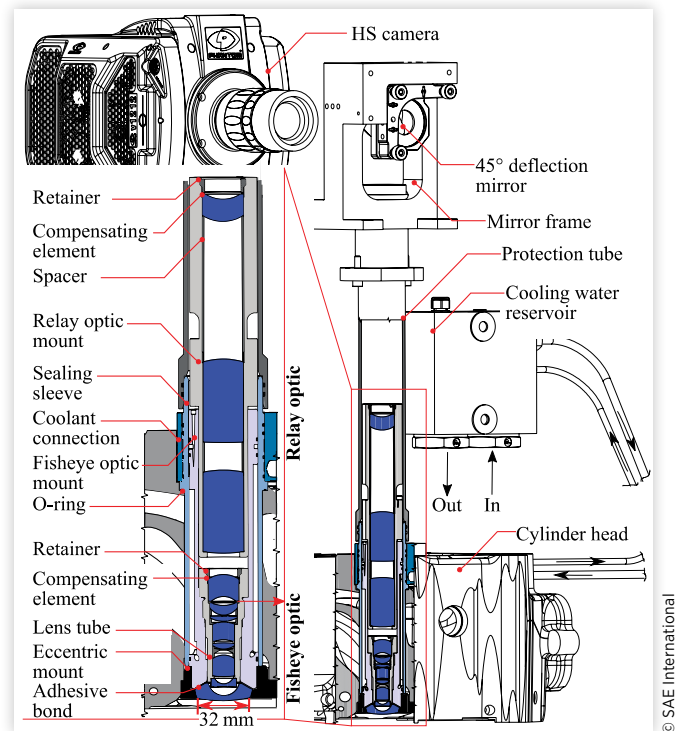
mount, the space between the latter and the sealing sleeve is filled with water supplied from the coolant connection, which forms two ring channels for inflow and outflow of the water delivered from the cooling water reservoir. Radially mounted O-rings at the bottom and top of the fisheye optic mount seal the cooling duct. A detailed description and numerical investigations follow in Subsection 4.5.

The fisheye endoscope consists of two parts—the fisheye optic with the typically shaped front lens directly facing the combustion chamber and the 2:1 relay optic, which transfers and magnifies the image of the fisheye optic via the mirror to the high-speed camera. As the design of the fisheye endoscope uses a silicon-based adhesive between the front lens of the fisheye optic and its mount, the bearable thermal engine load is limited to the permanently endurable temperature of the adhesive to 200°C. Furthermore, the first lens made from the cost-effective quartz glass offers better optical performance compared to sapphire. But the mechanical stability of quartz glass is four times less than sapphire. Therefore, the material choice reduces the endurable combustion peak pressure. The reduction in the engine load is explained in more detail in Subsection 4.6.

4.1. Optical Design of the Fisheye Optic

The fisheye optic design is based on a patent review of [22, 23, 24]. According to the available installation space in the

FIGURE 9 Lens design fisheye optic (SH = Principal plane, f = Focus, f′ = Back focus).
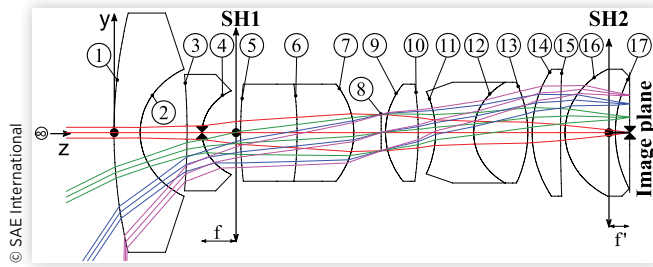
cylinder head and the quite similar optical properties of the first element, the design of [25] was used as a starting point and optimized with the optical design software OpTaliX Pro®. The optimization is performed with the components at room temperature. The adjustable back focus and the later-introduced relay optic can be used to compensate for the temperature-induced differences resulting from the use of the optics in an internal combustion engine. The final retro focus design commonly used for fisheye optics depicted in Figure 9 contains nine lenses with two color aberration corrective doublets.

The fisheye optic consists of a negative first group containing Surfaces 1-7 with a negative focus and a second positive group containing Surfaces 9-17. Table 2 summarizes the appropriate lens specifications. The optic offers an aperture number of 2.2 (numerical aperture 0.178) and an EFL (equivalent focal length) of 4 mm. The image diameter is 9.7 mm.

To judge the imaging quality, several image metrics of the imaging aberrations are available. Within the scope of this article, only the significant design parameters are enumerated. The design shows a slight coma aberration and transversal color aberration (TCA) as is stated by the third-order

TABLE 2 Lens specifications.

Surface	r (mm)	Distance (mm)	Material
1	79.52	3	HPFS7980
2	9.68	5.40	—
3	−102.02	1.74	H-LAF50B
4	6.36	4.43	—
5	69.53	6.51	ZF12
6	−55.34	6.51	H-LAK51A
7	−11.4	3.16	—
8	0	0.5	—
9	11.44	3.75	H-BAK7
10	−55.88	2.00	—
11	−14.76	4.39	H-ZF7LA
12	8.09	6.22	H-ZK9A
13	−18.04	0.5	—
14	17.31	3.28	H-LAK4L
15	289.52	0.5	—
16	9.80	5.80	H-K9L
17	18.54	1.63	—

FIGURE 10 Third-order aberration of the fisheye optic at room temperature (SPH = Spherical, ASTI = Astigmatism, DIST = Distortion, TCA = Transversal color, LCA = Longitudinal color, PETZ = Petzval curvature).
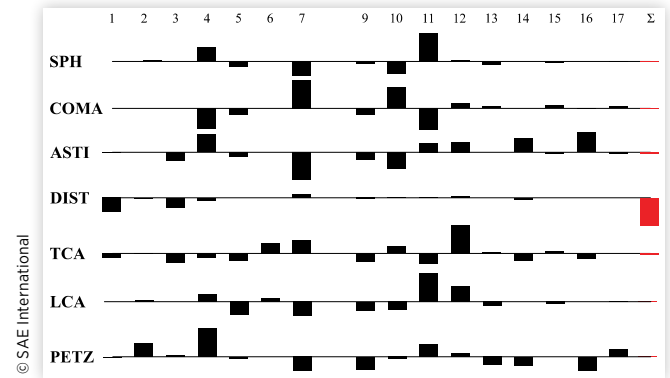
Seidel-aberration plot (cf. Figure 10), where the contribution of each surface to the total aberration is shown.

The large Petzval radius results in an almost flat image that is advantageous, especially with respect to the small image diameter. The system is nearly free of spherical aberrations and longitudinal chromatic aberrations. Coma, astigmatism, and color magnification error are optimized to a minimum at a sufficiently low level.

Common for fisheye optics, the f-theta distortion is of great interest as it is what enables imaging with a 180° FOV. The f-theta distortion is a necessary property that must be taken into account. The f-theta distortion with −25% results in a fisheye common barrel distortion.

Taking the higher-order aberrations into account, Figure 11 depicts the optical path difference (OPD) plot. The OPD measures the difference of the real wave front compared to the ideal form from the peak to the valley of a light wave. The tangential plane depicts quite a good correction with a slight axial color aberration in the outer regions whereas the sagittal plane depicts a common deteriorated wave, especially for the
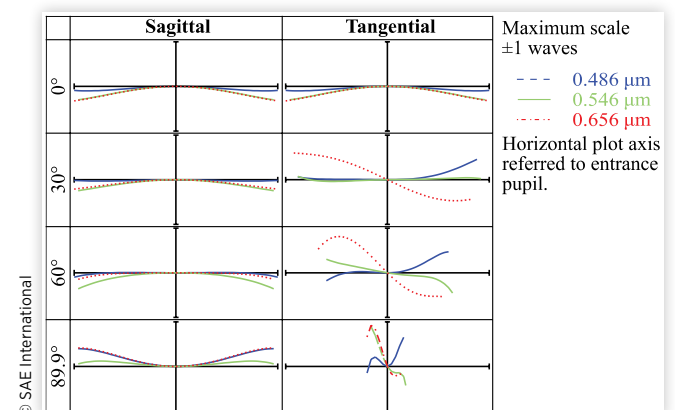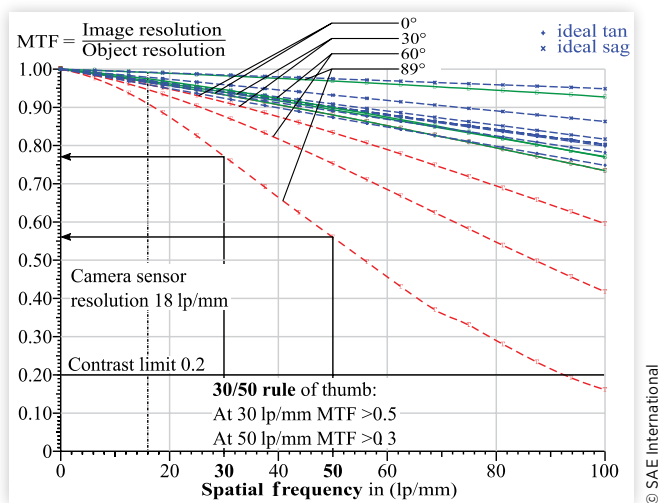
FIGURE 11 OPD of the fisheye optic.

FIGURE 12 MTF of the fisheye optic under room temperature.

© SAE International

FIGURE 13 Lens design relay optic with intermediate image from the fisheye optic.

© SAE International

maximum FOV due to a slight spherical aberration and coma. The shortened lines over the normalized diameter for the maximum FOV hint at vignetting in the system. Nevertheless, the sagittal aberrations measure less than half of the corresponding wavelength, which implies a rather good aberration correction.

The imaging quality represented by the modulation transfer function (MTF), as shown in Figure 12, exhibits a sufficient resolution above the contrast limit until 93 lp/mm. As a rule of thumb for high-quality lenses, the 30/50 condition according to [26] demonstrates rather perfect imaging of the optic, especially as the proposed values are all surpassed (cf. Figure 12). Compared to the camera resolution (cf. Figure 18), the optic shows a sufficient resolution.

4.2. Fisheye Endoscope

As the fisheye optic's image is not telecentric and the distance between the image and camera is quite large and enclosed by the tight protection tube (cf. Figure 8), the quite good aperture is degraded and results in a reduced light efficiency. Therefore, a further relay optic is introduced to improve image brightness. Especially due to the specific boundary conditions arising from the installation in a combustion engine, the temperature-dependent diffraction of each used material affects imaging. Therefore, the relay optic is optimized under these conditions using a front lens temperature of 265°C and a temperature of all subsequent elements (lenses and spacers) of 85°C resulting from the engine's temperature conditioning system. As the back focus is adjustable due to the positioning of the camera, a further adjustment is possible if the boundary conditions used are not met exactly.

The relay optic consists of six lenses with two doublets and is depicted in Figure 13. As the relay optic offers a magnification of 2:1, the image increases to a diameter of 19.4 mm.
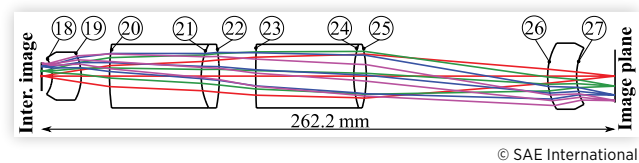
The distance between the camera and the image of the fisheye endoscope decreases by almost half from 554 mm to 295 mm.

Table 3 summarizes the lens specification for the relay design.

As the optical aberrations are affected by each lens in the system, the relay optic is optimized to minimize possible aberrations. Nevertheless, concerning the third-order aberrations depicted in Figure 14, the correction of the spherical aberration is increased compared to the sole fisheye optic.

Further coma and astigmatism aberrations increase when the relay optic is added, but range in a tolerable margin. The system offers a good color aberration correction and a quite flat image concerning the Petzval-curvature radius and image diameter. As the third-order aberrations affect the higher-order degradation of the image, an explicit presentation is not depicted as was done in Subsection 5.1 with the OPD. The image quality determined with the MTF is also affected by every optical element. Figure 15 depicts the degradation of the MTF by the relay optic. In contrast to the fisheye optic alone, the addition of the relay optic decreases the MTF concerning the contrast limit, which is 80 lp/mm in this article. As the 30/50 rule of thumb is satisfied, image resolution seems sufficient especially concerning the resolution of which the camera is capable.
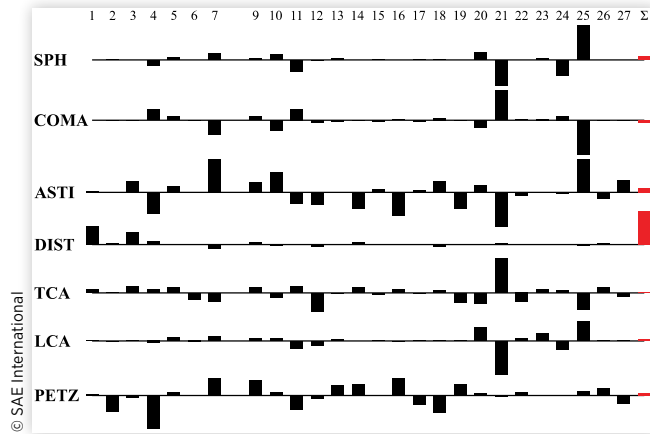
4.3. Tolerancing of the Fisheye Endoscope

Each element of the fisheye endoscope is subject to manufacturing-, assembly-, and material-related tolerances. These tolerances affect imaging quality further. The tolerances are

TABLE 3 Lens specification relay optic.

Surface	r (mm)	Distance (mm)	Material
18	−10.7	11.35	ZBAF17
19	−16.58	15.79	—
20	69.43	37.21	S-TIH57
21	24.76	8.53	S-LAL18
22	−71.43	15.26	—
23	130.53	45.0	H-ZLAF68B
24	28.98	17.46	S-LAM61
25	−46.03	76.88	—
26	21.75	10.77	S-FPM3
27	18.66	16.12	—

© SAE International

FIGURE 14 Third-order aberrations of the fisheye endoscope under operating temperature (SPH = Spherical, ASTI = Astigmatism, DIST = Distortion, TCA = Transversal color, LCA = Longitudinal color, PETZ = Petzval curvature).

FIGURE 16 Statistical tolerance analysis of fisheye endoscope at 30 lp/mm.

due to the inaccuracies of the lens itself (material-related such as dispersion variation, and shape) and variances when the lens is mounted (decenter and tilt of the lenses). Figure 16 depicts a statistical tolerance analysis for the fisheye endoscope using the Monte Carlo process implemented in OpTaliX Pro® with a 95% confidence value.

The design tolerances are chosen according to state-of-the-art manufacturing procedures and raw materials. The analysis uses the back focus as the sole compensator for a decrease in the mean MTF with an allowed degradation of 2%. The result shows an MTF value of >70% for 30 lp/mm at a cumulated probability of 100% for the FOV from 0° to 89°. This seems well suited, considering the 30/50 rule of thumb.

FIGURE 15 MTF of the fisheye endoscope at operating temperature.

4.4. Imaging System Image Quality Estimation

The fisheye endoscope imaging system consists of the fisheye endoscope itself, the Sigma f180 2.8 macro objective, and the Phantom v2012 high-speed color camera. Therefore, a higher MTF for the design procedure and tolerancing process is better since other components of the imaging system degrade the image quality. A final determination of image quality is depicted in Figure 17 with a real image from the combustion chamber of the test engine. Figure 17(a) illustrates the potential image resolution using a checkerboard calibration pattern with a rectangle size of 2.5 mm at a distance of 15 mm from the front lens of the fisheye endoscope. The resolution seems quite sufficient, especially as the combustion appears as a large-scale event as depicted in Figure 17(b). The image is taken from a combustion with a camera exposure time of 330 μs, which corresponds to a 1.5°CA at 750 rpm engine speed.

With respect to exposure time, the imaging system suffers from a loss of brightness, as an image recording rate of less than 1°CA would be preferable for the temporal resolution of combustion. This loss of brightness results from the already-mentioned increase in the aperture number due to the remaining transport of the image through the diameter-limited protection tube. Nevertheless, with respect to the small diameter of the front lens of 32 mm and the long distance from the image to the camera, even the usage of this exposure offers a quite good possibility of investigating the combustion process under near-realistic engine conditions.
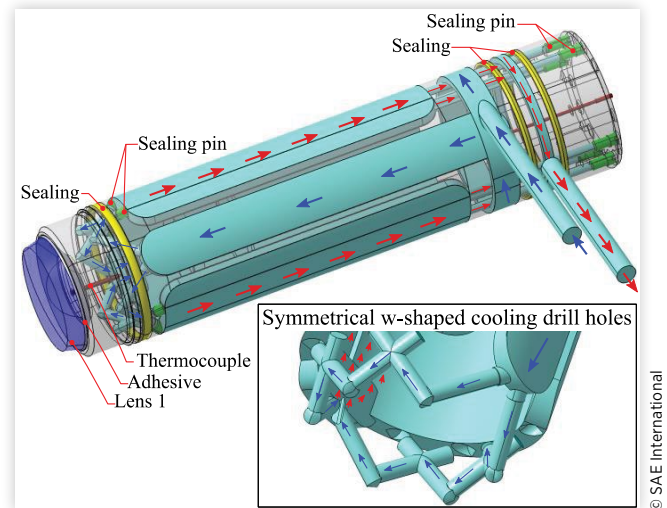
4.5. In-Stationary CHT Investigation

Realistic engine conditions entail high combustion temperature and pressure, which the optic, especially the front lens

FIGURE 17 (a) Imaging system quality. (b) Image brightness.

(a)

(b)

© SAE International

FIGURE 18 Fisheye optic cooling duct.

© SAE International
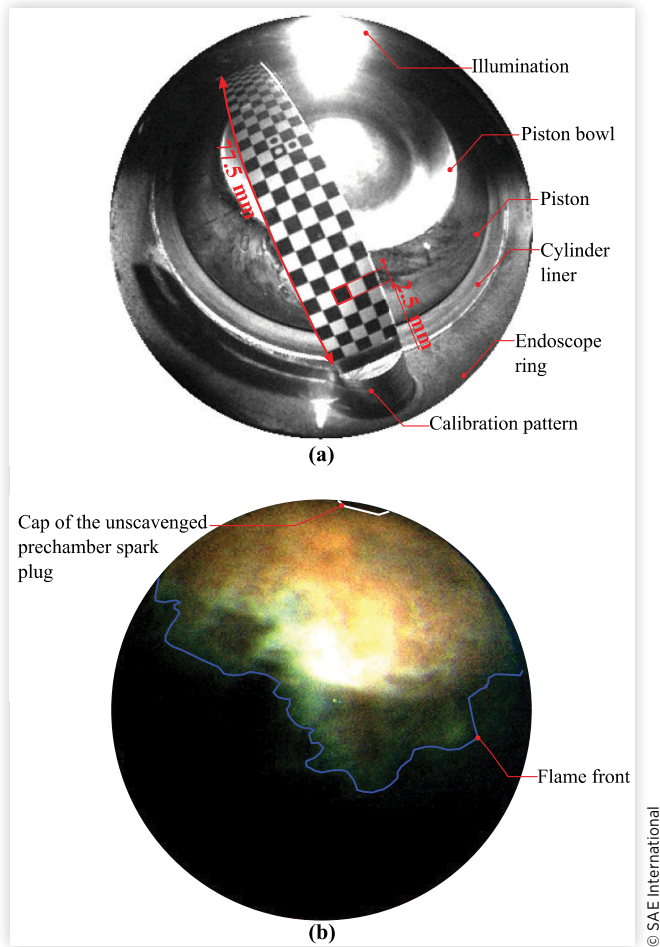
and its mount, has to withstand. As the mount of the front lens uses the same temperature-stable silicon glue up to 200°C, as in [16], a similar engine operation strategy and enhanced cooling of the optic has to be used to prevent the adhesive from overheating and failing. The skipped fire engine operation is also monitored using a thermocouple (TC) next to the adhesive (cf. Figure 18). Figure 18 also depicts the cooling duct of the upper part of the fisheye endoscope described in Section 5 without the sealing sleeve. To provide an effective cooling solution near the adhesive joint, symmetrical W-shaped cooling drill holes in the fisheye optic mount were added. The bores are sealed with pins to lead the water from the inlet ring channel to the outlet (cf. Figure 18). The outlet ring channel is connected to the cooling water volume using six riser bore-holes sealed with screwed and glued pins. The fisheye endoscope cooling water is pure water with an inlet pressure of 5 bar at 20°C. The critical temperature is estimated using an in-stationary CHT simulation. This simulation uses the same numerical model and worst-case boundary conditions as depicted in Figure 4. To account for the modifications necessary for the fisheye endoscope, the model includes the fisheye

endoscope assembly, except the lenses and mounts after the front lens. The lateral mounted endoscope and its air cooling are disregarded due to their lesser influence on the fisheye endoscope. The simulation lasts for 30 s with a time step of 1 ms. Figure 19 depicts the maximum lens temperature, maximum cylinder head temperature, maximum temperature in the adhesive, and the temperature at the TC introduced to monitor the skipped fire engine operation strategy.

The slow increase in the TC's temperature and maximum front lens temperature derived from the simulation results can be explained by the low heat conductivity of the silicon-based adhesive. The temperature increases slowly as long as the cooling system is capable of transporting the heat sufficiently. After crossing this temperature threshold, the temperature slope increases. The cylinder head displays the contrary behavior. After a short stabilization phase, the temperature slope decreases continuously. The results show that the engine could be run in the worst-case condition for at least 25.5 s until the temperature limit of the adhesive is

FIGURE 19 Simulated temperature over fired engine operation.


© SAE International
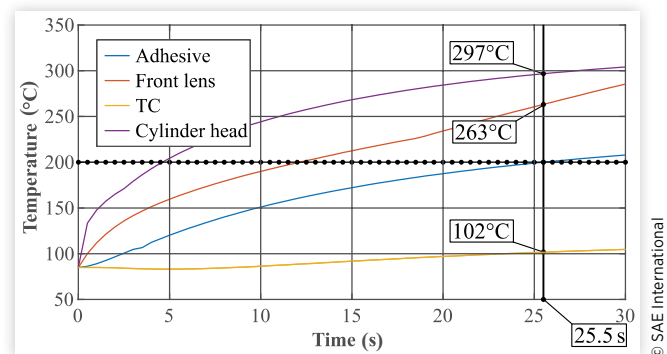
reached. This results in at least 318 fired engine cycles at 1500 rpm nominal speed and 159 at the half nominal engine speed. With 50 cycles that are used for image recording at the end of a test run, at least out of 268, 109 cycles could be used to gain near-stationary engine operation. Engine operation could be assumed to be almost stable as the cylinder head temperature seems nearly stable toward the end of the allowed fired operation time. This can be assumed, as the slope of the temperature decreases only incrementally by the end of the allowed fired operating time. The observation of near stable engine operation is necessary, as this kind of engine is normally used in stationary power generation. To gain realistic boundary conditions for the upcoming experiments observing the combustion, similar conditions compared to the all-metal engine have to be reached. With realistic engine behavior, the comparability between the results of the optical and all-metal engine can be ensured and improved. Furthermore, to better reach the stationary engine behavior, the adhesive is capable of a short-term overload of up to 250°C. This results in an elongated operation time to reach steady-state conditions. This elongated fired engine run time can be especially exploited if the adhesive layer can be inspected regularly. This is possible in the presented setup as the front lens has to be cleaned regularly depending on the degree of contamination. In addition, the thermal boundary conditions represent a worst-case estimation, which is not achieved due to the reduced engine load. The reduction of the load, especially the peak pressure, is due to the strength of the front lens and the modified cylinder head.

4.6. Mechanical Investigations

By inserting the fisheye endoscope instead of an exhaust valve, the cylinder head is weakened significantly in this area. Thus, in addition to the front lens and its bearing, it is primarily the cylinder head that determines the endurable engine load. Figure 20 shows the adjustments required to the simulation setup already shown in Figure 6.

The model uses the temperature boundary conditions from the previously shown transient CHT simulation at the time when the temperature limit is reached at the adhesive joint. The same temperature-dependent models as in Section 3 have been used to describe the material behavior. For the description of the adhesive's behavior, the model from [18] has been used due to its successful implementation. Particularly in the area of the enlarged valve bore in the cylinder head, vulnerable areas are revealed by the simulation results. These must be countered by a reduced peak pressure and, thus, possible reduced preload forces without falling below the bolt strength. This is necessary because design measures such as reducing the diameter of the optics have already been exhausted without further deterioration of the imaging quality. An endurable peak pressure of 18 MPa is calculated and equals about 80% of the maximum peak pressure of a comparable industrial gas engine. The front lens shows a plausible maximum stress of 26 MPa at the transition

FIGURE 20 FEM-contact definition of the fully optically engine configuration.
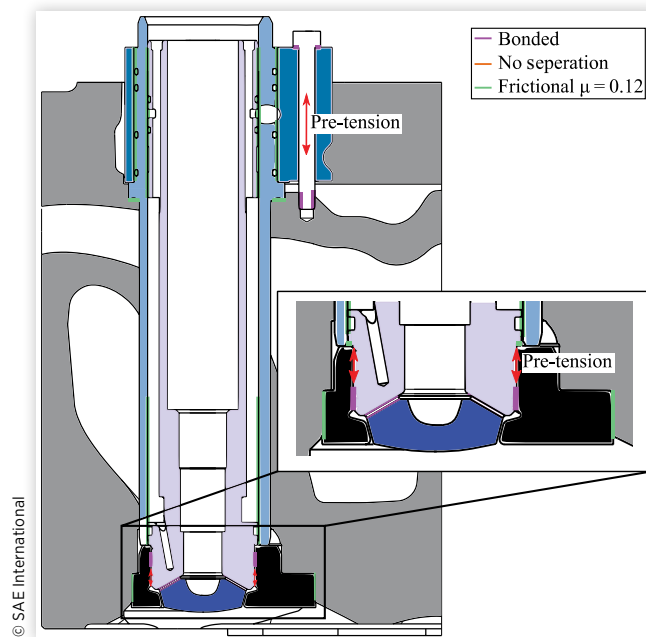
of the pressure shoulder to the inner radius of the lens depicted in Figure 21. This tensile stress originates from the temperature-dependent deformation of the fisheye optic mount induced by the bonded contact from the eccentric mount, which influenced the lens due to the modeled stiffness of the adhesive. This deformation is enhanced under the peak combustion pressure. Therefore, the stiffness of the fisheye optic mount and the contact definition between both parts are key enablers to enhance the lens' stability. As the stiffness is maximized without reducing the optics aperture number further by reducing the lens' diameter which leads to less light efficiency, the static safety margin of 1.96 (maximum tensile stress of Corning 7980 with 54 MPa) seems sufficient as the glue behavior is already validated in [18]. Further the definition of a bonded contact between the fisheye optic mount and eccentric mount simulates the worst case, disregarding the

FIGURE 21 Tensile stress of the first lens.
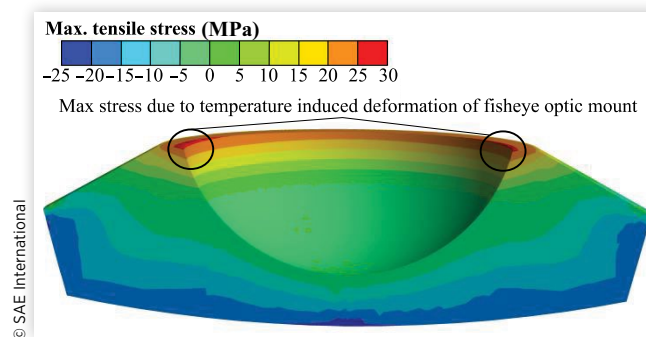
flexibility in the thread connection of both parts. For validation, the setup was statically pressurized in a preliminary test without failure. With this reduction of the combustion peak pressure, the tie rods preload could also be reduced. Hence the modified cylinder head also offers sufficient stability to run the engine under testing conditions. Still, intensified and regular observations of the critical locations should be considered.

5. Design of the Modified Valve Train

As the fisheye endoscope replaces an exhaust valve, the valve train on the exhaust side must be adjusted accordingly. The adjustment is depicted in Figure 22. The fixed position of the camshaft limits the possible offset of the exhaust rocker arm to the same position as the intake rocker arm. Therefore, the rocker arm has to be modified, as shown in Figure 22(b). Both rocker arms are mounted in a bracket fixed on a base plate. In addition, replacing the valve bridge with a cup for only one valve leads to a change in the valve train kinematics, as shown in Figure 22(b). Considering an equal maximum lift of the valve realized by an adapted cam, the adaptation results in a modified deflection angle of the ball joint with respect to the different rocker arm lengths between the original and modified version. The modified valve train kinematics with only one exhaust valve makes it necessary to evaluate the modifications with respect to the modified rocker arm durability and charge exchange. The detailed investigations are presented in the following sections.

5.1. Modified Gas Exchange Behavior

To determine the effects on the gas exchange behavior for the replacement of an exhaust valve two three-dimensional (3D)-CFD models are used. One model represents the engine using the lateral optical access and a series cylinder head—the reference configuration—and the second model represents the modified cylinder head, which is needed for mounting the fisheye optic and also the lateral optical access. Figure 23 depicts the investigated adaptation of the exhaust valve lift trace to equalize the gas exchange behavior between both configurations. The valve lift and the lift gradient influence the kinematics and are limited by the test engine's boundaries. The modified exhaust valve lift is the scaled profile of the reference trace.

This results in an increased cross section when the pressure in the combustion chamber is high to improve the gas exchange behavior. This is especially of interest when hydrogen or hydrogen methane blends are investigated to reduce the risk of backfire by an ignition of the fresh charge at hot residue gases (cf. [17]). A reduction in the exhaust backpressure is possible for all variants as the testing rig offers a controlled throttle to simulate the backpressure of a turbocharger. This modification reduces the in-cylinder temperature and affects combustion duration, ignitability especially of diesel, emissions, and efficiency [27]. It also reduces the thermal load on the adhesive bond, making engine operation with the optical access safer. The intake valve lift is not adapted and remains the same for all simulative investigations.

The boundary conditions for both simulation models are taken from a thermodynamic reference point with an all-metal engine. The simulation models are set up within the software CONVERGE CFD. The simulation is carried out without combustion for two cycles to ensure a stable gas

FIGURE 22 Modification exhaust valve train (IV = Intake valve, EV = Exhaust valve). (a) Overview. (b) Modification of rocker arm resulting in different paths of motion.
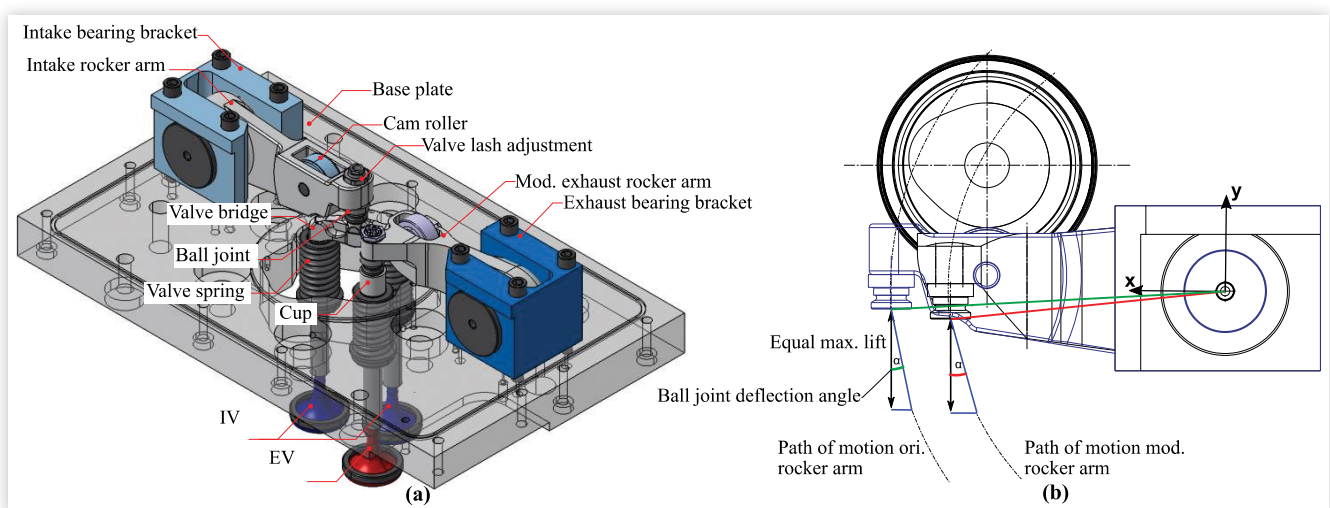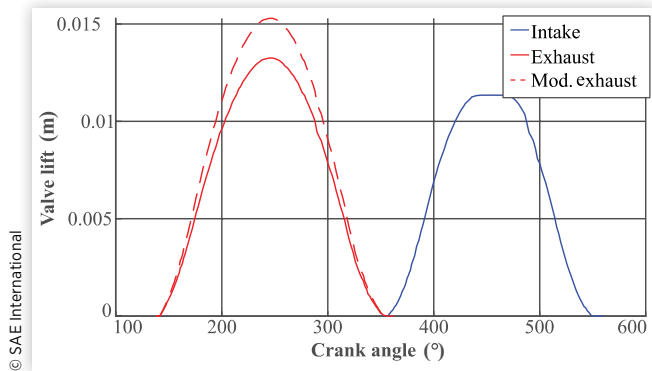
FIGURE 23 Realizable valve lift traces.

exhaust valve [cf. Figure 24(b)] with respect to the exhaust mass flow. As the mass is conserved over one cycle as blowby losses are disregarded for the simulation, the intake mass flow equals the exhaust mass flow. However, the increased valve lift contributes only 4% here. The maximum exhaust temperature behaves as expected—with an increased backpressure [cf. Figure 24(c)]. The combustion chamber pressure at exhaust valve closing and intake valve opening also behaves as expected, as the configuration of Simulation 5 with less backpressure and increased valve lift produces less counterpressure [cf. Figure 24(d)]. With the modified valve lift resulting in a similar gas exchange behavior compared to the reference model, the modified kinematics seems valid, and its effects on the modified rocker arm have to be investigated.

exchange. The combustion chamber pressure and the exhaust mass flow, reverse flow into the intake, and the combustion chamber gas temperature are used to judge the appropriate adjusted measure. Figure 24 summarizes the results. Simulation 5 with the maximum valve lift and an ambient backpressure offers the most equal reverse mass flow [cf. Figure 24(a)] into the intake with the least increase of 33%. This is due to the least pressure at intake valve opening, comparing Simulations 2, 3, 4, and 5. The reverse mass flow is calculated over the complete opening time of the intake valve. During this time, hot residual gas flowing back into the intake can cause backfire, so an increase of 33% seems a quite good compromise to realize with the depicted modifications. Only a reduction in backpressure to ambient conditions and a higher valve lift compensates for the replacement of the

5.2. Modified Exhaust Valve Kinematic

The omission of an exhaust valve results in a halved valve spring return force. This can lead to a lift-off of the cam and cam roller while the reduced mass inertia remains approximately the same. Modifying the rocker arm's rotational inertia of mass seems to be the most promising approach to counter this as the reduced forces allow for optimizing the geometry to a greater extent. Still the final design is made from titanium Grade 5, as a further reduction of a steel or aluminum variant was not valid due to high dynamic stresses. The cam roller is slightly diminished to decrease the rotational inertia and improve the unwinding condition. The decrease of the cam rollers' diameter is possible as the halved valve spring return

FIGURE 24 CFD results of exhaust valve lift and backpressure adaptation: Simulation 1 = Reference, Simulation 2 = Modified cylinder head, Simulation 3 = Reduced backpressure, Simulation 4 = Scaled valve lift, Simulation 5 = Reduced backpressure + scaled valve lift.
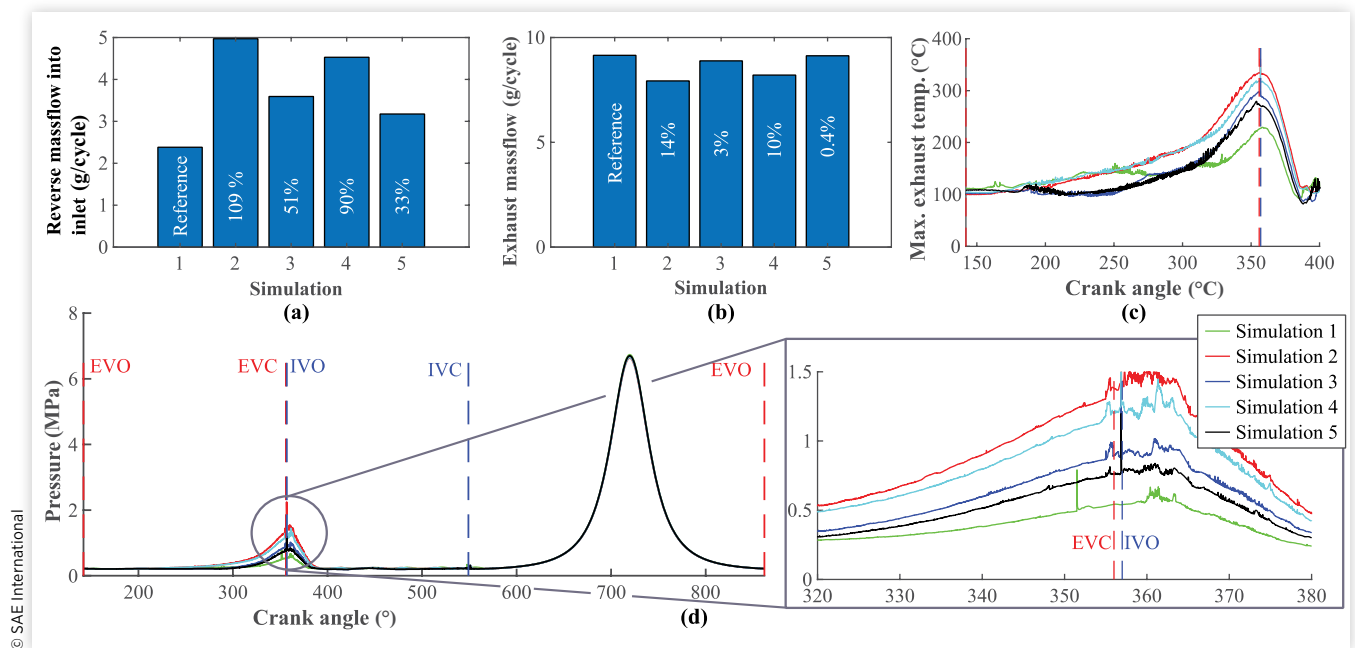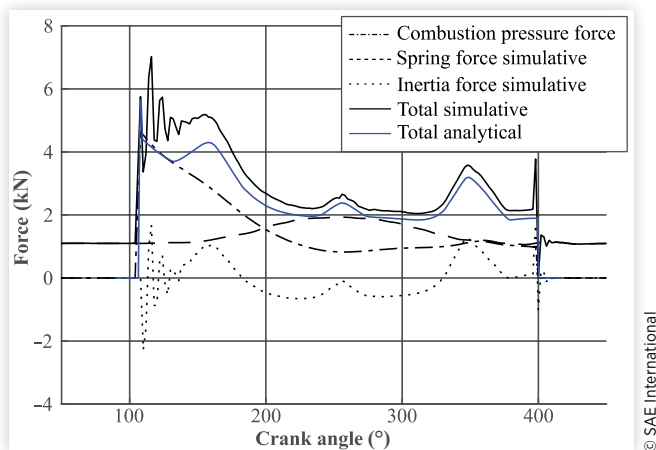
FIGURE 25 Exhaust valve actuation force.

© SAE International

FIGURE 26 Strength verification of the modified rocker arm.

© SAE International

force also decreases the contact pressure between cam and cam roller, which results in an almost-equal pit load-bearing capacity. The rotational inertia of the modified exhaust valve train could thus be reduced by 48% in contrast to the original design. Additionally, an adaptation of the cam profile is needed to realize the exhaust valve lift discussed before, which results in higher valve acceleration and an adapted valve actuation force. The multi-body simulation of the exhaust valve train is conducted using AVL's Excite software package. The model contains the complete valve train including the belt drive, two intake valves, and the modified exhaust valve. The model uses the overload engine speed of 2000 rpm as a worst-case scenario. Further, the maximum modified exhaust valve lift is set to 16 mm to consider manufacturing tolerances and gain safety reserves. To generate the suitable valve actuation force, the exhaust valve is subjected to a force resulting from mean combustion pressure scaled up to 20 MPa peak pressure. Analytical calculations verify the simulation results (cf. Figure 25). The simulative results are delayed in time due to dynamic effects which cannot be reproduced by the analytical calculation. Due to the combustion chamber pressure at the exhaust valve opening, the maximum valve actuation force at the valve side is about 7100 N. With respect to the lever ratio, a force of 7650 N is necessary to open the valve at this engine speed and combustion chamber pressure.

5.3. Modified Rocker Arm Strength Evaluation

The FEM models are set up in ANSYS Workbench according to cases one and two depicted in Figure 9 and are used to

TABLE 4 Material properties titanium Grade 5 (cf. [7]).

Tensile strength R_{mN}	895 MPa	Static safety margin	2.4
Yield stress R_{pN}	830 MPa	Dynamic safety margin	1.5
Fatigue strength	313 MPa		

© SAE International
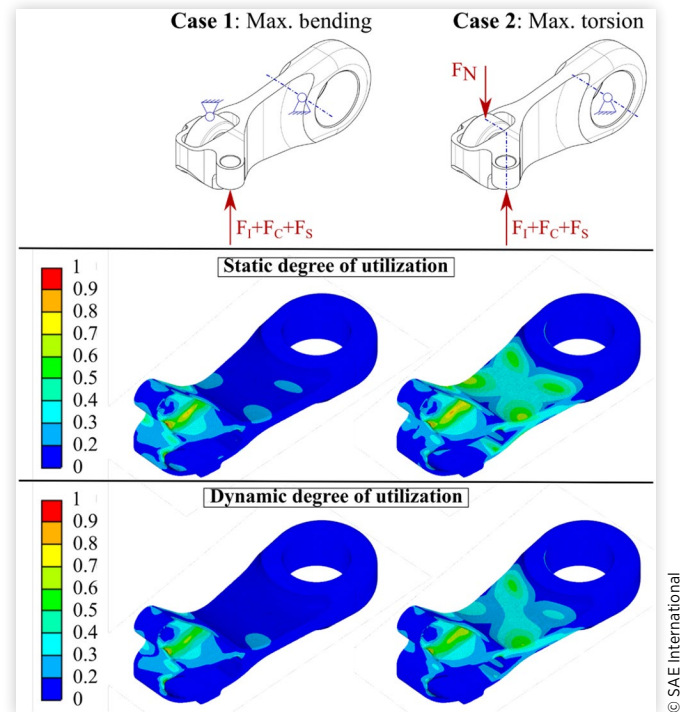
evaluate the static and dynamic degree of utilization calculated similar to [20] using the values listed in Table 4. The load applied as pulsating from 0 N to its maximum of $F_N = 7650$ N and $F_I + F_C + F_S = 7100$ N results from the kinematic analysis presented in the previous section and contains the inertia, combustion, and spring force.

With regard to a maximum possible bending and a maximum possible torsion, for both cases, the modified rocker arm made from titanium Grade 5 is not critical as the utilization ratios are less than 1 for static (0.96 and 0.87) and dynamic loads (0.85 and 0.80). Figure 26 depicts the calculated values. Due to this high material utilization, the choice of titanium seems justified. The high static utilization is intended for the valve train's overload case of 2000 rpm. While the engine is operated at 1500 rpm, the inertia force decreases by 43%. Additionally, the increased valve spring due to an increased valve lift results in a further safety margin of 6%. With this in mind, the rocker arm is stable for normal as well as for overload engine operating conditions.

6. Summary and Discussion

The modular design of the lateral and the fisheye endoscope access allows for individual as well as combined use of the access types.

The lateral access is realized by a ring integrated between the cylinder head and cylinder liner. It enables three different positions for mounting a UV-optimized endoscope. The small surface area of the endoscopic access in combination with an appropriate cooling concept makes this access suitable for stationary full-load engine operation. This is confirmed by the simulative tests shown. The vertical FOV shown is well suited for optical, as well as laser optical, investigations since two of the accesses are almost perpendicularly arranged to each other. By using the beam splitter, the visible and the UV part of the combustion can be observed synchronously with two cameras.

To extend the setup to a fully optically accessible engine, an outlet valve is replaced with the fisheye endoscope. It consists of two modular parts: the main 180° FOV fisheye optic and a relay optic with a magnification of 2:1. The design process is similar to the depicted procedure in [16] in which a starting point based on a literature-based design is optimized for use in a combustion engine. Key design challenges for the new design described in the current article are as follows:

- The limited dimension due to the available installation space
- Limited selection for the front element material due to thermal, mechanical, and chemical boundary conditions arising from combustion

In contrast to the optic shown in [16], the new optic is less than half the diameter and uses a much more cost-efficient quartz glass front lens instead of sapphire with no concern of birefringence. Additionally, the relay optic enhances the image diameter and brightness as much as possible, which is limited by the installation space, cost, and less image degradation.

The optics show good imaging quality with MTF > 0.3 at 50 lp/mm, or an object size of 0.01 mm. Test images taken from the combustion chamber using the entire optical system, including the camera and lens, confirm good imaging quality. Nevertheless, the fisheye endoscope is limited in its aperture number further due to the narrow and remaining image guidance through the protecting tube. As the availability of the low-dispersive materials is limited due to the thickness of the raw material, a compromise had to be found between:

- The number of elements in the relay optic as more elements degrade the image quality
- The thickness of the elements, which is limited by available raw material and manufacturing
- The cost of the expensive low-dispersion materials

Therefore, the relay optic has the sole purpose of minimizing the distance between the intermediate image and the camera. To improve brightness and image quality, several possibilities are conceivable:

- Extension of the relay optic and further optimization using, e.g., cost-intensive aspherical and gradient indexing lenses

- Replacement of the Sigma f180 2.8 objective with a further optimized relay optic
- Introducing glass fibers to redirect the fisheye optic's image to the camera

Similar approaches are used for a fisheye-like optic used to observe the combustion process in a horizontal engine with a 65 mm bore and 44 mm stroke used for lawnmowers (cf. [28]).

Nevertheless, imaging of the natural gas combustion process with a resolution of at least 1.5°CA is possible. As depicted, the recognition of the blue shimmering flame front is possible.

Due to the insertion of the fisheye endoscope and the necessary modifications of the cylinder head, a reduction in the combustion peak pressure to 80% of a comparable industrial gas engine is necessary to avoid failure of the cylinder head and the front lens. The fatigue for the critical cases was, therefore, examined in simulative investigations. Furthermore, a similar operation strategy as depicted in [16] is necessary to prevent the failure of the adhesive bond between the front lens element and its mount. A cooling of this bond lengthens the fired engine operating time. At least 25.5 s of a fired engine run is possible until the permanently tolerable temperature limit of 200°C of the adhesive is reached. This is indicated by the in-stationary CHT simulation results under worst-case conditions. This results in a quite sufficient number of fired engine cycles to reach almost stable engine operation. Considering a less critical engine operation point and the possible short-term overload temperature, an even longer duration seems possible.

An attempt has been made to compensate for the effects of the adjustment described above, especially on the charge change and thus on combustion behavior, by increasing the valve lift and reducing the exhaust backpressure. The 3D-CFD investigations confirm that a combination of both measures exhibits approximately the same behavior in terms of the gas mass flow returning via the intake valves and flowing out via the exhaust valve. This suggests an approximately equal residual gas mass with a changed distribution due to the higher pressure prevailing in the engine. Due to the higher pressure level in the exhaust valve opening, an increase in exhaust gas temperature must be accepted for the integration of the optics. Since no exhaust gas turbocharger is installed on the single-cylinder engine, this has no effect. The strength of the optimized titanium cam follower has been confirmed simulative up to an overload of 2000 rpm.

7. Conclusion and Outlook

The optical access developed herein consists of two individual usable setups. The full-load optical access especially developed with the least interference to the all-metal engine and a high load capacity is usable, e.g., for investigations of abnormal combustion as it is done in [17]. The lateral access design

presented here and its numerical treatment can be used as a guide to equip further large-bore engines with optical access. With this access, further optical and laser optical measurement techniques can be implemented to investigate combustion and emission formation under realistic conditions to further improve large-bore engines.

The fully optically engine setup using a fisheye endoscope is a less complex approach compared to a Bowditch type engine, but offers almost as much FOV and as many possible experimental setups. The design presented here is supplemented with a credible numerical treatment to demonstrate the feasibility regarding the component fatigue and especially the imaging quality of the optics. This procedure can also be used as a guide to transfer the design to other engines. In contrast to the full-load optical setup, the fully optical one shows more design changes compared to the all-metal engine needed to integrate the fisheye endoscope. CFD investigations of the in-cylinder flow show a possibility of reducing the difference of the gas exchange behavior due to the replaced exhaust valve. The presented design further shows the following improvements especially concerning the design presented in [16] on which it is based on.

- The optimized design space of the fisheye endoscope, which results in a 41% reduced diameter compared to [16].

- An increased optical imaging quality compared to [16].

- An equal mechanical stability of the fisheye endoscope compared to [16], especially as the less stable quartz glass material is used here.

- The optimized design can also be used in engines with an even larger bore with less modification due to the optimized design space.

To prove the reliability of the designs, an experimental comparison between the different engine setups from the all-metal engine to the fully optical one was conducted and will be presented in a further publication. Nevertheless, the presented optical setups provide an optimized optical access to a large-bore high-speed engine capable of different state-of-the-art optical and laser optical measurement techniques. These insights are needed to complement thermodynamic investigations of the all-metal engine to gain knowledge about the combustion of especially renewable fuels for further improvements.

Author Contribution

The complete writing, implementation, evaluation, and interpretation of the depicted simulative and experimental data and the final design of the optical test engine belong to Stephan Karmann. Hannes Röhrle supported the work during his master's thesis, developing the basic design of the optical test engine. Bernhard Klier supported the work during his semester thesis, developing the basic optical design of the fisheye endoscope. The remaining co-authors supported the work with their reviews.

Contact Information

Stephan Karmann
karmann@lvk.mw.tum.de

Definitions/Abbreviations

ASTI - Astigmatism

°CA - Degree crank angle

CFD - Computational fluid dynamics

CHT - Conjugate heat transfer

DIST - Distortion

EFL - Equivalent focal length

FEM - Finite element method

FEO - Fisheye optic

FOV - Field of view

HS - High speed

HTC - Heat transfer coefficient

LCA - Longitudinal color aberration

MBS - Multi-body simulation

MFB - Mass fraction burnt

MTF - Modulation transfer function

OPD - Optical path difference

PETZ - Petzval curvature

RANS - Reynolds-averaged Navier-Stokes equation

RMS - Root mean square

SPH - Spherical aberration

TC - Thermocouple

TCA - Transversal color aberration

References

1. Dierksheide, U., Meyer, P., Hovestadt, T., and Hentschel, W., "Endoscopic 2D Particle Image Velocimetry (PIV) Flow Field Measurements in IC Engines," *Exp Fluids* 33, no. 6 (2002): 794-800, https://doi.org/10.1007/s00348-002-0499-3.

2. Hultqvist, A., Christensen, M., Johansson, B., Richter, M. et al., "The HCCI Combustion Process in a Single Cycle - Speed Fuel Tracer LIF and Chemiluminescence Imaging," SAE Technical Paper 2002-01-0424, 2002, https://doi.org/10.4271/2002-01-0424.

3. Einecke, S., Schulz, C., and Sick, V., "Measurement of Temperature, Fuel Concentration and Equivalence Ratio Fields

Using Tracer LIF in IC Engine Combustion," *Appl Phys B* 71, no. 5 (2000): 717-723, https://doi.org/10.1007/s003400000383.

4. Pöllmann, S., Härtl, M., and Wachtmeister, G., "Injection Process of the Synthetic Fuel Oxymethylene Ether: Optical Analysis in a Heavy-Duty Engine," SAE Technical Paper 2020-01-2144, 2020, https://doi.org/10.4271/2020-01-2144.

5. Fatouraie, M. and Wooldridge, M., "Optical Investigation of the Effects of Ethanol/Gasoline Blends on Spark-Assisted HCCI," *Journal of Engineering for Gas Turbines and Power* 136, no. 8 (2014): 081507, https://doi.org/10.1115/1.4026862.

6. Sequino, L., Belgiorno, G., Di Blasio, G., Mancaruso, E. et al., "Assessment of the New Features of a Prototype High-Pressure "Hollow Cone Spray" Diesel Injector by Means of Engine Performance Characterization and Spray Visualization," SAE Technical Paper 2018-01-1697, 2018, https://doi.org/10.4271/2018-01-1697.

7. Beatrice, C., Belgiorno, G., Di Blasio, G., Mancaruso, E. et al., "Analysis of a Prototype High-Pressure 'Hollow Cone Spray' Diesel Injector Performance in Optical and Metal Research Engines," SAE Technical Paper 2017-24-0073, 2017, https://doi.org/10.4271/2017-24-0073.

8. Wellander, R., Rosell, J., Richter, M., Alden, M. et al., "Study of the Early Flame Development in a Spark-Ignited Lean Burn Four-Stroke Large Bore Gas Engine by Fuel Tracer PLIF," *SAE Int. J. Engines* 7, no. 2 (2014): 928-936, https://doi.org/10.4271/2014-01-1330.

9. Bowditch, F.W., "A New Tool for Combustion Research A Quartz Piston Engine," SAE Technical Paper 610002, 1961, https://doi.org/10.4271/610002.

10. Gleis, S., Frankl, S., Waligorski, D., Prager, D. et al., "Investigation of the High-Pressure-Dual-Fuel (HPDF) Combustion Process of Natural Gas on a Fully Optically Accessible Research Engine," SAE Technical Paper 2019-01-2172, 2019, https://doi.org/10.4271/2019-01-2172.

11. Gleis, S., Frankl, S., Prager, M., and Wachtmeister, G., "Optical Analysis of the Combustion of Potential Future E-Fuels with a High Pressure Dual Fuel Injection System," in *14th International AVL Symposium on Propulsion Diagnostics*, Baden-Baden, Germany, 2020.

12. Korb, B., Kuppa, K., Nguyen, H.D., Dinkelacker, F. et al., "Experimental and Numerical Investigations of Charge Motion and Combustion in Lean-Burn Natural Gas Engines," *Combustion and Flame* 212 (2020): 309-322, https://doi.org/10.1016/j.combustflame.2019.11.005.

13. Frankl, S., Gleis, S., and Wachtmeister, G., "Interpretation of Ignition and Combustion in a Full-Optical High-Pressure-Dual-Fuel (HPDF) Engine Using 3D-CFD Methods," in *CIMAC CONGRESS 19, 29th CIMAC World Congress on Combustion Engine, Meeting the Future of Combustion Engines*, Vancouver, BC, Canada, June 10-14, 2019.

14. Karmann, S., Prager, M., and Wachtmeister, G., "Conceptual Investigations on Full Optical Accessibility to Large-Bore

Medium-Speed Engines," *SAE Int. J. Engines* 12, no. 3 (2019): 291-308, https://doi.org/10.4271/03-12-03-0020.

15. Duong, J., "Combustion Visualization in a Large Bore Gas Engine," Thesis for the Degree of Licentiate in Engineering, Lund University, Lund, 2013.

16. Karmann, S., Friedrich, C., Prager, M., and Wachtmeister, G., "Realization of a Fully Optically Accessible Medium Speed Large Bore Engine Using a Fisheye Optic," in *ASME 2020 Power Conference*, Virtual, Online, 2020, https://doi.org/10.1115/POWER2020-16477.

17. Eicheldinger, S., Karmann, S., Prager, M., and Wachtmeister, G., "Optical Screening Investigations of Backfire in a Large Bore Medium Speed Hydrogen Engine," *International Journal of Engine Research* (2021), https://doi.org/10.1177/14680874211053171.

18. Karmann, S., Kunkel, C., Prager, M., and Wachtmeister, G., "A New Optical Access for Medium Speed Large Bore Marine Engines under Full-Load Operating Conditions," *SAE Int. J. Engines* 14, no. 6 (2021): 867, https://doi.org/10.4271/03-14-06-0052.

19. Eicheldinger, S., Bartkowski, T., Schröder, A., Prager, D. et al., "Experimental Investigation on the Influence of Brake Mean Effective Pressures up to 30 bar on the Behavior of a Large Bore Otto Gas Engine," SAE Technical Paper 2019-01-2224, 2019, https://doi.org/10.4271/2019-01-2224.

20. Maschinenbau, F., *Rechnerischer Festigkeitsnachweis für Maschinenbauteile aus Stahl, Eisenguss- und Aluminiumwerkstoffen*, 6th ed. (Frankfurt am Main, Germany: VDMA-Verl, 2012)

21. Unfug, F., "Experimentelle und numerische Untersuchung der Verbrennung eines mittelschnelllaufenden 4-Takt Dieselmotors," PhD dissertation, Logos Berlin, Berlin, 2013.

22. Nakagawa, J., Ultra_wide_angle_photographic lens. US Patent 3,741,630, 26 June, 1973.

23. Kweon Gyeongil, L.M., Fisheye lens. US Patent 8,064,149 B2, 22 November 2011.

24. Samy, A.M. and Gao, Z., "Simplified Compact Fisheye Lens Challenges and Design," *J Opt* 44, no. 4 (2015): 409-416, https://doi.org/10.1007/s12596-015-0260-y.

25. Laikin, M., *Lens Design*, 2nd ed. (New York: Marcel Dekker, 1995)

26. Sasián, J., *Image Evaluation/Introduction to Lens Design* (Cambridge: Cambridge University Press, 2019)

27. Sapra, H., Godjevac, M., Visser, K., Stapersma, D. et al., "Experimental and Simulation-Based Investigations of Marine Diesel Engine Performance against Static Back Pressure," *Applied Energy* 204 (2017): 78-92, https://doi.org/10.1016/j.apenergy.2017.06.111.

28. Wilson, T.S., "The Research and Development of In Situ Non-intrusive Optical and Temperature Diagnostics in an Internal Combustion Engine," PhD thesis, School of Engineering, University of Warwick, 2002.

B.4   Veröffentlichung 4 im Original

Karmann, S.; Eicheldinger, S.; Prager, M.; Jaensch, M.; Wachtmeister, G. Experimental Com-parison Between an Optical and an All-Metall Large Bore Engine. International Journal of Engine Research 2022,146808742210827. doi: 10.1177/14680874221082794.

Reprinted with permission from International Journal of Engine Research

©SAGE Publications

Experimental comparison between an optical and an all-metal large bore engine

Stephan Karmann[1] , Stefan Eicheldinger[2] , Maximilian Prager[2] ,
Malte Jaensch[2] and Georg Wachtmeister[1]

Abstract
Rising engine efficiency, increasingly stringent exhaust limits, and the use of synthetic and renewable fuels are all factors that demand a deeper knowledge of the combustion process. State-of-the-art investigations employ optical and laser-optical measurement techniques that rely on having optical access to the engine. In this paper, a new endoscopic system that provides full optical access to a high-speed large-bore engine is compared by thermodynamic experimentation to the equivalent all-metal engine. This comparison provides an insight into the altered combustion behavior resulting from modifying the engine to accommodate the optical elements. The successfully realized concept consists of two individually usable access points integrated in an engine with a bore of 170 mm and a stroke of 210 mm. The lateral endoscopic access is designed for full-load operating conditions and provides the best comparability to an all-metal engine. It is compared directly to the all-metal engine in the present investigations. Despite the changes in engine-out emissions from the optical engine, the experimental results display relatively equal combustion behavior in both setups. The lateral endoscopic access is then extended by adding a fisheye endoscope in place of one exhaust valve. This setup is compared to findings obtained with the endoscopic lateral access. The investigations reveal further deviations of the combustion process due to the more extensive modifications needed to fit the fisheye endoscope to the cylinder head. Nevertheless, the results display an overall good level of comparability of the combustion behaviors in these setups and, in turn, of the validity of further fundamental experiments based on the optical engine.

Introduction

As the energy revolution continues, the use of renewable energies is expanding. In the EU, for example, the share of power consumption attributable to renewable energies increased from 8.5% in 2004 to 18% in 2018 (cf. Pressemitteilung Eurostat[1]). In realizing a sustainable, cost-effective, and stable supply of energy in an industrialized and globalized world, the power to X process plays a key role in a sector-coupling approach. The power to X process stabilizes seasonal and regional fluctuations in residual loads by enabling the (long-term) storage of overproduced renewable energies in the form of renewable gaseous fuels such as hydrogen and methane and renewable synthetic liquid fuels such as OME. In existing infrastructures, synthetic methane or methane-hydrogen mixtures can replace fossil natural gas. In times of underproduction, renewably generated chemical energy carriers can be used to stabilize the energy supply, for instance by reconverting them to electricity and heat in combined heat and power plants. For this purpose, stationary gas engines are known to be a reliable and efficient technology. To investigate the effects of new synthetic fuels on combustion, optical and laser-optical measurement methods are required, together with thermodynamic

[1]Institute of Internal Combustion Engines, Technical University of Munich, Munchen, Bayern, Germany
[2]School of Engineering and Design, Technical University of Munich, Munchen, Germany

Corresponding author:
Stephan Karmann, Institute of Internal Combustion Engines, Technical University of Munich,Schragenhofstr. 31, Munchen, Bayern 80992, Germany.
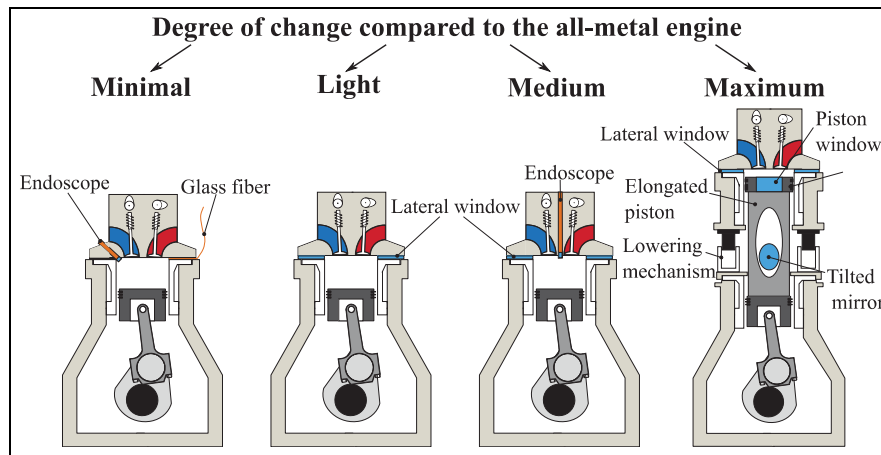Email: karmann@lvk.mw.tum.de

Figure 1. Degree of optical accessibility.

experiments. These techniques make it possible, for example, to assess the mixture composition during the gas exchange cycle; this has a direct effect on combustion, emission formation and combustion anomalies and, in turn, on engine efficiency. Combustion and the location of any anomalies that may occur (such as lube oil ignition, backfiring or knocking) can then be observed and understood. The basic prerequisite for these measurement techniques, which are already used widely in the passenger and truck vehicle displacement class to investigate synthetic fuels, for example (cf. Refs.[2–11]), is that the engine permits optical access. Neither optical access nor the investigation of large bore engines are very common (cf. Refs.[12–19]). According to Karmann et al.,[20] Bensing,[11] there are four basic types of optical access, depending on the degree of change that this necessitates in relation to the all-metal engine (cf. Figure 1).

As the degree of optical accessibility and the modification requirements increase, the comparability of the optical setup with the all-metal engine decreases. This is mainly due to the introduction of glass components, resulting in changes to the heat transfer, modified engine components to accommodate the optical design, and, in some cases, the need to adapt the engine operation mode. Optical access with the maximum scope for modification is constructed according to the Bowditch principle[21] and requires by definition:

- a modified crankshaft drive plus attendant changes to the tribological system of the piston and liner
- reduced engine speed due to increased inertia forces
- an increased proportion of glass components plus their temperature-sensitive mounts

Further adaptation of the operation to an often load-reduced skip fire operation mode is necessary. This approach is particularly common in the car and truck engine displacement class. Korb and Gleis present an application of this approach for a high-speed large-bore gas engine (cf. Refs.[22,13,23,19]). The effects of the maximum amount of change on engine behavior compared to the equivalent all-metal, for passenger-car-sized engines are shown in Colban et al.,[24] Kashdan et al.[25] and Kashdan and Thirouard[26] The engine-out emissions are particularly strongly affected. In order to overcome the disadvantages of the Bowditch approach in large bore engines, while also enabling maximum optical accessibility, an endoscopic method was developed for a high-speed large bore engine similar to that in Karmann et al.[27] This setup uses a fisheye endoscope to obtain a horizontal field of view inside the cylinder and a UV-optimized endoscope with an aperture angle of about 50° for a vertical field of view. This approach is in the medium change class according to Figure 1. The following describes the experimental comparison of the optical setup and all-metal engine that were performed to characterize the effects of the respective modifications on engine behavior.

Engine setup

Only a brief summary will be given here, as a detailed description of the three different engine setups can be found, for instance, in Eicheldinger et al.[28] for the all-metal engine and in Karmann et al.[29] for the optical setups. For simplification, the engine setups are denoted as 1 (all-metal engine), 2 (full-load optical setup) and 3 (full optical setup).

All-metal engine – setup 1

The all-metal engine is a single-cylinder research engine with a bore of 170 mm, a stroke of 210 mm, and a resulting displacement of 4.8 dm^3. The engine can run on both gaseous and liquid fossil and renewable fuels in a variety of combustion processes, such as HPDF (high pressure dual fuel,[13,30]) LPDF (low pressure dual fuel,[31]) or scavenged and unscavenged prechamber spark plugs.[32,28] Figure 2 shows the setup consisting of the cylinder head, cylinder liner and liner housing. The setup uses as well as all further settings the same
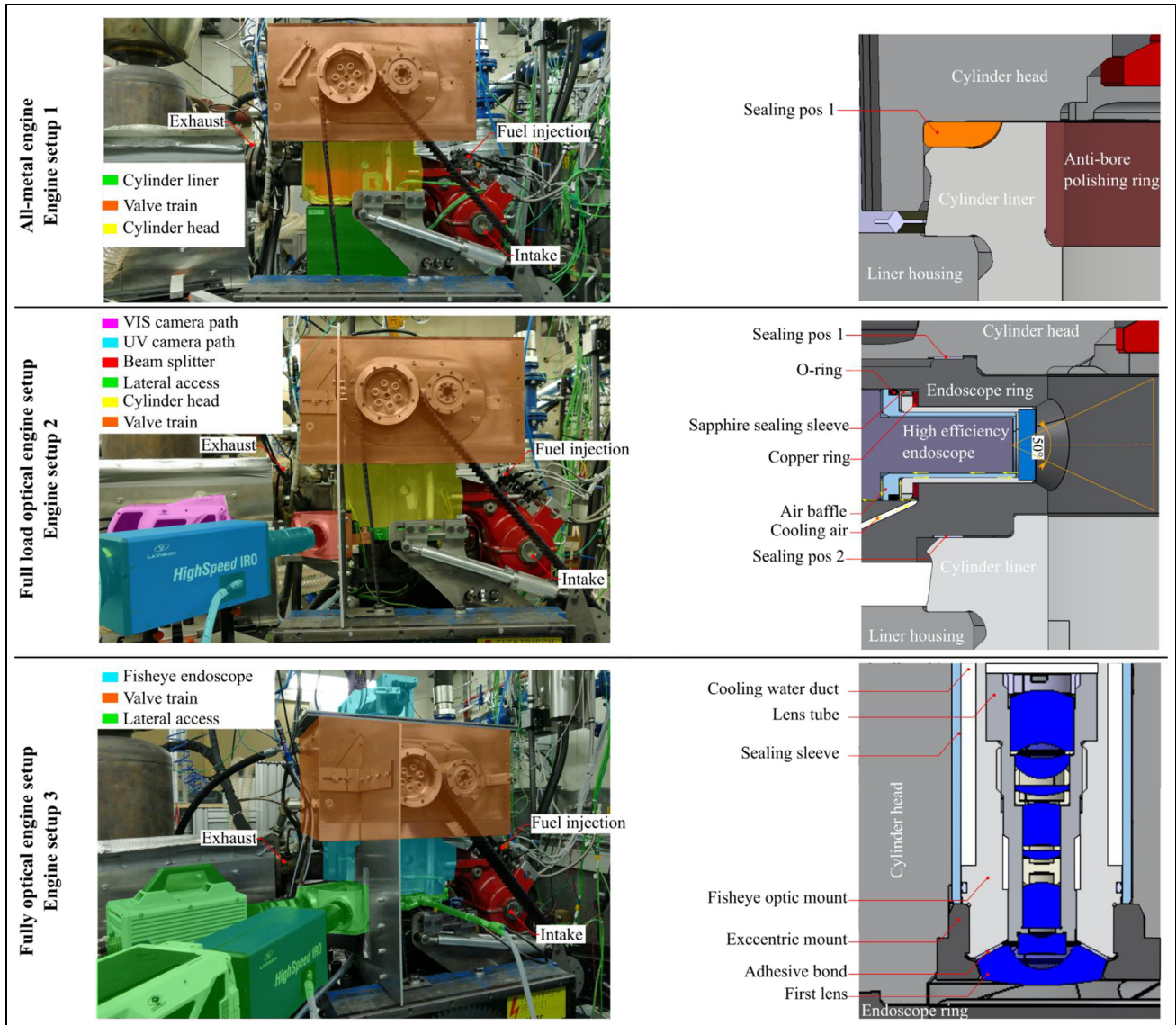
Figure 2. Overview of engine setups 1–3.

Full-load optical engine setup – setup 2

The optical setups are based on the design studies presented in Karmann et al.[33] and use the same testing rig infrastructure and base engine as Setup 1. The full-load optical setup consists of an endoscope ring integrated between the cylinder head and cylinder liner (cf. Figure 2). The endoscope ring is sealed with metal gaskets at Position 1 beneath the cylinder head and Position 2 on the liner. The setup uses adapted series parts, such as a slightly modified cylinder head and liner. To withstand continuous full-load operation conditions, water cooling is integrated into the endoscope ring. The endoscope assembly further provides a self-developed air cooling system. Further, the sapphire sealing sleeve from FOS Meßtechnik GmbH can withstand 300 bar and 600°C and is modified to suit the air cooling, as shown in Figure 3. The endoscope ring offers three mounting positions for the LaVision high efficiency UV endoscope. The endoscope has a field angle of 25°. A beam splitter is used to simultaneously record both UV and natural-flame chemiluminescence in the visible spectral range, (cf. Figure 2).

In contrast to the all-metal engine, the full-load optical engine setup has a cooling circuit in the upper section of the liner where the endoscope ring is introduced, resulting in a relatively low cylinder wall temperature in this region. Due to the altered material, the endoscope ring (42CrMo4) has a lower heat conductivity than the original cylinder liner, which decreases the cooling effect by about 13%. The endoscope ring is fitted by
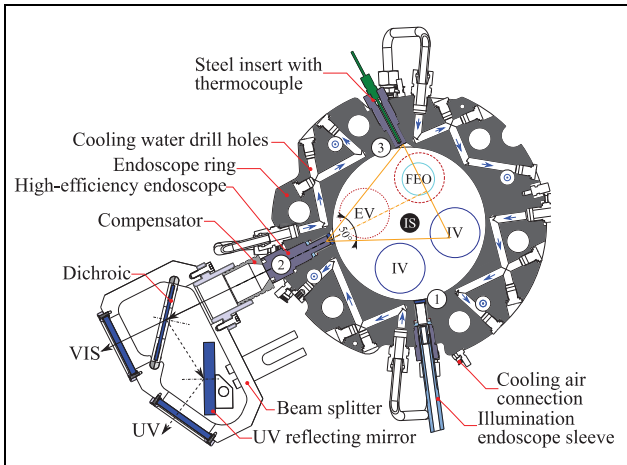
The parts are all commercially available series parts. The geometric compression ratio can be adjusted by inserting spacers between the liner housing and the base engine to modify the clearance height.

Figure 3. Horizontal sectional view of setup 2 and setup 3.

first removing the anti-bore polishing ring. As the overall run time of the engine during the tests was short, omitting this part is not critical. The presence of the endoscope ring increases the engine's dead volume by the second sealing height; this is also due to the recesses in the endoscope ring marking the endoscope positions. The dead volume arising from additional gaps due to the two sealing positions and the integration of the endoscope mounting holes increases to 1.75 times the dead volume of the all-metal engine (which equals an increase of 0.006l). To gain a constant compression ratio for the following experiments the clearance height was adjusted with the modification of the setup's liner housing and an adjustment of the spacers. The uncertainty of the geometric compression ratio amounts to ±0.05 for the geometric compression ratio of 11.6 used in the following experiments, mainly due to manufacturing tolerances. Due to the high fire land of the piston with 25 mm, no further modifications are necessary to integrate the endoscope ring.

Full optical engine setup – setup 3

The full optical engine setup (cf. Figure 2) combines Setup 2 with a modified cylinder head capable of supporting a fisheye endoscope replacing one of the exhaust valves. This alters the gas exchange behavior due to the increased exhaust back pressure. The same additional dead volume as in Setup 2 arises in Setup 3 on account of the integration of the endoscope ring. As the exhaust valve is replaced by the fisheye endoscope and its mount, the additional dead volume causes a loss in the geometric compression ratio of about 0.7% at the compression ratio of 11.6. Due to non-optimized spacers for the adjustment of the compression ratio, as well as the uncertainty due to the manufacturing tolerances of the fisheye optic mount and the modifications at the cylinder head to fit the assembly, this small loss was acceptable and the compression ratio is assumed as equal. The first lens is made from quartz glass and is directly mounted in the combustion chamber. The lens

is glued precisely to its mount using a temperature-stable silicon-based adhesive capable of withstanding a 200°C continuous and 250°C peak temperature. To prevent the adhesive bond from overheating and failing, a strategy is required similar to those used in Bowditch-design engines (cf. Section 1). In Setup 3, skip fire engine operation is feasible for at least 150 fired cycles, thanks to the specially designed cooling system for the fisheye endoscope. The operating strategy of setup 3 is further detailed in section 3.3. The engine peak pressure has to be reduced to prevent the cylinder head from failure, as it is weakened by the modifications needed for mounting the optic. Simulations estimate that a minimum peak pressure of 180 bar can be endured, as shown in Karmann et al[29]. The fisheye endoscope has a field angle of up to 180° and redirects the combustion's natural chemiluminescence via a 45° deflection mirror to the camera mounted outside the engine. The glass surface of the first lens diameter is 32 mm, which is only 3.5% of the bore area comparable less concerning the Bowditch principal with its large piston window.

Experimental setup and procedure

After the description of the different setup's designs the following summarizes briefly the testing rigs infrastructure equal for all three setups and the chosen experimental procedure.

Testing rig infrastructure

The test rig provides preconditioned and automated cooling water and oil supplies. Further, the test rig supplies pressure and temperature-controlled intake air at up to 9 bar. The air mass flow is measured using a rotary piston gas meter. The turbocharger is simulated by a controllable exhaust throttle, and the engine is connected to a coupled break, consisting of an induction machine and a dynamometer. The test rig provides both automated data acquisition and a control system. The fuel is natural gas from the municipal gas supply with a methane number of 90. The fuel mass flow is measured with a coriolis mass flow meter. The engine's exhaust pressure, intake pressure and combustion chamber pressure are indicated and logged by an automated measurement acquisition system. The recording rate of the fast measurement values is 0.1°CA. For combustion pressure recording the Kistler 6041B piezo-electric pressure transducer and 5011B charge amplifier are used. The measurement of the intake pressure is realized using a Kistler 4045A10 piezoresistive pressure transducer. The exhaust pressure is recorded with a Kistler piezoresistive pressure transducers 4075A10 in combination with a Kistler 7533B switching adapter. Both pressure transducers are connected to a corresponding Kistler charge amplifier 4603. To prove the plausibility of the recorded data, two slow pressure transducers in the intake and exhaust line of WIKA s10 type are used.

Setup and procedure

The full-load setup shown here is designed to be as close as possible in terms of its thermodynamic behavior to the all-metal engine with no lateral endoscopic access after a minimum of adjustments. The two setups are therefore compared directly. Further this comparison states the comparability of the findings described in Eicheldinger et al.[34] and Karmann et al.[35] with the all-metal engine.

The addition of the fisheye endoscope to the full-load setup can already be seen to have a significant effect, primarily on the gas exchange, and necessitates a reduction in the engine load (cf. Section 2). The two optical setups under reduced load are therefore compared and analyzed to determine the extent to which the combustion behavior is altered by the presence of the fisheye endoscope.

Water cooling for the fisheye optic was intended for the experiments, like it is described in Karmann et al.[29] Due to manufacturing issues that caused slight water leakage from the cooling duct into the lens setup, it had to be substituted by air cooling. Air cooling prevents contamination of the lens setting and still provides sufficient cooling to the lenses. Nevertheless, due to the reduced heat capacity and lower cooling capability of air, it was necessary to reduce the operation time of the fired engine. To compensate for this, the engine load was decreased further to a maximum peak pressure of 120 bar for the comparisons with the fisheye endoscope. Further, the engine's cooling water temperature was decreased by 5°C to extend the available measurement time. The nominal engine speed was reduced by 50% for both optical setups to prevent strong engine vibrations from affecting the cameras. Nevertheless, the designs without the cameras were still capable of achieving the nominal engine speed (cf. Karmann et al.[29]).

Table 1 shows the data of the two setups in the following comparison.

According to the detailed description given in Karmann et al.,[29] the exhaust valve lift was modified to account for the differences in gas exchange behavior. In contrast to the modification described in Karmann et al.,[29] the maximum lift of both valves is equalized. This is due to the use of a different cam profile in the experiment for Setups 1 and 2 than in the simulative investigations presented in Karmann et al.[29]

The intake valve lift is the same in all setups. The valve lift of the exhaust valve is changed slightly in setup 3 to take advantage of the higher in-cylinder pressure when the exhaust valve is open and to enhance the exhaust gas mass flow.

The maximum lift is achieved almost simultaneously in all setups. Reducing the valve overlap causes the exhaust valve in Setup 3 to close 15°CA earlier than in both other setups. Figure 4 shows the measured valve lift curves for the exhaust and intake. The maximum exhaust valve lift is equal in all setups. 148 consecutive cycles are recorded for all setups and used for thermodynamic data processing. Setup 2 and 3 use 50 out of 148 cycles for image recording due to limited storage capacity of the camera setup. At each of the indicated measurement points the filtered combustion chamber pressure curves are corrected using a two-point polytropic offset correction. With a tuned GT-Power TPA (three pressure analysis) model the burning duration and heat release rate are derived, taking into account the wall heat losses calculated according to GT's so called WoschniGT approach.

The IMEP coefficient of variance, which is an indicator of combustion stability, is calculated by equation (1). Therefore, the corrected pressure traces used come directly from the data acquisition system of the test rig (cf. Chen et al.[7]).

$$CoV_{IMEP} = \frac{\sqrt{\frac{1}{N} \cdot \sum_{i=1}^{N} (IMEP_i - IMEP_m)^2}}{IMEP_m} \cdot 100 \% \quad (1)$$
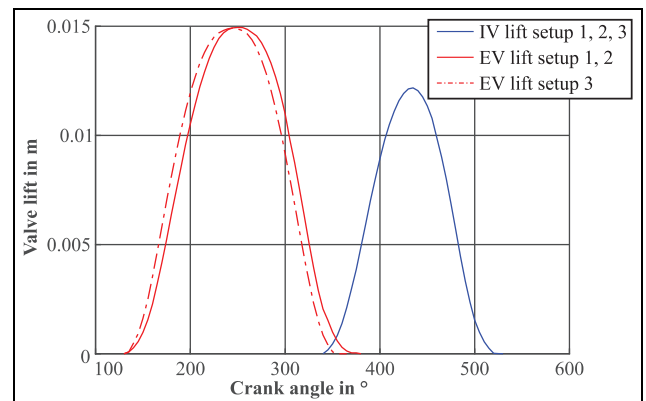
Table 1. Overview of the experimental setup.

	Comparison 1: Engine setup 1 Engine setup 2	Comparison 2: Engine setup 2 Engine setup 3
ε	11.6 ± 0.4%	11.6 ± 0.7%
Engine Load	IMEP 21 bar	IMEP 16 bar
Injection pressure	12 bar	12 bar
Ignition	Unscavenged prechamber spark plug	
Engine speed for experiments	750 rpm	
Nominal engine speed	1500 rpm	
Sol	350°CA bFTDC	
Fuel	Natural gas	
Bore	170 mm	
Stroke	210 mm	
Conrod length	480 mm	

Figure 4. Valve lift (EV = Exhaust valve, IV = Intake valve).

Skip fire operation strategy

As already mentioned, only engine setup 3 uses a skip fire operation strategy to keep the temperature limits of the fisheye endoscope in certain simulative estimated (cf. Karmann et al.[29]) bounds. Especially the temperature of the adhesive bond between the first lens of the optic and its mount limits the operation strategy and is therefore measured nearby for control. A similar approach was used in Karmann et al.[27] The start of the recording of thermodynamic values and the image capturing is controlled manually. Figure 5 shows the skip fire strategy for the measurement series of the CoC (center of combustion) variation for 10°CA aFTDC on the left of the image and on the right of the image for 8°CA aFTDC at an air-fuel equivalence ratio of 1.7. The CoC equals the 50% mass fraction burned. The image contains the temperature profile measured near the adhesive bond over the experiment time. The engine starts firing and reaches for the specified value of the CoC by online adjustment of the ignition timing to keep the CoC in the target with a range of ±1.5°CA. The air mass needed for a specific air-fuel equivalence ratio was defined in preceding tests with a constant amount of fuel to reach a specific load.

The thermodynamic data recording starts when the fisheye endoscope reaches a temperature limit specified in preliminary tests and covers 148 fired cycles. The start temperature of the image recording is no fixed value, but actually depends on the actual air-fuel equivalence ratio, load and CoC resulting in a faster or slower heat up and thus higher or lower end temperature of the fisheye endoscope. Therefore, the start temperature is preliminarily derived for each investigated point meeting the boundary conditions of not reaching the automatic shut off temperature and providing a sufficient amount of fired cycles for a sufficient settling time to reach a stable combustion state. The image recording of 50 cycles starts with an offset of about 50 cycles to the thermodynamic data capturing to gain more settling time for the combustion. Figure 5 shows the automatic shut off temperature of 125°C.

The automatic measurement acquisition system provides two different recordings. One uses a slow 1Hz circle for continuous data logging. The fast one uses a resolution of 0.1°CA for the indication of the intake, exhaust and combustion chamber pressure. The continuous data logging freezes for about 4 s shortly before the high resolution circuit finishes and uses the complete communication bandwidth between the real-time system and the control computer for storing the data. This results in Figure 5's visible logging freeze and the challenge not to pass the shut off temperature accidentally during this time without providing the actual control temperature, especially as this effect leads to a sudden temperature increase of about 5°C after finishing the data storing. A fired cycle sequence lasts on average for 74 s respectively 462 cycles.

After the fired cycles the fueling and ignition are shut off and the engine changes its operation from a fired to a motored one: the cool down cycles. During the unfired cycle sequence the engine cools down until reaching the start temperature of at most 85°C. Such a cool down duration was observed to last for up to 6 minutes depending on the endoscope's end temperature.

Emission measurement under skip fire operation

Gleis[13] investigated the response time of the same AVL FTIR as used for the following investigations under skip fire engine operation at a Bowditch type fully optically accessible HPDF engine. At least 70 fired cycles were needed before the measurement data recording reaches nearly constant emission levels. Nevertheless, as Gleis et al.[13] uses a much more stable diesel combustion process and no other investigation from literature for a prechamber spark ignited optically engine was found, Figure 6 proofs the here achieved settling time sufficient for plausible emissions behavior. The settling time for the measurement of the emissions depicted in Figure 5 includes the duration from start of combustion detected as the first increase in the effective engine
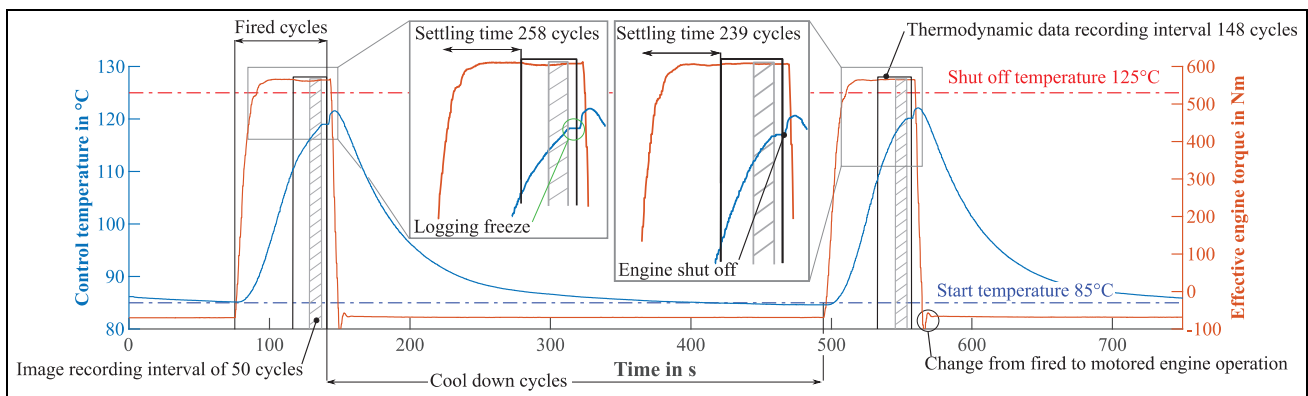

Figure 5. Skip fire operation strategy for air-fuel equivalence ratio 1.7 from left to right CoC variation for 10 and 8°CA aFTDC.
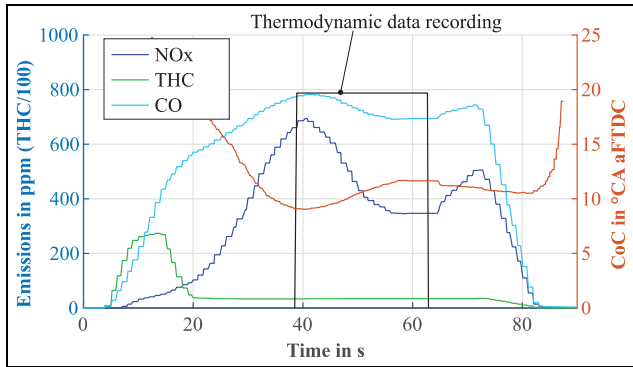
Figure 6. Emissions and CoC trace at air-fuel equivalence ratio 1.7 and CoC = 10°CA aFTDC (THC emissions are scaled by a factor of 100).

Figure 7. Gas and air mass traces at air-fuel equivalence ratio 1.7 and CoC = 10°CA aFTDC.

torque until the start of the thermodynamic data recording. Further, Figure 6 shows exemplarily the trace of the online calculated CoC and measured emissions traces over time for data recording. Emissions are recorded and then averaged with a moving average of the last 10 values before getting logged with 1HZ. The CoC is averaged over the last 148 working cycles and then logged with 1 HZ.

CO emissions show a maximum variation of 78.3 ppm during data logging, indicating that they are nearly constant throughout data recording. The THC emissions show even fewer deviations during the measurement interval. The increased variation of 314.2 ppm in NOx emissions during data logging is due to the high sensitivity of NOx formation to cyclic variations typical of spark ignited combustion processes. Since the emission traces of the remaining CoC variation show similar behavior in skip fire operation, the values can represent a clear trend in emission behavior over the conducted experiments and support the comparable behavior of engine Setup 3 with Setup 2. However, the comparison of absolute values, especially for NOx emissions is not recommended as long as no increase of stalling time is realized. To ensure that this variation in NOx emissions is not due to a fluctuating air to fuel equivalence ratio, Figure 7 examines air mass flow and fuel mass flow at a CoC of 10°CA aFTDC in skip fire operation.

The target gas mass flow of 8.44 kg/h is reached with a peak deviation of 0.35% during the recording period. The target air mass flow of 247.5 kg/h is achieved with a maximum deviation of 1.7% in the recording period. If the measurement uncertainty of the air mass flow meter and the coriolis gas flow sensor are also taken into account, the deviation of the air to fuel equivalence ratio can be specified. The target value of 1.7 can be reached within a deviation of ±0.027 respectively 1.58% during recording. This is sufficiently accurate for the investigations and for stable combustion.
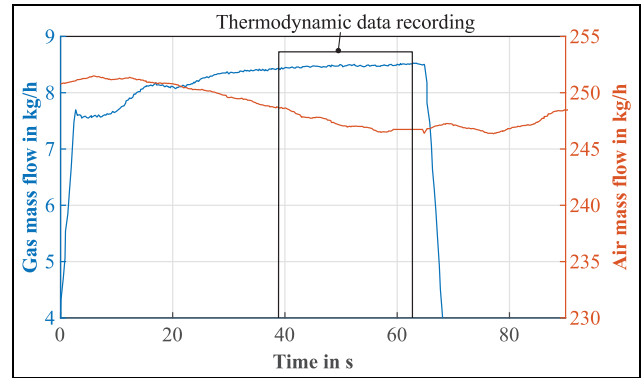
Experimental comparison between the all-metal engine and the full-load optical engine setup: Comparison I

To compare the all-metal engine with the full-load optical engine setup, an air-fuel equivalence ratio and CoC (center of combustion) which equals the MFB 50 (50% mass fraction burned) variation map is considered at a constant load of up to 21 bar IMEP (indicated mean effective pressure). The air-fuel equivalence ratio variation is evaluated in steps of 0.05 from 1.5 to 1.85. The uncertainty of the lambda calculation is 0.23% resulting from the accuracy of the measurement devices. The CoC is investigated at $8^{\pm 1}$, $10^{\pm 1.5}$, $15^{\pm 1.5}$, $20^{\pm 1.5}$ and $25^{\pm 1.5}$°CA aFTDC. The specified uncertainties are due to the engine control tolerances. Regarding the theoretical thermodynamic optimum, the following evaluation focuses on the CoC at 8°CA aFTDC. The measurement data are evaluated for combustion and emission behavior.

Combustion pressure

Figure 8 shows the recorded combustion pressure trace of Setups 1 and 2. Between compression from 80°CA bFTDC to FTDC at 0°CA, there is only a slight deviation in the pressure trace, resulting from different wall heat losses in the two setups. The maximum combustion pressure only deviates by 0.3 bar. The shift between the traces is due to a delay of 4.25°CA in the ignition timing of engine setup 1 due to a difference in the burn duration shown in Figure 9(a). During the expansion and exhaust stroke, the pressure traces are almost equal again.

Combustion behavior

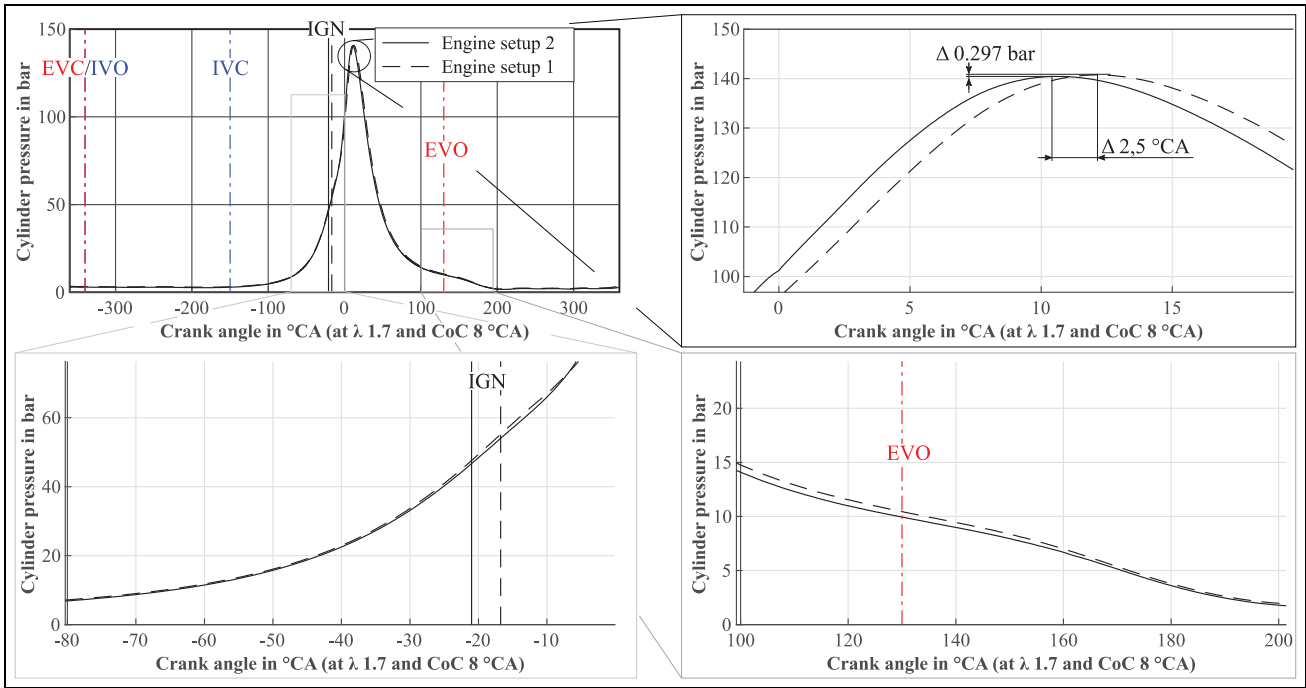Due to the difference in the ignition timing needed to reach the same CoC of the thermodynamic optimum at

Figure 8. Combustion pressure trace at an air-fuel equivalence ratio of 1.7 and CoC 8°CA aFTDC.
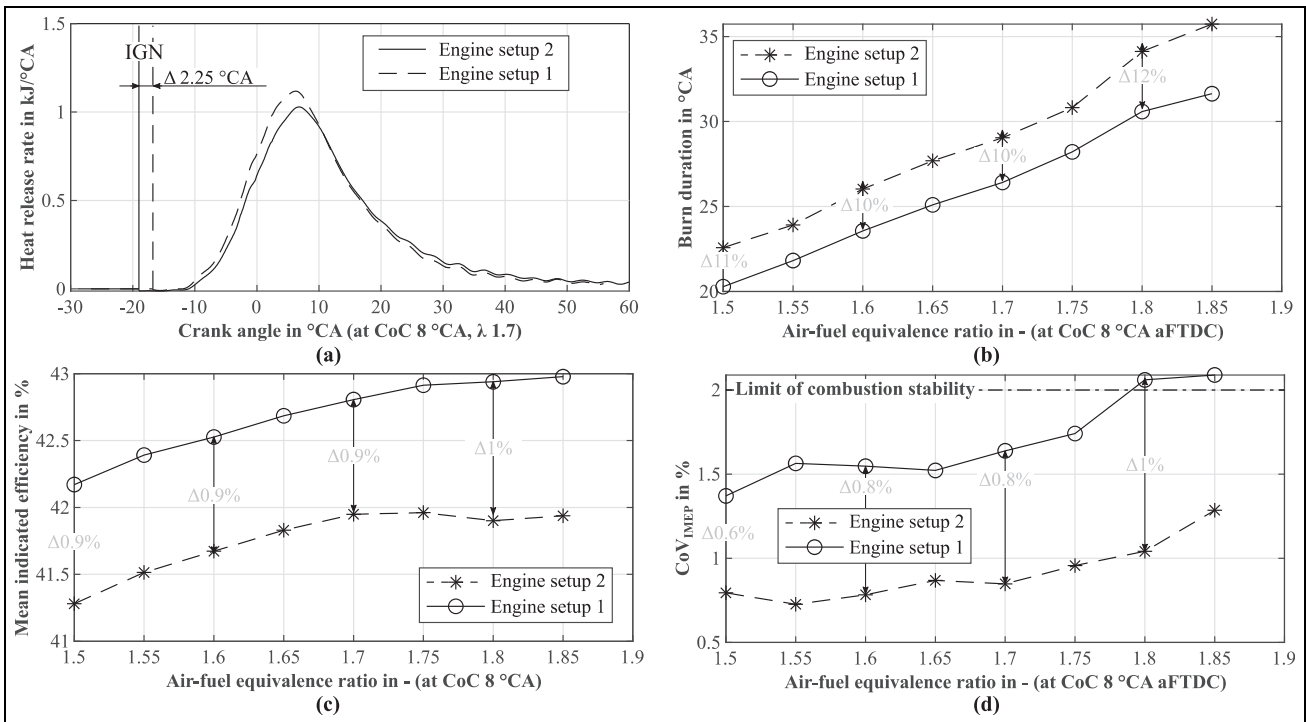

Figure 9. Combustion behavior in Comparison 1: (a) heat release, (b) burn duration MFB 10–90, (c) mean indicated efficiency, and (d) CoV$_{Imep}$.

8°CA, the heat release rate in Setup 1 is before the trace of engine setup 2 (cf. Figure 9(a)). This is also due to an apparent increased ignition delay in Setup 2. The maximum heat release is lower for Setup 2 and has a slightly slower trace, hinting at a decrease in combustion temperature and a possible different air-fuel distribution in the combustion chamber. The peak difference in the two traces is due to a slight increase in the wall heat loss and delayed combustion for Setup 2. The burn duration from MFB 10 to MFB 90 shows an almost constant offset of about 3°CA observed over the air-fuel equivalence ratio variation (cf. Figure 9(b)). This may be due

to cooler combustion chamber walls and increased quenching in Setup 2. The lower wall temperature is due to endoscope ring cooling, whereas engine setup 1 does not provide any cooling duct in the vicinity of the anti-bore polishing ring. The shorter burning duration in Setup 1 and the lower wall heat loss and dead volume lead to an increased indicated mean efficiency of at least 1% compared to engine setup 2, as shown in Figure 9(c). The variance coefficient of indicated mean effective pressure shows more unstable combustion in Setup 1, with differences of up to 1%. As the optimal thermodynamic center of combustion of 8°CA aFTDC is attained, ignition conditions such as pressure and temperature are at their optimum compared to later CoCs. The assumption made here is that due to the cooler combustion chamber a reduced laminar burning velocity creates less intense combustion concerning the heat release and pressure rise rate in Setup 2 than in Setup 1. Uneven fuel distribution in the fresh charge leads to uneven flame propagation, which is reflected as a pressure variation in the cycles. This has a negative effect on the uniformity of combustion from cycle to cycle. An increased level of cylinder charge temperature tends to amplify the inhomogeneous flame spreading. This effect affects Setup 2 less than setup 1 due to the cooler combustion chamber, which could cause the more stable combustion shown in Figure 9. A further detailed investigation is necessary to proof the extent of this influence. Furthermore, it can be assumed that the design adjustments lead to a change in the cylinder liner tension, which can increase the lube oil ingress via the piston ring pack. The spread of oil contributes to combustion stability as an additional, spatially distributed ignition source. Setup 1 in particular exceeds the limit of CoV_{IMEP} proposed in Park et al.[36] Moreover, the combustion stability decreases as the air-fuel equivalence ratio increases due to the reduction in laminar flame speed and the deterioration in the ignition conditions as the combustion becomes leaner.

Engine-out emissions

Engine-out emissions are measured with an AVL Sesam FTIR, and are shown in Figure 10. CO emissions increase continuously as the air-fuel equivalence ratio varies and display a colder after-burn phase in Setup 2 (cf. Figure 10(a)) than in Setup 1, which prevents the temperature-dependent oxidation of CO. This is because the decreased wall temperatures facilitate heat transfer into the wall, which reduces the burnt gas temperature and thus prevents further oxidation of CO. The decrease in CO at higher air-fuel equivalence ratios is due to the lower amount of oxidized fuel that can be discerned as the THC emissions increase, owing to the deteriorated lean combustion conditions. The mean increase in CO emissions from Setup 1 to Setup 2 is 32%.

The slightly lower mean combustion temperature does not decrease the NOx emissions shown in Figure 10(b). With only slightly lower thermal NOx formation in the flame front, both setups show almost equal NOx emissions. This indicates similar peak combustion temperatures and a different after burn phase, influenced in particular by the wall temperature of the combustion chamber. The high level of NOx emissions is due to the formation factors of time and temperature, as the reduced nominal engine speed doubles the formation time, and therefore, the NOx emissions of the engine at nominal speed are lower.

THC emissions are also higher in Setup 2 (cf. Figure 10). This is due to the slightly lower combustion temperature, resulting either in a longer burn duration (cf. Figure 9(a)), with a reduced laminar flame speed and increased quenching distance. The longer quenching distance is also due to the lower combustion chamber wall temperature. As the cold wall reduces the radical formation due to the increased heat transfer from the flame front to the wall, the combustion propagation deteriorates. Therefore, the near-wall regions, in particular contain unburnt hydrocarbons, especially methane. Furthermore, the full-load optical engine setup has an increased dead volume because of the two sealing positions, instead of only one in engine setup 1. Additionally, the gaps around the endoscope mounting positions are not covered by the flame and therefore hold unburnt gas. All in all, the dead volume of Setup 2 in contrast to Setup 1 is increased 1.75 times resulting in 0.006l (cf. section 2.2). Taking this into account, a
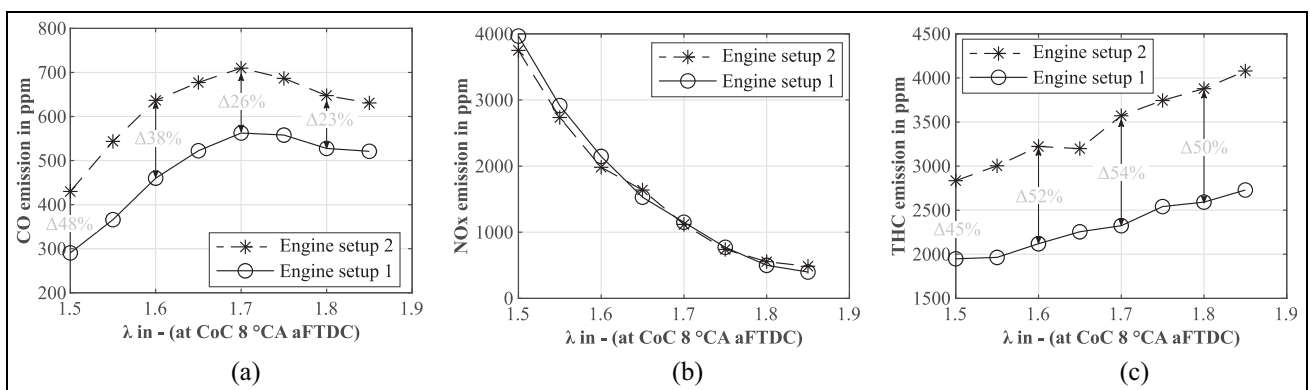

Figure 10. Emissions in comparison 1: (a) CO emission, (b) NOx emission, and (c) CO emission.

mean increase of 49% in THC emissions seems plausible as Korb[32] already mentions the dead volume reduction as a possible cause for a decrease in THC emissions of up to 30%. Simulative 3D-CFD investigations of the influence of dead volume and flame wall quenching on THC emissions in Kuppa et al.[37] point to a greater influence of the dead volume than the quenching.

Combustion chamber temperature

The cylinder head temperature is measured near the flame deck at four different locations between the valves in 4 mm ± 0.1 mm depth from the flame deck. The circumferential distribution is shown in Figure 11(a). Position 4 indicates the maximum cylinder head temperature, being located between the two exhaust valves. The cylinder head temperature shown in Figure 11(a) is almost equal in both engine setups, except at Position 4. The temperature difference at Position 4 is a result of the receded measurement position in Setup 2. This receded position is due to the equal raw parts strategy used for Setup 2 and 3. The two setups have the same basic modifications at the cylinder head for integrating the endoscope ring and the modifications for thermodynamic measurements, for example, the addition of thermocouples and a cylinder pressure sensor. Setup 3 requires further machining to integrate the fisheye endoscope, especially at the region of the exhaust valve. So the position of Thermocouple 4 is altered. The almost equal temperature at the other measurement positions

in the cylinder head is due to the cylinder head cooling duct being unmodified. Further, as the same amount of fuel energy is introduced, the same amount of heat is released, disregarding slight differences arising from the slightly altered combustion.

Setup 1 contains three thermocouples on the pressure side and three on the counter pressure side of the liner in a depth of 0.3 mm ± 0.1 mm. The nearest ones to the cylinder head (Positions 1 and 2 in Figure 11(b)) offer the best comparability to thermocouples in the endoscope ring. Therefore these are taken as input for the average value for the comparison of the two setups shown in Figure 11(b).

The endoscope ring contains seven thermocouples (not shown in Figure 11(b)). Three thermocouples can be positioned in the screw in positions (cf. Figure 3) using steel inserts with a 3 mm ± 0.1 mm distance from the combustion chamber wall surface to the tip of the thermocouple. Position A in Figure 11(b) has a steel insert fitted with a thermocouple. Three more monitor the temperature near these positions. The seventh thermocouple (Position B in Figure 11(b)) measures the wall temperature of the endoscope ring in the inlet half of the combustion chamber with a distance of 1.8 mm ± 0.1 mm from the thermocouple tip to the inner chamber surface.

Since the measurement positions of the two engine setups do not exactly match, the positions A and B shown in Figure 11(b) have been chosen, as they are the closest available. To simplify the comparison, the values are taken as a mean value. Hence, Setup 2 results in
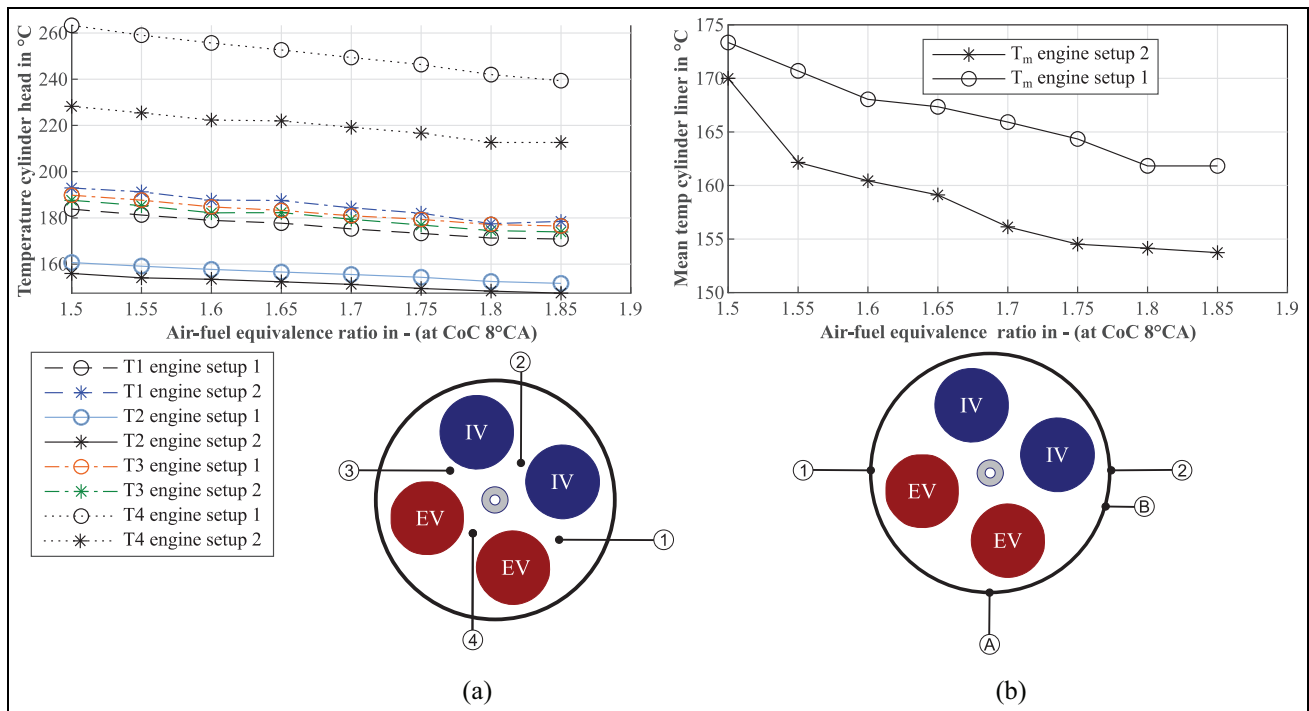

Figure 11. Wall temperature in Comparison 1: (a) cylinder head temperature and (b) mean cylinder wall temperatures (1–2 Setup 1) A–B (Setup 2).

a lower mean temperature of about 8°C. The temperature reduction resulting from endoscope ring cooling supports the explanation of the combustion behavior.

Experimental comparison between the full-load optical and fully optical engine setups: Comparison 2

To compare the full-load optical engine setup with the full optical engine setup, a CoC variation at a constant load of 16 bar IMEP and a constant excess air ratio of 1.7 is analyzed, as no complete variation map of the air-fuel equivalence ratio and CoC is available. Engine setup 3 runs in skip fire operation mode detailed in section 3.3, whereas Setup 2 runs continuously in normal steady state operation. This comparison can be used to evaluate the comparability of Setup 3 versus Setup 2 and the suitability of skip fire operation. The following section presents the measurement data for combustion and emissions and the observed behavior.

Combustion pressure

Figure 12 evaluates the combustion pressure trace at CoC 8°CA aFTDC for an air-fuel equivalence ratio of 1.7. Due to the relatively small difference in the ignition timing of 0.75°CA, the pressure traces show no shift and are almost equivalent. The compression phase also matches quite well, resulting in a comparable combustion process for both setups. Nevertheless, the maximum combustion pressure of the full optical engine is 3.3 bar lower than in the full-load optical engine setup,

resulting in a 3% deviation. This could be due to a slight deviation in the compression ratio as well as less intense combustion due to incomplete gas exchange and lower in-cylinder combustion temperatures. The lower gas exchange efficiency is related to the increased exhaust backpressure, as one exhaust valve is replaced by the fisheye endoscope, as described in Section 2. This behavior can be seen in Figure 12, as the combustion pressure after EVO is higher for Setup 3 than for Setup 2, even though the exhaust flap for simulating a turbocharger is fully open to compensate for this elevated pressure. In contrast, Setup 2 uses a simulated exhaust flap with a turbo charger efficiency of 75%.

Combustion behavior

The cumulative heat release rate shown in Figure 13(a) points to almost equal combustion behavior in both setups, as the start and ascent behaviors are quite similar. This can also be attributed to the very similar ignition timing with a difference of 0.75°CA.

The lower maximum of the heat release rate in Setup 3 supports the assumption that the combustion is less intense regarding a decreased laminar burning velocity. This has several reasons. One main effect is the lower combustion chamber wall temperature, which results in an increased heat loss toward the wall and therefore reduces the charge temperature at the beginning and during the combustion. Further, this effect supports a delayed ignition and contributes to a decreased heat release rate.

The modifications of the valve lift in Setup 3 decrease the effect of the remaining amount of residual
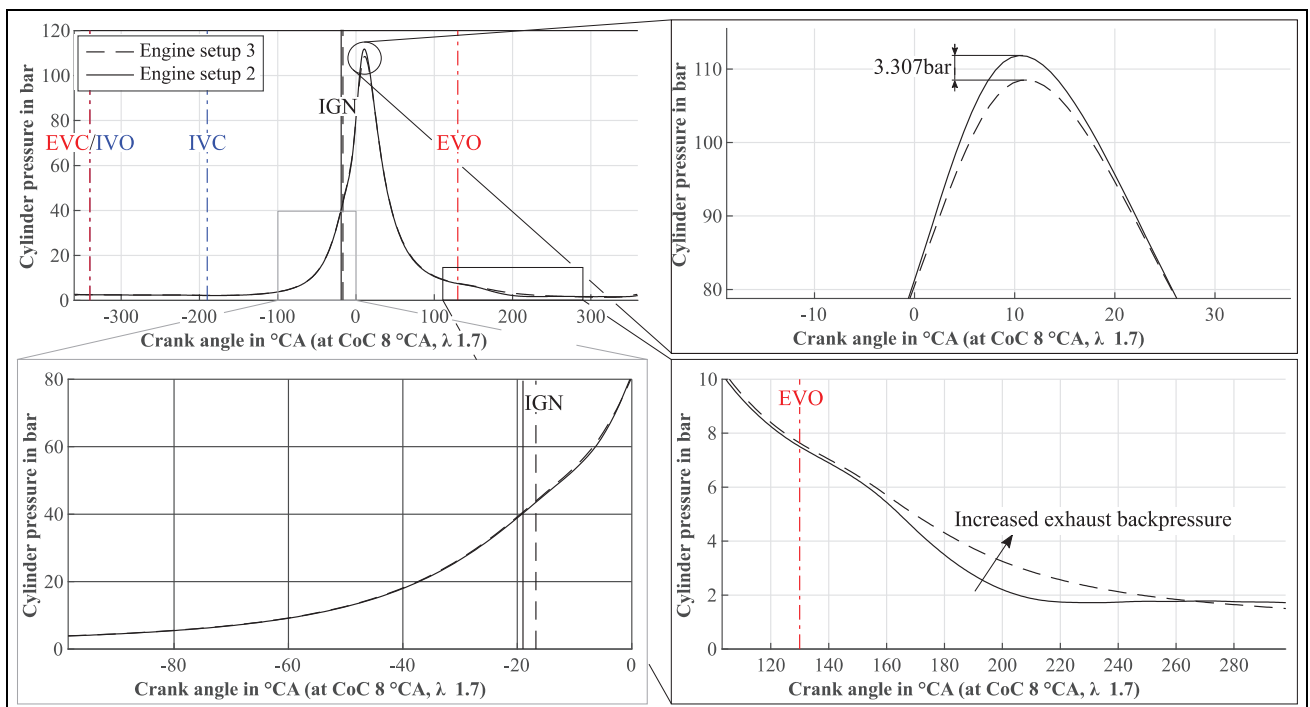

Figure 12. Combustion pressure at CoC 8°CA, air-fuel equivalence ratio 1.7 for comparison 2.
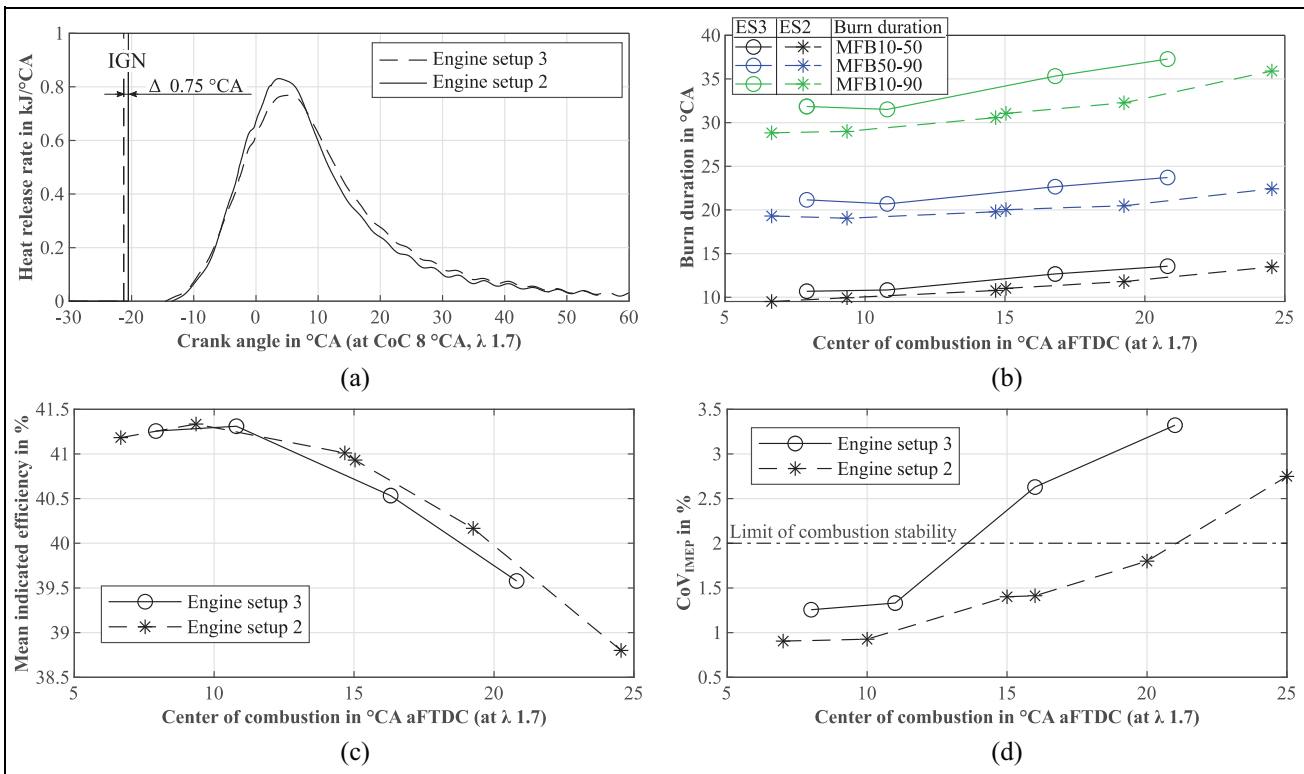
Figure 13. Combustion behavior in Comparison 2: (a) heat release, (b) burn duration (ES2 = engine setup 2, ES3 = engine setup 3), (c) mean indicated efficiency, and (d) CoV$_{Imep}$.

gas as only a small deviation of the ignition timing and a close matching heat release are observable. Further, the GT-Power model used for the TPA calculates a mean increase of the residual gas mass percent at combustion start over the experiments of 1.1%. Therefore, the slightly increased residual gas mass contributes to the delayed combustion.

Figure 13(b) shows the burn duration for the main combustion from MFB10-50, for the late combustion from MFB50-90 and the complete combustion duration from MFB10-90 for both engine Setups 2 and 3. For the main combustion, engine Setup 3 has a mean deviation of 1.4°CA to Setup 2. This hints that the main combustion matches quite well comparing both Setups providing almost similar combustion conditions. The late combustion duration shows a mean difference of 2.3°CA, which is 63% more than in the main stage of the combustion. This hints at a delayed combustion due to a decrease in the laminar burn velocity. As the combustion conditions deteriorate in this stage of the combustion, the reduction of the laminar burn velocity in engine Setup 3 further suffers from increased wall heat loss.

Nevertheless, the combustion durations are comparable, especially with CoCs near the thermodynamic optimum, supporting the combustion with good ignition and flame propagation conditions. With late CoCs the combustion conditions deteriorate resulting in a higher burn duration for each setup and therefore also in an increased difference because of the accumulation

of deviation over time. For the complete combustion duration, the mean difference over all experiments results in 12%.

The mean indicated efficiency is almost equal in both setups but deteriorates at late CoCs further in Setup 3 (cf. Figure 13(c)). For early CoCs, the combustion and ignition conditions are well matched and hardly any deviation is discernible even with the deterioration of the combustion in Setup 3 relative to Setup 2. This relative equality is also due to the higher combustion temperature and shorter burning duration at early CoCs of Setup 2, resulting in a shorter duration for wall heat loss and more complete combustion. Setup 3 on the other hand shows an efficiency drop due to the increased burn duration for late CoCs owing to the deteriorated combustion and ignition conditions. Since a late CoC results in delayed and more incomplete combustion, the efficiency decreases. This is especially true in Setup 3, as the quenching distance increases due to the colder combustion chamber wall and lower combustion temperature, resulting in even more incomplete combustion, also indicated by the increased amount of THC in the exhaust gas (cf. Figure 14(c)).

The combustion stability of Setup 3 undergoes deterioration in all investigations compared to the other setup, as only this setup operates in skip fire engine mode, which does not entirely reach the same stationary and stable engine operating conditions as in Setup 2. Figure 13(d) illustrates this behavior. Considering the

early center of combustion, the combustion destabilizes as the ignition conditions deteriorate. This does not get better as the engine continues to heat up and offers no stable ignition conditions. Nevertheless, both engine setups display the expected combustion behavior over the investigated CoC sweep at an air-fuel equivalence ratio of 1.7, which is an effect of the modifications. As the CoV_{IMEP} is derived directly from the measurements without consideration of the TPA model, the corresponding CoC points are also derived directly from the measurements, resulting in a slight offset compared to the CoC values derived from the TPA model.

Engine-out emissions

With respect to section 3.3, the emissions of CO and THC show a promising stable emission behavior, whereas the NOx emissions seem more unstable. Therefore, the findings especially concerning the NOx emissions can only be interpreted as tendencies not absolute values with the possible contributing effects explained for a profound overview.

With regard to the engine-out emission behavior in Comparison 2, both setups show almost the same level of CO emissions (cf. Figure 14(a)).

For late CoCs, the lower peak combustion temperature tends to increase CO emissions, but this effect is outweighed by the prolonged combustion, which leads to prolonged oxidation also in the exhaust gas. Finally, both setups have roughly equal THC emissions, as illustrated in Figure 14(c). Although Setup 3 operates in skip fire mode, the THC emissions are about 7% lower than in Setup 2. The increased amount of residual gas keeps unburnt fuel in the cylinder and increases the average gas temperature over the working cycle. Both promote the oxidation of THC.

The fewer NOx emissions shown in Figure 14(b) for Setup 3 is due to the lower peak combustion temperature resulting from the slightly increased recirculation of the in-engine exhaust gas and the skip fire operation and increased cooling. However, at the same time, the increased residual gas acts as a thermal insulator during the after burning phase and thus prevents wall heat loss, resulting in a higher post-oxidation temperature.

Combustion chamber temperature

The effects of the 5°C reduction in cooling water temperature and the skip fire engine operation are reflected in the temperature profiles of the cylinder head and the cylinder liner wall, which are shown in Figure 15.

The temperature measurement positions in the cylinder head are equal in both setups lying 4 mm ± 0.1 mm below the flame deck. The measurement positions in the endoscope ring are placed in a steel insert for positions A and C with a material coverage depth of 3 mm ± 0.1 mm. Position B is similar to the one used for comparison 1 and is positioned in a depth of 1.8 mm ± 0.1 mm. Position D is near the endoscope and has a distance of 7 mm ± 0.1 mm to the combustion chamber surface. The values shown are mean temperatures derived from all measurement positions in the cylinder head and the endoscope ring. This is plausible as the measurement positions are equal in both setups. Nevertheless, there is a considerable deviation of about 40°C in the cylinder head temperature and 20°C in the mean endoscope ring temperature. These deviations are mainly a result of skip fire engine operation and the lower cooling water temperature in Setup 3. As shown, this affects the combustion behavior to a limited extent. The limited effect could be due to the recirculation of in-cylinder exhaust gas. Since the remaining residual exhaust gas acts as thermal insulation, the heat flow to the combustion chamber wall decreases to a smaller extent. The hot remaining residual exhaust gas increases heat up of the fresh charge. As a consequence, the combustion temperature is high enough to result in combustion behavior that is almost equal to that of the full-load optical engine setup running in steady state operation conditions.
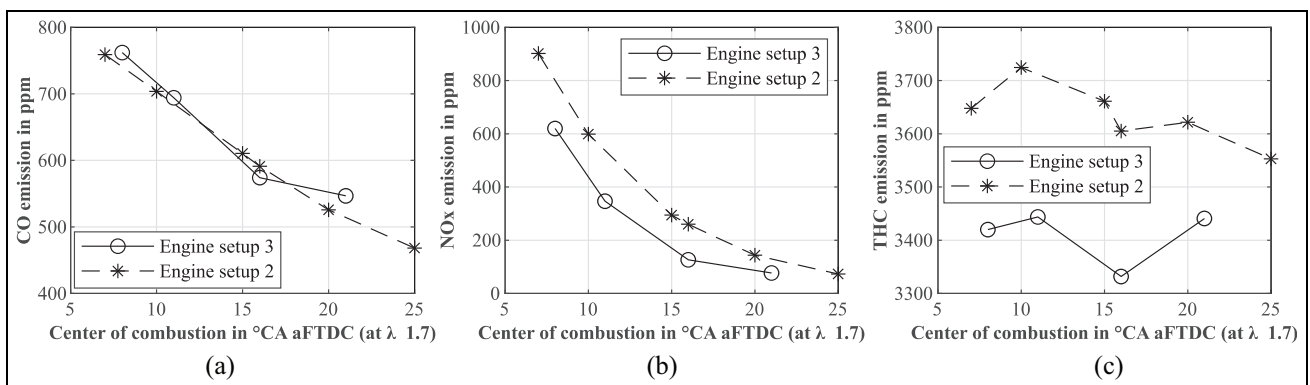

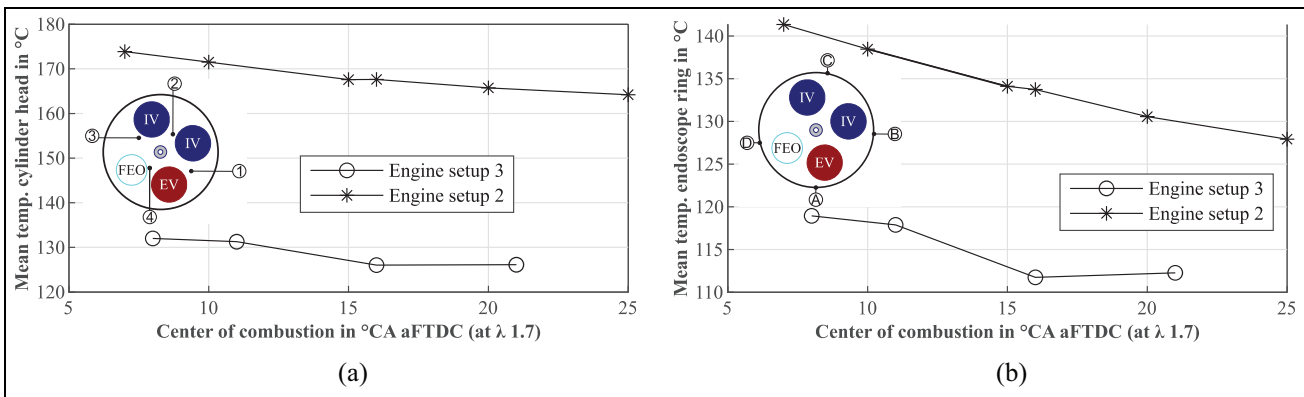**Figure 14.** Emission of comparison 2: (a) CO emission, (b) NOx emission, and (c) THC emission.

Figure 15. Wall temperature in Comparison 2: (a) mean cylinder head temperature and (b) mean cylinder wall temperature.

Summary and discussion

The aim of comparing the all-metal engine with the optical setup is to show the extent to which the two setups are comparable regarding their combustion behavior. Similar comparisons have already been made between a light duty truck engine with full optical access based on the Bowditch principle and the corresponding thermodynamic engine in Refs.[24–26]

However, no corresponding comparison has been conducted for the larger engine size examined in this study. Yet, differences in load compatibility, wall temperatures and, in turn, emissions have been found.

The modified full-load optical engine setup (Setup 2) can attain the nominal engine load of the all-metal engine (Setup 1). Nonetheless, this Comparison 1 displays slightly different combustion behavior. This is mainly due to the slightly lower combustion temperature resulting from the cylinder wall cooling of the optical elements, which are not found in the all-metal engine. This affects the laminar burn velocity, resulting in a slightly extended burn duration, a reduced mean indicated efficiency, and higher CO and THC emissions. Although the combustion behavior shows slightly different behavior, the differences between Setup 2 and Setup 1 are relatively small:

- 10% for the burn duration (MFB10-90)
- 1% for the indicated mean efficiency, and
- 0.5% for CoV_{IMEP}

In contrast, the THC emissions in the optical setup differ by almost 50%. Nevertheless, both setups display the same qualitative behavior and tendencies in the air-fuel equivalence ratio variations. Therefore, the investigations of the full-load optical engine setup are comparable with those conducted on the all-metal engine if one considers offset in the values. To determine if those offsets are constant throughout all operation points further investigations have to be carried out based on the test setups of comparison 1. If linearity between Setup 1 and 2 can be ascertained, a scaling model approach could be derived to transfer the findings of the optical full-load engine to the all-

metal engine. In addition, further design modifications can be applied to reduce the additional dead volume of Setup 2 for better comparability of the engine-out emissions.

Similarly, the difference between the full-load optical engine setup (Setup 2) and the full optical one (Setup 3) is quite small in terms of the heat release rate and combustion pressure trace. Although the adapted operation strategy of the full optical engine results in lower wall temperatures in the cylinder head and endoscope ring, it only affects the combustion behavior to a limited extent. The fueling of the engine as well as the air mass flow are stable during the measurement time resulting in reliable and comparable air-fuel equivalence ratios. Further, the effect of replacing the exhaust valve with the fisheye endoscope and its mount is simulated in GT-Power. The residual gas content increases by only 1.1% compared to the full-load optical engine.

Concerning the engine-out emissions the skip fire operation strategy has the highest impact on the NOx emissions as their occurrence proves very unstable during the measurement duration. This is especially due to the combustion process where cyclic variation have a great influence on the maximum combustion temperature and therefore on NOx formation. The THC and CO emissions on the other hand show a reliable behavior. Nevertheless, all investigated emission tendencies seem reasonable and can be explained by known factors.

All in all, despite some minor differences both optically accessible engines show a comparable behavior.

Comparing the full optical setup with the all-metal engine in an indirect comparison, a significant deviation in the cylinder wall temperature can be determined due to the adapted skip fire engine operation strategy, the reduced coolant temperature, and the enhanced cooling concept. Further, an altered amount of engine-out emissions between both setups have to be expected, but they also show comparable and predictable tendencies in emission formation. This is especially due to the more realistic thermodynamic behavior of the new full optical engine design which at least offers a longer fired operation time than a design according to Bowditch with only 70 fired cycles (cf. Gleis et al.[13]).

As for both optical setups the nominal engine speed has to be slowed by half to prevent the camera from damage, the transferability of the results have to be considered. As the engine speed directly affects the timescale, the mixture preparation and combustion are altered. This results in altered burn duration, emission formation and engine efficiency. The causes of the effects produced at a different engine speed are nevertheless transferable, as the timescale effect is also considered, and the results are evaluated with respect to this. All in all, the investigations display good comparability of the engine setups and hint at reliable quantifiable offsets.

Conclusion and outlook

The reliability of the optical designs is validated by experimental investigations to evaluate the comparability of the all-metal engine to the full-load optical setup as well as in an intermediate step a comparison of the setups to the full optical engine. The findings present the differences in engine behavior due to the modifications and adaptation of the engine's operating conditions. The results demonstrate good comparability in terms of combustion behavior. However, there is a discernible difference in the engine-out emissions. The insights obtained render further investigations feasible, the results of which can be evaluated and transferred to the behavior of the all-metal engine. Eicheldinger et al.,[34] for example, references the usability of the full-load optical engine design investigating abnormal combustion of the engine fueled with hydrogen. To improve the performance of the fisheye setup, water cooling of the fisheye endoscope could increase the load and measurement time until full steady-state engine operation is reached, resulting in increased comparability, particularly since the combustion stability and the NOx stability would increase.

Further investigations based on fisheye endoscopic access will be carried out in due course to gain an understanding of the use of in-cylinder combustion to push renewable fuels beyond existing limits.

Author contributions

The entire writing, implementation, evaluation and interpretation of the depicted experimental data and the design of the optical test engine belong to S. Karmann. S. Eicheldinger supported the experiments at the test rig. The remaining co-authors supported the work with their reviews.

Declaration of conflicting interests

The author(s) declared no potential conflicts of interest with respect to the research, authorship, and/or publication of this article.

Funding

The author(s) disclosed receipt of the following financial support for the research, authorship, and/or publication of this

ORCID iDs

Stephan Karmann https://orcid.org/0000-0002-0920-7222
Stefan Eicheldinger https://orcid.org/0000-0003-1211-1157
Maximilian Prager https://orcid.org/0000-0003-2507-6530
Malte Jaensch https://orcid.org/0000-0003-0550-1421

References

1. Pressemitteilung Eurostat. Erneuerbare Energien in der EU im Jahr 2018: Eurostat, https://ec.europa.Eu/eurostat/documents/2995521/10335442/8-23012020-AP-DE.pdf/ab13eb1f-fe9d-9a57-44b3-98f0011e8697 (2020, accessed 9 September 2021)
2. Hultqvist A, Christensen M, Johansson B, Richter M, Nygren J, Hult J, et al. The HCCI combustion process in a single cycle – speed fuel tracer LIF and chemiluminescence imaging. SAE technical paper 2002-01-0424, 2002.
3. Einecke S, Schulz C and Sick V. Measurement of temperature, fuel concentration and equivalence ratio fields using tracer LIF in IC engine combustion. *Appl Phys B* 2000; 71(5): 717–723.
4. Pöllmann S, Härtl M and Wachtmeister G. Injection process of the synthetic fuel oxymethylene ether: optical analysis in a heavy-duty engine. SAE technical paper 2020-01-2144, 2020.
5. Fatouraie M and Wooldridge M. Optical investigation of the effects of ethanol/gasoline blends on spark-assisted HCCI. *J Eng Gas Turbines Power* 2014; 136(8).
6. Lee C-f, Pang Y, Wu H, Hernández JJ, Zhang S and Liu F. The optical investigation of hydrogen enrichment effects on combustion and soot emission characteristics of CNG/diesel dual-fuel engine. *Fuel* 2020; 280: 118639.
7. Chen L, Wei H, Zhang R, Pan J, Zhou L and Feng D. Effects of spark plug type and ignition energy on combustion performance in an optical SI engine fueled with methane. *Appl Therm Eng* 2019; 148: 188–195.
8. Peñaranda A, Martinez Boggio SD, Lacava PT, Merola S and Irimescu A. Characterization of flame front propagation during early and late combustion for methane-hydrogen fueling of an optically accessible SI engine. *Int J Hydrogen Energy* 2018; 43(52): 23538–23557.
9. Jakob M. *Optical investigation of diesel-engine related combustion processes*. Dissertation, Aachen: Rheinisch-Westfälische Technische Hochschule, Germany, 2014.
10. Greis EA. *Laseroptische Untersuchungen des Verbrennungsprozesses in einem PKW-Dieselmotor*. Dissertation, Aachen: Rheinisch-Westfälische Technische Hochschule, Germany, 2007.
11. Bensing D. *Aufbau eines optisch zugänglichen Einzylinder-Viertaktmotors und charakterisierende Messungen*. Dissertation, Universität Duisburg-Essen, Duisburg, Germany, 2013.
12. Unfug F. Experimentelle und numerische Untersuchung der Verbrennung eines mittelschnelllaufenden 4-Takt Dieselmotors. Dissertation, Berlin: Logos Berlin, Germany, 2013.
13. Gleis S, Frankl S, Prager M and Wachtmeister G. Optical analysis of the combustion of potential future E-Fuels with a high pressure dual fuel injection system. In: *14. internationales AVL powertrain diagnostik symposium*, Baden-Baden, Germany, 2020.

14. Hult J and Mayer S. A methodology for laser diagnostics in large-bore marine two-stroke diesel engines. *Meas Sci Technol* 2013; 24(4) :45204.

15. Wellander R, Rosell J, Richter M, Alden M, Andersson O, Johansson B, et al. Study of the early flame development in a spark-ignited lean burn four-stroke large bore gas engine by fuel tracer PLIF. *SAE Int J Engines* 2014; 7(2): 928–936.

16. Duong J. *Combustion visualization in a large bore gas engine*. Thesis, Lund: Lund University, 2013.

17. Disch C and Waldenmaier U. *High-speed flame chemiluminescence investigations of prechamber jets in a lean mixture large-bore natural gas engine*, 27th CIMAC World Congress, Shanghai, China, 13–16 May 2013, Paper-No.: 79/1-16.

18. Tsekenis SA, Wilson D, Lengden M, Hyvönen J, Leinonen J, Shah A, et al. Towards in-cylinder chemical species tomography on large-bore IC engines with pre-chamber. *Flow Meas Instrum* 2017; 53: 116–125.

19. Korb B, Kuppa K, Nguyen HD, Dinkelacker F and Wachtmeister G. Experimental and numerical investigations of charge motion and combustion in lean-burn natural gas engines. *Combust Flame* 2020; 212: 309–322.

20. Karmann S, Prager M and Wachtmeister G. Conceptual investigations on full optical accessibility to large-bore medium-speed engines. *SAE Int J Engines* 2019; 12(3): 291–308.

21. Bowditch FW. A new tool for combustion research a quartz piston engine. SAE technical paper 610002, 1961.

22. Korb B and Gleis S. Auslegung und Entwicklung eines volloptischen Einzylinder-Großmotors mittels Ansys Workbench und einer vereinfachten FKM-Richtlinie. In: *Conference proceedings | Die Fachkonferenz zur Numerischen Simulation*. Grafing bei München, Darmstadt: CADFEM GmbH, 2015.

23. Gleis S, Frankl S, Waligorski D, Prager M and Wachtmeister G. Investigation of the High-Pressure-Dual-Fuel (HPDF) combustion process of natural gas on a fully optically accessible research engine. In: *2019 JSAE/SAE powertrains, fuels and lubricants international meeting*, Kyoto, Japan, 2019.

24. Colban WF, Kim D, Miles PC, Oh S, Opat R, Krieger R, et al. A detailed comparison of emissions and combustion performance between optical and metal single-cylinder diesel engines at low temperature combustion conditions. *SAE Int J Fuels Lubr* 2009; 1(1): 505–519.

25. Kashdan J and Thirouard B. Optical engines as representative tools in the development of new combustion engine concepts. *Oil Gas Sci Technol Rev IFP Energies Nouvelles* 2011; 66(5): 759–777.

26. Kashdan JT and Thirouard B. A comparison of combustion and emissions behaviour in optical and metal single-cylinder diesel engines. *SAE Int J Engines* 2009; 2(1): 1857–1872.

27. Karmann S, Friedrich C, Prager M and Wachtmeister G. Realization of a fully optically accessible medium speed large bore engine using a fisheye optic. In: *ASME 2020 power conference*, 4–5 August 2020. New York: ASME.

28. Eicheldinger S, Bartkowski T, Schröder A, Prager M and Wachtmeister G. Experimental investigation on the influence of brake mean effective pressures up to 30 bar on the behavior of a large bore otto gas engine. SAE technical paper 2019-01-2224, 2019.

29. Karmann S, Klier B, Röhrle H, Prager M and Wachtmeister G. Design of an endoscopic fully optically accessible high speed large bore engine. *Int J Engine Res* 2021; 15(6)

30. Frankl S, Gleis S and Wachtmeister G. Interpretation of ignition and combustion in a full-optical high-pressure-dual-fuel (HPDF) engine using 3D-CFD methods. In: *CIMAC CONGRESS 19, 29th CIMAC world congress on combustion engine, meeting the future of combustion engines*, Vancouver, BC, CA, 10–14 June 2019.

31. Weber S, Stegmann R, Prager M and Wachtmeister G. The effect of inlet valve timing and engine speed on dual fuel NG-diesel combustion in a large bore engine. *SAE Int J Engines* 2018; 11(2): 229–246.

32. Korb B, Prager M, Wachtmeister G, Kuppa K and Dinkelacker F. Ursachen und Reduzierung der CH4-Emissionen in Biogasmotoren; Teilvorhaben 1. Fachagentur Nachwachsende Rohstoffe e.V. (FNR), https://www.tib.eu/de/suchen?tx_tibsearch_search%5Baction%5D=download&tx_tibsearch_search%5Bcontroller%5D=Download&tx_tibsearch_search%5Bdocid%5D=TIBKAT%3A871460009&cHash=d7b46a65f628785a07a6541ca4302f28#download-mark(2016, accessed 2016 July 29).

33. Karmann S, Kunkel C, Prager M and Wachtmeister G. A new optical access for medium speed large bore marine engines under full-load operating conditions. *SAE Int J Engines* 2021; 14(6): 867–883.

34. Eicheldinger S, Karmann S, Prager M and Wachtmeister G. Optical screening investigations of backfire in a large bore medium speed hydrogen engine. *Int J Engine Res.* Epub ahead of print 20 October 2021. DOI: 10.1177/14680874211053171.

35. Karmann S, Eicheldinger S, Prager M and Wachtmeister G. Optical and thermodynamic investigations of a methane and hydrogen blend fueled large bore engine. *Int J Engine Res.* Epub ahead of print 3 January 2022. DOI: 10.1177/14680874211066735.

36. Park C, Kim C, Choi Y, Won S and Moriyoshi Y. The influences of hydrogen on the performance and emission characteristics of a heavy duty natural gas engine. *Int J Hydrogen Energy* 2011; 36(5): 3739–3745.

37. Kuppa K, Nguyen HD, Goldmann A, Korb B, Wachtmeister G and Dinkelacker F. Numerical modelling of unburned hydrocarbon emissions in gas engines with varied fuels. *Fuel* 2019; 254: 115532.

Appendix

Notation

AHRR	Apparent heat release rate
CoC	Center of combustion ≙ MFB 50
CHT	Conjugate heat transfer
FEO	Fisheye optic
FOV	Field of view
MFB	Mass fraction burned
FTDC	Firing top dead center
aFTDC	After firing top dead center
bFTDC	Before firing top dead center
EVO	Exhaust valve open
EVC	Exhaust valve close
IVO	Inlet valve open
IVC	Inlet valve close
OME	Oxymethylenether

B.5   Veröffentlichung 5 im Original

Karmann, S.; Eicheldinger, S.; Prager, M.; Wachtmeister, G. Optical and thermodynamic in-vestigations of a methane and hydrogen blend fueled large bore engine. International Journal of Engine Research 2022,146808742110667. doi: 10.1177/14680874211066735.

Reprinted with permission from International Journal of Engine Research

©SAGE Publications

Dear Stephan Karmann,

Thank you for your request. You may include the Final Published PDF (or Original Submission or Accepted Manuscript) in your dissertation or thesis, which may be posted in an Institutional Repository or database as specified in our journal author reuse policy.

Please accept this email as permission for your request. Permission is granted for the life of the edition on a non-exclusive basis, in the English language, throughout the world in all formats provided full citation is made to the original SAGE publication with a link to the appropriate DOI where possible. Permission does not include any third-party material found within the work.

Please contact us for any further use of the material and good luck with your dissertation!

Kind regards,

Mary Ann Price (*she/her*)
Senior Rights Coordinator

www.sagepublications.com

International Journal of
ENGINE RESEARCH

Optical and thermodynamic investigations of a methane and hydrogen blend fueled large bore engine

Stephan Karmann(iD), Stefan Eicheldinger(iD), Maximilian Prager(iD) and Georg Wachtmeister

Abstract
The following paper presents thermodynamic and optical investigations of the natural flame and OH radical chemiluminescence of a hydrogen enriched methane combustion compared to natural gas combustion. The engine under investigation is a port-fueled unscavenged prechamber 4.8 L single cylinder large bore engine. The blends under consideration are $2\%_V$, $5\%_V$, $10\%_V$, and $40\%_V$ of hydrogen expected to be blended within existing natural gas grids in a short and mid-term timeline in order to store green energy from solar and wind. These fuel blends could be used for stabilization of the energy supply by reconverting the renewable fuel CH_4/H_2 in combined heat and power plants. As expected, admixture of hydrogen extends the ignition limits of the fuel mixture toward lean ranges up to an air-fuel equivalence ratio of almost 2. No negative effect on combustion is observed up to an admixture of $40\%_V$ hydrogen. At $40\%_V$ hydrogen, abnormal combustion like backfire occurs at an air-fuel equivalence ratio of 1.5. The higher mixtures exhibit increased nitrogen oxide emissions due to higher combustion chamber temperatures, while methane slip and CO emissions are reduced due to more complete combustion. The optical investigation of the natural flame and OH radical chemiluminescence are in good agreement with the thermodynamic results verifying the more intense combustion of the fuel blends by means of the chemiluminescence intensity. Further, lube oil combustion and a continuing luminescence after the thermodynamic end of combustion are observed.

Introduction

A sustainable energy supply represents one of the greatest challenges of current and future generations. Fossil energy sources are finite and their conversion into energy with the associated generation of exhaust gases such as the climate-damaging CO_2 is harmful to the environment. **Sector coupling** pursues the approach of using renewable energy sources such as wind, biomass, solar and geothermal energy as primary energy sources to predominantly substitute fossil energy sources. This is intended to meet the energy needs of demand sectors such as households, commerce, trade and services, industry, and the mobility of goods and people in a sustainable way by reducing greenhouse gases to the point of neutrality. By coupling both energy production as the so-called supply sector, and energy use (demand

sector) via transportation and infrastructure, it should be possible to use and distribute the available energy more efficiently as shown in Figure 1.[1,2]

Due to high residual loads that originate from the seasonal and regional fluctuations of renewable energy production by solar and wind power plants, the energy supply is discontinuous. In order to ensure a sustainable and stable energy supply, short-term storage, as

Institute of Internal Combustion Engines, Technical University of Munich, Munich, Germany

Corresponding author:
Stephan Karmann, Institute of Internal Combustion Engines, Technical University of Munich, Schragenhofstr. 31, Munich, Bavaria 80992, Germany.
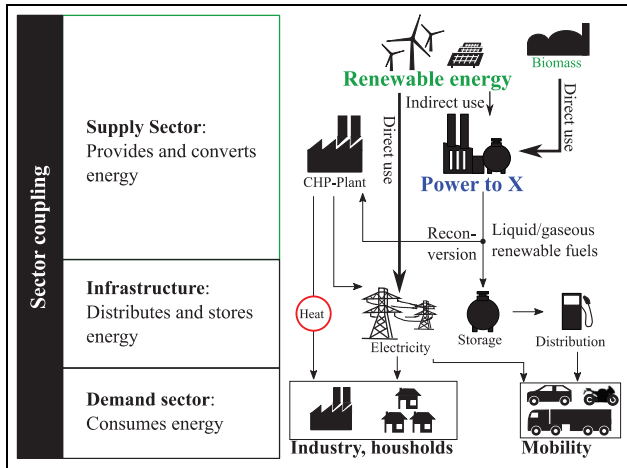Email: karmann@lvk.mw.tum.de

Figure 1. Overview of the sector coupling approach.

well as long-term storage solutions for environmentally friendly generated energy, are required. One possibility, especially for long-term storage, is the **Power to X** or **Power to Gas** process, which is of interest for the following investigations. For the Power to Gas process, excess electricity is used to produce hydrogen from water by means of electrolysis.

This chemical energy carrier can be stored directly in the natural gas grid with a capacity of $350 \, kWh/m^3$ (hydrogen) or further processed into methane with a capacity of $1100 \, kWh/m^3$. Both processes, electrolysis and the subsequent methanation, have a comparatively high efficiency of 64.1% and 51.3% (cf. Zapf[3]). In the future, further improvements in efficiency are expected for these technologies as a result of continuing technical development. Storing hydrogen is more complex than storing methane because the latter can directly replace natural gas and make use of already existing infrastructure. As Wahl and Kallo[4] and numerous studies, that is, Zapf[3] and Hüttenrauch et al.[5] show, the feasible maximum addition of hydrogen to a particular natural gas grid is strongly dependent on the local infrastructure (pipeline materials, kind of storage systems, etc.), the availability of hydrogen, and the consumers connected to the natural gas network (furnaces, CHPs, industrial processes, etc.).

In the US[6] mentions a possible 5%–15%$_V$ blend of hydrogen in the gas grid with less effort. For the European Union[7] refers to an actually regulated maximum up to 12%$_V$. For Germany[8] shows that a maximum proportion of 8.3%$_V$ could be added to the natural gas grid over the medium term up until 2030 and a maximum proportion of 43%$_V$ over the long term.

As combustion engines can serve as a bridging technology to convert these gas mixtures back into electricity on demand, the optimization of combustion processes for stationary gas engines to further improve their efficiency and environmental compatibility could contribute to a sustainable energy supply. For this

reason, a minimally invasive optical access system for a 4.8 L single-cylinder research gas engine has been developed and set up at the Institute of Internal Combustion Engines at the Technical University of Munich. This access enables optical and laser-optical investigations of the combustion under realistic engine conditions including up to full load for the investigation of combustion processes with renewable fuels and their mixtures. For the blends 0%, 2%, 5%, 10%, 20%, 40%$_V$ H_2–CH_4 the thermodynamic evaluations are shown in the following. Endoscopic high-speed images of the visible and UV chemiluminescence of the combustion with a focus on the burnout of the blends support the thermodynamic findings, promote the understanding of the combustion behavior and provide insights for potential optimization.

Effects of hydrogen blends on combustion: A brief literature review

Thermodynamic investigations

As mentioned in section 1, one storage option for the hydrogen generated with the power-to-gas process is to feed it into the public natural gas grid. For gas mixtures of hydrogen and methane or hydrogen and natural gas, the volumetric calorific value is reduced while the volume in the system remains constant. In addition, the methane number as an indicator for the gas mixture's knock resistance, changes due to its composition in the natural gas grid. This can lead to an increased risk of knocking during combustion for values below 80, where 100 equals pure methane with the highest knock resistance.[9] Therefore, investigations on engines that address these kinds of issues are of great importance. Figure 2 shows an overview of investigated hydrogen/natural gas mixtures in gas engines of different displacement classes (car, truck, marine, and stationary engine application), combustion processes (dual-fuel in diesel-gas, DFI/PFI-SI), ignition systems (spark plug, pre-chamber, pilot ignition) and approaches used in the investigations. Car and truck displacement class engines have been studied extensively and are already summarized in literature-based reviews (e.g. Wahl and Kallo,[4] Mehra et al.,[10] White et al.,[11] Sahoo et al.[12]). Figure 3 summarizes the generally observed effects in all of the various investigations caused by the addition of hydrogen.

The effects are explainable due to the different fuel specification of hydrogen in contrast to methane cf. Table 1. Additionally, Figure 4 depicts the laminar burning velocity for the investigated fuel blends of 2%$_V$, 5%$_V$, 10%$_V$, 40%$_V$, and the reference natural gas (NG), derived from an ideal reactor calculation conducted with Cantera. Obviously, the laminar burning velocity increases only slightly up to the 40%$_V$ hydrogen blend. For the lower hydrogen admixtures, the difference even diminishes as the air-fuel equivalence ratio increases.
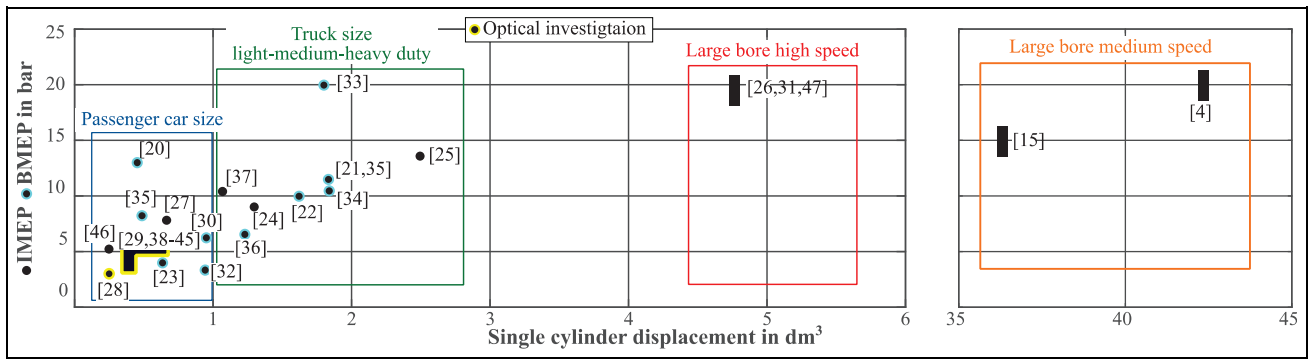
Figure 2. Literature review of HCNG fueled engines,[4,13–41] bars indicate an estimation as no value was indicated in the source.

Figure 3. Effects of hydrogen addition (blue = advantageous, red = disadvantageous).

Table 1. Fuel properties under normal condition (cf. Verhelst and Wallner[42]).

Fuel properties	H_2	CH_4
Density in kg/m^3	0.08	0.65
Ignitability in air in $\%_V$	4–75	5–15
Auto ignition temperature in air in K	858	813
Minimum ignition energy in mJ	0.02	0.28
Laminar burning velocity in m/s	1.85	0.38
Adiabatic flame temperature in K at $\lambda = 1$	2390	2226
Quenching distance in mm	0.64	2.03

The following combustion characteristics determine which effect and result of Figure 3 dominate the combustion behavior:

- The combustion process, such as lean, rich or stoichiometric
- The fuel preparation, such as direct injection or port fuel injection
- The ignition system, such as spark ignition or scavenged prechamber ignition

However, in general, all observed effects can be reduced back to the depicted basic causes of the change in:

- laminar burning velocity
- quenching distance
- ignitability
- ignition energy
- heating value

From Figure 2 it is clear that for so far only a few investigations have been performed with large bore engines for stationary or maritime applications using hydrogen-natural gas mixtures. Only Korb et al.[43] demonstrates the effects of hydrogen admixtures of $0\%_V$–$30\%_V$ for large bore engines. The results obtained from thermodynamic measurements show that even a small admixture of hydrogen improves combustion (higher burning rate). The lean burning limit (combustion stabilization) is extended, THC (up to 30% reduction compared to NG) and formaldehyde (up to 23% reduction compared to NG) emissions (complete combustion, lower C-atom content) are reduced, and a slight increase in efficiency of 0.2% is achieved with the same NO_x emissions as without admixture.

Near the knock limit, pre-ignition was observed for increased hydrogen admixtures. The cause of this is suspected to be spontaneous ignition of the more reactive hydrogen (low ignition energy and self-ignition temperature) at hot spots and residual gas in the combustion chamber. Kaj et al.[19] the influence of hydrogen-natural gas mixtures is investigated up to a maximum of $40\%_V$ for a marine DF application and a stationary power generation engine using a spark plug both with 35.6 L displacement per cylinder. Slight efficiency improvements with constant NOx emissions and a reduction of THC up to the knock limit was confirmed with increasing hydrogen admixture, and pre-ignition similar to the investigations of Korb et al.[43] was observed.

Reducing the THC-emissions resulting in less methane slip of such engines is of equal importance because the global warming potential over a 100-year time horizon for methane is 28 times higher than that for CO_2 (cf. Core Writing Team et al.[44]). Replacing methane with hydrogen further decreases possible methane slip by the reduction of methane in the fuel. In each of the experiments, the ignition timing was
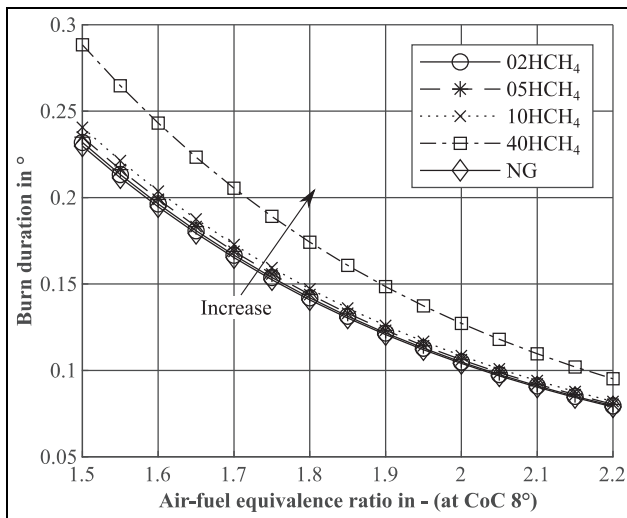
Figure 4. Laminar burning velocity at compression end like conditions.

Figure 5. Combustion emission spectra, and OH bandpass filter (cf. Arias et al.[47]).

adapted to achieve an optimum for the operating conditions. Different compression ratios (10–11–12.6) and their influence on the maximum hydrogen admixture (~40%v, ~28%v, ~16%v) have also been investigated. Wahl and Kallo[4] conducted investigations for an engine with a displacement of 42.3 L and a scavenged prechamber for mixtures up to a maximum of 20%v hydrogen addition, achieving similar results to those described by Korb.[43]

Optical investigations

Complex chemical reactions take place during engine combustion when the reactants (fuel and air) are converted under pressure and temperature. Those are the main influences on emission formation and the quality of the combustion (thermodynamic efficiency). Optical and laser-optical measurement methods make it possible to investigate and analyze the combustion process without influencing it. This allows conclusions to be drawn about which chemical products are formed during combustion and which conditions (lambda distribution) led to the formation of the products. The occurrence of the combustion products depends on the combustion process (rich/lean, premixed/diffusive combustion) and the fuel use. Figure 5 is an overview of the radicals formed during combustion and in which bandwidth they emit light when formed and are thus detectable. In addition to the discontinuous spectra, there are also continuous spectra, which occur as broadband background radiation from combustion. Broadband emitting radicals are, for example, CO2*(340–650 nm), HCO*(250–410 nm), and HCHO*(340–523 nm) (cf. Catapano et al.[45] and Gaydon[46]).

The blackbody radiation of soot formation calculated according to Arias et al.[47] also belongs to the broadband background emission with increasing
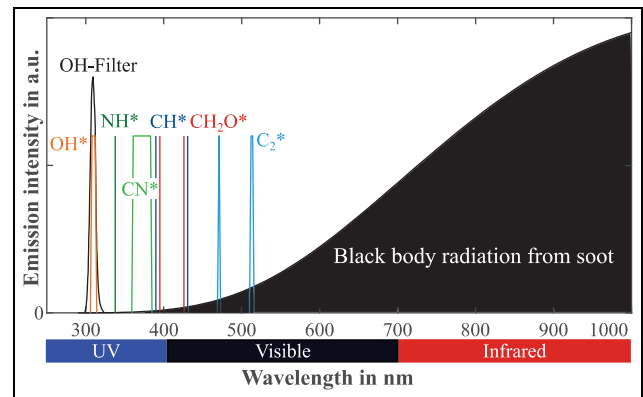
intensity for higher wavelengths. The formation of radicals and their intensities change during combustion dependent on the combustion process and the fuel used. Spectroscopic investigations on a PFI engine with spark plug ignition according to[23,33,39,48] show that CN*, NH*, and C_2* are mainly detectable during ignition, whereas OH* and CH* are observable as indicators of a reaction in the flame over the entire combustion process. OH* can also be observed during the hot after burning phase (cf. Reyes et al.[49]). The formation of the C_2* radical is proportional to the carbon content of the fuel and is reduced when hydrogen/methane blends are used. In addition, the intensity of OH* radicals increases with increasing hydrogen percentage during combustion dependent on temperature and air-fuel equivalence ratio (cf. Catapano et al.[45] and Gaydon[46]). The optical studies which can be found in literature (cf. Figure 2) also show the progress of the flame front, its nature (strongly distorted/uniform) and the space possibly covered by flame expansion, simply by observing the chemiluminescence of the combustion. This allows statements to be made about the increased laminar flame speed, better flammability and thus extension of the lean burning limit, and the higher combustion intensity correlated with an increased OH* concentration, which affects the thermodynamic efficiency. For stationary or marine engines, we are not currently aware of any other optical investigations with natural gas/methane/hydrogen mixtures in literature. Thus, the following results could be of benefit in this respect by expanding the understanding of methane/hydrogen combustion in large bore engines.

Test bench design

The research engine setup that was used for the investigations is quite similar to Korb et al.,[25] but the engine includes an additional endoscopic minimal optical lateral access as depicted in Figure 6. The research engine is designed to match different ignition systems, such as
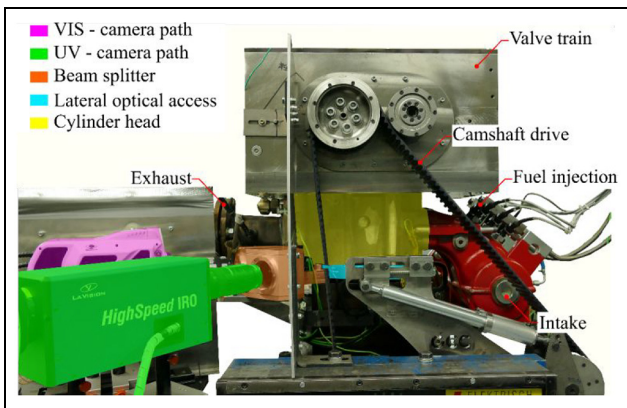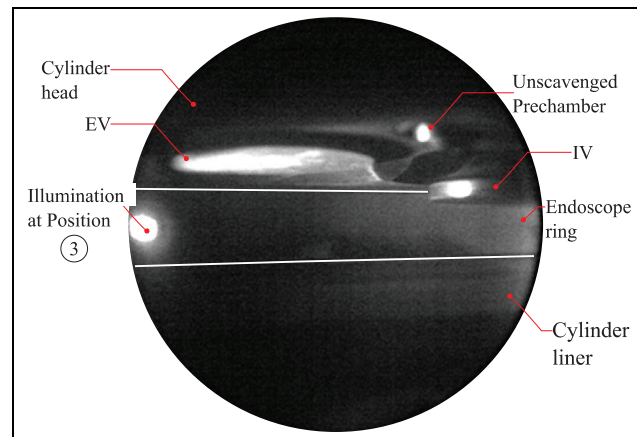
Figure 6. Engine setup at the testing rig.

Table 2. Engine properties.

Bore in mm	170
Stroke in mm	210
Displacement in dm^3	4.76
Compression ratio	11.6
Ignition system	Unscavenged prechamber spark plug
Engine speed in rpm	750
IMEP in bar	~21

a scavenged and un-scavenged pre-chamber, spark plugs and pilot fuel injection systems in combination with port fuel injected gaseous or liquid fuels as can be seen in Eicheldinger et al.[50,51] Figure 6 depicts a setup with the port fuel injection relatively close to the cylinder head, into the receiver. Table 2 summarizes the engine specifications for the setup used here. Two overhead camshafts driven by a belt actuate two exhaust and two intake valves. The exhaust backpressure of a turbocharger is simulated using a controlled throttle. A turbocharger efficiency of 75% was emulated during all experiments.

The test rig includes a conditioning system for cooling water and oil as well as for the charge air supply. The engine's exhaust, intake and combustion chamber are indicated and logged by an automated measurement acquisition system with the recording rate of 0.1°CA. The Kistler 6041B piezoelectric pressure transducer and 5011B charge amplifier are used for combustion pressure recording. Measurements of exhaust and intake pressures are realized using the Kistler piezo resistive pressure transducers 4045A10 and 4075A10 and the corresponding charge amplifier 4603. Two slow pressure transducers in the intake and exhaust of WIKA s10 type are used to plausibilize the recorded data.

The hydrogen methane mixtures are obtained ready-mixed in 300 bar bundles and injected into the intake via six automotive injectors.

The optical investigations are carried out using a minimally invasive endoscopic lateral optical access with a maximum comparability to the thermodynamics

Figure 7. Field of view of the UV enhanced endoscope.

or all-metal engine without optical adaptions (cf. Figure 6). The endoscope ring is designed for continuous full load engine operation using an additional appropriate cooling duct (cf. Figure 8) to prevent increased thermal-induced stress and failure. To briefly summarize the design, it comprises an endoscope ring mounted between the cylinder head and cylinder liner. Three mounting positions for endoscopes can be used simultaneously or individually while sealing the remaining accesses with steel inserts equipped with a thermocouple to investigate the combustion chamber wall temperature. The piston and piston rings are equivalent to those of the all-metal test engine without an optical access. The cylinder head and liner are series parts with slight modifications to fit the endoscopic full load optical engine. Using the same parts as for the all-metal engine enhances the comparability and transferability of results between both engine setups.

For the upcoming experiments, position two (cf. Figure 8) is used with a suitable field of view to observe the combustion focusing on quenching at the cylinder walls and during the after burning-phase. Figure 7 depicts the resulting field of view. As the EV and IV are in the focus plane their imaging has sufficient contrast. The unscavenged pre-chamber is out of focus and therefore blurry, but sufficiently visible to determine its location on the images. The endoscope is mounted in the optic ring with a special sapphire sealing tube from FOS Messtechnik GmbH, which is resistant up to 300°C and 300 bar and utilizes an air cooling system (cf. Figure 8).

LaVision's high-efficiency endoscope with a field of view of ~25° enhanced for the ultraviolet spectral range of 280–350 nm was installed for the test setup. A beam splitter similar to Gleis et al.[52] makes it possible to simultaneously record the visible range of the combustion (cf. Figure 5) and the ultraviolet spectral range, especially the chemiluminescence of the OH-radical comparable to Di Iorio et al.,[23] Catapano et al.,[33,34] Di Iorio et al.[38,48] The visible path is recorded by a color imaging Phantom v2012 high-speed camera equipped
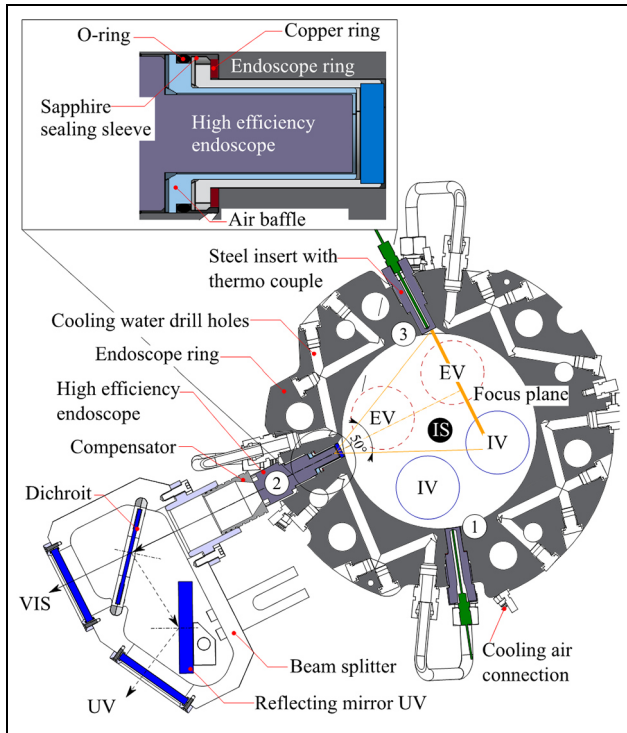
Figure 8. Sectional view of the lateral optical access.

Table 3. Properties of natural gas used.

Methane number	90	N_2 in %$_V$	0.2
Methane in %$_V$	95.7	Ethane %$_V$	3.2
CO_2 in %$_V$	0.7	Butane %$_V$	0.0695
Argon in %$_V$	0.1	H_2	–

with a Wallimex f# 2.8, f100 objective. A monochromatic Phantom v2011 camera equipped with high speed intensified relay optics and a filter for OH* detection (cf. Figure 5) with a spectral range of 300–315 nm (cf. Figure 5) captures the natural UV emissions of the combustion.

Evaluation of thermodynamic results

The following sections summarize the experimental results on the effects of hydrogen addition.

Experimental procedure

The experiments cover the fuel blends: 2/98%$_V$, 5/95%$_V$, 10/90%$_V$, 40/60%$_V$ Hydrogen/Methane and NG as reference fuel. Table 3 summarizes the properties of the natural gas used. The hydrogen concentration is below the detection limit resulting in hydrogen-free natural gas. The investigated ratios represent possible amounts of blending, that is, for German gas infrastructure during the short and medium-term expansion of renewable energies according to Hartmut.[53]

For each fuel, an air-fuel equivalence ratio and a center of combustion variation was conducted at a constant fuel energy amount resulting in max. 21 bar IMEP (Indicated Mean Effective Pressure). The engine speed was reduced from its nominal value of 1500–750 rpm as a necessary precaution to protect the cameras mounted on the testing rig from damage caused by the engine's

vibrations. The air-fuel equivalence ratio was varied from ratios indicating the start of abnormal combustion until the start of misfire in steps of 0.1 by keeping the amount of energy constant and adapting the air mass flow. When increasing the amount of hydrogen admixture, the fuel mass was decreased to keep the energy amount constant. The center of combustion variation within a ±1°CA tolerance includes the crank angles 25°, 21°, 16°, 11°, and 8°CA aFTDC for each step of the fuel air ratio. This results in an adaption of the spark timing angle for the different investigated fuels. The injection of the gaseous fuel starts at 350°CA bFTDC for all investigations with a pressure of 12 bar into the intake manifold.

About 125 consecutive recorded cycles at each measurement point are used in a tuned GT-Power v2021 TPA (three-pressure-analysis) model. Its gas exchange calculation uses the intake and exhaust pressure traces recorded on the test bench. In combination with the measured, corrected and mean combustion pressure trace, the burning rate, burning duration and further related quantities are derived for the following analysis of the experiments. The IMEP coefficient of variance as an indicator for the combustion stability is calculated according to equation (1) (cf. Chen et al.[36]).

$$CoV_{IMEP} = \frac{\sqrt{\frac{1}{N} \cdot \sum_{i=1}^{N} (IMEP_i - IMEP_m)^2}}{IMEP_m} \cdot 100\%$$

(1)

The indicated mean efficiency is calculated according to equation (2) using the indicated mean effective pressure resulting from the integral of the engine speed n and the fuel-flow dependent energy. These values are taken directly from the measurements.

$$\eta_i = \frac{0.5 \cdot n \cdot \oint p \cdot dV}{H_u \cdot \dot{m}_B} \cdot 100\%$$

(2)

Influence of H2 admixture on the combustion process

Burning duration (MFB10-90). As an admixture of hydrogen increases the laminar flame speed (cf. Figure 4), the natural gas shows the highest burning duration over the MFB and air-fuel equivalence ratio variation depicted in Figure 9(a) and (b). With an increase of the air-fuel equivalence ratio, the burning duration
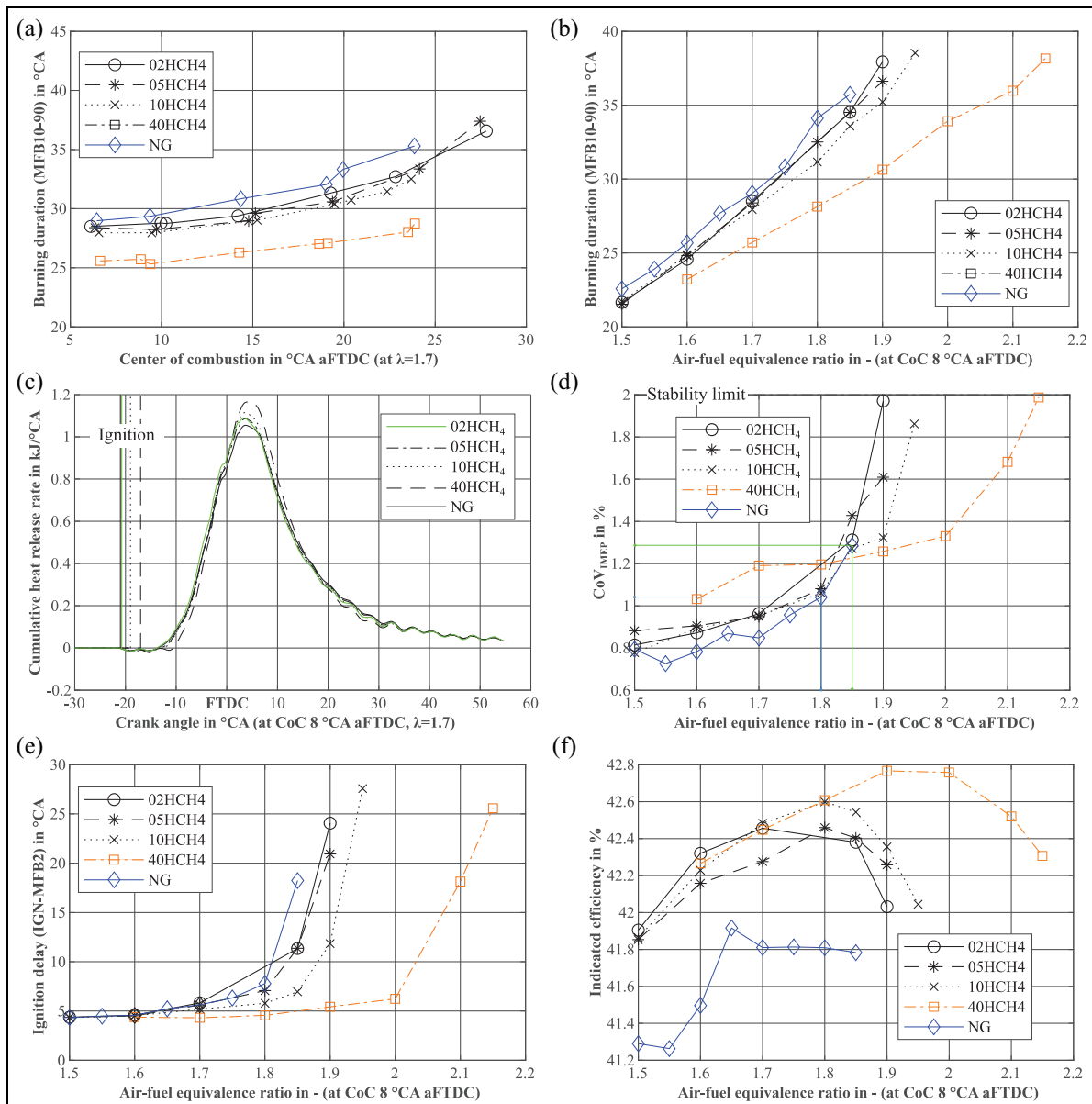
Figure 9. Combustion evaluation of the fuel blends: (a) burning duration over a CoC variation at λ 1, (b) burning duration over a λ variation at CoC 8°CA aFTDC, (c) gross heat release rate at CoC 8°CA aFTDC and λ 1.7, (d) cyclic variation of the IMEP at CoC 8°CA aFTDC and λ 1.7 (e) ignition delay over a λ variation at CoC 8°CA aFTDC, and (f) indicated efficiency of a λ variation at CoC 8°CA aFTDC.

increases as the flame speed decreases. This behavior is observable for all fuel blends (cf. Figure 9(b)). The highest amount of hydrogen at $40\%_V$ has, as expected, the lowest burning duration at an air-fuel equivalence ratio of 1.6 at MFB50 = 8°CA aFTDC with at least 23.3°CA respectively 5.2 ms at 750 rpm. The adaption of the MFB50 results in earlier ignition timing for the lower hydrogen-containing gases. This leads to delayed combustion as pressure and temperature decrease at ignition resulting in a longer combustion duration as depicted in Figure 9(a). Figure 4 shows that the laminar burning velocity is quite similar for the $2\%_V$, $5\%_V$, and $10\%_V$ blends compared to NG. This also results in quite similar burning durations with a maximum

deviation between NG and the $10\%_V$ blend of 2.3°CA at an air-fuel equivalence ratio of 1.8.

In combination with a short burning duration, the indicated efficiency increases while a short combustion results in more complete combustion and reduced wall heat losses. Figure 9(f) depicts the indicated efficiency over a variation. This effect can also be explained by the cumulative heat release rate.

Cumulative heat release rate. The gross heat release rate depicted in Figure 9(c) indicates faster and more intense combustion with an increasing admixture of hydrogen. Furthermore, the ignition timing retards with an increased hydrogen admixture due to a reduced ignition

delay as depicted in Figure 9(e) and a higher laminar flame speed.

Coefficient of variance (CoV). Figure 9(d) depicts the Coefficient of Variance of the IMEP. The behavior of the CoV_{IMEP} can be explained in that with a rich charge composition and an early center of combustion better conditions for ignition and flame propagation exist. The admixture of hydrogen leads to less stable combustion compared to the reference of NG especially for the $40\%_V$ hydrogen blend. For the remaining blends, the CoV_{IMEP} is only slightly higher than that of the NG reference fuel.

The admixture of hydrogen enhances the ignitability and the reactivity of the fuel. As already shown, this leads to fast and intense combustion with a high combustion temperature and pressure increase. At worst, abnormal combustion such as knocking or pre-ignition can occur, the latter being especially induced by oil ingress which degrades the combustion stability. Abnormal combustion, especially pre-ignition, causes a much faster pressure increase resulting in a cycle with much higher IMEP than for normal combustion cycles. This effect can contribute to the instability of combustion.

Furthermore, unstable combustion can occur because of the fuel distribution. For the investigated fuel blends the combustion is rather more independent of the fuel distribution than for NG due to the higher laminar burning velocity and better ignitability. In lean mixtures, especially for NG, the flame propagation decreases until misfire occurs as the charge could not be ignited and the combustion stability deteriorates. By contrast, the better ignitability of the fuel blends facilitates ignition in the first place, enhances the misfire limit, and stabilizes the combustion, as proven by the reduced CoV_{IMEP} over the increased hydrogen admixture above the air-fuel equivalence ratio of 1.8.

However, the possibility of an accumulation of fuel at one place in the combustion chamber also exists. This is especially conceivable because with an increase in the hydrogen admixture, the fuel valves located in the intake manifold have to extend their opening time to inject the energy-equivalent amount of fuel. Due to this, the time available for mixture preparation decreases. With a shortened mixture preparation time, the local combustion becomes richer resulting in an intensified combustion with a faster and higher pressure increase and thus a higher CoV_{IMEP}.

Nevertheless, the CoV_{IMEP} of even NG is quite reasonable because the limit of 2% proposed by Park et al.[54] is not reached. The explanation for this is the unscavenged pre-chamber spark plug that already enhances the ignition at a thermodynamic optimum CoC (Center of Combustion) in respect of the ignition conditions.

Indicated efficiency. Up to an air-fuel equivalence ratio of 1.7, the indicated efficiency shows only minor differences between the $2\%_V$, $5\%_V$, and $10\%_V$ blends. This is mainly because the laminar combustion velocity does not vary much and the combustion conditions are advantageous here compared to leaner combustion. The reference fuel NG provides the lowest indicated efficiency. This is primarily due to incomplete combustion which becomes more complete with the increasing admixture of hydrogen.

With a further increase in the air-fuel equivalence ratio, it becomes obvious that a higher hydrogen fraction in the fuel extends the lean running limit leading directly to a higher indicated mean efficiency. A further increase in the air-fuel equivalence ratio over each corresponding maximum leads to non-sufficient ignition conditions and misfire. With an admixture of $40\%_V$, the indicated mean efficiency can be increased up to almost 43%. The behavior of the $40\%_V$-hydrogen blend exhibits an efficiency that is 0.06% lower than the $2\%_V$ hydrogen blend at an air-fuel equivalence ratio of 1.6. This slight difference can be explained by taking the higher heat loss of the $40\%_V$ mixture into account, which results from higher combustion temperatures due to more intense and fast combustion and a reduced quenching distance.

Ignition delay. The ignition delay is calculated as the temporal difference between the time at which fuel is first consumed and MFB2. It represents an expected behavior. The highest hydrogen admixture provides the lowest ignition delay due to the highest laminar burning velocity as well as the early ignition timings resulting in better temperature and pressure conditions for the ignition. The delay increases for very lean combustion as ignition and combustion conditions deteriorate. The delay also increases with a decreasing admixture.

As the ignition delay appears quite low until an air-fuel equivalence ratio of 2 is reached for the $40\%_V$ hydrogen admixture, the ignition is quite stable. This supports the assumption that the charge distribution influences the fuel blend less for high hydrogen admixtures as even areas with a relatively lean charge distribution are now ignitable.

Effects of hydrogen admixture on emissions

The effects of air-fuel equivalence variations on the THC emissions that correspond to the methane slip as well as on the NO_x and CO_2 emissions regulated by law, are discussed in the following.

THC emissions. The THC emission behavior is depicted in Figure 10(a). With an increase in the H_2 admixture, the CH-ratio (cf. Table 4) decreases leading to a lower
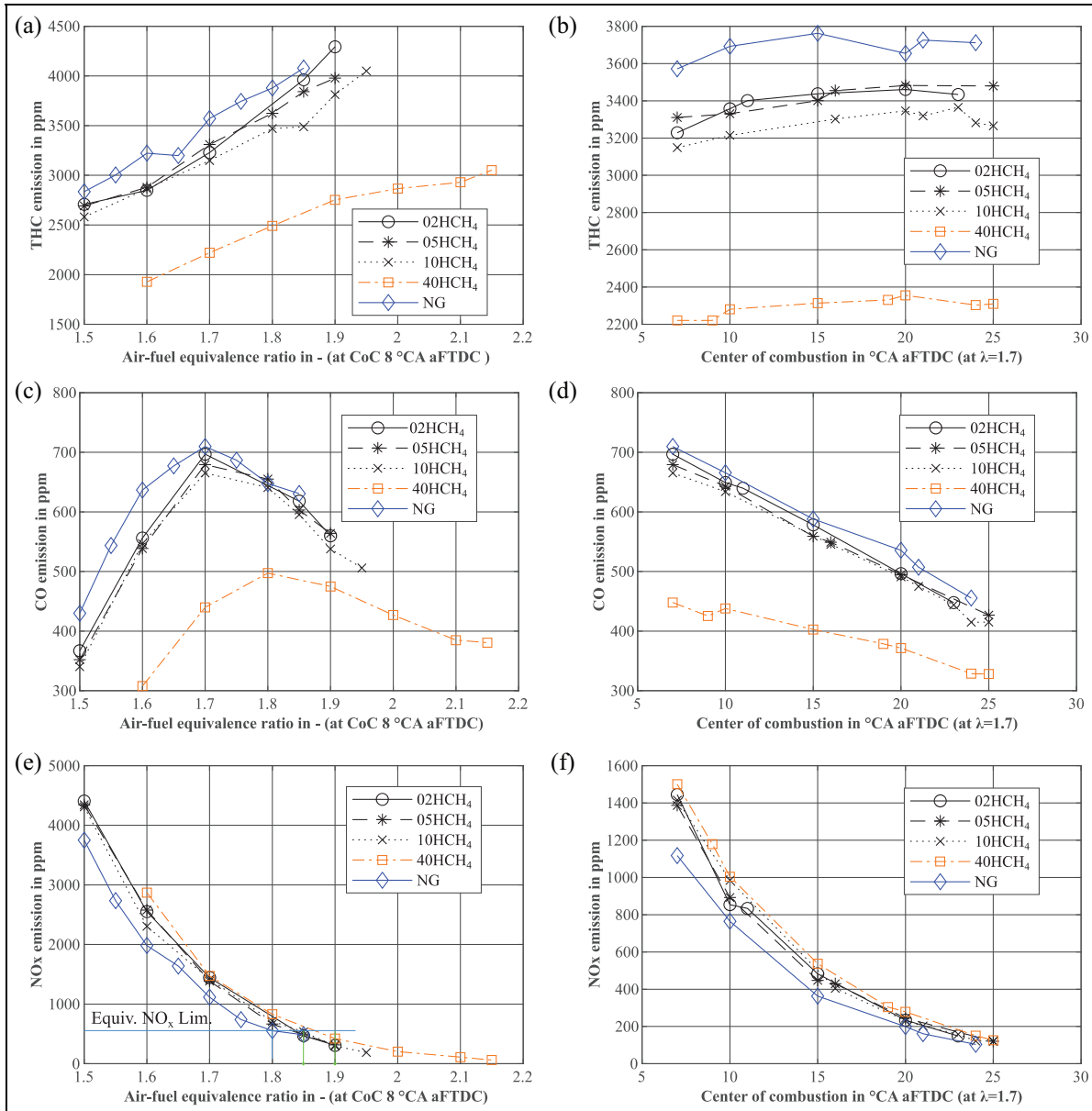
Figure 10. Emission: (a) THC emission of a λ variation at a CoC 8°CA aFTDC, (b) THC emission of an CoC variation at λ of 1, (c) CO emission of λ variation at a CoC 8°CA aFTDC, (d) CO emission of an CoC variation at a λ of 1.7, (e) NOx emission of a λ variation at a CoC 8°CA aFTDC, and (f) NOx emission of an CoC variation at a λ of 1.7.

Table 4. Properties of the used fuels.

	NG	2HCH$_4$	5HCH$_4$	10HCH$_4$	40HCH$_4$
H2 in %$_V$	0	2	5	10	40
CH-ratio in -	0.25	0.247	0.243	0.236	0.183
ϱ in kg/m^3	0.657	0.655	0.653	0.649	0.61
H_u in MJ/kg	50.01	50.21	50.51	51.06	55.86
λ_{St}	17.23	17.28	17.35	17.49	18.66

amount of hydrocarbons and therefore to lower THC emissions. Furthermore, as the laminar burning velocity and the reactivity increase, the quenching distance also decreases with an increasing admixture of hydrogen and

the combustion consumes almost the entire fuel. This means a lower amount of unburnt fuel than arises for NG from gaps not covered by the flame. With a more lean combustion regime, THC emissions increase.

Combustion becomes more unstable as indicated by the CoV_{IMEP} (cf. Figure 9(d)) increasing for leaner combustions. This instability results in more unburnt fuel and thus increased THC emissions. A lower laminar burning velocity for lean combustion defines this behavior for all investigated fuels. During the CoC variation, THC emissions decrease with an increase in the hydrogen admixture due to improved combustion behavior based on the higher laminar burning velocity of hydrogen (cf. Figure 10(b)). Where the late adjustment of the center of combustion is concerned, the THC emissions increase only slightly. This can be attributed to the favorable ignition behavior of the unscavenged prechamber spark plug. In addition, the oxidation of THC in the exhaust pipe due to increasing exhaust gas temperatures counteracts the retarded CoC. Furthermore, the air-fuel equivalence ratio is not yet particularly susceptible to misfiring and thus offers good ignition and combustion conditions.

CO emissions. CO emissions can be used as an indicator for the completeness of carbon oxidation during the combustion and especially the after-burning phase. The emissions reach a minimum under lower air-fuel equivalence ratios because here the temperature in the combustion chamber and the exhaust gas temperatures are higher than under lean conditions (cf. Figure 10(c)). At a higher combustion chamber temperature, the carbon oxidation is enhanced resulting in almost complete oxidation to CO_2. CO emissions increase under higher air-fuel equivalence ratios (up to 1.7 and 1.8 for $40\%_V$) as the combustion temperature decreases. With a further increase of the air-fuel equivalence ratio, CO emissions start to decrease as the experiments reach almost the lean running limit. This results in incomplete combustion visible as an increase in the THC emissions. With an increased amount of unburned fuel, the formation of CO during combustion becomes less likely. This also contributes to a decrease in CO emission levels as lean combustion conditions are approached. The emission trend is practically the same for all fuels, but reduced in its overall amount with an increased admixture of hydrogen. This can be explained by the increased amount of hydrogen when the in-cylinder temperature is increased, thus enhancing the carbon oxidation. Further probable causes for the CO decrease during the air-fuel equivalence ratio increase could be the increased amount of oxygen and a slight increase in the in-cylinder temperature. The increase in oxygen leads to more complete oxidation and therefore to reduced CO emissions. The oxygen further serves as thermal insulation preventing heat loss at the cylinder wall. Instead of losing heat due to wall cooling, the surplus oxygen is heated up which enhances the oxidation of the fuel. The CoC variation depicted in Figure 10(d) verifies the reduction in CO emissions as the hydrogen admixture is increased. With an early center of combustion, the duration of the combustion decreases resulting in less time for oxidation and therefore a higher quantity of CO emissions. With longer combustion duration, the combustion is being delayed resulting in a higher exhaust temperature, which increases the carbon oxidation in the after-burning phase.

NOx emissions. The NOx emissions depicted in Figure 10(e) behave in a manner contrary to that observed for THC emissions. With an increase of hydrogen in the fuel and a richer combustion, NO_x emissions increase. The reason for this is that NO_x emission formation is primarily temperature driven. With an increase in the air-fuel equivalence ratio, the in-cylinder temperature decreases as do the NOx emissions. NO_x formation is also driven by the amount of oxygen (prompt NO_x). Therefore, the quantity of oxygen due to the lean air-fuel equivalence ratio contributes to the prompt NO_x formation for all operating points of the experiment. For the mixture with $40\%_V$ hydrogen and the maximum combustion chamber temperature, no significant increase in NOx emissions compared to the remaining fuels is apparent. Here the third factor for NOx formation has to be considered. The dwell time at high temperatures with high quantities of oxygen is also important for NOx formation. As the $40\%_V$ hydrogen blend provides the lowest burning duration (cf. Figure 9(b)) the dwell time under the necessary conditions is shorter. The CoC variation exhibits similar behavior (cf. Figure 10(f)). With an early center of combustion, the combustion chamber temperature is at its maximum resulting in a high amount of temperature-related NOx emissions. With a late center of combustion, this effect diminishes. Analogously to the air-fuel equivalence ratio variation, the highest amount of hydrogen in the fuel causes the maximum NOx emissions over the complete CoC variation due to the increased combustion temperature.

Nevertheless, cutting the engine's nominal speed by half, by reducing it from 1500 to 750 rpm results in a NOx emission level that is even higher than when running at nominal speed. This must also be considered for better charge mixing and more time available for combustion. Furthermore, the time available for the end of combustion especially the after-burning phase is longer resulting in reduced overall CO and THC emissions compared to the nominal engine speed.

Outcome. For an operation range further extended toward efficient lean combustion and decreased thermal NOx emissions, the admixture of hydrogen up to $10\%_V$ to NG appears to be a suitable measure without a significant risk of abnormal combustion up to an air-fuel equivalence ratio of 1.5. For higher admixture levels, an air-fuel equivalence ratio of 2 is possible but is associated with abnormal combustion starting from an air-fuel equivalence ratio of 1.5, and increased NOx emissions compared to lower admixtures as will be shown in the following. A compromise between

emissions and combustion stability has to be the goal of the engine operation strategy as emissions are regulated by law while combustion stability influences fluctuations in the power output.

Evaluation of the optical results

The optical results include the natural OH radical (OH*) representing the flame front and indication of combustion, the natural flame chemiluminescence as an indicator of black body radiation arising during carbon oxidation in a sooty diffusive combustion that is visible as bright luminosity (cf. section 2.2) and the broadband background radical lumination as an indication of combustion. The visible blue part of the combustion arises from a lean premixed flame especially from CH and C_2 radicals, as described in section 2.2. The natural OH radical chemiluminescence is captured with intensified relay optics at a constant gain for all investigations and bandpass filtered at 309 nm as depicted in Figure 5. Due to the high quantity of optical data, the following evaluation neglects the $2\%_V$ and $5\%_V$ hydrogen admixture.

Pre- and postprocessing

The image preprocessing includes a file format conversion and excerption of the region of interest (ROI). Further, a mean image over the 50 recorded engine cycles for each 0.8 °CA recorded image is calculated. A calibration of the endoscope allows registering of the images of both cameras and creating an overlay of the UV-image information with the combustion observed in the visible spectral range. The postprocessing includes the intensity trace calculation as a summation of all pixel intensities within the ROI, normalized by the actual visible field of view in pixels at the specific °CA the image was captured at. A constant threshold is introduced to filter background noise from the images. Figure 11 depicts the described procedure as well as the percentage of the visible part of the field of view (FOV) that is generally limited by the piston movement covering the endoscopic access. At 4.8°CA aTDC the FOV starts increasing reaching 100% at 29.6°CA. The FOV starts decreasing at 29.6°CA bTDC and is fully covered starting at 4.8°CA bTDC lasting for 9.6°CA.

Air-fuel equivalence ratio and CoC variation

The evaluation of the air-fuel equivalence ratio and the center of combustion variation is conducted using the intensity information derived from the mentioned pre-processing as depicted in Figure 12. It shows the natural OH-radical chemiluminescence (OH*) as well as the natural flame chemiluminescence arising from the different species. Each image in Figure 12 depicts the luminosity trace for three different air-fuel equivalence ratios from 1.6 to 1.8 indicated with a different line style for the specific fuel marked with different colors at the corresponding CoC presented in each line. Each trace's brightness is scaled to the maximum arising intensity per visible area over the investigated CoC and air-fuel equivalence ratio. Further Figure 12 shows the MFB95 which is usually taken as the end of combustion (EoC). As the FOV corresponds to the piston movement, the ignition and the first part of the flame initiation and propagation are not visible. This results in an almost similar start of the intensity trace and a non-fitting maximum compared to the heat release rate. This must be kept in mind when evaluating the depicted intensity traces as indicators for the thermodynamic trends explained in section 4.

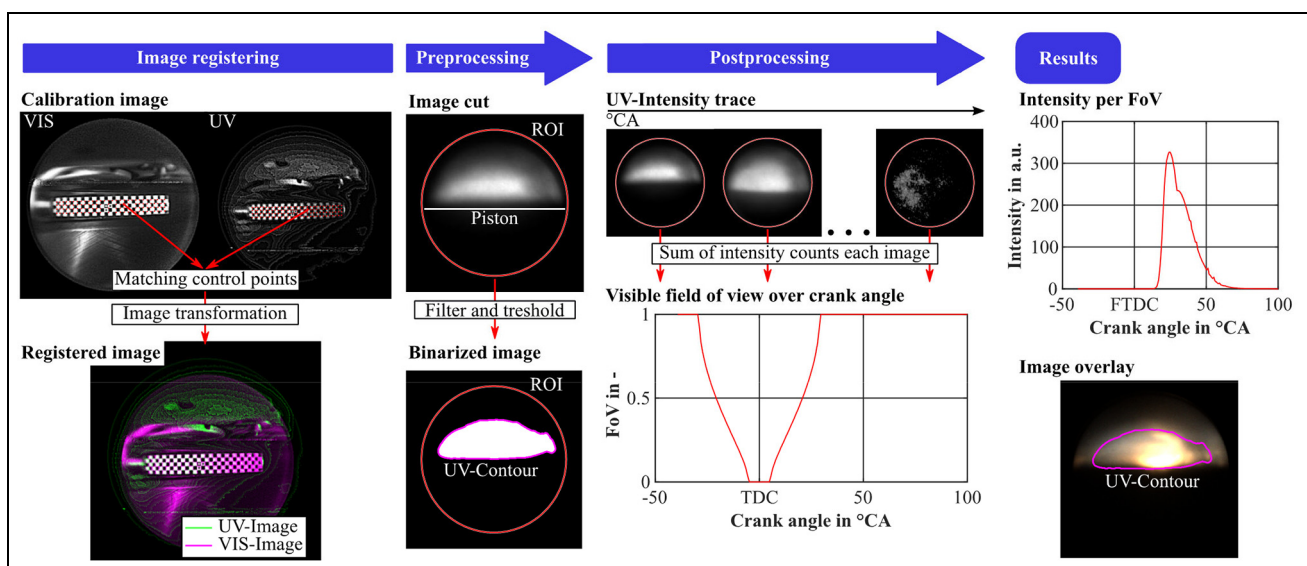*Air-fuel equivalence ratio variation.* The $40\%_V$ admixture induces the most intense combustion, due to the highest

Figure 11. Image processing procedure comprising image registration preprocessing, postprocessing, and result visualization.
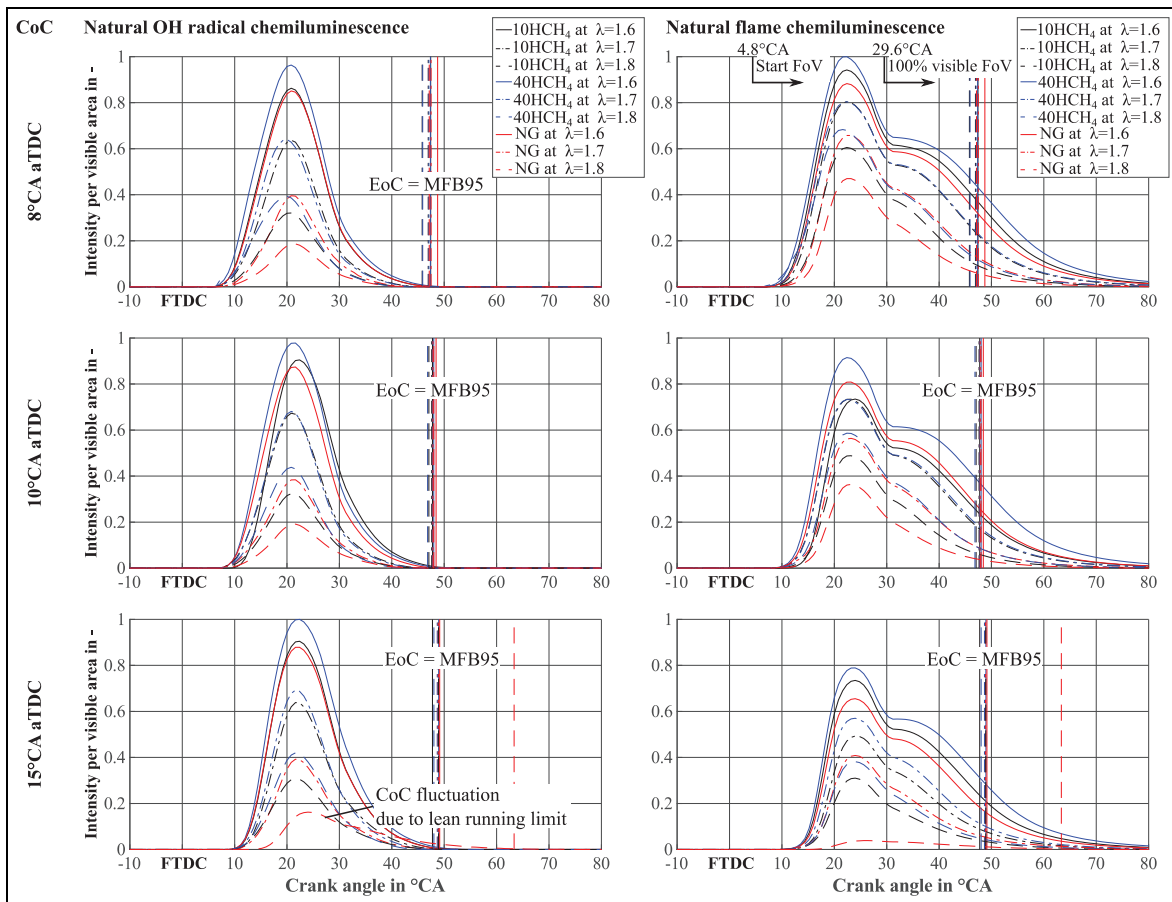
Figure 12. Evaluation of the natural OH radical and flame chemiluminescence due to CoC and air-fuel equivalence ratio variation.

amount of natural OH radical chemiluminescence resulting from the highest combustion temperature and the increased amount of hydrogen available for reaction kinetics as is also investigated in Catapano et al.[45] The natural flame chemiluminescence confirms this assumption at an air-fuel equivalence ratio of 1.6 due to high combustion temperature and therefore high black body radiation as its intensity correlates with T^4 and increased production of broadband combustion radicals such as the CO_2^*, HCO^*, $HCHO^*$ radicals (cf. Catapano et al.[45]). With a decrease in the hydrogen admixture, the intensity in both traces decreases. Further, an increase in the air-fuel equivalence ratio toward a combustion at high air-fuel equivalent ratios lowers the combustion temperature and thus the visible combustion intensity to almost half the intensity for an air-fuel equivalence ratio of 1.8 when compared to the richest combustion at an air-fuel equivalence ratio of 1.6. In combustions with a reduced air-fuel equivalence ratio and an admixture of hydrogen, the laminar burning velocity increases. This can be observed in the slope of the intensity trace that acts as an indicator for the flame speed. For the 10HCH4 and the NG, both traces are quite similar for rich combustion with an air-fuel equivalence ratio of 1.6. With leaner combustion, the behavior of both fuels starts to differ. This is due to the diminishing combustion conditions at higher air-fuel

equivalence ratios, which affect the natural gas more than the fuel blends due to the higher reactivity of hydrogen, and thus extend the lean running capability of the fuel blends. The reduction in the THC and CO emissions and the increase in NOx emissions as depicted in section 4 can also be explained by the intensity traces. With an elongated trace, the maximum admixture depicts a slightly enhanced combustion duration resulting in an extended time for oxidation of CO and fuel residues. The increased intensity also induces a higher combustion temperature enhancing the thermal NOx formation. As the combustion duration decreases with an increased air-fuel equivalence ratio, the CO and THC emissions increase whereas the thermal NOx emissions decrease as the combustion luminosity decreases. In particular, the natural flame chemiluminescence recorded in the visible spectral range indicates an ongoing luminosity continuing after the end of the UV- bandpass filtered images of the natural OH radical and after the MFB95 indicating the end of combustion. This indicates that, after the combustion and flame front propagation, which correlates quite well with the EoC at MFB95, further oxidation of remaining radicals under reduced temperature and pressure takes place. Similar behavior of a spark-ignited natural gas optical engine is, for example, reported in Dumitrescu et al.[55] The fact that the

oxidation is temperature-driven is apparent because with a decrease in hydrogen admixture and increase in the air-fuel equivalence ratio, the intensity lasts for a much shorter time span.

CoC variation. With the variation of the CoC the depicted intensity trace maximum shifts accordingly for both spectral ranges. However, the maximum does not correspond to the combustion center at MFB50 because the influence of the increase in CoC is also visible. Contrary to expectations, the latest CoC at 15°CA aTDC shows the highest intensity of OH radicals. This can be explained by the fact that with a later CoC, ignition occurs later than with an early CoC. Thus, the air-fuel mixture starts burning later during the cycle. As the intensity of the OH radicals correlates with the progress of the combustion, it is postponed as well and thus reaches higher intensities later when the piston clears the FOV. Further, the slope of the intensity trace is slightly greater for the late CoC when compared to the early CoC. Since the crank angle range in which there is no FOV is relatively short and the shift of the CoC from early to late is also only 7°CA, the effects on the OH radical intensity trace are comparatively low. The visible spectral range behaves as expected because the OH radicals' luminosity occurs earlier than the combustion of radicals in the visible spectral range. The intensity of the natural flame chemiluminescence decreases with a late CoC. The late ignition timing for late CoCs causes this when the combustion is not as advanced as for an early CoC. It results in an observable combustion propagation after ignition dominated by a blue cold premixed flame with generally lower intensity. This is visible at the start of the intensity trace that slightly shifts to a later °CA as the camera with the chosen exposure time is not capable of recognizing this low intensity resulting from the cold flame. Further, due to the later ignition timing and thus less favorable ignition conditions, combustion is more retarded than for combustion with an early CoC. This is visible as a lower slope and a shifted MFB95 for late CoC.

The comparison between each fuel for the CoC variation is as expected because of the reactivity of hydrogen compensating for the disadvantages of a late CoC. The emission formation in particular can be classified by the intensity of the natural flame luminescence as a measure of the combustion intensity and thus combustion temperature. NOx decreases as the late CoC results in a reduced combustion temperature, whereas the THC emissions increase. CO emissions decrease with a retarded combustion as a higher exhaust gas temperature is available for oxidation. The CoC influence on OH radical intensity is distinctly lower in contrast to the air-fuel equivalence ratio. This is due to the missing view of the piston bowl because of the piston movement and thus a non-observable start and first propagation of the combustion.

Combustion image series

Figure 13 depicts the averaged images of the recorded cycles at the specific MFB points from MFB50 as CoC to MFB95 as EoC for both the maximum investigated hydrogen admixture and the reference fuel NG. Further, the average of the cylinder pressure and cumulative heat release rate as well as the MFB points are highlighted. The images show the visible part of the combustion and the overlaid natural OH radical chemiluminescence as an outer contour plot derived from the postprocessing of the UV imaging as described in subsection 5.1. The combustion between MFB50 until MFB70 is less intense as well as being mostly covered by the piston, and the image's intensities were therefore scaled for better visibility by a factor of 20 until the combustion becomes visible.

Dependency of heat release rate and image series. The main combustion takes place in the piston bowl. The flame initialization and propagation, which correlates with the OH radical intensity and distribution is not detectable. This is due to the setup's vertical field of view, which is covered by the piston at the beginning and is only gradually released with the piston movement. The piston starts to uncover the FOV notable at MFB50 in Figure 13 for both fuels. Thus, only the late part of the combustion is observable. Therefore, the depicted image series intensities of the natural OH radical and the flame's chemiluminescence do not match the heat release trace due to the missing information during the main combustion in the piston bowl. With the opening FOV at MFB50 the visible intensity increases until it reaches the camera's maximum recordable value at MFB80. Due to this, it is recognizable that the highest depicted intensity respectively the largest depicted OH-contour at MFB80 does not correlate with the maximum heat release rate. Nevertheless, the setup allows a focus on the late combustion because the OH radical is a species which is present even after the main combustion phase depicting areas with ongoing reactions (cf. Reyes et al.[49]). The bandpass-filtered natural OH radical chemiluminescence correlates with the maximum visible intensity. The highest brightness concentrates at the image center and diminishes to the left toward the combustion chamber walls (cf. Figure 13). This means the hot after burning phase concentrates in this region. As the images are an integral of the line of sight, the high intensity could also be caused by this. The amount of natural OH radical chemiluminescence changes its location from the upper region to the center of the observed area in the combustion chamber. This indicates a shift of the combustion reaction toward the burnout phase from the combustion chamber walls to the center of the cylinder between MFB80 and MFB90. At these MFB values, the heat release is almost finished and the main part of the fuel has been consumed. The in-cylinder temperature as well as the in-cylinder
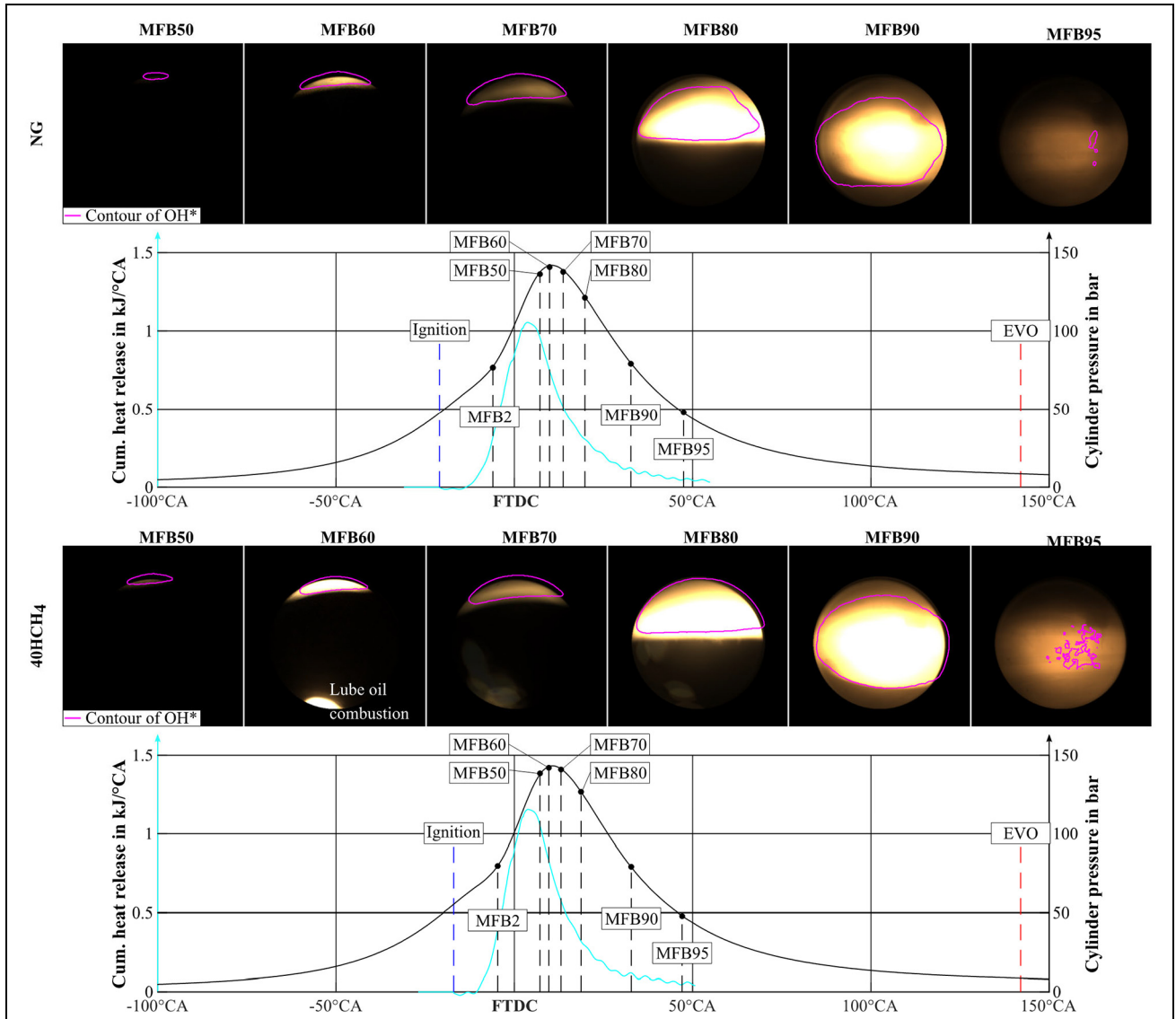
Figure 13. Image mapping for MFB50 to MFB95 at CoC = 8°CAaFTDC and λ = 1.7 for NG and 40HCH$_4$.

pressure decrease until finally the natural OH radical chemiluminescence disappears at MFB95 at which point almost all of the fuel has been consumed and the reaction chain of the fuel stops. Although no natural OH radical chemiluminescence is visible, the visible spectral part of the combustion depicts continuing luminosity.

Comparison of the image series for 40HCH4 and NG. Comparing both fuels, the blend exhibits a slightly higher intensity and higher coverage of the visible area. This hints for the decreased quenching distance of the blend and a more intense burnout phase during the combustion. The natural OH radical chemiluminescence also exhibits quite a large captured area for the fuel blend. This is due to the increased laminar burning velocity as well as the increased combustion temperature. It is evident that the visible combustion continues

after the defined EoC and visible OH radicals. This emission could be caused by water vapor which increases with the admixture of hydrogen (cf. García-Armingol and Ballester[56]). Also, carbon oxidation or combustion of lube oil could be possible other reasons because the temperature is sufficiently high for those effects. Lube oil combustion is particularly visible for the maximum hydrogen admixture at MFB60, 70, and 80. As the images represent the average over 50 consecutive recorded cycles it has to be considered that the lube oil combustion with its strong intensity resulting from the black body radiation of the sooty combustion may occur in only one of the cycles. Nevertheless, an increase of hydrogen could lead to lube oil combustion in the top land of the piston as the quenching distance decreases with increasing hydrogen percentages. This could also hint at increased combustion instability due to increasing hydrogen admixture and the possible brightness after the EoC coming with this.
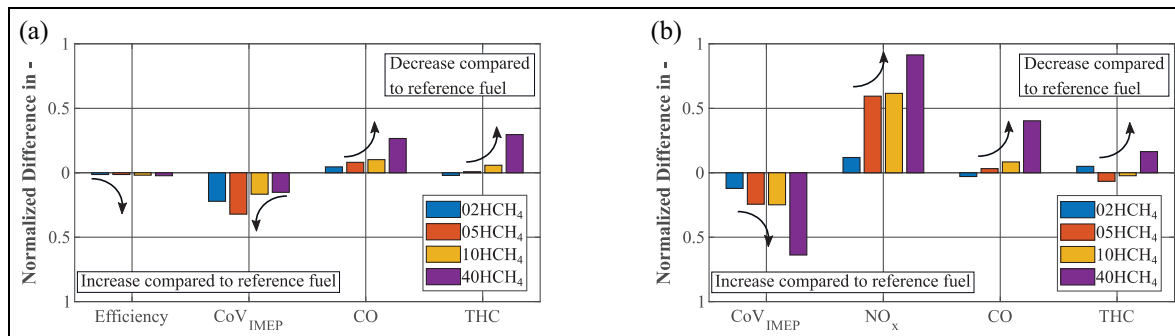
Figure 14. Influence of hydrogen admixture on selected values at: (a) NOx equivalent limit and (b) best indicated efficiency.

Summary and discussion

Using current technology over the medium term, up to $10\%_V$ hydrogen could be fed into the natural gas grid for long-term storage of renewable energies. It is planned to feed smaller proportions of up to $5\%_V$ into the grid in the short term. In the long term, with technological upgrades, up to $40\%_V$ hydrogen could be admixed. In addition, natural gas can be completely substituted by synthetic methane. The admixture of hydrogen changes the combustion behavior in gas engines for coupled electricity and heat generation. This is because the fluid properties of the admixed hydrogen differ from those of methane of which natural gas is mainly comprised or by which it can be substituted (see Table 4).

The presented investigations of the combustion of HCH_4 mixtures with fractions of $2\%_V$, $5\%_V$, $10\%_V$, and $40\%_V$ hydrogen show that up to an admixture of $10\%_V$ and with a center of combustion close to the thermodynamic optimum, only small differences relative to the reference investigations with natural gas in the combustion behavior and the emission formation can be observed. This is partly due to the engine, which has already been optimized for natural gas operation. Admixing hydrogen extends the lean burning limit and thus further improves efficiency. The addition of hydrogen reduces THC emissions due to more complete combustion. However, at the same time, an increase in NOx emissions due to higher combustion temperatures can be observed. Those could be controlled by appropriate exhaust gas after treatment systems and in-engine by an increase in the air-fuel equivalence ratio. The depicted decrease of the combustion stability of the fuel blends could be due to an increased burning velocity instability that occurs particularly with lean mixtures. These flame front instabilities have been investigated by experiments in a constant-volume combustion bomb in Reyes et al.[57] Further, the instability increase could also be due to mixing formation fluctuations resulting from the fuel injection into the receiver quite close to the cylinder head providing only a short length for mixing. Further, the injection duration of the fuel blends has to be extended when increasing hydrogen admixture to equal

the same amount of fuel energy contributing to a shortened mixing time. Moreover, the fuel blends are much more sensitive to lube oil ignition due to the higher reactivity of hydrogen resulting in a higher amount of cyclic variation leading to reduced combustion stability.

In summary, the effects of admixing hydrogen to methane can be illustrated by two typical variations. The first starts with an equivalent NOx limit for the fuels determined by the reference fuel NG at 8°CA CoC. For this NOx limit equivalent, the corresponding air-fuel equivalence ratio is determined for the fuel blends (cf. Figure 10(e)) at which the values depicted in Figure 14(a) are evaluated. This equivalent NOx limit is applied to the next available measurement point. Figure 14(a) depicts the results as the difference relative to the reference fuel. The arrows in the figure indicate the trend emerging from the experiments. At an equivalent NOx limit, the indicated efficiency increases slightly due to the possible lean combustion and is necessary to achieve the same NOx limit because of an increased combustion temperature at a higher hydrogen admixture. As already mentioned, the CoV_{IMEP} increases only slightly for the maximum hydrogen admixture because the hydrogen in particular, is responsible for stabilizing combustion at lean air-fuel equivalence ratios. The CO emissions decrease with an increase in the hydrogen admixture due to the necessary leaner combustion resulting in an oxygen excess for a moderate combustion temperature decrease. The THC emissions also decrease with increased admixture of hydrogen due to improved combustion.

The second example uses the maximum indicated efficiency of each fuel to determine the appropriate air-fuel equivalence ratio at which the remaining values are evaluated. Figure 14(b) depicts the results at an indicated efficiency of almost 42% for the reference fuel NG. The deterioration of the combustion instability is due to the chosen air-fuel equivalence ratio and the other mentioned effects. As the best indicated efficiency occurs for lean combustion, the NOx emissions decrease as the combustion temperature decreases. The other emissions show quite similar behavior, depending strongly on the chosen air-fuel equivalence ratio. The behavior of the $5\%_V$ and $10\%_V$ admixtures of

hydrogen, which is contrary to the expected behavior, results in an increase in the THC emissions of relatively small magnitude and is thought to be due to the more unstable combustion at the corresponding air fuel ratios. Nevertheless, the admixture of hydrogen shows an explainable and predictable behavior confirming the depicted influence derived from the literature review in section 2.

The optical investigations use a UV-enhanced endoscope with its vertical field of view to record the band-pass-filtered UV spectral range to observe the natural OH radical chemiluminescence. Using a beam splitter the visible spectral range recorded simultaneously depicts the broadband luminosity of various combustion radicals as depicted in Figure 5. The optical investigations are evaluated by focusing on the derivation of the intensity trace normalized by the actual FOV which is limited by the piston movement within the line of view. Both results consistently demonstrate the influence of the hydrogen admixture on the combustion and therefore both seem reliable.

Analyzing the image series, a direct correlation between the intensities and the heat release rate is not possible due to the lack of information during the main combustion where the field of view is covered by the piston and therefore not detectable. Nevertheless, the image series gives a good insight into the late combustion stage depicting the shift of combustion toward the burnout phase away from the combustion chamber walls toward the center of the cylinder. Further, the EoC with diminishing natural OH radical chemiluminescence is visible in Figure 13 and correlates with the thermodynamic calculation. Moreover, the images captured within the visible spectral range show an ongoing reaction beyond the EoC defined at MFB95 with an increasing intensity due to hydrogen admixture. Several possible effects may be responsible here. For example, the water vapor produced during combustion exhibits absorption bands in the near IR range which can be excited by transverse influences. The hydrogen admixture would enhance this effect. Likewise, due to the high exhaust gas temperatures, carbon oxidation of unburned fuel or lubricating oil can still occur here. Nevertheless, the end of the natural OH radical chemiluminescence is consistent with the MFB95 and the end of combustion

Conclusion and outlook

The investigations on the effect of hydrogen admixture on natural gas combustion confirm that the addition of hydrogen up to $10\%_V$ does not result in any significant restrictions or deviations from combustion with natural gas. It is only in a moderately lean range that differences in engine operating behavior can occur. Above all, the disadvantage of increased thermal NOx emission formation can straightaway be partially compensated for by further changing the combustion

conditions toward higher air-fuel equivalent ratios. On the other hand, the effects of the slight deterioration in combustion stability on the fluctuations in torque and power output should be evaluated for the respective applications in a full-engine test. Nevertheless, the limit of 2% CoV_{IMEP} is not exceeded in the presented experiments. Only in a very lean range approaching the lean running limit is an increased diversification of the engine operating behavior identifiable with increasing admixture of hydrogen. In respect of this, the combustion could be improved by adapting the ignition timing to a NOx-equivalent reference of NG.

The conducted optical investigations of the natural OH radical and flame emissions are consistent with the findings of the thermodynamic investigations. Luminosity lasting beyond the EoC in the flame emission recordings was apparent in all experiments. Further flame spectroscopy investigations are needed to clarify which wavelengths are involved in detail, in order to get an insight into the reacting species. For future investigations involving the lateral access, a recess in the piston would provide a view into the piston bowl for better observation of ignition and flame front propagation to supplement the current results. Alternatively, a horizontal field of view could be implemented to facilitate viewing into the piston bowl.

In order to be able to judge the transferability of the results of the optically accessible engine compared to the behavior of an all-metal engine, comparative measurements were carried out to determine the differences in behavior. The results allow the conclusion to be drawn that high similarity exists and these results will be presented in a future publication.

Author contributions

The optical setup (development and design) as well as the processing and interpretation of the thermodynamic and optical data belong to S. Karmann. S. Eicheldinger supported the experiments on the testing rig. The remaining co-authors supported the work with their reviews.

Declaration of conflicting interests

The author(s) declared no potential conflicts of interest with respect to the research, authorship, and/or publication of this article.

Funding

ORCID iDs

Stephan Karmann https://orcid.org/0000-0002-0920-7222
Stefan Eicheldinger https://orcid.org/0000-0003-1211-1157
Maximilian Prager https://orcid.org/0000-0003-2507-6530

References

1. Wietschel M, Plötz P, Pfluger B, et al. *Sektorkopplung: Definition, Chancen und Herausforderungen*. Working Paper Sustainability and Innovation 01/2018 Fraunhofer, Karlsruhe, 2018.
2. Wietschel M, Plötz P, Klobasa M, et al. Sektorkopplung – Was ist darunter zu verstehen? *Zeitschrift für Energiewirtschaft* 2019; 43(1): 1–10.
3. Zapf M. *Stromspeicher und Power-to-Gas im deutschen Energiesystem: Rahmenbedingungen, Bedarf und Einsatzmöglichkeiten*. Wiesbaden: Springer Vieweg, 2017.
4. Wahl J and Kallo J. Quantitative valuation of hydrogen blending in European gas grids and its impact on the combustion process of large-bore gas engines. *Int J Hydrogen Energy* 2020; 45(56): 32534–32546.
5. Hüttenrauch J, Müller-Syring G, Krause H, et al. *Integration fluktuierender erneuerbarer Energien durch konvergente Nutzung von Strom-und Gasnetzen- Konvergenz Strom- und Gasnetze: Abschlussbericht KonStGas*. Freiberg: DBI – Gastechnologisches Inst, Mai 2017.
6. Melaina M, Antonia O and Penev M. Blending hydrogen into natural gas pipeline networks: a review of key issues. *Hydrogen Knowledge Centre*, https://www.h2knowledgecentre.com (2013, accessed 1 November 2021).
7. Yoo Y, Glass N and Baker R. *Review of hydrogen tolerance of key power-to-gas (P2G) components and systems in Canada: final report*. Canada, 2017 https://doi.org/10.4224/23002611.
8. Krause H, Giese A, Dörr H and Brückner H-J. *Hauptstudie zur Analyse der volkswirtschaftlichen Auswirkungen von Gasbeschaffenheitsschwankungen auf die Sektoren des Gasverbrauchs und deren Kompensation Phase 1 Hauptstudie Gasbeschaffenheit: Abschlussbericht*. Bonn: Deutscher Verein des Gas- und Wasserfaches e. V, 2016.
9. Weber S and Baumgartner L. Einfluss H2-Zumischung zum Erdgas auf den Betrieb von Gasmotoren: Untersuchung des Einflusses von H2-Zumischungen aus der Windenergie in das Erdgasnetz und die Auswirkungen auf den Betrieb, insbesondere von Gasmotoren [Abschlussbericht Vorhaben Nr. 1159]. Frankfurt am Main, 2014. (Heft 1056 – 2014).
10. Mehra RK, Duan H, Juknelevičius R, Ma F and Li J. Progress in hydrogen enriched compressed natural gas (HCNG) internal combustion engines – a comprehensive review. *Renew Sustain Energ Rev* 2017; 80: 1458–1498.
11. White C, Steeper R and Lutz A. The hydrogen-fueled internal combustion engine: a technical review. *Int J Hydrogen Energy* 2006; 31(10): 1292–1305.
12. Sahoo BB, Sahoo N and Saha UK. Effect of engine parameters and type of gaseous fuel on the performance of dual-fuel gas diesel engines—A critical review. *Renew Sustain Energ Rev* 2009; 13(6–7): 1151–1184.
13. Akansu S, Kahraman N and Ceper B. Experimental study on a spark ignition engine fuelled by methane–hydrogen mixtures. *Int J Hydrogen Energy* 2007; 32(17): 4279–4284.
14. Sagar SM and Agarwal AK. Experimental investigation of varying composition of HCNG on performance and combustion characteristics of a SI engine. *Int J Hydrogen Energy* 2017; 42(18): 13234–13244.
15. Li H, Liu S, Liew C, et al. An investigation of the combustion process of a heavy-duty dual fuel engine supplemented with natural gas or hydrogen. *Int J Hydrogen Energy* 2017; 42(5): 3352–3362.
16. Lounici MS, Boussadi A, Loubar K and Tazerout M. Experimental investigation on NG dual fuel engine improvement by hydrogen enrichment. *Int J Hydrogen Energy* 2014; 39(36): 21297–21306.
17. Tsujimura T and Suzuki Y. The utilization of hydrogen in hydrogen/diesel dual fuel engine. *Int J Hydrogen Energy* 2017; 42(19): 14019–14029.
18. McTaggart-Cowan GP, Rogak SN, Munshi SR, Hill PG and Bushe WK. The influence of fuel composition on a heavy-duty, natural-gas direct-injection engine. *Fuel* 2010; 89(3): 752–759.
19. Kaj P, Jenny S, Gilles M and Hanna B. *Hydrogen as fuel for Wärtsilä gas engines*. 28th CIMAC World Congress, 6–10 June 2016, Helsinki.
20. Kawauchi S, Korb B, Wachtmeister G, Tsuru D, Takasaki K and Junichi H. *Understanding of combustion process in apremixed lean burn gas engine fueled withhydrogen enriched natural gas*. 28th CIMAC World Congress, 6–10 June, Helsink, 2016.
21. Bhasker JP and Porpatham E. Effects of compression ratio and hydrogen addition on lean combustion characteristics and emission formation in a compressed natural Gas fuelled spark ignition engine. *Fuel* 2017; 208: 260–270.
22. Biffiger H and Soltic P. Effects of split port/direct injection of methane and hydrogen in a spark ignition engine. *Int J Hydrogen Energy* 2015; 40(4): 1994–2003.
23. Di Iorio S, Sementa P and Vaglieco BM. Analysis of combustion of methane and hydrogen–methane blends in small DI SI (direct injection spark ignition) engine using advanced diagnostics. *Energy* 2016; 108: 99–107.
24. Hora TS, Shukla PC and Agarwal AK. Particulate emissions from hydrogen enriched compressed natural gas engine. *Fuel* 2016; 166: 574–580.
25. Korb B, Kawauchi S and Wachtmeister G. Influence of hydrogen addition on the operating range, emissions and efficiency in lean burn natural gas engines at high specific loads. *Fuel* 2016; 164: 410–418.
26. Lim G, Lee S, Park C, Choi Y and Kim C. Effects of compression ratio on performance and emission characteristics of heavy-duty SI engine fuelled with HCNG. *Int J Hydrogen Energy* 2013; 38(11): 4831–4838.
27. Liu J, Duan X, Yuan Z, Liu Q and Tang Q. Experimental study on the performance, combustion and emission characteristics of a high compression ratio heavy-duty spark-ignition engine fuelled with liquefied methane gas and hydrogen blend. *Appl Therm Eng* 2017; 124: 585–594.
28. Park C, Kim C, Choi Y and Lee J. Operating strategy for exhaust gas reduction and performance improvement in a heavy-duty hydrogen-natural gas blend engine. *Energy* 2013; 50: 262–269.
29. Park C, Lee S, Lim G, Choi Y and Kim C. Full load performance and emission characteristics of hydrogen-compressed natural gas engines with valve overlap changes. *Fuel* 2014; 123: 101–106.
30. de Santoli L, Lo Basso G and Bruschi D. Energy characterization of CHP (combined heat and power) fuelled with hydrogen enriched natural gas blends. *Energy* 2013; 60: 13–22.
31. Tangöz S, Akansu SO, Kahraman N and Malkoç Y. Effects of compression ratio on performance and

emissions of a modified diesel engine fueled by HCNG. *Int J Hydrogen Energy* 2015; 40(44): 15374–15380.

32. Lee C-F, Pang Y, Wu H, Hernández JJ, Zhang S and Liu F. The optical investigation of hydrogen enrichment effects on combustion and soot emission characteristics of CNG/diesel dual-fuel engine. *Fuel* 2020; 280: 118639.

33. Catapano F, Di Iorio S, Magno A, Sementa P and Vaglieco BM. A comprehensive analysis of the effect of ethanol, methane and methane-hydrogen blend on the combustion process in a PFI (port fuel injection) engine. *Energy* 2015; 88: 101–110.

34. Catapano F, Di Iorio S, Sementa P and Vaglieco BM. Analysis of energy efficiency of methane and hydrogen-methane blends in a PFI/DI SI research engine. *Energy* 2016; 117: 378–387.

35. Di Iorio S, Magno A, Mancaruso E and Vaglieco BM. Analysis of the effects of diesel/methane dual fuel combustion on nitrogen oxides and particle formation through optical investigation in a real engine. *Fuel Process Technol* 2017; 159: 200–210.

36. Chen L, Wei H, Zhang R, Pan J, Zhou L and Feng D. Effects of spark plug type and ignition energy on combustion performance in an optical SI engine fueled with methane. *Appl Therm Eng* 2019; 148: 188–195.

37. Peñaranda A, Martinez Boggio SD, Lacava PT, Merola S and Irimescu A. Characterization of flame front propagation during early and late combustion for methane-hydrogen fueling of an optically accessible SI engine. *Int J Hydrogen Energy* 2018; 43(52): 23538–23557.

38. Di Iorio S, Sementa P and Vaglieco BM. Optical diagnostics for the analysis of hydrogen–methane blend combustion in internal combustion engines. In: Barbir F, Basile A and Veziroğlu TN (eds) *Hydrogen energy conversion*. Amsterdam/ Boston/Cambridge: Elsevier/WP Woodhead Publishing, 2016, pp.233–261.

39. Merola SS, Di Iorio S, Irimescu A, Sementa P and Vaglieco BM. Spectroscopic characterization of energy transfer and thermal conditions of the flame kernel in a spark ignition engine fueled with methane and hydrogen. *Int J Hydrogen Energy* 2017; 42(18): 13276–13288.

40. Soltic P and Hilfiker T. Efficiency and raw emission benefits from hydrogen addition to methane in a prechamber–equipped engine. *Int J Hydrogen Energy* 2020; 45(43): 23638–23652.

41. Korb B, Kuppa K, Nguyen HD, Dinkelacker F and Wachtmeister G. Experimental and numerical investigations of charge motion and combustion in lean-burn natural gas engines. *Combust Flame* 2020; 212: 309–322.

42. Verhelst S and Wallner T. Hydrogen-fueled internal combustion engines. *Prog Energy Combust Sci* 2009; 35(6): 490–527.

43. Korb B, Kawauchi S and Wachtmeister G. Einfluss des H2 Gehalts auf das Brennverfahren von magerbetriebenen Erdgasmotoren im Hinblick auf heutige und zukünftige Emissionsgrenzwerte. In: *9th Dessau gas engine conference*, 16–17 April 2015, Dessau-Roßlau.

44. Core Writing Team, Pachauri RK and Meyer LA. Climate change 2014 synthesis report, https://www.ipcc.ch/site/assets/uploads/2018/05/SYR_AR5_FINAL_full_wcover.pdf (2014, accessed 1 November 2021)

45. Catapano F, Di Iorio S, Sementa P and Vaglieco BM. Characterization of CH4 and CH4/H2 mixtures combustion in a small displacement optical engine. *SAE Int J Fuel Lubricants* 2013; 6(1): 24–33.

46. Gaydon AG. *The spectroscopy of flames.* 2nd ed. Dordrecht, The Netherlands: Springer, 1974.

47. Arias L, Torres S, Sbarbaro D and Farias O. Photodiode-based sensor for flame sensing and combustion-process monitoring. *Appl Opt* 2008; 47(29): 5541–5549.

48. Di Iorio S, Sementa P and Vaglieco BM. Experimental investigation on the combustion process in a spark ignition optically accessible engine fueled with methane/hydrogen blends. *Int J Hydrogen Energy* 2014; 39(18): 9809–9823.

49. Reyes M, Tinaut FV, Giménez B and Pastor JV. Effect of hydrogen addition on the OH* and CH* chemiluminescence emissions of premixed combustion of methane-air mixtures. *Int J Hydrogen Energy* 2018; 43(42): 19778–19791.

50. Eicheldinger S, Bartkowski T, Schröder A, Prager M and Wachtmeister G. Experimental investigation on the influence of brake mean effective pressures up to 30 bar on the behavior of a large bore Otto gas engine. SAE technical paper 2019-01-2224, 2019.

51. Eicheldinger S, Prager M, Wachtmeister G, Nguyen HD, Dohrmann S and Dinkelacker F. Development of a combustion process for gas engines with mean effective pressure above 30 bar while complying with the TA-Luft. In: *11th Dessau gas engine conference*, Dessau-Roßlau, 11–12 April 2019, pp. 44–56.

52. Gleis S, Frankl S, Waligorski D, Prager M and Wachtmeister G. Investigation of the High-Pressure-Dual-Fuel (HPDF) combustion process of natural gas on a fully optically accessible research engine. In: SAE Technical Paper 2019-01-2172, 2019. https://doi.org/10.4271/2019-01-2172.

53. Hartmut K. Untersuchungen der Auswirkungen von Gasbeschaffenheitsänderungen auf industrielle und gewerbliche Anwendungen, https://www.dvgw.de (2014, accessed November 2021).

54. Park C, Kim C, Choi Y, Won S and Moriyoshi Y. The influences of hydrogen on the performance and emission characteristics of a heavy duty natural gas engine. *Int J Hydrogen Energy* 2011; 36(5): 3739–3745.

55. Dumitrescu CE, Padmanaban V and Liu J. An experimental investigation of early flame development in an optical spark ignition engine fueled with natural Gas. *J Eng Gas Turbine Power* 2018; 140(8): 082802.

56. García-Armingol T and Ballester J. Flame chemiluminescence in premixed combustion of hydrogen-enriched fuels. *Int J Hydrogen Energy* 2014; 39(21): 11299–11307.

57. Reyes M, Tinaut FV, Horrillo A and Lafuente A. Experimental characterization of burning velocities of premixed methane-air and hydrogen-air mixtures in a constant volume combustion bomb at moderate pressure and temperature. *Appl Therm Eng* 2018; 130: 684–697.

Appendix

Notation

aFTC	After firing top dead center
aTDC	After top dead center
bFTC	Before firing top dead center
BMEP	Brake mean effective pressure
bTDC	Before top dead center

CA	Crank angle	IV	Intake valve
CHP	Combined heat and power	MFB	Mass fraction burned
CoC	Center of combustion	NG	Natural gas
COV	Coefficient of variance	PFI	Port fuel injection
DF	Dual fuel	ROI	Region of interest
DFI	Direct fuel injection	SI	Spark ignition
EOC	End of combustion	THC	Total hydrocarbon
EV	Exhaust valve	λ	Air-fuel equivalence ratio
FOV	Field of view	$\%_V$	Volume percentage
FTDC	Firing top dead center		
IMEP	Indicated mean effective pressure		

B.6   Veröffentlichung 6 im Original

Karmann, S.; Eicheldinger, S.; Prager, M.; Jaensch, M.; Wachtmeister, G. Optical and Thermodynamic Investigations of a Methane- and Hydrogen-Blend-Fueled Large-Bore Engine Using a Fisheye Optical System. *Energies* 2023, *16*, 1590. https://doi.org/10.3390/en16041590

Reprinted with permission from MDPI Energies.

Optical and Thermodynamic Investigations of a Methane- and Hydrogen-Blend-Fueled Large-Bore Engine Using a Fisheye Optical System

Stephan Karmann [1,*], Stefan Eicheldinger [2], Maximilian Prager [2], Malte Jaensch [2] and Georg Wachtmeister [1]

[1] Institute of Internal Combustion Engines, Technical University of Munich, 80333 Munich, Germany
[2] Institute of Sustainable Mobile Drivetrains, Technical University of Munich, 80333 Munich, Germany
* Correspondence: karmann@lvk.mw.tum.de

Abstract: The following paper presents thermodynamic and optical investigations of hydrogen-enriched methane combustion, showing the potential of a hydrogen admixture as a means to decarbonize stationary power generation. The optical investigations are carried out through a fisheye optical system directly mounted into the combustion chamber, replacing one exhaust valve. All of the tests were carried out with constant fuel energy producing 16 bar indicated mean effective pressure. The engine under investigation is a port-fueled 4.8 l single-cylinder large-bore research engine. The test series compared the differences between a conventional spark plug and an unscavenged pre-chamber spark plug as an ignition system. The fuel blends under investigation are 5 and 10%v hydrogen mixed with methane and pure natural gas acting as a reference fuel. The thermodynamic results show a beneficial influence of the hydrogen admixture on both ignition systems and for all variations concerning the lean running limit, combustion stability and indicated efficiency, with the most significant influence being visible for the tests using conventional spark plugs. With the unscavenged pre-chamber spark plug and the combustion of the 10%v hydrogen admixture, an increase in the indicated efficiency of 0.8% compared to NG is achievable. The natural chemiluminescence intensity traces were observed to be predominantly influenced by the air–fuel equivalence ratio. This results in a 20% higher intensity for the unscavenged pre-chamber spark plug for the combustion of 10%v hydrogen compared to the conventional spark plug. This is also visible in the evaluations of the flame color derived from the dewarped combustion image series. The investigation of the torch flames also shows a difference in the air–fuel equivalence ratio but not between the different fuels. The results encourage the development of hydrogen-based fuels and the potential to store surplus sustainable energy in the form of hydrogen in existing gas grids.

Keywords: optical engine; large-bore engine; hydrogen–methane blend; port fuel injection; fisheye optic

1. Introduction

Sustainable energy production is a key issue in reducing the extent of climate change. For up to 150 years, the internal combustion engine (ICE) has been a key enabling technology for mobile and stationary power generation whilst being continuously optimized and improved. Thereby 25% of the world's power demand is satisfied through the use of ICEs, producing 10% of the world's greenhouse emissions (cf. [1]). Even with the increasing electrification of mobility, the ICE is a promising technology in the environment of Power to X. Hereby, surplus green energy provided by solar and wind sources is used to produce sustainable liquid fuels, such as oxymethylene ethers [2–5], or gaseous fuels, such as methane, hydrogen, and blends for storage and distribution. Onorati et al. [6] emphasize the possibilities of hydrogen in ICEs for sustainable energy production as well as the

need for further investigations, especially regarding hydrogen and derived synthetic fuels. As of now, in the field of large-bore engines, these investigations are still rare (cf. [7]) but not of less importance, as these engines are used for stationary power supply and are the driving force of freight transportation.

To provide the means for such investigations, a new kind of optical accessibility for large-bore engines was developed (cf. [8]), realized (cf. [9]), improved (cf. [10]) and presented in the following to investigate the combustion process of hydrogen methane blends. The admixture of hydrogen to methane is promising in many aspects regarding the optimization of the different fuel properties summarized in Table 1. The high stability of the tetrahedral molecule structure of methane causes its high stability and, therefore, its lower ignitability, whereas hydrogen is highly ignitable, improving the ignitability of mixtures. This results in improved lean-running conditions (cf. [7,11–15]). Additionally, with the increased admixture of hydrogen, the probability of abnormal combustion increases due to the higher ignitability of hydrogen. With the following investigated low admixture of 5 and 10%$_v$, these drawbacks are negligible, as [7] already shown, and as the following results will state. Therefore, these amounts tend to be a suitable way in the short- and mid-term timespan to replace fossil natural gas and can possibly be stored in natural gas grids. Further, the high laminar burning velocity of hydrogen improves combustion efficiency and the lean-running limits of fuel blends in contrast to the low laminar burning velocity of pure methane (cf. [7,11–14]). Due to the lower carbon-to-hydrogen ratio of the fuel blends, the CO_2 emission decreases, which is further supported by more stable lean-running combustion. One drawback of the admixture of hydrogen is the higher adiabatic flame temperature of hydrogen, resulting in increased NOx emissions, especially for higher amounts of hydrogen admixture (cf. [7,11–14]).

Table 1. Fuel properties under normal conditions (cf. [16].)

Fuel Properties	H$_2$	CH$_4$
Density in kg/m^3	0.08	0.65
Ignitability in air in %$_v$	4–75	5–15
Auto ignition temperature in air in K	858	813
Minimum ignition energy in mJ	0.02	0.28
Laminar burning velocity in m/s	1.85	0.38
Adiabatic flame temperature in K at $\lambda = 1$	2390	2226
Quenching distance in mm	0.64	2.03

The combustion of hydrogen/methane mixtures basically follows the chemical reaction process of methane, altered in the elementary reaction steps according to the content of hydrogen and the combustion conditions (cp. [17]). Figure 1 shows the flame spectrum of methane combustion with its common radicals formed during combustion. The hydroxyl radical (OH*), as a main component in the chemical combustion process with its peak at 309 nm, starts forming at 1600 K and is observable during the main combustion process determining the flame front as well as after the main combustion [18,19]
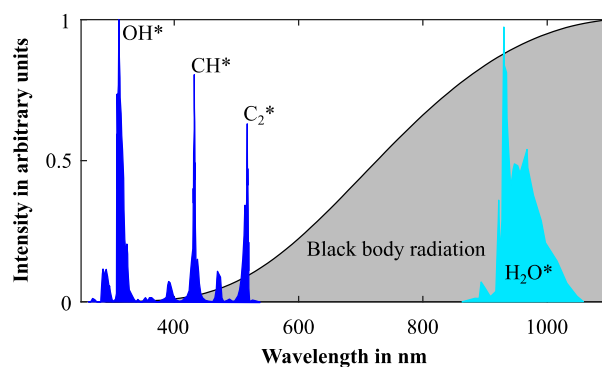
Figure 1. Intensity spectra of methane combustion (data taken from [20–22].)

To distinguish the flame front, the CH radical (CH*), as an intermediate product of the hydrocarbon combustion to the final product CO_2, is a further possible indicator. The CH* mostly forms in regions with slight excess fuel and high temperatures. In addition, the CH* consumption by the flame is faster than the one of OH* and is responsible for the flame's blue color. Hence, the CH* is also an indicator for the prompt NO-formation as the radical is bonding with the air's nitrogen to HCN and finally to NO ([18,20,23]).

The C_2 radical (C_2*), with its peak at 517 nm, forms with a high concentration for premixed combustion under low air–fuel equivalence ratios. Further, C_2* can act as a core for the polymerization of soot, thus presenting a first indicator for incomplete combustion. During combustion, the C_2* radical radiates a large part of the combustion heat. C_2* is responsible for flame colors ranging from yellow to green. ([18,19,24])

Further, background radiation originating from the broadband spectrum of CO_2* (@340–650 nm), HCO* (@340–523 nm) and HCHO* (340–523 nm) (cp. [19,25]) exists, which is not included in Figure 1. Another major occurrence is the black body radiation from soot incandescence arising, e.g., from lube oil ignition, which partly overlays the combustion radical spectra. For the addition of hydrogen to the combustion of methane in a continuous burner [26], reduced global radical emission spectra can be observed, especially for the carbon-based radicals (CH*, C_2*, CO_2*); this can be expected, as with an increased amount of hydrogen, the amount of methane decreases, and thus the amount of carbon atoms required to form these radicals diminishes. On the other hand, the global intensity of the OH* radicals decreases despite the higher amount of hydrogen for the higher admixtures. This can be explained by the reduction of the CH* radical, which reacts with O_2 and forms the hydroxyl radical.

Similar findings are presented in [27] for non-premixed combustion with an emphasis on the importance of CH* radicals for OH* radical formation. The more hydrogen admixture, the more the global emission spectra differ from the typical methane emission, with more H_2O radicals (H_2O*) in the infrared region appearing due to an increasing amount of water (cf. [26]). Nevertheless, [20] mentions that this spectrum mainly arises from thermal excitation and less from chemical reactions. This was also observed in [7], especially after the combustion end was marked as 95% MFB. The H_2O* radical is responsible for the red color of the flame.

Di Iorio [28,29] optically investigated the already mentioned increased laminar flame speed of higher hydrogen percentages using a Bowditch type (cp. [30]) passenger-car-size fully optical single-cylinder research engine. The flame front was detected through observations of the OH* and CH* radicals that were identified as flame front indicators.

As optical investigations of methane/hydrogen mixture combustion in large-bore applications are quite rare (cp. [7]), the following presents thermodynamical and optical measurement results of the combustion of NG, 5/95 and 10/90%v hydrogen mixtures. The optical results are derived from the natural flame chemiluminescence captured with a new type of optical access.

2. Experimental Setup and Procedure

The test bench used in the following experiments is described in [7,31,32] and has already been used in different setups for other investigations. Therefore, the following sections only briefly summarize the main experimental setup and procedure.

2.1. Engine Setup

Table 2 summarizes the main dimensions of the test engine. The fully optically accessible engine consists of two access types—a lateral optical ring and a vertical fisheye endoscope, both shown in Figure 2. The lateral access is realized by inserting an intermediate ring between the cylinder head and the cylinder liner. It contains different mounting positions for an endoscope. For the following experiments, these positions were sealed with steel inserts, as no camera or illumination was used. The fisheye endoscope replaces an exhaust valve and realizes a view from the top.

Table 2. Engine properties.

Bore	170 mm
Stroke	210 mm
Connecting rod length	480 mm
Displacement	4.76 dm^3
Compression ratio	11.6
Ignition system	Unscavenged pre-chamber spark plug Spark plug
Engine speed	750 rpm
IMEP	16 bar

This top view is captured using a high-speed camera mounted outside of the engine to protect the camera from the engine oscillations, so the image is redirected by a 45° deflection mirror toward the camera. The camera is equipped with a Sigma macro-objective. The camera and the fisheye endoscope are aligned using a laser pointer mounted at the end of the endoscope, projecting the laser beam over the deflection mirror to the sigma objective. On the front of the objective, a blend can be mounted. Behind this blend, a mirror redirects the laser beam back to the laser pointer. The perfect alignment is reached as soon as the laser beam distinguishes and is not visible at the blend or the pointer itself. This proper alignment is especially important for the developed image post-processing algorithm mentioned in Section 4. The compensation of any relative motion between the camera and the fisheye endoscope, on the other hand, can be derived from the post-processing. As a reference point for this, a bright spot generated with an LED is rigidly fixed to the mirror frame.

The optically enhanced engine is capable of an extended skipped fire engine operation with at least a fired operation time of 74 s, resulting in 462.5 fired cycles at 750 rpm (cf. [33]). The description of the operation strategy as well as a comparison between the optical setup and the all-metal engine, can be found in [33]. A detailed description of the test bench design and its development can be found in [10].
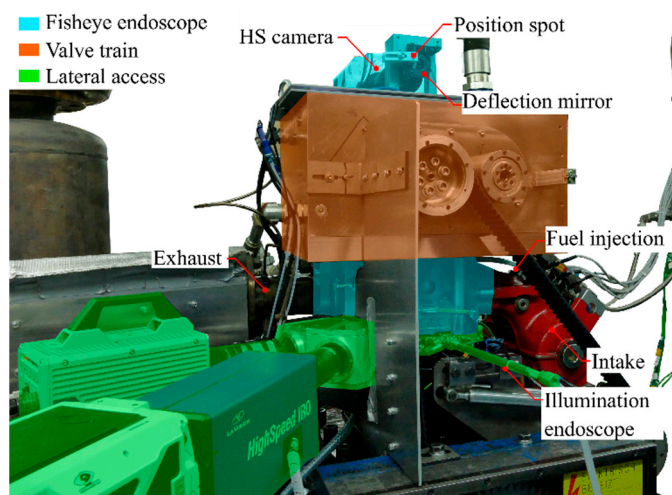
Figure 2. View of the engine setup at the test rig.

2.2. Test Bench Infrastructure

The test bench features automated feeding of the preconditioned media for the cooling water, oil, air, gaseous, and liquid fuel. The natural gas was obtained from the municipal gas network. The gas mixtures are provided directly from the premixed gas bundles. The gas supply pressure is kept constant at 12 bar using a dome pressure regulator before supplying it to the engine's six gas injectors, three of each located at one inlet runner. The gas mass flow is measured using a Coriolis gas flow meter. The screw-type compressor is capable of supplying charged air up to 9 bar. The air mass flow is measured using a rotary piston gas meter. To simulate a turbocharger pressure drop while upholding a constant turbocharger efficiency, a controllable flap is integrated into the exhaust path. A dynamometer is coupled with an induction machine to account for the high-power output of the single-cylinder engine. The test bench has an automated data acquisition system working with two different recording frequencies. The high-frequency resolution of 0.1 °CA captures the intake, exhaust, and combustion pressure. To record the combustion pressure, a Kistler 6041B piezoelectric pressure transducer and a 5011B charge amplifier are used. The intake pressure measurement uses a Kistler 4045A10 piezoelectric pressure transducer. The 4075A10 Kistler piezoelectric pressure transducer for the exhaust pressure measurement is coupled with a Kistler 7533B switching adapter to prevent the sensor from long-time exposure to high exhaust gas temperatures. The intake and exhaust pressure transducers are connected to a corresponding Kistler charge amplifier of type 4603 and plausibilized with a slow pressure measurement using a WIKA s10-type sensor. In addition to the automated data acquisition, an automated engine control system based on the National Instruments c-Rio and PIX system offers the possibility of both automated and manual control. An AVL Sesam FTIR conducts the measurement of exhaust species concentration. A description of measurement accuracy can be found in [33]. Those systems present state-of-the-art measurement techniques and equipment, and the measurements carried out show reproducible and small errors.

2.3. Fuel Properties

The experiments investigate the following fuel blends: 5/95, 10/90%v Hydrogen/Methane and NG as reference fuels in comparison. These mixtures represent potential replacements for fossil natural gas in the natural gas grid infrastructure and are, therefore, relatively easily usable in the near future. Table 3 summarizes the properties of the municipal natural gas used. This mixture is assumed to be hydrogen-free, as the hydrogen concentration is below the detection limit.

Table 3. Properties of natural gas.

Methane Number	90	N$_2$ in %v	0.2
Methane in %v	95.7	Ethane %v	3.2
CO$_2$ in %v	0.7	Butane %v	0.0695
Argon in %v	0.1	H$_2$	-

Table 4 directly compares the fuel properties of the tested blends in contrast to the reference fuel, natural gas. The properties are derived from an experimental gas analysis conducted by a certified laboratory. The properties differ not much, so direct replacement seems possible.

Table 4. Properties of the used fuels.

	NG	5HCH$_4$	10HCH$_4$
H$_2$ in %v	0	5	10
CH-ratio in -	0.25	0.243	0.236
ϱ in kg/m^3	0.657	0.653	0.649
H_u in MJ/kg	50.01	50.51	51.06
λ_{St}	17.23	17.35	17.49

2.4. Experimental Procedure and Settings

The investigations include a variation of the equivalence air–fuel ratio (λ) from 1.5 to 1.8 in steps of 0.1 with an increasing amount of air while keeping the amount of fuel constant. The equivalence air–fuel ratio is within an uncertainty of 0.23% resulting from the measurement devices. Further, the center of combustion (CoC), defined as a 50% amount of burnt fuel, varied in four discrete steps of 7 ± 2°, 11 ± 1°, 15 ± 2 and 20 ± 2 °CA aFTDC within the indicated limit throughout all equivalence air–fuel ratios. The adaption of the CoC results in an adaption of the spark timing. All variations are carried out for each fuel of Table 4 and for each ignition system with a common spark plug and an unscavenged pre-chamber spark plug. All investigations test a constant amount of fuel energy within a tolerance of 2%, necessitating an adjustment of the amount of fuel according to the extent of the hydrogen admixture. This results in an indicated mean effective pressure of up to 16 bar. Further, the geometric compression ratio of 11.6 was kept constant for all investigations.

The following thermodynamic results (burning duration, ignition delay, heat release rate, combustion temperature) are derived from a tuned GT-Power three pressure analysis (TPA) using the temperature results of 125 consecutive recorded engine cycles. Inputs for the calculation were the directly measured combustion chamber, inlet and exhaust pressures, which are averaged and corrected with a two-point offset. In the following presented burning duration, indicated efficiency, heat release rate and ignition delay are derived from the TPA. The CoV is derived directly from the measurement data using Equation (1) (cf. [34]).

$$CoV_{IMEP} = \frac{\sqrt{\frac{1}{N}\sum_{i=1}^{N}(IMEP_i - IMEP_m)^2}}{IMEP_m} \cdot 100\,\% \tag{1}$$

The indicated efficiency was calculated using direct measurements according to Equation (2).

$$\eta_i = \frac{0.5 \cdot n \cdot \oint p \cdot dV}{H_u \cdot \dot{m}_B} \cdot 100\,\% \tag{2}$$

For a detailed overview of the experimental setting, Table 5 summarizes the boundary conditions of the engine's media supply.

In contrast to [7,31,35], the herein presented investigations use the fully optically accessible engine and compare the combustion of an unscavenged pre-chamber spark plug

to the combustion of a conventional spark plug using hydrogen methane blends and natural gas as a reference fuel. This first-of-its-kind optical investigation uses a fisheye optical system to observe these combustions. Further, the optical results are evaluated and compared to the thermodynamical findings.

Table 5. Boundary conditions.

Air inlet temperature	45 °C
Gas inlet temperature	50 °C
Turbocharger emulator flap	Fully open
Cooling water inlet temperature	70 °C
Inlet pressure fuel gas	12 bar
Inlet oil temperature	80 °C

3. Evaluation of Thermodynamic Results

The following sections summarize the thermodynamic results derived from the experiments to determine the effects of hydrogen admixture on the combustion process.

3.1. Burning Duration (MFB10-90)

The burning duration shown in Figure 3 is observed over a variation of the air–fuel equivalence ratio at a constant CoC of 8 °CA aFTDC (Figure 3a,b) and over a CoC variation at a constant air–fuel equivalence ratio of 1.7 (Figure 3c,d). The burning duration consists of the two timespans from the 10% mass fraction burned (MFB10) to 50% MFB (MFB50) and from 50% MFB to 90% MFB (MFB90). The division in these two parts shows the different influences of the admixture on the ignition and main combustion determined between the MFB10-50 and on the late combustion and burnout determined between MFB50-90. Regarding the ignition and main combustion, natural gas shows the longest burning duration in both engine setups using the conventional spark plug (SP) and the unscavenged pre-chamber spark plug (UP-SP). The 10HCH$_4$ fuel mixture shows the lowest burning durations in both engine setups. Especially for high air–fuel equivalence ratios, the hydrogen admixture becomes more effective as the ignition and combustion conditions deteriorate. This improved lean burning behavior can be explained by taking the fuel properties of hydrogen into account, especially the improved ignition and laminar burning velocity (cf. [36]). Nevertheless, for lower air–fuel equivalence ratios, the influence of the hydrogen admixture on the combustion turns out to be smaller, as the ignition and combustion conditions are sufficient for both ignition systems used. Comparing both ignition systems, the unscavenged pre-chamber spark plug leads to a better ignition with a shorter burning duration and shows a greater impact of the hydrogen admixture at higher air–fuel equivalence ratios. Additionally, the unscavenged pre-chamber allows a stable engine operation with natural gas and 10HCH$_4$ at an air–fuel equivalence ratio of 1.8, whereas using the conventional spark plug leads to considerable misfiring and unstable conditions during the skipped fire engine operation and is, therefore, not shown. The main combustion recorded over a variation of the CoC at constant air–fuel equivalence ratio also depicts a reasonable behavior as the burning duration decreases for both ignition systems with earlier CoC, respectively, ignition timings. Furthermore, natural gas depicts the longest combustion and ignition durations for the conventional spark plug (cf. Figure 3c).

The second stage of the combustion, which includes the burnout, shows a similar behavior as the main stage of the combustion for the air–fuel equivalence ratio variation (cf. Figure 3b). Increasing air–fuel equivalence ratios lead to elongated combustion durations as the laminar burning velocity decreases. Concerning the CoC variation, earlier ignition timings lead to earlier CoC, decreasing the burning duration. An increased influence is recognizable as the CoC is later than 15 °CA aFTDC. Nevertheless, the admixture

of hydrogen improves the combustion of late CoCs as the laminar burning velocity is increased. This improves burnout and affects the emissions as well as the efficiency of the combustion.
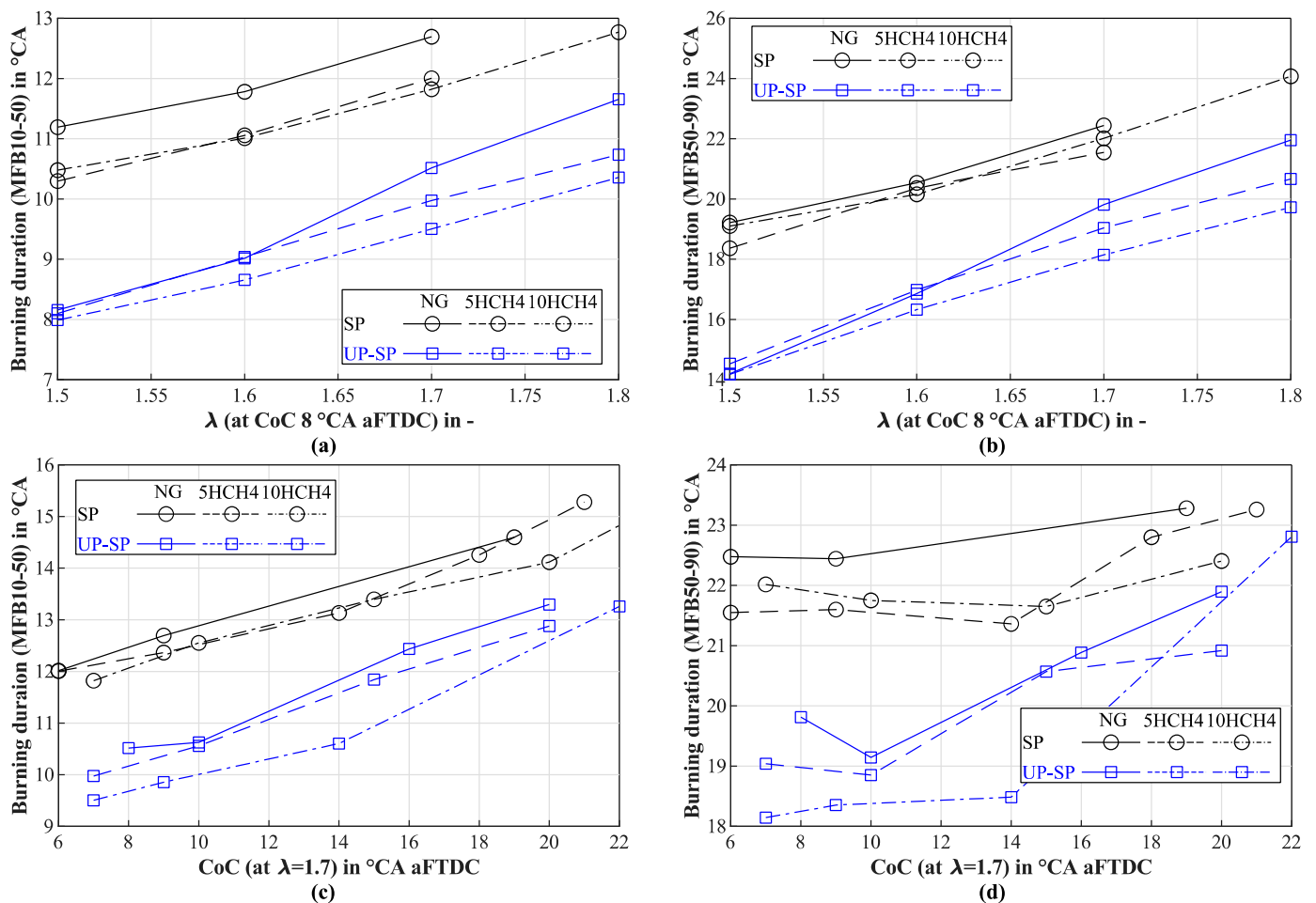

Figure 3. (**a**) Burning duration from 10–50 MFB at constant CoC = 8 °CA aFTDC; (**b**) Burning duration from 50–90 MFB at constant CoC = 8 °CA aFTDC; (**c**) Burning duration from 10–50 MFB at constant λ = 1.7; (**d**) Burning duration from 50–90 MFB at constant λ = 1.7.

3.2. Ignition Delay

The ignition delay shown in Figure 4 is calculated from the ignition timing until MFB2. It is obvious that the unscavenged pre-chamber spark plug reduces the ignition delay significantly, especially for higher air–fuel equivalence ratios. At the air–fuel equivalence ratio of 1.7, the difference between the ignition delay for NG is 18 °CA, for 5HCH$_4$ 11 °CA and 10HCH$_4$ 12.5 °CA. This is especially due to local air–fuel equivalence disturbances influencing the formation of a spark core in contrast to the unscavenged pre-chamber spark plug. In addition, due to the optimized design of the unscavenged pre-chamber's overflow bores, the turbulence in the pre-chamber can be increased to enhance the ignition and growth of the flame kernel (cf. [37]). Further, with increased air–fuel equivalence ratios, the local concentration of fuel near the conventional spark plug decreases, which deteriorates the initiation of the combustion as well as the propagation of the flame front starting at the conventional spark plug. The admixture of hydrogen especially supports the ignition using the conventional spark plug, whereas the effect of both hydrogen mixtures is almost equal. With the unscavenged pre-chamber spark plugs, the effect of the hydrogen addition is almost negligible for the here used amount and shows a clear improvement only at higher air–fuel equivalence ratios. Similar findings in [7] support the results.
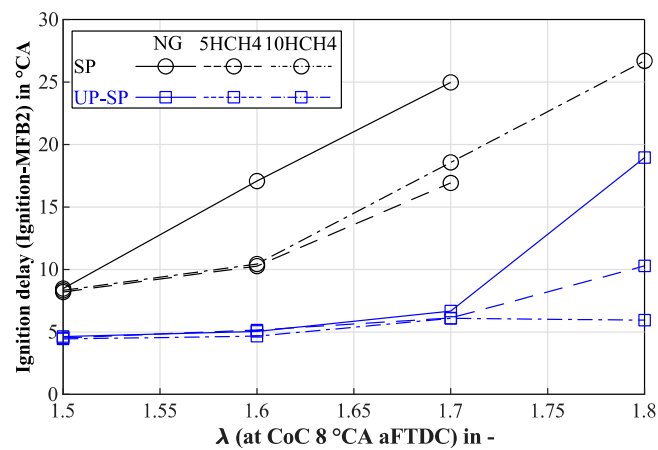
Figure 4. Ignition delay at constant CoC = 8 °CA aFTDC.

3.3. Coefficient of Variance (CoV)

Figure 5 shows the coefficient of variance (CoV) of the indicated mean effective pressure calculated according to Equation (1). Figure 5 also includes the stability limit of 2%, according to [38]. By covering a larger volume during ignition with the unscavenged prechamber, combustion runs more stable than using the conventional spark plug. With increasing air–fuel equivalence ratios, the combustion becomes more unstable as the cyclic variations increase until a misfire occurs. Especially for the conventional spark plug, this results in misfiring and, therefore, exceeds the stability limit. Even with the highest amount of hydrogen admixture used, here, the combustion using a conventional spark plug for ignition exceeds the stability limit at an air–fuel equivalence ratio of 1.8. The investigation results had to be neglected as severe misfires led to absolutely unstable conditions, especially as the engine was operated under skipped fire operation. For the unscavenged pre-chamber spark plug, the admixture of hydrogen is much more beneficial and stabilizes the combustion, if only at higher air–fuel equivalence ratios, whereas at lower air–fuel equivalence ratios, almost no influence is visible. Further, the admixture is low enough that the effects of lube oil ignition cannot deteriorate the combustion stability, as experienced in [7], leading to abnormal combustion. Especially taking the skipped fire operation condition of the optical engine into account, the stabilization of the combustion with an increased admixture of hydrogen is beneficial, resulting in higher combustion temperatures, faster heat-up of the engine and, therefore, improved ignition and combustion conditions.
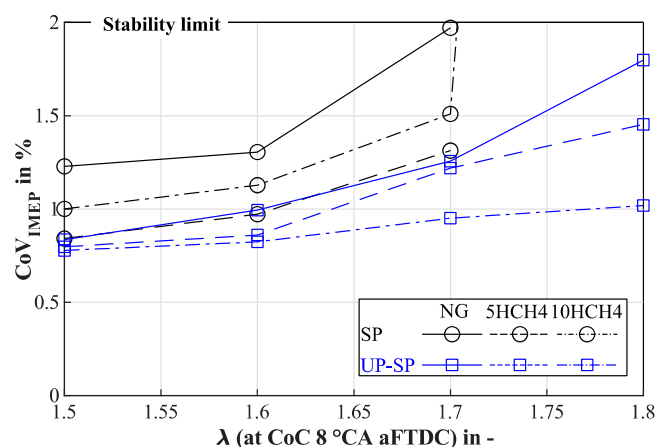

Figure 5. CoVIMEP at constant CoC = 8 °CA aFTDC.

3.4. Indicated Efficiency

Figure 6 includes the indicated efficiency at a constant CoC of 8 °CA aFTDC and at a constant air–fuel equivalence ratio of 1.7 each, with a variation in the air–fuel equivalence ratio, respectively, the CoC. The indicated efficiency was calculated using Equation (2) from filtered, corrected and averaged measurement data. The unscavenged pre-chamber spark plug shows higher indicated mean efficiency due to better ignition and, therefore, faster combustion for the air–fuel equivalence ratio as well as CoC variation. As the lean running limit is increased, this results in higher efficiency at higher air–fuel equivalence ratios for the unscavenged pre-chamber, whereas the spark plug is not capable of the ignition of lean mixtures resulting in misfires and decreased efficiency (cf. Figure 6a). Especially for higher air–fuel equivalence ratios, the benefit of hydrogen admixture is recognizable as the efficiency is increased compared to NG due to stable ignition and combustion. For lower air–fuel equivalence ratios, the effect is less decisive as the ignition conditions here a better compared to higher air–fuel equivalence ratios. Figure 6b shows the effect of the CoC influence on the indicated efficiency. With late CoCs, the efficiency of both ignition systems deteriorates as the combustion duration increases, leading to higher wall heat losses, exhaust gas temperatures and less usable heat for the pressure increase. Nevertheless, an admixture of hydrogen improves the indicated efficiency as it increases the laminar burning velocity of the fuel blend compared to NG.
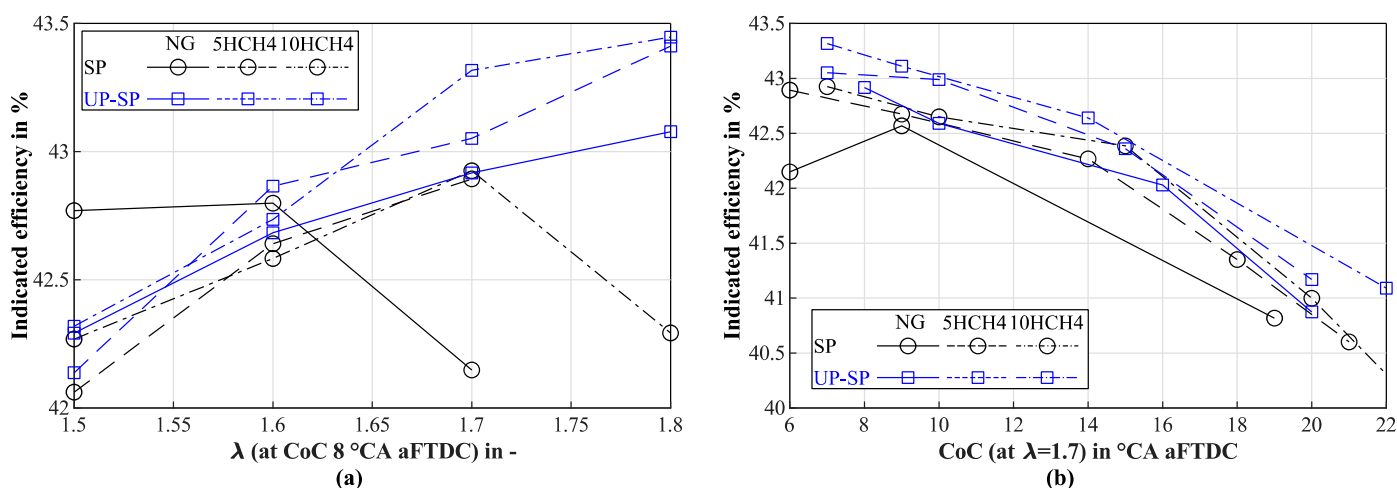

Figure 6. (**a**) Indicated efficiency at constant air–fuel equivalence ratio of 1.7; (**b**) Indicated efficiency at constant CoC of 8 °CA aFTDC.

3.5. Apparent Heat Realease Rate (AHRR)

Figure 7 shows the heat release rate for both ignition systems and investigated fuels at a constant CoC of 8 °CA aFTDC and an air–fuel equivalence ratio of 1.7. Concerning the ignition system, the unscavenged pre-chamber shows later ignition timings due to a reduced ignition delay (cf. Figure 4) and reduced burning durations (cf. Figure 3).

The conventional spark plug needs much earlier ignition timings to overcome the deteriorated ignition behavior. Further, the addition of hydrogen only slightly alters the timing. The admixture results in a steeper heat release and higher peaks, as well as a retarded burnout. This supports the increased indicated efficiency of the combustion of the fuel blends (cf. Figure 6). Compared to the unscavenged pre-chamber spark plugs, Figure 7b shows a much steeper and faster combustion with increased peak value and a further retarded burnout, resulting in an increased indicated efficiency. The addition of 2%$_v$ is only of less influence concerning the heat release, while the ignition delay of NG and 5HCH$_4$ are almost equal. Nevertheless, the peak value is 1.3 °CA earlier and 4.6% higher. The maximum hydrogen admixture shows the highest heat release peak, resulting in fast combustion.
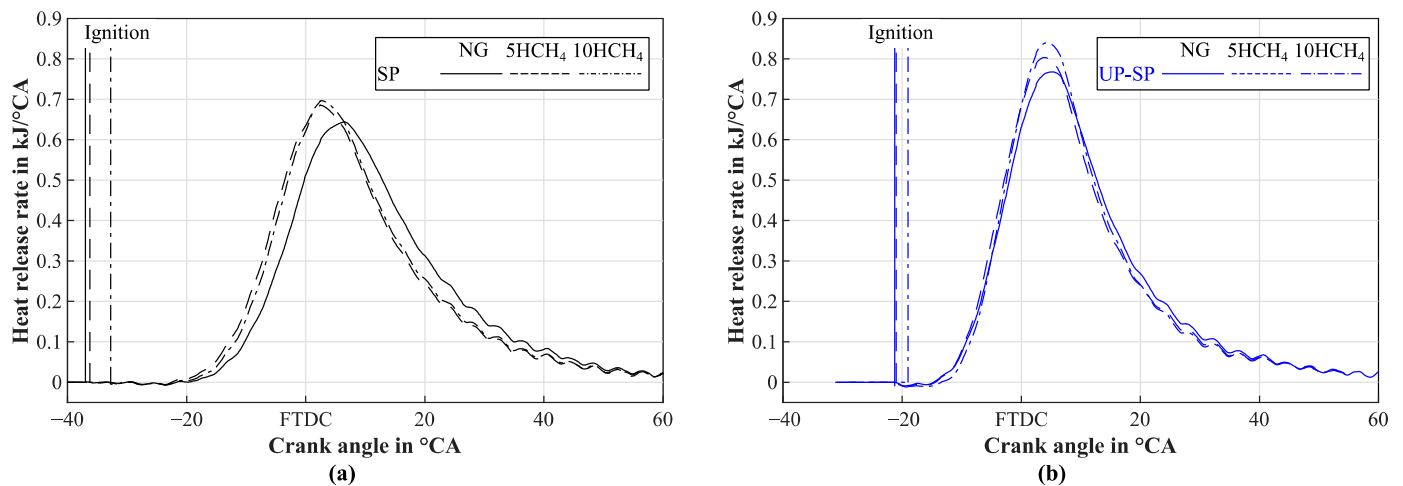
Figure 7. (**a**) Heat release rate for spark plug at CoC = 8 °CA aFTDC and air–fuel equivalence ratio 1.7; (**b**) Heat release rate for unscavenged spark plug at CoC = 8 °CA and air–fuel equivalence ratio 1.7.

4. Evaluation of the Optical Results

The optical investigations focus on intensity traces of the natural flame chemiluminescence to support the findings of the thermodynamically derived results. A comparison of images at specific points in the combustion cycle can be used to derive differences in the combustion between the two ignition systems and the different investigated fuels.

4.1. Procedure of the Image Evaluation

The pre- and post-processing follow the approach detailed in [35]. Figure 8 summarizes the preprocessing procedure implemented in Matlab. The preprocessing includes basic image arithmetic to rotate and mirror the image, the compensation of the image movement, a cutout of the ROI (region of interest) and a debayering to derive the colored images. The post-processing includes the un-distortion of the images as well as a simplified reprojection algorithm detailed in Section 4.4. For this, a special calibration of the complete fisheye endoscope is necessary. The procedure behind the calibration is explained in detail in [35]. The calibration is carried out using the Kannala Brandt [39] approach. It is compared to an alternative approach in [35] and chosen as the most applicable. The calibration leads to the forward projection function shown in Figure 9, with a maximum angle of 97.2° and a maximum image radius of 203 px.
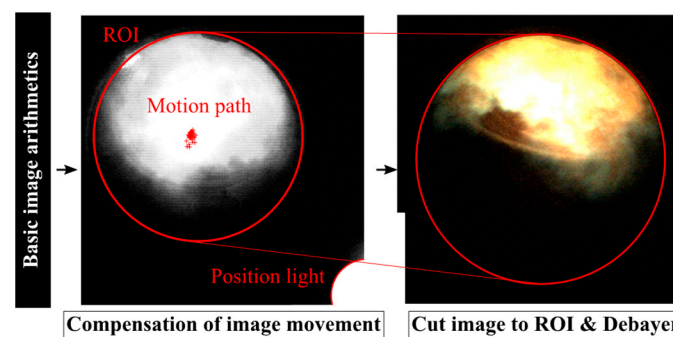
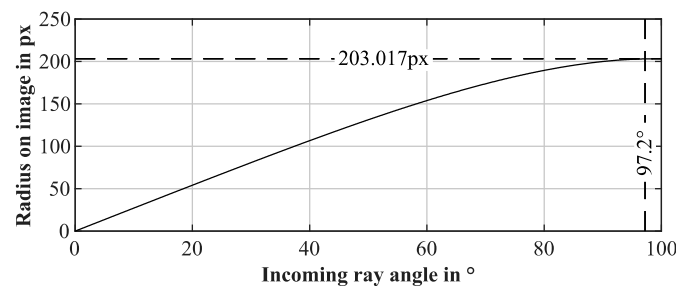

Figure 8. Preprocessing of images.

Figure 9. Forward Projection function derived from calibration.

The calibration for the imaging was carried out on a setup outside the engine with similar mounting conditions as at the engine (cf. Figure 10). The alignment of the camera towards the optic at the testing rig and at the calibration setup uses a laser beam extinction. The calibration setup outside the testing rig facilitates a homogenous illumination, as well as the usage of the calibration pattern with a size of 297 mm × 42 mm × 10 mm. The pattern consists of 17 columns and 12 rows, resulting in 204 regular black and white squares with 176 usable control points and 325 unique distances between them. To estimate the accuracy of the calibration, a reprojection of the calibration pattern to six different offsets from the first lens is carried out. For each reprojection, the algorithm shown in [35] was used to derive the visible distances between the control points. Figure 11 shows the standard deviation of the derived distance to the real one with 25 mm.

The quality of the results is dependent on the accuracy of the detection algorithm used to derive the control points from the image, the precision of the calibration itself and the accuracy of the measurement of the distance between the optic and the pattern. Especially due to the detection of the control points herein carried out with [40], the distance proves especially influential as its accuracy also determines the calibration quality. Further, the typical optical distortion effect of a fisheye optic can be seen in the results. With the object closer to the lens, the object becomes more distorted, resulting in a deteriorated resolution and, thus, a higher standard deviation. The higher standard deviation for the 24 mm distance results from the almost doubled amount of detectable and useable distances to determine the value. Here, the imaging results of the investigations can be used to derive a better estimation of the optic's accuracy. With an averaged standard deviation over all distances, a deviation of 3.3 mm compared to the engine's bore 2% proves a less comparable deviation. A mean value over all investigated distances seems valid, as the observed natural chemiluminescence is an integral field of sight method.

To further improve the accuracy of the reprojection algorithm, a tuning of the camera's position in the real world can be carried out if at least the real-world coordinates of one point in the image are known. Two visible control points in the image were used for this and compared to the digital mockup of the testing rig. The analysis showed a mean error of 3.2 mm for the reprojection and, thus, imaging accuracy.
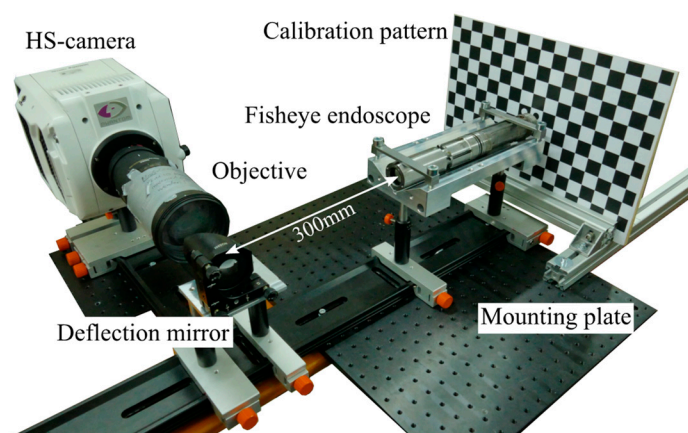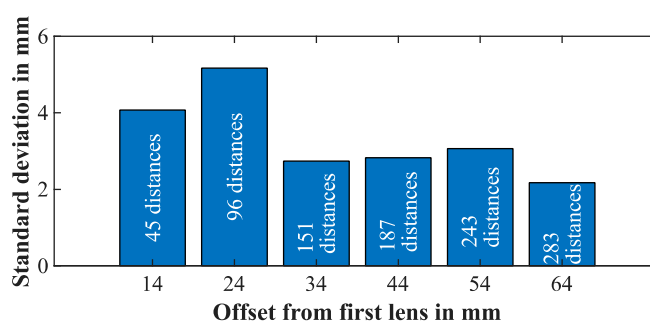
Figure 10. Calibration Setup.

Figure 11. Standard deviation of distance between control points.

4.2. Evaluation of the Natural Chemiluminescence Intensity Trace

Figure 12 shows the mean intensity trace over all recorded cycles for the CoC of 8, 10 and 15 °CA aFTDC and the different air–fuel equivalence ratios 1.5, 1.6, 1.7 and 1.8. Column 1 contains the traces for the unscavenged pre-chamber sparkplug, whereas column 2 shows the traces for the conventional spark plug. All traces are normalized relative to the maximum arising intensity for the unscavenged pre-chamber spark plug of CoC 8 °CA aFTDC and λ 1.5 to compare the intensity traces among the different CoC and air–fuel equivalence ratios as well as for both ignition systems. As already shown in the evaluation of the thermodynamic results, it is not capable of a stable ignition, respectively, combustion for the air–fuel equivalence ratio of 1.8, so no characteristic behavior can be determined. Thus, they are not included in the optical evaluation. According to Figure 12, a postponed center of combustion results in a less intense natural flame chemiluminescence. This can be explained by a reduced combustion temperature, resulting in a less intense broadband luminosity of the combustion.

The comparison of the combustion temperature derived from the TPA model with the intensity for the unscavenged pre-chamber spark plug at λ 1.5 and 1.8 for $10HCH_4$ and NG under the CoC variation is shown in Figure 13. Here, the decrease in the combustion temperature with higher air–fuel equivalence ratios as well as with late CoCs is visible. In particular, for the CoC of 15 °CA aFTDC, the maximum occurring temperature is retarded for all air–fuel equivalence ratios. This results from delayed and slow combustion under these conditions.
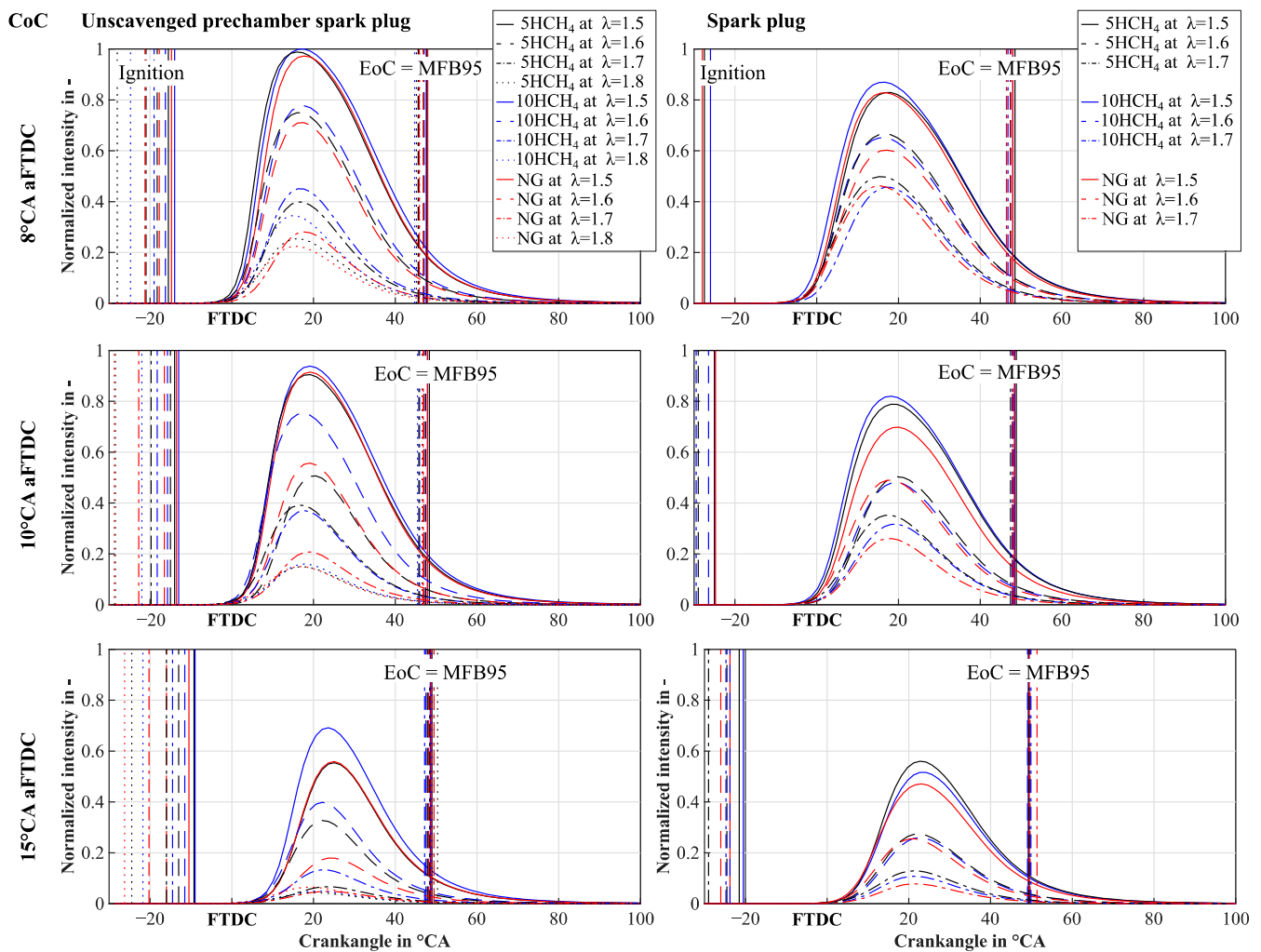
Figure 12. Intensity trace of the natural chemiluminescence for a CoC and air–fuel equivalence ratio variation comparing an unscavenged pre-chamber sparkplug to a spark plug.
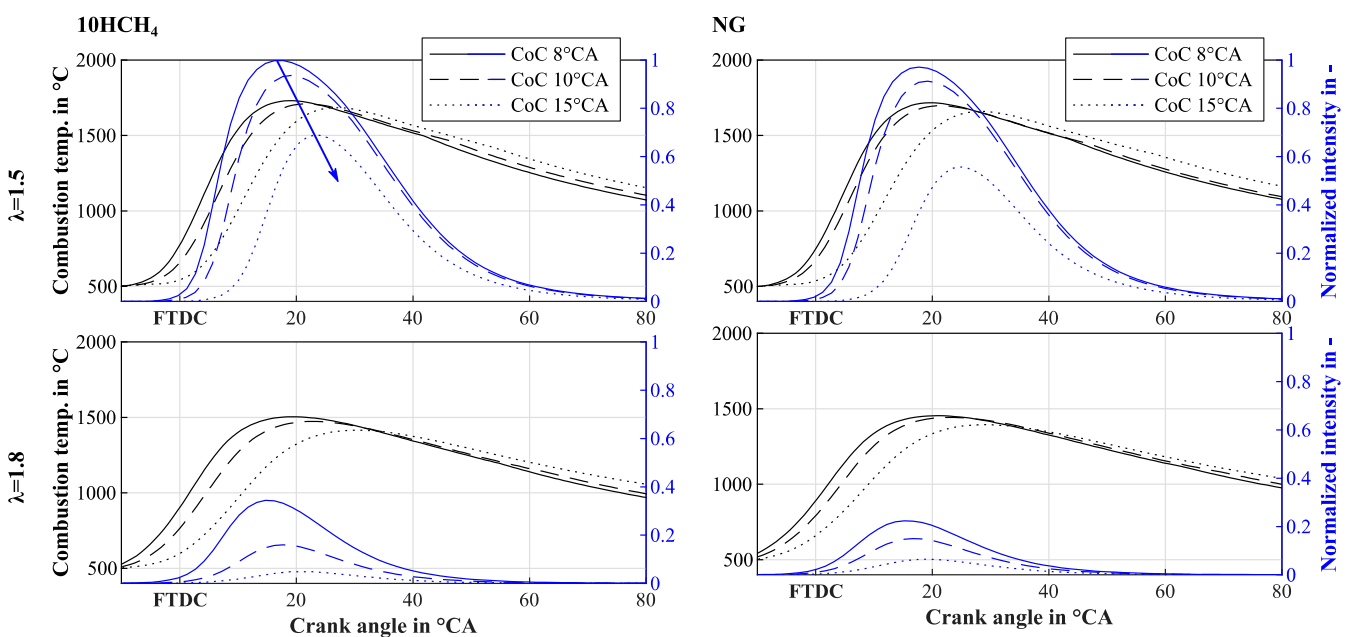

Figure 13. Normalized intensity traces and combustion temperatures for CoC variation at λ = 1.5 and 1.7 for the unscavenged pre-chamber spark plug.

Further, the conditions for the chain branching mechanism of the combustion deteriorate towards lower pressure and temperature during the combustion for late CoCs. This behavior is observable for both ignition systems, and an even lower intensity can be observed for the conventional spark plug due to a lower ignition performance, leading to an even more deteriorated combustion for later CoCs. The behavior of the air–fuel equivalence ratio variation seems valid, taking higher combustion temperatures (cf. Figure 13) and faster combustion into account. The higher combustion temperature arises from lower air–fuel equivalence ratio values due to a higher amount of fuel and less surplus air. In addition, a higher broadband luminosity from less quenching between the excited combustion molecules with oxygen for lower air–fuel equivalence ratios results in higher intensity (cf. [41,42]). The faster combustion leads to an early generation of chemiluminescence arising from carbon-based radicals with higher energy content, resulting in more intense radiation. This can be observed in Figure 13, as for low air–fuel ratios and early CoCs, the intensity's maximum is within 1 °CA difference between the temperature and intensity trace. For late CoCs, the combustion slows down, and the offset between the temperature and the intensity increases to almost 3 °CA. This becomes even more for high air–fuel equivalence ratios, as quenching and a further decrease in burning velocity occur. A difference of 10 °CA develops between the two maxima. The behavior between the maximum admixture of 10%v hydrogen and the NG is similar.

For the unscavenged pre-chamber spark plugs, the 10%v hydrogen admixture shows the highest natural flame chemiluminescence intensity due to the highest combustion temperature (cf. Figure 13) with the most broadband radiation. This difference becomes more obvious as the ignition and combustion conditions deteriorate for a higher air–fuel equivalence ratio and a later CoC. The increased amount of hydrogen in the mixture counteracts the deteriorated conditions for ignition and combustion. Especially for the lowest air–fuel equivalence ratio of 1.5 and the earliest CoC of 8 °CA aFTDC, the difference between the fuel mixtures and the reference fuel NG is quite small. The same behavior can be observed in Figure 13 when comparing NG and $10HCH_4$ at λ 1.5. The combustion temperatures are quite equal, with a difference of 40 °C for the earliest CoC and also for the CoC 10 °CA aFTDC. With the late CoC 15 °CA aFTDC, the influence becomes remarkable. This is due to the optimal ignition conditions at early CoC, a low air–fuel equivalence ratio and stable and complete combustion, resulting in high combustion temperatures and, thus, the high intensities of the broadband radiation. Those operating points are also quite similar because of the limited resolution of the camera, as all images are captured with the same exposure time for comparability. Nevertheless, as already shown in section three, the unscavenged pre-chamber spark plug shows a stable ignition, even for the deteriorated conditions at late CoC and high air–fuel equivalence ratios, and all used fuel mixtures. The results show similar behavior as mentioned in [7]. However, the end of combustion marked as MFB95 cannot be correlated with the natural chemiluminescence as further intensity above the MFB95 is visible. Similarly to what was discussed in [7], this can result from excited water forming during the after-combustion phase. Especially with a higher content of hydrogen and a lower air–fuel equivalence ratio, the intensity after the end of combustion is higher, resulting from higher combustion temperatures.

The offset of the CoC and the center of intensity (CoI) shows a mean value of 13.98 °CA and a standard deviation of 2.2 °CA for the unscavenged pre-chamber spark plug. The offset between the CoC and CoI for the conventional spark plug shows a mean value of 14.29 °CA and a standard deviation of 2.2 °CA. The difference between the CoI and the CoC of both ignition systems for all the investigated variations seems almost constant with at least 14 °CA.

4.3. Evaluation of Combustion Image Series

Figure 14 shows the combustion image series for the MFB5, MFB10, MFB50 and MFB95 at 8° CoC and an air–fuel equivalence ratio of 1.5 and 1.7 for the unscavenged pre-chamber spark plug for NG and a 10%v admixture of hydrogen. The image intensities are

scaled individually for each MFB for better visibility but are constant for the different fuels. The images are taken from the 25th recorded cycle out of 50 and are not depicting the mean value.
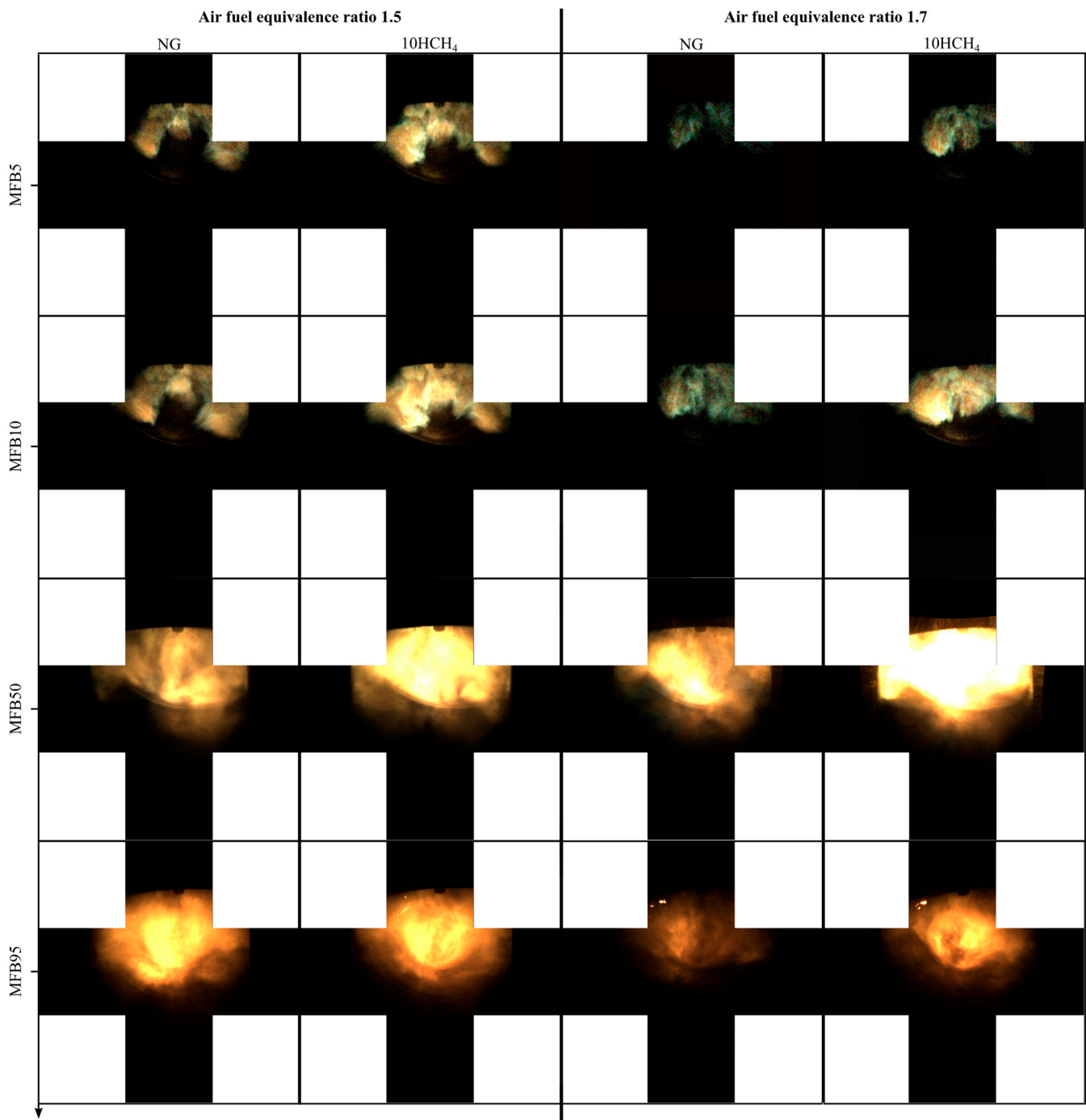

Figure 14. Combustion image series for MFB5, 10, 50 and 95 for the unscavenged pre-chamber spark plug at 8° CoC and air–fuel equivalence ratio of 1.5 and 1.7.

Further, the images are dewarped using five different pinhole projections (cf. [35]), resulting in the specific display format. Figure 15 shows the same arrangement for the conventional spark plug. As already described in Section 1, the radicals arising during combustion are responsible for the flame's color. A comparison of the two fuels for the respective air–fuel equivalence ratio shows only a few differences in the color composition of the flame for both ignition systems. For the air–fuel equivalence ratio of 1.5 using the

unscavenged pre-chamber spark plug (cf. Figure 14), only the early stages of the combustion of NG and 10HCH₄ at points MFB5 and MFB10 show blue areas at the flame front. These can be attributed to the formation of CH* in the outer edges of the flame, the reactive flame front. In the early stages of the combustion of 10HCH₄, some yellow areas can already be seen in the flame, which can indicate higher combustion temperatures as well as faster combustion leading to the earlier formation of more C_2*.
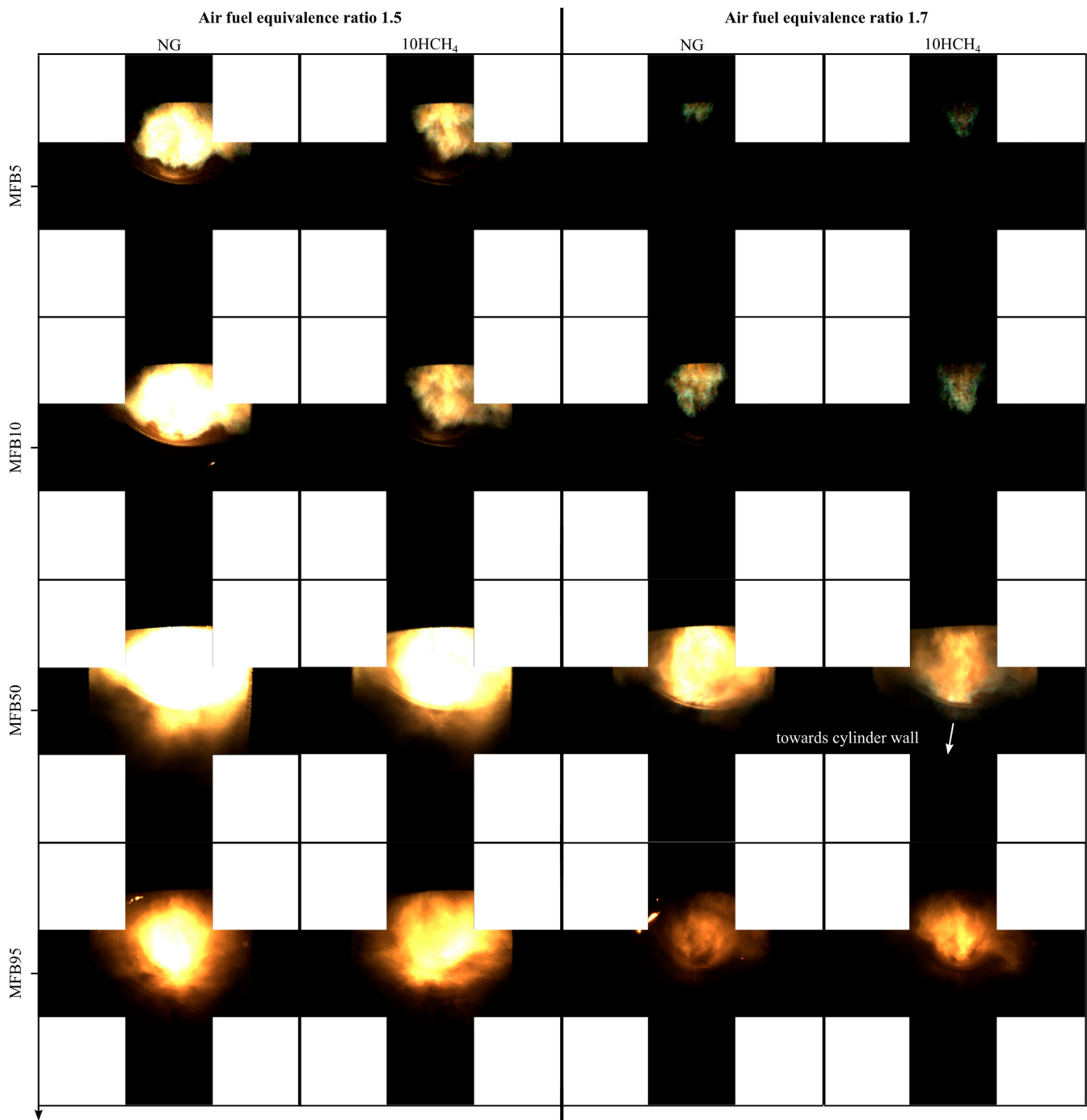

Figure 15. Combustion image series for MFB5, 10, 50 and 95 for the conventional spark plug at 8° CoC and air–fuel equivalence ratio of 1.5 and 1.7.

With MFB5, both flames show a reddish portion, which can be an indicator of the formation of water. The center of combustion shows a strong yellow flame, indicating a

high combustion temperature and the resulting strong black body radiation and C_2^* formation. Further, there are reddish areas at the boundaries of the deep yellow parts of the flame. This intensifies as the flame progresses toward the burnout phase and is clearly visible for MFB95. Here, a bright yellow core is now formed, blending into the red spectral range in the direction of the combustion chamber wall.

At the air–fuel equivalence ratio of 1.7, a clearly more pronounced blue component for the combustion of natural gas in the early stages of combustion compared to the mixture with 10%v hydrogen is visible. Due to the lower combustion temperatures in areas of leaner λ, a lower temperature-dependent background radiation, as well as a lower production of C_2^*, is to be expected. Nevertheless, the flame with a higher hydrogen content and thus a higher combustion temperature already shows first reddish (MFB5) and then first yellow (MFB10) areas. Further, these are due to the stronger black-body radiation of burning carbon at higher combustion temperatures at MFB50. During the burnout phase and the end of combustion (MFB95), shifted portions of the flame can also be seen in the direction of the combustion chamber wall as well as in the center, colored in the red spectral range, which could be attributed to the formation of thermally excited H_2O^*.

A comparison of the two λ shows a clearly higher blue portion of the color for higher oxygen content, at least for the early phases of the combustion caused by the CH^* that is well visible because of the lower superimposed background radiation and a slower combustion velocity. At the end of combustion and during the burnout phase, the images with a leaner air–fuel equivalence ratio show a slightly more pronounced shift into the reddish range. This is also resulting from weaker background radiation and lower temperatures during the burnout resulting from an overall lower combustion temperature.

For the conventional spark plug test series (cf. Figure 15), an almost similar behavior can be observed. For low air–fuel equivalence ratios, blue parts in the flame front at the early stage of combustion hint at CH^* formation. At an air–fuel equivalence ratio of 1.7, the images show a slight blue part at the edges of the flame at CoC, which is propagating toward the combustion chamber wall. These are visible as the combustion temperature is lower compared to the experiments using the unscavenged pre-chamber spark plug and, therefore, is less concealed by background radiation. Further, the slower combustion for high air–fuel ratios and the conventional spark plug results in a delay in the radical formation. The higher intensities displayed for the natural gas compared to the 10HCH4 combustion at an air–fuel equivalence ratio of 1.5 arise from the cyclic variations.

Comparing the images of the unscavenged pre-chamber spark plug and the conventional spark plug in Figures 14 and 15, a different flame propagation is visible. Especially in the early stage of the combustion, the areas ignited by the torch flames are visible in Figure 14, whereas Figure 15 shows a more compact area of the flame for the conventional-spark-plug-ignited combustion.

4.4. Evaluation of Torch Rays

For the unscavenged pre-chamber spark plug, a closer look at the early stages of the combustion shows the formation of torch flames originating from the unscavenged pre-chamber spark plug combining to create a continuous flame front (cf. Figure 16). Due to the position of the fisheye optical system, not all of the unscavenged pre-chamber spark plug's torch flames are visible in the recordings, as the rest is covered by the cap of the ignition system itself. Figure 16 shows the recorded image series for the 10HCH4 fuel at CoC 8 °CA aFTDC with an air–fuel equivalence ratio of 1.7. The images depicted are mean-value images over the 50 recorded cycles. The image recognition results of the detection algorithm used to extract the four visible torch flames out of a total of seven are included in Figure 16. The torch flames all have a bluish color indicating a quite high concentration of CH^* responsible for the flame's blue color that is overlayed with yellow and orange, hinting at carbon-based radiation as the °CA advances. Figure 17 shows the arrangement of the torch flames. The algorithm for extracting the torch flame contour stops when a continuous bright flame front forms. Since not all torch flames can be detected

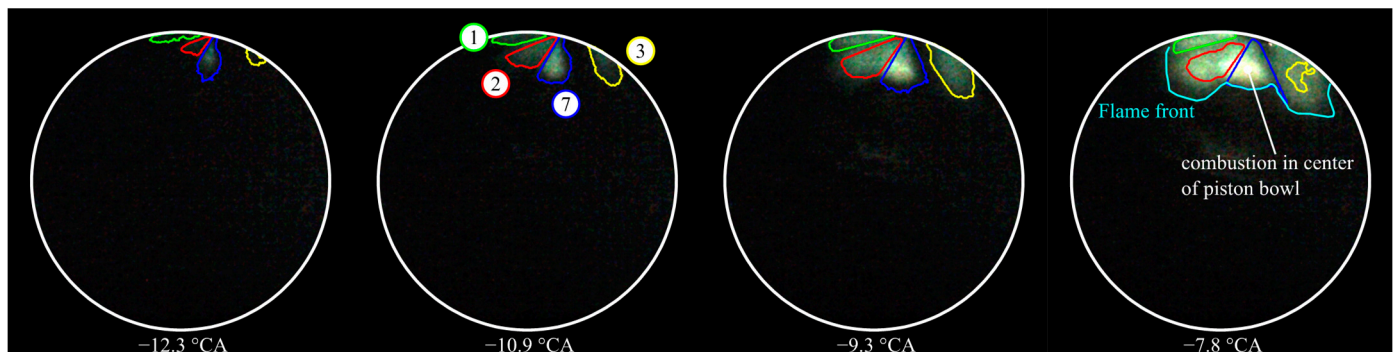equally well, the following evaluation concentrates on the one pointing downward with the number 7.

Figure 16. Image series of torch ray of 10HCH₄ at CoC = 8 °CA AFTDC and λ = 1.7 (numbers indicate torch ray).

It has the shortest distance to the piston bowl and even extends as far as the bowl itself, as will be shown in Figures 18 and 19. Figure 17 shows the detailed proceeding for the reprojection post-processing, which is similar to the one presented in [35]. The reprojection plane used for the post-processing is perpendicular to the connection vector of the orthogonal projection points of the camera and ignition system origins to the horizontal base plane. After the virtual reprojection, the length of the torch flame L can be derived from the post-processed images. This is undertaken for both fuels of NG and 10HCH₄ at the CoC of 8 °CA aFTDC and air–fuel equivalence ratios of 1.5, 1.6 and 1.7. Figures 18 and 19 summarize the results. Both figures show the mean value images of the 50 recorded cycles and are dewarped and individually scaled regarding their intensities for better visibility. Each figure contains the derived torch flame length, L, estimated as the max distance of the torch flames flame front to the engine's flame deck (cf. Figure 18). Further, three different points on the piston bowl's omega shape are overlayed to verify the length of L in accordance with the piston position over the engine rotation (s1–s3 cf. Figure 18).
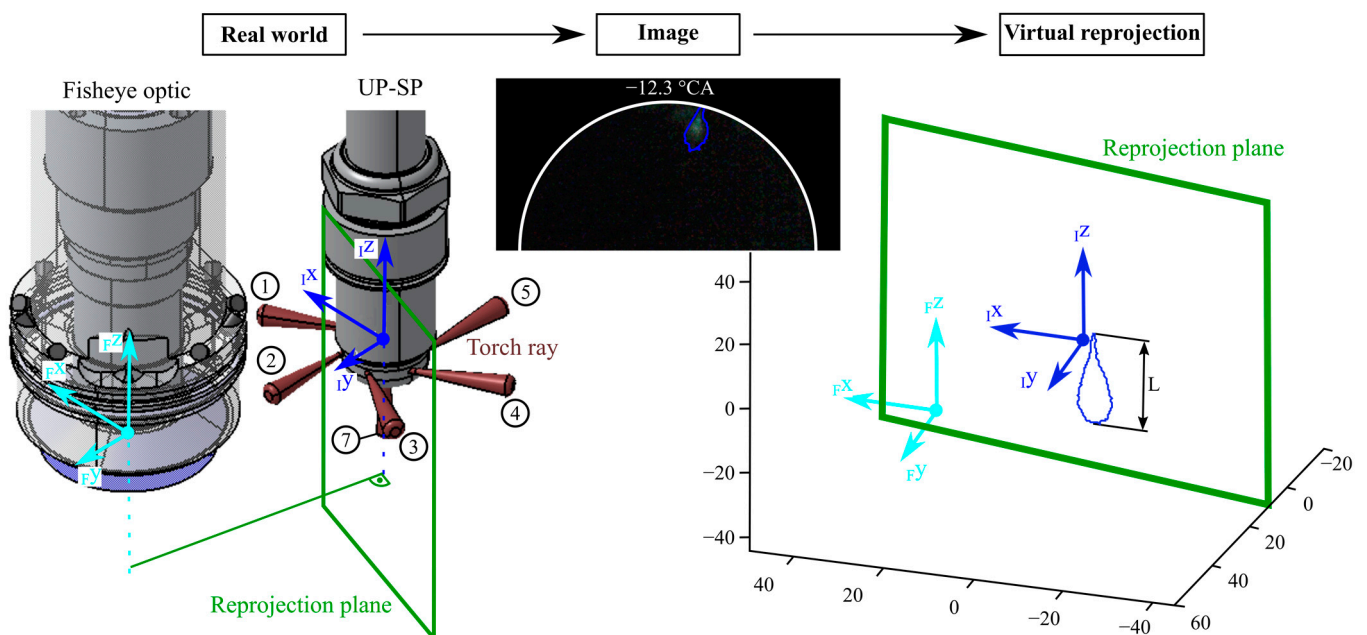

Figure 17. Proceeding of virtual reprojection to derive the torch ray length L using the visible natural chemiluminescence (numbers indicate the different torch rays).

Comparing the derived length of L with these distances, it becomes evident that the detected torch flame is being redirected within the piston bowl. The tip of the torch flame touches the highest point of the piston at s1 even before the images are captured, as the derived length is always larger than s1. Due to the omega-shaped piston bowl and the squish flow, the flame is redirected towards the lowest point of the piston shape marked as s3. This can be recorded as the used measurement technique is an integral line of sight method, which captures all the intensity along a line of sight. Especially for the highest air–fuel equivalence ratio resulting in the slowest combustion, the development of the torch flame and the interaction of flame number 7 with the piston bowl can be seen for both fuels. The tip of flame 7 is growing stronger perpendicularly to the flame axis and shows a higher intensity as here, a larger volume already ignites and contributes to the captured intensity. The first part of flame torch 7, at about one-third from its origin, is very narrow and compact, hinting at a high flame velocity and momentum at the exit of the unscavenged pre-chamber. The other three visible torch flames are difficult to distinguish from the background noise. During combustion, the horizontally aligned torch flames progress along the jet axis, but mainly perpendicular to it, so that the combustion chamber formed by the cylinder head and piston bowl is covered increasingly by the flames. This can be explained, among others, by the swirl and squish flow of the engine as well as by the mounting position of the unscavenged pre-chamber spark plug. The mounting position prevents the horizontally aligned torch flames from propagating too deep into the combustion chamber in the direction of the torch flame axis as their paths intersect partially with the engine's valves. For lower air–fuel equivalence ratios, the combustion progress is so fast that only a few pictures can be captured. Here, the torch rays also develop more quickly and show bright combustion that is already turning yellow, implying a later stage of combustion and C_2^*-based chemiluminescence with a higher intensity. The MFB5 is identified to occur after the flame torches form a continuous flame front and at crank angles later than the depicted 7 °CA bFTDC. The detected length, L, of torch flame 7 is of a quite similar length for both fuels, as the torch flame reaches the piston bowl and is thus limited to the maximum possible length s3 within the algorithm's reprojection accuracy (cf. Section 4.1). The mean images of the torch flame of both fuels also show quite similar intensities and very similar colors. This may be due to the comparable low admixture of hydrogen with only 10%v. As also observed in [43], the 10%v admixture shows a modest increase in the laminar burning velocity.
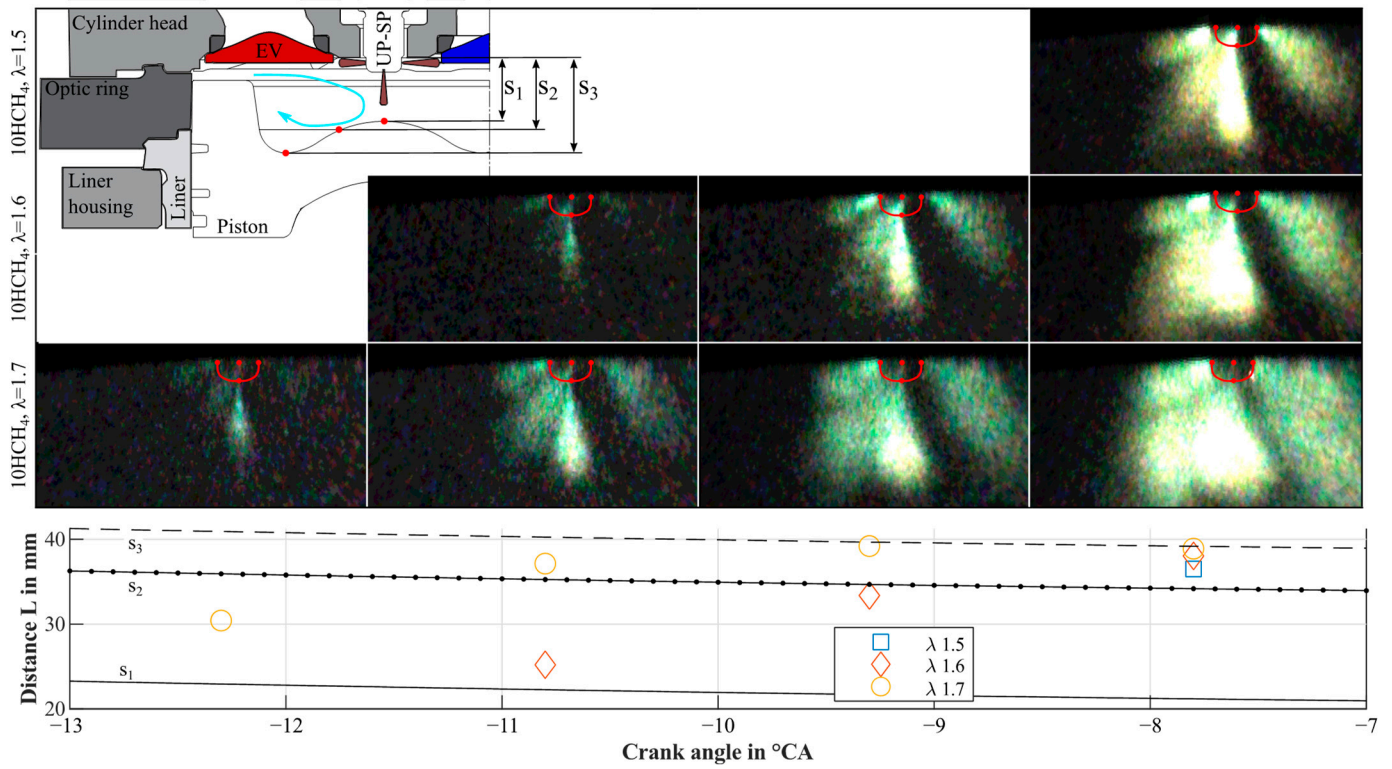
Figure 18. Torch ray images for 10HCH$_4$ at CoC = 8 °CA AFTDC and λ = 1.5, 1.6, 1.7. Distances s measured from the flame deck to the piston bowl.

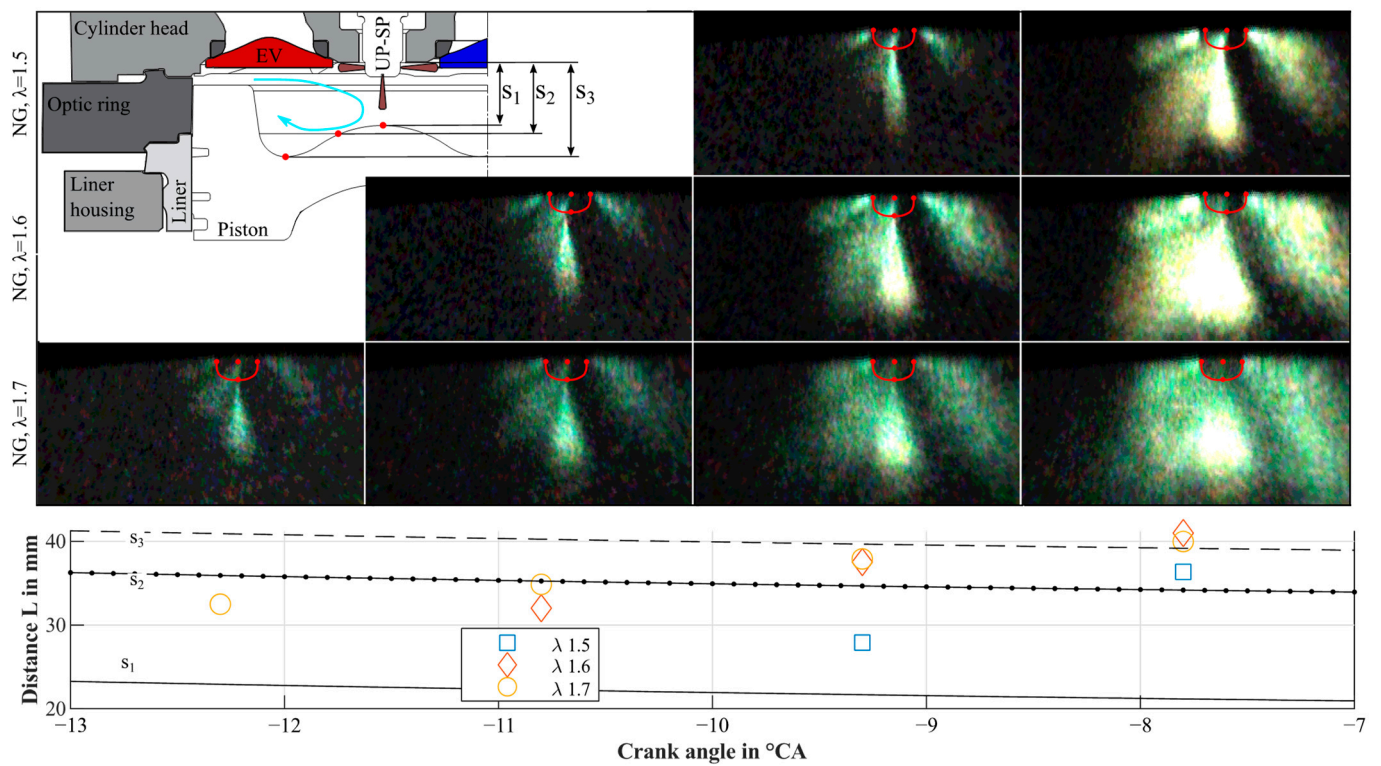**Figure 19.** Torch ray images for NG at CoC = 8 °CA AFTDC and λ=1.5, 1.6, 1.7. Distances s measured from the flame deck to the piston bowl.

5. Summary and Discussion

5.1. Thermodynamic Results

The thermodynamic results all show plausible and explainable behavior that is also comparable to the combustion within an all-metal engine, as shown in [33]. This means that the setup is capable of a sufficient fired run time to stabilize the combustion and record the measurement data. The skipped fire operation mode even benefits from the admixture of hydrogen by a faster heat up of the combustion chamber and a faster stabilization but it also increases the thermal load onto the optical components. The herein investigated two different volume percentages of hydrogen cause no abnormal combustion and are, therefore, suitable for the engine by solely adapting the spark timing.

The results of the test series show that even with a small amount of hydrogen admixture, the combustion process gains higher efficiency and combustion stability because of the enhanced lean running limit. This is especially true for the setup with a conventional spark plug but is also beneficial for the unscavenged pre-chamber spark plug. Here, the combination with the admixture of hydrogen enhances the lean running limit further as the ignition and combustion benefit from the higher laminar burning velocity of the hydrogen. With the elongation of the lean running limit, a NOx equivalent running strategy seems possible (cf. [7]) despite the higher combustion temperatures arising from the admixture of hydrogen that increase the NOx concentration.

5.2. Optical Results

The imaging was conducted using a fisheye optical system that was mounted in the cylinder head. Due to the integration of the optic into the engine using a non-central mount a large part of the extensive field of view is not usable. Regarding optical quality, the optic is capable of images with a resolution of 1.5 °CA, resulting in 330 μs gate time. With this setting, a sufficient intensity and usable field of view are possible to even capture the early stage of the combustion, especially for the unscavenged pre-chamber spark plug.

Compared to the spectrometer investigations of premixed methane and blended methane/hydrogen combustion in a continuous burner presented in [26,44], the admixture of 10%$_v$ hydrogen has no significant influence on the combustion spectra intensities. Therefore, the assumption of a similar spectrum of the methane and fuel blend combustion seems feasible. Further, [45] show the influence of the air–fuel equivalence ratio and the admixture of hydrogen on the flame emission. With high air–fuel equivalence ratios for natural gas flames, the intensity of the CH* (@431 nm) decreases, whereas the emission of the C$_2$* (@516 nm) radical vanishes, which is also responsible for the yellow part of the flame. The recorded natural chemiluminescence intensities seem, therefore, mainly dominated by the air–fuel equivalence ratio (cf. traces in Section 4.2 and combustion images in Section 4.3). This results in strong intensities from background radiation at low air–fuel equivalence ratios and overlays the much weaker intensities of the intermediate species, e.g., CH*, which is formed mostly in the reactive flame front. Further, the higher burning velocity supports a faster conversion of the fuel and thus offers less time for the intermediate radical's radiation.

The presented intensities traces (cf. Section 4.2) of the natural flame chemiluminescence show a clear difference between the unscavenged pre-chamber spark plug and the conventional spark plug and some slight changes between the NG and the highest tested amount of hydrogen admixture of 10%$_v$. A higher intensity of the natural flame chemiluminescence for hydrogen admixtures hints at combustion with higher temperatures and, thus, assuming the same energy content for all tests, proves the combustion to be more efficient. Further, a faster increase in the intensity traces leads to a faster combustion, resulting in a faster heat release.

The Interpretation of the flame color uses dewarped images and supports the temperature, respectively, air–fuel equivalence ratio dominated intensities, as well as the findings from [26,44,45]. With colder combustion temperatures at high air–fuel equivalence

ratios and a slower combustion, a more blue part of the flame is visible and less overlayed by background radiation as well as the more intense C_2* radical vanishes at high air–fuel equivalence ratios (cf. [45]).

For the investigation of the torch flame, dewarped mean value images and the presented reprojection algorithm are used.

The virtual reprojection method is used to have a first look at the torch flame development using mean value images of the early stage of the combustion with the unscavenged pre-chamber spark plug. The used virtual reprojection underlies simplifications assumption and inaccuracies such as:

-   The contour extraction uses predefined sectors for each torch flame and a global threshold in each sector for image binarization. The threshold is optimized to reduce the standard deviation of the extracted contour over the different thresholds.
-   The reprojection is dependent on the accuracy of the optic's calibration.
-   Due to the used integral line of sight method used here, intersecting or overlayed intensities lie in the same line of sight and cannot be distinguished. This deteriorates the accuracy of the torch flame recognition and thus decreases the quality of the virtual reprojection compared to laser-based investigations using specific and determined sheets for observation.
-   As the engine uses a swirl in the charge air movement and the torch flame number seven is aligned with the cylinder bore axis, the influence arising from the swirl onto the torch flame is almost negligible.
-   As natural chemiluminescence images are used, it is not possible to distinguish between the combustion radicals.
-   The usable signal noise ratio is low for the detection of the torch flame.

Nevertheless, the virtual reprojection is a simple method to have the first easy-to-use comparison of the carried out natural chemiluminescence measurements to characterize the observed combustion. Further, the method can be used in case of a comparison with CFD results by deriving the same views with the same herein-used projection method.

Korb [46] presents different ignition regimes of a scavenged pre-chamber for different holes of the pre-chamber as well as different cycles. Xu [47] presents time-resolved optical investigations of the natural OH* radical chemiluminescence in an RCEM for an unscavenged pre-chamber spark plug igniting natural gas. Due to a missing lift-off length of the observed ignition, the combustion is flame based. The RCEM used in these experiments shows interference of the torch flame oriented parallel to the cylinder axis with thy piston.

The presented investigation uses mean value images to derive the torch flame contour. The mean value reduces the effect of the occurring cyclic variation and supports the derivation of a more reliable contour as background noise becomes less effective.

Nevertheless, even with the mean value of all recorded images in one cycle, there seems to be no lift-off length between the cap of the unscavenged pre-chamber spark plug and the torch flame, especially for the torch flame 7. With this, the assumption of a predominant flame-based ignition, combustion seems more comprising.

The evaluation of torch flame 7's length shows the interaction with the piston bowl and the in-cylinder flow with an increased reactivity at the tip. The interaction seems similar for both investigated fuels under the reprojection accuracy. The remaining visible torch rays show a predominantly evaluation perpendicular to the flame axis, which ignites the combustion chamber. This seems to be due to the in-cylinder flow and the mounting position.

For the low air–fuel ratio of only two, one image could be captured where a torch flame is visible. This is due to the good ignition and flame propagation conditions in the combustion chamber of the selected experimental point. A higher capture rate seems to be necessary to record the complete development of the torch flame, especially at low air-to-fuel ratios. Both investigated fuels show a similar behavior in the development of the

torch flames when comparing intensities and color. This is due to the decreased deviation of both fuel properties, as also stated in [40].

6. Conclusions and Outlook

The paper presents in detail:

- The thermodynamic comparison of the combustion of NG, 5HCH$_4$ and 10HCH$_4$ in two test series using an unscavenged pre-chamber spark plug and a conventional spark plug under CoC and air–fuel equivalence ratio variations.
- The optical comparison of the natural chemiluminescence intensity of the combustion of NG, 5HCH$_4$ and 10HCH$_4$ using an unscavenged pre-chamber spark plug and a conventional spark plug under a CoC and air–fuel equivalence ratio variation.
- The interpretation of the flame color for NG and 10HCH$_4$ at two stages of air–fuel equivalence ratio at CoC of 8 °CA aFTDC for both ignition systems.
- A discussion of the visible natural chemiluminescence of the torch flame from images that are post-processed by a virtual reprojection method.

The following conclusions could be derived from the results:

- Hydrogen admixture leads to faster combustion for the unscavenged pre-chamber spark plug compared to pure NG investigations and the tests of the conventional spark plug.
- For a CoC of under 15 °CA aFTDC, the burning duration decreases for both ignition systems and fuels.
- The unscavenged pre-chamber spark plug offers less ignition delay compared to the conventional spark plug. Using the unscavenged pre-chamber spark plugs, the influence of the here-used amount of hydrogen admixture is almost negligible.
- The admixture of hydrogen improves combustion stability. This holds true, especially for the conventional spark plug but has only a minor effect for the unscavenged pre-chamber spark plug.
- The indicated mean efficiency increases with increasing amounts of hydrogen and reaches its maximum for the herein investigated unscavenged pre-chamber spark plug and maximum admixture of hydrogen.
- The apparent heat release rates of both hydrogen admixture levels are of similar quality for each ignition system. In detail, the conventional spark plug shows a slower and less intense heat release compared with the unscavenged pre-chamber spark plug.
- The beneficial effect of the hydrogen admixture becomes especially visible for higher air–fuel equivalence ratios.
- The intensity of the natural chemiluminescence increases mainly in proportion to the air–fuel equivalence ratio and the resulting burn velocity and is at its maximum for low air–fuel equivalence ratios and 10HCH$_4$ for the tests with the unscavenged pre-chamber spark plug.
- After the thermodynamic end of combustion at MFB95, a remarkable intensity of the natural chemiluminescence remains. The intensity also follows the combustion temperature and can be a hint for thermal excited water.
- The flame coloring at characteristic operation points during combustion (MFB 5, 10, 50, 95) develops proportionally to the intensity trace of the natural chemiluminescence and, thus, also the air–fuel equivalence ratio.
- For lower combustion temperatures at high air–fuel ratios, a higher content of blue is visible in the flame leading to the assumption of a higher emergence of CH* and less overlayed broadband luminosity as well as less C$_2$* radiation which vanishes for high air–fuel ratios. Further, a slow burn velocity supports the visibility of the CH* emissions.
- High combustion temperatures at low air–fuel ratios result in an intense yellow flame that originates from broadband emissions and those of the C$_2$* radicals. Due to the

low content of the hydrogen admixture at low air–fuel ratios, enough carbon seems available to advance their local formation.

- The end of the combustion shows a more reddish flame concentrated in the center of the combustion chamber, hinting at thermally excited H_2O.

The early stage of combustion using the unscavenged pre-chamber spark plug shows no obvious differences between both fuels concerning the color of the flame and the intensity. Only the influence of the air–fuel equivalence ratio is obvious, resulting in faster combustion with a more yellow flame under fuel-rich conditions.

The correlation of the optical results with the thermodynamic ones shows a reasonable behavior of the combustion. It also proves the feasibility and comparability of the developed alternative fully optically accessible engine and emphasizes the potential of further enhancement to gain more quantitative measurements, e.g., with a similar approach as presented in [23]. Further, the development of a UV-transmission fisheye endoscopic system would support laser-based measurement techniques as well as the observation of the flame's natural OH-chemiluminescence. With such an optic, the testing and development of large-bore engines that can run on pure hydrogen and not only admixtures are possible. It allows the complete decarbonization of combustion engines and thus realizes the usage of a purely sustainable energy supply. Nevertheless, the presented investigations for the admixture of 10%v to methane shows already several advantages, even for the unscavenged pre-chamber spark plug. With this, a content of 10%v hydrogen in the natural gas grid seems already feasible from the point of view of stationary energy generation using combined heat and energy plant units, which can be the first step towards sustainable energy generation. Further investigations on the infrastructure of the gas grid are necessary to avoid risks for other consumers than combustion engines connected to the natural gas grid.

Nomenclature

aFTDC	After firing top dead center	FTDC	Firing top dead center
aTDC	After top dead center	ICE	Internal combustion engine
bFTDC	Before firing top dead center	IMEP	Indicated mean effective pressure
bTDC	Before top dead center	MFB	Mass fraction burned
CA	Crank angle	NG	Natural gas
CoC	Center of combustion as 50% burnt mass fraction		
CoI	Center of intensities	ROI	Region of interest
COV	Coefficient of variance	SP	Spark plug
DF	Dual fuel	UP-SP	Unscavenged pre-chamber spark plug
EOC	End of combustion	THC	Total hydrocarbon
FOV	Field of view	λ	Air–fuel equivalence ratio
		%v	Volume percentage

References

1. Reitz, R.D.; Ogawa, H.; Payri, R.; Fansler, T.; Kokjohn, S.; Moriyoshi, Y.; Agarwal, A.; Arcoumanis, D.; Assanis, D.; Bae, C.; et al. IJER editorial: The future of the internal combustion engine. *Int. J. Engine Res.* **2020**, *21*, 3–10. https://doi.org/10.1177/1468087419877990.
2. Pöllmann, S.; Härtl, M.; Wachtmeister, G. *Injection Process of the Synthetic Fuel Oxymethylene Ether: Optical Analysis in a Heavy-Duty Engine*; SAE Technical Paper Series; SAE: Warrendale, PA, USA, 2020. https://doi.org/10.4271/2020-01-2144.
3. Held, M.; Tönges, Y.; Pélerin, D.; Härtl, M.; Wachtmeister, G.; Burger, J. On the energetic efficiency of producing polyoxymethylene dimethyl ethers from CO_2 using electrical energy. *Energy Environ. Sci.* **2019**, *12*, 1019–1034. https://doi.org/10.1039/c8ee02849d.
4. Pélerin, D.; Gaukel, K.; Härtl, M.; Jacob, E.; Wachtmeister, G. Potentials to simplify the engine system using the alternative diesel fuels oxymethylene ether OME1 and OME3−6 on a heavy-duty engine. *Fuel* **2020**, *259*, 116231. https://doi.org/10.1016/j.fuel.2019.116231.
5. Gelner, A.D.; Höß; R; Zepf, A.; Härtl, M.; Wachtmeister, G. *Engine Operation Strategies for the Alternative Diesel Fuel Oxymethylene Ether (OME): Evaluation Based on Injection Rate Analyzer and 0D-/1D-Simulation*; SAE Technical Paper Series; SAE: Warrendale, PA, USA, 2021. https://doi.org/10.4271/2021-01-1190.
6. Onorati, A.; Payri, R.; Vaglieco, B.; Agarwal, A.; Bae, C.; Bruneaux, G.; Canakci, M.; Gavaises, M.; Günthner, M.; Hasse, C.; et al. The role of hydrogen for future internal combustion engines. *Int. J. Engine Res.* **2022**, *23*, 529–540. https://doi.org/10.1177/14680874221081947.
7. Karmann, S.; Eicheldinger, S.; Prager, M.; Wachtmeister, G. Optical and thermodynamic investigations of a methane and hydrogen blend fueled large bore engine. *Int. J. Engine Res.* **2022**, *23*, 846–864. https://doi.org/10.1177/14680874211066735.
8. Karmann, S.B.; Prager, M.; Wachtmeister, G. Conceptual Investigations on Full Optical Accessibility to Large-Bore Medium-Speed Engines. *SAE Int. J. Engines* **2019**, *12*, 291–308. https://doi.org/10.4271/03-12-03-0020.
9. Karmann, S.B.; Kunkel, C.; Wachtmeister, G. A New Optical Access for Medium Speed Large Bore Marine Engines under Full-Load Operating Conditions. *SAE Int. J. Engines* **2021**, *14*, 867–883. https://doi.org/10.4271/03-14-06-0052.
10. Karmann, S.B.; Röhrle, H.; Klier, B.; Prager, M.; Wachtmeister, G. Design of an Endoscopic Fully Optically Accessible High-Speed Large-Bore Engine. *SAE Int. J. Engines* **2022**, *15*, 117193. https://doi.org/10.4271/03-15-06-0042.
11. Mehra, R.K.; Duan, H.; Juknelevičius, R.; Ma, F.; Li, J. Progress in hydrogen enriched compressed natural gas (HCNG) internal combustion engines—A comprehensive review. *Renew. Sustain. Energy Rev.* **2017**, *80*, 1458–1498. https://doi.org/10.1016/j.rser.2017.05.061.
12. White, C.; Steeper, R.; Lutz, A. The hydrogen-fueled internal combustion engine: A technical review. *Int. J. Hydrogen Energy* **2006**, *31*, 1292–1305. https://doi.org/10.1016/j.ijhydene.2005.12.001.
13. Sahoo, B.; Sahoo, N.; Saha, U. Effect of engine parameters and type of gaseous fuel on the performance of dual-fuel gas diesel engines—A critical review. *Renew. Sustain. Energy Rev.* **2009**, *13*, 1151–1184. https://doi.org/10.1016/j.rser.2008.08.003.
14. Wahl, J.; Kallo, J. Quantitative valuation of hydrogen blending in European gas grids and its impact on the combustion process of large-bore gas engines. *Int. J. Hydrogen Energy* **2020**, *45*, 32534–32546. https://doi.org/10.1016/j.ijhydene.2020.08.184.
15. Zhen, X.; Li, X.; Wang, Y.; Liu, D.; Tian, Z. Comparative study on combustion and emission characteristics of methanol/hydrogen, ethanol/hydrogen and methane/hydrogen blends in high compression ratio SI engine. *Fuel* **2020**, *267*, 117193. https://doi.org/10.1016/j.fuel.2020.117193.
16. Verhelst, S.; Wallner, T. Hydrogen-fueled internal combustion engines. *Prog. Energy Combust. Sci.* **2009**, *35*, 490–527. https://doi.org/10.1016/j.pecs.2009.08.001.
17. Di Sarli, V.; Di Benedetto, A. Laminar burning velocity of hydrogen–methane/air premixed flames. *Int. J. Hydrogen Energy* **2007**, *32*, 637–646. https://doi.org/10.1016/j.ijhydene.2006.05.016.
18. Stocker, R. Bestimmung Verbrennungsrelevanter Größen in Flammen mit Laseroptischen Verfahren. Ph.D. Thesis, Fakultät für Maschinenwesen, Technische Universität München, München, Germany, 2004.
19. Gaydon, A. *The Spectroscopy of Flames*; Springer: Dordrecht, The Netherlands, 1974. Available online: https://ebookcentral.proquest.com/lib/kxp/detail.action?docID=6560931 (accessed on 28 December 2022).
20. Oh, S.; Park, Y.; Seon, G.; Hwang, W.; Do, H. Impacts of N_2 and CO_2 diluent gas composition on flame emission spectroscopy for fuel concentration measurements in flames. *Int. J. Heat Mass Transf.* **2020**, *149*, 119174. https://doi.org/10.1016/j.ijheatmasstransfer.2019.119174.
21. Brockhinke, A.; Krüger, J.; Heusing, M.; Letzgus, M. Measurement and simulation of rotationally-resolved chemiluminescence spectra in flames. *Appl. Phys. B Laser Opt.* **2012**, *107*, 539–549. https://doi.org/10.1007/s00340-012-5001-1.
22. Karmann, S.; Mühlthaler, M.; Prager, M.; Wachtmeister, G.; Unfug, F. *A Method for Measuring in-Cylinder λ-Distribution in Medium-Speed DF Engines*; Lehrstuhl für Verbrennungskraftmaschinen: Munich, Germany, 2016. Available online: http://www.hercules-2.com/sites/default/files/pub/D2.1_634135_A%20method%20for%20measuring%20in-cylinder%20--distribution%20in%20medium-speed%20DF%20engines.pdf (accessed on 31 January 2017).
23. Sun, Z.; Ma, Z.; Li, X.; Xu, M. Flame Emission Characteristics in a Direct Injection Spark Ignition Optical Engine Using Image Processing Based Diagnostics. In Proceedings of the ASME Internal Combustion Engine Fall Technical Conference—2018: Presented at ASME 2018 Internal Combustion Engine Fall Technical Conference, San Diego, CA, USA, 4–7 November 2018.
24. Warnatz, J.; Maas, U.; Dibble, R.W. *Verbrennung: Physikalisch-Chemische Grundlagen, Modellierung und Simulation, Experimente, Schadstoffentstehung*, 3rd ed.; Springer: Berlin/Heidelberg, Germany, 2001.

25. Catapano, F.; Di Iorio, S.; Sementa, P.; Vaglieco, B.M. Characterization of CH_4 and CH_4/H_2 Mixtures Combustion in a Small Displacement Optical Engine. *SAE Int. J. Fuels Lubr.* **2013**, *6*, 24–33. https://doi.org/10.4271/2013-01-0852.

26. García-Armingol, T.; Ballester, J. Flame chemiluminescence in premixed combustion of hydrogen-enriched fuels. *Int. J. Hydrogen Energy* **2014**, *39*, 11299–11307. https://doi.org/10.1016/j.ijhydene.2014.05.109.

27. Oh, J.; Noh, D.; Ko, C. The effect of hydrogen addition on the flame behavior of a non-premixed oxy-methane jet in a lab-scale furnace. *Energy* **2013**, *62*, 362–369. https://doi.org/10.1016/j.energy.2013.09.049.

28. Di Iorio, S.; Sementa, P.; Vaglieco, B.M. Experimental investigation on the combustion process in a spark ignition optically accessible engine fueled with methane/hydrogen blends. *Int. J. Hydrogen Energy* **2014**, *39*, 9809–9823. https://doi.org/10.1016/j.ijhydene.2014.04.065.

29. Di Iorio, S.; Sementa, P.; Vaglieco, B.M. Optical diagnostics for the analysis of hydrogen–methane blend combustion in internal combustion engines. In *Woodhead Publishing Series in Energy, Number 85, Hydrogen Energy Conversion*; Barbir, F., Basile, A., Veziroğlu, T.N., Eds.; Elsevier/WP Woodhead Publishing: Amsterdam, The Netherlands; Boston, MA, USA; Cambridge, UK, 2016; pp. 233–261.

30. Bowditch, F.W. *A New Tool for Combustion Research a Quartz Piston Engine*; SAE Technical Paper; SAE: Warrendale, PA, USA, 1961. https://doi.org/10.4271/610002.

31. Eicheldinger, S.; Karmann, S.; Prager, M.; Wachtmeister, G. Optical screening investigations of backfire in a large bore medium speed hydrogen engine. *Int. J. Engine Res.* **2021**, *23*, 893–906. https://doi.org/10.1177/14680874211053171.

32. Weber, S.; Stegmann, R.; Prager, M.; Wachtmeister, G. The Effect of Inlet Valve Timing and Engine Speed on Dual Fuel NG-Diesel Combustion in a Large Bore Engine. *SAE Int. J. Engines* **2018**, *11*, 229–246. https://doi.org/10.4271/03-11-02-0015.

33. Karmann, S.; Eicheldinger, S.; Prager, M.; Jaensch, M.; Wachtmeister, G. Experimental comparison between an optical and an all-metal large bore engine. *Int. J. Engine Res.* **2022**. https://doi.org/10.1177/14680874221082794.

34. Chen, L.; Wei, H.; Zhang, R.; Pan, J.; Zhou, L.; Feng, D. Effects of spark plug type and ignition energy on combustion performance in an optical SI engine fueled with methane. *Appl. Therm. Eng.* **2019**, *148*, 188–195. https://doi.org/10.1016/j.applthermaleng.2018.11.052.

35. Karmann, S.B.; Weber, S.; Stürzl, W.; Prager, M.; Jaensch, M.; Wachtmeister, G. Development of an Optical Investigation Method for Diesel and Oxymethylene Ether Spray in a Large-Bore Dual-Fuel Engine Using a Fisheye Optical System. *SAE Int. J. Engines* **2023**, *16*. https://doi.org/10.4271/03-16-05-0036.

36. Dong, C.; Zhou, Q.; Zhang, X.; Zhao, Q.; Xu, T.; Hui, S. Experimental study on the laminar flame speed of hydrogen/natural gas/air mixtures. *Front. Chem. Eng. China* **2010**, *4*, 417–422. https://doi.org/10.1007/s11705-010-0515-8.

37. Röthlisberger, R. An Experimental Investigation of a Lean Burn Natural Gas Prechamber Spark Ignition Engine for Cogeneration. 2005. Available online: https://doi.org/10.5075/epfl-thesis-2346 (accessed on 27 December 2022).

38. Park, C.; Kim, C.; Choi, Y.; Won, S.; Moriyoshi, Y. The influences of hydrogen on the performance and emission characteristics of a heavy duty natural gas engine. *Int. J. Hydrogen Energy* **2011**, *36*, 3739–3745. https://doi.org/10.1016/j.ijhydene.2010.12.021.

39. Kannala, J.; Heikkilä; J; Brandt, S.S. Geometric Camera Calibration. *Wiley Encycl. Comput. Sci. Eng.* 2008, 13, 1–12.

40. Strobl, K.H.; Sepp, W.; Fuchs, S.; Paredes, C.; Smisek, M.; Arbter, K. DLR CalDe and DLR CalLab. Oberpfaffenhofen, Germany. Available online: http://www.robotic.dlr.de/callab/ (accessed on 27 December 2022).

41. Greis, E.A. Laseroptische Untersuchungen des Verbrennungsprozesses in Einem PKW-Dieselmotor. Ph.D. Thesis, Fakultät für Maschinenwesen, Rheinisch-Westfälische Technische Hochschule, Aachen, Germany, 2007.

42. Geßenhardt, C. Endoskopische Bestimmung des Temperaturfeldes im Brennraum von Ottomotoren mittels laserinduzierter Fluoreszenz. Ph.D. Dissertation, Universität Duisburg-Essen, Fakultät für Ingenieurweissenschaften, Abteilung Maschinenbau, Duisburg, Germany, 2013.

43. Nilsson, E.J.; van Sprang, A.; Larfeldt, J.; Konnov, A.A. The comparative and combined effects of hydrogen addition on the laminar burning velocities of methane and its blends with ethane and propane. *Fuel* **2017**, *189*, 369–376. https://doi.org/10.1016/j.fuel.2016.10.103.

44. García-Armingol, T.; Ballester, J. Influence of fuel composition on chemiluminescence emission in premixed flames of $CH4/CO2/H2/CO$ blends. *Int. J. Hydrogen Energy* **2014**, *39*, 20255–20265. https://doi.org/10.1016/j.ijhydene.2014.10.039.

45. Ballester, J.; Hernández, R.; Sanz, A.; Smolarz, A.; Barroso, J.; Pina, A. Chemiluminescence monitoring in premixed flames of natural gas and its blends with hydrogen. *Proc. Combust. Inst.* **2009**, *32*, 2983–2991. https://doi.org/10.1016/j.proci.2008.07.029.

46. Korb, B. Beitrag zur Charakterisierung des Homogenen Magerbrennverfahrens bei Großgasmotoren mittels Experimenteller Methoden im Hinblick auf Verbrennung, Wirkungsgrad und Emissionen. Ph.D. Thesis, TUM School of Engineering and Design, Technische Universität München, München, Germany, 2021.

47. Xu, G.; Kotzagianni, M.; Kyrtatos, P.; Wright, Y.M.; Boulouchos, K. Experimental and numerical investigations of the unscavenged prechamber combustion in a rapid compression and expansion machine under engine-like conditions. *Combust. Flame* **2019**, *204*, 68–84. https://doi.org/10.1016/j.combustflame.2019.01.025.